ANNUAL REPORT
of
THE INSTITUTE OF PHYSICS
ACADEMIA SINICA

VOLUME 13 DECEMBER 1983

THE INSTITUTE OF PHYSICS, ACADEMIA SINICA
TAIPEI, TAIWAN, REPUBLIC OF CHINA

中央研究院物理研究所集刊

發 行 人 (Publisher)
林 爾 康 (E. K. Lin)

執行編輯 (Executive Editor)
胡 進 錕 (C.-K. Hu)

The Annual Report is published annually by the Institute of Physics, Academia Sinica, Taipei, Taiwan 115, Republic of china.

中央研究院物理研究所集刊

第十三卷

中央研究院物理研究所印行

CONTENTS 目 錄

ARTICLES

FLUID MECHANICS AND ATMOSPHERIC PHYSICS

ABSTRACT

THEORETICAL PHYSICS

NUCLEAR PHYSICS

SOLID STATE PHYSICS AND BIOPHYSICS

FLUID MECHANICS AND ATMOSPHERIC PHYSICS

ERRATA

Ta-You Wu: A NOTE ON EINSTEIN'S RELATION OF TRANSITION PROBABILITIES

On page 1, "." should be put after Equations (1) and (5); "," should be put after line 9, and Equations (3) and (4).

On page 2, "," should be put after Equation (8); "N'_m" of Equation (9) should be replaced by "N_m".

A NOTE ON EINSTEIN'S RELATION OF TRANSITION PROBABILITIES

Ta-You Wu

Academia Sinica, Taipei

In Einstein's theory of Planck's formula (1917), the basic relation is

$$N_n B^m_{\uparrow n} \phi_\nu = N_m B^m_{\downarrow n} \phi_\nu + N_m A^m_{\downarrow n} \tag{1}$$

On using the Boltzmann theorem

$$N_m = N_n e^{-\beta(E_m - E_n)} \tag{2}$$

and the condition that

$$\lim_{\beta h \nu \to 0} \phi_\nu = \frac{8\pi\nu^2}{c^3} kT$$

one arrives at

$$B^m_{\uparrow n} = B^m_{\downarrow n} \tag{3}$$

$$A^m_{\downarrow n} = \frac{8\pi h\nu^3}{c^3} B^m_{\downarrow n} \tag{4}$$

and

$$\phi_\nu = \frac{8\pi h\nu^3}{c^3} \frac{1}{e^{\beta h\nu} - 1} \tag{5}$$

The purpose of the present note is to point out that when the system of particles obey the Bose-Einstein or the Fermi-Dirac statistics, the relation (2) must be modified accordingly. It is well known that

$$\frac{N_n}{N} = \frac{1}{e^{-\gamma + \beta E_n} - a}, \qquad a = \begin{Bmatrix} 1 \\ 0 \\ -1 \end{Bmatrix} \quad \text{for} \begin{Bmatrix} \text{B.E.} \\ \text{Boltzmann} \\ \text{F.D.} \end{Bmatrix} \tag{6}$$

It can be shown then the relation (1) in general becomes*

$$N_n B^m_{\uparrow n} \phi_\nu = N_m B^m_{\downarrow n} \phi_\nu + N_m A^m_{\downarrow n} \left(1 + a \frac{N_n}{N}\right) \tag{7}$$

where

$$a\,\frac{N_o}{N} = \left\{ \begin{array}{c} \dfrac{1}{e^{-\gamma+\beta E_n}-1} \\ 0 \\ -\dfrac{1}{e^{-\gamma+\beta E_n}+1} \end{array} \right\} \text{for} \left\{ \begin{array}{l} \text{B.E.} \\ \text{Boltzmann} \\ \text{F.D.} \end{array} \right\} \text{system} \qquad (8)$$

and relations (3), (4), (5) remain valid.

The meaning of the $a\,\frac{N_n}{N}$ in (7) is clear. For the F. D. case, when $N_n = 0$, the transition rate of $m \longrightarrow n$ is $N_m A_n^m$. When $N_n \neq 0$, the Pauli principle reduces this rate by $\frac{N_n}{N}$. For the B. E. case, the transition rate of $m \longrightarrow n$ is enhanced by $\frac{N_n}{N}$. For the Boltzmann case the transition probability for $m \longrightarrow n$ is independent of N_n. This is in accord with Brillouin's derivation of (6).

* The relation (1) should in fact be replaced by

$$N_n B_n^m \left(1 + a\,\frac{N_m}{N}\right) \phi_\nu = N_m B_n^m \left(1 + a\,\frac{N_n}{N}\right) \phi_\nu + N_m' A_n^m \left(1 + a\,\frac{N_n}{N}\right), \qquad (9)$$

the argument being that given in the end paragraph. But in view of $B_n^m = B_n^m$ (3), this relation (9) reduces to (7).

Introducing statistical weights g_m, g_n for states m, n does not change the result above.

PHENOMENOLOGICAL RENORMALIZATION GROUP APPROACH TO PHASE TRANSITIONS

Chin-Kun Hu

Institute of Physics, Academia Sinica

Nankang, Taipei, Taiwan, R. O. C.

P. Kleban

Department of Physics and Astronomy and

Laboratory for Surface Science and Technology

University of Maine at Orono

Orono, Maine 04469, U. S. A.

A phenomenological renormalization group (PRG) transformation is formulated based on the idea that the renormalization group (RG) transformation can be considered as a process of replacing the original system by another one with fewer degrees of freedom but having the same or approximately the same free energy. As in Nightingale's PRG theory, only the inverse temperature (β) or external field (h) conjugate to the order parameter of the system is allowed to vary in the PRG transformation. It is found that the susceptibility diverges proportional to the number of particles in the system at first order transitions. The behavior of the correction to such finite-size scaling is also discussed. As a demostration, this formulation is applied to the two-dimensional Ising model and it is found that its susceptibility has the expected behavior. Some theoretical problems related to our formulation are also discussed.

I. INTRODUCTION

The calculation of the macroscopic properties of thermodynamic systems, such as phase diagrams and critical parameters, from given interactions between constituent particles of the systems, is one of the central problems of statistical mechanics. Before 1971, the methods used in such calculations included mean field theory[1], diagonization of the transfer matrix[2, 3], series expansion[4], and Monte-Carlo simulation[5] Each of these methods has certain advantages and disadvantages. For the two-dimensional Ising model with nearest neighbor (nn) interaction only, one can diagonize[2] the transfer matrix for an arbitrary number of spins to obtain the exact free energy, and hence specific heat, critical point etc., of the system. But for Ising models with more complicated interactions or

in higher space dimensions, one can diagonize only transfer matrices for small finite numbers of column or surface spins. Thus one can not calculate very accurate critical points and exponents which are manifestation of interactions among infinite number of particles with different length scales in given space dimensions. The Monte-Carlo simulation and mean field method have similar difficulties when dealing with systems at critical points. On the other hand, although the series expansion method[4] becomes very complicated when applied to high order term calculations and systems with complicated interactions, it does produce some reliable critical parameters for certain model systems[4].

In the first half decade of the 1960's, both experimental and theoretical results indicate that the critical exponents satisfy certain equalities which motivated Widom[6] in 1965 to introduce the scaling hypothesis for the free energy of a system near its critical point. In 1966. Kadanoff[7] presented a heuristic argument, called the Kadanoff construction, that provides intuitive support for the scaling hypothesis. The Kadanoff construction was eventually mathematically realized as a systematic calculation procedure when Wilson[8] introduced the renormalization group (RG) method to statistical physics. In the RG calculations of physical quantities, the contributions from different length scales are taken into acccunt and the qualitatively correct and even quantitatively accurate results can thus be obtained[9].

In the first few years after 1971, people usually carried out RG transformation in momentum space. In recent years, more attention has been paid to the position space renormalization group (PSRG) transformation. One of the reasons for this change is that lattice-gas models of certain experimentally available physical or chemical absorption systems on surfaces correspond to certain spin models[10] and the calculation of phase diagrams for such spin models is possible using PSRG methods. The PSRG methods often employed are the Niemeijer-van Leeuwen method[11], Kadanoff's variational approximation[12, 13], and Migdal-Kadanoff approximation[14,15]. Each of these methods also has certain virtues and limitations. The Niemeijer-van Leeuwen method is based on the assignment of block spin (i.e. transformed spin variable) to a certain number of site spins according to the majority rule in a system with a finite number of site spins. The complexity of the calculation increases

exponentially with the number of site spins in a given RG transformation. In Kadanoff et al.'s lower bound variational approximation[12, 13] only spins in the same primitive unit cell of the lattice can have nonzero couplings. The RG transformation in the Migdal-Kadanoff[14, 15] approximation is very simple, but this method is applicable directly to models with the nn interactions only. These limitations greatly reduce the possibility of direct application of the methods[11-15] to lattice-gas models for certain physically realizable systems. Besides such limitations. systematic errors of the PSRG methods just mentioned can easily reach 5 - 20%, and there is apparently no easy systematic way to reduce such errors.

In 1976, Nightingale[16] proposed a phenomenological renormalization group theory for second order phase transitions based on the finite-size scaling of the correlation length at second order phase transition temperatures. In this theory, the ratios among the coupling constants for the spins of the transformed and the original systems are assumed to be the same and only the inverse temperature(β) and magnetic field(h , coupling with order parameter) can be adjusted to satisfy the finite-size scaling of the correlation length ξ_n for simi-infinite n x ∞ spin systems, where n is the number of spins in a column. ξ_n can be calculated frcm the largest (λ_1) and second largest (λ_2) eigenvalues of the transfer matrix for n column spins as $\xi_n = 1/\ln(\lambda_1/\lambda_2)$. This method can be applied to spin models with complicated couplings among spins. The accuracy of such calculations can be increased easily by increasing n. Thus this is a very powerful method for calculating critical points and indices at second order phase transitions. However, this method can not be applied generally to locate first order phase transition points and thus can not be used to calculate the complete phase diagrams for many experimentally interesting systems.

The purpose of this paper is to formulate a phenomenological renormalization group (PRG) theory which has the advantages of Nightingale's theory and can also be systematically applied to first order phase transitions. The basic idea of our approach had been reported in 1981 American Physical Society march meeting[17] and also in a short paper[18]. Our approach, which will be reported in section 2, proceeds directly from previous PSRG developments and Nightingale's theory and

is based on the following ideas: (1) the RG transformation can be considered as a systematic way to replace the original system by a system with fewer degrees of freedom but having the same or approximately the same free energy; the ratios among the coupling constants for the spins of the transformed and the original systems are assumed to be the same and only β or h is adjusted to satisfy the requirement that the transformed and the original systems have the same or approximately the same free energy, (2) the RG transformation becomes more and more accurate when the fraction of the degrees of freedom subtracted each time in succesive RG transformations becomes less and less, (3) if there is a first or second order phase transition at $\beta = \beta_c$, $h = h_c$, then (β_c , h_c) is a fixed point of the RG transformation.

Based on the above ideas, we derive a scaling relation for the susceptibility at the fixed points of large systems, where the scaling power is a maximum at first order transitions. We will also discuss corrections to such scaling relations in finite systems. In the formulation of Sect. II, some of the assumptions made in the previous paper[18] are either not necessary or more comprehensible from a unified physical picture. The connection with traditional RG transformations[11-15] is also more clear. In Sect. III, we apply our formulation to the two-dimensional Ising model and find that the susceptibility has the expected behaviour. In Sect. IV, some theoretical problems related to our theory are discussed. A brief conclusion is given in Sect. V.

II. GENERAL FORMULATION

Our formulation is based on the following interpretation of the RG transformation. Let us take the application of the Niemeijer-van Leeuwen method[11] to the two-dimensional spin model on a square lattice as an example:

(2.1) Interpretation of a Conventional RG Transformation.

Suppose we have Ising spins, $s_1, \cdots\cdots s_N$, on a two-dimensional square lattice as shown in Fig.1 with interaction Hamiltonian $H (s_1, \cdots\cdots s_N)$. In the following, we shall use s(i, j) to denote spin s at coordinate (i, j). Some examples of s spin coordinates are shown in Fig. 1. To define a Niemeijer-van Leeuwen RG transformation, we define cell spins, $t_1, \cdots\cdots t_{N'}$, (N' = N/4),

on the lattice with doubled lattice constant also shown in Fig.1. We will use t(i, j) to denote a spin t on a lattice point, [i, j] where i and j are integers and " [ ] " indicates that t spins are on a lattice with doubled lattice constant. The purpose of the RG transformation is to find an effective Hamiltonian $H'(t_1, \cdots\cdots t_{N'})$ for the cell spins which has the same or approximately the same free energy as that calculated from $H (s_1, \cdots\cdots s_N)$. However, this is not an easy problem for $N \to \infty$. To make the calculation possible, one breaks the whole lattice into small 4 x 4 blocks of site spins as indicated by broken lines in Fig. 1. The broken lines break all coupling between site spins on different 4 x 4 blocks, e.g. s(2, 1) with s(1, 0), s(2, 0), and s(3, 0). To restore partially the loss of energy caused by the broken lines, one imposes a periodic boundary condition for each block of 4 x 4 site spins, e.g. the couplings between s(2, 1) and s(1, 0), s(2, 0), and s(3, 0) are replaced by the couplings between s(2, 1) and s(1, 4), s(2, 4), and s(3, 4). We thus have a block potential, e.g. v(s(1, 1) .....s(4, 4)) $\equiv v (s_1, \cdots\cdots s_{16})$, for each block of 4 x 4 site spins. From $v (s_1, \cdots\cdots s_{16})$, it is quite straightforward to calculate the block potential $v'(t[1 , 1] , \cdots\cdots t [2 , 2]) \equiv v'(t_1, \cdots\cdots t_4)$ for cell spins:

$$\exp (v'(t_1, \cdots\cdots , t_4) = \sum_{s_1, \cdots\cdots s_{16}} \exp (v (s_1, \cdots\cdots s_{16}) + T (t_1, \cdots\cdots t_4 ; s_1, \cdots\cdots s_{16})), \qquad (1)$$

where $T(t_1, \cdots\cdots t_4 ; s_1, \cdots\cdots s_{16})$ satisfies:

$$\sum_{t_1, \cdots\cdots t_4} \exp (T (t_1, \cdots\cdots t_4 ; s_1, \cdots\cdots s_{16})) = 1 \qquad (2)$$

to ensure that $v'(t_1, \cdots\cdots t_4)$ and $v(s_1, \cdots\cdots s_{16})$ have the same free energy. $v'(t_1, \cdots\cdots t_4)$ can be expanded as a summation of the invariant functions of $t_1, \cdots\cdots t_4$ with the coupling constants as expansion coeficients, which include the configuration independent constant C_o' . C_o' can also be calculated from the equation:

$$C_o' = \sum_{t_1, \cdots\cdots t_4} v'(t_1, \cdots\cdots t_4)/NCF, \qquad (3)$$

where NCF is the total number of configurations for $t_1, \cdots\cdots t_4$. The coupling constants except C_o' can be put together as a vector K'. It is then assumed that

the t spins within a block and the t spins in the neighboring blocks have the same coupling constant, e.g. the nearest neighbor coupling between t(1, 0) and t(1, 1) is the same as the nearest neighbor coupling between t(1, 1) and t(1, 2). We thus arrived at the Hamiltonian $H'(t_1, \cdots\cdots t_{N'})$ for cell spins with $\vec{K}'$ as the coupling constant vector. Let f(K) and f(K') denote the free energy per spin calculated from Hamiltonian with K and K' as coupling constant respectively, then

$$f(\vec{K}) \cong (f(\vec{K}') + K_0'(\vec{K}))/L^2 \qquad (4)$$

where L = 2 is the scale factor, $K_0' = C_0'/4$ is the background energy per cell spin for the transformed system. Equation (4) is only approximately, rather than exactly true, because the RG transformation of (1) only gives the approximate free energy for the transformed system. We can carry out the next step of RG transformation by breaking the lattice for $t_1, \cdots\cdots t_{N'}$, into 4 x 4 blocks of spins as indicated by the solid line in Fig. 1 and then proceeding in the same way as before. Such RG transformations can be carried out step by step until a fixed point is reached, where the free energy for the remaining degrees of freedom can be easily calculated. Thus Niemeijer-van Leeuwen's RG transformation[11] can be considered as a process of replacing original systems by other systems with fewer degrees of freedom, which have approximately the same free energy as the original system. We can also give a similar interpretation to the Migdal-Kadanoff[14, 15] and Kadanoff et al's[12, 13] lower bound RG transformation, where the free energy of the transformed system is a lower bound to the free energy of the original system. From this interpretation, it is easy to understand that there are appreciable errors in such RG transformations, because a large fraction of coupling bonds among spins are broken (in Niemeijer-van Leeuwen's method) or removed (in Migdal-Kadanoff approximation and Kadanoff et al's lower bound RG transformation) in each RG transformation. On the other hand, if only a small fraction of the bonds are broken in each RG transformation, more accurate results can be obtained. This is one of our basic motivations for the phenomenological RG transformation.

(2.2) Phenomenological RG Transformation.

For the purpose of easy presentation and comparison with prior methods, we formulate the phenomenological RG(PRG) transformation for spin models on a two-dimensional square lattice. This formulation can obviously be extended to three-

dimensions and other lattices.

As in the previous case, suppose we have Ising spins $s_1, \cdots\cdots s_N$ on a two-dimensional square lattice as shown in Fig. 2 with interaction Hamiltonian $H(s_1, \cdots\cdots s_N)$. The spins can have more complicated couplings than those in the previous case. We shall use s(i, j) to denote the spin on lattice point (i, j), where i and j are integers. To define a PRG transformation, we divide the lattice into n x m blocks of site spins as indicated by broken lines in Fig. 2. The broken lines break all coupling between site spins on different n x m blocks of site spins, e.g. s(n, 2) with s(n+1, 1), s(n+1, 2), and s(n+1, 3). To compensate for the loss of energy caused by broken lines, we impose periodic boundary condition for site spins on n x m blocks, e. g. the coupling between s(n, 2) and s(n+1, 1), s(n+1, 2), and s(n+1, 3) are replaced by couplings between s(n, 2) and s(1, 1), s(1, 2), and s(1, 3) respectively. We thus have an interaction potential $v(s(1, 1), \ldots s(n, m)) \equiv v(s; n, m)$ for nm site spins. The free energy of the nm site spins with the block potential v(s; n, m) can be calculated and is denoted by F(n, m; β , h), where β is the inverse temperature and h is an external field coupling with the order parameter. Now we define n'm' spin variables t(1, 1),... t(n', m') inside each nm block of site spins, where $1 < n/n' = m/m' = L$ = linear scale factor and t(1, 1), ... t(n', m') assume the same spin components as s (e.g., if s = $\pm$ 1, then t=$\pm$1). We also assume that the t spins couple in the same way as the s spins (including periodic boundary condition). Their block potential for a given configuration is denoted by v'(t(1, 1), ... t(n', m')$\equiv$v'(t; n', m'). As in the case of Niemeijer-van Leeuwen's RG transformation, we can establish the RG transformation by the requirement that the free energy calculated from v'(t';n', m') should be the same as that calculated from v(s; n, m). One possible way to realize this requirement is to introduce a generating function T(t(1, 1), ... t(n', m'); s(1, 1), ... s(n, m)) $\equiv$ T(t; s) which satisfies the normalization condition:

$$\sum_{(\,\,)\ s(1,1),\cdots,s(n,m)} \exp(v(s;n,m)+T(t;s)) = 1 , \qquad (5)$$

and v'(t; n', m') is related to v(s; n, m) by the transformation:

$$\exp(v'(t;n',m')) = \sum_{s(1,1),\cdots s(n,m)} \exp(v(s;n,m) + T(t;s)) . \qquad (6)$$

Eqs. (5) and (6) ensure that the free energy calculated from v'(t; n', m') is the same as that calculated from v(s; n, m) as is the case for (1) and (2). As in an ordinary RG transformation, v'(t; n', m') also contains a configuration independent constant C_o (n, m, n', m', β , h) which can be calculated from the equation:

$$C_o'(n,m,n',m',\beta,h)=\sum_{t(1,1),\ldots t(n',m')} v'(t;n',m')/NCF, \quad (7)$$

where NCF is the number of terms in the configuration summation of (7). It is easy to show that

$$\frac{\partial^2}{\partial h^2} C_o'(n,m,n',m',\beta,h)\geq 0, \quad (8)$$

$$\frac{\partial^2}{\partial \beta^2} C_o'(n,m,n',m',\beta,h)\geq 0. \quad (9)$$

Equations (8) and (9) will be used later in the discussion of the scaling behavior of magnetic susceptibility and specific heat at phase transition points. C_o' of (7) can be considered as a background energy of the t spin system arising from elimination of some degrees of freedom in the original s spin system. Thus C_o' becomes less and less important as $\frac{nm}{n'm'} \to 1^+$ and n, m, n', and m' tend to large numbers.

For the large values of n, m, n', and m', where the RG transformation is expected to be more accurate, it is difficult to carry out the transformation of (6) in practice. Thus we take the configuration sum over t(1, 1), ... t(n', m') on both sides of (6) and have the equation:

$$F(n,m;\beta,h)=F(n',m';\beta',h')+C_o'(n,m,n',m',\beta,h), \quad (10)$$

where F(n, m,; β , h) and C_o' (n, m, n', m', β , h) are defined above and F(n', m'; β' , h') is the free energy calculated from the configuration dependent part of v(t; n', m') (i.e. exclude the contribution from C_o'). We will use (10) as our PRG transformation equation.

Now dividing (10) by nm, we have:

$$f(n,m;\beta,h)=L^{-d}[f(n',m';\beta',h')+K_o'(n,m,n',m',\beta,h)]. \quad (11)$$

Here d=space dimensions, f(n, m; β , h) = F(n, m; β , h)/nm, f(n', m'; β' , h') = F(n', m'; β' , h')/n'm', and K_o' (n, m, n', m', β , h) = C_o (n, m, n', m', β , h)/n'm'. Eq. (11) is the PRG transformation for the transformed variables

β' , h', and K_o' . In later discussions, we will consider the RG transformation only in a particular direction perpendicular to the β or h axis in the (β , h) plane, e.g. we fix β (or h) and change h(or β) only. For the moment, suppose we know β' and h' for the transformed system. We then use β' and h' as coupling parameters for the infinite t spins system whose free energy per spin is denoted by f(β' , h'). f(β' , h') satisfies approximately the equation:

$$f(\beta,h)\cong L^{-d}[f(\beta',h')+K_o'(n,m,n',m',\beta,h)], \quad (12)$$

where f(β , h) is the free energy per spin of the original infinite s spin system. The difference between (11) and (12) should be noted; the former is the PRG transformation equation for β' or h', similar to (1) in an ordinary RG transformation, while (12) is the approximate equation for the free energy per spin of the infinite system, similar to (4) in an ordinary RG transformation.

Now we fix $\beta' = \beta$ and allow h' to change in (11) and (12) then take the derivative of (12) with respect to h to obtain the equation:

$$M(\beta,h)=L^{-d}[(\frac{\partial h'}{\partial h})M(\beta,h')+\frac{\partial}{\partial h}K_{o,h}'(n,m,n',m',\beta,h)], \quad (13)$$

where the subscript h has been included in $K_{o,h}'$ to indicate that only h is allowed to vary in the PRG transformation. Suppose the original Hamiltonian $H(s_1,\ldots s_N)$ is an even function of $s_1,\ldots s_N$ at h = 0. Then the second term on the right-hand side of (13) is zero at h = 0. In this case if

$$\Delta M(\beta,0)=M(\beta,0^+)-M(\beta,0^-)\neq 0, \quad (14)$$

we have

$$(\frac{\partial h'}{\partial h})=L^d. \quad (15)$$

This is the condition of the first order transition considered by B. Nienhuis and M. Nauenberg[19]. Now we fix $\beta' = \beta$ and take the second derivative of (11) with respect to h at h = 0 and have:

$$\chi(n,m,\beta,h)=L^{-d}(\frac{\partial h'}{\partial h})^2\chi(n',m';\beta,h')$$
$$+L^{-d}[\frac{\partial}{\partial h}(\frac{\partial h'}{\partial h})M(n',m';\beta,h')$$
$$+\frac{\partial^2}{\partial h^2}K_{o,h}'(n,m,n',m',\beta,h)], \quad (16)$$

Since h' is an odd function of h, the second term on the right-hand side is zero at h = 0. As n, m, n' and m' $\to\infty$ and nm/n'm' $\to 1^+$, the first term on the right-hand side of (16) becomes singular at phase transition points, but the last term is still regular or much less singular than the first term, which will be discussed further in section (4.4). Thus we can neglect the last term and have:

$$\chi(n, m, \beta, 0) = L^d \chi(n', m', \beta, 0), \qquad (17)$$

where (15) for a first order transition at h = 0 has been used. For large but finite n, m, n', and m', (17) can be considered as an approximate equation of finite-size scaling at a first order transition. At the second order transition, we have[9]:

$$\left(\frac{\partial h'}{\partial h}\right) = L^{d-\beta/\nu}. \qquad (18)$$

Following a similar procedure and argument to derive (17), we have:

$$\chi(n, m, \beta, 0) = L^{d-2\beta/\nu}\chi(n', m', \beta, 0), \qquad (19)$$

at second order transitions for large n, m, n', and m'. Since $\beta/\nu > 0$, we conclude from (17) and (19) that χ (n, m, β, 0) increases with n and m most rapidly at a first order transition. This can be used as a criterion to locate the first order transition point. For this purpose, we define the function:

$$\begin{aligned}\Delta\chi(n, m, n', m', \beta, h) &= \chi(n, m, \beta, h) - L^d\chi(n', m', \beta, h') \\ &= \left(L^{-d}\left(\frac{\partial h'}{\partial h}\right)^2 - L^d\right)\chi(n', m', \beta, h') \\ &+ L^{-d}\left[\frac{\partial}{\partial h}\left(\frac{\partial h'}{\partial h}\right)M(n', m', \beta, h')\right. \\ &\left. + \frac{\partial^2}{\partial h^2}K'_o(n, m, n', m', \beta, h)\right]. \qquad (20a)\end{aligned}$$

From (8), (17), (19), (20a), and the statement following (16), it is obvous that for large but finite n, m, n', and m',

$$\Delta\chi(n, m, n', m', \beta, h = 0) \geq 0 \qquad (20b)$$

at first order transition points, and

$$\Delta\chi(n, m, n', m', \beta, h = 0) < 0 \qquad (20c)$$

at second order transition points or points where there is no transition. Thus if we plot $\Delta\chi$ (n, m, n', m', β, h) as a function of h at a first order transition temperature, there will be a region of positive sign near h = 0 even for quite large (but finite) n, m, n', and m'. This behavior can be used to identify the region of first order transitions (see next section for an example).

Now we fix h' = h = 0 and allow β' to change in (11) and (12). The first derivation of (12) with respect to β and the second derivative of (11) with respect to β are given by:

$$U(\beta, 0) = L^{-d}\left[\left(\frac{\partial\beta'}{\partial\beta}\right)U(\beta', 0) + \frac{\partial}{\partial\beta}K'_{o,\beta}(n, m, n', m', \beta, 0)\right], \qquad (21)$$

$$\begin{aligned}&C(n, m, \beta, 0) \\ &= L^{-d}\left(\frac{\partial\beta'}{\partial\beta}\right)^2 C(n', m', \beta', 0)(\beta/\beta')^2 + L^{-d}\left[\beta^2\frac{\partial}{\partial\beta}\left(\frac{\partial\beta'}{\partial\beta}\right)U(n', m', \beta', 0)\right. \\ &\left. + \beta^2\frac{\partial^2}{\partial\beta^2}K'_{o,\beta}(n, m, n', m', \beta', 0)\right], \qquad (22)\end{aligned}$$

where $U(\beta, 0) = \frac{\partial}{\partial\beta}f(\beta, 0)$, $U(\beta', 0) = \frac{\partial}{\partial\beta'}f(\beta', 0)$,

$C(n, m, \beta, 0) = \beta^2\frac{\partial^2}{\partial\beta^2}f(n, m, \beta, 0)$, $C(n', m', \beta', 0) = \beta'^2\frac{\partial^2}{\partial\beta'^2}f(n', m', \beta', 0)$. If β_c is a fixed point of (11) at h = 0 and

$$U(\beta_c, 0) = U(\beta + \varepsilon, 0) - U(\beta - \varepsilon, 0) \neq 0 \qquad (23)$$

for positive $\varepsilon \to 0^+$, then it follows from (21) that:

$$\frac{\partial\beta'}{\partial\beta} = L^d \qquad (24)$$

at the first order transition temperature β_c. At a second order phase transition temperature, we have[9]:

$$\frac{\partial\beta'}{\partial\beta} = L^{(d/\nu - \alpha)}. \qquad (25)$$

As n, m, n', and m' $\to\infty$ and nm/n'm' $\to 1^+$, the first term on the left-hand side of (22) become singular at phase transition points, but the last two terms are still regular or much lesser singular than the first term, which will be discussed

further in section (4.4); thus we can neglect the last two terms and have:

$$C(n, m, \beta_c, 0) = L^d C(n', m', \beta_c, 0) \qquad (26)$$

at first order transition points and

$$C(n, m, \beta_c, 0) = L^{d(\alpha/(2-\alpha))} C(n', m', \beta_c, 0) \qquad (27)$$

at second order phase transition points. Since α for second order phase transitions is generally less than 1, we concluded from (26) and (27) that C increases with n and m mostly rapidly at first order transition points. This can also be used as a criterion to locate the first order transition point. If it happens that $\frac{\partial}{\partial \beta'} \frac{\partial \beta'}{\partial \beta} = 0$ in (22), which is not always true, then following the argument given before for $\Delta\chi$ of (20), we expect that $\Delta C(n, m, \beta, 0) = C(n, m, \beta, 0) - L^d C(n', m', \beta, 0)$ will show a region of positive sign around the first order transition points. Thus in this case, we can locate a first transition temperature from the behavior of ΔC.

III. AN EXAMPLE : SPIN-1/2 ISING MODEL

Now we will apply the formulation of section 2 to the Ising model on a square lattice with the nearest neighbor (nn) interaction to demonstrate that (20) can actually be used to locate the region of first order transitions. The Hamiltonian for the Ising model is given by:

$$\beta H = -K \sum_{(ij)} \sigma_i \sigma_j - h \sum_i \sigma_i \qquad (28)$$

where the first and the second summations extend over all nn bonds and sites of the lattice, respectively; σ_i , $\sigma_j = \pm 1$. The model of (28) on a square lattice has a second order transition at h = 0, $T_c = K_c^{-1} = (0.44068....)^{-1}$, and a line of first order transitions for h = 0, $T < T_c$. When we apply (20) to locate the region of first order transitions for fixed n and n', and varied m and m', we expect to get more and more accurate results by increasing m and m', because the fractions of broken bonds decrease as m and m' increase. In the limit $m \to \infty$, $m' \to \infty$: We get the best result for fixed n and n'. In the limit $m \to \infty$, the magnetization per spin for the n x ∞ system is given by:

$$M(n, \infty, K, h) = \frac{1}{n} \langle \psi_0 | \sum_{i=1}^{n} \sigma_i | \psi_0 \rangle , \qquad (29)$$

where ψ_0 is the eigenvector corresponding to the largest eigenvalue λ_0 of the transfer matrix R for the n column spins of the n x ∞ system. An efficient procedure to find λ_0 and ψ_0 for R can be found in Nightingale's paper[16]. The magnetic susceptibility per spin for the n x ∞ system $\chi(n, \infty, K, h)$ can be calculated from $M(n, \infty, K, h)$ by numerical differentiation. For very small h, we have:

$$\chi(n, \infty, K, 0) = M(n, \infty, K, h) / h , \qquad (30)$$

because $M(n, \infty, K, h = 0) = 0$ for the semi-infinite system. For given K, h, and n, we choose n' = n - 1 and calculate the quantities:

$$\Delta\chi(n, \infty, K, h) = \chi(n, \infty, K, h) - \left(\frac{n}{n-1}\right)^d \times \chi(n-1, \infty, K, h) , \qquad (31)$$

for very small h. The behaviour of $\Delta\chi / n^2$ as a function of K is shown in Fig. 3 for n = 5, 8, and 10. From Fig. 3, we may conclude that (20) can actually be used to locate the region of the first order transitions accurately.

IV. DISCUSSION

Some theoretical problems related to our formulation of Sect. II are discussed as follows:

(4.1) If there is a line of first order transition with a discontinous order parameter for $T < T_c$ and there is a second order transition at $T = T_c$ (e.g. two-dimensional Ising mo-el), then $\frac{\partial h'}{\partial h}$ equals L^d for $T < T_c$ and $L^{d-\beta\nu}$ at $T_c = T_c$. It seems that this is an unpleasant feature in our theory, because $\frac{\partial h'}{\partial h}$ appears to be a discontinuous function of T at $T = T_c$. However, the above result follows from the fact that we keep β fixed during PRG transformation and systems at different T or β should be considered as distinct because they can not transform from one into another. Thus we can not consider $\frac{\partial h'}{\partial h}$ as a function

of T in our treatment. Here we give a physical meaning to our PRG transformation with fixed T. A RG transformation can be considered as viewing the system from different length scales or at different distances from the system. If we apply a very small magnetic field h on a system at $T < T_c$, then there is a net magnetization in the direction of h. However, if we view the system on the microscopic scale, the spins of the system still flip quickly between up and down states. If we go away from the system, that corresponds with the situation after RG transformation, the spins of the system appear to be more rigid. If T of the system is allowed to vary in RG transformation, then one can interpret the situation by saying that the system is at $T' < T$, i.e. RG transformation transforms the system from T to $T' < T$. However, in our PRG transformation, T is fixed and one can interpret the situation (spins are more rigid.) by saying that a larger external magnetic field h' is applied to the system. By fixing T in PRG transformation, we force h = 0 for any T to be a fixed point in PRG transformation and thus have the result $\frac{\partial h'}{\partial h} = L^d$ at first order transtion temperatures.

(4.2) It has been pointed out[20] that the calculation of the spontaneous magnetization of the two-dimensional Ising model by C. N. Yang[21] and also E. W. Montroll, R. B. Potts, and J. C. Ward[22] is in fact a calculation of $(\chi_N / N)^{1/2}$ for $N \to \infty$. Thus $\chi_N \propto N$ when $T < T_c$. This holds for periodic boundary conditions, for which zero field susceptibility per spin χ_N may be written as a sum of N two-spin correlation function $< s_i \, s_j >$, since the magnetization m_N vanished identically. This result may be extended to some other Ising models with periodic boundary condition. These results are consident with our derivations of Sect. II.

(4.3) In the exact results mentioned above, the periodic boundary condition is crucial for the result that $\chi_N \propto N$. In the formulation of Sect. II, we also use the periodic boundary condition for n x m and n' x m' blocks of site and cell spins respectively. Such periodic boundary conditions follow naturally in our formulation, because we use the extra coupling arising from the periodic boundary condition to compensate for the loss of energy due to the breaking of bonds between different blocks of spins. However, our formulation also allows the free

boundary condition, but we expect that it will give less acurate result, e.g. in the location of first order transition region by using (20).

(4.4) In the derivation of (17), (19), (26), and (27) it has been said that the first term on the left-hand side of (16) and (22) is most singular and dominate the behavior of χ and C as n, m, n', and m' $\to \infty$ and nm/n'm' $\to 1^+$. It is reasonable to expect that this is indeed the case, because χ and C are associated with n'm' degrees of freedom and $\frac{\partial^2}{\partial h^2} K'_{o,h}$ and $\frac{\partial^2}{\partial \beta^2} K'_{o,\beta}$, are associated with nm-n'm' degrees of freedom, which is much smaller than n'm' in the limit nm/n'm' $\to 1^+$.

(4.5) It has been suggested by R. B. Griffiths, P. A. Pearce[23], and T. W. Burkhardt[24] that some RG transformations in the thermodynamic limit might be singular. However, in our formulation of Sect. II, only an infinitesimal fraction of the degrees of freedom are removed in the PRG transformation, a situation similar to the case of the exact RG transformation by Hilhorst et al.[25], and we don't actually take the thermodynamic limit (we just take the limit of large but finite n, m, n', and m'), it is reasonable to expect that our PRG transformation is also regular and free from the singularity of the free energy of the thermodynamic system.

(4.6) Recently, the result $\chi_N \propto N$ has been obtained by Fisher and Berker[26], Blöte and Nightingale[27], and Hu[28] using other methods. However, in such treatments there is no result concerning the correction to scaling at first order transitions (see (20b)).

(4.7) In the derivation of (17), (19), (20), (26), and (27), we don't actually solve the PRG transformation equation but only use certain reasonable properties of the transformation (e.g. the existence of T in (5) and (6)), similar situations are not rare in other branches of physics. For example, in the field theory of elementary particle physics, the PCT (parity, charge conjugation, and time reversal) symmetry is not obtained from the solution of the field equation but derived from certain properties of the field[29].

V. CONCLUSION

We have used a phenomenological renormalization group transformation to derive the finite-size scaling at first order phase transitions including the behavior of the correction term. We demonstrate in the simple Ising model that these results can be used to locate the region of first order transitions accurately. It is expected that the same technique can be applied to locate the rigion of first order phase transitions for other spin models where the exact solution is not available.

VI. ACKNOWLEDGEMENT

We are indebted to Professors R. B. Griffiths, W. -D. Chen, J. P. Valleau, S. G. Whittington, and A. J. Guttmann for useful discussions on the paper. The work was supported by the Office of Naval Research, USA, when the first draft of the paper was completed. One of the auther (C. K. Hu) was supported by the National Science Council of the Republic of China when the final version of the paper was completed.

REFERENCES

(1) H. E. Stanley, Introduction to Phase Transitions and Critical Phenomena. Oxford University Press, New York/Oxford, 1971, p.79.

(2) L. Onsager, Phys. Rev. 65, 117(1944).

(3) L. K. Runnels, in Phase Transitions and Critical Phenomena V.2 edited by C. Domb and M. S. Green. Academic Press, London/New York, 1972, p.305.

(4) C. Domb and M. S. Green (editors), Phase Transitions and Critical Phenomena V.3. .Academic Press, London/New York, 1974.

(5) K. Binder (editor), Monte-Carlo Methods in Statistical Physics. Springer-Verlag, Berlin/New York, 1979.

(6) B. Widom, J. Chem. Phys. 43, 3892 and 3898 (1965).

(7) L. P. Kadanoff, Physics 2, 263 (1966).

(8) K G. Wilson, Phys. Rev. B4, 3174, 3184 (1971).

(9) S. K. Ma, Modern Theory of Critical Phenomena. W. A. Benjamin, Inc., London, 1976.

(10) M. N. Barber, Phys. Reports 59, 375 (1980).

(11) a. T. Niemeijer & J. M. J. van Leeuwen Phys. Rev. Lett. 31, 1412 (1973), and Physica (Utrecht) 71, 17 (1974).

b. M. Nauenberg & B. Nienhuis, Phys. Rev. Letts 33, 944, 1598 (1974).

(12) L. P. Kadanoff, A. Houghton, and M. C. Yalabik, J. Stat. Phys. 14, 171 (1976).

(13) C.-K. Hu and P. Kleban, J. Comp. Phys. 43, 289 (1981).

(14) A. A. Migdal, Sov. Phys. JETP 42, 743 (1976).

(15) L. P. Kadanoff, Ann. Phys. (N. Y.) 100, 359 (1976).

(16) M. P. Nightingale, Physica 83A, 561 (1976); Phys. Lett. 59A, 486 (1977); Proc. Kon. Ned. Akad. Wet. Series B. 82, 235, 245, 269 (1979).

(17) C.-K. Hu and P. Kleban, Bull. Am. Phys. Soc. 26, 241 (1981).

(18) P. Kleban and C.-K. Hu, Bull. Am. Phys. Soc. 27, 92, 325 (1982).

(19) B. Nienhuis and M. Nauenberg, Phys. Rev. Lett 35, 477 (1975).

(20) T. D. Schultz, D. C. Mattis and E. Lieb, Rev. Mod. Phys. 38, 856 (1964).

(21) C. N. Yang, Phys. Rev. 85, 808 (1952).

(22) E. W. Montroll, R. B. Potts, and J. C. Ward, J. Math. Phys. 4, 308 (1963).

(23) R. B. Griffiths and P. A. Pearce, Phys. Rev. Lett. 41, 917 (1978); J. Stat. Phys. 20, 499 (1979).

(24) T. W. Burkhardt, Phys. Rev. Lett. 43, 1629 (1979).

(25) H. J. Hilhort, M. Schick. and J. M. J. van Leeuwen, Phys. Rev. B19, 2479 (1979); H. J. F. Knops and H. J. Hilhorst, Phys. Rev. B19, 3689 (1979).

(26) M. E. Fisher and A. N. Berker, Phys. Rev. 26, 2507 (1982).

(27) H. W. Blöte and M. P. Nightingale, Physica 112A, 405 (1982).

(28) C.-K. Hu, Phys. Rev. B1, Vol. 29, April (1984).

(29) R. F. Streater and A. S. Wightman, PCT, Spin and Statistics, and All That. W. A. Benjamin, Inc., New York, 1964.

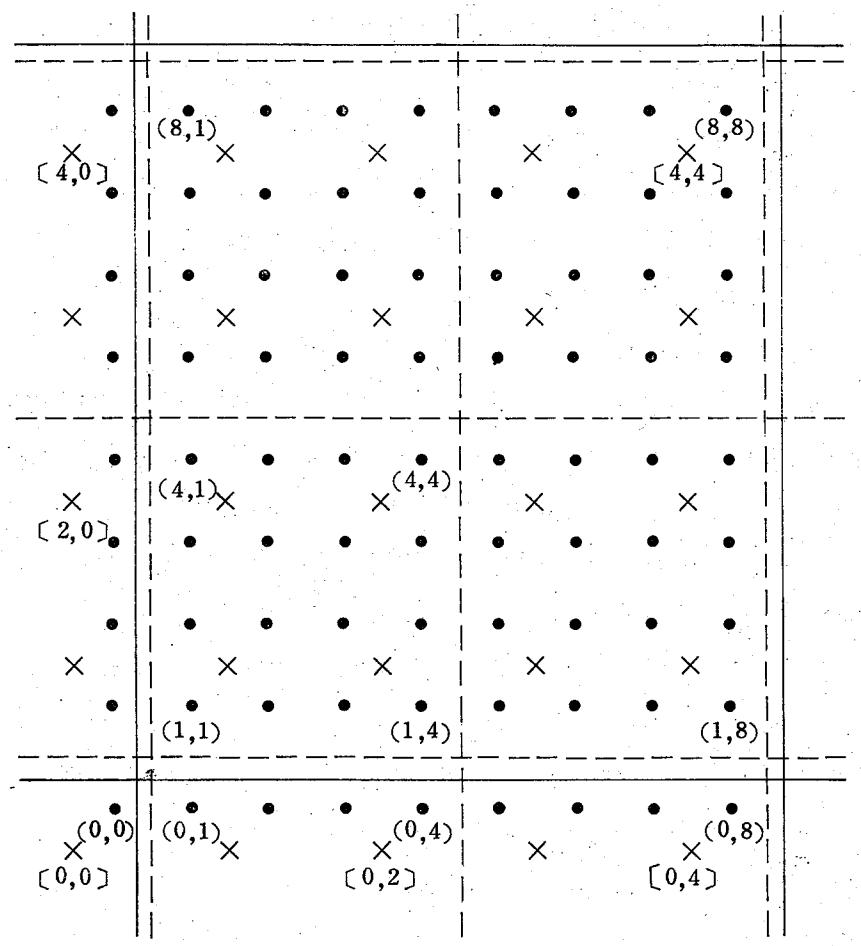

Fig. 1. Lattices and coordinates for the original spins $s_1,....s_N$ (•) and the transformed spins $t_1,....t_{N'}$(x) of the RG transformation. The coordinates for s and t spin are denoted by (i, j) and [k, l] respectively, where i, j, k and l are integers and the unit for [k, l] is double that for (i, j). Note that the origin for (i, j) and [k, l] are different. Some examples of (i, j) and [k, l] are shown in the diagram. In the RG Transformation, the site spins are divided into 4 x 4 blocks as indicated by the dotted lines. The 16 site spins(s) inside each block are transforme into 4 cell spins(t) by equation (1). For detail, see section (2.1).

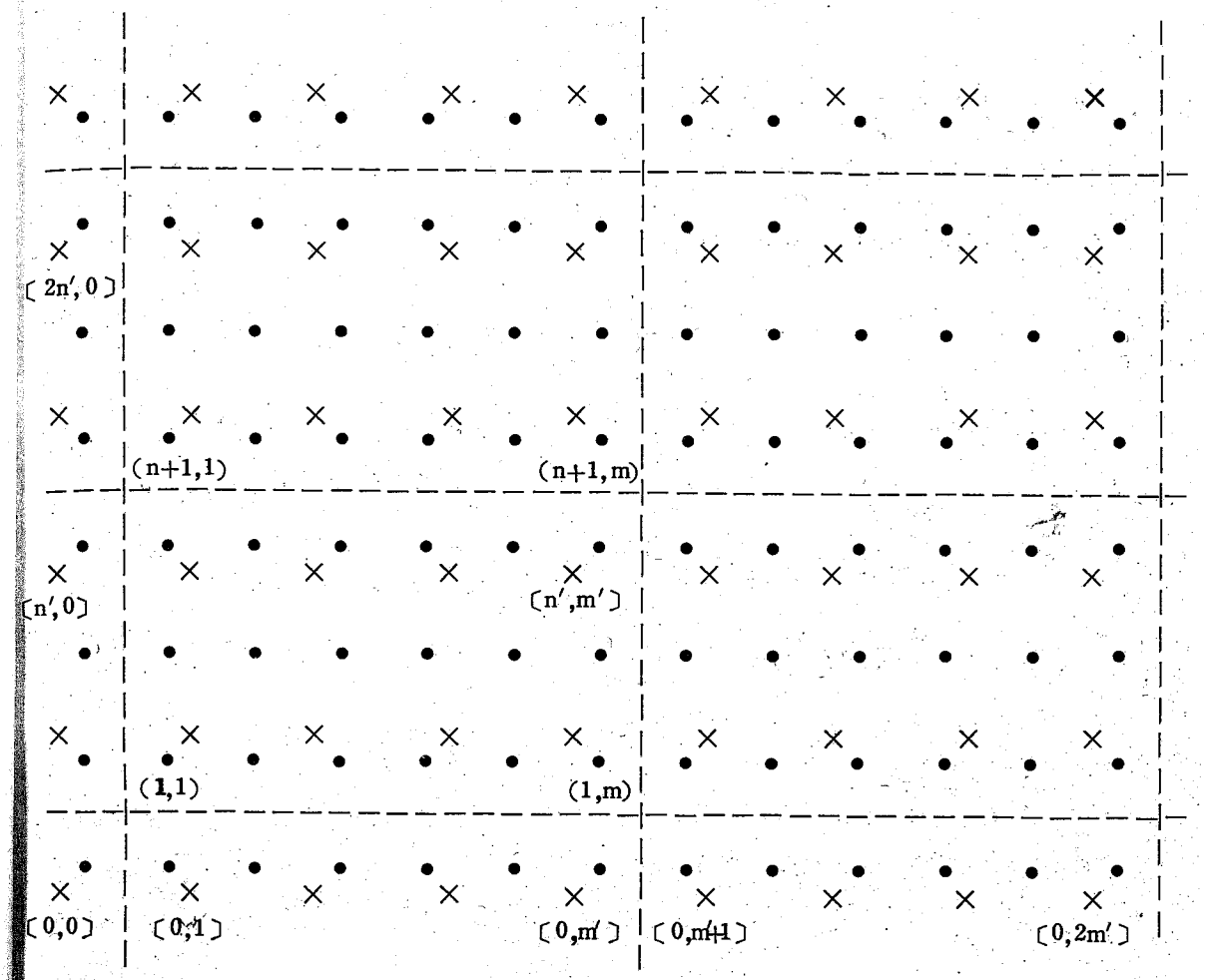

Fig. 2. Lattices and coordinates for the original spins $s_1,....s_N$ (•) and the transformed spins $t_1,....t_{N'}$(x) of the PRG transformation. The coordinates for s and t spin are denoted by (i, j) and [k, l] respectively, where i, j, k and l are integers and the unit for [k, l] is double that for (i, j). Note that the origin for (i, j) and [k, l] are different. Some examples of (i, j) and [k, l] are shown in the diagram. In the PRG transformation, the site spins $s_1,....s_N$ are divided into n x m blocks as indicated by the dotted lines. The mn site spins(s) inside each block are transformed into m'n' cell spins(t) by equation (6) or (11), where m/m'=n/n'=L=linear scale factor. For detail, see section (2.2). In this figure m=6, n=3, m'=4, n'=2 and L=1.5.

whose cell potential have 90^o rotation symmetry but do not have the permutation symmetry. They extended the MKVM to the two-parameter case, i.e. p_1 and p_2 are determined by minimizing the single cell free energy, and applied the method to calculate the critical points for the Baxter model[8] with several sets of coupling constants. Were Huang and Shih's two-parameter modified Kadanoff variation method justifiable, then to calculate derivatives of the free energy for the two-dimensional square-lattice Ising model with 90^o rotation symmetry, one should extend Hu and Kleban's method[5] from one parameter to two parameters. The latter is expected to be much more complicated than the former. In this note, we will prove that when applied to square-lattice Ising models with 90^o rotation symmetry, the RG transformation in the two-parameter modified Kadanoff variational method breaks the 90^o rotation symmetry if $|p_1| \neq |p_2|$. Since the transformed systems are expected to have the same symmetry properties as the original system, it is inappropriate to apply the two-parameter method to the spin model with 90^o rotation symmetry, e.g. the Baxter model. Hu and Kleban's method[5] with only one variational parameter is still appropriate for the square-lattice Ising models with 90^o rotation symmetry.

The most general form of the cell potential for the square-lattice Ising models with 90^o rotation symmetry and up-down symmetry may be written as[5]:

$$\nu(\sigma_1,\sigma_2,\sigma_3,\sigma_4) = K_o + K_{nn}(\sigma_1\sigma_2 + \sigma_2\sigma_3 + \sigma_3\sigma_4 + \sigma_4\sigma_1) + K_{nnn}(\sigma_1\sigma_3 + \sigma_2\sigma_4) + K_4\sigma_1\sigma_2\sigma_3\sigma_4 . \quad (1)$$

Here K_o , K_{nn} , K_{nnn} and K_4 denote a constant, nearest-neighbour (nn), next-nearest-neighbour (nnn), and four-spin interactions, respectively, $\sigma_1,\sigma_2,\sigma_3$, and σ_4 are four spins located clock-wise on a typical unit cell as shown in Fig. 1 and $\sigma = \pm 1$. It follows from equation (1) that:

$$\nu(1,1,1,1) = \nu(-1,-1,-1,-1) , \quad (2)$$

$$\begin{aligned}&\nu(1,1,1,-1)=\nu(1,1,-1,1)=\nu(1,-1,1,1)\\ &=\nu(-1,1,1,1)=\nu(-1,-1,-1,1)=\nu(-1,-1,1-1)\\ &=\nu(-1,1,-1,-1)=\nu(1,-1,-1,-1) , \end{aligned} \quad (3)$$

$$\begin{aligned}&\nu(1,1,-1,-1)=\nu(1,-1,-1,1)\\ &=\nu(-1,-1,1,1)=\nu(-1,1,1,-1) , \end{aligned} \quad (4)$$

$$\nu(1,-1,1,-1)=\nu(-1,1,-1,1) . \quad (5)$$

Thus there are four independent cell potentials, say $\nu(1,1,1,1)$, $\nu(1,1,1,-1)$, $\nu(1,1,-1,-1)$ and $\nu(1,-1,1,-1)$, which are linerar functions[5] of four independent parameters in equation (1).

Using the two-parameter form of the generating function given by equation (5) of Ref. (7), the RG transformation from the original cell potentials $\nu(\sigma_1,\sigma_2,\sigma_3,\sigma_4)$ to the transformed cell potentials $\nu(\mu_1,\mu_2,\mu_3,\mu_4)$ may be written as:

$$\begin{aligned}&\exp[\nu'(\mu_1,\mu_2,\mu_3,\mu_4)]\\ &= \sum_{\sigma_1\sigma_2\sigma_3\sigma_4} \exp[4\nu(\sigma_1,\sigma_2,\sigma_3,\sigma_4) + p_1(\mu_1\sigma_1 + \mu_3\sigma_3) + p_2(\mu_2\sigma_2 + \mu_4\sigma_4)] \,/\, \{\exp[p_1(\sigma_1+\sigma_3) + p_2(\sigma_2+\sigma_4)]\\ &+ \exp[-p_1(\sigma_1+\sigma_3) - p_2(\sigma_2+\sigma_4)]\} , \end{aligned} \quad (6)$$

where μ_1, μ_2, μ_3 and μ_4 are four spins located clockwise on a typical unit cell of the transformed system as shown in Fig. 1 and $\mu = \pm 1$

If the cell potentials $\nu'(\mu_1,\mu_2,\mu_3,\mu_4)$ have the same symmetry properties as the original systems, then $\nu'(\mu_1,\mu_2,\mu_3,\mu_4)$ must satisfy equations (2) to (5). On the other hand, to show that $\nu'(\mu_1,\mu_2,\mu_3,\mu_4)$ do not have the same symmetry properties as the original system, one only needs to show that cell potentials $\nu'(\mu_1,\mu_2,\mu_3,\mu_4)$ do not satisfy certain equality in equations (2) to (5).

It follows from equation (6) that:

$$\begin{aligned}\exp[\nu'(1,1,1,-1)] &= \frac{\cosh 2p_1}{\cosh 2(p_1+p_2)} Z_1^4 + (2\cosh 2p_2 + \frac{2}{\cosh 2p_2}) Z_2^4 + 2\cosh 2p_2 Z_3^4\\ &+ \frac{\cosh 2p_1}{\cosh 2(p_1-p_2)} Z_4^4 , \end{aligned} \quad (7)$$

and

$$\exp\left[\nu'(1,1,-1,1)\right]=\frac{\cosh 2p_2}{\cosh 2(p_1+p_2)}Z_1^4 + \left(2\cosh 2p_1+\frac{2}{\cosh 2p_1}\right)Z_2^4 + 2\cosh 2p_1\, Z_3^4 + \frac{\cosh 2p_2}{\cosh 2(p_1-p_2)}Z_1^4 \qquad (8)$$

where

$$Z_1 = e^{\nu(1,1,1,1)}, \qquad (9)$$

$$Z_2 = e^{\nu(1,1,1,-1)}, \qquad (10)$$

$$Z_3 = e^{\nu(1,1,-1,-1)}, \qquad (11)$$

and

$$Z_4 = e^{\nu(1,-1,1,-1)}. \qquad (12)$$

When $p_2 = p_1$ or $p_2 = -p_1$, we have $\nu'(1, 1, 1, -1) = \nu'(1, 1, -1, 1)$. Since Z_1, Z_2, Z_3, and Z_4 are independent parameters, when

$$|p_1| \neq |p_2| \qquad (13)$$

we have

$$\nu'(1,1,1,-1) \neq \nu(1,1,-1,1), \qquad (14)$$

i.e. the cell potentials $\nu'(\mu_1,\mu_2,\mu_3,\mu_4)$ do not have the 90^0 rotation symmetry.

For the Baxter model[8], K_{nn} of equation (1) should be zero and we have:

$$\nu(1,1,1,1) = \nu(1,-1,1,-1) \qquad (15)$$

and

$$Z_1 = Z_4 . \qquad (16)$$

When Z_1 and Z_4 of equations (7) and (8) satisfy the equality of equation (16), we still have equation (14) if equation (13) is still true.

In conclusion, we have shown that the two-parameter RG transformation[7] could not preserve the 90^0 rotation symmetry of the square-lattice Ising model when $|p_1| \neq |p_2|$. Therefore, it is inappropriate to apply this method to the square-lattice Ising model with 90^0 rotation symmetry, e.g. the Baxter model.

ACKNOWLEDGEMENT

The author thanks Professors Y. -M. Shih and W. -D. Chen for useful discussions. This work was supported by the National Science Council of the Republic of China under Grant No. NSC73-0204-M001-03.

REFERENCES

(1) L. P. Kadanoff, A. Houghton, and M. C. Yalabik, J. Statist, Phys. 14, 171 (1976).

(2) S. L. Katz and J. D. Gunton, Phys. Rev. B 16, 2163 (1977).

(3) Y. M. Shih, et al., Phys. Rev. B 19, 529 (1979).

(4) M. N. Barber, J. Comput. Phys. 34, 414 (1980).

(5) C. -K. Hu and P. Kleban, J. Comput. Phys. 43, 289 (1981).

(6) C. -K. Hu and P. Kleban, Phys. Rev. B 25, 6760 (1982).

(7) H. -M. Huang and Y. -M. Shih, Phys. Lett. 89 A, 257 (1982).

(8) R. J. Baxter, Ann. Phys. (NY) 70, 193 (1972).

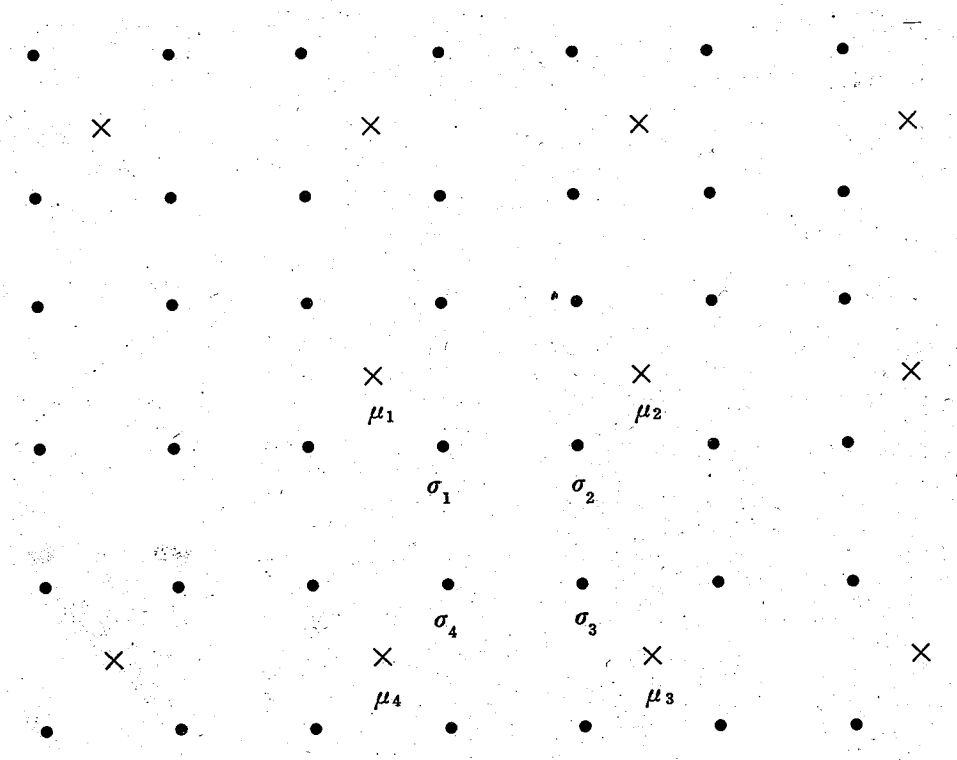

Fig. 1. The original σ -spin system (•) and the transformed μ -spin system (X) on square lattices. Note that the lattice constant of the latter is twice that of the former.

GAMMA TRANSITIONS IN ^{124}Te FOLLOWING THE BETA DECAY OF ^{124}Sb*

D. Wang, E. K. Lin, G. C. Jon and C. W. Wang
Institute of Physics, Academia Sinica
Nankang, Taipei, Taiwan, R. O. C.

The γ -radiation following the beta decay of 60.2d ^{124}Sb from thermal neutron capture in ^{123}Sb has been investigated with a Ge(Li) detector and a Ge(Li)-NaI(T ℓ) coincidence spectrometer. A total of 38 γ -rays was observed and the directional correlation has been measured for the 1248.6 keV → 602.6 keV → 0, 1325.6 keV → 602.6 keV → 0, 2293.9 keV → 602.6 keV → 0 and 2693.8 keV → 602.6 keV → 0 cascades. The energies, intensities and the multipole mixing ratios of the γ -rays in ^{124}Te have been deduced. The populated levels of ^{124}Te were identified up to 2.775 MeV. A previously unreported γ -transition was observed between levels at 2521 keV and 1958.1 keV.

1. INTRODUCTION

In recent years considerable attention has been devoted to the nuclear spectroscopy by decay scheme studies. The population of levels in ^{124}Te following the radiocative decays has been the topic of many investigations by Grabowski et al[1], Baker et al[2], Behar et al[3], Meyer et al[4], and Auer et al[5] from the decay of ^{124}Sb, and by Ragaini et al[6] from the decay of ^{124}I. The results have been comprehensively compiled by Ledered and Shirley[7] in "Table of Isotope", which have established the presence of numerous excited states of ^{124}Te up to ~ 3 MeV excitation. In particular, the lower excited states below 2091.5 keV have been extensively investigated, they exhibit somewhat vibrational pattern in nature. It is believed that the vibrational model with a pairing-plus-quadrupole force and coupling of the core to the shell model states of the two protons outside the closed shell[8] would be the most successful to describe the low-lying level scheme of ^{124}Te. However, the structure of the higher excited states of ^{124}Te are not well established. Several I^π assignments remain uncertain. Experimentally, there appeares some inconsistencies in the directional correction data for the casecade transitions from the higher excited levels, and discrepancies with the theoretical

* Supported by the National Science Council, Republic of China.

model exist. It seems necessary to require more experimental information for further studies.

The experimental works of the thermal neutron capture reaction on heavy nuclei with use of high resolution Ge(Li) detector in this laboratory have been extensively investigated to study the nuclear level scheme for several years. It is purpose of the present investigation on the beta decay of ^{124}Sb to provide additional experimental information on the level scheme of ^{124}Te and to confirm I^{π} assignments by observation of $\gamma - \gamma$ coincidence and directional correlations. Emphasis has been made in the present work to investigate the γ-rays which represent the transition between levels above 1249 keV in ^{124}Te.

2. EXPERIMENTAL METHOD

Radioactive sources of ^{124}Sb were obtained through the thermal neutron capture reaction in ^{123}Sb by the irradiation of 1 mg isotropically enriched sample powder (98.23% in ^{123}Sb and 1.77% in ^{121}Sb) with thermal neutron flux of about 5 x 10^{11} n-cm^{-2}-sec^{-1} for 10 hours in the reactor of national Tsinghua University. The sample was irradiated in a sealed capsules. After irradiation, the sample was taken out from reactor and was allowed for cooling in a period of 30 days, since the half life of the ^{124}Sb and ^{122}Sb activities is known to be 60.2d and 2.8d, respectively. The small amounts of ^{121}Sb impurity admixture in the sample apparently cause no interference in the present measurement of γ-rays from the beta decay of ^{124}Sb.

The experiments were based on conventional measurements carried out in nuclear spectroscopy with radiative sources. Singles spectra of γ-rays were taken mainly with a 43-cm^3 coaxial ORTEC Ge(Li) detector and standard low-noise amplifiers. The data were accumulated in a Camberra 4096-channel analyzer. To measure coincidence a Ge(Li)-Na(Tℓ) spectrometer was applied. A block diagram of electronic circuit used in the coincidence measurement is given in Fig. 1. The Ge(Li) detector was kept fixed, while the NaI(Tℓ) scintillation detector was allowed to rotate an angle as desired. The detailed description of the apparatus and methods of data treatment is given in previous papers.

3. RESULTS AND ANALYSIS

A. Singles γ-ray spectrum

Singles γ-ray spectra of ^{124}Te from beta decay of ^{124}Sb as viewed with Ge(LI) detector is presented in Figs. 2-5. Typical resolution obtained in the present measurement was 2.8 keV (FWHM) for ^{60}Co 1333 keV peak. Fig. 2 shows the γ-ray spectrum in the low-energy portion (240 keV - 740 keV). The higher energy portion of the γ-ray spectrum is shown in Figs. 3-5. A total of 48 γ-rays was observed. The γ-ray at 602.6 keV is seen to be quite intensive. Peaks due to ^{124}Te are seen up to 2182.3 keV. Among 48 peaks, thirty-eight were identified belonging to the energy levels in ^{124}Te by using half-life decay testing method; while seven of the others at 241.8 keV, 251.7 keV, 583.2 keV, 911.5 keV, 1461.0 keV, 1765.0 keV, and 2205.7 keV were arised from natural background, and the rest at 669.1 keV, 1069.0 keV, and 1180.0 keV are attributed to pair production. For all 38 γ-rays, the corresponding transitions in ^{124}Te were identified. The γ-ray appeared at 563.9 keV was found to represent a new transition between the 2521.5 keV and 1958.1 keV levels in ^{124}Te, it was not previously reported.

The energies of γ-rays observed in Figs. 2-5, the relative intensities and the classification of the 38 transitions between levels of ^{124}Te are listed in Table 1, where the available information on the energies of γ-rays from previous work is also listed in the third column for comparison.

The energy and efficiency calibration were derived from standard γ-ray sources. Also, the known energies of photo peaks arised from natural background measured at the same time as shown in the singles spectrum were used in the calibration. Photo peak efficiencies for the Ge(Li) detector were determined by using standard gamma sources with conventional method. From the first least square fit in the calibration, the relation between γ-ray energy and number of channel c was obtained as E(keV) = 0.705c + 82.2.

Energies of the observed γ-rays were then accurately determined as given in the second column of Table 1. It is seen that the determined energies agree very with previous measurement.

branching ratios for many transition lines were determined in the present

investigation. Table 2 shows the determined branching ratios for transitions from the 2293.9 keV, 2039.2 keV, 1958.1 keV, and 1325.6 keV levels in ^{124}Te. Our results were found in agreement with previous work[7] within 50%.

B. $\gamma-\gamma$ coincidence measurements

A 3" x 3" NaI(Tℓ) scintillator was used as the gating detector for Ge(Li)-NaI(Tℓ) coincidence measurements, and standard fast-slow coincidence was employed with resolving time of $\sim$ 5 ns. The coincidence measurements were carried out with a proper gate set over the 602.6 keV, which corresponds to the energy of γ-ray emitted in the transition from the first excited state to ground state of ^{124}Te. The energy interval selected by this gating may contain contributions arised from the 602.6 keV, 632.5 keV, 646.0 keV and 722.9 keV radiations.

Typical γ-ray coincidence spectra are shown in Fig. 6. It is seen that a total of 16 rays was observed in the coincidence spectra. Of these 16 γ-rays, six arise from the higher excited states of ^{124}Te in a cascade transition to the first excited state (2^+) at 602.6 keV and then to the ground state; four represent the cascade transitions arising from higher excited states of ^{124}Te to the second excited state (4^+) at 1248.6 keV; and three are attributed to the cascade transitions from higher excited states of ^{124}Te to the third excited state (2^+) at 1325.6 keV. The results of the coincidence measurements are summarized in Tables 3 and 4.

Relative intersities for the γ-rays appeared in the coincidence spectra have been calculated. Their values are relatively comparable to those of the corresponding γ-rays appeared in the singles γ-ray spectra, except the one at 968.3 keV which is seen to have comparably larger intensity appeared in the singles spectra because of contribution of the γ-ray at 969.2 keV from background ^{208}Ac.

C. Directional Correlation Measurement

Directional correlation measurements were carried out with an attempt to study the cascade transitions in ^{124}Te arising from higher excited states to the first excited state at 602.6 keV and then to the ground state. We set gating over the 602.6 keV as in the case of the coincidence measurement. Data were taken at angles θ = 90°, 105°, 120°, 135°, 165° and 180° for four cascades 1248.6 keV $\rightarrow$ 602.6 keV $\rightarrow$ 0, 1325.6 keV $\rightarrow$ 602.6 keV $\rightarrow$ 0, 2293.9 keV $\rightarrow$ 602.6 keV - 0, and 2693.8 keV $\rightarrow$ 602.6 keV $\rightarrow$ 0. The observed photo-peak areas were fitted to a linear combination

of Lagendre polynominal $P_L(\theta)$ by a CYBER 172 computer.

It has been shown that at a given angle the correlation function $W(\theta)$ for γ-cascade $I_a(L_1,L_1')I_b(L_2,L_2')I_c$ between three levels I_a, I_b, I_c of an even-even nucleus could be simply expressed[9] as follows:

$$W(\theta) = A_0 + A_2P_2(\theta) + A_4P_4(\theta)$$

where correlation coefficients A_L are defined in terms of the multipole mixing ratio δ of Krane and Steffen[10]. Referring to the first transition in the cascade, δ is given by

$$\delta = \langle I_a \,||\, L_1+1 \,||\, I_b\rangle / \langle I_a \,||\, L_1 \,||\, I_b\rangle$$

For the cascade transitions investigated, the cascade mode is $I_a(L_1,L_1+1)\,2^+(2,0)0^+$, anisotropy $A(\delta)$ is given in terms of coefficients A_2 and A_4

$$A(\delta) = \frac{\frac{3}{2}A_2 + \frac{5}{8}A_4}{1 - \frac{1}{2}A_2 + \frac{3}{8}A_4}$$

We have written a computer program for correlation coefficients A_L and anisotropy $A(\delta)$ for different I_a, and L_1, and from the calculated A_L we then extract the multipole mixing ratio.

Experimentally we obtain coefficient A_2^{exp} and A_4^{exp} from the least square fit to the measured correlation function $W(\theta)$. Figs 7 and 8 show the correlation functions and decay scheme from cascades 1248.6 keV $\rightarrow$ 602.6 keV $\rightarrow$ 0, 1325.6 keV $\rightarrow$ 602.6 keV $\rightarrow$ 0, 2293.9 keV $\rightarrow$ 602.6 keV $\rightarrow$ 0, and 2693.8 keV $\rightarrow$ 602.6 keV $\rightarrow$ 0. The dot represents the measured values of the correlation function $W(\theta)$. With the experimental data at 90° and 180°, we obtain anisotropy

$$A^{exp}(\delta) = \frac{W(180°) - W(90°)}{W(90°)}$$

The results on the measured coefficients A_2^{exp} and A_4^{exp}, and anisotropy $A^{exp}(\delta)$ are listed in Table 5 and compared with the calculated values. The agreement is seen to be satisfactory.

4. SUMMARY AND DISCUSSION

In the obtained coincidence spectra we identified many two γ-rays in the

cascade transitions between energy levels of ^{124}Te, the decay scheme of ^{124}Te between levels up to 2775.1 keV is established as shown in Fig. 9. It is seen that there are a large number of transitions feeding the first 2^+ level at 602.6 keV. Our result is in good agreement with most earlier investigations(7).

The three lowest excited states of ^{124}Te are well known to be 0^+, 2^+, and 4^+ respectively as described by the hydrodynamical vibrational mode(11). In the present work, we established 13 levels above the 1248.6 keV 4^+ level. Ref. 5 indicates the presence of one level at 2710.6 keV. No supporting evidence was found for this level in the present work. We observed a γ-ray at 563.9 keV, which represents a new transition between the 2521.5 keV and 1958.1 keV levels and is proposed to be associat with M3/E2 mode.

Among 13 levels identified, the levels at 1325.6 keV, 2039.2 keV, and 2091.5 keV were all assigned(7) to be 2^+; the level at 1958.1 keV has been carefully investigated by Behar et al(3) and their measurements on the directional correlations and polarization-directional corrections have determined a unique spin assignment of 4^+ for the 1958.1 keV level; and the level at 2293.9 keV was known(7) to be 3^-; while the I^π assignment of the other levels at 2182.5 keV, 2225.0 keV, 2322.9 keV, 2483.4 keV and 2521.5 keV were all uncertain. From analysis of data obtained in the directional correlation measurements for the 646-603, 723-603, 1691-603, and 2091-603 cascades in the present work, we obtain evidence for the I^π assignment of levels at 1248.6 ke 1325.6 keV, 2293.9 keV and 2693.8 keV to be 4^+, 2^+, 3^- and 3^-, respectively.

Table 6 and Fig. 7 summarize results of the directional correlation measurements for the above mentioned cascades. For the 646-604 and 2091-603 cascades the values o A_L coefficients and δ are consistent, respectively, with a 4^+-2^+-0^+ spin sequence of a nearly pure E2 character, and with a 3^--2^+-0^+ spin sequence of a nearly E1 chara This supports the spin and parity assignment 4^+ for the 1248.6 keV level and 3^- for the 2693.8 keV level. Our directional correlation results for the 723-603 and 1691-603 cascades agree, respectively a 2^+-2^+-0^+ spin sequence of a probable E2 multipola with M1 admixture (δ = -3.5 for the 723 keV transition), and a 3^--2^+-0^+ spin sequence of a probable E1 multipolarity with M2 admixture (δ = -0.05 for the 1691 ke transition). We have evidence that the 1325.6 keV and 2293.9 keV levels are 2^+ and 3^- respectively. The δ -values determined in the present work for the mixing ratio

of above four cascades agree quite well with the obtained in the work of Baker et al(2).

In conclusion, the structure of ^{124}Te nucleus is very complex. It is believed that the results of this work offer evidences concerning some highly excited states of ^{124}Te and provide useful experimental information for the detailed theoretical description of the nucleus ^{124}Te.

ACKNOWLEDGEMENT

We are grateful to Mr. G. C. Kiang for his suggestions and discussion as well as assitance in the initial phase of the experiment, and to the Institute of Nuclear Engineering, National Tsinghua University for providing assistance in the irradiation of samples.

REFERENCES

(1) Z. W. Grabowskik K. S. Krane and R. M. Steffen, Phys. Rev. 3C, 1649 (1971).
(2) K. B. Baker, J. H. Hamilton, A. V. Ramayya and G. Highland, Nucl. Phys. A186, 493 (1972).
(3) M. Behar, G. Garcia Bermudez, A. Filevich and M. C. Cambiaggio, Phys. Rev. 12C, 767 (1976).
(4) R. A. Meyer, W. B. Walters and R. C. Razaini, Nucl. Phys. A127, 959 (1969).
(5) I. P. Auer, J. J. Reidy and M. L. Wiedenbeck, Nucl. Phys. A124, 199 (1969).
(6) R. C. Ragaini, W. B. Walters, A. A. Noyes, and R. A. Meyer, Phys. Rev. 187, 1721 (1969).
(7) C. Michael Lederer and Vriginia S. Shirley, Table of Isotopes (7th ed.), John Wiley & Sons, Inc. New York.
(8) E. Degrieck and G. Vanden Berghe, Nucl. Phys. 141 (1974).
(9) M. E. Rose, Phys. Rev. 93, 477 (1954).
(10) K. S. Krane and R. M. Steffen, Phys. Rev. C2, 724 (1970).
(11) A. Bohr and B. R. Mottelson, Mat. Tys, Dan. Vid. Selsk. 27, No. 16 (1963).

Table 1 Energies, intensities, and classifications of the transitions in ^{124}Te

Peak No.	Energy		Relative Intensity	Classification
	Present Work	Ref. 7		
1	241.8±0.3		0.696±0.009	From Ra-226
2	336.0±0.3	335.8	1.012±0.009	2293.9 1958.1
3	351.7±0.3		0.592±0.007	From Ra-226
4	370.9±0.4	370.4	0.393±0.006	2693.8 2322.9
5	400.2±0.4	400.0	1.073±0.009	2793.8 2293.9
6	443.9±0.2	443.99	1.445±0.011	2483.4 2039.2
7	468.9±0.4	468.6	0.551±0.007	2693.8 2225.0
8	511.0			
9	525.3±0.2	525.5	0.903±0.009	2483.4 1958.1
10	563.9±0.2		0.543±0.007	2521.5 1958.1
11	583.2±0.3		0.524±0.007	From Tℓ-208
12	602.6	602.72	602.550±0.23	602.6 g.s.
13	632.5±0.2	632.4	0.555±0.007	1958.1 1325.6
14	646.0	645.82	42.784±0.060	1248.6 602.6
15	669.1		4.900±0.020	From 1691.2(D)
16	709.6±0.2	709.31	3.417±0.017	1958.1 1248.6
17	713.7±0.3	713.82	5.133±0.021	2039.2 1325.6
18	722.9±0.2	722.78	53.788±0.067	1325.6 602.6
19	735.6±0.4	735.8	0.670±0.008	2693.8 1958.1
20	790.8±0.3	790.8	3.235±0.017	2039.2 1248.6
21	817.1±0.2	816.8	0.251±0.005	2775.1 1958.1
22	856.1±0.3	856.9	0.061±0.002	2182.5 1325.6
23	899.2±0.5	899.8	0.060±0.002	2225.0 1325.6
24	911.5		0.332±0.005	From Ac-228
25	968.3±0.3	968.2	7.227±0.025	2293.9 1325.6
26	976.5±0.3	976.4	0.094±0.003	2225.0 1248.6
27	1045.3±0.3	1045.24	6.419±0.023	2293.9 1248.6
28	1069.0		1.047±0.009	From 2091.3 (D)
29	1180.0		2.359±0.014	From 1691.2 (S)
30	1325.8±0.2	1325.5	4.146±0.019	1325.6 g.s.
31	1355.5±0.2	1355.2	2.693±0.015	1958.1 602.6
32	1368.2±0.4	1368.2	6.014±0.023	2693.8 1325.6
33	1376.0	1376.0	0.602±0.007	2701.6 1325.6
34	1436.8±0.3	1436.7	2.784±0.015	2039.2 602.6
35	1445.1±0.4	1445.2	0.487±0.006	2693.8 1248.6
36	1461.0		1.552±0.011	From K-40
37	1489.1±0.3	1489.0	1.451±0.011	2091.5 602.6
38	1526.5±0.2	1526.3	1.033±0.009	2775.1 1248.6
39	1579.9±0.3	1579.9	0.951±0.009	2182.5 602.6
40	1622.6±0.3	1622.4	0.063±0.002	2225.0 602.6
41	1691.2±0.3	1691.2	100.000±0.092	2293.9 602.6
42	1720.3		0.197±0.004	2322.9 602.6
43	1765.0		0.101±0.003	From Ra-226
44	1918.8±0.2	1918.6	0.088±0.003	2521.5 602.6
45	2038.9±0.3	2039.3	0.116±0.003	2039.2 g.s.
46	2091.3±0.4	2091.0	9.071±0.027	2693.8 602.6
47	2182.3±0.3	2182.6	0.054±0.002	2182.5 g.s.
48	2205.7		0.018±0.001	From Ra-226

Table 2 Branching ratios for transitions from the 2293.9keV, 2039.2 keV, 1958.1 keV, and 1325.6 keV levels in ^{124}Te.

Level energy (keV)	γ-energy (keV)	Branching ratio	
		Present Work	Ref. 7
2293.9	336.0	0.196±0.002	0.079
	968.3	2.740±0.01	1.84
	1045.3	2.490±0.01	1.85
	1691.2	49.000±0.045	49.00
2039.2	713.7	1.310±0.007	2.40
	790.8	0.880±0.004	0.75
	1436.8	1.020±0.007	1.02
	2038.9	0.050±0.001	0.061
1325.6	722.9	13.460±0.015	11.3
	1325.8	1.420±0.006	1.42
1958.1	632.5	0.130±0.003	0.16
	709.6	0.850±0.004	1.43
	1355.5	0.930±0.006	0.93

Table 3 Results of the coincidence measurements

Peak No.	Energy (keV)	Relative Intensity	Transition	
			From	to
1	602.6	500.10±3.4	602.6	g.s.
2	646.0	36.89±0.92	1248.6	602.6
3	669.1	5.15±0.34	From 1691.2 (D)	
4	709.6	2.99±0.26	1958.1	1248.6
5	713.7	5.00±0.57	2039.2	1325.6
6	722.9	49.40±1.07	1325.6	602.6
7	790.8	2.83±0.26	2039.2	1248.6
8	968.3	2.50±0.24	2293.9	1325.6
9	1045.3	6.00±0.37	2293.9	1248.6
10	1325.8	2.89±0.10	1325.6	g.s.
11	1355.5	2.86±0.21	1958.1	602.6
12	1368.2	6.12±0.38	2693.8	1325.6
13	1436.8	2.89±0.20	2039.2	602.6
14	1526.5	1.01±0.16	2775.1	1248.6
15	1691.2	100.00±1.50	2293.9	602.6
16	2091.3	9.41±0.47	2693.8	602.6

Table 5 Results on the measured angular correlation coefficients and anisotropy

Transition	Expermental			Calculated
	A_2	A_4	Anisotropy	Anisotropy
$1249(I_1) \rightarrow 603(2^+) \rightarrow 0(0^+)$	0.100 ± 0.012	0.0081 ± 0.013	0.181 ± 0.095	0.167
$1326(I_1) \rightarrow 603(2^+) \rightarrow 0(0^+)$	0.148 ± 0.025	0.2800 ± 0.030	0.336 ± 0.090	0.386
$2294(I_1) \rightarrow 603(2^+) \rightarrow 0(0^+)$	-0.031 ± 0.016	-0.0002 ± 0.019	-0.013 ± 0.055	-0.046
$2694(I_1) \rightarrow 603(2^+) \rightarrow 0(0^+)$	-0.071 ± 0.021	0 ± 0.035	-0.089 ± 0.176	-0.103

Table 6 Summary of the directional correlation measurements

Transition	Experimental		χ^2	Calculated values					Reference 2	
	A_2	A_4		I_1	L_1	A_2	A_4	δ_1	A_2	A_4
$1249(I_1) \rightarrow 603(2^+) \rightarrow 0(0^+)$	0.100	0.0081	0.174	4	2	0.102	0.0091	0	0.095	0.003
	± 0.012	± 0.013							± 0.001	± 0.011
$1326(I_1) \rightarrow 603(2^+) \rightarrow 0(0^+)$	0.148	0.280	1.48	2	1	0.142	0.302	$-3.5^{a)}$	0.136	0.270
	± 0.025	± 0.030							± 0.009	± 0.015
$2294(I_1) \rightarrow 603(2^+) \rightarrow 0(0^+)$	-0.031	-0.0002	1.716	3	1	-0.0309	-0.0002	$-0.05^{b)}$	-0.068	-0.011
	± 0.016	± 0.019							± 0.005	± 0.011
$2694(I_1) \rightarrow 603(2^+ \rightarrow 0(0^+)$	-0.071	0	0.913	3	1	-0.0714	0	0	-0.067	-0.038
	0.021	0.035							± 0.012	± 0.018

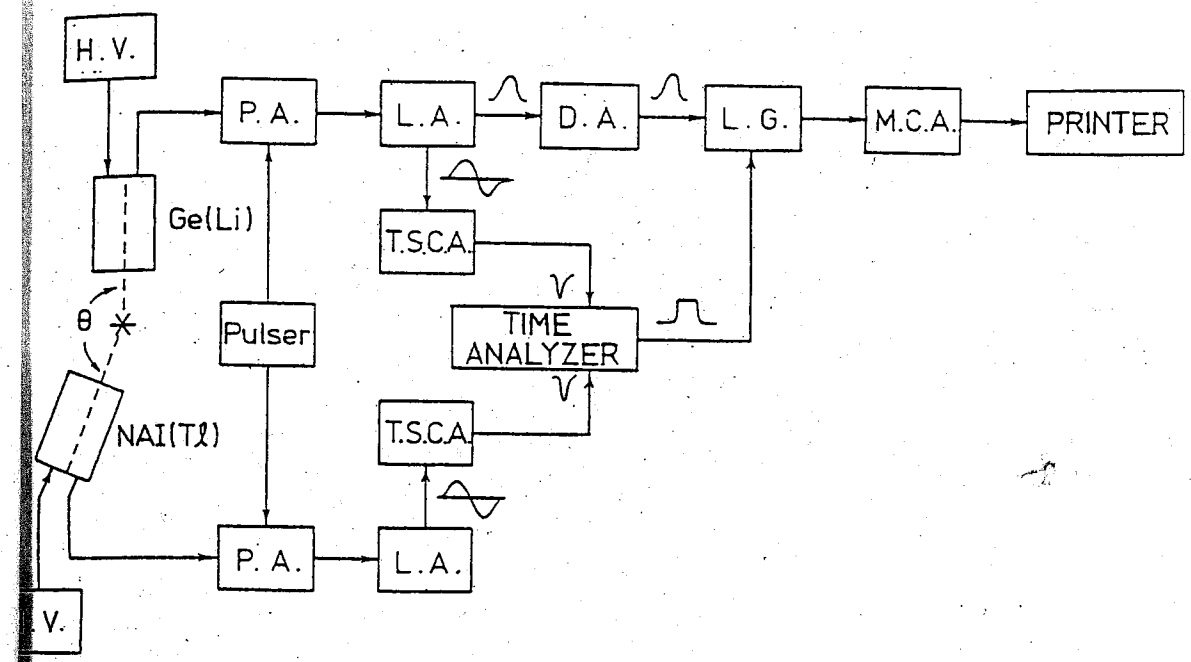

Fig. 1. Block diagram of electronics used in the coincidence measurement.

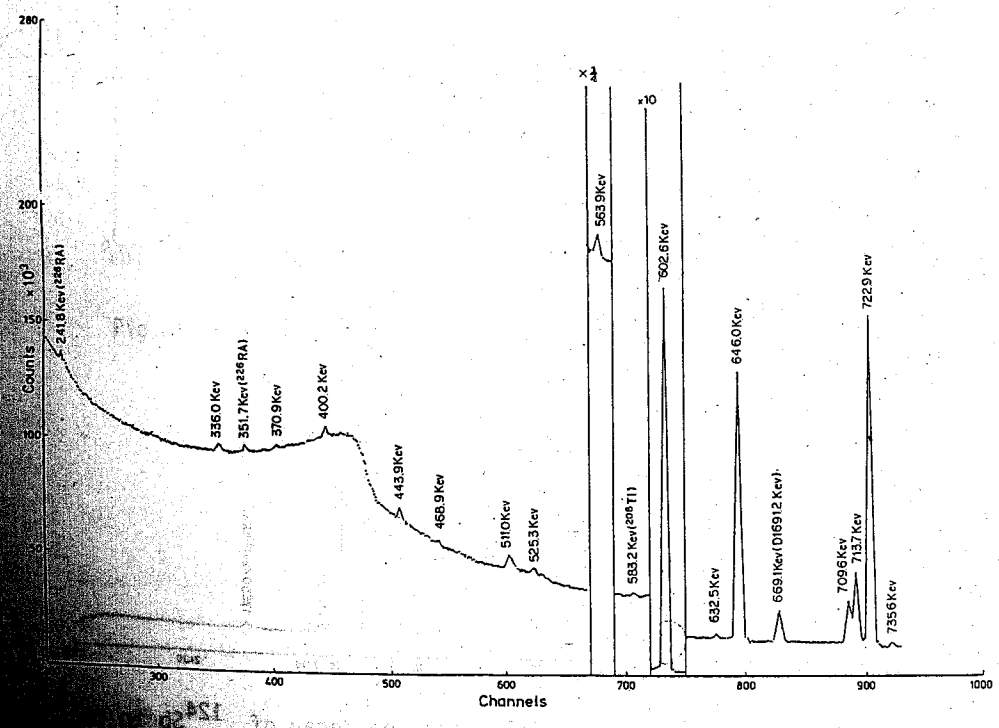

Gamma-ray singles spectrum following the decay of ^{124}Sb in the energy range of 240-740 keV.

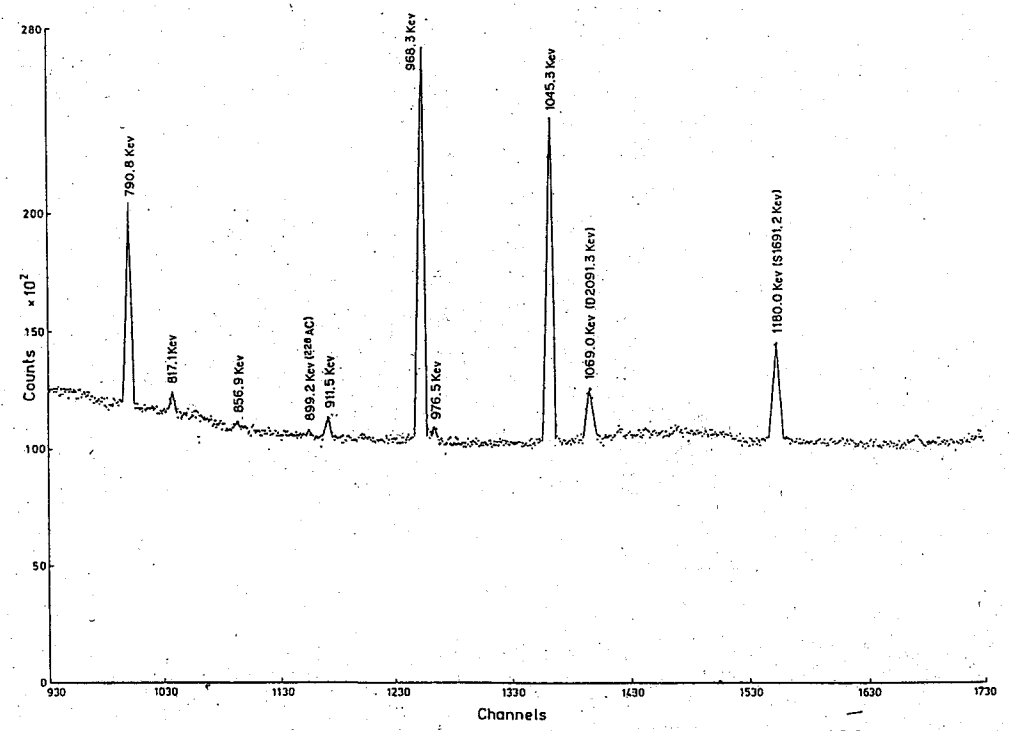

Fig. 3. Gamma-ray singles spectrum following the decay of ^{124}Sb in the energy range 740-1320 keV.

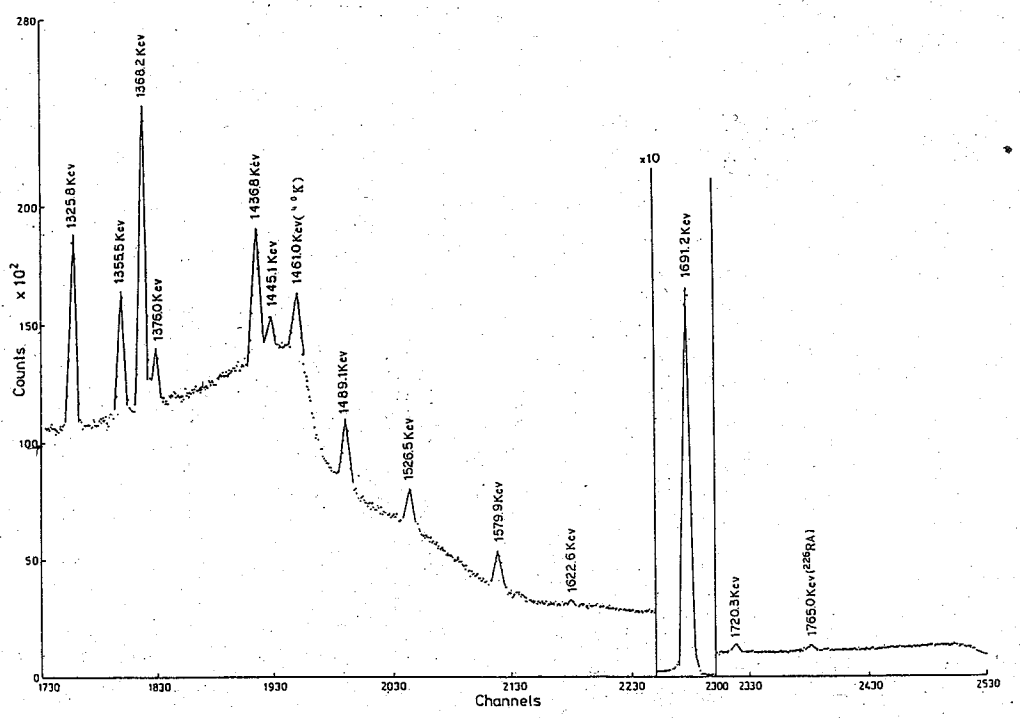

Fig. 4. Gamma-ray singles spectrum following the decay of ^{124}Sb in the energy range of 1320-1890 keV.

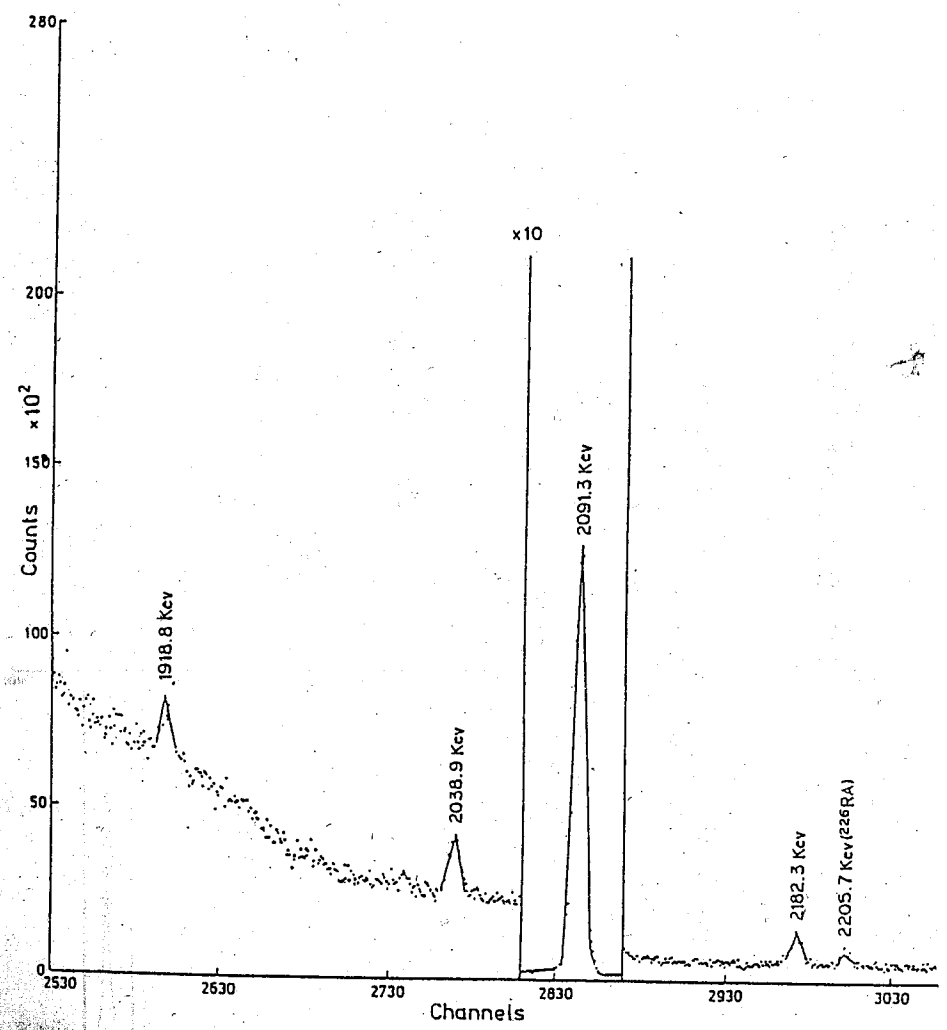

Fig. 5. Gamma-ray singles spectrum following the decay of ^{124}Sb in the energy range of 1890-2230 keV.

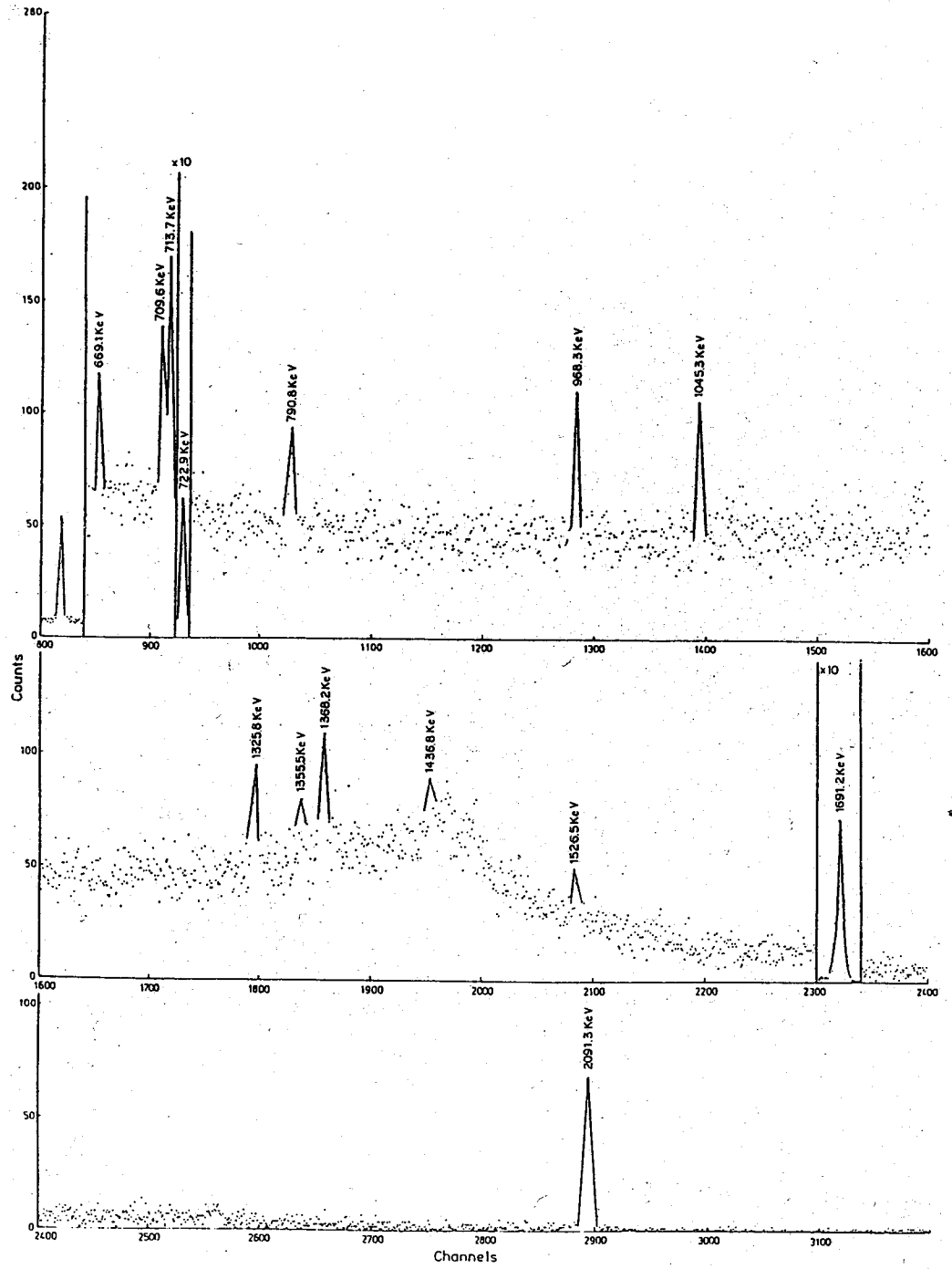

Fig. 6. Gamma-ray coincidence spectrum gated at 602.6 keV.

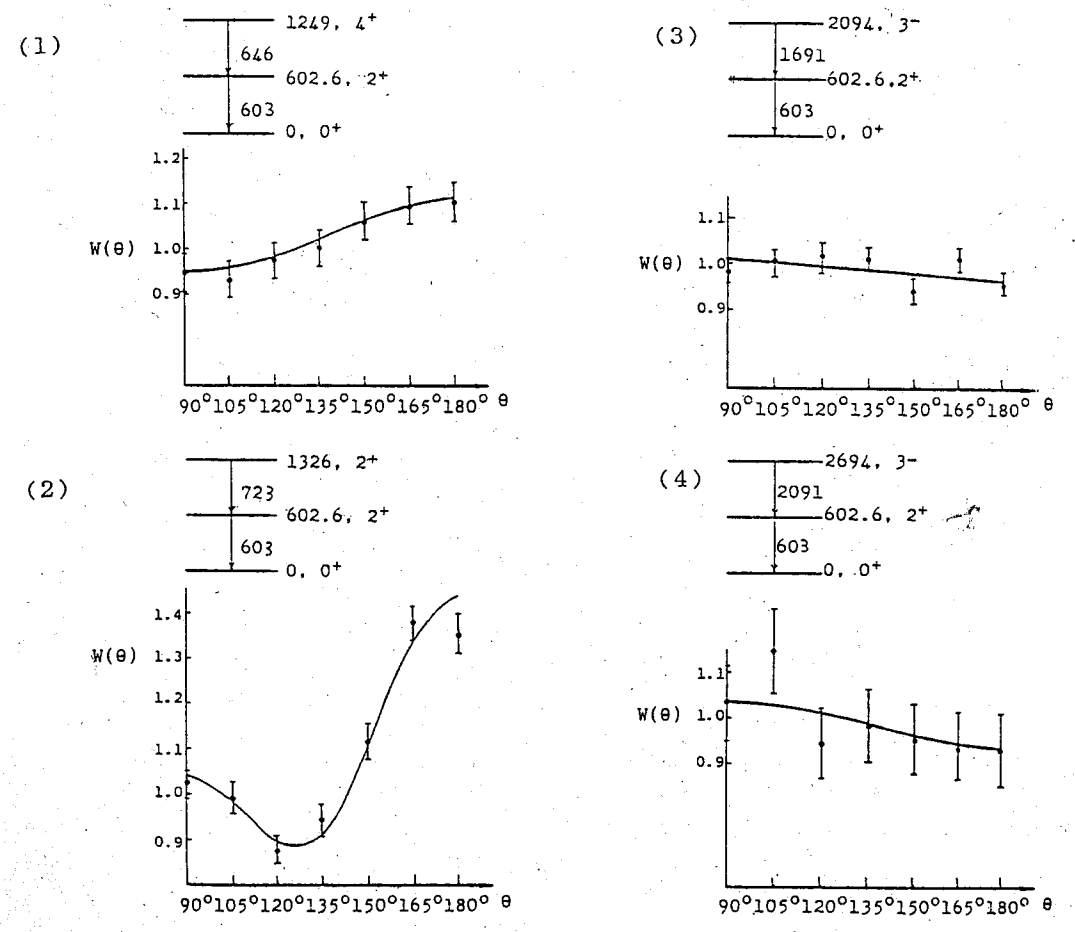

Fig.7. The fitted angular correlation function and the experimental data of (1) 646-603 cascade, (2) 723-603 cascade, (3) 1691-603 cascade, (4) 2091-603 cascadem.

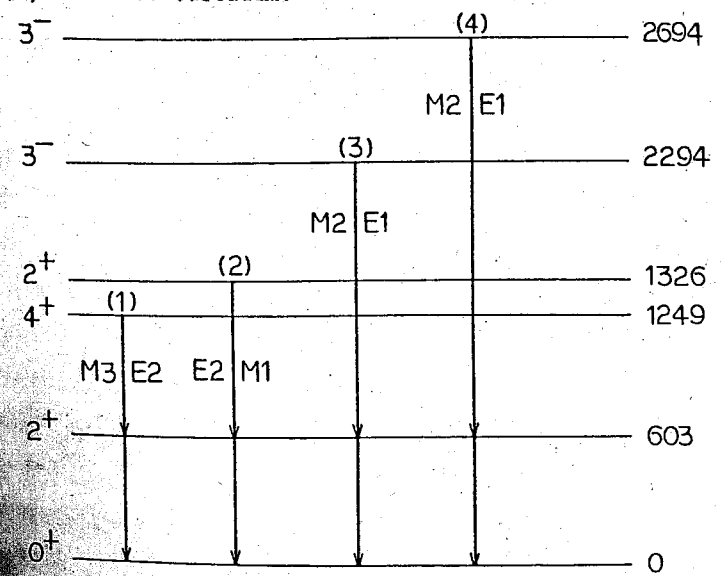

Fig. 8. The ^{124}Te decay scheme from (1) 646-603, (2) 723 -603, (3) 1691-603 and (4) 2091-603 cascades.

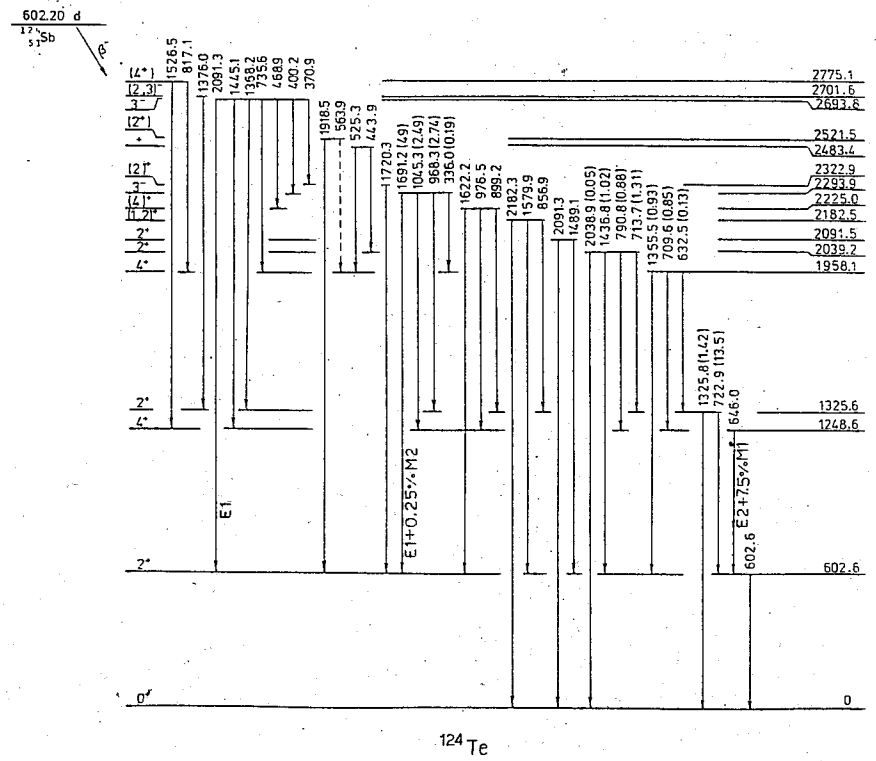

Fig. 9. The decay scheme of ^{124}Te.

本所新建大樓伽瑪背景之分析

王　　定

仲　　慶

摘　要

利用本所原子核小組73c.c HpGe 伽瑪線偵測器量取本所新建大樓三個不同房間之伽瑪背景，可發現有51條伽瑪射線，此51條伽瑪線經分析及確定分別由八個不同放射源所放出，除 ^{40}K 核種外，^{208}Tl，^{212}Bi，^{212}Pb，^{228}Ac來自釷系，^{214}Bi，^{214}Pb，^{224}Ra 來自鈾系。比較分析此三處伽瑪背景，對相同能量而不同房間瑪伽射線間之相對強度其差別不超過15%，其次利用HpGe偵測器對不同能量伽瑪射線之效率關係計算本所大樓伽瑪背景劑量約爲 0.3 9 ± 0.06 毫倫琴／週，遠較一般保健物理所定有關生物反應之許可劑量爲低。

壹、緒　言

宇宙射線及地表所存在之天然放射性核種是伽瑪背景的主要來源。此微量伽瑪背景對人體之影響，到目前爲止還所知有限。一般建築物內伽瑪背景主要來源爲建築材料內之天然放射性核種，主要爲釷（Th）系、鈾（U）系與鉀－40（^{40}K）核種[1]。由於宇宙射線大部份被阻擋於屋外，因此一般室內伽瑪背景劑量較室外爲低[2][3]。對於一般伽瑪放射性或原子核物理實驗室，此微量之伽瑪背景會造成量度伽瑪線譜上之若干嚴重干擾，因此一般伽瑪放射性或原子核物理實驗室均將伽瑪背景之認定及量度作爲必要之工作之一，以免其影響實驗結果之分析。

本所新建大樓於本年(73)七月完成，爲求對原子核實驗室及大樓內其他實驗室之伽瑪背景有一普遍之瞭解，本實驗利用本所原子核小組現有之 73 cc. HpGe 伽瑪偵測器，量度大樓內三個不同房間之伽瑪背景，分析比較此三處伽瑪背景不同能量伽瑪射線間之相對強度，並與已知原舊大樓有關伽瑪背景之資料做一比較，由HPGe 偵測器對不同伽瑪射線之不同效率，計算伽瑪背景之劑量，並列表說明其生物效應之微小。

貳、實驗分析與結果

本實驗利用HPGe高分解力偵測器量取伽瑪背景線譜，此偵測器對 ^{60}Co 1332.47 Kev 伽瑪射線之分解力爲 2.8 KeV，並利用 Canberra Series 80 型多頻道分析儀記錄實驗數據，實驗分三個不同房間量取伽瑪背景線譜。

A室：114 號原子核實驗室

B室：113 號原子核實驗室

C室：大廳

每一室量取伽瑪背景線譜之時間均爲 24 小時。

分析此三室伽瑪背景線譜，均可發現 51 條伽瑪射線，將A室之伽瑪線譜繪於圖一，圖一中括弧內之同位素表示此條伽瑪射線之來源核種，圖一中 238.63 KeV，241.98 KeV 與 1588.3 KeV，1593.3 KeV兩組伽瑪射線係由於偵測器之分解力有限而無法完全分開，將此三組伽瑪線譜，以 1460.75 KeV 伽瑪射線之强度定爲 100 單位，校正每組伽瑪射線間之相對强度，與 1979 年所刋登本所舊大樓有關伽瑪背景之資料[4]作一比較，列於表一，表一中伽瑪射線能量係根據 1978 年所收集 " Table of Isotope " 一書[5]所錄，相對强度之誤差係統計誤差，由表一中來源一欄共可發現八種伽瑪背景來源核種，其中 ^{208}Tl，^{212}Bi，^{212}Pb，^{228}Ac 四核種來自釷系，^{214}Bi，^{214}Pb，^{226}Ra 三核種來自鈾系，表一中所列本所舊大樓資料其伽瑪射線僅發現 18 條，係由於量取伽瑪背景時間不足之故。

由表一中比較A，B，C三室同能量伽瑪射線間之相對强度，發現其差別最多不超過 25 %，比較A，B，C三室有關 1460.95 Kev 伽瑪射線相對强度之比爲 1 : 0.938 : 0.925，以此比值校正A，B，C三室同能量伽瑪射線間之相對强度，取 17 條强度較强之伽瑪射線列於表二，表二中相對强度之誤差亦係統計誤差，由表二可發現A，B，C三室間實際伽瑪背景强度之差別不超過 15 %。

其次假設伽瑪背景線源對圓柱狀偵測器晶體（Crystel）面是均勻的劑量分佈[1]，由 73 cc.HPGe 偵測器對伽瑪光子之效率關係[6]，

$$\ln(EFF) = -0.37(\ln E)^2 + 4.27(\ln E) - 14.4 \quad \cdots\cdots(1)$$

EFF：效率　　E：伽瑪射線能量

計算A室伽瑪背景劑量爲 0.39 毫倫琴 / 週，根據A，B，C三室伽瑪背景相對强度之差別不超過 15 %，故可得本所新建大樓伽瑪背景劑量約爲 0.39 ± 0.06 毫倫琴 / 週，將 1972 年所著 " 保健物理 " 一書[7]有關放射線劑量法與生物反應列於表三，由表三可看出本所大樓內之伽瑪背景劑量距 0.3 倫琴 / 週之許可劑低約 10^{-3} 倍。

參考文獻

(1)熊建華、張賜元著，核子科學，第十九卷，第四期，223 頁（民國七十一年十二月）。

(2) Wayne M. Lowder, Ascher Segall, and William J. Condon, Environmental Radiation Survey in Northern New England, In The Natural Radiation Environment (J. A. S. Adams and A. M. Lowder, Eds.), p.907. Univ. of Chicago Press, Chicago, 1964.

(3) Cecil Pinkerton, William Y. Chen, R. G. Hutchins, and Ralph E. Schrohenloher, Background Radioactivity Monitoring of a Pilot Study Community in Washington Country, Maryland. In The Natural Radiation Environment (J. A. S. Adams and A. M. Lowder, Eds.), p.919, Univ. of Chicago Press, Chicago, 1964.

(4)江紀成等著，中央研究院物理研究所集刋第九卷，31 頁（民國六十八年）

(5) C. Michael Ledever and Virginia S. Shirley, Table of Isotopes (7th ed.), John Wiley & Sons, Inc. New York.

(6)本所原子核組實驗所收集之有關 73 c.c. HPGe偵測器對不同能量伽瑪射線效率資料。

(7)D. J. Rees 著，黃則夫譯，保健物理，228 頁，民國六十一年出版。

表一：新大樓與舊大樓伽瑪背景强度之比較

伽瑪射線能量 (KeV)	相對强度 新建大樓 A室	B室	C室	舊大樓	來源
186.18	7.75 ± 0.08	7.97 ± 0.10	8.49 ± 0.19		^{226}Ra
209.3	5.09 ± 0.06	5.39 ± 0.09	5.26 ± 0.15		^{228}Ac
241.98(238.63)	87.87 ± 0.26	84.48 ± 0.32	89.66 ± 0.61	72.19	^{214}Pb(^{212}Pb)
270.2	6.23 ± 0.07	6.14 ± 0.09	6.43 ± 0.16		^{228}Ac
277.4	3.00 ± 0.05	2.53 ± 0.06	2.66 ± 0.10		^{208}Tl
295.21	19.30 ± 0.12	19.78 ± 0.15	20.24 ± 0.29	36.43	^{214}Pb
300.11	5.00 ± 0.06	5.22 ± 0.08	5.52 ± 0.15		^{212}Pb
327.6	3.91 ± 0.05	4.38 ± 0.07	4.16 ± 0.14		^{228}Ac
338.3	15.83 ± 0.11	15.27 ± 0.14	15.20 ± 0.25	17.16	^{228}Ac
351.92	34.27 ± 0.16	37.19 ± 0.21	36.24 ± 0.39	36.43	^{214}Pb
409.8	1.76 ± 0.04	1.98 ± 0.04	1.83 ± 0.09		^{228}Ac
463.0	5.52 ± 0.06	5.74 ± 0.08	5.09 ± 0.15		^{228}Ac
510.72	17.65 ± 0.11	16.87 ± 0.14	18.80 ± 0.28	29.96	^{208}Tl
562.6	0.86 ± 0.03	0.94 ± 0.03	0.90 ± 0.06		^{228}Ac
583.14	34.62 ± 0.16	33.74 ± 0.21	32.61 ± 0.36	33.65	^{208}Tl
609.31	32.85 ± 0.16	33.65 ± 0.21	36.55 ± 0.39	30.86	^{214}Bi
665.45	1.22 ± 0.03	0.92 ± 0.03	0.98 ± 0.06		^{214}Bi
727.3	7.40 ± 0.07	6.96 ± 0.09	7.71 ± 0.18	11.30	^{212}Bi
768.36	3.87 ± 0.05	3.81 ± 0.06	3.99 ± 0.13		^{214}Bi
786.0	1.78 ± 0.04	2.01 ± 0.05	2.09 ± 0.08		^{214}Pb
795.0	3.74 ± 0.05	4.23 ± 0.07	4.26 ± 0.13		^{228}Ac
806.17	0.73 ± 0.02	0.91 ± 0.03	0.88 ± 0.06		^{214}Bi
835.6	1.06 ± 0.03	0.89 ± 0.03	0.85 ± 0.06	6.31	^{228}Ac
839.2	0.66 ± 0.02	0.72 ± 0.03	0.79 ± 0.06		^{214}Pb
860.4	4.59 ± 0.06	4.55 ± 0.08	4.35 ± 0.13	7.42	^{208}Tl
911.1	24.53 ± 0.14	23.18 ± 0.17	22.85 ± 0.31	18.89	^{228}Ac
934.06	2.00 ± 0.04	2.11 ± 0.05	1.98 ± 0.08		^{214}Bi
968.8	18.79 ± 0.12	18.13 ± 0.15	18.85 ± 0.28	17.24	^{228}Ac
1120.29	8.78 ± 0.08	8.52 ± 0.10	9.11 ± 0.20	7.00	^{214}Bi
1155.19	1.34 ± 0.03	1.31 ± 0.04	1.24 ± 0.07		^{214}Bi
1238.11	4.79 ± 0.06	4.67 ± 0.08	4.81 ± 0.14	3.88	^{214}Bi
1280.96	0.62 ± 0.02	0.78 ± 0.02	0.58 ± 0.05		^{214}Bi
1377.67	1.85 ± 0.04	1.97 ± 0.05	1.63 ± 0.08		^{214}Bi
1407.98	1.25 ± 0.03	1.42 ± 0.04	1.03 ± 0.07		^{214}Bi
1460.75	100	100	100	100	^{40}K
1496.2	0.42 ± 0.02	0.62 ± 0.03	0.54 ± 0.05		^{228}Ac
1509.23	0.95 ± 0.03	1.08 ± 0.04	1.06 ± 0.07		^{214}Bi
1588.3(1593.3)	6.33 ± 0.07	7.11 ± 0.10	7.12 ± 0.17		^{228}Ac(^{208}TlD)
1620.6	0.86 ± 0.03	0.92 ± 0.03	0.90 ± 0.06		^{212}Bi
1630.7	0.94 ± 0.03	1.19 ± 0.04	1.14 ± 0.07		^{228}Ac
1661.3	0.69 ± 0.02	0.84 ± 0.03	0.83 ± 0.06		^{214}Bi
1729.6	1.23 ± 0.03	1.49 ± 0.04	1.47 ± 0.08		^{214}Bi
1764.51	7.55 ± 0.07	7.79 ± 0.10	8.29 ± 0.18	8.84	^{214}Bi
1847.42	1.10 ± 0.03	1.11 ± 0.04	0.98 ± 0.06		^{214}Bi
2103.3	3.53 ± 0.05	3.79 ± 0.07	3.63 ± 0.12	5.21	^{208}Tl S
2118.55	0.49 ± 0.02	0.59 ± 0.03	0.48 ± 0.05		^{214}Bi
2204.21	1.99 ± 0.04	2.24 ± 0.05	2.38 ± 0.10		^{214}Bi
2447.8	0.63 ± 0.02	0.77 ± 0.03	0.83 ± 0.06		^{214}Bi
2614.5	21.43 ± 0.13	22.25 ± 0.17	22.82 ± 0.23		^{208}Tl

表二：A，B，C三室同能量伽瑪背景强度之比較

來源	伽瑪射線能量 (KeV)	相對强度 A室	B室	C室
^{40}K	1460.75	1 ± 0.003	0.938 ± 0,003	0.925 ± 0.006
^{208}Tl	583.14	1 ± 0.005	0.914 ± 0.006	0.871 ± 0.010
	2614.5	1 ± 0.006	0.974 ± 0.007	0.985 ± 0.011
^{212}Bi	727.3	1 ± 0.010	0.882 ± 0.012	0.964 ± 0.023
^{212}Pb	300.11	1 ± 0.012	0.979 ± 0.015	1.021 ± 0.025
^{214}Bi	609.31	1 ± 0.005	0.961 ± 0.006	1.029 ± 0.011
	1120.29	1 ± 0.009	0.910 ± 0.011	0.960 ± 0.021
^{214}Pb	295.21	1 ± 0.006	0.961 ± 0.008	0.970 ± 0.013
	351.92	1 ± 0.005	1.018 ± 0.006	0.978 ± 0.011
^{226}Ra	186.18	1 ± 0.010	0.965 ± 0.012	1.013 ± 0.022
^{228}Ac	209.3	1 ± 0.012	0.993 ± 0.016	0.956 ± 0.027
	270.2	1 ± 0.011	0.924 ± 0.013	0.955 ± 0.024
	338.3	1 ± 0.007	0.905 ± 0.008	0.888 ± 0.014
	463.0	1 ± 0.012	0.975 ± 0.014	0.853 ± 0.025
	911.1	1 ± 0.006	0.886 ± 0.007	0.862 ± 0.011
	968.8	1 ± 0.006	0.905 ± 0.007	0.928 ± 0.013
	1588.3	1 ± 0.012	1.054 ± 0.015	1.040 ± 0.025

表三　放射線劑量法與生物反應

劑量法 劑量，（倫琴）	劑量率	照射情況*	生物反應
0.3	每週	T	可能沒有（許可劑量）
1	每日（年計）	T	白血球減少症
1.5	每週	L	可能沒有（手及手指的許可劑量）
25	單次劑量	L	瘤細胞內的染色體破裂（組織培養）
50-100	累積的小劑量	L	基因突變使得自生率每代增加二倍。
60	單次劑量	L	磷酸活性退化
200	單次劑量	T	噁心
300	單次劑量	L	100kV 的紅斑劑量（小範圍）
300-500	單次劑量	T	男性的 LD_{50}（50 %致死量）
300-600	單次劑量	L（卵巢）	女性絕育
400	單次劑量	L	可逆性脫毛
400-500	10-50 γ/日	T	臨床復原
500	單次劑量	L	200kV 的紅斑劑量（小範圍）
600-800	單次劑量	L（睪丸）	男性絕育
600-900	300γ/日或小劑量		放射線內障
1000	單次劑量	L	鐳的紅斑劑量
1000-1500	200-300γ/日	L	骶阻滯
1000-2500	200-300γ/日	L	顯著的放射性敏感癌反應
1500	200-300γ/日	L（卵巢）	卵巢截除（女性）
1500-2000	200-300γ/日	L	唾腺功能停止
1800-2000	200-300γ/日	L（胃）	胃酸缺乏
2000	單次劑量	L	2MeV 的紅斑劑量
2000-3000	200-300γ/日	L（腎臟）	放射線胃炎
2500-6000	200-300γ/日	L	中等放射線敏感癌反應
2700-3000	單次劑量	L	溼性脫皮，但皮膚會復原：100kV 放射線（小範圍）
3600-5000	200-300γ/日	L	皮膚極限（單門靜脈，200kV，5×5 厘米範圍）
4000-5000	200-300γ/日	L	神經組織極限
5000-6000	200-300γ/日	L	胃腸道極限
5000-7000	200-300γ/日	L	溼性脫皮，但皮膚會復原（單門靜脈 2000 至 3000 kV 放射線，10 × 10 厘米範圍）
～50000	10-100γ/日	L	生癌

*T＝total body（全身）；L＝local（局部）。
＋此處使用的劑量率單位γ/日＝倫琴/日。

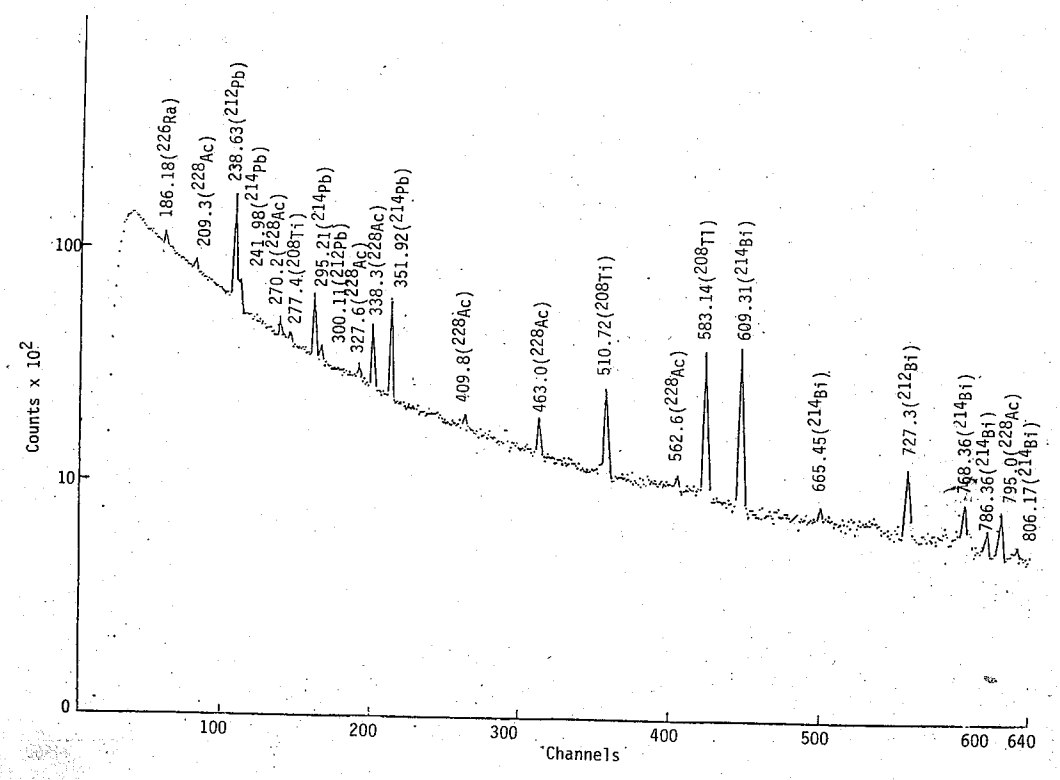

圖一　A室伽瑪背景線譜（180 KeV- 810 KeV）

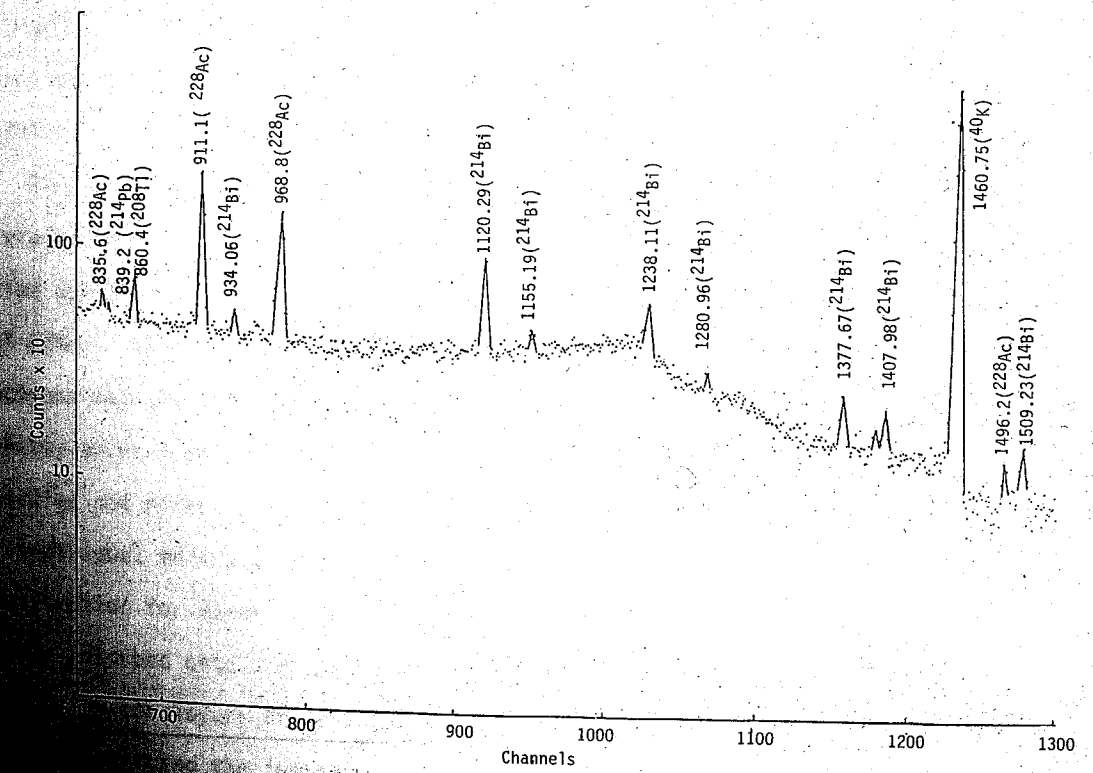

圖一　A室伽瑪背景線譜（810 KeV- 1520 KeV）

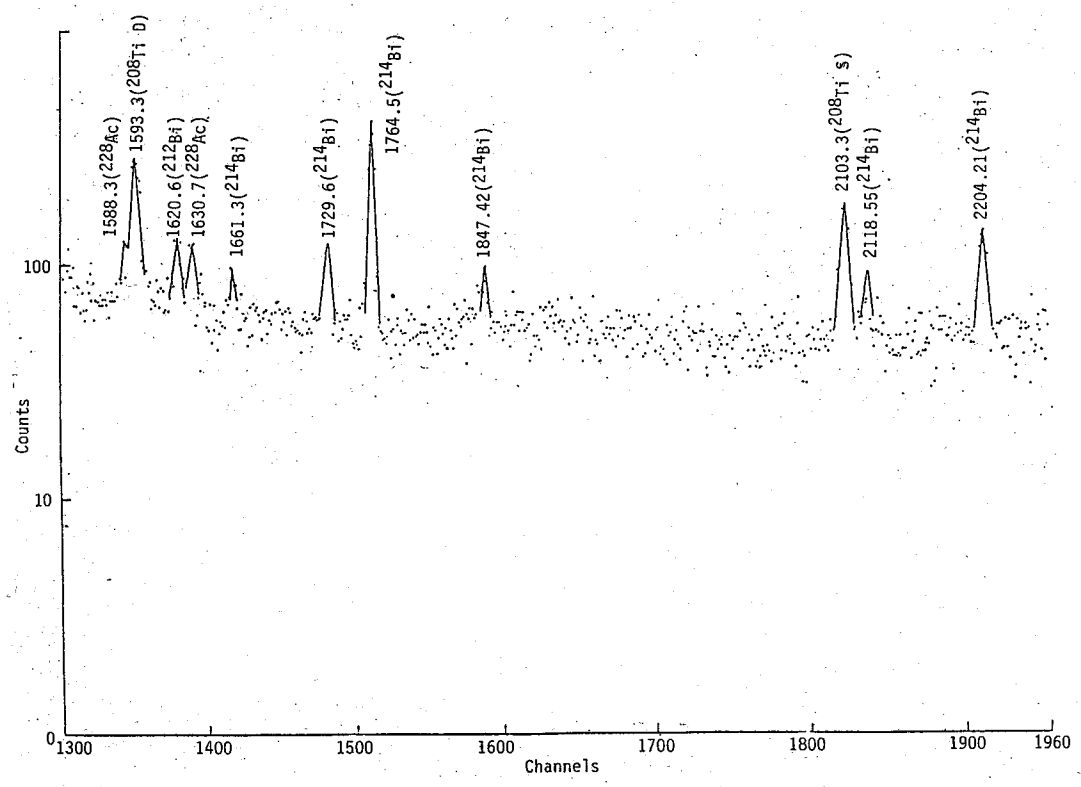

圖一　A室伽瑪背景線譜（1520 KeV - 2230 KeV ）

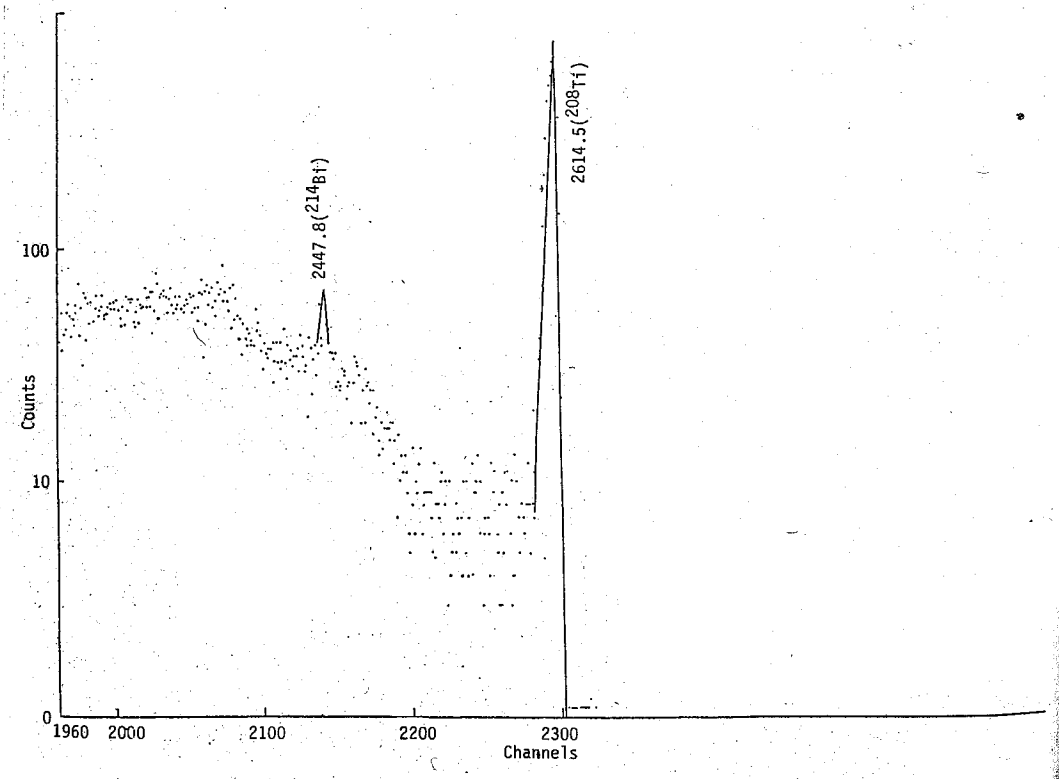

圖一　A室伽瑪背景線譜（2230 KeV - 2620 KeV ）

A NEW THEORY OF SURFACE ENHANCED RAMAN SCATTERING

Chun Chiang

Institute of Physics Academia Sinica

Nankang, Taipei, Taiwan, R. O. C.

It is proposed that the π electrons of p-orbitals in the adsorbed melecules may delocalize via the metal, thus the electrons excited by the photon impacted on the molecule may not only provoke Raman scattering in that particular molecule, but may also delocalize to other molecules and provoke Raman scattering in other molecules. This increases the effective cross section and leads to the enhancement of the Raman scattering. Many data may be explained with the present theory.

Since the discoverty of intensive Raman line of pyridine molecules adsorbed on the silver electrode (1), intensive effort has been directed to elucidate this surface enhanced Raman scattering (SERS). Many theories have been proposed for its explanation, see for example reference (2, 3), no theory seems to have been accepted overwhelmingly. Here we would like to propose a simple mechanism for its explanation.

When molecules are adsorbed onto the metal such as Ag, Au, Cu, etc., if the molecules have the lone pair electrons or π electrons, these electrons may delocalize and transmit through the metal medium so that they may interact and influence each other. When these electrons in a single molecule are excited, the excited electrons may transmit to other molecules via metal as well. Thus not only the directly excited molecule will contribute to the Raman intensity, other adsorbed molecules not directly excited may also contribute to the Raman intensity, namely, individual molecules become effectively a "giant molecule" and the effective cross section for Raman scattering is increased. Since large amount of molecules adsorbed onto the metal, thus an intensity enhancement factor of 10^6 may be monolayers of molecules adsorbed. Also, the metal surface provides an ing the photons, which can also excite the electrons. These excited grate to the adsorbed molecules and contribute to the Raman singnals,

leading to SERS. The proposal that the electrons are delocalized in the system also predicts that the polarizability of the molecules is increased, since ample electrons can be supplied in response to any change of field or environments. This also contribute to the SERS.

The exact interaction between the adsorbed molecules and metal may vary case by case, the π electrons of the molecules may form a π complex with the metal or the lone pair of the molecule may donate a bond to the metal or the electrons may turnel through the barrier. However, as long as the electrons can delocalize in the molecule and migrate or tunel to the metal, and in turn, the carriers in metal may also migrate or turnel to the adsorbed molecules, the SERS will be exhibited. For this reason, the best molecules showing this SERS are those with π electron double bond, especially those with conjugated double bond.

For effective communication of electrons between adsorbed molecules and metal, the surface properties, especially, the surface charge, will play an important role. The residue charges on the surface can attract the molecules, and facilate the electronic delocalization of electron between the molecules and the metal, thus electronically processed surface shows SERS. The electrons may also deposit on top of the metal surface curvature, this is also the reason why irregular surface shows larger enhancement of Raman signals.

The present theory relies on the delocalization of electrons among various molecules adsorbed. Thus the recent discovery (14, 15) that the SERS may be due to the carbonized non-crystalline phase between the pyridine and the metal can be easily incorporated within this theory, since the carbonized phase can also provide a means for the delocalization of electrons.

This simple theory may explain or predict many other experimental data as follows:

1. Since it is the π electron of the double bond which delocalizes and comunicates within the system, the SERS effect will be stronger for the vibration mode of the atoms having the π electrons. Thus the double bond or triple bond strechi will show strong enhancement, whereas the C-H vibration in the same molecule show litter enhancement. Also, CH_4 and C_2H_6 should not show SERS. These a indeed observed (4, 5).

2. Since the delocalized electrons can migrate freely to various location, the energy fluctuation would be larger. Also, due to the interaction among the molecules and between the molecule and the metal, the energy state will be broadened and SERS spectrum will be broadened as indeed observed by Moskovits and DiLella (4, 5). Metiu and Palk have suggested the possibility of coupling of the molecular vibration to the electronic degrees of freedom of the matal (6), but no dotail has been given yet. From another point of view, the photons in a single adsorbed molecule is trapped in that single molecule, thus its life time is longer, whereas, the photons in "giant molecule" can transport to other site and makes transition there, the increased possibility of transition makes the life time smaller. Concequently, the SERS spectrum will be broadened. That the electron transition in adsorbed molecules will display shorter lifetimes and lower energies has been reviewed befoere (8), the present theory emphisizes further the interaction among the adsorbed molecules as a source of broadening.
3. It is observed that for several layers of alkene molecules adsorbed on metal, besides a very enhanced, broadened and shifted peck, there is also a weaker, unbroadened, unshifted peck located at the same frequency as in polycrystaline material (5). The very much enhanced, shifted peck may be explained by the conjugated "giant molecule"; the delocalization of electrons in double bond will lessen the double bond character and the double bond vibration frequency will be shifted to the lower value. The unshifted pack may be explained as due to the local field such as image field effect (9, 10) or surface plasmon effect (4), which may not only acting at the first lager, but acting at second or third layer as well. These effects are weaker and may not necessarily cause broadening of frequency shifting.

According to the present theory, the larger is the size of the metal substrate, the more is the molecules adsorbed, and the more enhancement is the scattering. However, it should note that the larger is the size of the metal, the more po- will be the dissipation of the excited electrons in the bulk of the Thus there is an optimum size for which the SERS will be the maximum. (7) have found that the films which show the largest Raman signals of isolated islands of approximatly 200-400A dimensions. Taking

the surface area as 5×10^5 Å^2 and the attached molecule area as 10 Å^2 the number of adsorbed molecules is 5×10^4 and this is approxcimatly the SERS enhancement factor. The possibility that the energy of the excited delocalized electrons may also be dissipated in the metal matrix explains the fact that the background Raman continum intensity is also increased.

5. If the photons or excited electrons involve in other optical process such as luminescence or absorption, then this luminescence or absorption should also be enhanced. This is indeed observed (11, 12, 13).

In Conclusion, by proposing that the electrons in the adsorbed molecules may delocalize so that all the individual moleules may effectively becomes a "giant molecule", the SERS may be explained. Many data may be explained with this idea.

REFERENCES

(1) M. Fleischmann, P. J. Hendra, A. J. McQuillan, Chem. Phys. Lett. 26, 123 (1974).

(2) T. E. Furtak, J. Reyes, Surf. Sci. 93, 351 (1980).

(3) R. K. Chang, T. E. Furtak, Ed. Surface Enhanced Raman Scattering, Plenum, New York (1982).

(4) M. Moskovits and D. P. DiLella, Chem. Phys. Lett. 73, 500 (1980).

(5) M. Moskovits and D. P. DiLella, in Surface Enhanced Raman Scattering, Ed. Chang, Furtak, Plenum, New York pp.243 (1982).

(6) H. Metiu and E. Palke, J. Chem. Phys, 69, 2574 (1978).

(7) J. G. Bergman, D. S. Chemla, P. F. Liao, A. M. Glass, A. Pinczuk, R. M. Hart and D. H. Olson, Opt. Lett, 6, 33 (1981).

(8) R. R. Chance, A. Prock and Sibley in: Advances in Chemical Physics, Vol. 37, Eds. I. Prigogine and S. Rice (1978) p.1.

(9) F. W. King, R. P. Van Duyne and G. C. Schatz, J. Chem. Phys, 69, 4472 (1978).

(10) S. Efrima and H. Metiu, Chem. Phys. Letters 60, 59 (1978).

(11) G. Ritchie, E. Burstein and R. B. Stephens, Bull. Am. Phys. Soc. 26, 359 (198

(12) A. Hartstein, J. R. Kirtley, and J. G. Tsang, Phys. Rev. Lett. 45, 201 (1980)

(13) A. M. Glass, P. F. Liao, J. G. Bergman and D. A. Olson, Opt. Lett, 5, 368 (19

(14) R. P. Cooney, M. W. Howard, M. R. Mahoney and T. P. Mernagh, Chem. Phys. Let 79, 459 (1981).

(15) T. P. Mernagh and R. P. Cooney, J. Raman Spectroscopy, 14, 138 (1983).

ATOMIC AND ELECTRONIC PROCESSES OF SWITCHING IN AMORPHOUS THIN FILMS*

Chun Chiang

Institute of Physics Academia Sinica

Nankang, Taipei, Taiwan, R. O. C.

It is proposed that the conversion of C_3° from C_2° leads to the switching. Since C_3° has more connection points, the conductivity of C_3° is higher and large current favours the C_3° species; thus increasing the current increas the C_3° density and less voltage is needed to sustain the same amount of current. This explains the S shaped negative resistance. The concept is simple and the mathematics for quantitative calculation is manageable.

Switching in amorphous thin films is an important phenomenon. Despite its intensive research[1] its explaination is still a controversy.

Recently, Kastner et. al.[2] propose an important concept of valence alteration pair (VAP) to explain the properties of Chalcogenide amorphous thin films. Using this concept, Petersen and Adler[6] propose that if certain minimum amount of valence alternational pairs are present, the Mott transition may be initiated by carrier generation induced by field to form the C_3° band by the reaction $C_3^+ + e^- \rightarrow$ C_2° or $C_1^- + e^+ \rightarrow C_3^\circ$, thus producing the high conductivity state; below a critical VAP density, no switching can occur. The carrier density in the ON state is independent of the VAP density, however, the current in ON state increases with filament size. Also, Adler et. al.,[3] propose that the field-induced carrier generation can neutralize the charge traps(C_3^+, C_1^-), when all the traps are filled carriers can transit the sample with an enhanced mobility andthe generation power required to keep the traps filled is reduced. The carrier is dependent on electrode (no interband generation) and the filment growth with area to maintain constant current density. Since both of these models depends on the carrier generation by field induction, it seems that S shaped negative conductance may not be one of these mechanism.

---

* Physics Letters, 1984.

The purpose of this letter is to propose another mechanism, which utilizes the concept of VAP in another form. The mechanism proposed is the current mediated conversion of C_2° and C_3°, where C_2° and C_3° represent the chalcogenide elements with two bonds and three bonds respectively. In the normal state, C_2° is the lowest neutral state, however, two neighboring C_2° may interact such that C_3° are formed

$$2\,C_2^\circ \rightleftarrows 2\,C_3^\circ\,(e^*) \qquad (1a)$$

where the star indicates that the neutral C_3° has an electron in high energy state (antibonding state in this case). This electron may further transport to other low energy site such as the dangling bond and release the energy

$$2\,C_3^\circ\,(e^*) \rightarrow 2\,C_3^+ + 2\,e + \text{energy} \qquad (1b)$$

Two neighboring C_2° may also react to form one C_3° and one dangling bond such as

$$2\,C_2^\circ \rightleftarrows C_3^\circ\,(e^*) + C_1^\circ \qquad (2a)$$

The high energy state electron also can transport to C_1° and release the energy

$$C_3^\circ\,(e^*) + C_1^\circ \rightarrow C_3^+ + C_1^- + \text{energy} \qquad (2b)$$

Eqs. (1) and (2) may also be expressed in a diagramatic way in Fig. 1.

In the normal film in OFF state, there are certain number of C_2° elements with bond strain or being too much crowded, so that Eq. (1) proceeds to the right and energy is released. Also there are certain number of atoms located far away in the forming process such that dangling bonds are formed, namely,

$$C_2^\circ \rightarrow 2\,C_1^\circ \qquad (3)$$

Since there are equal probability for the atoms to be displaced too crowdly or too loosely, thus equal number of C_3^+ and C_1^- will be formed from Eqs. (1) and (3). Eq. (2) also produces equal number of C_3^+ and C_1^-. The electrons in C_3^+, C_1^- and C_2° in OFF state are all paired, thus this can explain the observed data that no EPR signals are observed in chalcogenide film.

If passing current through the film, the electrons in C_1^- is excited to the excited state or conduction band, Eqs. (1b) and (2b) are essentially reversed; namely, energy is provided such that electron is excited into the high energy anti-bonding state C_3°. Since C_3° lattice has more connection points with other species this is the low resistance path and electrons will choose C_3° lattice as the conducting path. If no C_3° path is available, the electron has to pass through lattice via hopping process and the local energy will be higher and this is the

preferable path. As more current passing through the film, the C_3° lattice will be used up and more current has to use the C_2° species as conducting path. However, since a large excitation energy is needed for the electron to be excited into the conduction band and since C_2° species have less connection points, its conductivity is less; thus, by passing equal amount of current through the film, the local energy via the path of C_2° lattice is higher than that via the path of C_3° lattice. For this reasons, the film prefers the C_3° lattice and the C_2° species will be transformed to C_3° species according to Eq. (1a) or (2a) and depending on the environment of neighboring atoms. This kind of transformation may be termed current mediated structure transformation. This idea may be put in an equation as

$$F(I) + 2C_2^\circ \rightleftarrows G(I) + 2C_3^\circ \qquad (4)$$

where F(I) and G(I) represent the energy produced when current passing through C_2° lattice or C_3° lattice respectively. Since the electron in C_3° species is in excited state already and also its resistivity is less, thus $G(I) < F(I)$, and higher current favours the C_3° species and Eq. (4) proceeds to the right. Furthermore, a film with more C_3° species will have less resistivity and less voltage drop, thus increasing the current will increase the C_3° species and decrease the voltage drop. When most of the C_2° species have been transformed to C_3° species, then increasing the current will increase the voltage drop again. This mechanism explains the S shaped negative conductance satisfactorily. Note that in this transformation process, only electronic bonding is changing and not much atomic displacement is involved, thus the process can be very fast. If relatively large atom displacement is involved, then permenent change may occure such as in memory process or the forming process.

In a film the high energy stress occurs near the boundary between C_2° and C_3° species, the C_2° near the C_3° has high tendency to transform to C_3°, thus C_3° will [illegible] nucleus and a conducting filament will be formed before the switching starts. [illegible] initiation of switching process, the filament will grow in size with current [illegible] transformed to C_3° around the C_3° filament and the voltage will drop. [illegible] state consistes mostly the C_2° and equal number of C_3^+ and C_1^-; the [illegible] consistes mostly the C_3° species; in the S shaped negative conductance [illegible] consists a mixture of C_2° and C_3°. The properties of ON and OFF [illegible] in following table:

State	ON State	Off State	Mixed State
Species	C_3°	C_2° , C_3^+, C_1^-	C_3° , C_2°
Excitation Energy	Little or non (electron in anti-bonding orbital)	Large (from lone pair to conduction band)	Medium
Carriers	More	Less	Medium
Connection Network	Three connection points	Two connection points in average	Medium
Conductivity	Large	Small	Medium
dI/dV	Positive	Positive	Negative

Chiang[4, 5] previously has formulated a quantitative switching theory by proposing two configurations co-exist in the film. The theory was able to explain many experimental data such as delay time, triensient ON characteristics, etc.. The present communication provides the specific details about the species of the configuations. These configurations are also consistant with the other properties such as no EPR signal is observed and the conductivity is of $e^{-E/KT}$ type. The major difference between this theory and those proposed by Adler et al[3] and Peterson and Adler[2] is that the present theory depends on the conversion of C_2° to C_3° , the excitation and traping of C_3^+ and C_1^- determine only the conduction in OFF state but may contribute very little to the switching process. On the other hand, those by Adler et al and Peterson and Adler depend on a fixed minimum amount of C_3^+ and C_1^- pairs present in the OFF state, below which no switching can occur; the number of the pairs is not changed, however, the excitation of C_3^+ and C_1^- species or the conversion of C_3° from C_3^+ and C_1^- , not from C_2° , leads to switching. Also in the present theory, the growth of filament size determines the S shaped negative conductance, and it is a mixture state of C_3° and C_2° ; however, the other theory conjecture on the growth of filament size with the current in the ON state and it is not quite clear how does the S shaped negative conductance occur.

In conclusion, a structure conversion induced by current is proposed, the concept is simple and the mathematics is managable and it is able to explain many experimental data.

REFERENCES

1) D. Adler, H. Henisch, N. Mott, Rev. Mod. Phys. 50, 209 (1978).

2) M. Kastner, D. Adler, and H. Fritzsche, Phys. Rev. Lett. 37, 1504 (1976).

3) D. Adler, M. S. Shur, M. Silver, S. R. Ovshinsky, J. Appl. Phys. 51(b), 3289 (1980).

4) C. Chiang, Phys, Stat. Sol. (a) 54, 735 (1979).

5) C. Chiang, Sol. Stat. Comm. 39, 111 (1981).

6) K. E. Petersen and D. Adler, J. Appl. Phys. 50, 5065 (1979).

FIGURE LEGEND

Fig. 1. (a) A diagramatic representation of Eq. (1a).
(b) A diagramatic representation of Eq. (2a). The lone pair is represented by two dots and the & represents the electron in high energy anti-bonding state.

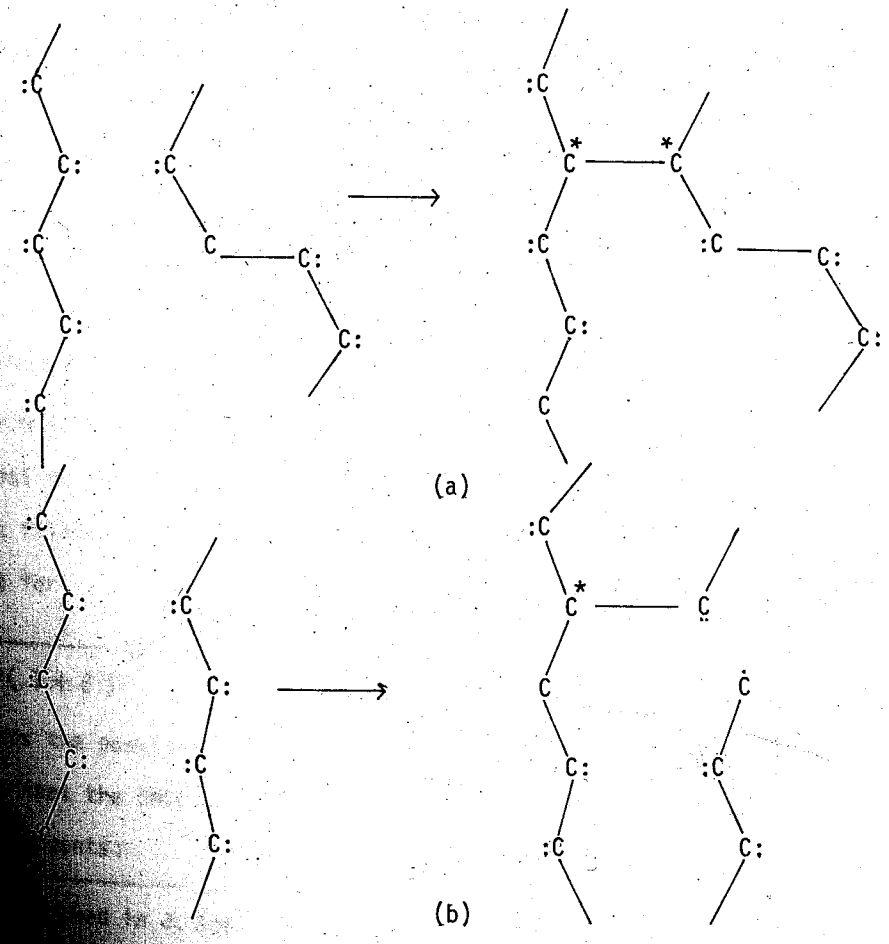

ON TRAPPING AND SWITCHING IN SEMICONDUCTORS: A COMMENT*

Chun Chiang
Institute of Physics Academia Sinica
Nankang, Taipei, Taiwan, R. O. C.

Adler et al. propose that field-induced filling of traps may lead to S shaped negative differential conductance, and using the existance of two solutions of electron concentration for a given applied field as evidence for it. We comment on the conditions for this existance of two solutions and its significance to the SNDC

Intensive effort has been directed to the elucidation of switching mechanism of amorphous thin films. Recently, Adler et al[1] have proposed that the field-induced filling of positively and negatively charged traps may lead to S shaped negative differential conductance (SNDC). Using the hypotheses that the field induced generation rate of electron hole pair is equal to the rate of electronic filling to the acceptor or the rate of hole filling to the negative traps, they derived the following equations

$$P/N|_{\pm} = \frac{1}{2}(\lambda^{-1} - 1 - \xi) \pm \{[\frac{1}{2}(\lambda^{-1} - 1 - \xi)]^2 - \xi\}^{\frac{1}{2}} \qquad (1)$$

and

$$N = [N_0 + \lambda(1 \mp P/N)]/[1 - (P/N)] \qquad (2)$$

where P or N is proportional to the concentration of holes or electrons, λ is proportional to field, N_0 is a constant and ξ is the ratio of the rate of electronic filling to the rate of the hole filling to the traps. From this, they claim that for

$$\frac{1}{2(1+\xi)} \leqq \lambda \leqq \frac{1}{[1+\xi^{\frac{1}{2}}]^2} \qquad (3)$$

exists the possibility of two solutions for P or N at a given λ, thus ing that the SNDC characteristics is present. We like, however, to make comments:

---

shed in J. Appl. Phys. (1984).

1. According to their mathematical derivation, the condition for the existance of two possible solutions for P or N should be

$$\frac{1}{2(1+\xi)} < \lambda < \frac{1}{[1+\xi^{\frac{1}{2}}]^2}, \quad \xi < 1 \tag{4}$$

Namely, the equal signs in Eq. (3) should be droped and the condition that $\xi < 1$ should be imposed. Fig. 1 (a) or 1(b) is a plot of Eq. (2) with ξ = 5 or 0.5 respectively, it can be seen that two positive solutions do not exist in Fig. 1(a). Note that two negative solutions exist for $0.083 < \lambda < 0.095$ but physically is not possible. Fig. 1(b) indicates that two positive solutions exist for $0.33 < \lambda < 0.34$. There are solutions existing in other region of λ, however N or P is either negative or imaginary and is physically impossible, thus it is not ploted in the diagram.

2. There are certain regions where no solution exists, indicating that the mechanism breaks dawn and is unrealistic, thus cast serious doubts of the validity of their mechanism.

3. Adler et al[1] claim that the existance of two possible solutions for a given λ indicates that the SNDC characteristic is present; however, the existance of two possible solutions only indicate that the NDC characteristic is present and is not sufficient to explain the whole story of SNDC. To fully explain the SNDC, it is required to demonstrate that three possible solutions should exist for a given λ, rather than two (as shown in their Fig. 8). A switching equation for amorphous thin films with three possible solutions for a given value of field has been derived[2], also, this equation has solution for all region of field and seems to have beteer ability to elucidate the switching mechanism.

REFERENCES

(1) D. Adler, M. S. Shur, M. Silver, S. R. Ovshinsky, J. Appl. Phys. 51, (6), 328 (1980).

(2) C. Chiang, Physica Status Solidi (a) 54, 735 (1979).

FIGURE LEGEND

Fig. 1. Plot of equation (2) with N_o = 0.07. For 1(a), ξ = 5, for 1(b), ξ =0.5.

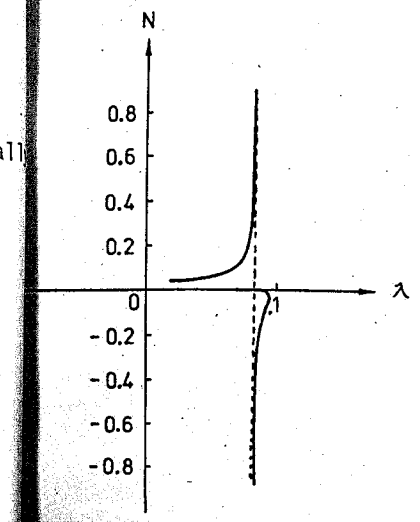

Fig. 1(a)

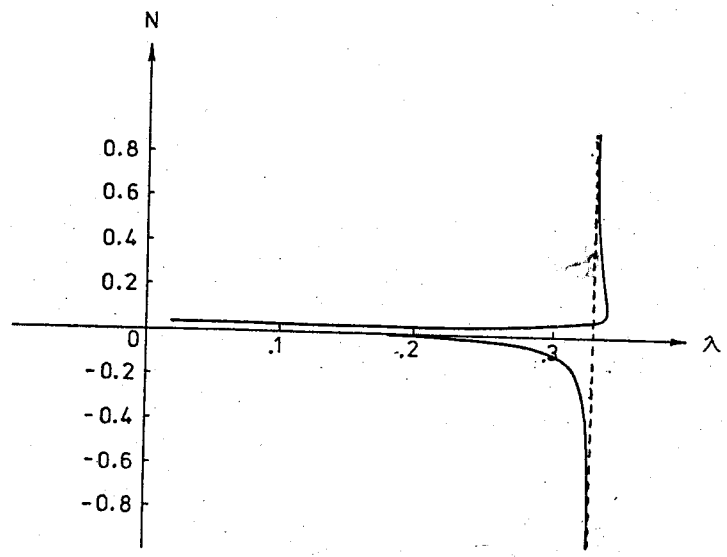

Fig. 1(b)

LONG-WAVELENGTH LATTICE VIBRATIONS OF CRYSTALLINE HCl AND HBr

Chia-Nan Chang (1), and Wan-Sun Tse(2)

Department of Electronic Engineering and Technology,

National Taiwan Institute of Technology(1) and Institute

of Physics, Academia Sinica, Nankang, Taipei, Taiwan, R. O. C. (2)

Lattice dynamics calculations of crystalline orthorhomic HCl and HBr in phase III are studied by using the Born-Von Karman model with seven interactomic force constants which is capable of giving good agreement between the observed and calculated zone centre ($\vec{q} \simeq 0$) frequencies. The calculated results show that the forces between atoms in different chains and different planes are much weaker than those between nearest neighbors in the same linear chain.

1. INTRODUCTION

Solid HCl and HBr are isomorphic molecular crystals which has been the subject of several experimental and throretical studies[1-7]. They both have three solid phases[1]. In phase I and II, the hydrogen atoms are disorded and the unit cell has 4 molecules. In the low temperature phase III, the hydrogens are fully ordered and the crystal structure is ordered orthorhombic with space group C_{2v}^{12} ($Bb2_1m$) The molecules form planar zig-zag hydrogenbonded chains, with two molecules in the primitive unit cell on sites of Cs symmetry. The three-dimensional structure of these zig-zag chains is shown in figure 1.

Based on a group theoretical analysis[2], the lattice and stretching vibrations for $q = 0$ of these crystals are classified into twelve non-degenerate normal modes in accordance with their symmetries. There are three translational ($A_1 + B_1 + A_2$) four librational modes ($A_1 + B_1 + A_2 + B_2$) corresponding to the external ons of rigid molecules. In addition, there are also two stretching modes $+ B_1$) . The A_1 mode is the in-plane vibration of the two molecules cell and is totally symmetric. The B_1 mode is the antisymmetric hich alternate molecules are exactly out of phase.

s been two major methods of long-wavelength lattice dynamics calculation

of crystalline HCl and HBr. The first one[3], using the Buckingham exp-six potential considers the angular force of bonds indirectly by placing a point charge on each at of the bonds and is complex in calculation. The second one[4], using the Born-Von Karman harmonic potential, neglects all the forces between the atoms in different zig-zag chains and is not physically appealing. In this paper, a simple three dimensional model is proposed. This model takes into account the atomic forces between atoms of adjacent zig-zag chains and considers the angular forces of bonds directly. The parameters of this model are adjusted to attempt to interpret those normal modes of vibrations obtained from spectroscopic techniques[1-2].

In section2, the model of the long-wavelength lattice dynamics calculation of a crystal is developed and then the parameters of the model adopted are explained. In section 3, the calculated results and discussions are presented.

2. THEORY AND MODEL ADOPTED

As a result of thermal fluctuations, each atom in a crystal is displaced from its equilibrium position by a small amount $\vec{u}\begin{pmatrix}\mu\\ \ell\\ k\end{pmatrix}$ where $\vec{u}\begin{pmatrix}\mu\\ \ell\\ k\end{pmatrix}$ represents the displacement of the ℓ^{th} atom of the k^{th} kind in the μ^{th} cell of the crystal. In the Born-Von Karman's approximation of harmonic force between atoms in a crystal, the equations of motion for each atom of the crystal are

$$M_k \ddot{u}_\alpha \begin{pmatrix}\mu\\ \ell\\ k\end{pmatrix} = - \sum_{\mu',\ell',k',\beta} \phi_{\alpha\beta} \begin{pmatrix}\mu & \mu'\\ \ell & \ell'\\ k\ ; & k'\end{pmatrix} u_\beta \begin{pmatrix}\mu'\\ \ell'\\ k'\end{pmatrix} \tag{1}$$

where $\phi_{\alpha\beta}\begin{pmatrix}\mu & \mu'\\ \ell & \ell'\\ k\ ; & k'\end{pmatrix}$ is the negative of the force exerted in the α-direction on the atom $\begin{pmatrix}\mu\\ \ell\\ k\end{pmatrix}$ when atom $\begin{pmatrix}\mu'\\ \ell'\\ k'\end{pmatrix}$ is displaced a unit distance in the β-direction all other atoms being kept at their equilibrium position.

As usual, we choose the displacement $u\begin{pmatrix}\mu\\ \ell\\ k\end{pmatrix}$ in a travelling-wave form of wavevector $\vec{q}$ with its corresponding amplitude independent of the cell (μ)[8][9]. In the long wavelength limit ($\vec{q} = 0$) and for nontrivial solutions of the various amplitudes in each unit cell, we can obtain the following secular equation for the crystal as

$$\left| D_{\alpha\beta}\begin{pmatrix}\mu & \mu'\\ \ell & \ell'\\ k\ ; & k'\end{pmatrix} - \omega^2\, \delta_{\alpha\beta}\, \delta_{\ell\ell'} \delta_{kk'} \right| = 0 \tag{2}$$

where $D_{\alpha\beta}\begin{pmatrix}\mu & \mu'\\ \ell & \ell'\\ k\ ; & k'\end{pmatrix} = (M_k M_{k'})^{-1/2} \sum_{\beta,\ell',k'} \phi_{\alpha\beta}\begin{pmatrix}\mu & \mu'\\ \ell & \ell'\\ k\ ; & k'\end{pmatrix}$ is an element of the long wavelength mass reduced dynamical matrix D.

The eigenvalues of the dynamical matrix D are the squared frequencies of the phonons, ω^2, and the matrix which diagonalised D is the matrix of phonon eigenvectors. The problem of obtaining the phonon frequencies and eigenvectors at long wavelength limit then consists of constructing D and diagonalising it.

In this three-dimensional interacting model, the interaction of H...H, H...Cl and H...Br between adjacent zig-zag chains in different planes were assummed to be negligible due to the lighter mass of hydrogen, while the range of interactions of Cl...Cl and Br... Br were limited to their first nearest neighbors with the central force constant ξ[9]. The model is outlined in Figure 2, and all the force constants are shown. The range of interaction of each hydrogen atom and halogen atom is limited to its fourth-nearest neighbors in each planar zig-zag chain structure. Assuming central force constants between one atom to the other atoms are taken to its first to fourth nearest neighbors only (represented respectively as α, β, λ and γ) and the axially symmetric angular force constants[10] are taken to its first and second nearest neighbors (represented respectively as δ_2 and δ_1), the dynamical matrix interaction for those four atoms (2 molecules of HCl or HBr) in one unit cell can be obtained as following (expressed in dyadic forms):

$$\phi\begin{pmatrix}1 & 1\\ 1\ ;\ 1\\ H & N\end{pmatrix}=\phi\begin{pmatrix}1 & 1\\ 1\ ;\ 1\\ N & H\end{pmatrix}=-[(\hat{i}\hat{i}+\hat{k}\hat{k})\delta_2+\hat{j}\hat{j}(\alpha)],$$

$$\phi\begin{pmatrix}1 & 1\\ 1\ ;\ 2\\ H & N\end{pmatrix}=\phi\begin{pmatrix}1 & 1\\ 2\ ;\ 1\\ N & H\end{pmatrix}=-[(\hat{i}\hat{i}+\hat{k}\hat{k})\delta_1+\hat{j}\hat{j}(\beta)],$$

$$\phi\begin{pmatrix}1 & 1\\ 1\ ;\ 2\\ H & H\end{pmatrix}=\phi\begin{pmatrix}1 & 1\\ 2\ ;\ 1\\ H & H\end{pmatrix}$$

$$=-\left(\frac{\gamma}{P}\right)[\hat{i}\hat{i}(a^2+b^2)\cos^2\theta+\hat{j}\hat{j}(x)-(\hat{i}\hat{j}+\hat{j}\hat{i})(W)]$$

$$\phi\begin{pmatrix}1 & 2\\ 1\ ;\ 2\\ H & N\end{pmatrix}=\phi\begin{pmatrix}1 & -2\\ 2\ ;\ 1\\ N & H\end{pmatrix}$$

$$=-[\hat{i}\hat{i}\left(\frac{\varepsilon}{Q}\right)(a+b)^2\cos^2\theta+\hat{j}\hat{j}\left(\frac{\varepsilon}{Q}\right)(V^2)-(\hat{i}\hat{j}+\hat{j}\hat{i})\left(\frac{\varepsilon}{Q}\right)(V)(a+b)\cos\theta]$$

$$\phi\begin{pmatrix}1 & 1\\ 2\ ;\ 2\\ H & N\end{pmatrix}=\phi\begin{pmatrix}1 & 1\\ 2\ ;\ 2\\ N & H\end{pmatrix}$$

$$=-[\hat{i}\hat{i}(\alpha\cos^2\theta+\delta_2\sin^2\theta)+\hat{j}\hat{j}(\alpha\sin^2\theta+\delta_2\cos^2\theta)+\hat{k}\hat{k}(\delta_2)],$$

$$\phi\begin{pmatrix}1 & \pm 3\\ 1\ ;\ 2\\ N & N\end{pmatrix}=\phi\begin{pmatrix}1 & \pm 5\\ 2\ ;\ 1\\ N & N\end{pmatrix}=-\frac{\xi}{S}[\hat{i}\hat{i}(d^2\sin^2\frac{\phi}{2})+\hat{j}\hat{j}(T^2)+\hat{k}\hat{k}(c^2)$$

$$-(\hat{i}\hat{j}+\hat{j}\hat{i})(T)(d\sin\phi)\pm(\hat{i}\hat{k}+\hat{k}\hat{i})(c)(d\sin\phi)\pm(\hat{j}\hat{k}+\hat{k}\hat{j})(c)(T)],$$

$$\phi\begin{pmatrix}1 & -2\\ 2\ ;\ 1\\ H & N\end{pmatrix}=\phi\begin{pmatrix}1 & +2\\ 1\ ;\ 2\\ N & H\end{pmatrix}=-[\hat{i}\hat{i}(\beta\cos^2\theta+\delta_1\sin^2\theta)+\hat{j}\hat{j}(\beta\sin^2\theta$$

$$+\delta_1\cos^2\theta)+\hat{k}\hat{k}(\delta_1)-(\hat{i}\hat{j}+\hat{j}\hat{i})(\tfrac{1}{2})(\beta-\delta_1)\sin 2\theta]$$

$$\phi\begin{pmatrix}1 & \pm 6\\ 2\ ;\ 1\\ N & N\end{pmatrix}=\phi\begin{pmatrix}1 & \pm 4\\ 1\ ;\ 2\\ N & N\end{pmatrix}=-\frac{\xi}{S}[\hat{i}\hat{i}(Y^2)+\hat{j}\hat{j}(Z^2)+\hat{k}\hat{k}(c^2)$$

$$-(\hat{i}\hat{j}+\hat{j}\hat{i})(Y)(Z)\pm(\hat{i}\hat{k}+\hat{k}\hat{i})(c)(Y)\pm(\hat{j}\hat{k}+\hat{k}\hat{j})(c)(Z)] \quad (3)$$

where $P=a^2+b^2+2ab\sin\theta$

$Q=(a+b)^2+2a(a+b)\sin^2\theta+a^2$

$R=d^2+b^2-2bd\sin\theta+c^2$

$S=d^2+(a+b)^2+c^2-2d(a+b)\cos(\frac{\phi}{2})$

$T=(a+b)-d\cos(\frac{\phi}{2})$

$V=a+(a+b)\sin\theta$, $W=2ab\cos\theta+\frac{1}{2}(a^2+b^2)\sin 2\theta$

$U=(a+b)+a\sin\theta$

$X=(a^2+b^2)(1+\sin^2\theta)+4ab\sin\theta$

$Y=(a+b)\cos\theta-d\sin(\frac{\phi}{2})$

$Z=(a+b)\sin\theta+d\cos(\frac{\phi}{2})$

$\theta=\phi-90°$

Each element $\phi_{\alpha\beta}\begin{pmatrix}\mu & \mu'\\ \ell & \ell'\\ k\ ;\ k'\end{pmatrix}$ of the dynamical matrix $\phi\begin{pmatrix}\mu & \mu'\\ \ell & \ell'\\ k\ ;\ k'\end{pmatrix}$ in Eq. (3) were calculated by the following formula[10]

$$\phi_{\alpha\beta}\begin{pmatrix}\mu & \mu'\\ \ell & \ell'\\ k\ ;\ k'\end{pmatrix}=-\{(\phi_r-\phi_t)\frac{[x_\alpha\begin{pmatrix}\mu'\\ \ell'\\ k'\end{pmatrix}-x_\alpha\begin{pmatrix}\mu\\ \ell\\ k\end{pmatrix}][x_\beta\begin{pmatrix}\mu'\\ \ell'\\ k'\end{pmatrix}-x_\beta\begin{pmatrix}\mu\\ \ell\\ k\end{pmatrix}]}{R^2}+\phi_t\delta_{\alpha\beta}\}$$

where ϕ_r and ϕ_t are respectively the central force constant and the axially symmetric force constant (if it exists) between atoms $\begin{pmatrix}\mu\\ \ell\\ k\end{pmatrix}$ and $\begin{pmatrix}\mu'\\ \ell'\\ k'\end{pmatrix}$, and R the distance between these two atoms, and $x_\alpha\begin{pmatrix}\mu\\ \ell\\ k\end{pmatrix}$ and $x_\beta\begin{pmatrix}\mu'\\ \ell'\\ k'\end{pmatrix}$ are the coordinates of these two atoms in the α direction and β direction respectively (α, β = x, y, z). The structural properties of the phase III crystals are listed in Table 1.

The condition that the value of the force on each atom is invariant under a rigid body translation of the crystal, we have the following condition of force constants[9],

$$\phi_{\alpha\beta}\begin{pmatrix}\mu & \mu\\ \ell & \ell\\ k\ ; & k\end{pmatrix}=-\sum_{\substack{\mu\neq\mu'\\ \ell\neq\ell'\\ k\neq k'}}\phi_{\alpha\beta}\begin{pmatrix}\mu & \mu'\\ \ell & \ell'\\ k\ ; & k'\end{pmatrix} \tag{4}$$

This equation is important in the construction of Eq. (2).

3. RESULTS AND DISCUSSIONS

The equations of motion for the four atoms in the x, y and z direction, relating the seven interacting constants, established a 12 x 12 dynamical matrix as discussed in previous section. The force constants were then adjusted to give optimum agreement between the observed[2] and the calculated frequencies. All the calculations and fittings were performed on a VAX 11/780 computer using the Jacobi rotation method. The optimized values of the force constants and the results of the calculations as compared with the experimental values are summarized in Table 2. The assignment of the symmetry of each mode was made by studying the transformation properties of the eigenvectors of the dynamical matrix and by comparison between the calculated values and the experimental values.

From Table 2, it is seen that not only the calculated two in-plane translational mode frepmencies (A_1+B_1) are in good agreement with those from experiments, but also the calculated low frequency out-of-plane A_2 translational mode is also in good match with the observed values due to fact that in this three-dimensional model inter-planar forces are included. This is a much better result compared with previous two-dimensional model calculation on solid HCl ($28.5cm^{-1}$ compared with $61cm^{-1}$) and solid HBr ($18cm^{-1}$ compared with $45cm^{-1}$). The two stretching (A_1+B_1) modes are also very well fitted. However, the overall agreement between the calculated and observed librational frequencies is less than satisfactory. The larger errors of the librational modes may be caused by the electric moments in crystalline HCl and HBr[3][7], which bring into play long-range electrostatic forces between the atoms and limit the accuracy of this harmonic model. Note that the pure translational modes are not identically equal to zero because of the round off errors produced during the diagonalization procedure. (In the construction of Eq. (2), the conditions of equilibrium of the pure translational modes have been taken into account by using Eq. (4)).

The comparsions of the directions of the force components due to various force constants with that of vibrational modes reveal three interesting facts. (1) α and β are closely related to the eigenfrequencies of the two stretching modes A_1 & B_1 (2) γ and ϵ determine mostly the eigenfrequencies of the in-plane modes $B_1(T)$, $A_1(T)$ & $B_1(L)$, but the splitting of these frequencies are determined by ξ, δ_1 and δ_2. (3) The eigenfrequencies of the three out-of-plane modes $A_2(T)$, $A_2(L)$ & $B_2(L)$ are determined wholly by ξ , δ_1 are δ_2 , since only forces of these three force constants have force components along the z-direction.

It can be found that the angular force constants δ_1 and δ_2 have the vibrational effect of deforming the angle ϕ between the bonds, and are important in getting satisfactory explanations of the observed results. A pure central force model, with zero values of δ_2 and δ_1 and two additional interplanar force constants was also analyzed and found to be unable to give a reasonable fitting between the calculated and observed eigenfrequencies and eigenvectors. This fact indicates that the binding force of molecular bond and hydrogen bond are both central and noncentral in character.

The model adopted in these calculations of crystalline HCl and HBr shows good overall fitting between the observed and calculated frequencies. The average deviation for solid HCl is 9.1% while that for solid HBr is 6.0%. These deviations are smaller than the corresponding values of the planar model that were proposed by Chang et al recently[4]. A comparsion between the optimized values of all force constants shows that the force between atoms in different chains and different planes are much smaller than those between nearest neighbors in the same chain. It seems that this three dimensional model is reasonably successful in the long-wavelength lattice dynamics calculations of crystalline HCl and HBr in their low temperature phase.

4. REFERENCES

[2] [illegible]esel and B. H. Torrie, Can. J. Phys. 55, 592 (1977).

[3] [illegible]n and A. Anderson, Chem. Phys. Lett. 17. 104 (1972).

[4] [illegible]out and J. W. Leech, Solid State Phys. 7, 3245 (1974).

(4) C. N. Chang, W. S. Tse, and L. Chang, Chin, J. Phys. 25, No. 1, 21 (1983).

(5) M. Ito, M. Suzuki and T. Yokoyama, J. Chem. Phys. 50, 2949 (1969).

(6) R. Savcie and A. Anderson, J. Chem. Phys. 40, No.2, 548 (1966).

(7)D. E. Stogryn and A. P. Stogyrn, Molec. Phys. 11, 371 (1966).

(8) G. S. Pawley, Phys. Stat. Sol. (b) 49, 475 (1972).

(9) A. A. Maradudin, E. W. Montroll, G. M. Weiss and I. P. Ipatova. The Theory of Lattice Dynamics in the Harmonic Approximation. 2-nd edn. p.14, Academic press. (1971).

(10) N. Wakabayashi and R. M. Nicklow, Neutron Scattering and Lattice Dynamics of Material with Layered Structures. p.413 Addision-Wesly Publishing. (1979).

Table 1. Structural properties of the phase III crystal[c]

	HCl	HBr
Molecular bond length a(Å)	1.275	1.414
Hydrogen bond length b(Å)	2.413	2.513
Distance between two adjacent planes of zig-zag chains: c(Å)	2.900[a]	3.040[b]
Half distance between two adjacent chains in the same plane d(A)	2.558	2.790
Angle between the molecular bond and the hydrogen bond ϕ ($\theta = \phi - 90°$)	93°31'	91°48'

(a) estimated values from Ref. (5).

(b) estimated values from Ref. (6).

(c) The values of a,b,d and ϕ of the crystals are from Refs. (4), (5) and (6).

Table 2. Calculated frequencies and force constant for solid HCl and HBr in phase III (cm^{-1})

Assignment		HCl Obs[2](18K)	HCl Calc. (this work)	HBr Obs[2](18K)	HBr calc. (this work)
A_1	Acoustic	0	0.076	0	0.108
B_1	Acoustic	0	0.705	0	0.949
B_2	Acoustic	0	0.753	0	0.984
A_2	(o/p)T	61	66.01	45.0	45.85
A_1	(i/p)T	88.5	84.40	61.0	60.124
B_1	(i/p)T	114	110.4	75.5	76.94
A_2	(o/p)L	141.5	198.7	147	189.4
B_2	(o/p)L	223	201.2	207	190.4
A_1	(i/p)L	336	320.2	297	282.71
B_1	(i/p)L	409	449.3	376	394.39
A_1	(i/p)S	2697	2699.9	2395	2393.2
B_1	(i/p)S	2741.5	2720	2431	2410.2

Optimized force constants: (in units of 10^5 dyne/cm).

HCl		HBr	
α	: 413500	α	: 327500
β	: 7320	β	: 8350
γ	: 3700	γ	: 2720
ε	: 3580	ε	: 2550
ξ	: 1180	ξ	: 1340
δ_1	: 780	δ_1	: 680
δ_2	: 1560	δ_2	: 1450

out of plane; i/p in plane; L, libration; T, translation; S, streching.

Figure 1. The three-dimensional structure of phase III solid HCl and HBr. The symbols H_ℓ^μ and N_ℓ^μ represent the ℓ^{th} hydrogen atom and the ℓ^{th} halogen atom respectively in the μ^{th} primitive unit cell of the crystal. N represent Cl or Br atom.

Figure 2. Force constants of phase III solid HCl and HBr adopted in the calculation described in this paper.

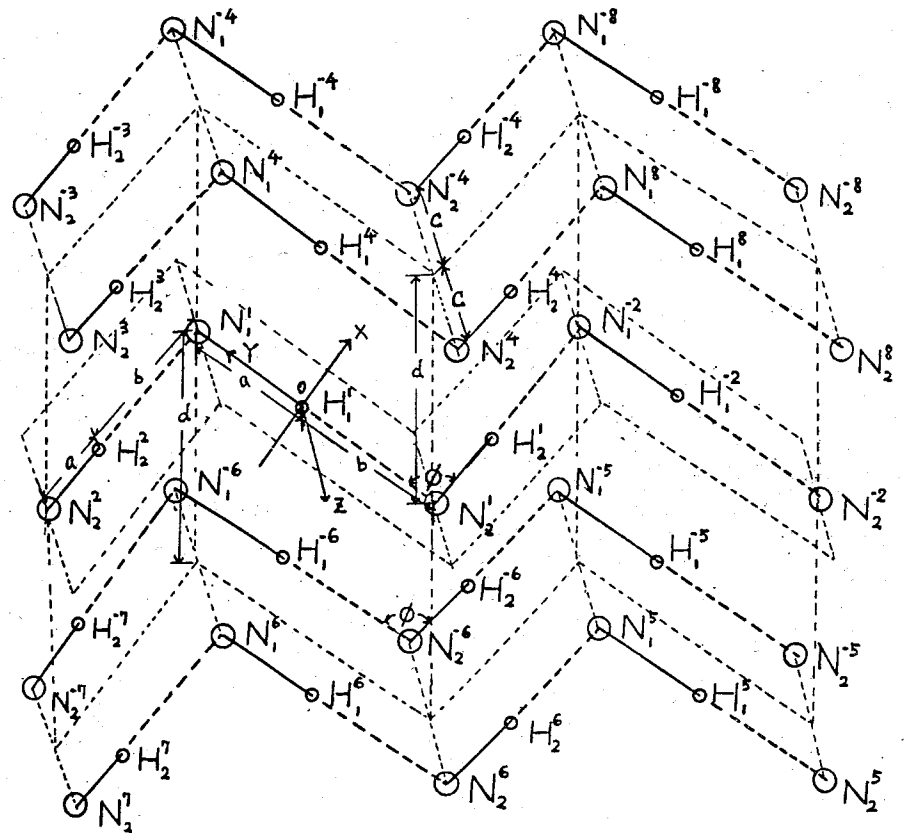

Fig. 1.

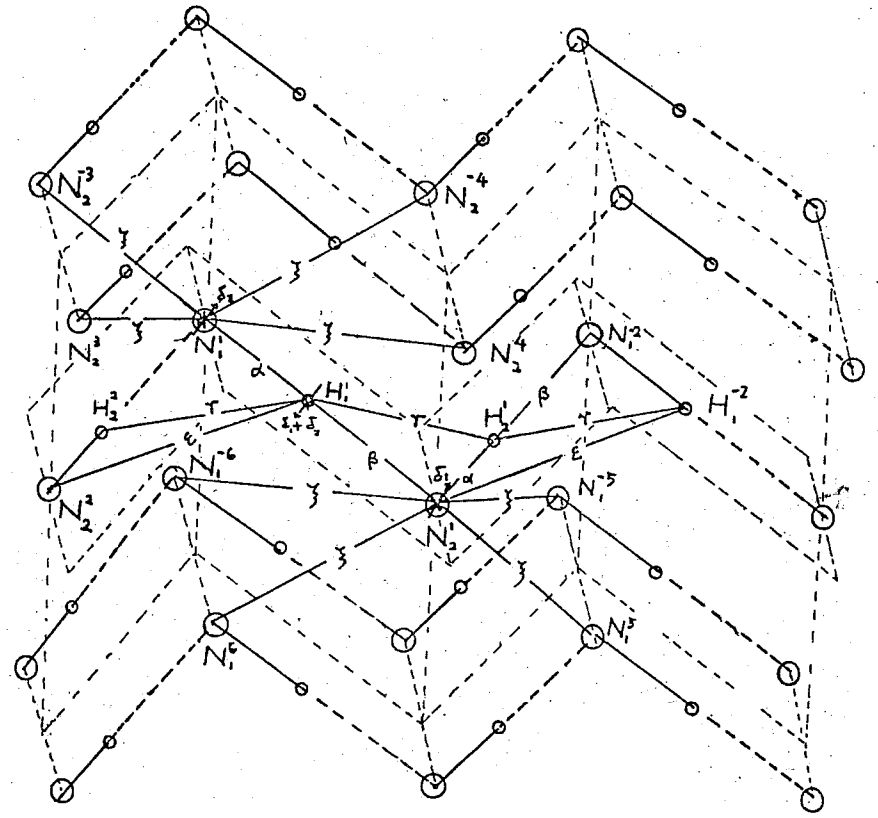

Fig. 2.

RAMAN SPECTRA OF CRYSTALLINE SILICON AND GERMANIUM TETRACHLORIDES

W. S. Tse and C. C. Chen[1]

Institute of Physics, Academia Sinica,

Nankang, Taipei, Taiwan (115), R. O. C.

Laser Raman spectra of polycrystalline samples of silicon and germanium tetrachlorides have been observed for the lattice and intramolecular vibrational regions at 80K. Comparisons are made with the spectra of known crystalline $TiCl_4$, and the observed peaks of $GeCl_4$ are classified into translational and librational model. Classification scheme: 78.

The Raman spectra of these molecular tetrachlorides in the liquid state has been studied previously (1, 2), but there has been no systematic study of these tetrachlorides in the solid state including external and internal vibrations. The Raman spectra of polycrystalline $SiCl_4$ and $GeCl_4$ in the internal mode region have been recorded by clark and Hunter (3). In this letter we report a comprehensive study of the high resolution Raman spectra of the tetrachlorides of silicon and germanium as polycrystalline films at 80K including both internal and external vibrations.

The Raman spectra were excited by the 5145 Å line of 200-400mW from a Spectra Physics 170-00 argon ion laser using a standard 90° scattering configuration. The scattered light was dispersed by a Spex 1401 double monochromator and was detected by an EMI 9558 QA photomultiplier which was cooled down to -20°C. Photon-electron pulses were then processed through the SSR 1120 amplifier/discriminator and then converted into analog signal by the SSR 1105 photon counter/data converted console. The low temperature sample cell was a Pyrex made double layer dewar and was discussed in a previous paper (4). Frequencies reported here were estimated to be accurate within ±1 cm⁻¹ for sharp features.

The lattice spectra of both samples at 80K are shown in Figure 1 and the

[1] Department of Physics, Soochow University, Taipei, Taiwan (111), R. O. C.

peak positions are listed in Table 1. The low frequency Raman spectra of these two crystals have not been reported except some preliminary results was obtained by one of us (5). Complete X-ray data are available for titanium tetrachloride (6) at 241K and tin tetrachloride (6, 7) at 234K which have the tin tetrabromide structure (6, 7) with the monoclinic space group $P2_1/c$ and Z=4. No Structural data is availabl for crystalline silicon and germanium tetrachlorides but it is believed that $SiCl_4$ and $GeCl_4$ crystals could be the same structures as $TiCl_4$ and $SnCl_4$ (6). The group theoretical analysis based on the known crystal structure of $TiCl_4$ predicts six Raman active librational modes and also six Raman active translational modes (4). In previous paper (4) it has been shown that the lattice spectra of $TiCl_4$ and $SnCl_4$ are similar to each other in peak shapes and relative intensities because these two crystals have similar structures. It is the aim of this work to study and compare the nature of the lattice modes with the hope that they will provide some information about the crystal structures of the two unknown samples of $GeCl_4$ and $SiCl_4$ and try to classify the lattice modes.

From Figure 1, there are obvious similarities between the results of the Raman spectra of $GeCl_4$ and $TiCl_4$ both in spectral band shapes and relative intensities except the corresponding weak features are absent in $GeCl_4$ spectrum. This shows that the crystal structure of $TiCl_4$ and $GeCl_4$ may be similar to each other. In solid $TiCl_4$ spectrum the lattice modes consist of ten peaks and a simple model (4) shows that the lattice modes are classified into translational and librational motions. The basic assumption of such simple model says that to determine a first approximation to the lattice frequencies, we consider the intermolecular interactions between the molecules in $TiCl_4$ and $GeCl_4$ may be identical provided that crystalline $TiCl_4$ and $GeCl_4$ have similar structure and also their lattice dimensions are nearly the same. Since the crystalline $SnCl_4$ and $TiCl_4$ have the same structure and also their lattice dimensions are nearly the same (4), and that the molecular weight of $GeCl_4$ and the intramolecular bond length r_{Ge-Cl} are more closely related to $TiCl_4$ than $SnCl_4$. Hence lattice dimensions of $GeCl_4$ and $TiCl_4$ may nearly the same when they form isostructural crystals.

The molecules can perform translational or librational motions at a lattice site in the crystal. The frequencies are calculated from the following two simp

expressions:

$$\nu_T = \frac{1}{2\pi}\sqrt{\frac{K_T}{M}}$$

$$\nu_L = \frac{1}{2\pi}\sqrt{\frac{K_L}{I}}$$

where K_T and K_L are the relevant force constants and in this case we will assume them nearly the same in both samples because of the identical intermolecular interactions. Applying the above simple idea we have

$$\nu_T \propto \frac{1}{\sqrt{M}} \quad \text{and} \quad \nu_L \propto \frac{1}{r_{X-Cl}}$$

Where r_{X-Cl} is the intramolecular bond length and M is the total molecular mass. The frequency ratios $\nu(TiCl_4)/\nu(GeCl_4)$ are obtained by pairing off the observed peaks in $TiCl_4$ and $GeCl_4$ spectra according to their relative intensities and relative spectral band shapes as shown in Table 2. The theoretical ratio for the translational modes is 1.063, while that for the librational modes is 0.952. From Table 2, we note that the three lowest lattice modes all have values close to 1.063 and hence are mostly translational motion in nature. The next four higher frequency peaks have the ratio values close to 0.952 and therefore these peaks may be associated with librational motions. On the other hand, the lattice spectrum of crystalline $SiCl_4$ is different from the spectrum of $TiCl_4$ and $GeCl_4$ in relative intensities and spectral band shapes so that we cannot apply the above simple model to distinguish which are translational or librational modes. Therefore, its structure may be different from $TiCl_4$ and $GeCl_4$.

Raman spectra of the internal modes of these two crystals were also recorded [illegible] The regions of all four fundamentals have been examined and that the [illegible] and crystal splittings have also been observed. However, the results are [illegible]ubstantially different from those of Clark and Hunter (3) except the intensity [illegible] the $\nu_1(A_1)$ mode components of $SiCl_4$. The splitting of the $\nu_1(A_1)$ [illegible] into five bands is isotopic in origin arising from the two isotopes [illegible] Five tetrachloride species occur with abundances: $X^{35}Cl_4$ (32.54%), $X^{35}Cl_2{}^{37}Cl_2$ (20.5%), $X^{35}Cl^{37}Cl_3$ (4.43%) and $X^{37}Cl_4$ [illegible]ording to Clark and Hunter (3) the intensity of the $Si^{35}Cl_4$

band and that of $Si^{35}Cl_3{}^{37}Cl$ at liquid nitrogen temperature is nearly the same. However, for our polycrystalline sample, we found that the observed ratio close to the calcualted abundance ratio (0.772). The other observed splittings (isotopic and crystalline field splittings) in the intramolecular vibrational regions are similar to Clark and Hunter's (3) work and so will not be discussed here.

The authors would like to thank Dr. H. Chang and N. T. Liang for fruitful discussions.

REFERENCES

(1) K. Nakamoto, Infrared Spectra of Inorganic and Cordination Compounds, (Wiley, New York 1970).

(2) R. J. H. Clark and C. J. Willis, Inorg, Chem, 10(1971) 28.

(3) R. J. H. Clark and B. K. Hunter, J. Chem. Soc., 15A(1971) 2999.

(4) W. S. Tse, C. C. Chen, H. Chang and N. T. Liang, J. Raman Spectro., (Accepted for Publication).

(5) W. S. Tse, Ph. D. Thesis, (University of Waterlo 1980).

(6) P. Brand and H. Sachmann, Z. Anorg, Chem., 321 (1963) 269.

(7) P. Brand and H. Sachmann, Acta. Cryst., 16(1963) 446.

FIGURE CAPTIONS

Figure 1. The lattice Raman spectra of Crystalline $GeCl_4$ and $SiCl_4$ at 80K. The asterisk (*) indicates a plasma line. Spectral resolution is 1 cm^{-1}. The inserted figure is the spectrum of crystalline $TiCl_4$ (4).

Table 1. The lattice frequencies of crystalline $GeCl_4$ and $SiCl_4$ at 80K.

Frequency (cm^{-1})	
$GeCl_4$	$SiCl_4$
25.0	25.0
33.5	30.0
40.0	33.0
49.0	36.0
51.0	40.0
54.5	46.0
68.0	55.0

Table 2. Comparison of the lattice frequencies of $GeCl_4$ measured in this work with $TiCl_4$ frequencies at 80K (4).

$\sqrt{M(GeCl_4)/M(TiCl_4)} = \sqrt{214.4/189.71} = 1.063$ (T)

$r(GeCl_4)/r(TiCl_4) = 2.08/2.185 = 0.952$ (L)

Frequency (cm^{-1})		$\frac{\nu(TiCl_4)}{\nu(GeCl_4)}$	Assignment
$TiCl_4$	$GeCl_4$		
25.3	25.0	1.012	T
35.1	33.5	1.047	T
42.0	40.0	1.050	T
48.3	49.0	0.985	L
51.0	51.0	1.000	L
54.8	54.5	1.005	L
65.5	68.0	0.805	L

T = translational mode.

L = librational mode.

$M(GeCl_4)$ = total mass of $GeCl_4$

$M(TiCl_4)$ = total mass of $TiCl_4$

$r(GeCl_4)$ = bond length between Ge and Cl atoms.

$r(TiCl_4)$ = bond length between Ti and Cl atoms.

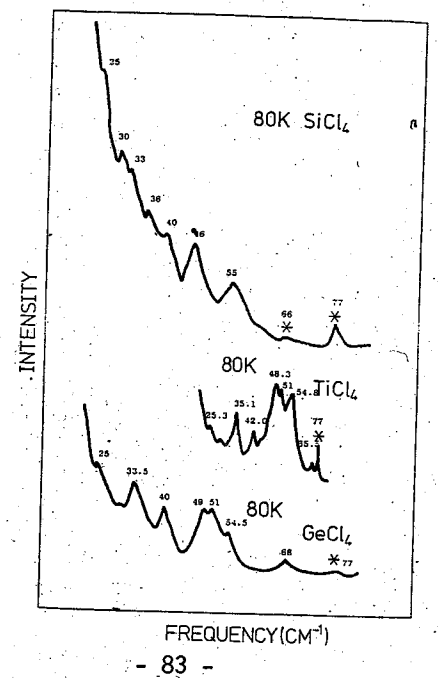

EFFECT OF HALOPERIDOL AND NOMIFENSINE ON THE DOPAMINE AUTO-REGULATION IN RAT

W. K. Wang, L. S. Jenq, T. L. Hsu and Y. Chiang

Biophysics Laboratory, Institute of Physics,

Academia Sinica Taipei,

Taiwan, 115, R. O. C.

Haloperidol [1-3] has long been identified as an antagonist to dopamine postsynaptically. Some study[4-5] on synaptosomal preparation also showed that it antagonize the inhibitory effect of apomorphine which has been characterized as a dopamine agonist that preferentially bind presynaptic dopamine receptor[6,7]. However, we found that haloperidol would not antagonize dopamine auto-inhibition. It's inhibitory effect and dopamine auto-inhibition were additive. This suggests that we might need to refine our terminology and separate the presynaptic and postsynaptic effect of drugs.

Spragu-Dawley rat (180-230 g) were killed by decapitation. The corpus striatum was dissected on ice and homogenized in 10 Vols. 0.32 M sucrose using teflon pestle tissue homogenizer. After centrifigation at 1000g for 15 min, 50 $\mu\ell$ aliquots of the synaptosome-containing supernatant were incubated with 150 $\mu\ell$ physiological medium as described before[(8)], only some NaH_2PO_4 were replaced by $NaHCO_3$ to give final pH of 7.4 after equilibration with 95%. O_2 - 5% CO_2 at 37°C. Dopamine (DA) and haloperidol (HD) were added to the incubation medium with 10 $\mu\ell$ 0.1 M phosphorous buffer pH 7.4 as carrier. DA formation was calculated from the $^{14}CO_2$ output from [1—^{14}C] tyrosine, averaged over 50 minutes of incubation to 120 minutes of incubation. The rate of dopamine synthesis was about of that at pH = 6.6. We shifted to this pH because it is a more physiological

10^{-5} M added to the incubation mixture reduced $^{14}CO_2$ release to 76.2±1.8% from 5 preparation) of its normal rate.

10^{-6} M reduced the $^{14}CO_2$ release to 89.8±1.9% (mean±S.D. from 5 the normal rate, HD at 10^{-7} M had no significant effect.

CO_2 released from the preparation with HD and DA compare to the one with HD alone were summerized in Table 1. The presentce of HD doesn't change the auto-inhibition effect of DA. Only the one with HD (10^{-5}) and DA (10^{-6}) seemed to have some blocking effect. Fig. 1 showed some of these data.

The HD alone acted like DA, it behaved like a agonist presynaptically. It did not antagonize DA auto-inhibition either. This was not the some as that of apomorph whose inhibitory effect can be blocked by HD. Actually this may be the reason why HD is such a strong DA blocking agent[9], it blocked DA effects post-synaptically as well as inhibited DA synthesis presynaptically. From these results, we also see that the traditional way to define agonist and antagonist should be refined to separate the presynaptic and postsynaptic effect. The most effective blocking agonist will be the one like haloperidol, it worked as agonist presynaptically and as antagonist postsynaptically. While the most effective stimulating agent will be the one which does the reverse.

We thank Janssen Pharmaceutica for sending pure-haloperidol.

Table I. $\frac{^{14}CO_2 \text{ release (DA+HD)}}{^{14}CO_2 \text{ release HD}}$

Concentration of DA / Concentration of HD	10^{-5} M	10^{-6} M
10^{-5} M	38.6 ± 6.53 (4)	95.0 ± 2.33 (4)
10^{-6} M	42.6 ± 6.48 (6)	89.3 ± 3.78 (5)
10^{-7} M	37.9 ± 2.82 (5)	91.5 ± 1.79 (5)
0	40.1 ± 7.93 (4)	89.7 ± 3.50 (8)

DA : Dopamine HD: Haloperidol,

the data present as Mean ± S. D. (No of experiments)

REFERENCES

(1) Clement-Cormirer, Y. C., Kebabian, J. W., Petzold, G. L. & Greengard, P., Proc. Natn, Acad. Sci. U. S. A. 71, 1113-1117 (1974).

(2) Miller, R. J., Horn, A. S. & Iversen, L. L., Molec Pharmac 10, 759-766, (1974).

(3) Bochaert, J. Tassin, J. P., Thierry, A. M., Glowinski, J., & Premont, J., Brain Res. 232, 391-400 (1977).

(4) Christiansen J. & Squires, R. J. Pharm., Pharmac. 26, 367-369 (1974).

(5) Iversen, L. L., Rogawski, M. A., Miller, R. J., Molec. Pharmac. 12, 251-262 (1976).

(6) Nagy, J. I., Lee, T., Seeman, P. and Fibiger, H. C., Nature 274, 278-281 (1978).

(7) Raiteri, M., Cervoni, A. M., Carmine, R. O., Levi, G., Nature 274, 706-708 (1978).

(8) Wang, W. K., Chiang, Y., Jenq, L. S., Chen, N. K., Nature 296, 354 (1982).

(9) Staurton, D. A., Magistretti, P. J., Koob, G. F., Shoemaker, W. J., & Bloom, F. E., Nature 299, 72-74 (1982).

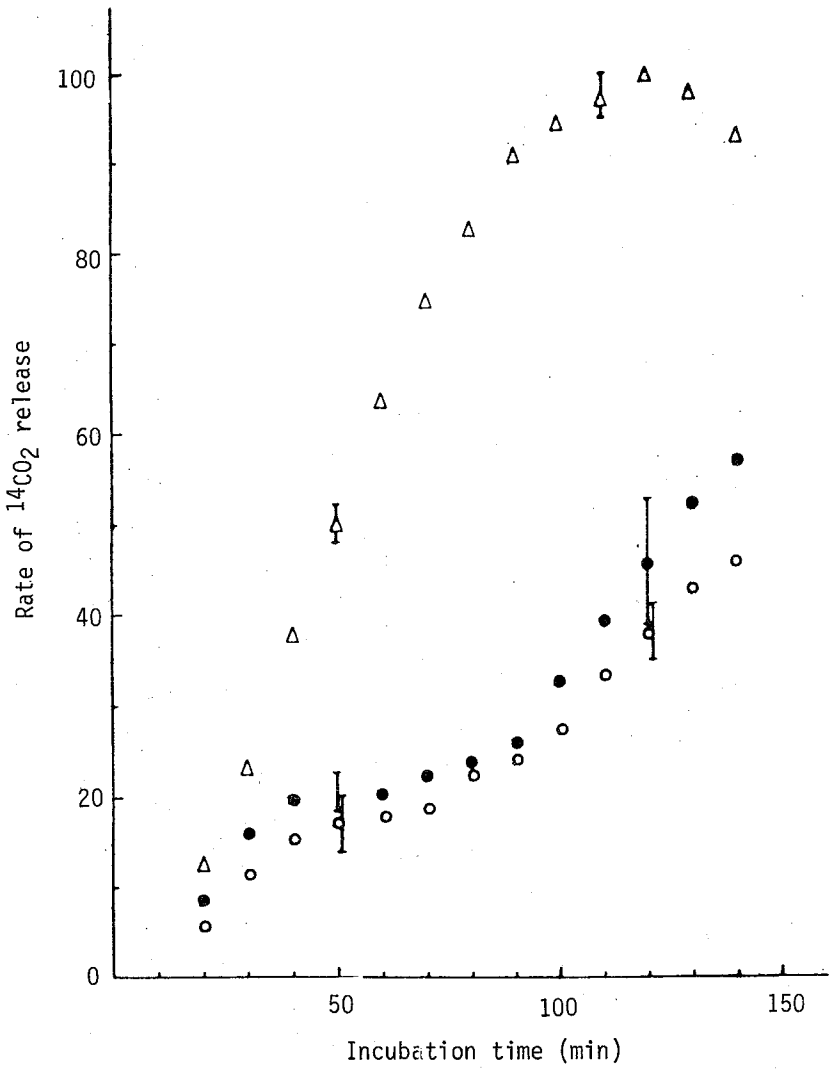

Fig. 1. Rate of $^{14}CO_2$ release from labelled tyrosine plotted against incubation time, error bar shown are standard deviation (mean ± S. D. for six preparations). Dopamine at 1 x 10^{-5} M added to the preparation (●) strongly inhibited dopamine synthesis. Haloperidol at 1 x 10^{-6} M together with dopamine at 1 x 10^{-5} M (o) further inhibited dopamine biosynthesis, Δ , control.

A VARIATIONAL-KINEMATICAL MODEL FOR FLOW OVER COMPLEX TERRAIN

Len-Fu W. Chang, Robert R. Hwang, Shwu-Ching Lin
Institute of Physics,
Academia Sinica, Nankang,
Taipei, Taiwan, R. O. C.

A variety of wind measurement systems may exist over region characterized with complex topography. These various systems include the mandatory rawindsound observation and the surface wind measurement. These observed wind field is inherent with different kinds of error, including resolution ability and vertical extend of measuring. Furthermore, topography effect may limit their representability. In this study, a variational-kinematical algorithm is adopted with mass continuity and topography as the constraints for analysis of wind flow over complex terrain. Case study is performed with flow over northern part of Taiwan.

I. INTRODUCTION

The analyses of wind and/or flow pattern over the region characterized by complex terrain are important procedure for many different applications. The wind energy survey over a specific region needs long term wind statistics at several locations where the adequate wind observations are not available. On the orther hand, estimation of the air pollutants and/or radioactive materials transport and dispersion for the purpose of environmental control, also requires the wind-flow pattern analysis. In general, a veriety of wind measurement systems may exist in a specific region. These various wind data sources include the rawindsound observations, surface wind observations, or some special pilot-balloom observations. These different measurement systems may be inherent with different kinds of error, different resolution ability, furthermore, the terrain may impose the limitation for their spacial representability. Thus, the intorpolation techanique is not suitable to obtain wind information at locations without direct observations.

In this paper, we devise a variational-kinematical algorithm to analyze the wind-flow pattern over complex terrain.

KINEMATICAL-VARIATIONAL ANALYSIS ALGORITHM

The analysis of flow pattern over a region of complex terrain is achieved by the variational method (Sasaki, 1958; 1970 a, b) with the kinematic (mass continuity and terrain boundary conditions) relationships as the constraint. For different purporses, Sherman (1978), and Dickerson (1978) formulated the variational algorithms to analyze the flow field over the complex terrain. Although, their approach to the problem differes slightly, both require the initial guess of vertical velocity in the computational domain. This kind of approach may cause uncertainty inherent in the calculated variance. However, this drawback may be adjusted through the using of different weighting factors for horisontal wind components and the vertical wind component in the models of Sherman and Dickerson. Furthermore, the performance of variational analysis depends very much upon the prescribed model depth within which mass balance is assumed to be maintained. Recently, Endlich et. al. (1982) have modified Sherman's algorithm, utilizing terrain following coordinate system and different laws for wind profiles. In the following, we proceed to develop a new variational analysing scheme, and through case studies to exame the performance of proporsed scheme.

For most applications, terrain following coordinate defined as

$$\hat{Z} = Z - E(x, y), \tag{1}$$

is convinent to incorporate into the analysing scheme. Here, the terrain elevation above the sea-level is denoted by E(x, y). The Boussinesq incompressible fluid continuity equation can be expressed as

$$\frac{\partial u}{\partial x} + \frac{\partial v}{\partial y} + \frac{\partial \hat{w}}{\partial \hat{z}} = 0 , \tag{2}$$

where $d\hat{z}/dt = \hat{w}$ The variational algorithm based on minimizing the variance between observed wind and analyzed wind can be formulated as

$$J = \iiint [\frac{1}{2}(u - u_0)^2 + \frac{1}{2}(v - v_0)^2 + \lambda (\frac{\partial u}{\partial x} + \frac{\partial v}{\partial y} + \frac{\partial \hat{w}}{\partial \hat{z}})] dx dy d\hat{z}, \tag{3}$$

In (3), λ is the so-called Lagrangian multiplier, and continuity equation (2) is imposed as the constraint condition. The direct interpolating wind components at each grid point are denoted by u_0 and v_0, respectively. The stationary condition of (3) yields the Euler-Lagrange equations:

$$u = u_0 + \frac{\partial \lambda}{\partial x} , \tag{4}$$

$$v = v_0 + \frac{\partial \lambda}{\partial x} , \tag{5}$$

$$\frac{\partial \lambda}{\partial z} = 0 \quad , \text{ and} \tag{6}$$

$$\frac{\partial u}{\partial x} + \frac{\partial v}{\partial y} + \frac{\partial \hat{w}}{\partial \hat{z}} = 0 , \tag{7}$$

Equation (4) - (7) are subjected to the natural boundary condition,

$$\iiint [\frac{\partial}{\partial x}(\lambda \delta u) + \frac{\partial}{\partial y}(\lambda \delta v) + \frac{\partial}{\partial \hat{z}}(\lambda \delta \hat{w})] dx dy d\hat{z} = 0, \tag{8}$$

derived from the variational problem. The condition (8) implied that at the lateral boundary we may adjust the horizontal wind components to satisfy the mass continuity relationship; while at the upper and lower boundary, the vertical velocity component $\hat{w}$ must be specified. The Physical lower boundary condition is

$$\hat{w} = 0 , \quad \text{at} \quad \hat{z} = 0 \tag{9}$$

At the upper boundary ($\hat{z}$ = H), we may assume that the prevailing flow is not disturbed by the surface inhomogeneity, such that the prevailing flow above H is quasi-horizontal; then

$$\hat{w} = -\vec{v}(H) \cdot \nabla E \tag{10}$$

After some manipulation of (4) - (10), it yields the analyzing equation for our problem,

$$\frac{\partial^2 \lambda}{\partial x^2} + \frac{\partial^2 \lambda}{\partial y^2} = -\frac{1}{H}\int_0^H (\frac{\partial u_0}{\partial x} + \frac{\partial v_0}{\partial y}) dz - \frac{1}{H}[\vec{v_0}(H) + \nabla \lambda] \cdot \nabla E , \tag{11}$$

KINEMATICAL-VARIATIONAL ANALYSIS ALGORITHM

The analysis of flow pattern over a region of complex terrain is achieved by the variational method (Sasaki, 1958; 1970 a, b) with the kinematic (mass continuity and terrain boundary conditions) relationships as the constraint. For different purporses, Sherman (1978), and Dickerson (1978) formulated the variational algorithms to analyze the flow field over the complex terrain. Although, their approach to the problem differes slightly, both require the initial guess of vertical velocity in the computational domain. This kind of approach may cause uncertainty inherent in the calculated variance. However, this drawback may be adjusted through the using of different weighting factors for horisontal wind components and the vertical wind component in the models of Sherman and Dickerson. Furthermore, the performance of variational analysis depends very much upon the prescribed model depth within which mass balance is assumed to be maintained. Recently, Endlich et. al. (1982) have modified Sherman's algorithm, utilizing terrain following coordinate system and different laws for wind profiles. In the following, we proceed to develop a new variational analysing scheme, and through case studies to exame the performance of proporsed scheme.

For most applications, terrain following coordinate defined as

$$\hat{Z} = Z - E(x, y), \tag{1}$$

is convinent to incorporate into the analysing scheme. Here, the terrain elevation above the sea-level is denoted by E(x, y). The Boussinesq incompressible fluid continuity equation can be expressed as

$$\frac{\partial u}{\partial x} + \frac{\partial v}{\partial y} + \frac{\partial \hat{w}}{\partial \hat{z}} = 0 , \tag{2}$$

where $d\hat{z}/dt = \hat{w}$ The variational algorithm based on minimizing the variance between observed wind and analyzed wind can be formulated as

$$J = \iiint [\frac{1}{2}(u - u_0)^2 + \frac{1}{2}(v - v_0)^2 + \lambda (\frac{\partial u}{\partial x} + \frac{\partial v}{\partial y} + \frac{\partial \hat{w}}{\partial \hat{z}})] \, dx dy d\hat{z}, \tag{3}$$

In (3), λ is the so-called Lagrangian multiplier, and continuity equation (2) is imposed as the constraint condition. The direct interpolating wind components at each grid point are denoted by u_0 and v_0, respectively. The stationary condition of (3) yields the Euler-Lagrange equations:

$$u = u_0 + \frac{\partial \lambda}{\partial x} , \tag{4}$$

$$v = v_0 + \frac{\partial \lambda}{\partial x} , \tag{5}$$

$$\frac{\partial \lambda}{\partial z} = 0 \quad , \text{ and} \tag{6}$$

$$\frac{\partial u}{\partial x} + \frac{\partial v}{\partial y} + \frac{\partial \hat{w}}{\partial \hat{z}} = 0 , \tag{7}$$

Equation (4) - (7) are subjected to the natural boundary condition,

$$\iiint [\frac{\partial}{\partial x}(\lambda \delta u) + \frac{\partial}{\partial y}(\lambda \delta v) + \frac{\partial}{\partial \hat{z}}(\lambda \delta \hat{w})] dx dy d\hat{z} = 0, \tag{8}$$

derived from the variational problem. The condition (8) implied that at the lateral boundary we may adjust the horizontal wind components to satisfy the mass continuity relationship; while at the upper and lower boundary, the vertical velocity component $\hat{w}$ must be specified. The Physical lower boundary condition is

$$\hat{w} = 0 , \quad \text{at} \quad \hat{z} = 0 \tag{9}$$

At the upper boundary ($\hat{z}$ = H), we may assume that the prevailing flow is not disturbed by the surface inhomogeneity, such that the prevailing flow above H is quasi-horizontal; then

$$\hat{w} = -\vec{v}(H) \cdot \nabla E \tag{10}$$

After some manipulation of (4) - (10), it yields the analyzing equation for our problem,

$$\frac{\partial^2 \lambda}{\partial x^2} + \frac{\partial^2 \lambda}{\partial y^2} = -\frac{1}{H}\int_0^H (\frac{\partial u_0}{\partial x} + \frac{\partial v_0}{\partial y}) dz - \frac{1}{H}[\vec{v_0}(H) + \nabla \lambda] \cdot \nabla E , \tag{11}$$

with the imposed lateral boundary condition,

$$\lambda = 0 \qquad (12)$$

ANALYSIS PROCEDURE AND RESULTS

The domain of wind flow analysis is shown in Figure 1. A rectangular grid system, with horizontal grid distance of 4 Km, is used to represent the flow field. The vertical grids are unevenly spaced, at 10, 50, 100, 200, 400, 600, 800, 1000 meters above the ground. The terrain elevation E(x, y) is shown in Figure 1, and is digitized at each grid point to served as the input data of the model. For verification of the model and adjustment of the optimum model height, H, ten different cases are tested. During the the testing run of the model, surface wind observations from twelve stations and one rawindsound report have been used as the input data. Under two hundred meters altitude above the ground, vertical wind profile of 1/7th power law is used to extrapolate the surface wind data upward. While above the two hundred meters altitude, homogeneous wind flow from the rawindsound report is used. The objective analysis scheme by Barnes (1973) is used to interpolated observed wind data to each grid points. The filtering characteristics inherent in Barnes scheme can be selected by choosing different parameters in interpolation algorithm. In this study, due to the sparsity of observing stations, the radius of influence of the interpolation scheme is choosed about 10 grid point distance (the 63% response function value), as shown by Figure 2. The content of the ten testing cases is listed in Table 1. In these cases, significantly different flow patterns are intentively selected to represent the typical winter and summer wind fields over northorn Taiwan. In summer season, surface heating causes strong local circulation embedding in the relatively weak prevailing flow. While, in winter season, wind flow pattern is controled largely by northest monson and the local terrain. The performance of the variational-kinematical model is checked through these case study.

From equation (11), it can be seen that the prescribed model depth, H, influences the performance of the model a great deal. Since, by (10), it is assumed that the prevailing flow over the complex terrain area becomes undisturbed and quasi-

horizontal flow without singnificant vertical motion at the level H. An objective prccedure to determine H is as follows, Define

$$H = \alpha \, E_{rms} \, , \qquad (13)$$

where

$$K^2_{rms} = \frac{1}{G-1} \sum_{i=1}^{G} E_i^2 \, , \qquad (14)$$

The rcot mean square value of terrain elevation over the analyzing area (the model domain) is denoted by E_{rms}, and is defined by (14). In (14), the total number of grid points is denoted as G, for the testing cases, G = 31 x 20. Over the model domain, the value of Krms is 526 meter. The optimun value of H is determined via variation of the value of α, such that the mean square value, σ^2, between analyzed winds, u_c, v_c, and the observed winds, u_o and v_o, is minimum. That is

$$\sigma^2 = \frac{1}{N-1} \sum_{i=1}^{N} [(u_c - u_o)_i^2 + (v_c - v_o)_i^2] \, , \qquad (15)$$

where, N is equal to ten (number of cases) multipling by twelve (the number of observing stations). The results from testing runs are shown in Figure 3. For the value of α between 1.6 to 2.6, the values of root mean square deviation σ^2 are about the same. This is corresponding to the values of H between 850 meters to 1360 meters. Beyond this range, the error increases tremendously. For this reason, we prescribed the model depth, H, to be 1000 meter. This happens to be coincidence with the typical depth of the planetary boundary layer. The numerical solution of (11) is via the typical over-relaxation method for Helmholtz type partial differential equation. However, the arrangement of grid points for wind components and the Lagrange multiplier, λ must be staggered according to Sasaki et. al. (1978).

The typical winter time surface flow patterns are shown in Fig. 4 - Fig. 11. The observed surface winds at twelve stations are shown in Fig. 4, Fig. 7, Fig. 10, and Fig. 12, respectively, for four out of the ten selected cases. In winter time, when east China-continental high pressure system moving eastward, northern Taiwan experiences northeartern to southeastern prevailing winds. Fig. 5 shows the analyze

surface wind flow pattern, this is obtained by observations from 12 surface stations. It can be seen that notheastern prevailing flow is deflected by the major mountain ridge of Taiwan island. While, in the Taipei valley, the wind direction becomed eastern, and the wind speed is relatively slow. In order to check the performance of the wind analyzing model, we delete two wind reports at Taipei station (station 692) and Keelung Station (station 694) as the input data to the model. The result is shown in Fig. 6. Comparison between Fig. 5 and Fig. 6, it can be seen the model is capable in revealing the wind condition at data sparse area, when the flow is largely controlled by terrain forcing. Fig. 10 to Fig. 13 show similar prevailing flow condition (judging from the reports from the station located at northeast offshore of Taiwan island), but difference in time. In summer (shown, in Fig. 12 and 13), due to stong surface heating the high land areas become the major confluence flow centers, while the Taipei valley endures low wind speed and diffulent flow condition. This situation is not prominent in winter.

The verification of the model is judged by the percentage error by comparing the reported winds at Taipei station and Keelung Station with the model anlayzed winds, while these two station's reports are deleted from the input data. The error, DEV, is defined as

$$DEV = \frac{\sum_{i=1}^{N} [(u_c - u_o)_i^2 + (v_c - v_o)_i^2]}{\sum_{i=1}^{N} [u_o^2 + v_c^2]_i} \qquad (16)$$

In (16), since there are ten different case studies, and two deleting stations, the number of N is 20. From the testing runs of the model, the DEV value is found to be 18.69%.

CONCLUSION

The proposed variation-kinematical model for analyzing wind characteristics at data sparse area has been checked for flow patterns at northern Taiwan island. In this study, it has been found that the performance of the model is sensitive to the prescribed depth of model domain. Since, this is the key factor affecting the

assumption of mass balance of flow field over complex terrain. We proporsed that the model depth should proportion to the root-mean-squre value of terrain elevation over the analyzing domain. By intentively, deleting reports from two observing stations as the imput, it is found that the interpolation ability of wind characteristics at data sparse area from the model calculation is quite well, the percentage error as defined by (16) is about 18%.

From this study, we are confident that this wind analyzing model is capable in serving as a preliminary tool in the wind energy survey problem or mesoscale transport of air pollutants in complex terrain area like northern Taiwan island.

REFERENCES

(1) Barnes, S. L., 1973: Mesoscale Objective Map Analysis Using Weighted Time-series Observation. NOAA Tech. Memo., ERL-NSSL-62.

(2) Dickerson, M. H., 1978: MASCON - A Mass Consistent Atmospheric Flux Model for Regions with Complex Terrain. J. Appl. Meteor., 17, 241-253.

(3) Endlich, R. M., F. L. Ludwig, C. M. Bhumeralker, and M. A. Estorque, 1982: A Diagnostic Model for Estimating Winds at Potential Sites for Wind Turbines, J. Appl. Meteor., 21, 1441-1454.

(4) Sasaki, Y., 1958: An Objective Analysis Based on the Variational Method. J. Meteor. Soc. Japan, 36, 77-88.

(5) _____, 1970a: Some Basic Formalisms in Numerical Variational Analysis. Mon. Wea. Rev., 98, 875-883.

(6) _____, 1970b: Numerical Variational Analysis Formulated under the Constraints Determined by Long-wave Equations and Low-pass Filter, Mon. Wea. Rev., 98, 8 884-898.

_____, P. S. Ray, J. S. Goerss, and P. Soliz, 1978: Inconsistent Finite Differencing Errors in the Variational Adjustment of Horizontal Wind Component, Meteor. Soc. Japn, 57, 88-92.

Sherman, C. A., 1978: A Mass-consistent Model for Wind Fields over Complex Terrain, J. Appl. Meteor., 17, 312-319.

Table 1. Content of Case Studies

Case No.	Time	Prevailing Wind*
1	1983, 1, 30; 14LT	N, 10 m/sec
2	1983, 1, 30; 23LT	NE, 12 m/sec
3	1983, 1, 31, 17LT	E, 10 m/sec
4	1983, 2, 1; 08LT	SW, 5 m/sec
5	1983, 2, 1; 14LT	SSE,10 m/sec
6	1983, 2, 1; 23LT	NE, 3 m/sec
7	1982, 7, 8; 23LT	SSW, 3 m/sec
8	1982, 7, 9; 02LT	2, 6 m/sec
9	1982, 7, 9; 11LT	SE, 5 m/sec
10	1982, 7, 9; 20LT	SSE, 3 m/sec

*Prevailing winds are indicated by surface wind reports at Pon-chia-yu island about 300 Km northest of Taipei.

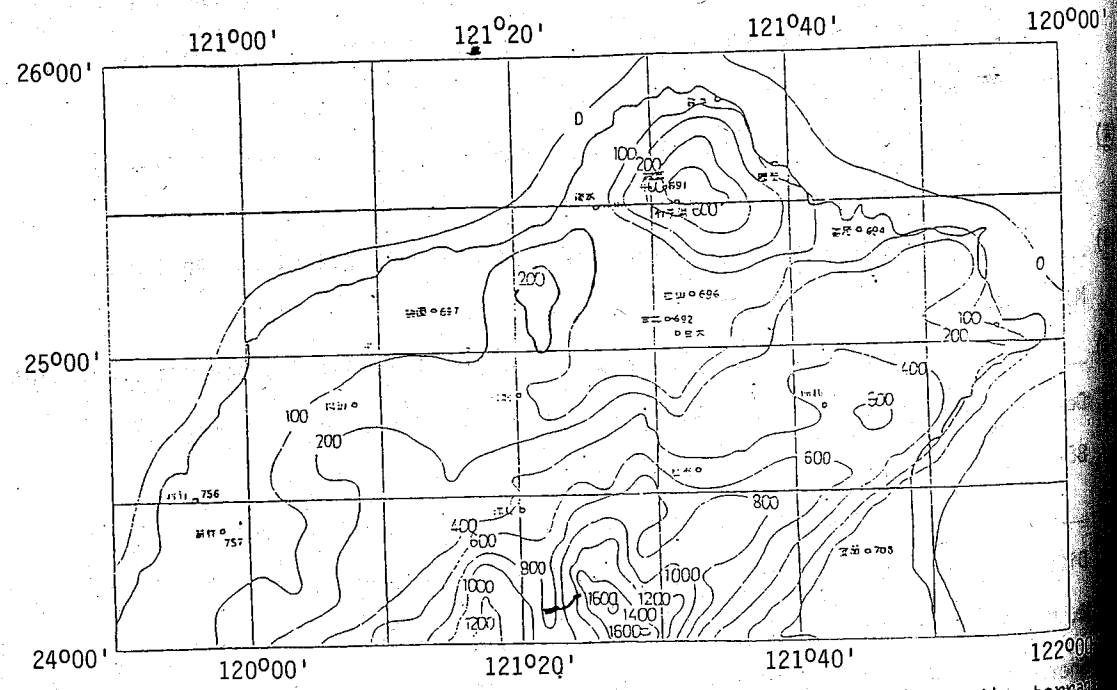

Fig. 1. The topography of Northern Taiwan, The contour-lines indicate the terra elevation above the sea-level (in meters).

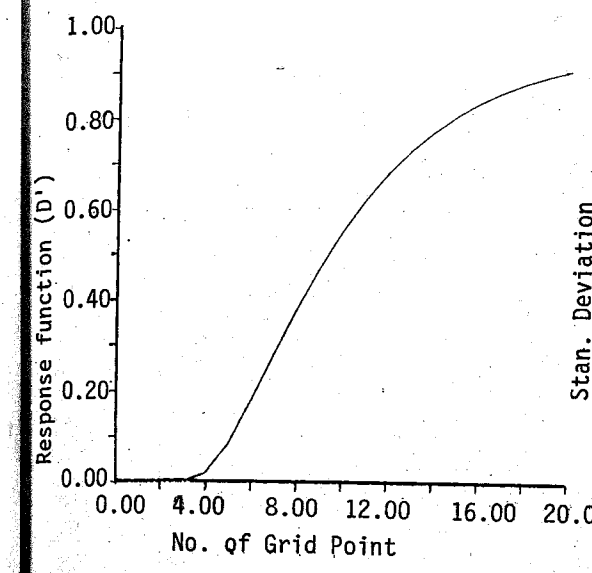

Fig.2. The response function of the objective analysis scheme (Barns scheme). The distance between grid points in 4.Km.

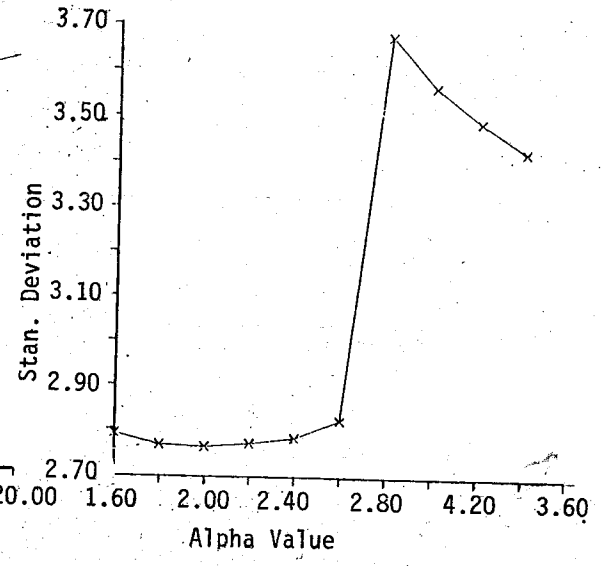

Fig.3. The relation defined by (13), (14) and (15).

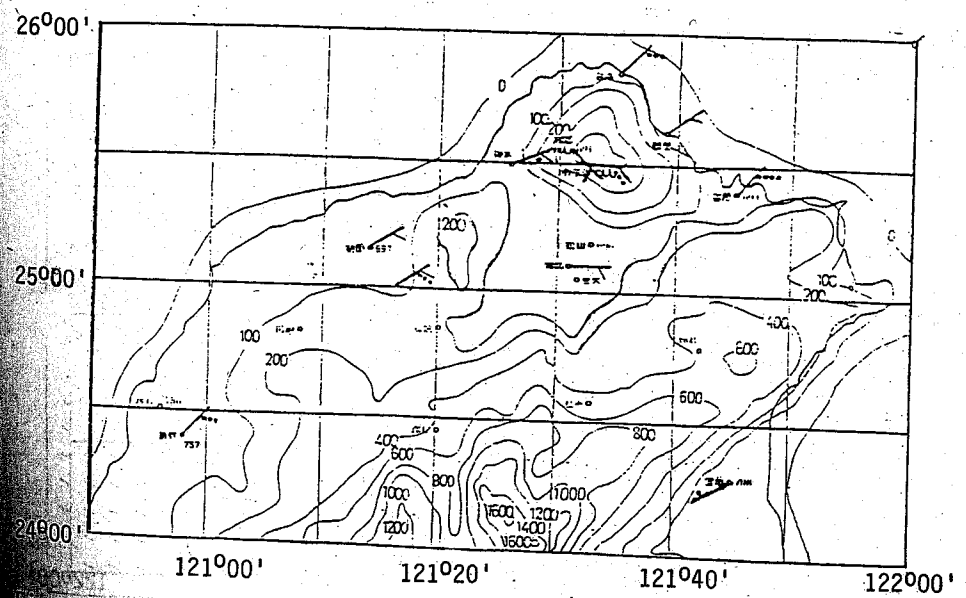

Fig. 4. The observed surface winds of case 2. A full-bar represents 10 m/sec, half-bar for 5 m/sec, and dot for 1 m/sec.

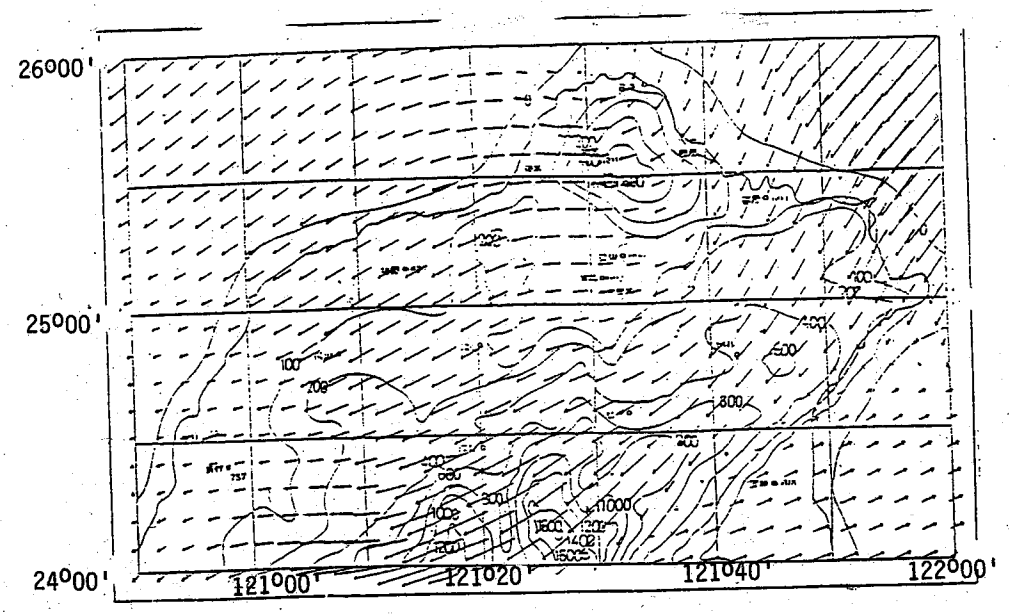

Fig. 5. The analyed surface wind pattern for case 2, in this analysis, 12 surface wind reports are used as the input data.

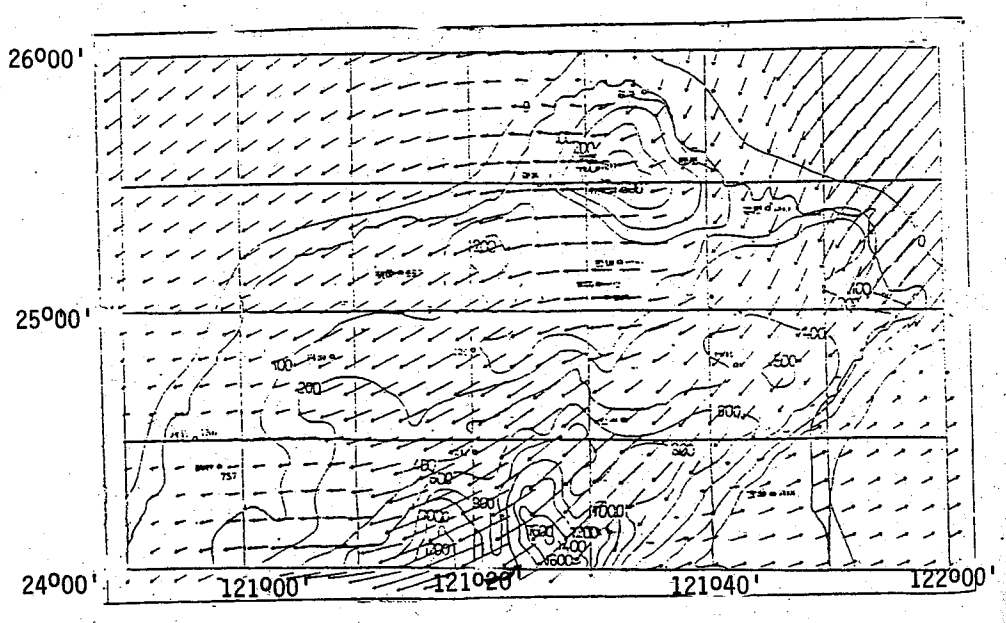

Fig. 6. Same Fig. 5, Except wind reports at Taipei (Station No. 692), Keelung (Station No. 694) are omitted in the input data.

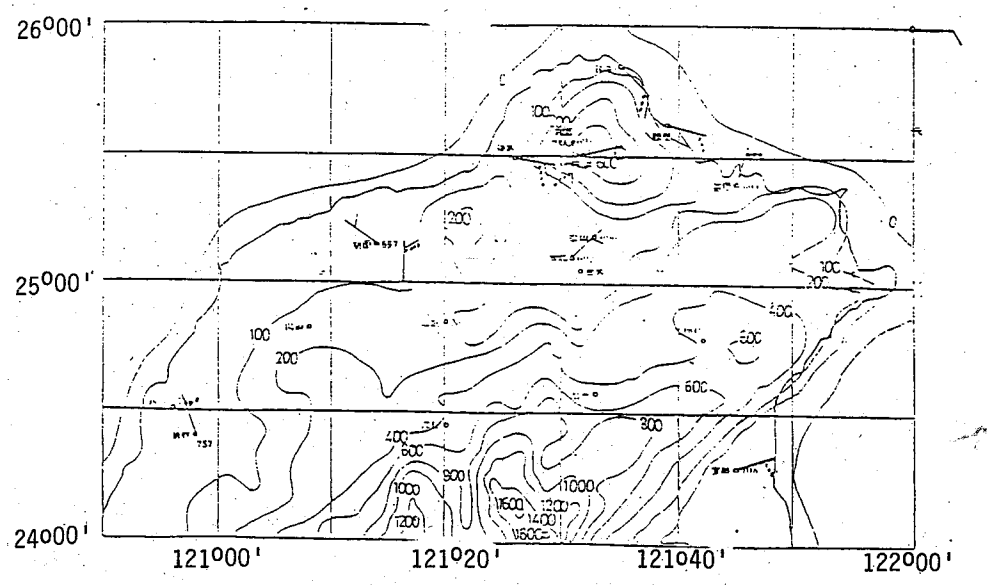

Fig. 7. The observed surface winds of case 3.

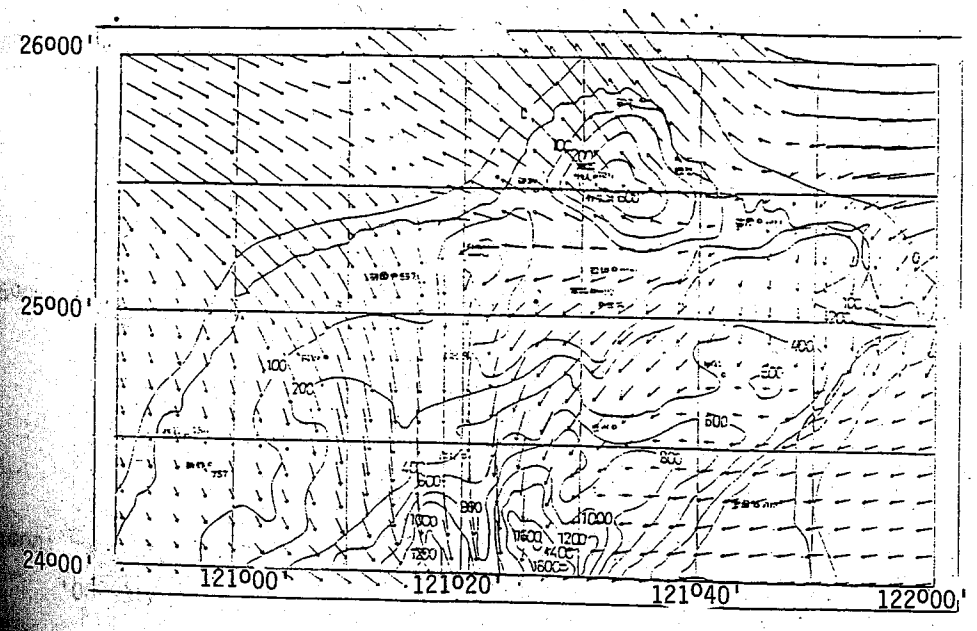

Fig. 8. The analyzed surface wind pattern for case 3. There is a total of 12 surface wind reports are used as the input data.

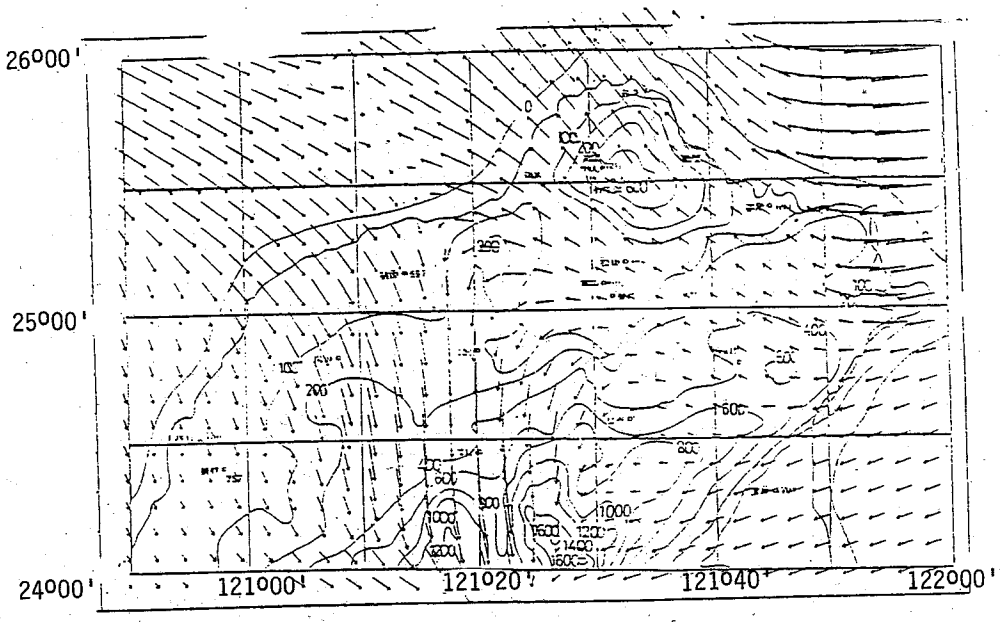

Fig. 9. Same as Fig. 8, except wind report at Taipei and Keelung are omitted in the input data.

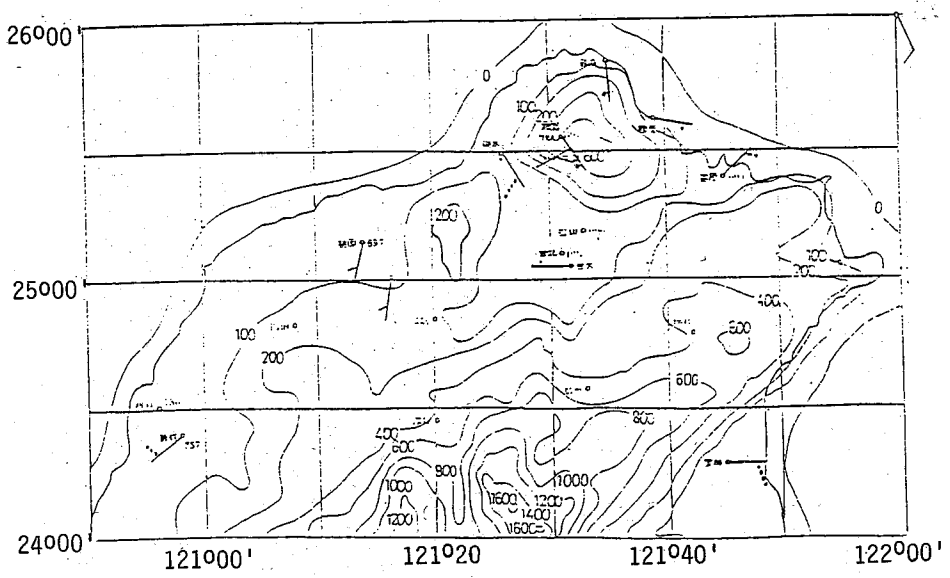

Fig. 10. Observed surface wind for case 5.

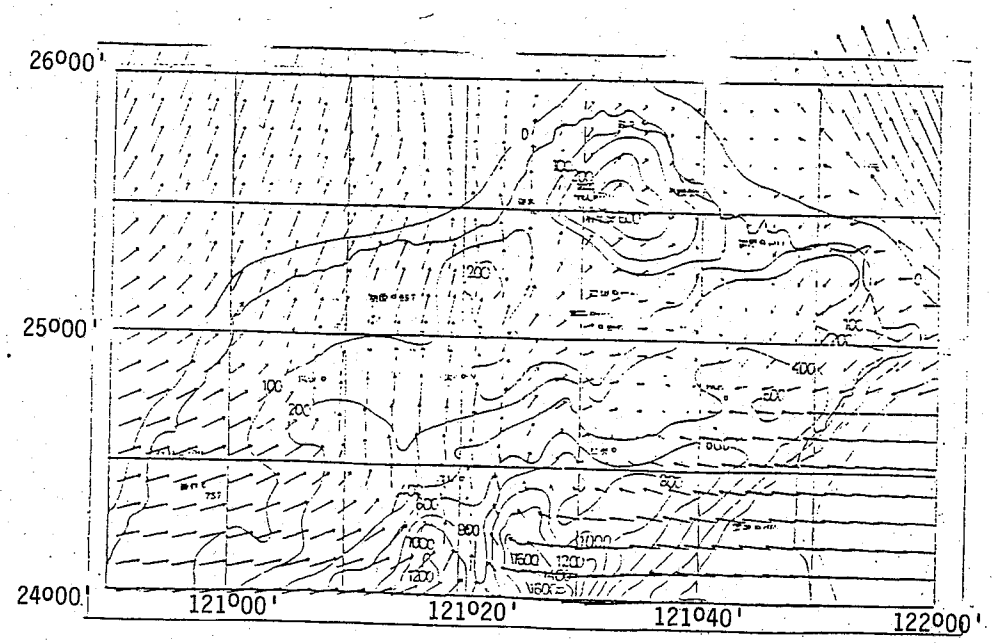

Fig. 11. The analyzed surface wind pattern for case 5.

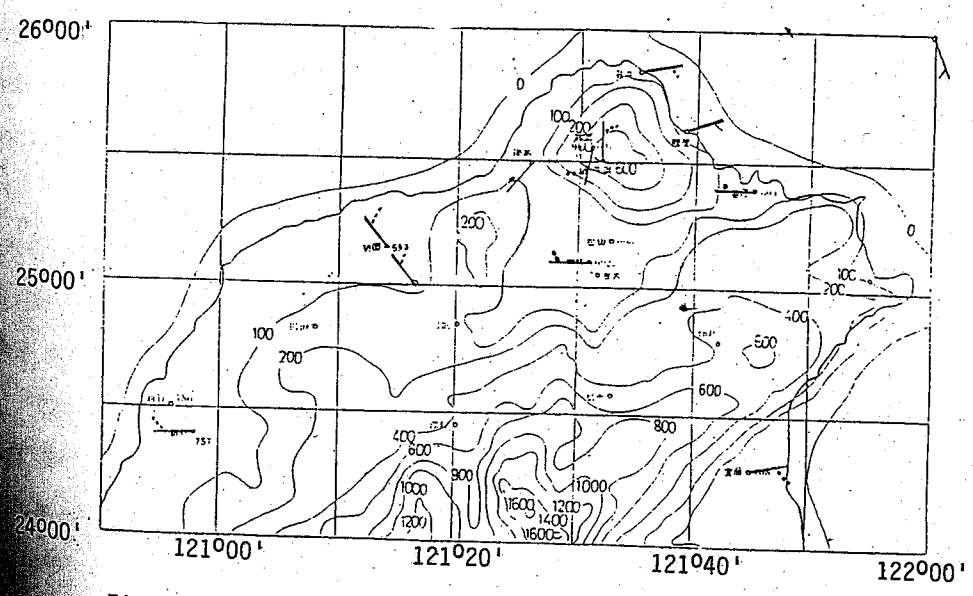

Fig. 12. The observed surface winds for case 9.

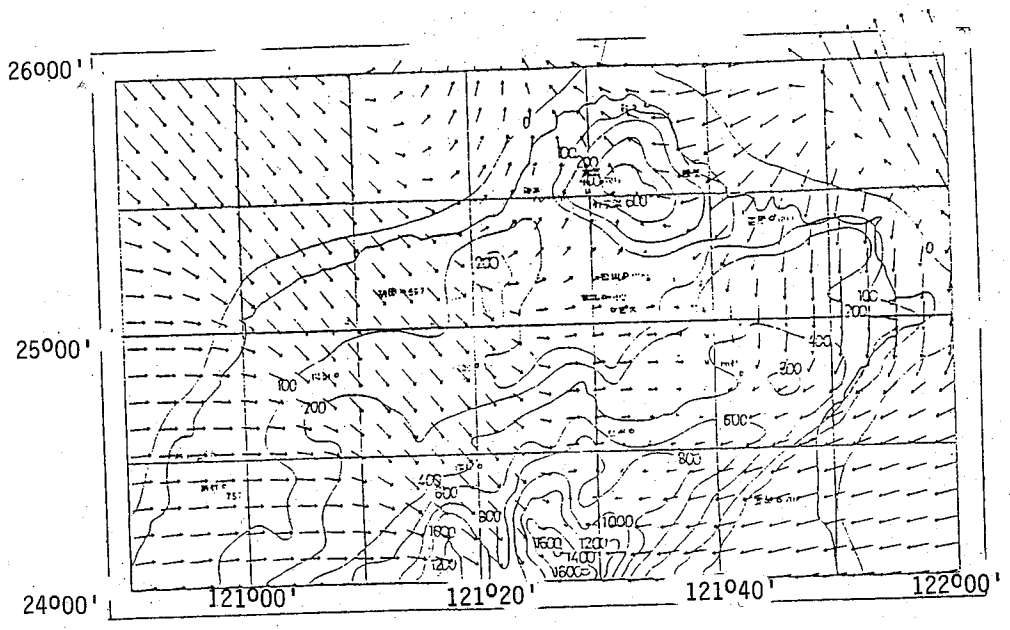

Fig. 13. The analyzed surface wind pattern for case 9.

THEORETICAL STUDY OF ROCKET EXHAUST PLUMES
PART I: CHARACTERISTICS METHOD

L. C. Chien, C. T. Wang, W. J. Liang and F. L. Chen
Institute of Physics
Academia Sinica, Nankang,
Taipei, Taiwan, R. O. C.

The method of characteristics has been developed to investigate the underexpanded rocket exhaust plumes. According to the plume structure, the computational procedures are set up similar to the formation process of actual flow. The method are employed on solving the plumes of two standard nozzles under different conditions and the plume of Thor missile exhausts into supersonic ambient flow. The results are compared with the existing solutions. For an object comparison, furthermore, the results got by finite difference method are devoted to calculating the same plumes stated previously. It is found that the results obtained with these two different numerical simulations are in good agreement.

INTRODUCTION

The rocket exhaust gases from highly underexpanded nozzles operating in low pressure condition results in large billowing plumes. Figure 1 shows a typical underexpanded rocket exhaust plume from a single-engine missile. Between the jet shock and the air shock, there is a turbulent mixing layer in which the air mixes with the exhaust flow. The air shock is the outer limit of the region in which the exhaust flow influences the air flow while the jet shock is the inner limit. Consequently, the flow in the region bounded by the jet shock and Mach disc is identical to the flow that would result when exhausting into vacuum.

Recent interest in rocket exhaust plumes has been stimulated by many design problems that arised when the exhaust gas left nozzle. For example, problems involving the effects of the plume impinging on the other vehicles, ground surface, and even on it own vehicle have received considerable attention. Still another case of great concern is the severe attenuation of communication signals between a space vehicle and ground control caused by the presence of free electrons in the plume. Other problems caused by large billowing plumes, such as the easy-detection of due to infared radiation exited from plume, cannot be avoid avoided but to

understand the plumes.

The method of characteristics are first used to calculate plume flowfiled. In the method characteristics solution, the flow at the lip of nozzle is expanded through a Prandtl-Meyer expansion fan to the pressure calculated at the dividing streamline. After the exhaust flow passes through the expansion region, it is turned by the dividing causing characteristics of the same family to coalesce and form the jet shock. The jet shock is of increasing strength as it moves downstream and, thereafter, decreases when it reaches the maximum diameter. One of the classical reports applying the method of characteristics of calculate plumes is by Love et al (1). However, in this report the so-called "fold-back" method employing in characteristics net results that the calculatings are valid only in the region near exit surface. This simplification has been eliminated by Andrew et al (2). And the resulting plume flowfield has been experimentally verified by Vick et al (3). There are some other investigators, Cassanoval et al (4) and Reis et al (5), are devoted to applying the method of characteristics on plume flowfield.

In addition to the method of characteristics technique for compating inviscid plume flowfields, Boyton and Thomson (6) have recently devised a Lagrangian finite-difference technique which can be applied to the solution of inviscid as well as viscous plume flowfield. Their technique has been extended by incorporating chemical non-equilibrium and turbulent transport capability into the analysis by Tannehill (7). This method will be discussed in detail in part II of this subject.

Both the method of characteristics and the Lagrangian finite-difference technique require a considerable amount of effort and computer time. This has prompted several investigators to dévelop approximate method which can be quickly applied to problem of determining the gross plume structure. They are, such as, Albini (8), and Hubbard (9). These approximate methods are able to determine the geometry of the plume shape, jet shock location, and internal pressure distribution.

However, the characteristics method, still, is a highly efficient technique for calculating the inviscid supersonic flow.

In the present paper, the authors developed a method of characteristics which the numerical calculating procedures are set up in similar to the formation process of actual flow. It is devoted to calculating the inviscid, rotational plume flowfield. The results obtained are, then, employed on comparison with the existing solutions.

GOVERNING EQUATIONS

In this section the equations necessary for computing the supersonic flowfield on a rocket exhaust plume are presented. The equations are applicable to both viscous and inviscid flowfield, and the flowfield including non-equilibrium chemical reactions if the proper terms are retained.

According to the derivation of Edelman and Weilerstein (10), the general equations for steady flow of a reacting mixture of perfect gases are:

Global continuity equations:

$$\nabla \cdot \rho \overline{V} = 0 \tag{1}$$

Species continuity equations:

$$\nabla \cdot \rho C_i \overline{V} = \rho \dot{W}_i - \nabla \cdot \overline{J}_i \tag{2}$$

Momentum equations:

$$\nabla \cdot [(\rho \overline{V})\overline{V}] = -\nabla P + \nabla \cdot \overline{\overline{\tau}} \tag{3}$$

Energy equations:

$$\nabla \cdot \rho \overline{V} H = \nabla \cdot (\overline{\overline{\tau}} \cdot \overline{V}) - \nabla \cdot \overline{Q} - \nabla \cdot \sum_{i=1}^{N} h_i J_i \tag{4}$$

Equation of state:

$$P = \rho \overline{R} T \sum_{i=1}^{N} \frac{C_i}{M_i} \tag{5}$$

where H is the total enthalpy, subscript i represnets the ith species from a total N.

In these equations, the viscous shearing stress $\overline{\overline{\tau}}$ is given for a Newtonian fluid and the heat transfer term Q can be evaluated by Fourier law. The diffusional mass flux term $\overline{J}_i$ can be applied by Fick's law (11). Accordingly, the species production term $\dot{W}_i$ represents the production rate of the ith species from the system of chemical reactions can be given by the classical Arrhenius law (12).

In order to simplify the above equations, some assumptions will be employed on the plume flowfield. In the high altitude, the assumption of frozen flow can be employed everywhere in the plume flowfield (13). Also, due to the results got by Tanne-

hill (7), it is shown that the reacting processes influent the plume slightly. So that the mass production term, $\dot{W}_i$, is neglected here; similarly, the mass diffusion term, $\dot{J}_j$ can be ignored due to the transition to turbulent is delayed. So that, the species continuity equation (2) would not be considered; and the species number N is equal to one. This simplification avoids the complex iteration in computational procedure. Furthermore, at high altutide the viscosity of the flowfield is small due to the ambient low pressure. Then, the viscous terms in equations (3) and (4) are negligible. Finally, assuming there is no heat transfer in the plume flowfield, the heat transfer term $\vec{Q}$ is equal to zero. The subject, depends on the assumptions made above, appears to be a steady, inviscid and frozen flowfield problem.

The flow in the plume will be taken as isentropic along the streamline. That would lose no generality because the existance of the gradient in entropy and stagnation entropy normal to the streamline makes the flow rotational in the flowfield. It satisfies the physical phenomena that the flow is rotational after the ambient flow passes through bow shock uniformly. Accordingly, the governing equations become:

Global continuity equations (6)

$$\nabla \cdot (\rho \overline{V}) = 0$$

Momentum equations: (7)

$$\nabla \cdot [(\rho \vec{V}) \vec{V}] + \nabla \rho = 0$$

Energy equations: (8)

$$\nabla \cdot (\rho \vec{V} H) = 0$$

Equation of state: (9)

$$P = \rho \overline{R} T$$

For an isentropic flow along the streamline, the energy equation may be replaced by speed of sound equation (14): (10)

$$\nabla \cdot (\vec{V} P) - a^2 \nabla \cdot (\vec{V} \rho) = 0$$

Taking the plume as a two-dimensional flowfield, equations (6), (7) and (10) can be transformed into characteristics and compability equations as follows:

Characteristic equations: (11)

$$(\frac{dy}{dx})_0 = x_0 = \frac{v}{u}$$

$$(\frac{dy}{dx})_\pm = x_\pm = \tan (\theta \pm \alpha) \quad (12)$$

Compability equations:

$$\rho \overline{V} \, d \overline{V} + dp = 0 \quad (13)$$

$$dp - a^2 d\rho = 0 \quad (14)$$

$$\frac{\sqrt{M^2 - 1}}{\rho \overline{V}^2} d\rho_\pm \pm d\theta_\pm + \zeta \left[\frac{\sin\theta \; dx_\pm}{yM \cos (\theta \pm \alpha)} \right] = 0 \quad (15)$$

where $\zeta = 0$ for planar flow, and $\zeta = 1$ for axisymmetric flow. The index +, - and 0 denoted C_+, C_- and C_0 characteristic curves, respectively.

These equations are sloved to determine the location and physical properties of the points through which the characteristics pass. Together with the oblique shock equations (14), they described the plume flowfield completely.

NUMERICAL PROCEDURE

The supersonic flow exhausted from the nozzle of rocket into ambient low pressure flowfield caused rapidly expansion near the nozzle lips. Originated from the lips, the expansion waves spread over in the flowfield comprised the Prandtl-Meyer expansion fan. Between the exhaust surface and the Prandtl-Meyer expansion fan, there locates a unifrom region, i.e., Mach cone. In this region, the physical properties are almost keep constant (for circular nozzle only). The characteristic lines which penetrate through the prandtl-Meyer expansion fan are the expansion waves. These waves, then, reflect from the plume boundary with becoming compression ones. The jet shock is formed by the coalescence of these reflected compressive waves. As moving downstream, a normal shock forms due to the increases of pressure ration between the flowfield of plume and ambient. If the ambient flow is supersonic, an oblique shock will happen outside of the plume boundary.

The calculating procedures of the method of characteristics used here would be developed similar to that of actual flow. A segment of typical characteristics network is shown in Figure (2). The calculation started from the exit surface. From the exit surface, lots of characteristic lines with different family exited and formed a characteristics network in Mach cone. The outerest characteristic line of

Mach cone is called Leading Characteristic Line (L. C. Line). Many expansive characteristics spread outward from L. C. Line in the prandtl-Meyer expansion region. In whole flowfield, there exist right-running characteristic lines C_- and left-running characteristic line C_+ . The expansion waves belong to the right-running characteristic line C_- . On the other hand, the left-running characteristic lines across the expansion region would reflect from the plume boundary with becoming compressive waves. These compressive characteristic lines coalesced and formed the jet shock. The computation continued with truncating one of the coalesced characteristics and the other one still moved downward.

The program is developed with the calculation procedure stated as above. It can analyze planner or axisymmetric flow. The Prandtl-Meyer expansion fan is set up so that the right-running expansion waves are uniformly spread. This is done by making the pressure difference between two near waves decrease as pressure decreases. If an error occurs in an arithmetic subrouting (THERMO), a new point is insert in the previous right-running line, and the current line is recalculated. This action is displayed in the output flowfield may be truncated along a left-running wave reflected from the axis under user control. This reduced the computer time considerably. It is also found that the characteristics net needs to be fine for the distored region.

RESULTS AND DISCUSSION

The method of characteristics developed in this paper is employed in solving inviscid plumes exhausted by rocket under difference pressure ratios and exit conditions. The results are compared with the existing solution of irrotational flow and the finite-difference solutions.

The primary parameters which influence exhaust plume profile are exit Mach number M_j , nozzle lip angle θ_N , specific heat ratio γ and the ratio between exit pressure P_j and ambient pressure $P\infty$. To investigate the physical phenomena affected by these four parameters, the program is devoted to solving the plume flowfield under various conditions due to changing those parameters. First, the effect of exit Mach number is observed (Figure 3). Five plumes' profiles are shown for different M_j = 1.5 (0.5) 3.5. The shape inflated as decreased Mach number. It

because the faster the exit flow, the less the influence by ambient flow pressure. On the upper-left corner in figure 3 showed the relationship between M_j and plume radius under different pressure ratios. It found that the influence of M_j increased as pressure ratio increased. Likewise, the effect of pressure ratio is observed in the same way (Figure 4). The high pressure ratio causes the inflection of plume shape. Furthermore, different lip angle influents the plume shape greatly (Figure 5). The exit flow expands dominately as lip angle becomes large. The specific heat ratio of the gas of the exit flow also has a considerable influence on the plume shape (Figure 6). High value of γ denotes the gas absorbed more energy with increasing one degree of absolute temperatue. So that, the higher γ caused large velocity of exit flow under same difference of temperature. That is the reason why the higher value of γ induces the small diameter of plume.

After analyzing the physical phenomena found that the results are resonable, the program is devoted to solving plumes of two standard nozzles, conical and circular nozzle, under three different conditions to compare with the existing solutions (Table I). The initial turning angle will be solved firstly. The flow angle through which the flow will expand is the difference between the Prandtl-Meyer expansion angles corresponding to the jet-boundary Mach number and exit Mach number. It is

$$\alpha_N = \nu_1 + \nu_N + \theta_N \tag{16}$$

where α_N is the turning angle υ_1 and ν_N are the Prandtl-Meyer expansion angle with respect to the boundary and exit Mach number, respectively. And θ_N is the lip angle as stated before. The calculated results under different pressure ratios of the two nozzles are compared with those obtained by Andrews et al (10) nicely (Figure 7). The method of characteristics can predict the flow near the exit surface well although may be under different calculation procedures.

Various plumes' shapes which are obtained under three different conditions of nozzle I and nozzle II (Figure 8 and 9). The results would compare with those got Andrew et al (10) which are evaluated in the irrotational flowfield. It is found the plumes with rotational flow are fatter than the plumes with irrotational Physically, uniform flow pass through bow shock will induce the flow to be onal. Furthermore, it needs iteration in calculation process for rotational ecause there are three characteristic lines pass through one node. But it is

not for the irrotational flow because there are only two characteristic lines for one node. This causes the numerical error which will propagate downstream and reduce that the solution is unacceptable in the downstream flowfield. Figure 10 is the plume exhausted by nozzle II under pressure ratio equals to 23800, i.e., almost under the vacuum ambient condition. In this figure, one can inspect obviously the coalescence of the reflected compressive waves which forms the jet shock. There are 40 right-running characteristic lines in the Prandtl-Meyer expansion fan. The characteristics net in the Mach cone is too crowded to show here. The propagate of Mach waves in the flowfield is one of the features of the characteristics method. This can be observed in Figure 10 easily.

On the nodes of characteristics net, there are some physical properties, such as pressure, temperature and Mach number, which are solved previously. In Figures 11, 12 and 13, the distributions of pressure, temperature and Mach number for nozzle I under case 1 are shown with the iso-valued curves. Observing the pressure distribution, there exists a pressure jump near the plume boundary. That is the result caused by jet shock. Again, it is found that the isobars formed close regions near the axis and expanded outward gradually with decreasing values. Contractly, the influence of ambient conditions propagates inward step by step. That is why the region far away from boundary is called "undisturbed region". On the upper-left corner, the Prandtl-Meyer expansion fan is shown with the pressure decreased outward rapidly. Similary, the undisturbed region can also be found in the distribution of temperature and Mach number. In these figures, there exist unreasonable bubble that is caused by coarse characteristics net in the flowfield. The uniform region, Mach cone, can be inspected by the value of first iso-valued curve on each figure equals to the exit condition. In addition, one can find that the temperature and pressure decreased as move downstream. This is induced by the ambient low pressure and temperature flowfield. On the other hand, for isentropic flow the decreasing of temperature causes the increasing Mach number. These properties developed downstream in this way until a normal shock happened. Behind the normal shock, called Mach disc, the flow becomes subsonic (not shown here).

The plumes obtained before are under the still ambient flow condition. For investigating the influent of ambient supersonic flow, the plumes of Thor missile

which exhausted into a supersonic flowfield are calculated with the method of characteristics developed in the paper. The results are compared with those obtained by Tannehill (7) (Figure 14 and 15). The plume shape obtained by the method of characteristics are fatter than the result of Tannehill obtained by Lagrangian finite-difference method. Furthermore, the pressure distribution along surface A in Figure 14 is compared in Figure 15. Care must be taken here that the data of Tannehill shown in Figure 15 are enlarged ten times in scale. Because the origin data shown by Tannehill are obviously unreasonable because they are too small for the exit condition. By adjusting in this way as Figure 15, the data of this paper and Tannehill before jet shock are compared nicely. But it is not for the data in jet shock layer. The detailed discussion of these distored results can be found in Chen (15).

For making an objectly comparison of the results got by the method of characteristics developed in this paper, the authors follows the Lagrangian finite-difference method developed by Boyton and Thomson (6) with some modifications to calculate the plume stated above. The detailed procedures and results are to be published as the second part of this study about rocket exhaust plumes. Here, this developed method under modifications made by the authors is employed on solving the plume exhaust by Thor missile to make an object comparison between the results of method of characteristics and Tannehill. In Figures 16, 17 and 18 are shown the comparisons got by these two different numerical approaches. The plume shapes got by method of characteristics and Lagrangian finite-difference method are almost matched each other. The pressure distributions along surface A in Figure 16 have also the results in good agreement. In addition, the temperature distributions along surface A are almost in the same result (Figure 18). The matched results got by two different numerical approaches proved the reliability of method of characteristics developed in this paper. As the disagreement data of Tannehill, the authors thought it as the wrong values of plume conditions given in his paper.

To predict the location of Mach disc, the pressure distribution downstream of shock is shown in Figure 19. The Mach disc happened at the location where the ssure down tream of the jet shock reaches a minimum (16). The location obtained sima and Radtke is 33 meters downstream from the exit surface. And the press- stribution in Figure 19 reaches a minimum about 35 meters downstream.

Finally, to compare with the experimental data, the curvature of plume boundary near the nozzle lips is investigated here. Under constant exhausted velocity, the curvatures with various pressure ratios are calculated as shown in Figure 20. These results are compared with those got by Love et al (1). As shown in this Figure , for M_j = 2.0, the experimental results (1) is 8.2, theoretical result (1) is 7.6, and the investigated result got here is 7.75.

CONCLUSION

The method of characteristics was developed in investigate the supersonic, inviscid plume under various altitudes with frozen, rotational flowfield. This method was employed on solving two standard nozzles under different cases and the plume of Thor missile exhausted into supersonic ambient flow. This method can predict the plume shape and internal structure of plume flowfield rapidly and accurately.

The computer excution time required to calculate the plume flowfield, which based on 20 nodes on exit surface and 20 pieces of Prandtl-Meyer expansion waves truncated at the 10th waves afterwards, is about 26 seconds for CDC CYBER-74 computer.

REFERENCES

(1) Love, E. S., Grigsby, C. E., Lee, L. P., and Woodling, M. T. Experimental and theoretical studies of axisymmetric free jets. United states National Aeronautics and space Administration Technical Report R-6, 1959.

(2) Andrews, E. H., Jr., Vick, A. R., and Craidon, C. B. Theoretical boundaries and internal characteristics of exhaust plumes from three different supersonic nozzles. United States National Aeronautics and Space Administration Technical Note D-2650. 1965.

(3) Vick, A. R., Andrews, E. H., Jr., Dennard, J. S., and Craidon, C. B. Comparisons of experimental free-jet boundaries with theoretical results obtained with the method of characteristics. United States National Aeronautics and Space Administration Technical Note D-2327. 1964.

(4) Reis, R. J., Aucoin, P. J., and Stechman, R. C. "Predition of Rocket Exhaust

Flowfields." J. Spacecraft, Vol. 7, No. 2, pp.155-159, 1970.

(5) Cassnova, R. A. "Expansion of Jet into a Vacuum", Eleventh International Symposium on Combustion, Univ. of Calif. Berkeley, Calif. 1966.

(6) Boynton, F. P. and Thomson, A. Numerical computation of steady, supersonic two-dimensional gas flow in natural coordinates. Journal of Computational Physics 3:379-398. 1969.

(7) Tannehill, J. C. Numerical computation of intermediate altitude rocket exhaust plumes, including nonequilibrium chemical reactions and diffusion. Ph. D. Thesis, Iown State Univ. Ames, Iowa. 1969.

(8) Albini, F. A. Approximate computation of underexpanded jet structure. American Institute of Aeronautics and Astronautics Journal 3:1535-1537, 1965.

(9) Hubbard, E. W. Approximate calculation of highly underexpanded jets. American Institute of Aeronautics and Astronautics Journal 4:1877-1879, 1966.

NOMENCLATURE

a : Speed of sound, m/sec.

C_i : Mass fraction of species i.

H : Total enthalpy, KJ/Kg.

h_i : Enthalpy of element i, KJ/Kg.

$\bar{J}_i$: Mass diffusion rate of element i.

M : Mach number.

M_j : Molecular weight of element i.

N : Number of element.

p : Pressure, newton/m^2.

q : Heat flow vector, J/sec.

R : Gas constant, Nm/Kg, mole.^oK.

u : Velocity in x direction, m/sec.

v : Velocity in y direction, m/sec.

V : Velocity ($\sqrt{v^2+u^2}$), m/sec.

$\dot{w}_i$: Production rate of species i.

ρ : Density, Kg/m^3.

τ : Stress tensor, Newton/m^2.

υ : Prantle-Meyer expansion angle (degree).

θ : Flow angle (degree).

α : Shock angle (degree).

INDEX

o : Along streamline.

+ : Along left-running characteristics.

- : Along right-running characteristics.

N : On the lips of nozzle.

Table 1. Nozzles exit and operating conditions for this study

		Nozzle I (circular arc)	Nozzle II (conical)	Thor nozzle
M_j		5.35	3.39	2.986
P_j (atm)		7.42×10^{-3}	3.237×10^{-1}	0.617
T_j (°K)		2000	2000	2060
θ_N (degree)		0	19.5	0
r_j (m)		6.464×10^{-2}	1.054×10^{-2}	0.5791
γ		1.24	1.18	1.210
P_∞ (atm)	case 1	7.510×10^{-4}	2.158×10^{-2}	1.3425×10^{-3}
	case 2	3.945×10^{-5}	1.360×10^{-3}	
	case 3	1.372×10^{-6}	1.360×10^{-5}	
T_∞ °K		200	200	266.15
M_∞				5.117
P_j / P_∞	case 1	9.88	15	459.6
	case 2	188.1	238	
	case 3	5410	23800	
Ambient Flow		Still	Still	Supersonic

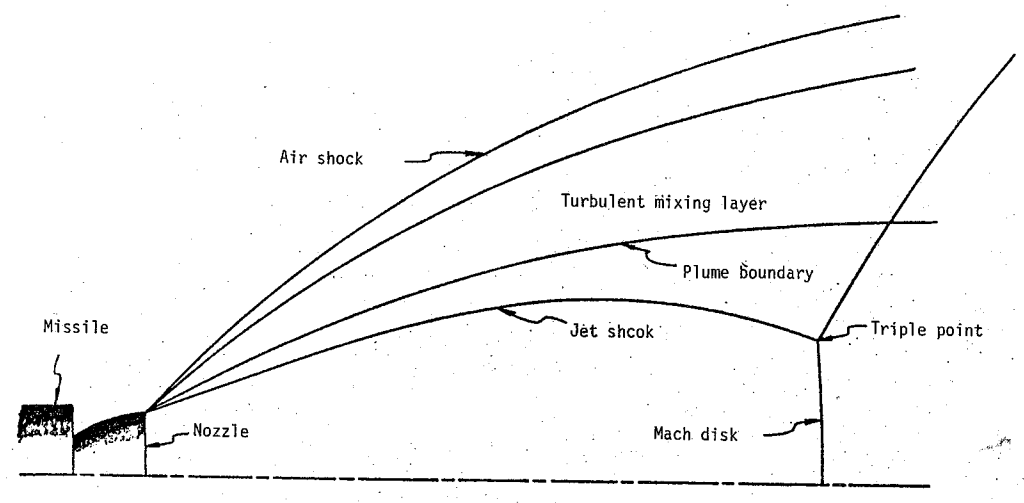

Figure 1. The underexpanded rocket exhausted plume.

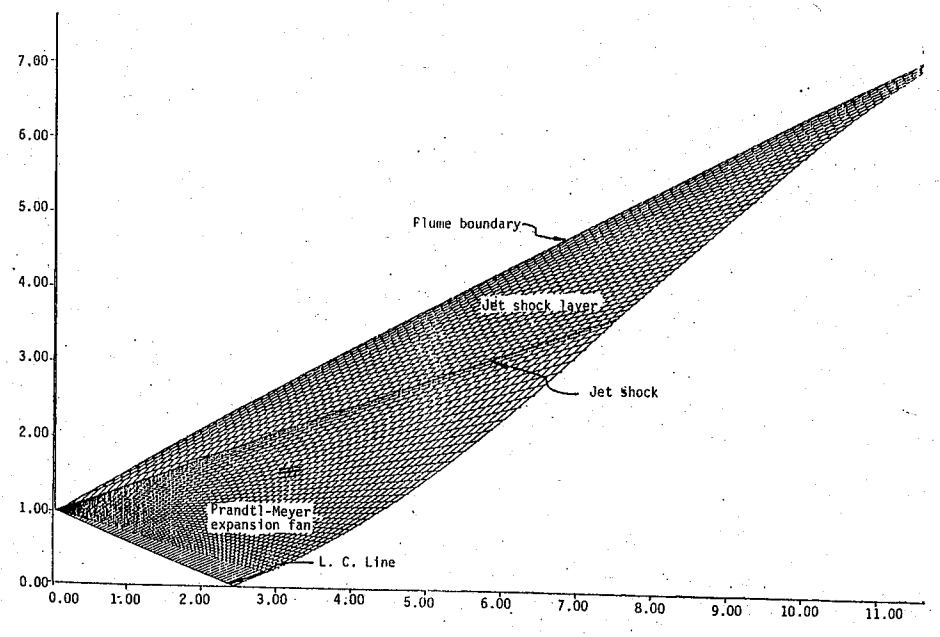

Figure 2. The structure of characteristic net of rocket exhausted plume.

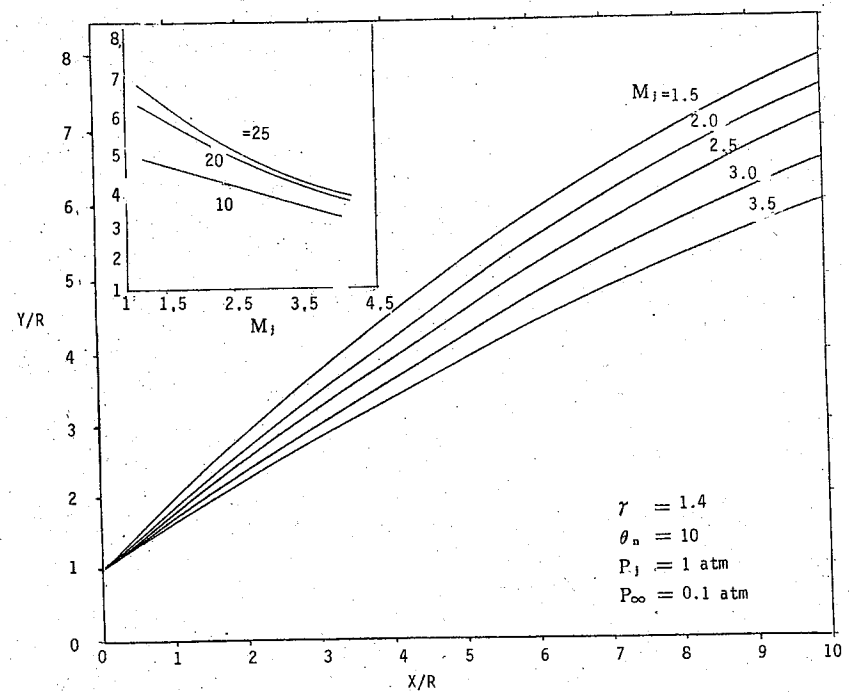

Figure 3. The effect of exiting Mach number on the plume profile. The diagram on the upper left corner shows that the relation between the radius of the plumes on X/R-4 and the exiting Mach number base on different pressure ratio.

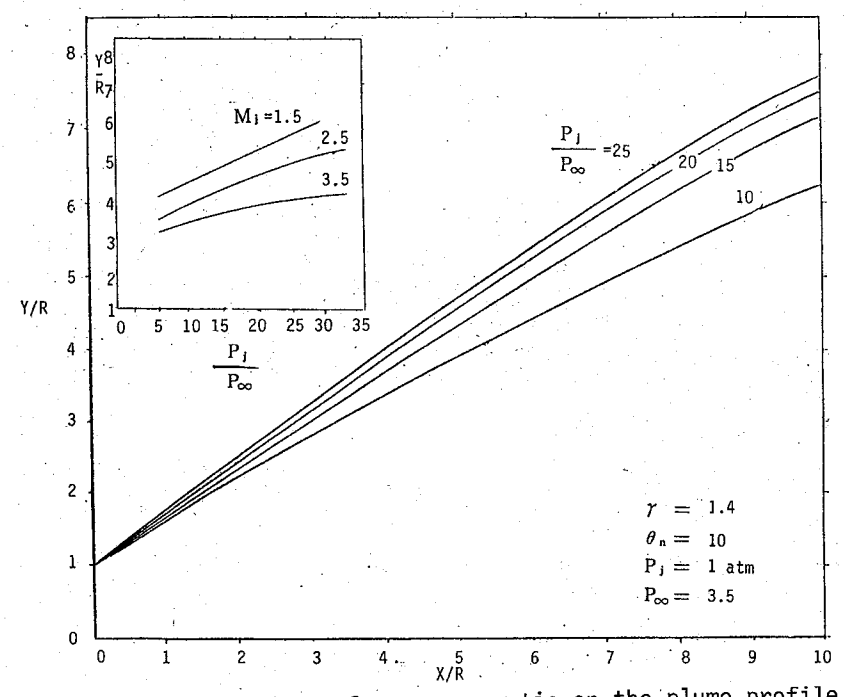

Figure 4. The effect of pressure ratio on the plume profile The diagram on the upper left corner shows that the relation between the radius of the plumes on X/R=4 and the pressure ratio base on different exiting Mach numbers.

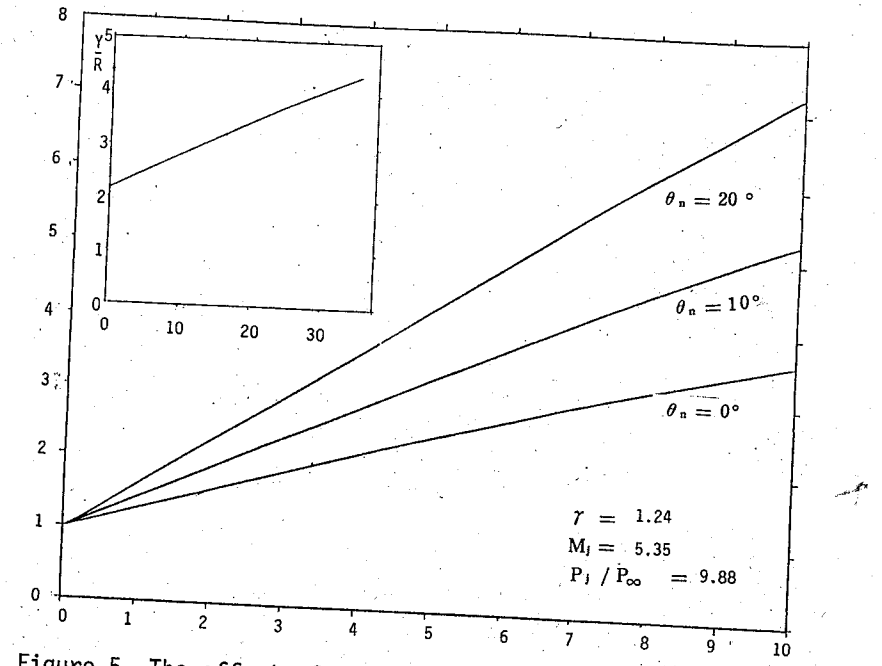

Figure 5. The effect of nozzle lip angle on the plume profile. The diagram on the upper left corner shows that the relation between the radius of the plumes on X/R=5 and the nozzle lip angle.

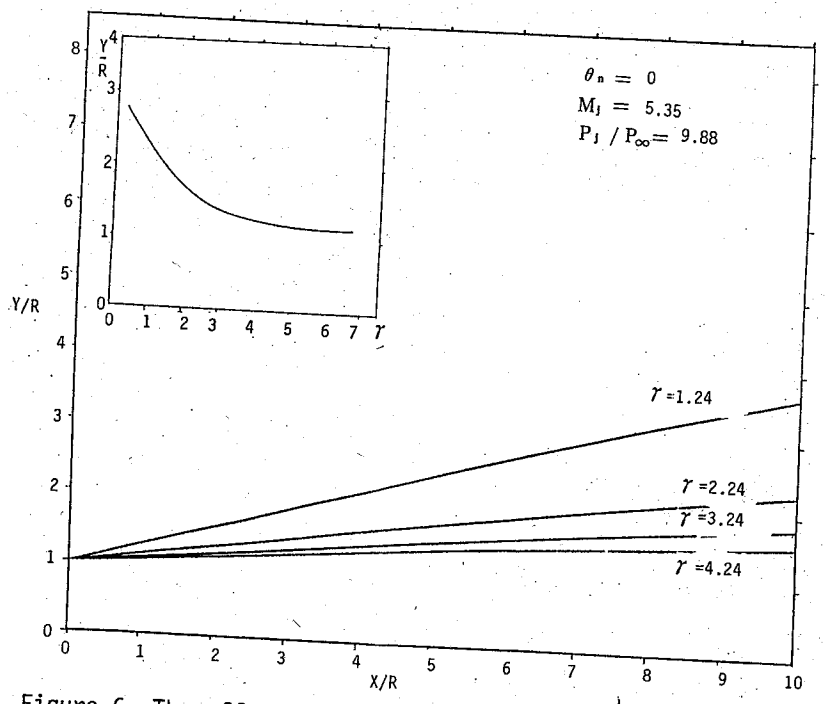

Figure 6. The effect of the ratio of specific heat on the plume profile. The diagram on the upper left corner shows that the relation between the radius of the plumes on X/R=5 and the ratio of specific heat.

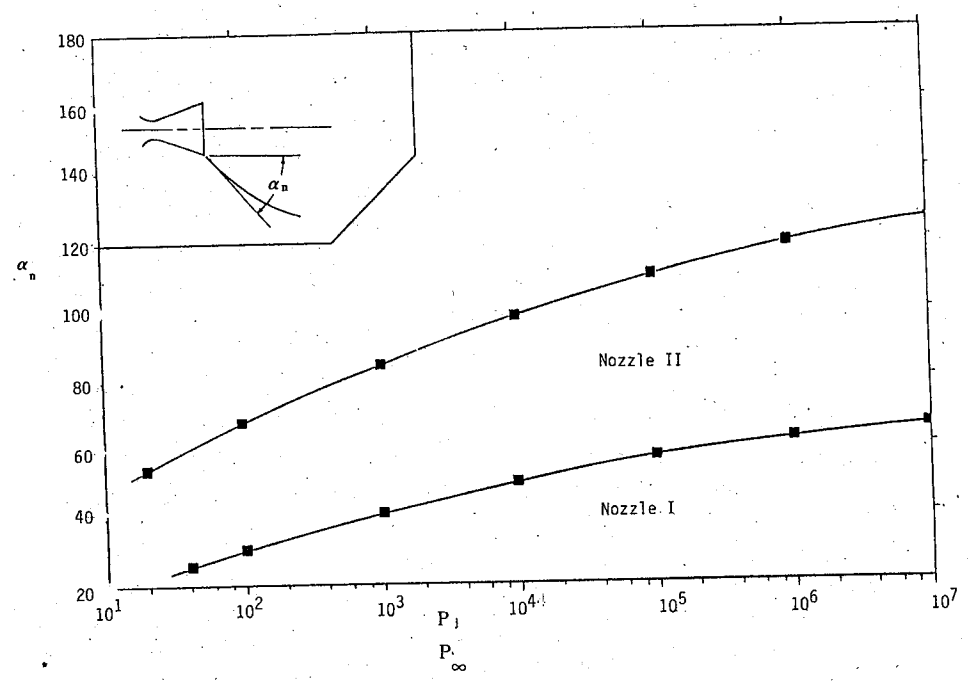

Figure 7. The relation between initial turning angle and the pressure retio. ◪ ;Andrew (1965); — : this study.

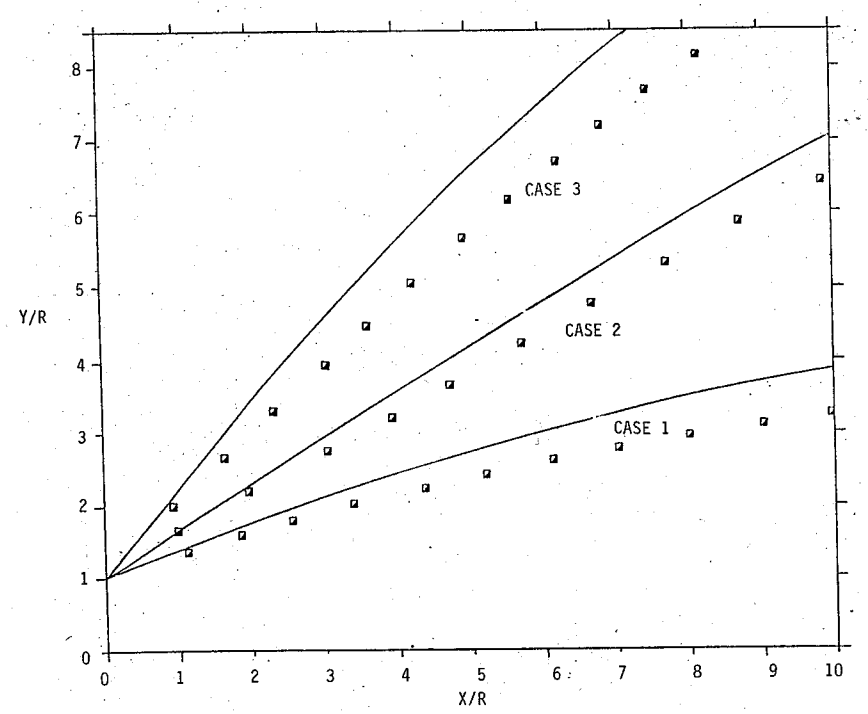

Figure 8. The plume profile of nozzle I under different ambient conditions.
◪: Andrew (1965, irrotational flow); ___: this study (rotational flow).

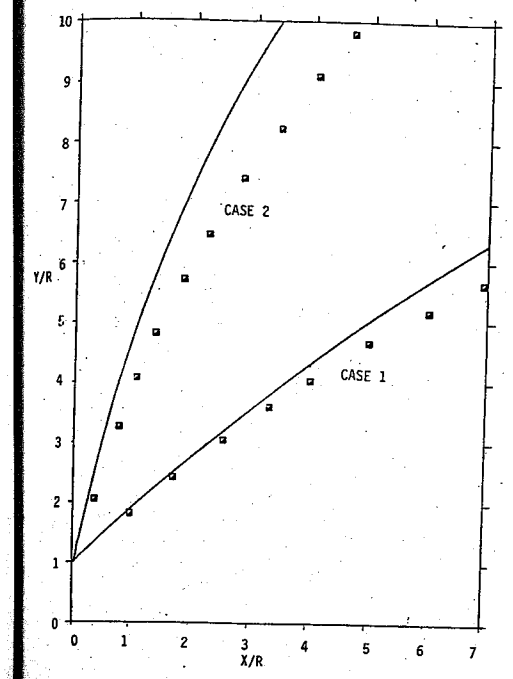

Figure 9. The plume profile of nozzle II under different ambient conditions. ◪: Andrew (1965, irrotational flow); ___: this study (rotational flow).

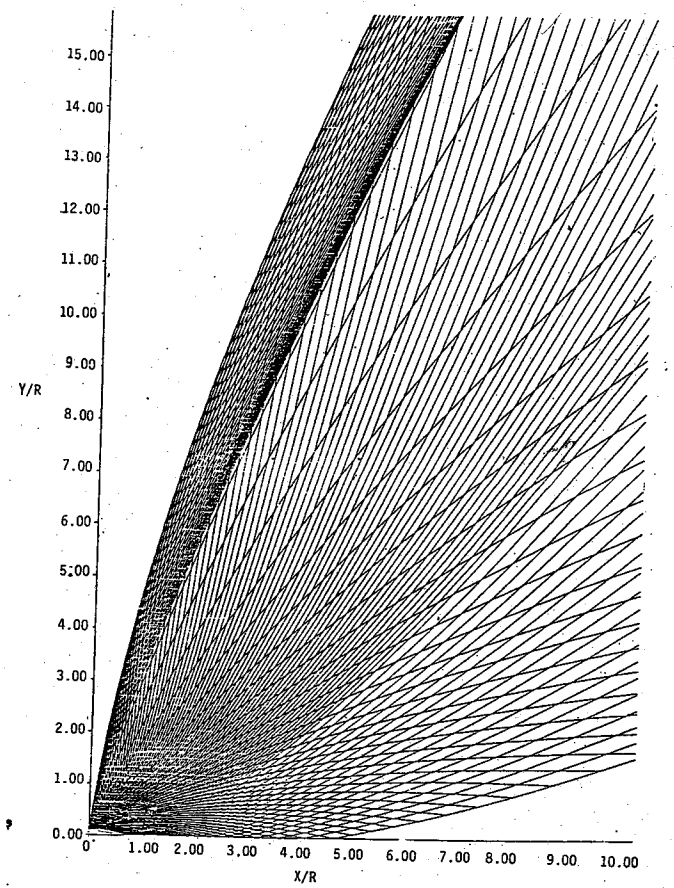

Figure 10. The characteristic net of plume exhausted by nozzle II.

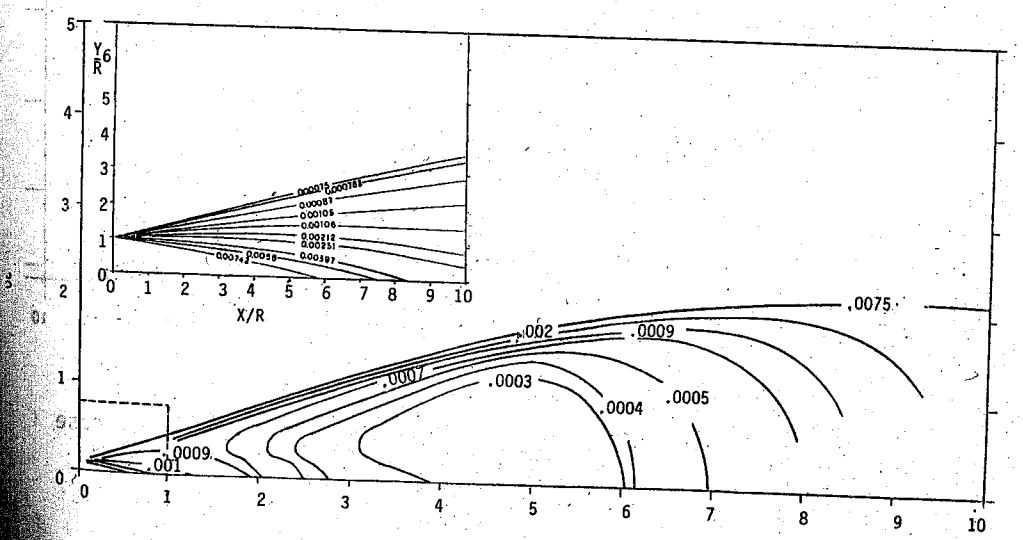

Figure 11. Pressure distribution of plume exhausted by nozzle I, case I, The diagram on the upper left corner is the plume flow field near nozzle in enlarged scale.

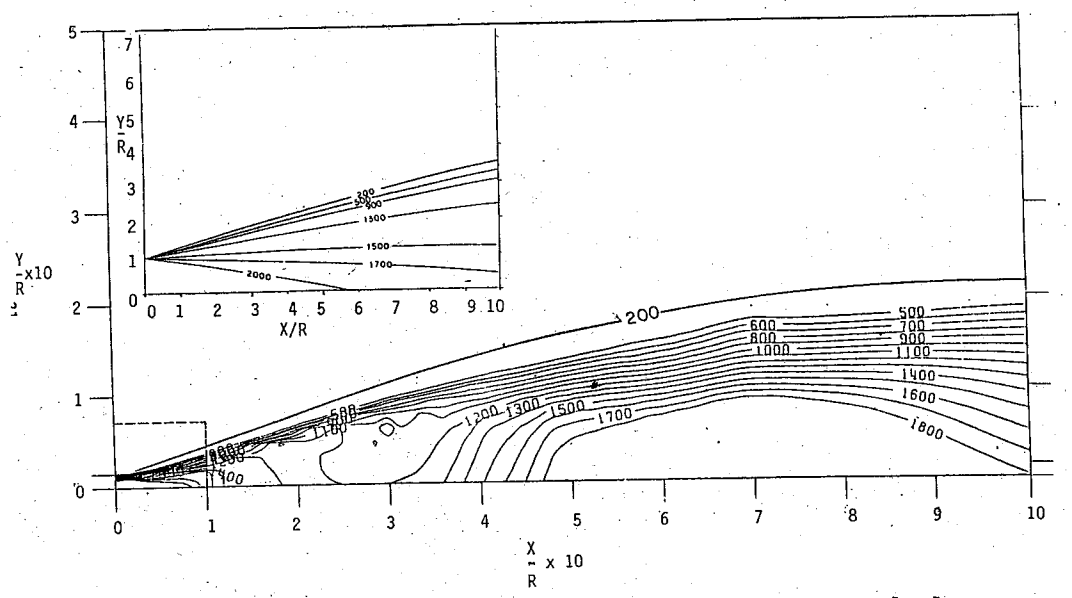

Figure 12. Temperature distribution of plume exhausted by nozzle I, case I. The diagram on the upper left corner is the plume flow field near nozzle in enlarged scale.

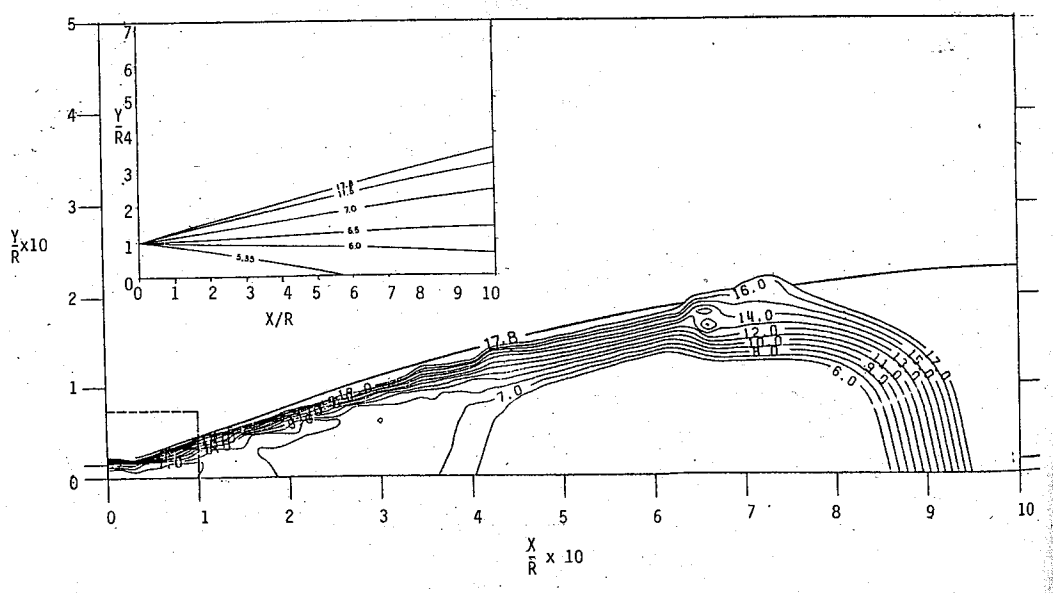

Figure 13. Mach number distribution of plume exhausted by nozzle I, case I. The diagram on the upper left corner is the plume flow field near nozzle in enlarged scale.

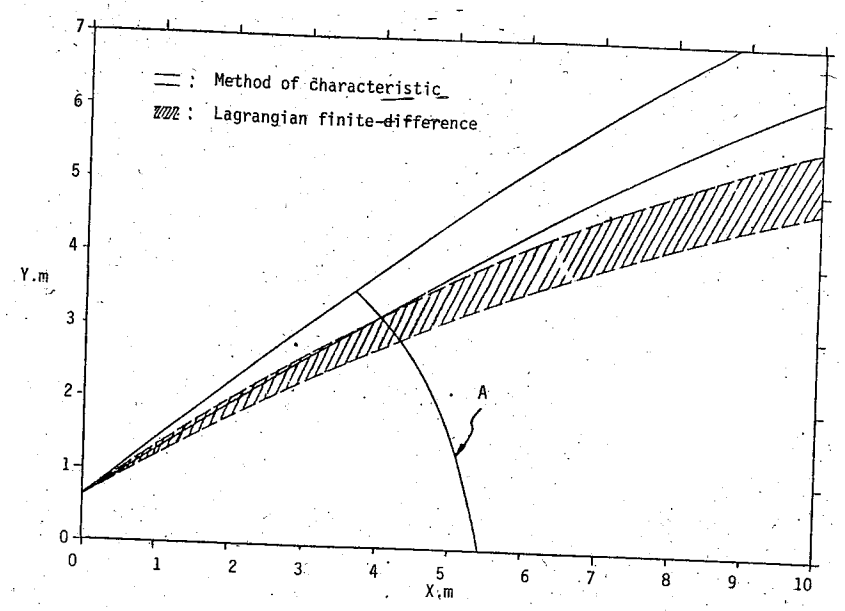

Figure 14. Thor plumes got by method of characteristics and Largrangian finite difference method (Tannehill).

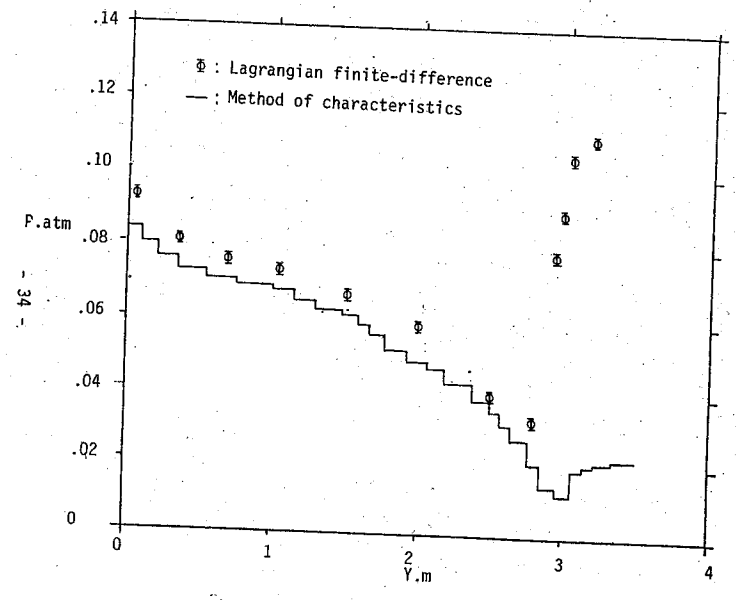

Figure 15. Pressure along surface A in Figure 14.

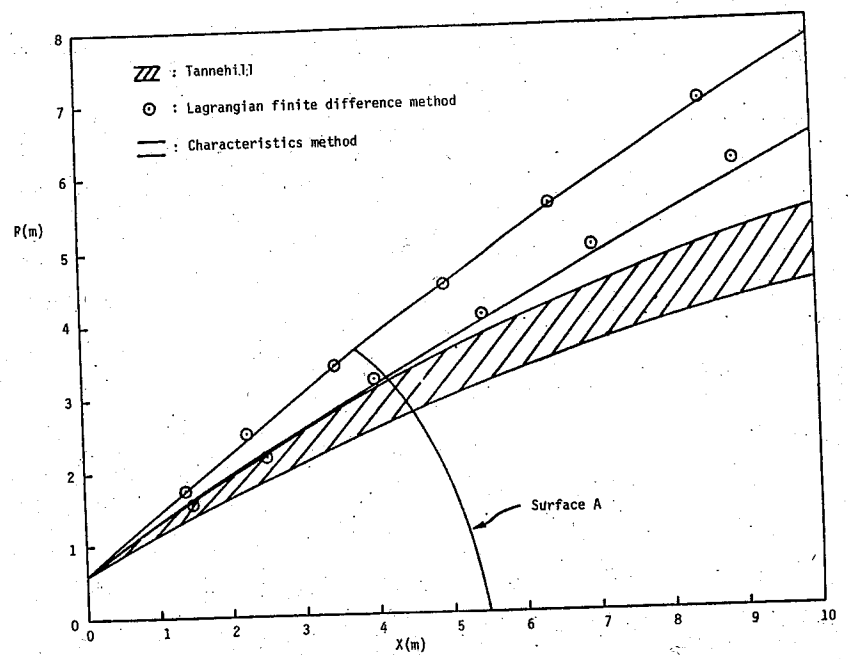

Figure 16. Thor plumes of three results got by different numerical techniques.

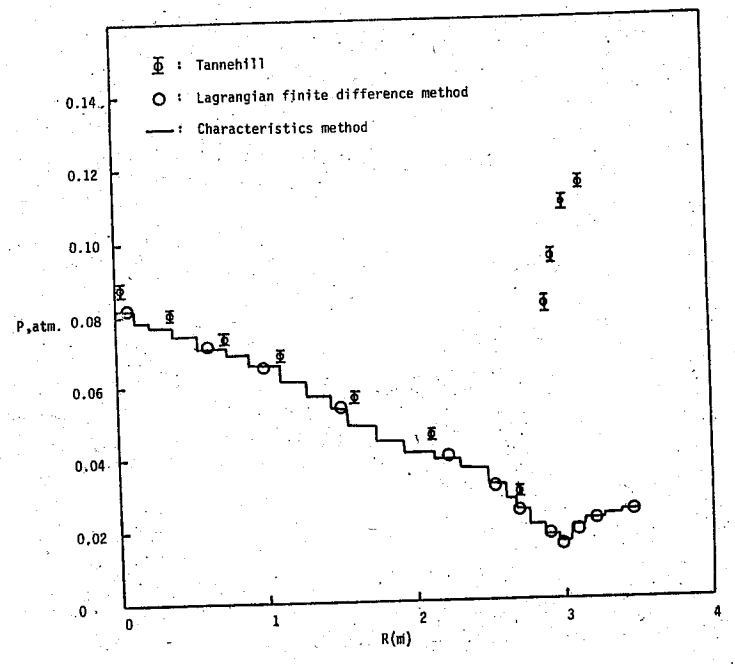

Figure 17. Pressure distributions along surface A in Figure 16 with three different numerical techniques.

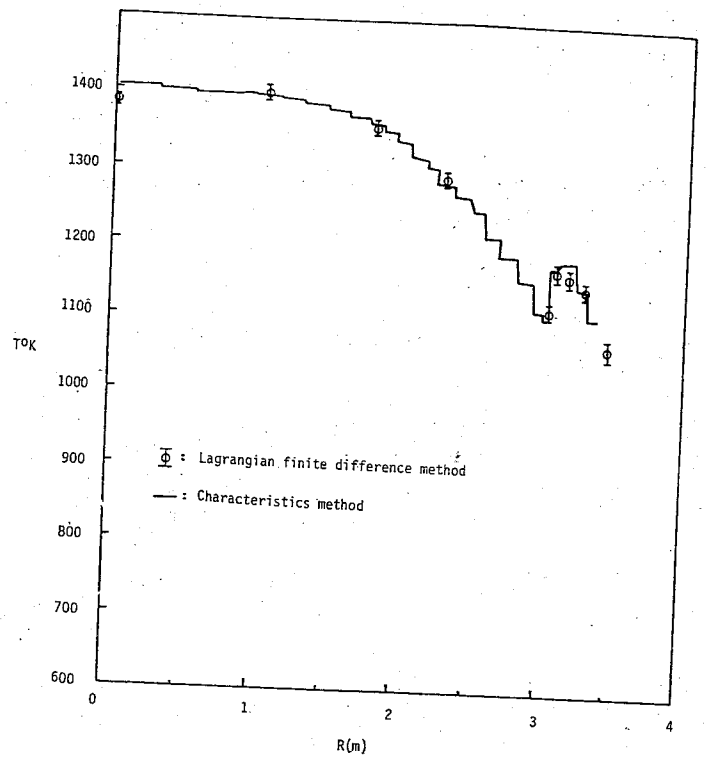

Figure 18. Temprature distributions along surface A in Figure 16 with two different numerical techniques.

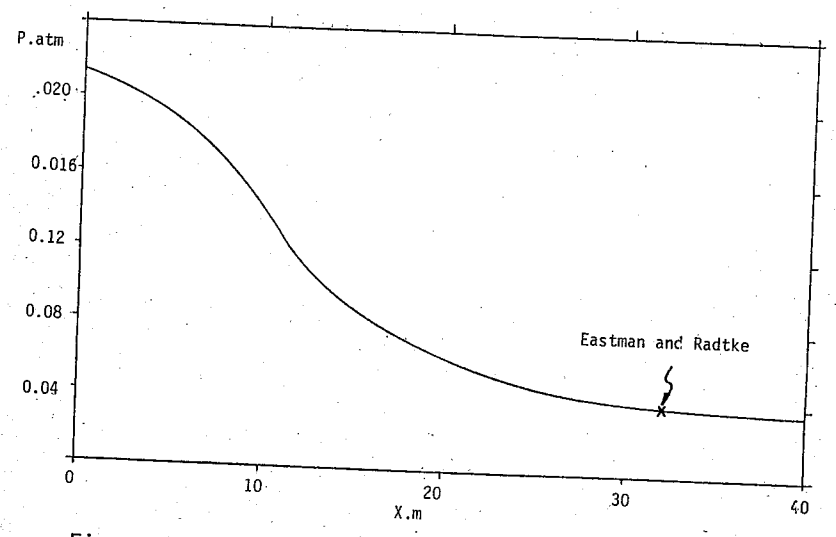

Figure 19. Pressure along jet shock of Thor plume. The location of normal shock is estimated by the method developed by Eastman by Radtke (1962).

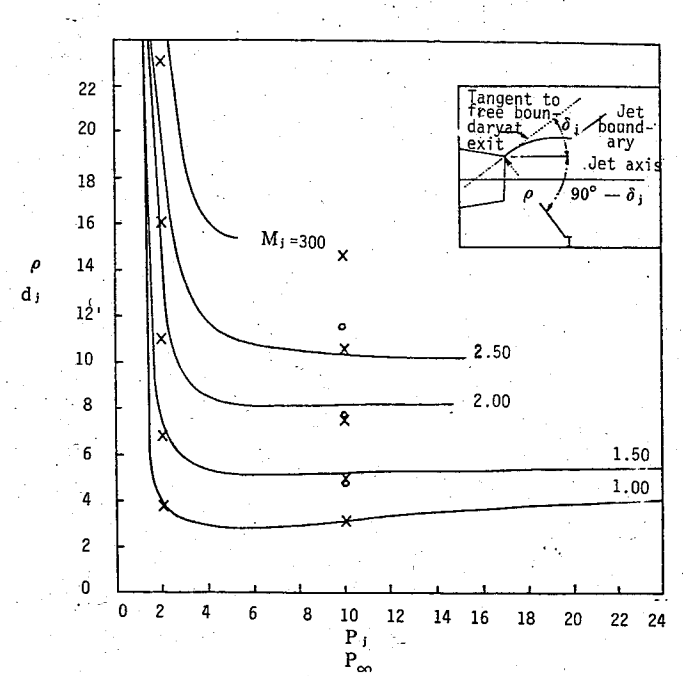

Figure 20. The curvatures of plume boundary at nozzle lip versus to pressure ratio and and Mach number.
—: Love (1); x; characteristics method; o : this study.

THEORETICAL STUDY OF ROCKET EXHAUST PLUMES PART II: FINITE-DIFFERENCE METHOD

L. C. Chien, C. T. Wang, W. J. Liang and F. L. Chen
Institute of Physics
Academia Sinica Nankang,
Taipei, Taiwan, R. O. C.

The rocket exhaust plumes under various altitudes are investigated by finite difference method. This numerical technique operates in the natural coordinates system and marches downstream from a surface of the nozzle exit. By this technique, the flow properties in rocket exhaust plumes are thus calculated and compared with those obtained by method of characteristics. The results obtained by the different numerical techniques are compared and agree excellently.

Finally, the flow properties along the axis and radial direction in the undistrubed region are investigated to aprove the assumption of undisturbed region in the calculating procedure is reasonable.

INTRODUCTION

The Lagrangian finite difference method and the method of characteristics are the two conventional computation methods used in investigating supersonic flow. In the method of characteristics solution, the shock is located by the coalesence of the characteristic lines of same family (1). The flowfield near the nozzle exit can be accurately predicted by the method (2). However, this numerical procedure exhibits computational difficulties for the cases of the low ambient pressure and high exit Mach number. Under these conditions, the characteristics of opposite family will eventually diverge unless the mesh size is refined, and the calculation can't be continued to great distances from the nozzle in an efficient manner.

In addition to the method of characteristics technique for computing inviscid plume flowfields, Boyton and Thomson (3) have recently devised a Lagrangian finite difference technique which can be applied to the solution of inviscid as well as viscous plume flowfields. In this method, the computation procedure was first based on determining the undisturbed, internal inviscid flow by expanding the test gases to a vacuum. Next, the initial locations of the jet shock and divi-

ding streamline are determined. Then, let the region between the jet shock and dividing streamline propagate into the previously calculated undisturbed flows.

Both the method of characteristics and the Lagrangian finite difference method required a considerable amount of effort and computation time. Some approximate methods are developed to predict the gross plume structure (4-6). These inviscid methods are excellent to determined the plume shape, jet shock location, and the internal pressure distribution.

In this study, the Lagrangian finite difference method are employed on solving the inviscid plume flow. The computation procedure was developed by the analysis of Boyton (3) for rocket exhaust plumes under various altitudes. The results obtained by this study are compared with those by method of characteristics (7). Also, the assumptions made for the computation procedure are approved by investigating that the structure of undisturbed region is independent with the boundary condition.

EQUATIONS AND COMPUTATIONAL PROCEDURE

The equations necessary to describe the rocket exhaust plume are shown in part one of this subject (7). For a two-dimensional or axially symmetric flow of an inviscid fluid, in which the gradients of pressure, temperature, and velocity are assumed much smaller in the direction of flow than normal to it, the equations simplified by using an order of magnitude analysis can be written in natural coordinate as follows:

Global continuity:

$$\frac{\partial}{\partial s}(\rho A u) = 0 \tag{1}$$

Streamwise momentum:

$$\rho u \frac{\partial u}{\partial s} + \frac{\partial p}{\partial s} = 0 \tag{2}$$

Normal momentum:

$$\rho u^2 \frac{\partial \theta}{\partial s} + \frac{\partial p}{\partial n} = 0 \tag{3}$$

Energy:

$$\rho u \frac{\partial}{\partial s}\left(h + \frac{1}{2} u^2\right) = 0 \tag{4}$$

State:

$$p = \rho \overline{R} T \tag{5}$$

Here s is the distance along a streamline, n the distance normal to it. These equations are transformed directly by equations (6) to (9) in PART I of this study. In those equations, by setting the normal pressure gradient term equal to zero, the boundary layer equations are obtained. These equations are similar to those derived by Boyton and Thomson (3) if relevant terms are included.

The Lagrangian finite-difference method developed by Boyton and Thomson (3) is employed on solving these equations. The flowfield is divided into a grid system which is composed of streamlines and the orthogonal surface (Figure 1). In the convention, the kth streamtube is bounded on the left by the kth streamline for an observor facing downstream, and the orthogonal surfaces are indexed ℓ. In each streamtube the properties are constant in the orthogonal direction but vary between orthogonal surfaces.

The start the calculation, data along an initial orthogonal surface are required. These data include the flow properties in the streamtubes, the positions, and flow angles of the dividing streamlines. In addition, the boundary conditions on either side of the flow must be specified. The curvature of the kth streamline at the initial ℓth surface is evaluated using normal momentum equation. This procedure is repeated for each streamline so that all streamtube areas, $A_{K,\ell+1}$ at the new surface can be calculated. Then, the remaining conservation equations can be integrated directly along the streamtubes in the usual manner. Each surface is calculated twice. For the second pass, average values between old and new surfaces are used. The computation marches downstream in this manner until the calculation in terminated.

This scheme is explicit and is therefore subject to instabilities unless the step size is limited. The stable step size is given as (3):

$$\delta S \leq \frac{1}{2} \delta n \left[\left(M^2 - 1 \right)^{-\frac{1}{2}} \right]^{-1} \tag{6}$$

The location of grid point at new orthogonal surface can be obtained by stepping downstream a stable stepping distance δS using a circular arc or a straight line to approximate the streamline curvature.

Rewritten in finite-difference form, equations (1) to (5) become:

Global continuity:

$$\dot{m}_k = \rho_{k,\ell}\, u_{k,\ell}\, A_{k,\ell} = \rho_{k,\ell+1}\, u_{k,\ell+1}\, A_{k,\ell+1} \tag{7}$$

Streamwise momentum:

$$\dot{m}_k \left(u_{k,\ell+1} - u_{k,\ell} \right) + \overline{A}_k \left(P_{k,\ell+1} - P_{k,\ell} \right) = 0 \tag{8}$$

Normal momentum:

$$-\left[\frac{\partial \theta}{\partial S}\right]_{k,\ell} = \left[\frac{4\,(2\pi\gamma_{k,\ell})^j}{u_{k,\ell} + u_{k+1,\ell}}\right]\left[\frac{P_{k+1,\ell} - P_{k,\ell}}{\dot{m}_k + \dot{m}_{k+1}}\right] \tag{9}$$

Energy:

$$\dot{m}_k \left(h_{k,\ell+1} - h_{k,\ell} + \frac{1}{2} u^2_{k,\ell+1} - \frac{1}{2} u^2_{k,\ell} \right) = 0 \tag{10}$$

State:

$$P_{k,\ell+1} = \rho_{k,\ell+1}\, \overline{R}\, T_{k,\ell+1} \tag{11}$$

where j is 0 for planar flow, 1 for axisymmetric flow.

With $A_{K,\ell+1}$ calculated as stated before, there are 5 unknow $P_{K,\ell+1}$, $T_{K,\ell+}$, $\rho_{K,\ell+}$, $u_{K,\ell+1}$ and $h_{K,\ell+1}$ can be got by solving equations (7) to (11) simultaneously.

BOUNDARY CONDITIONS

The natural coordinate system employed in this paper allows several different types of boundary conditions to be easily incorporated. First, the symmetry axis can be taken as a streamline. Likewise, dividing streamlines can be used directly if the outside ambient pressure of Newtonian impact pressure is specified

$$P_b = P_\infty + \rho_\infty u^2{}_\infty \sin^2 \left(\theta_b - \theta_\infty \right) \tag{12}$$

Shocks in the flowfield are calculated in a discontinuous way. That is, the undisturbed region is calculated initially by exhausting flow into vacuum and then the shocked region is computed using the shock as a boundary discontinuity which propagates into the previously calculated undisturbed region. The shock angle and conditions downstream of the shock can be obtained by requiring that the shock turn the flow parallel to the nearest streamline being carried in the calculation. The shock angle σ can be determined from (8).

$$\zeta^3 + b\zeta^2 + c\zeta + d = 0 \tag{13}$$

where

$$\zeta = \sin^2\sigma$$

$$b = -\frac{\left(M^2_\infty + 2 \right)}{M^2_\infty} - \sin^2\delta'$$

$$c = \frac{2M^2_\infty + 1}{M^4_\infty} + \left[\frac{(\gamma+1)^2}{M^4_\infty} + \frac{\gamma+1}{M^2_\infty}\right]\gamma \sin\delta' \tag{14}$$

$$d = -\frac{\cos^2\delta'}{M^4_\infty}$$

using the Newton-Raphson method. The pressure and temperature downstream of the shock are then obtained from

$$P_s = P_\infty \left[\frac{2\gamma M^2_\infty \zeta - (\gamma - 1)}{\gamma + 1}\right] \tag{15}$$

and

$$T_s = T_\infty \left[\frac{P_s}{P_\infty}\right] \frac{(\gamma-1)M^2_\infty \zeta + 2}{(\gamma+1)M^2_\infty \zeta} \tag{16}$$

RESULTS AND DISCUSSION

In this section, various comparisons are made between the results obtained using the Lagrangian finite difference method and the method of characteristics of PART I (7). By assuming inviscid and no chemical reaction, the rocket exhaust plumes under various altitudes are calculated. In addition, the exhaust gas are not allowed to mix with the air and the position of dividing streamline is determined by assuming that the pressure acting on the outside of the dividing streamline is the newtonian shocklayer pressure, equation (12).

In computing the nozzle exhaust plume flowfield, the exhaust flow must be first expanded into vacuum. This calculation is necessary in order to describe the region bounded by the jet shock and the Mach disc. This region is called undisturbed region.

Because very low pressures near the nozzle lips will cause the streamtube areas

to increase greatly, a large number of small streamtubes must be placed near the nozzle lip to initiate the calculation. Some of the streamlines and orthogonal surfaces for this expansion are shown in Figure 2. There are 43 initial streamtubes on the exhaust surface. The calculating steps downward uniformly near the initial surface and increases the step distance as goes far away. The pressure and temperature distributions in this vacuum plume are shown in Figure 3 and 4 respectively. It is found that the isobars and isothermal lines are spread out from inner region gradually. In other words, the boundary effect propagates into the flow region step by step and will decay to form the undisturbed region.

The next step is to locate the initial positions of the jet shock and dividing streamline. In the present calculation, the initial jet shock and dividing streamline locations were obtained using the characteristics method program developed in PART I (7). This is a very convenient and accurate method for locating these two locations (Figure 20 in PART I). Once the jet shock is located, the jet shock layer can be calculated letting the jet shock propagate into the previously calculated undisturbed vacuum plume. The flow properties in the jet shock layer far downstream were not very dependent on the initial conditions (8). The location of the dividing streamline and jet shock determined by the method of characteristics and Lagrangian finite difference method are shown in Figure 5 for comparison with satisfactory agreement. The reason for the uncoincidence between the calculated results and the results of Tannehill (9) is explained in PART I in detail. The pressure distribution along surface A in Figure 5 is shown in Figure 6. Also shown is the temperature distribution in Figure 7.

To get more advanced investigate, nozzle exhaust plumes under various altitude are calculated by the method of characteristics and the Lagrangian finite-difference method. Three cases used in PART I are adapted here compare the results of these two numerical techniques (Figure 8). The invicid plumes' profile got by these two numerical techniques are shown excellent agreement in comparison. But there exists obvious unccincidence between these results and those of irrotational flowfield. It is shown here that the more complicate calculation in rotational flowfield in this study results in the more accurate results than those of irrotational flow-

field calculation, which is with less iteration.

The structures of these plume flowfields are also investigated here. Figure 9 to Figure 11 show the pressure, temperature and Mach number distributions along the vertical line at X/R = 5. On these figures, it is found that these properties in the undisturbed region almost coincide each other without any effect due to the boundary variation. Reaching near the boundaries, these properties were induced to conform with the boundary conditions. It is found in these figures the property distributions were departed near the plume boundaries. For investigating the undisturbed region in detail, the property distributions along the axis of the plume were investigated in Figure 12 to 14. Independent with the various ambient conditions, the property distribution of plumes along the axis coincide each other as same as those along vertical line in the undisturbed region. Also shown a phenomenum is that the properties along axis in the Mach cone region. It is the result of the flow exhausted from a circular arc nozzle (2).

CONCLUSION

The Lagrangian Finite Difference Method is employed in investigating the nozzle exhaust plumes. The results are used to compare with those got by method of characteristics developed in PART I of this subject. After study from different point of views, the results got by these two numerical techniques are found in nice comparison. this is due primary to the calculating procedures of these two numerical techniques are developed by physical meaning. Furthermore, the assumptions of the undisturbed region and the shock layer are shown reasonable by the calculated results.

Unfortunately, there is no experimental data to the knowledge of the authors with which the rocket exhaust plumes under various conditions can be compared. This is due to the difficulties in setting up the test apparatus, a rocket nozzle and external air stream.

REFERENCES

(1) Love, E. S., Grigsby, C. E., Lee, L. P., and Woodling, M. T. Experimental and

theoretical studies of axisymmetric free jets. United States National Aeronautics and Space Administration Technical Roport R-6, 1959.

(2) Eastman, D. W. and Radtke, L. P. Two-dimensional or axially symmetric real gas flows by the method of characteristics. Boeing Company Document D2-10599, 1962.

(3) Boynton, F. P. and Thomson, A. Numerical Computation of steady supersonic two-dimensional gas flow in natural coordinates. Journal of Computational Physics 3: 379-398, 1969.

(4) Albini, F. A. Approximate computation of underexpanded jet structure. American Institute of Aeronautics and Astronautics Journal 3: 1535-1537, 1965.

(5) Hubbard, E. W. Approximate calcuation of highly underexpanded jets. American Institute of Aeronautics and Astronautics Journal 4:1877-1879, 1966.

(6) Luce, R. W. and Jarvinen, P. O. An approximate method for predicting plume sizes for nozzle flow into still air. American Institute of Aeronautics and Astronautics Journal 6: 182-183, 1968.

(7) Chien, L. C., C. T. Wang, W. J. Liang and P. L. Chen. Theoretical Study of Rocket Exhaust Plumes. PART I: Characteristics Method Annual Report of Institute of Physics, Academia Sinica Mechanical Engineering. Vol. 13, 1983.

(8) Tannehill, J. C. Numerical Computation of Intermediate Altitude Rocket Exhaust Plumes, Including Nonequilibrium Chemical Reactions and Diffusion. Ph. D. Dissertation, Iowa State University, 1969.

(9) Amer Aeronautical Laboratory. Amer Research Staff. Equations, tables, and charts for compressible flow. United State National Advisory Committee for Aeronautics Report 1135, 1953.

NOMENCLATURE

A : Area of streamtube

h : Enthalpy

M : Mach number

$\dot{m}$: Mass flow rate

n : Coordinate in normal direction

P : Pressure

$\bar{R}$: Gas constant

T : Temperature

s : Coordinate in streamwise direction

S : Stable step size

r : Radius

u : Velocity in streamwise direction

ρ : Density

θ : Flow angle

δ' : Shock deflection angle

γ : Ratio of specific heats

ζ : $\sin^2 \sigma$, equation (13)

σ : Shock angle

INDEX

∞ : Freestream condition

b : Boundary condition

ℓ : Condition in ℓh surface

s : Condition behind shock

j : 0 for plannar flow, 1 for axisymmetric flow

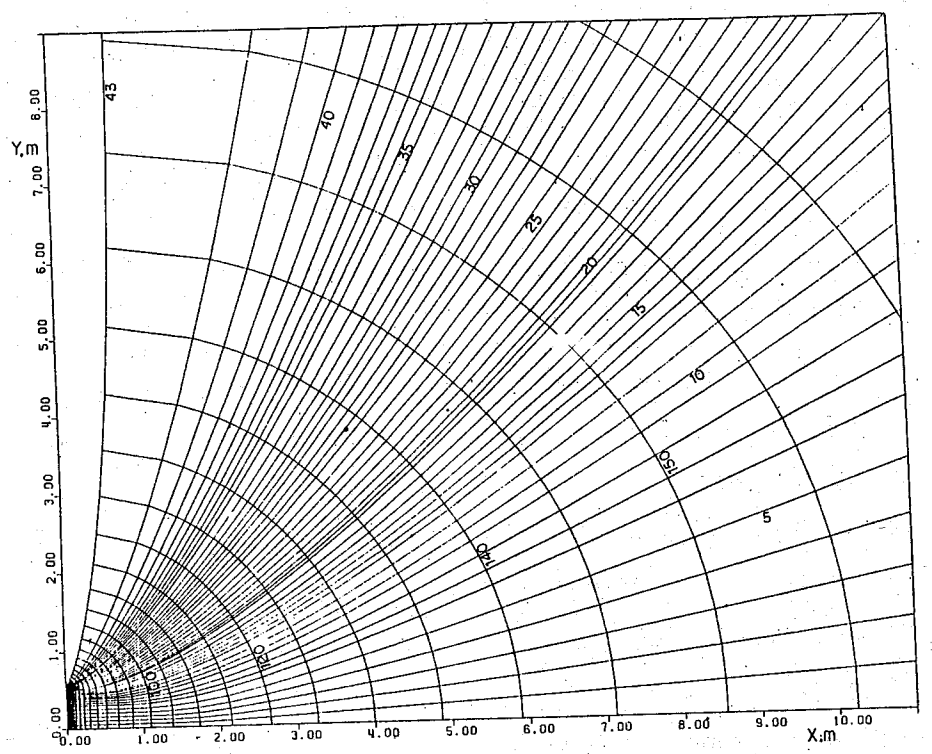

Figure 2. The streamtubes of vaccum plume.

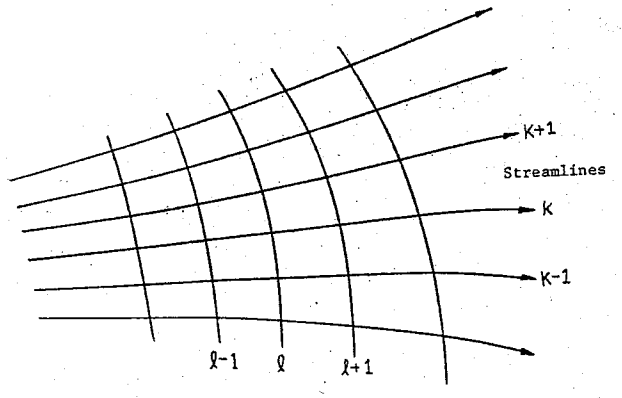

Orthogonal surfaces

Figure 1. Lagrangian finite difference mesh.

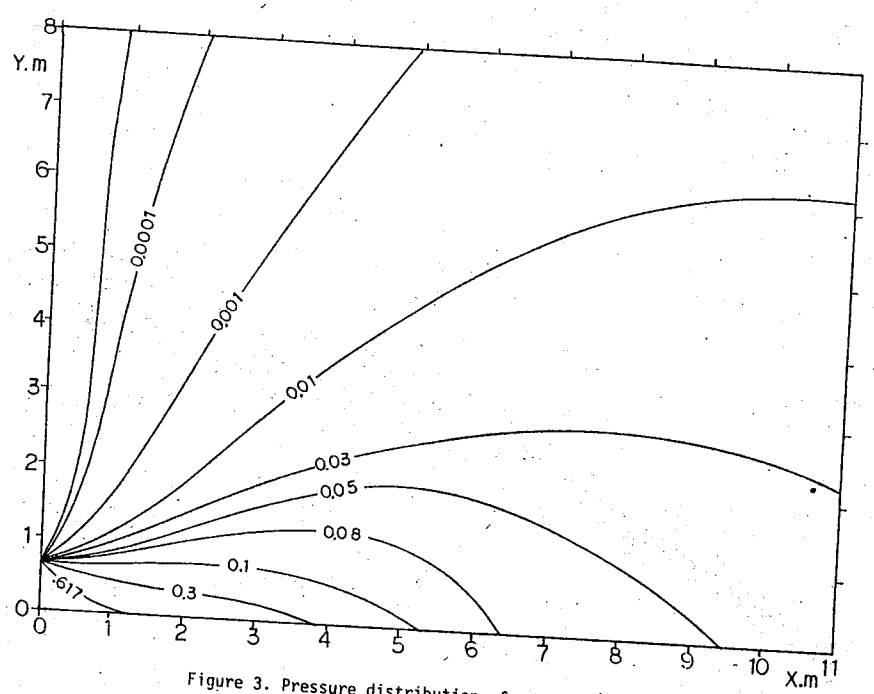

Figure 3. Pressure distribution of vaccum plume (atm).

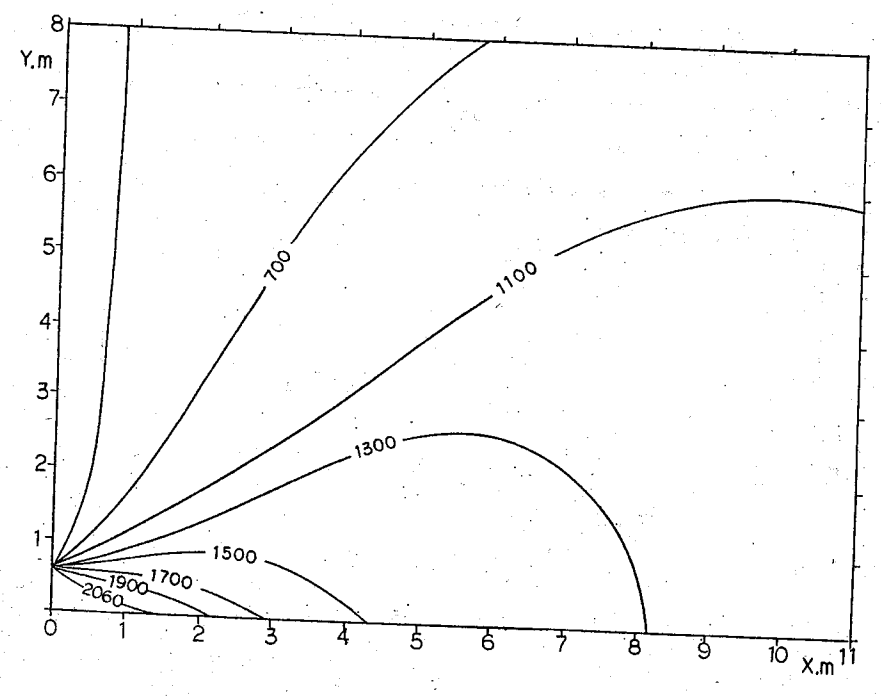

Figure 4. Temperature distribution of vaccum plume (^{o}K).

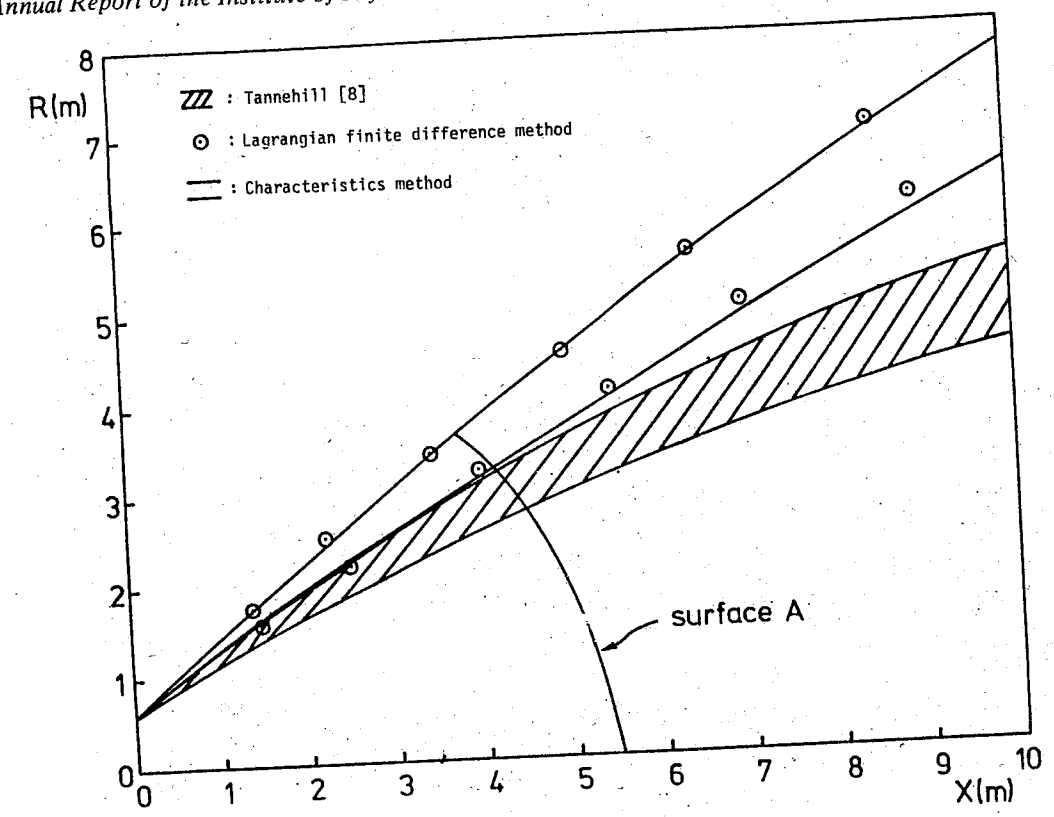

Figure 5. Profiles of Thor exhaust plume. Comparison among the results got by Lagrangian finite difference metnod, characteristics method, and those of Tannehill [8].

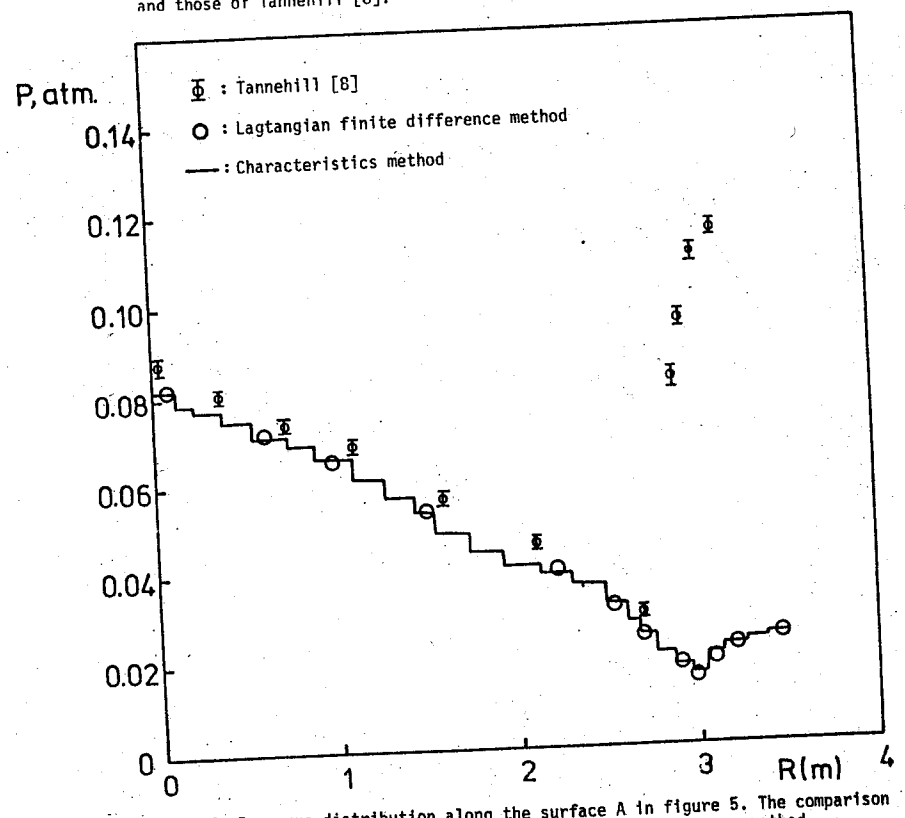

Figure 6. Pressure distribution along the surface A in figure 5. The comparison among the results got by Lagrangian finite difference method, characteristics method, and those of Tannehill [8].

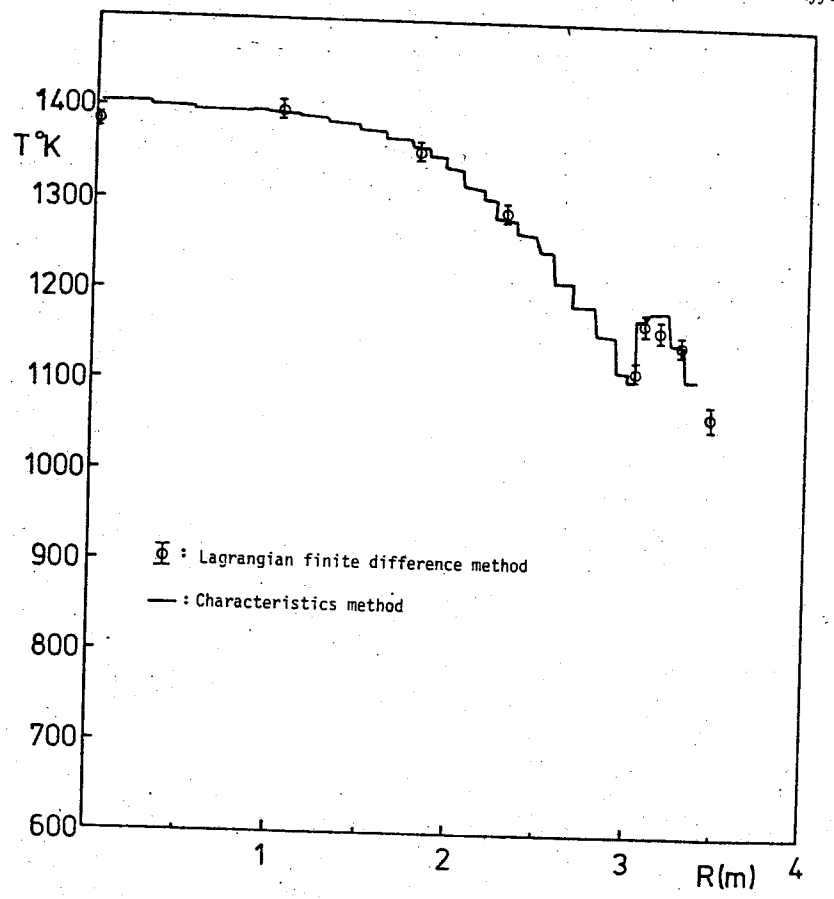

Figure 7. Temperature distribution along surface A in figure 5. The comparison between the results got by Lagrangian finite difference method and characteristic method.

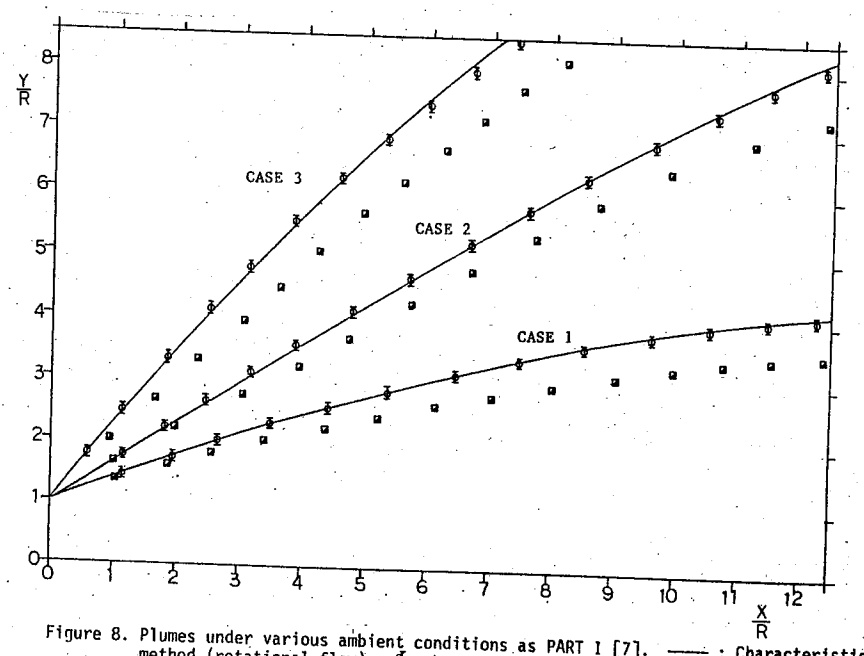

Figure 8. Plumes under various ambient conditions as PART I [7]. —— : Characteristics method (rotational flow); Ø : Lagrangian finite difference method; ◪ : Characteristics method (irrotational flow).

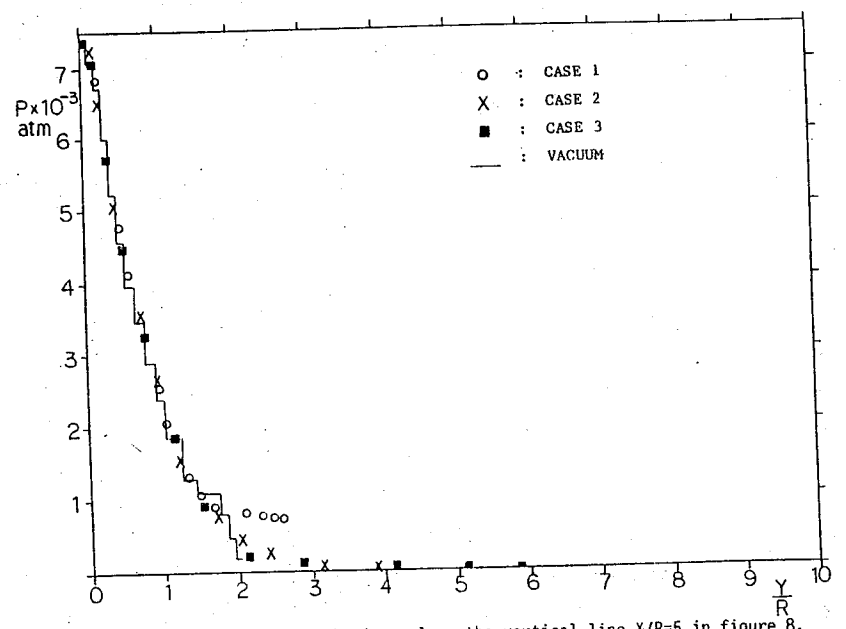

Figure 9. Pressure distributions along the vertical line X/R=5 in figure 8.

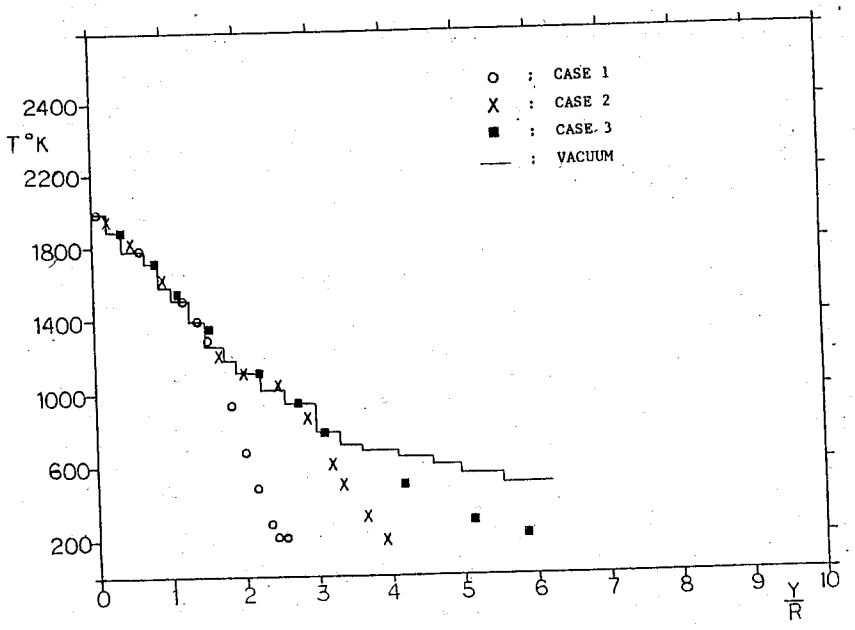

Figure 10. Temperature distributions along the vertical line X/R=5 in figure 8.

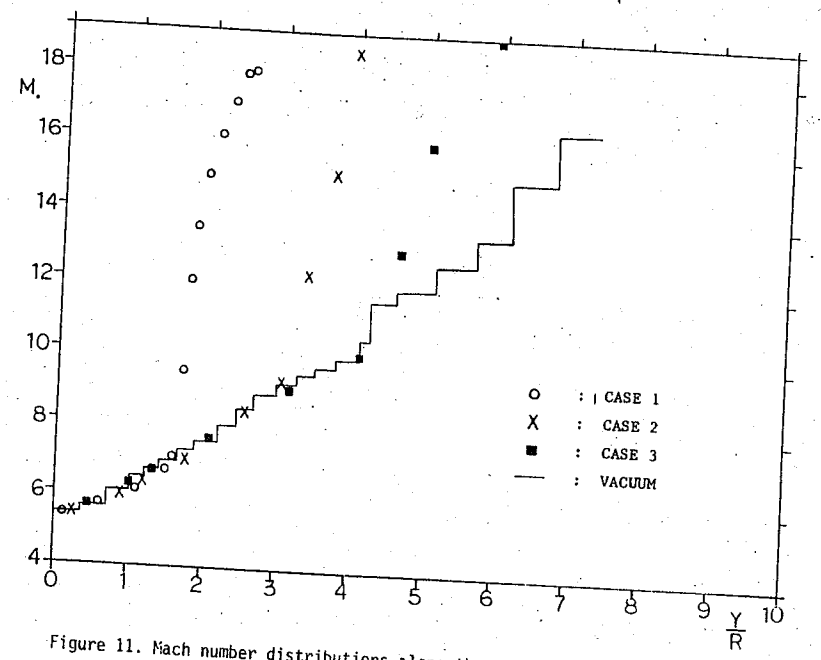

Figure 11. Mach number distributions along the vertical line X/R=5 in figure 8.

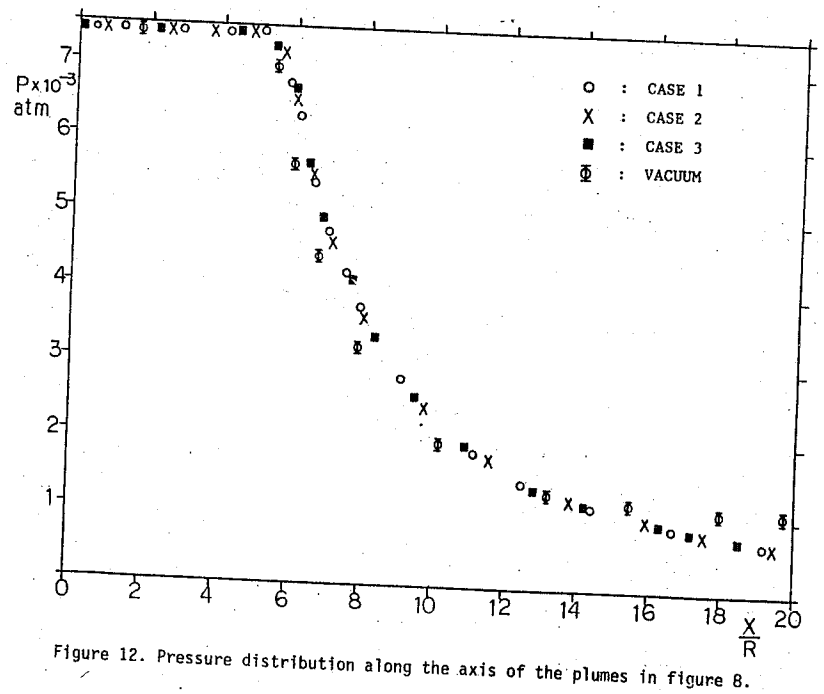

Figure 12. Pressure distribution along the axis of the plumes in figure 8.

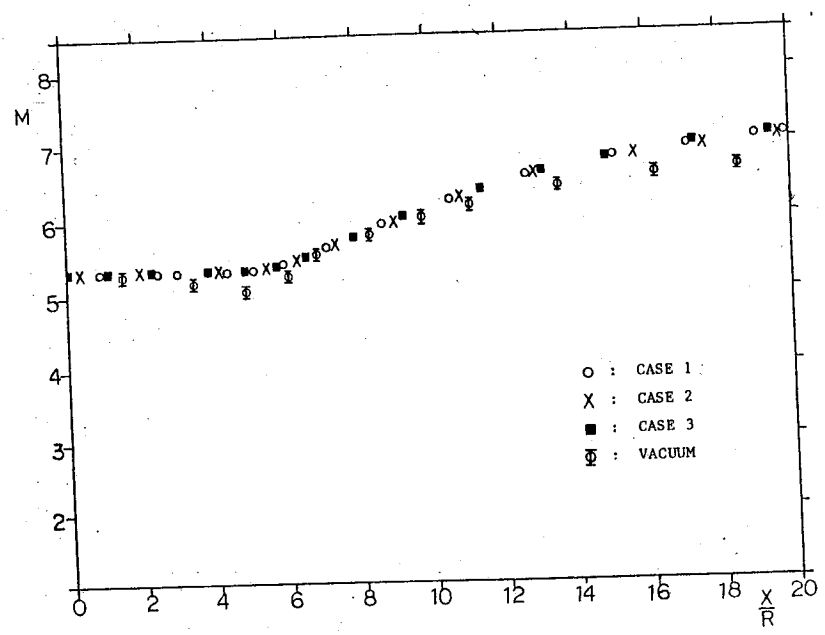

Figure 14. Mach number distributions along the axis of the plumes in figure 8.

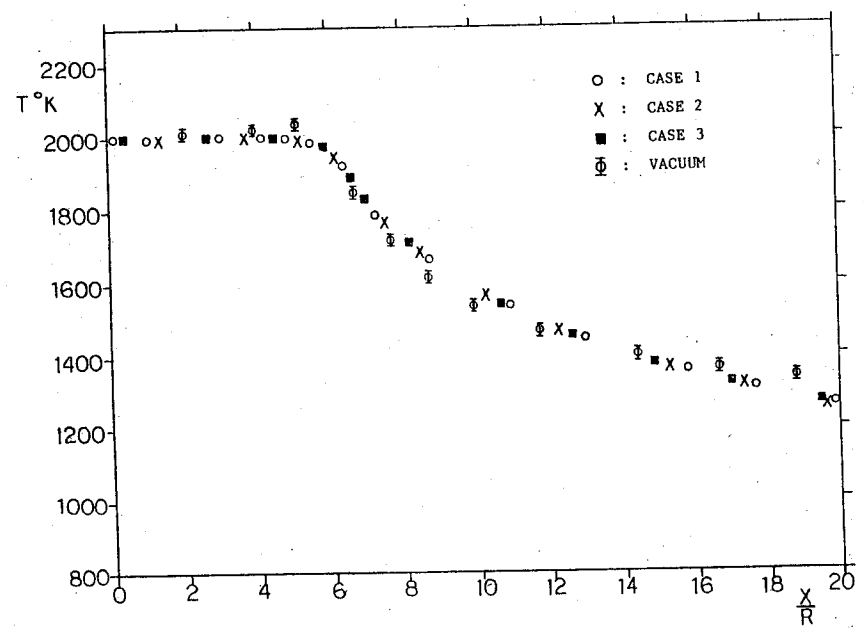

Figure 13. Temperature distribution along the axis of the plumes in figure 8.

THEORETICAL STUDY OF ROCKET EXHAUST PLUMES PART III: VISCOUS EFFECT

L. C. Chien, C. T. Wang, W. J. Liang and F. L. Chen
Institute of Physics
Academia Sinica, Nankang,
Taipei, Taiwan, R. O. C.

Due to the strong interaction between the rocket exhaust plume and the supersonic ambient flow, the viscous effect should not be ignored when the mixing layer become dominate the entire plume flow. The Lagrangian finite-difference scheme is employed here on solving the equations which include viscous terms. To investigate the viscous effect on the plume flow, the Thor plumes are calculated for both laminar and turbulent flows to compare with that for inviscid flow. It is found that the viscous phenomena dominate the plume flow when the shock layer width become as large as the diameter of nozzle exit.

INTRODUCTION

The inviscid calculations described in PART I and II are excellent for predicting the plume shape, jet shock location, and the internal flow structure. However since the air is not allowed to mix with the rocket exhaust flow, the viscous transport effects are totally ignored. The viscous layer due to the mixing of rocket exhaust flow and ambient supersonic flow will increase in size until it completely dominates the entire flowfield. The viscous terms of the governing equations for supersonic plume flowfield will become the same order of magnitude as other terms in those equations when the viscous layer size becomes as large as the diameter of the nozzle exit surface. Under this circumstance, the viscous effect should not be ignored any more.

To consider the strongly viscous transport effect on the plum flow, several investigators (1-3) have used the standard boundary layer equations to represent the mixing layer in the plume. However, when using the boundary layer equations to govern the mixing layer, several problems immediately become apparent. First of all, this representation is valid only in the region near the nozzle exit or far from the nozzle exit where the mixing layer is very thin or fully developed, respectively. The second drawback is that a zero radial pressure gradient is assumed.

This turns out to be a poor approximation for the turbulent mixing layer.

Still, the major drawback in using conventional boundary layer equations to represent the mixing layer in the plume lies in the problem of determining the coupling effects between the two surrounding inviscid flows and the mixing layer. Iteration techniques must be employed which are based on the boundary layer displacement thickness. This makes the computation very difficult.

A scheme developed by Thomson (4) and Boynton (5) used new equations which were derived from the Navier-Stokes equations using an order of magnitude analysis in which the gradients of pressure, temperature, and velocity are assumed much smaller in the direction of flow than in a direction normal to the flow. The resulting equations are somewhat similar to the boundary layer equations but include a normal momentum equation.

Two techniques have been proposed to solve this set of equations. The first technique (6, 7) uses a modified method of characteristics procedure in which viscous forcing terms are used. The second technique is a Lagrangian finite-difference procedure which has been applied by Thomson and Boynton (8) principally to the solution of high altitude rocket exhaust plumes. This procedure is more efficient than the previously mentioned modified method of characteristics procedure because in it the characteristic mesh becomes very compressed at high Mach numbers.

In the Lagrangian finite-difference scheme, the flowfield was described into a grid consisting of streamtubes and the surfaces orthogonal to them. Initially, the vacuum plume was calculated to be the boundary conditions of the following computation. With the initial locations of jet shock and dividing streamling determined by method of characteristics, the viscous layer bounded by jet shock and dividing streamline propagates into the previously calculated undisturbed vacuum plume. The entire viscous layer can be solved without iteration using this method.

Due to complicated structure of the plume flowfield, there exists no scheme which can be employed on solving the entire plume flowfield. A modular approach developed by Dash et al (9) has been implemented permitting variations in the mode of operation to accommodate the changing environment. Via this approach, the model can be operated in modes encompassing those available in all current plume models.

The entire computation procedures are built around the selt-contained plume modules discussed in reference 9.

In the present study, the Lagrangian finite-difference scheme is employed here on solving the viscous mixing layer of the plume flowfield. The governing equations derived by Edelman and Weilerstein (10) which were shown in PART I (11) are solved without considering the concentration diffusion. The larminar transport is assumed initially in order to simplify the derivation. After the final forms of the larminar equations are obtained, they are transformed to their turbulent counterparts. The Thor plume was calculated for both the laminar and turbulent flow to compare with the inviscid plume. The pressure and temperature distributions are also investigated for the viscous effect on the plume.

ANALYTICAL DEVELOPMENT

The general equations for the steady flow of a reacting mixture of perfect gas derived by Edelman and Weilderstein (10) are shown in PART I (11). In the following analysis, laminar transport is assumed initially to simplify the derivation. After the final form of the larminar equations are obtained, they are transformed to their turbulent counterparts by the conventional turbulent boundary layer Theory (12).

The general equations can be rewritten in natural coordinate system by order of magnitude analysis assumed the gradient of pressure, temperature, velocity and species concentrations are substantially smaller in the direction of flow than in a direction normal to the flow. After derived by Tannehill (12) and assumed for the non-reacting flow in this study, these equations became as follow:

Global continuity:

$$\frac{\partial}{\partial s}(\rho A u) = 0 \tag{1}$$

Streamwise momentum:

$$\rho u \frac{\partial u}{\partial s} + \frac{\partial p}{\partial s} = \frac{1}{r j} \frac{\partial}{\partial n}\left[r^{j} \mu \frac{u}{n} \right] \tag{2}$$

Normal momentum:

$$\rho u^2 \frac{\partial \theta}{\partial s} + \frac{\partial p}{\partial n} = 0 \tag{3}$$

Energy:

$$\rho u \frac{\partial H}{\partial s} = \frac{1}{r^j} \frac{\partial}{\partial n} \left[r^j \frac{\mu}{Pr} \frac{\partial H}{\partial n} \right] + \frac{1}{r^j} \frac{\partial}{\partial n} \left[r^j \left(1 - \frac{1}{Pr} \right) \mu u \frac{\partial u}{\partial n} \right] \tag{4}$$

State:

$$P = \rho \bar{R} T \tag{5}$$

where j = 0 is for plannar flow, j = 1 for axisymmitric flow. Equations (1) to (5, are suitable to describe the two-dimensional or axially symmetric flow of a non-reacting, viscous, heat-conducting fluid without considering the mass diffusion. Here, the total enthalpy H is function of temperature and velocity. So that, there are five equations for five unknowns once the streamlines have been located and the streamtube areas defined.

The present equations (1 to 5) can be rewritten for the turbulent flow with the turbulent counterparts replacing the relevant variables. These equations are transformed into turbulent equations by an intuitive argument which uses information gained from convectional turbulent boundary layer theory. According to applying on a turbulent mixing layer, the resulting turbulent boundary layer equations, in terms of time-averaged flow variables, are:

Global continuity:

$$\frac{\partial}{\partial s} (\rho u A) = 0 \tag{6}$$

Streamwise momentum:

$$\rho u \frac{\partial u}{\partial s} + \frac{\partial P}{\partial s} = \frac{1}{r^j} \frac{\partial}{\partial n} \left[r^j \varepsilon_v \frac{\partial u}{\partial n} \right] \tag{7}$$

Normal momentum:

$$\rho u^2 \frac{\partial \theta}{\partial s} + \frac{\partial P}{\partial n} = 0 \tag{8}$$

Energy:

$$\rho u \frac{\partial H}{\partial s} = \frac{1}{r^j} \frac{\partial}{\partial n} \left[r^j \frac{\varepsilon_v}{Pr_t} \frac{\partial H}{\partial n} \right] + \frac{1}{r^j} \frac{\partial}{\partial n} \left[r^j \left(1 - \frac{1}{Pr_t} \right) \varepsilon_v u \frac{\partial u}{\partial n} \right] \tag{9}$$

State;

$$P = \rho \bar{R} T \tag{10}$$

where ε_v and Pr_t are the eddy viscosity and turbulent Prandtl number, respectively. In addition, note that all variables are now time-averaged quantities. For the special case of compressible turbulent mixing most investigators modified the incompressible eddy viscosity expressions of Prandtl (13) either by performing a transformation which relates the compressible flow to an incompressible flow or by including a representive density (14). In present study, the latter form of modification is used in an expression proposed by Edelman and Fortune (15). This expression, which is constant across the width of the mixing layer, is written as

$$\varepsilon_v = \frac{\Delta Y}{C} \left[(\rho u)_{max} - (\rho u)_{min} \right] + 0.0485 \tag{11}$$

where ΔY is the mixing layer width, C is constant. The value of C was set equal to 900 and the turbulent Prandtl number was 1.2 (12) in this study.

The Lagrangian finite-difference method is employed on solving the equations mentioned above which contain both hyperbolic and parabolic types if the flow is supersonic everywhere. The flowfield is divided by the streamlines and the orthogonal surfaces. The calculating procedures are similar to those stated in PART II (16). However, because the flow is considered to be viscous here, the conservation equations cannot be integrated directly along the streamtubes after the new orthogonal surface had been calculated. Consequently, these conservation equations must be solved in finite-difference form. The calculation is arranged so that all momentum, energy lost from one streamtube reappears in the adjancent streamtube. The stable step size for the explicit scheme used here is now set as:

$$\delta s \leq \frac{1}{2} \delta n \left[\frac{1}{Re} + (M^2 - 1)^{-1/2} \right]^{-1} \tag{12}$$

In finite-difference form, these equations become those as shown below after some arrangements from Tannehill (12):

Global continuity:

$$m_k = \rho_{k,l} u_{k,l} A_{k,l} = \rho_{k,l+1} u_{k,l+1} A_{k,l+1} \tag{13}$$

Streamwise momentum:

$$\dot{m}_k(u_{k,l+1}-u_{k,l})+\bar{A}_k(P_{k,l+1}-P_{k,l})=\Delta_k[r_k^j\,\tau_k\,\delta s_k](2\pi)^j \quad (14)$$

Normal momentum:

$$-\left[\frac{\partial\theta}{\partial s}\right]_{k,l}=\left[\frac{4(2\pi r_{k,l})^j}{u_{k,l}+u_{k+1,l}}\right]\left[\frac{P_{k+1,l}-P_{k,l}}{\dot{m}_k+\dot{m}_{k+1}}\right] \quad (15)$$

Energy:

$$\dot{m}_k\left(h_{k,l+1}-h_{k,l}+\frac{1}{2}u^2_{k,l+1}-\frac{1}{2}u^2_{k,l}\right)$$

$$=\Delta_k\left[r_k^j\left(Q_k+\frac{1}{2}\left(u_k^2+u^2_{k,l}\right)\right)^{1/2}\tau_k\right] \quad (16)$$

State:

$$P_{k,l+1}=\rho_{k,l+1}\bar{R}T_{k,l+1} \quad (17)$$

where

$$\bar{\tau}_k=\overline{2(2\pi r)^j u_k\rho_k\mu}\;\overline{\frac{u_{k+1}-u_k}{\dot{m}_{k+1}-\dot{m}_k}} \quad (18)$$

$$\bar{\theta}_k=\overline{2(2\pi r)^j u_k\rho_k}\;\overline{\frac{C_p\mu}{Pr}}\;\overline{\frac{T_{k+1}-T_k}{\dot{m}_{k+1}+\dot{m}_k}} \quad (19)$$

In these equations, the operator Δ_k takes the difference in the bracket quantity across the kth streamtube; the variable with bar indicates the average value of the variable during the step downstream is to be used. The relationship between the enthalpy h and the total enthalpy H is shown below:

$$H=h+\frac{1}{2}u^2 \quad (20)$$

If the eddy viscosity and Turbulent Prandtl number replaced the viscosity and Prandtl number in these finite-difference equations, equations (13) to (19) became the turbulent equations again for the time-averaged variables.

RESULTS AND DISCUSSION

As the plume exhausted into the supersonic flowfield, there happened viscous transport process dominatly on the plume boundary. To consider the viscous effec

the viscous term in equations shown in PART I (11) are included in the computation of this study. Because the viscous transport phenomena is due to the velocity difference between the surpersonic plume flow and supersonic ambient flow, the viscous effect is investigated in the shocklayer only. In this study, both the laminar and turbulent flow are considered to simulate the flow in the shocklayer.

The computating procedures are the same as stated in PART II (16). The plume exhausted into vacuum was first calculated to be the boundary conditions for calculating the shock layer. After that, the initial locations of the jet shock and dividing streamline are calculated by the method of characteristics used in PART I (11). The laminar flow was first taken to simulate the shocklayer flow. In the viscous calculation, the number of streamtubes on the initial surface which situated between the initial locations of jet shock and dividing streamline can be set equal to that used in inviscid case. Usually 5 is the suitable number for the calculation. The number of streamtube will increase as goes downstream. However, since the streamtubes are continually added to the calculation as the shocklayer propagates downstream, the calculation will become repititions and complicated. In addition, the computation time is essentially inversely proportional to the square of the tube width (8). So that, it is necessary to combine tubes from time to time. A new streamtube is added when the mass flux approximates the average of those in the other streamtubes; and the tubes are combined when they are in the similar conditions (8). In the program, there is a parameter which will keep the number of streamtubes not exceed a certain value.

The viscous Thor plumes for both laminar flow and turbulent flow are investigated here and shown in Figure 1 to compare with that for inviscid flow. The locations of the dividing streamline and jet shock near the nozzle exit surface computed by the present viscous calculations were identical to the locations determined in the inviscid calculation. Further downstream from the exit surface, the jet shock and the dividing streamline displace outward slightly from their inviscid locations.

The reason why the viscous effect is dominate in the downstream is that the terms of the viscous terms are the same as other those of terms in the governing

equations when the width of shocklayer grows up to the value of the width of nozzle exit surface. However, physically, the viscous effect causes the increase of the flow velocity in normal direction. In addition, the pressure gradient along the othogonal surface in shocklayer is greater for viscous flow than inviscid flow. See Figure 2. That is why the shocklayer grows fatter as goes downstream.

To investigate the pressure and temperature distributions in the shocklayer, the results got from both the viscous and inviscid calculations along the surface B in Figure 1 are shown in Figure 2 and 3. They are found being coincident except that the gradients in normal direction are larger for the viscous flow. Due to the great convective the temperature gradient in normal direction for turbulent flow is larger than that of either the laminar or the inviscid flow.

As an conclusion, it is found that the viscous effect for the supersonic flow is less dominate than that for the incompressible flow. That is because the convection terms in the governing equations for supersonic flow are in larger order than the viscous terms. However, in the incompressible flow, the convection terms and the viscous terms are almost in the same orders.

CONCLUSION

Viscous calculation is employed on investigating the visous effect on the plume flowfield. The viscous transport process affects the plume dominatly when the mixing layer grows up as the width of the layer is as large as that of nozzle exit. The normal gradients of pressure and temperature in mixing layer are larger for turbulent flow than for larminar flow. Under using the Lagrangian finite-difference scheme, the after-burning process can be included in the calculating procedure. In addition, to investigate the complete plume flow, the analysises of both viscous inviscid and gas/particle interactions are necessary to be involved.

NOMENCLATURE

A : Area of streamtube.

C : Constant in eddy viscosity expression.

C_p : Specific heat.

h : Enthalpy.

H : Total enthalpy.

m : Mass flow rate.

M : Mach number.

n : Coordinate in normal direction.

P : Pressure.

Pr : Prandtl number.

Pr_t : Turbulent Prandtl number.

r : Radius.

$\bar{R}$: Universal gas constant.

Re : Reynolds number.

s : Coordinate in streamwise direction.

T : Temperature.

u : Velocity in streamwise direction.

ΔY : Width of mixing layer.

Δk : Difference across kth streamtube.

δn : Width of streamtube.

δs : Step in streamwise direction.

ε_v : Eddy viscosity.

θ : Flow angle.

μ : Viscosity coefficient.

π : 3.1415926

ρ : Density.

τ : Shear stress.

SUBSCRIPTS

k : Condition in streamtube K.

k+1 : Condition in streamtube K+1.

o : Condition at old surface.

n : Condition at new surface.

Annual Report of the Institute of Physics, Academia Sinica, Vol. 13. 1983.

線源光化學污染物擴散模式之原理與應用勘誤表

圖九至圖十四文字說明中之同圖十七改爲同圖八。

圖十六至圖二十一文字說明中之同圖二十四改爲同圖十五。

圖二十三至圖二十八文字說明中之同圖三十一改爲同圖二十二。

圖三十至圖三十五文字說明中之同圖三十八改爲同圖二十九。

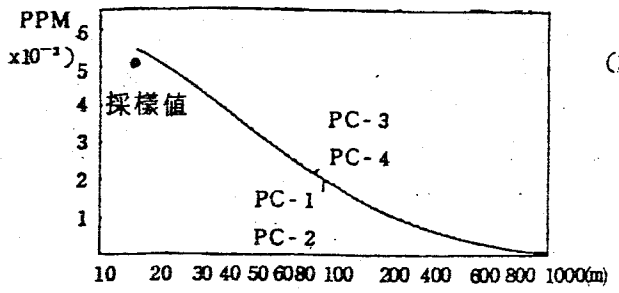

圖八　模式計算個案第一組情況下，NO_2濃度隨距離變化的情形。實線表第一、二組光化學反應濃度變化情形，虛線表第三、四組情形。

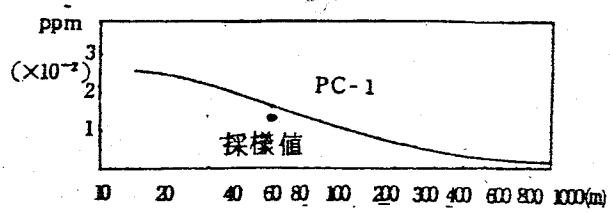

圖十五　模式計算個案第二組情況下NO濃度隨距離變化的情形（Ⅱ）。

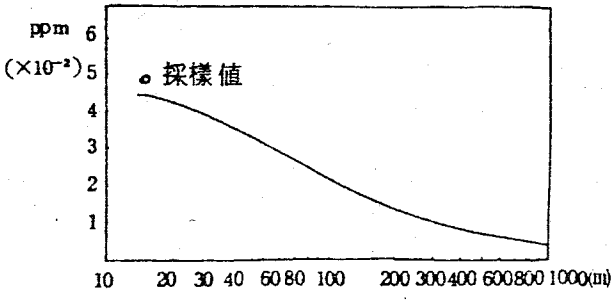

圖二十九　模式計算個案第四組情況下NO濃度隨距離變化的情形。

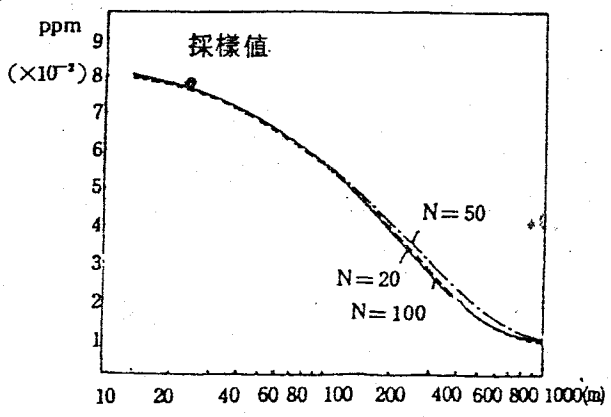

圖二十二　模式計算個案第三組情況下NO濃度隨距離變化的情形。採樣點和計算點在層區間分100格時非常接近。N表層區間分格數。

REFERENCES

(1) Libby, P. A. Theoretical analysis of turbulent mixing of reactive gases with application to supersonic combustion of hydrogen. American Rocket Society Journal 32: 388-396. 1962.

(2) Rczsa, R. B. Preliminary review of turbulent jet-mixing and afterburning in rocket exhaust plumes. Chrysler Corporation Space Division Technical Bulletin AE-64-79, 1964.

(3) Vasiliu, J. Turbulent mixing of a rocket exhaust jet with a supersonic stream including chemical ractions. Journal of the Aerospace Sciences 29:19-28, 1962.

(4) Thomson, J. A. L. High altitude rocket plume structure. General Dynamics Convair Report GD/C-DBE65-023, 1965.

(5) Boynton, F. P. The multitube supersonic flow computer code. Gernal Dynamics Convair Report GDC-DBE67-003, 1967.

(6) Vick, A. R., Cubbate, J. M. and Andrews, E. H., Jr. Rocket exhaust plume problems and some recent related research. Unpublished mimeographed paper presented at a Specialists Meeting on the Fluid Dynamic Aspects of Space Flight, Marseille, France, April 1964. Ames, Iowa; Department of Aerospace Engineering, Iowa State University of Science and Technology. Ca. 1969.

(7) Farmer, R. C., Prozan, R. J., McGimsey, L. R., and Ratliff, A. W. Verification of a mathematical model which represents large, liquid rocket-engine exhaust plumes. American Institute of Aeronautics and Astronautics Paper 66-650. 1966.

(8) Boynton, F. P. and Thomson, A. Numerical Computation of steady, supersonic two-dimensional gas flow in natural coordinates. Journal of Computational Physics 3:379-398. 1969.

(9) Dash, S. M. Pergament, H. S., and Thorpe, R. D. A Modular Approach for the Coupling of Viscous and Inviscid Processes in Exhaust Plume Flows. 17th Aerospace Science Meeting, 79-0150, 1979.

(10) Edelman, R. and Weilerstein, G. Mixing and combustion in supersonic flow with lateral pressure gradient effects. General Applied Science Laboratories,

Inc. Technical Report 636, 1968.

(11) Chien, L. C. and Chen, F. L. Theoretical Study for Rocket Exhaust Plumes. PART I Characteristics Method to be Published on the Journal of Chinese Mechanical Engineering.

(12) Tannehill, J. C. Numerical Computation of Intermediate Altitude Rocket Exhaust Plumes, Including Nonequilibrium Chemical Reactions and Diffusion. Ph. D. dissertation, Iowa State University, 1969.

(13) Schlichting, H. Boundary layer theory. 4th ed. New York, New York, McGraw-Hill Book Company, Inc. 1960.

(14) Eggers, J. M. Velocity profiles and eddy viscosity distributions downstream of a Mach 2.22 nozzle exhausting to quiescent air. United States National Aeronautics and Space Administration Technical Note D-3601, 1966.

(15) Peters, C. E., Peters, T., and Billings, R. B. Mixing and burning of bounded coaxial streams. Arnold Engineering Development Center Technical Report 65-4, 1965.

(16) Chien, L. C., and Chen F. L., Theoretical Study of Rocket Exhaust Plumes. PART II: Finite-Difference Method. To be published on the Journal of Chinese Mechanical Engineering.

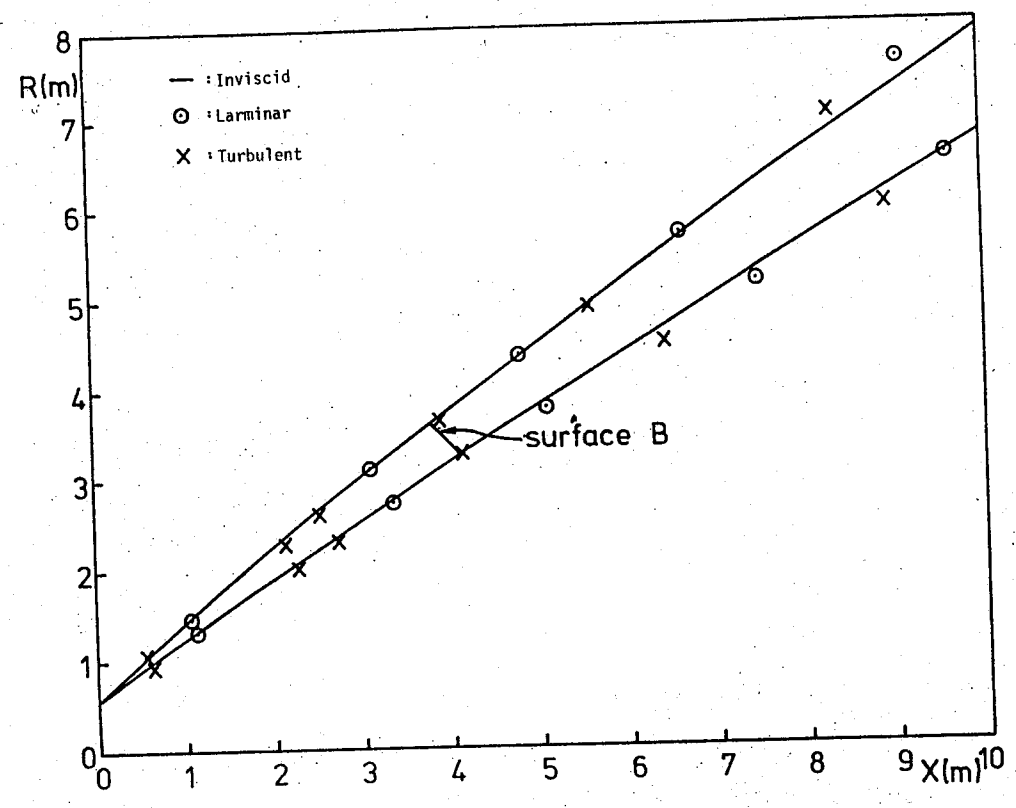

Figure 1. Thor plumes for larminar flow, turbulent flow and inviscid flow.

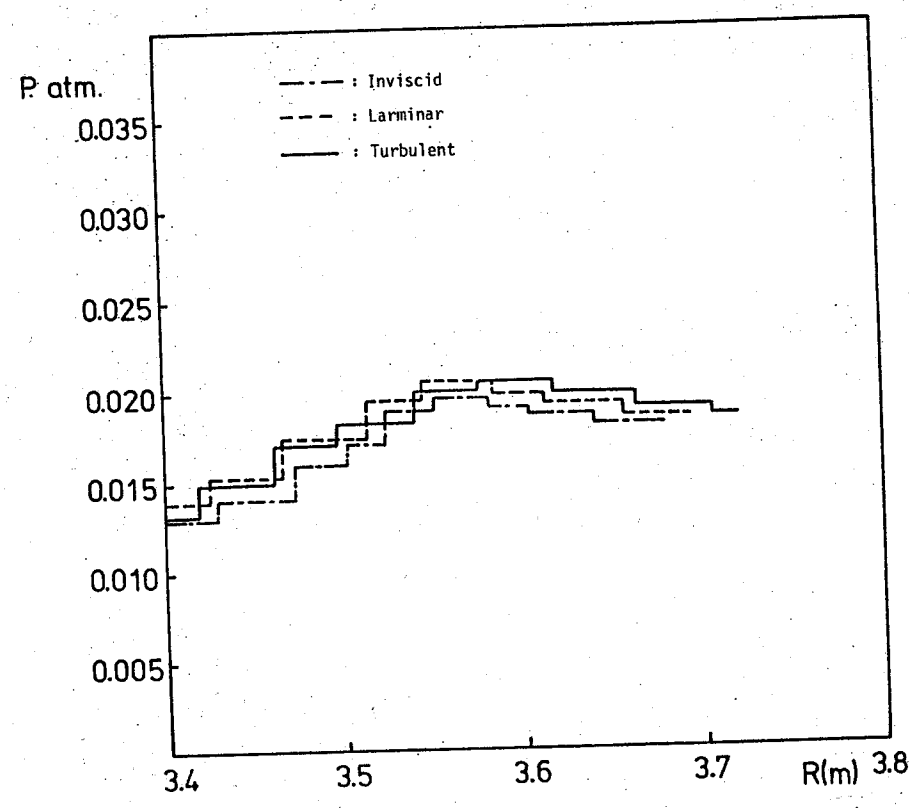

Figure 2. Pressure distributions along the surface B of figure 1.

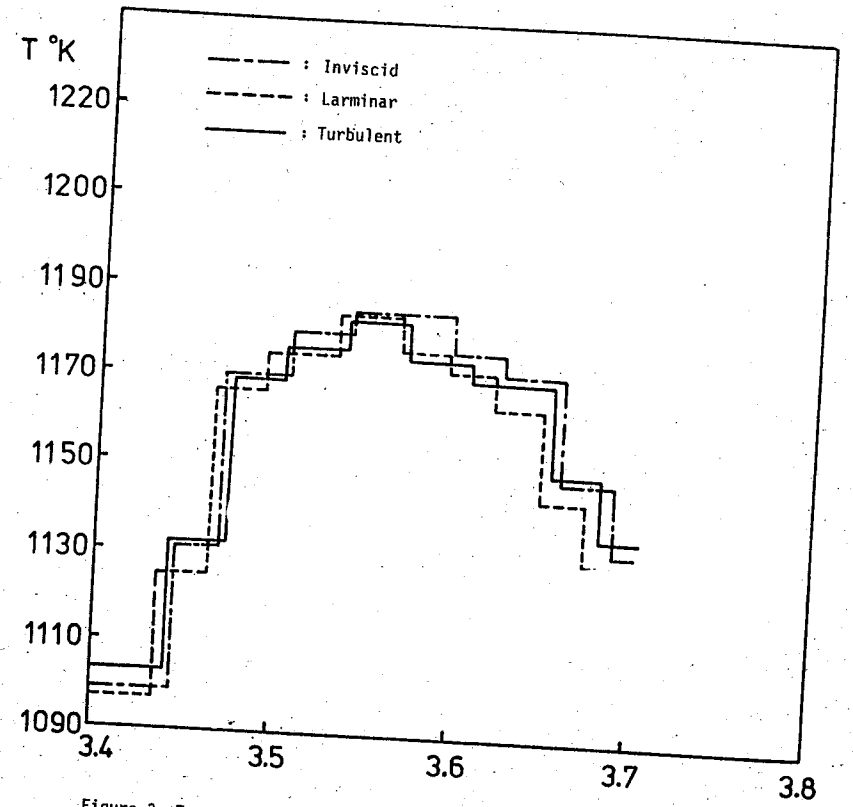

Figure 3. Temperature distributions along the surface B in figure 1.

垂直浮昇射流在流動密度層變水域中之浮昇與混合研究

黃　榮　鑑
中央研究院物理研究所
蔣　德　普
國立台灣大學造船工程研究所

摘　要

本文藉因次分析、數學模式、實驗等程序，探討具橫向流動之密度層變水域裡，垂直入射兼具啓始動量與密度差異射流之浮昇發展特性。

以因次分析方法推導流況參數 $N = GM_j^2 / B_j^2$ 作爲界分射流形態爲浮流、浮昇射流、動量射流之有效參數，且射流體總體性質物理量無因次參數和流況參數N之間，存在一定的函數次方關係式（3—a）～式（3—c）。實驗資料配合斷面積分法建立之數學模式演算，發現Taylor 捲增概念閉合控制方程式之捲增關係式採Abraham 建議但經本文修正之式（8—e）較佳，捲增係數 α_1 射流形態與流況參數N間有一演化趨勢式(9)，模式之可行性就其與實驗間之誤差分佈、軌跡趨勢而言尚稱良好，且在速度比k值相當小（$k < 4$）時仍能適用，顯示模式之優越性；進而以實驗及數學模式演算驗證因次分析推導之無因次函數間次方關係，推求可供海洋放流工程設計參考之簡便公式與圖表。

壹、緒　言

隨著經濟的茁長與生活水準的提昇，都市污水及工業廢水的排除量相對的日與俱增；然而河川涵容能力有限、廢水處理廠擴建速度無法與之配合再加上經濟效益的考慮，致使如何利用廣大海洋水域自然的力量來稀釋淨化污廢水，已成爲各國環境流體力學家們竭力研究的項目之一。海洋放流措施爲經初級或二級處理後之污廢水，以管道輸送至海面下約60公尺深地帶排放，因其與週遭水體間速度、密度差異而相混合，再藉海流帶動逐步擴散；此一過程中污廢水可能浮昇的最大高度、稀釋程度、浮昇平衡位置爲工程師設計海洋放流所面臨之最重要問題；由於放流管排除污廢水之力學特性與浮昇射流流場相似，吾人可藉研究一兼具速度、密度差異之射流，在橫向流動密度層變流場中浮昇發展特性模擬之。

依控制射流體物理量可將發展階段分爲近域、遠域。前者受控於射流體與環境水域

間差異引致之捲增、浮昇效應，爲第一次擴散階段；後者受控於環境水域亂流引致之亂流擴散，爲第二次擴散階段；本文之探討限於前者。

本問題理論解析上有二大機件：捲增及阻力關係式。捲增概念係由Morton, Taylor & Turner 〔 1 〕引入，用以閉合斷面積分法建立之數學模式，Taylor 〔 2 〕繼而假設捲增速度與射流體中心速度成正比，然而在複雜情況下捲增關係式之選定仍是意見紛紜；捲增係數不爲一定值常數而和射流形態有一演化趨勢〔 3 〕，有關浮昇射流在靜止層變水域中之浮昇與混合研究，黃〔18〕等曾作了系列的探討，在橫向流動水域裡因捲增關係式之不同仍未有定論。橫向流動量傳遞於射流體的阻力作用由Fan〔 4 〕、Abrabam 〔 5 〕率先以水流通過圓柱體所受阻力之形式予以考慮，阻力係數經Chan、Lin & Kennedy 〔 6 〕實驗指出在近域裡其與速度比K值有關。實驗方面近年來以Wright之一系列研究〔 7,8,9 〕較爲突出，其以因次分析方法推導若干特性長度配合實驗資料探討射流問題。

本文首先由與問題有關之諸因數著手，經由因次分析提出一界分射流形態之無因次參數、探討在不同射流形態下射流體總體物理量和N之函數次方關係；理論探討上以斷面積分法建立數學模式，藉實驗資料分析捲增關係式之適用性、界定捲增係數、驗證數值模式之可行性，進而檢視因次分析所推論者。

貳、因次分析

因次分析爲一數學程序，係將某一現象有關之因數就因次歸納整理，組合成相當數學模式解答之無因次函數關係式；吾人可藉之與實驗及數學模式相驗證，在適當範圍內其形式簡便可提供工程設計參考。於本問題有關因數可分爲三類，其分別爲：

1. 射流體總體性質物理量：本文探討浮昇最大高度H_m 、浮昇平衡高度H_e、浮昇最高點比質量流率V_m （ 稀釋率可由V_m / V_j 表之 ）。
2. 啟始排放條件：以流率表示下有啟始比質量流率$V_j = R^2 u_j$ 、啟始比動量流率$M_j = u_j V_j$ 、啟始比浮量流率$B_j = (\Delta\rho_j / \rho_{aj}) g V_j$。
3. 環境水域性質：密度層變參數$G = (g / \rho_{aj}) (d\rho_a / dy)$ 、水平流速U_a

諸因數間關係可由下式表示：

$$f (P_i, V_j, M_j, B_j, G, U_a) = 0 \qquad i = 1, 2, 3 \qquad (1-a)$$

式中： $P_1 = H_m$, $P_2 = H_e$, $P_3 = V_m$

又，射流體比質量流率因捲增效應沿發展路徑迅速增加，此一效應係受控於射流體與週遭水體間速度、密度差異，而和啟始比質量流率之相關性甚弱；故V_j 僅在排放口附近有其影響力，於式(1－a) 中其與 P_i 之相關性可予忽略，且就形態而言V_j 已含括於M_j 、B_j二因數內，爲簡化因次分析〔 7, 9, 10 〕將之略去改寫爲：

$$f' (P_i, M_j, B_j, G, U_a) = 0 \qquad i = 1, 2, 3 \qquad (1-b)$$

上式中有五個物理量，具時間、長度二個基本因次，由Buckinghm π－定理知其至多可組成三個無因次參數，分別爲：

$$\left(\frac{H_m B_j^{1/2}}{M_j^{3/4}}, \frac{H_e B_j^{1/2}}{M_j^{3/4}}, \frac{V_m B_j^{1/2}}{M_j^{5/4}} \right) \sim f_{BM} \left(\frac{G M_j^2}{B_j^2}, \frac{U_a M_j^{1/4}}{B_j^{1/2}} \right) \qquad (2-a)$$

定義：流況參數$N = G M_j^2 / B_j^2$ 爲啟始排放條件中動量、浮量二驅動力比值之無因次參數〔 11 〕；若射流啟始驅動力爲浮量主控，此時N之階數相當小（ 如$N \sim 10^{-3}$ ）射流形態趨向於浮流，則式(1－b) 略去M_j 經因次分析得：

$$\left(\frac{H_m G^{3/8}}{B_j^{1/4}}, \frac{H_e G^{3/8}}{B_j^{1/4}}, \frac{V_m G^{5/8}}{B_j^{3/4}} \right) \sim f_B \left(\frac{U_a}{G^{1/8} B_j^{1/4}} \right) \qquad (2-b)$$

反之，若射流啟始驅動力爲動量主控，此時N之階數相當大（ 如$N \sim 10^3$ ）射流形態趨向於動量射流，則式(1－b) 略去B_j 經因次分析得：

$$\left(\frac{H_m G^{1/4}}{M_j^{1/4}}, \frac{H_e G^{1/4}}{M_j^{1/4}}, \frac{V_m G^{1/4}}{M_j^{3/4}} \right) \sim f_M \left(\frac{U_a}{G^{1/4} M_j^{1/4}} \right) \qquad (2-c)$$

式(2－a)、(2－b)、(2－c) 中各無因次參數經適當配比後，可合併寫爲一通式：

$$\left(\frac{H_m B_j^{1/2}}{M_j^{3/4}}, \frac{H_e B_j^{1/2}}{M_j^{3/4}} \right) \sim N^{-3/8} \cdot f'_{HB} \left(\frac{H_m G^{1/2}}{U_a} \right) \qquad \text{浮　流}$$

$$\sim f'_H \left(N, \frac{H_m G^{1/2}}{U_a} \right) \qquad \text{浮昇射流}$$

$$\sim N^{-1/4} \cdot f_{HM} \left(\frac{H_m G^{1/2}}{U_a} \right) \qquad \text{動量射流} \qquad (3-a、b)$$

$$\frac{V_m B_j^{1/2}}{M_j^{5/4}} \sim N^{-5/8} \cdot f_{VB} \left(\frac{V_m G}{U_a^3} \right) \qquad \text{浮　流}$$

$$\sim f_V \left(N, \frac{V_m G}{U_a^3} \right) \qquad \text{浮昇射流}$$

$$\sim N^{-1/4} \cdot f_{VM} \left(\frac{V_m G}{U_a^3} \right) \qquad \text{動量射流} \qquad (3-c)$$

爲檢視射流體總體性質物理量無因次參數和參數N間次方關係是否如上所示，及提供簡單無因次式供海洋放流工程設計參考，以之進行複迴歸分析：

$$\frac{H_m B_j^{1/2}}{M_j^{3/4}} \sim N^p \cdot \left(\frac{H_m G^{1/2}}{U_a} \right)^m \qquad (4-a)$$

$$\frac{H_e B_j^{1/2}}{M_j^{3/4}} \sim N^q \cdot \left(\frac{H_e G^{1/2}}{U_a} \right)^n \qquad (4-b)$$

$$\frac{V_m B_j^{1/2}}{M_j^{5/4}} \sim N^r \cdot \left(\frac{V_m G}{U_a^3} \right)^\ell \qquad (4-c)$$

$p, q \sim -3/8$, $r \sim -5/8$ 浮　流

$\sim [-3/8, -1/4]$, $\sim [-5/8, -1/4]$ 浮昇射流

$\sim -1/4$, $\sim -1/4$ 動量射流 (4－d)

參數次方p、q、r是否如式（4－d）所示，參數次方m、n、ℓ之值爲何，將由實驗及數學模式演算驗證及求得。

叁、數學模式

射流問題之近域模式處理方法可分爲二類。其一爲從Navier-Stokes方程式著手將之以亂流擾動項代入展開，藉假設一亂流模式閉合控制方程式再以數值方法解析，由於高階非線性方程式之複雜性，此種方法缺乏實用性。其二爲在射流體斷面沿軸向速度、密度差具動力相似性假設下，以斷面積分法建立射流體質量、動量、浮量守恆方程式，藉Taylor 捲增概念閉合後得一組一階擬線性常微分方程式，再以數值方法求解（謂之Similarity Solution）；此一數學模式物理意義至爲明顯且易於數值計算，於探討射流總體性質工程觀點上具有實用性，本文循此解析射流問題。

一射流體控制方程式：

射流體之發展（如圖1）自勢心區頂點後已達完全發展之亂流，此時射流體實際斷面爲腎形其內有二個對稱渦性流動（如圖2）；今假設斷面爲圓形、軸向對稱，且渦性流動甚弱可以不計其對射流體發展之影響，則斷面上沿軸向速度、密度差分佈可接受相似性假設處理〔4,12〕，設其可由高斯分佈近似〔1,4,12,13〕表爲：

$$(u-U_a\cos\theta)=(u_c-U_a\cos\theta)\cdot\exp(-r^2/b^2) \qquad (5\text{—a})$$

$$(\rho_a-\rho)=(\rho_{ac}-\rho_c)\cdot\exp(-r^2/\lambda^2b^2)=\Delta\rho_c\cdot\exp(-r^2/\lambda^2b^2) \qquad (5\text{—b})$$

由Boussinesq 假設並定義射流體特性半徑R：射流體斷面上速度u所攜之物理量可分爲二部份，一爲（$u-U_a\cos\theta$）所攜，一爲$U_a\cos\theta$所攜；作爲斷面積分時前者可將式（5－a）、（5－b）代入利用高斯分佈特性計算化簡，後者則需有一適量邊界作爲積分上限方能計算，然而在高斯分佈假設下射流體無邊界（趨近於∞）可言。今假想一半徑爲R之斷面其上速度$\overline{u}$爲均勻分佈，設此一斷面上之比質量流率、比動量流率和（$u-U_a\cos\theta$）所攜者相同，即：

$$\pi R^3\overline{u}=\int_0^\infty(u-U_a\cos\theta)(2\pi r\,dr)$$

$$\pi R^2\overline{u}^2=\int_0^\infty(u-U_a\cos\theta)^2(2\pi r\,dr)$$

解之得$R=\sqrt{2}\,b$，此值含括高斯分佈特性及質量、動量流率均衡之物理意義，據此定義一射流體特性半徑R作爲計算速度$U_a\cos\theta$所攜之物理量。

則通過射流體斷面之比質流率$\overline{V}$、比動量流率M、比浮量流率B，經由式（5－a）、（5－b）計算化簡後爲：

$$V=\int_A u\cdot dA=\pi b^2(u_c+U_a\cos\theta) \qquad (6\text{—a})$$

$$M=\int_A u^2\cdot d_A=\frac{1}{2}\pi b^2(u_c+U_a\cos\theta)^2 \qquad (6\text{—b})$$

$$B=\int_A\frac{\rho_a-\rho}{\rho_{aj}}u\cdot dA=\pi\lambda^2b^2\cdot\frac{\Delta\rho_c}{\rho_{aj}}\cdot\left(U_a\cos\theta+\frac{U_c-U_a\cos\theta}{1+\lambda^2}\right) \qquad (6\text{—c})$$

假設：(1)流況爲定常態、不可壓縮流動、流體黏滯效應不顯著，(2)環境水域亂流引致亂流擴散及射流體縱向延散，遠小於射流體與週遭水體間速度、密度差異捲增所產生之側向混調，(3)地球自轉Coriolis Force 及流軸偏斜向心力等均甚小可予不計；則依質量守恆、動量守恆、浮量守恆、軌跡幾何關係，射流體發展控制方程組可寫如：

質量守恆 $$\frac{d(\overline{V})}{ds}=E \qquad (7\text{—a})$$

動量守恆$\overrightarrow{X}$ $$\frac{d(M\cos\theta)}{ds}=F_e+(e_\theta)\cdot F_D\sin\theta \qquad \begin{matrix}若\,\theta>0\,,e_\theta=1\\ \theta<0\,,e_\theta=-1\end{matrix} \qquad (7\text{—b})$$

$\overrightarrow{Y}$ $$\frac{d(M\sin\theta)}{ds}=-F_b-(e_\theta)\cdot F_D\cos\theta \qquad (7\text{—c})$$

浮量守恆 $$\frac{d(B)}{ds}=V\cdot\left(\frac{d\rho_a}{dy}/\rho_{aj}\right)\cdot\frac{dy}{ds} \qquad (7\text{—d})$$

軌跡幾何 $$\frac{d(\chi)}{ds}=\cos\theta \qquad (7\text{—e})$$

$$\frac{d(y)}{ds}=\sin\theta \qquad (7\text{—f})$$

式中：

捲增量$E=2\pi RV_e$

捲增力$F_e=E\cdot U_a$

阻　力$F_D=C_D\cdot\frac{(U_a\sin\theta)^2}{2}(2R)$

浮　力$F_b=\int_A\frac{\rho_a-\rho}{\rho_{aj}}g\cdot dA=\pi\lambda^2b^2g\cdot\frac{\Delta\rho_c}{\rho_{aj}}$

式（7－a）～（7－f）係一組擬線性常微分方程組，自變數爲s，應變數爲x、y、θ、b、u_c、$\Delta\rho_c/\rho_{aj}$；在決定捲增關係使之閉合及給予適當初值條件後得以數值方法求解，本文以Fourth-Order Runge-Kutta Method 運算之，於電腦程式中設定計算所需精度上，下限控制條件，自動調整演算間距Δs 以節省計算機時間。

二捲增關係式：

閉合斷面積分法建立數學模式之捲增概念係由Morton〔1〕提出，繼之Taylor〔2〕建議：假設捲增速度V_e與射流體軸心速度u_c成正比$V_e=\alpha u_c$，α爲捲增係，其後研究本問題學者大都在此一構架上嘗試適用於不同狀況下之捲增關係式，其中Fox〔3〕、Hirst〔14〕及黃、王〔18〕等藉雷諾應力分佈具動力相似性之假設，出適用於靜止水域（密度層變或均質）之捲增關係式較具解析性，其將α分爲二部，α_1、α_2：

$$V_e=\left(\alpha_1+\frac{\alpha_2\sin\theta}{F_\ell^2}\right)u_c \qquad (8\text{—a})$$

式中： $\alpha_2=\lambda^2(2\lambda^2-1)/(H\lambda^2)$ ， $F_t^2=u_c^2/(gb\cdot\Delta\rho_c/\rho_{aj})$

在密度均勻水域有橫向流動情況下，Abraham〔5〕將捲增關係式表爲：

$$V_e=\alpha_1(u_c-U_a\cos\theta)+\alpha_3(U_a\cos\theta)\cdot\sin\theta \qquad (8-b)$$

綜合式（8－a）、（8－b）可將具橫向流動密度層變水域裡捲增關係式表爲：

$$V_e=(\alpha_1+\alpha_2|\sin\theta|/F_t^2)(u_c-U_a\cos\theta)+\alpha_3(U_a\cos\theta)\cdot|\sin\theta| \qquad (8-c)$$

式中 θ 爲流軸偏斜角度因子，因捲增與路徑角度無關故修正爲 $|\sin\theta|$ 。

密度層變水域裡以式（8－c）捲增關係式閉合控制方程式之數學模式作數值演算時，$\Delta\rho_c$ 隨射流體發展有正、負相間出現之振盪現象（如圖3），F_t^2 爲 $\Delta\rho_c$ 函數將隨之變化，致使捲增量在計算上有向內捲進（正）與向外捲出（負）之別；作者以爲 $\Delta\rho_c$ 隨射流體發展之振盪現象是合理的，但就捲增而言不論是向內捲進抑是向外捲出均爲一混調過程，射流體比質量流率均應沿發展路徑持續增加（可由實驗觀察得知），按此式（8－c）宜加修正爲：

$$V_e=(\alpha_1+\alpha_2|\sin\theta|/|F_t^2|)(u_c-U_a\cos\theta)+\alpha_3(U_a\cos\theta)\cdot|\sin\theta| \qquad (8-d)$$

或爲： $V_e=\alpha_1(u_c-U_a\cos\theta)+\alpha_3(U_a\cos\theta)\cdot|\sin\theta|$ (8－e)

式（8－d）、（8－e）何者爲佳，將藉實驗與數學模式演算驗證之。

三捲增係數：

1. α_1 ：依前人研究〔3〕不爲一定值常數而與射流形態有關，於射流趨向浮流者其值大於射流趨向動量射流者；依前述因次分析流況參數N可視爲界分射流形態有效參數，本文嘗試以之爲界分原則界定之。

2. α_2 ：依前人研究〔14〕$\lambda=1.11$（動量射流）至1.16（浮流）間，當 F_t^2 相當小時此一差異方對捲增量計算有所影響，故逕採 $\lambda=1.16$ ，則 $\alpha_2=0.97$ 。

3. α_3 ：Richards 〔15〕實驗資料指出在密度均勻水域裡其值爲0.5，本文將之延用至密度層變水域裡。

4. C_D ：依Chan,Lin & Kennedy 實驗資料〔6〕，於近域裡 C_D 和速度比 $k=u_j/U_a$ 之分佈如圖四，由其分佈趨勢本文假設當 $k>10$ 時 $C_D\sim0.8$ 。

四初值條件：勢心區頂點各量之推求

1. S_o,θ_o ：採Schatzmann〔16〕實驗迴歸式

$$S_o=(6.2-20.0/k)D_j$$

$$\theta_o=\pi(1.0-1.22/k)/2$$

2. b_o ：假設排放口至勢心區頂點間浮力，阻力變化甚小可予不計，則二者垂直方動量應相同，積分式（7－c）得：

$$b_o=\left(\frac{2.0}{\sin\theta_o}\right)^{1/2}\cdot\frac{u_j}{(u_c+U_a\cos\theta)}\cdot R_j$$

3. u_{co} ：$u_{co}=u_j+U_a\cos\theta_o$

4. $\Delta\rho_{co}/\rho_{aj}$ ：排放口至勢心區頂點間浮量守恆，積分式（7－d）省略微小項次後得：

$$\frac{\Delta\rho_{co}}{\rho_{aj}}=\frac{R_j^2}{\lambda^2 b_o^2}\cdot\frac{u_j}{\frac{u_j}{1+\lambda^2}+U_a\cos\theta}\cdot\frac{\Delta\rho_j}{\rho_{aj}}$$

肆、實　驗

「實驗」對問題之分析是相當重要的，於學理上可界定數學模式中諸係數、驗證模式可行性；更可藉之檢視因次分析推導之無因次函數次方關係是否正確，進而求出相當於數學模式解答之簡便公式與圖表供工程設計參考。本問題所需模擬之環境水域具密度層變又有橫向流動，故應用相對速度原理以「於靜止之密度層變水域裡，有一等速運動垂直排放之射流」模擬之；又爲避免排放口運動過程干擾到水域密度層變，而將排放口安設於水面下適當位置由上往下排放。實驗在一長3.7公尺、寬0.3公尺、深0.3公尺壓克力水槽中進行，實驗方法與步驟〔17,18〕簡述如下：

1 密度層變水域：利用鹽水填加方法，在水槽中每二公分由下而上充填不同鹽量之鹽水14層（如圖5），其過程約需6～7小時；填妥之水域各層密度差異在不受擾動情況下，由於分子擴散作用將漸趨緩和，靜置10～20小時（視層變梯度、室溫而定）後，水域密度將呈線性分佈（如圖6）。

2 相對速度：在水槽上方架設二支平行於水槽二側鋼軌供台車行走，台車上安設由三組滑輪及一組變速馬達組成之傳動系統，利用可變電壓器改變電源電壓（40～110伏特），使台車在不同速度（1.0～8.0公分／秒）下前進；排放口架設於水槽橫斷面中心位置之台車上並伸入水面下適當位置，則由台車帶動可使排放口在水域中依所需速度前進（如圖7）。

3 流場顯現：利用架設於台車上方光箱（箱內面鋪錫紙、1 kw 水銀燈一具），以光箱底面1毫米寬之狹縫將光源集中射出照射在射流體（排放溶液配有染料Rhodamine W.T）中心斷面上，利用射流體與環境水域間明暗程度差異得以攝得其發展軌跡（如圖8）；照相器材爲Nikom、F_2、50 mm 鏡頭、附自動捲片裝置之相機，將之固定於台車側下方隨車前進，拍攝時使用1 LFORD ASA 400 高感光度底片、快門爲一秒、光圈視染料濃度而定在2.8～5.6間。

實驗過程中，最大排放量僅達水域體積之0.003％，其對定常態假設之影響極微可忽略之；本文實驗共計26組，實驗數據如表一編號501～506，攝得射流體軌跡中心位如圖9.1～9.26。

伍、結果與討論

先以實驗結果比較捲增關係式何者爲佳、界定捲增係數、驗證模式可行性，進而以

實驗、數學模式驗證因次分析推導之無因次函數次方關係。

一分別以式（8－c）、（8－d）、（8－e）捲增關係式進行數學模式演算，以演算得軌跡和圖 9.1～9.26 實驗軌跡作比較，結果顯示式（8－d）、（8－e）較式（8－c）爲佳，蓋式（8－c）不滿足射流體應隨其發展路徑不斷增大之物理現象。

二以表一實驗資料中浮昇最大高度爲基準，比較式（8－d）、（8－e）捲增關係式進行數學模式演算所求出 α_1 最佳值（浮昇最大高度演算值最接近實驗值時之 α_1）和流況參數N之關係，結果發現：

1.式（8－e）捲增關係式所求出 α_1 最佳值和N有較佳之相關性。

2.式（8－d）捲增關係式在速度比甚小（$k<5$）時，最大浮昇高度演算值遠小於實驗值，茲以表一編號86實驗資料（$k=3.3$）演算作一說明：

⑴圖 10.1 爲演算軌跡比較：式（8－d）、（8－e）演算得浮昇最大高度分別爲 $3.2D_j$、$14.7D_j$ 而實驗值爲 $14.8D_j$，式（8－d）演算值與實驗值相去甚遠且此不準確性經測試分析知與 α_1、α_3 值大小無關。

⑵圖 10.2 爲捲增量計算比較：於此例中式（8－d）所描述捲增配比爲 $\alpha_2|\sin\theta|/|F_\ell{}^2|\cdot(u_c-U_a\cos\theta)\ll\alpha_1(u_c-U_a\cos\theta)$，$\alpha_3(U_a\cos\theta)\cdot|\sin\theta|$ 此一配比甚不合理；且在射口附近捲增量高達射流體比質量流率之1.7倍，不合理的龐大捲增迅速消彌了射流體週遭水體密度差異的浮昇效應，又射流體動量所具浮昇力遭橫向流動壓制，射流體無法向上浮昇致使演算結果偏低。

據此，作者以式（8－e）作爲閉合控制方程式之捲增關係式。

三因次分析式（2－a）中參數 $U_aM_j{}^{1/2}$，就形態而言與流況參數 $N=GM_j{}^2/B_j{}^2$ 相類似，亦可視爲啟始排放條件動量、浮量＝驅動力比值之無因次參數；但依本文分析結果其與 α_1 之相關性較弱，故本文採 $N=GM_j{}^2/B_j{}^2$ 作爲界分射流形態及選定捲增係數 α_1 之有效參數。所求出 α_1 和N間關係大致爲：

$N\sim[0,1]$	，	$\alpha_1\sim0.053$	， 射流形態～浮　流
$\sim[1,10]$	，	~0.045	， 浮昇射流
$\sim[10,\infty]$	，	~0.034	， 動量射流

四以式（8－e）捲增關係式、式⑼捲增係數 α_1 進行數學模式演算，就軌跡趨勢、射流體浮昇最大（平衡）高度驗證模式可行性，其結果分述如下：

1.軌跡趨勢：演算及實測比較如圖 9.1～9.26，其趨勢及吻合程度尚佳。

2.浮昇最大高度 H_m（實驗資料如表一）：實驗值 H_{me}、計算值 H_{mn} 間誤差 $ER1=(H_{me}-H_{mn})/H_{me}$ 列如表一 10a，其分佈大致爲

$|ER1|<5\%$ 佔 53％ ，$|ER1|<10\%$ 佔 84％

$|ER1|<15\%$ 佔 91％ ，$|ER1|<20\%$ 佔 97％

3.浮昇平衡高度 H_e（實驗資料如表二）：實驗值 H_{ee}、計算值 H_{en} 間誤差 $ER2=(H_{ee}-H_{en})/H_{ee}$ 列如表二 10b，其分佈大致爲

$|ER2|<5\%$ 佔 47％ ，$|ER2|<10\%$ 佔 68％

$|ER2|<15\%$ 佔 80％ ，$|ER2|<20\%$ 佔 90％

就軌跡趨勢、誤差分佈而言模式可行性尚稱良好，且在速度比相當小（$k<4$）時本模式仍能準確預測更顯其優越性。

五以實驗點啟始排放條件因數 M_j、B_j，環境水域性質因數 G、U_a，配合浮昇最大（平衡）高度實驗值 H_{me}（H_{ee}），浮昇最高點比質量流率計算值 V_m（稀釋率 V_m/V_j 列如表一 8a），按式（4－a）、（4－b）、（4－c）作複迴歸分析；結果發現參數次方 m、n、ℓ 等隨射流形態變動範圍很小可以一定值視之，其分別爲 2/5、2/5、－1/5；以 $(H_{me}B_j{}^{1/2}/M_j{}^{3/4})\cdot(H_{me}G^{1/2}/U_a)^{-2/5}\sim N$、$(H_{ee}B_j{}^{1/2}/M_j{}^{3/4})\cdot(H_{ee}G^{1/2}/U_a)^{-2/5}\sim N$ 及 $(V_mB_j{}^{1/2}/M_j{}^{5/4})\cdot(V_mG/U_a{}^3)^{1/5}\sim N$ 在雙對數座標格紙上作圖（如圖 11.1、11.2、11.3）藉之檢視參數N之次方 p、q、r，結果發現其與因次分析推導之式（3－a）、（3－b）、（3－c）相當接近，經整理後得：

$$\frac{H_mB_j{}^{1/2}}{M_j{}^{3/4}}=C_1\cdot N^p\cdot\left(\frac{H_mG^{1/2}}{U_a}\right)^{2/5}\qquad(10\text{－a})$$

$$\frac{H_eB_j{}^{1/2}}{M_j{}^{3/4}}=C_2\cdot N^q\cdot\left(\frac{H_eG^{1/2}}{U_a}\right)^{2/5}\qquad(10\text{－b})$$

$$\frac{V_mB_j{}^{1/2}}{B_j{}^{5/4}}=C_3\cdot N^r\cdot\left(\frac{V_mG}{U_a{}^3}\right)^{-1/5}\qquad(10\text{－c})$$

$N\sim[0,1]$，射流形態～浮　流，$C_1=2.20$，$p=-0.352$〔理論值－0.375〕

$C_2=2.18$　$q=-0.355$〔理論值－0.375〕

$C_3=2.01$　$r=-0.622$〔理論值－0.625〕

$\sim[1,10]$，～浮昇射流，$C_1=2.42$，$p=-0.305$

$C_2=$ —　$q=$ —

$C_3=1.97$　$r=-0.458$

$\sim[10,\infty]$，～動量射量，$C_1=1.77$，$p=-0.272$〔理論值－0.250〕

$C_2=1.93$　$q=-0.260$〔理論值－0.250〕

$C_3=1.04$　$r=-0.272$〔理論值－0.250〕

（10－a）、（10－b）、（10－c）相關係數均在 0.95 以上，在適當範圍內與圖 11.1、11.2、11.3 可供海洋放流工程設計參考。

陸、結　論

本文探討具橫向流動之密度層變水域裡，兼具啟始動量與密度差異射流之混合發展過程由因次分析、數學模式演算、實驗驗證等步驟，獲致結論如下：

在速度密度差具動力相似性假設下，採 Taylor 捲增概念閉合斷面積分法建立射

流體控制方程式之近域數學模式，就射流體總體性質而言其結果是可以接受的。

2. 捲增關係式在有橫向流動水域裡，當 k 值較小時式（ 8 － d ）不適用，採 Abraham 建議經本文修正之式（ 8 － e ）則能有良好的預測。

3. 本文建立之數學模式就軌跡趨勢、浮昇最大（平衡）高度演算，在與實驗比較下模式可行性尚稱良好，且在 $k < 4$ 時仍能適用益顯其優越性。

4. 因次分析推導之流況參數 $N = GM_j^2 / B_j^2$ ，可作爲界分射流形態及選定捲增係數 α_1 之有效參數，其演化情形如式(9)。

5. 實驗及數學模式演算驗證了因次分析方法推導之無因次參數函數間次方關係。式（10—a）、（10—b）、（10—c） 及圖 11.1 ， 11.2 ， 11.3 相當於數學模式解答，其形式簡便在適當範圍裡當對工程設計有所助益。

參考文獻

1. Morton, B., Taylor, G. I. & Turner, J. S., "Turbulent Gravitational Convection from Maintained and Instantaneous Sources," Journal of the Royal Society, London, England, A234, 1956.
2. Taylor, G. I., "Flow Induced by Jets," Journal Aero/Space Science. Vol. 25, 1958.
3. Fox, D. B., "Forced Plume in a Stratified Fluid," Journal of Geophysical Research, Vol. 75, 1970.
4. Fan, L. N., "Turbulent Buoyant Jets into Stratified or Flowing Ambient Fluids," W. M. Keck Laboratory of Hydraulics and Water Resources, Report No. KH-R-15, California Institute of Technology, Pasadena, California. 1967.
5. Abraham, G., "The Flow of Round Buoyant Jets Issuing Vertically into Ambient Fluid Flowing in a Horizontal Direction," Delft Hydraulics Laboratory, Delft, Netherlands, Report No. 81, 1971.
6. Chan, T. L., Lin, J. T. & Kennedy, J. F., "Entrainment and Drag Forces of Deflected Jets," Journal of the Hydraulics Division, ASCE, Vol. 102, 1976.
7. Wright, S. J., "Mean Behavior of Buoyant Jets in a Crossflow," Journal of the Hydraulics Division, ASCE, Vol. 103, 1977.
8. Wright, S. J., "Effects of Ambient Crossflows and Density Stratification on the Characteristic Behavior of Round Turbulent Buoyancy Jets," California Institute of Technology Report No. KH-R-36, 1977.
9. Wright, S. J., Wong, D. T. & Zimmerman, K. E., "Outfall Diffuse Mechanics in Stratified Ambient Fluid," Journal of the Hydraulics Division, ASCE, Vol. 108, 1982.
10. Alavian, V. & Hoopes, J. A. "Thermal Fronts in Heated Water Discharges," Journal of the Hydraulics Division, ASCE, Vol. 108, 1982.
11. Fisher, H. B., et al., Mixing in Inland & Coastal Waters, Academic Press, Inc. New York, 1977.
12. Rouse, H., Yih, C. B. & Humphreys, H. W., "Gravitational Convection from a Boundary Source," Tellus, Vol. 4, 1952.
13. Baumgartuer, D. J., & Trent, D. S., "Ocean Outfall Design Part 1 Liteaature Review and Theoretical Development," United States Department of the Interior Federal Water Quality Administration, 1970.
14; Hirst, E., "Buoyant Jets Discharged to Quiescent Stratified Ambients," Journal of Geophysical Research, Vol. 76, 1971.

15. Richards, J. M., "Experiments on the Motion of Isolated Cylindrical Thermals Through Unstratified Surroundings," International Journal of Air and Water Pollution, Vol. 7, 1963.
16. Schatzmann, M., "Auftriebsstrahlen in Naturlichen Stromungen-Entwicklung eines Mathematischen Modells," Thesis Pressented to Universitat Karlsruhe, in Karlsruhe, Germany, 1967.
17. 黃榮鑑、周文輝、王燦汶，“密度層變流中的擴散及其在海洋放流之應用”國立台灣大學水工試驗所試驗報告第52號，1977。
18. 黃榮鑑、王德忠、蔡西銘，“垂直浮昇射流在靜止密度層變水域中之浮昇與混合研究”，土木水利，十卷三期，37～59頁，1983。
19. 黃榮鑑，“二維密度層變流通過障礙受阻的研究”，中國工程學刊五卷三期，167～177頁，1982。
20. Jirka, G. H. & Fong, L. M., "Vortex Dynamic and Birfurcation of Buoyant Jet in Crossflow," Journal of the Engineering Mechanics Division, ASCE, Vol. 107, 1981.

符號說明

(x, y)	：笛卡爾座標系統	s	：射流體軸心位置
V	：射流體比質量流率	θ	：射流體軸向$\vec{s}$與x軸向$\vec{x}$交角
M	：射流體比動量流率	G	：水域密度層變參數
B	：射流體比浮量流率	U_a	：水域橫向流動速度
E	：捲增量	F_b	：浮　力
V_e	：捲增速度	F_D	：阻　力
F_e	：捲增力	C_D	：阻力係數
F_l	：局部密度福祿數	k	：速度比
R	：射流體特性半徑	N	：流況參數
D_j	：排放口直徑	H	：　體浮昇高度
R_j	：排放口半徑	ρ	：射流體時均密度
u	：射流體時均速度	ρ_a	：環境水域密度
λ	：擴散比	$\Delta\rho$	：同位置之環境水域與射流體間密度度差異
α	：捲增係數，α_1，α_2，α_3	b	：高斯分佈特性半徑
$(\ )_j$	：排放口位置	$[\ ]_e$	：實驗值
$(\ )_m$	：浮昇最高位置	$[\ ]_n$	：數學模式演算值
$(\ )_e$	：浮昇平衡位置	$ER1$	：$ER1 = (H_{me} - H_{mn}) / H_{me}$
$(\ )_o$	：勢心區頂點位置	$ER2$	：$ER2 = (H_{ee} - H_{en}) / H_{ee}$
$(\ )_c$	：射流體軸心位置		

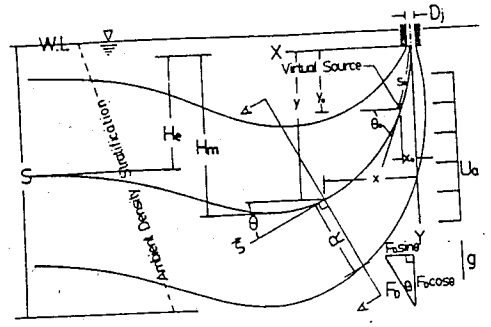

圖 1　射流體發展示意圖

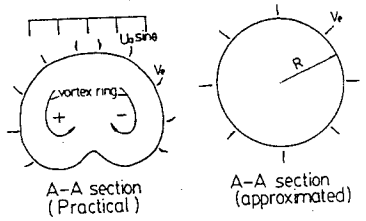

圖 2　射流體橫斷面

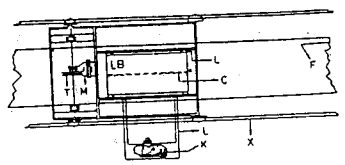

圖 7　實驗設備頂視圖

X：鋼軌
B：電源
M：馬達
V：電壓控制
T：傳動系統
E：排放管線
G：閥門
H：浮盆
I：鐵架
L：連桿
LB：光箱
C：狹縫（１mm）
K：相機
A：１KW水銀燈
F：環境水域水槽
D：鹽水拌合槽
P：鹽水充填管線

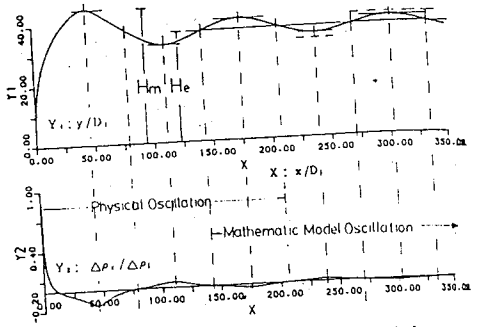

圖 3　密度層變水域振盪現象

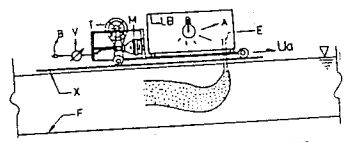

圖 8　實驗設備側視圖

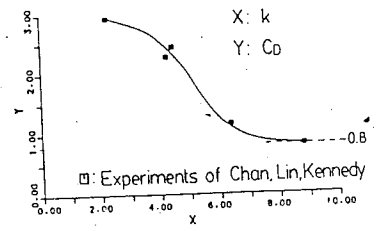

圖 4　阻力係數和速度比關係

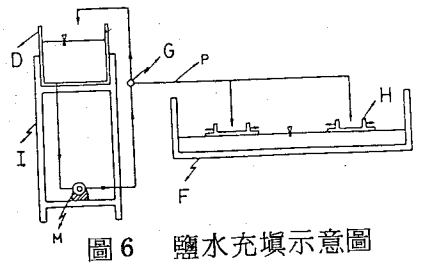

圖 6　鹽水充填示意圖

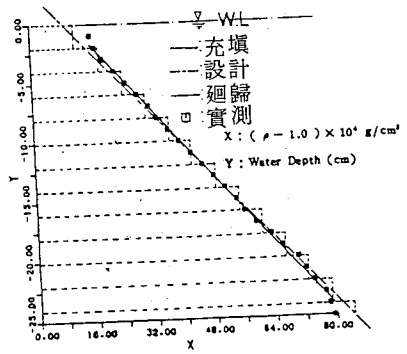

圖 5　環境水域密度層變

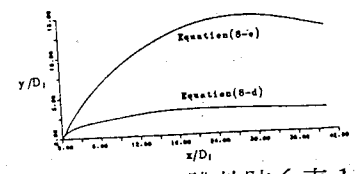

圖 10.1　射流體軌跡（表 1 No. 86）

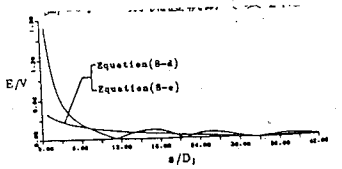

圖 10.2　射流體捲增量（表 1 No. 86）

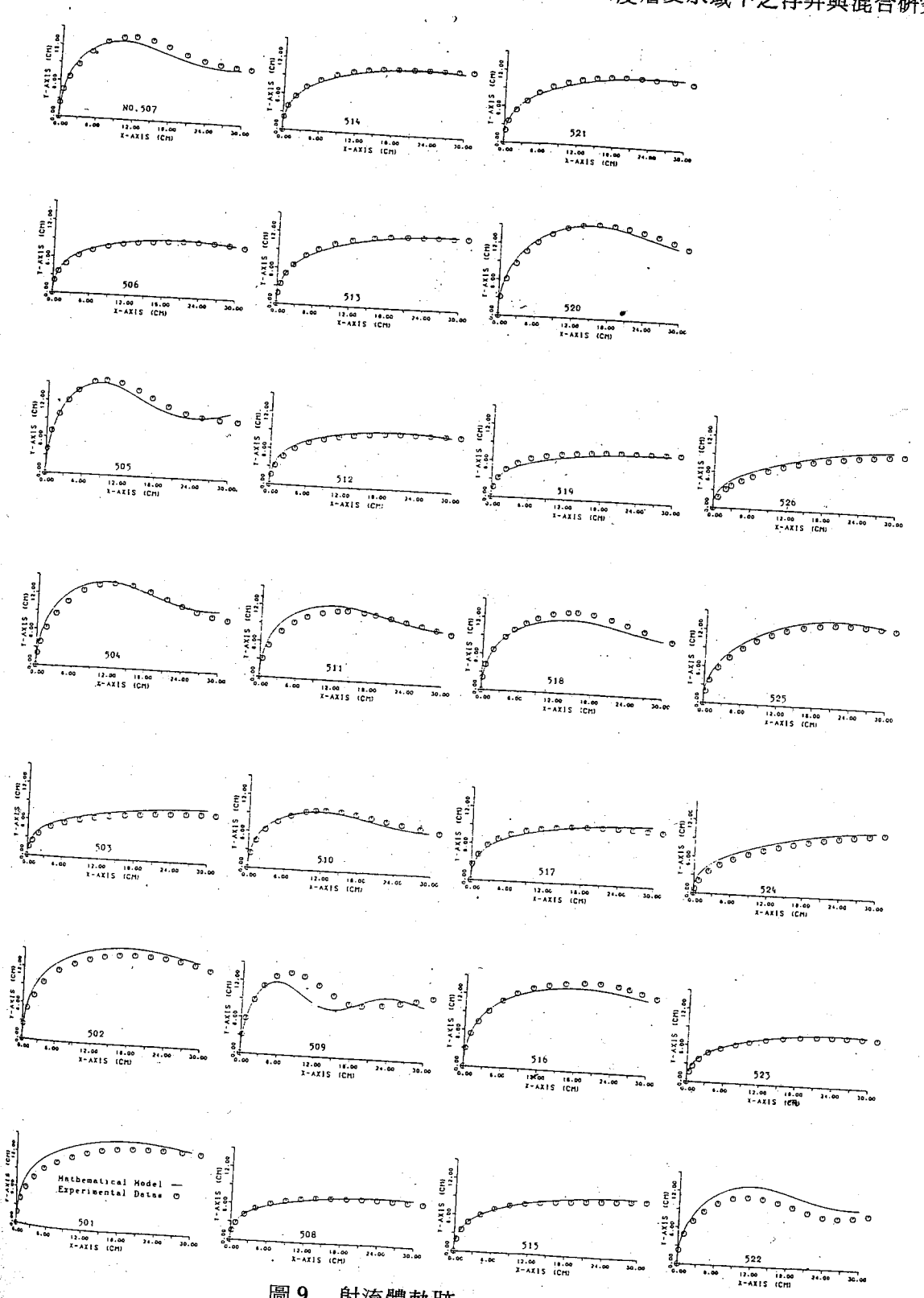

圖 9　射流體軌跡

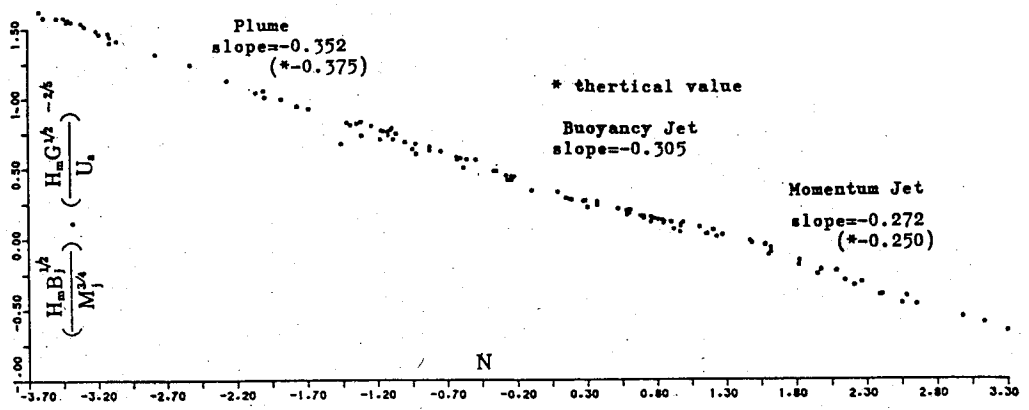

圖 11.1 $\frac{H_m B_j}{M_j^{3/4}} \sim N^p \cdot \left(\frac{H_m G^{1/2}}{U_a}\right)^m \qquad m = 2/5$

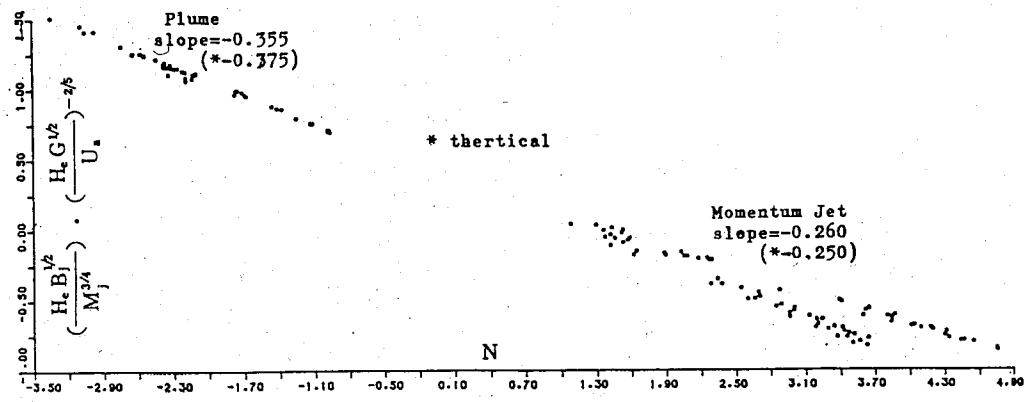

圖 11.2 $\frac{H_e B_j}{M_j^{3/4}} \sim N^q \cdot \left(\frac{H_e G^{1/2}}{U_a}\right)^n \qquad n = 2/5$

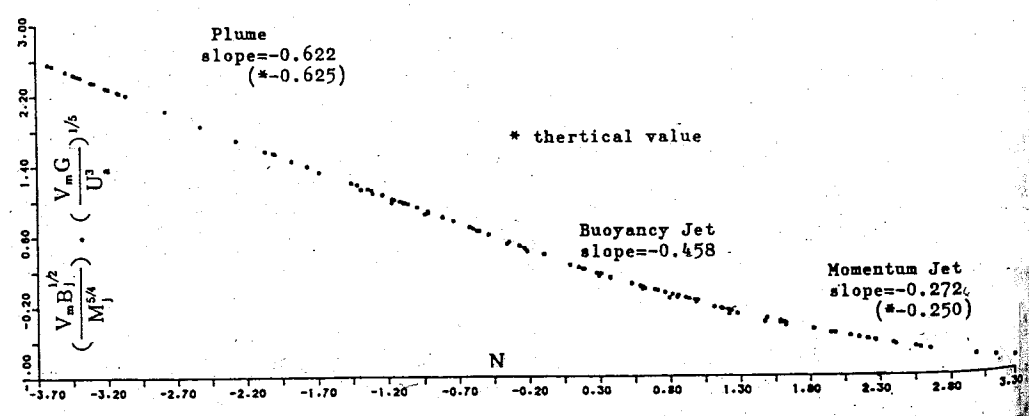

圖 11.3 $\frac{V_m B_j}{M_j^{5/4}} \sim N^r \cdot \left(\frac{V_m G}{U_a^3}\right)^\ell \qquad \ell = -1/5$

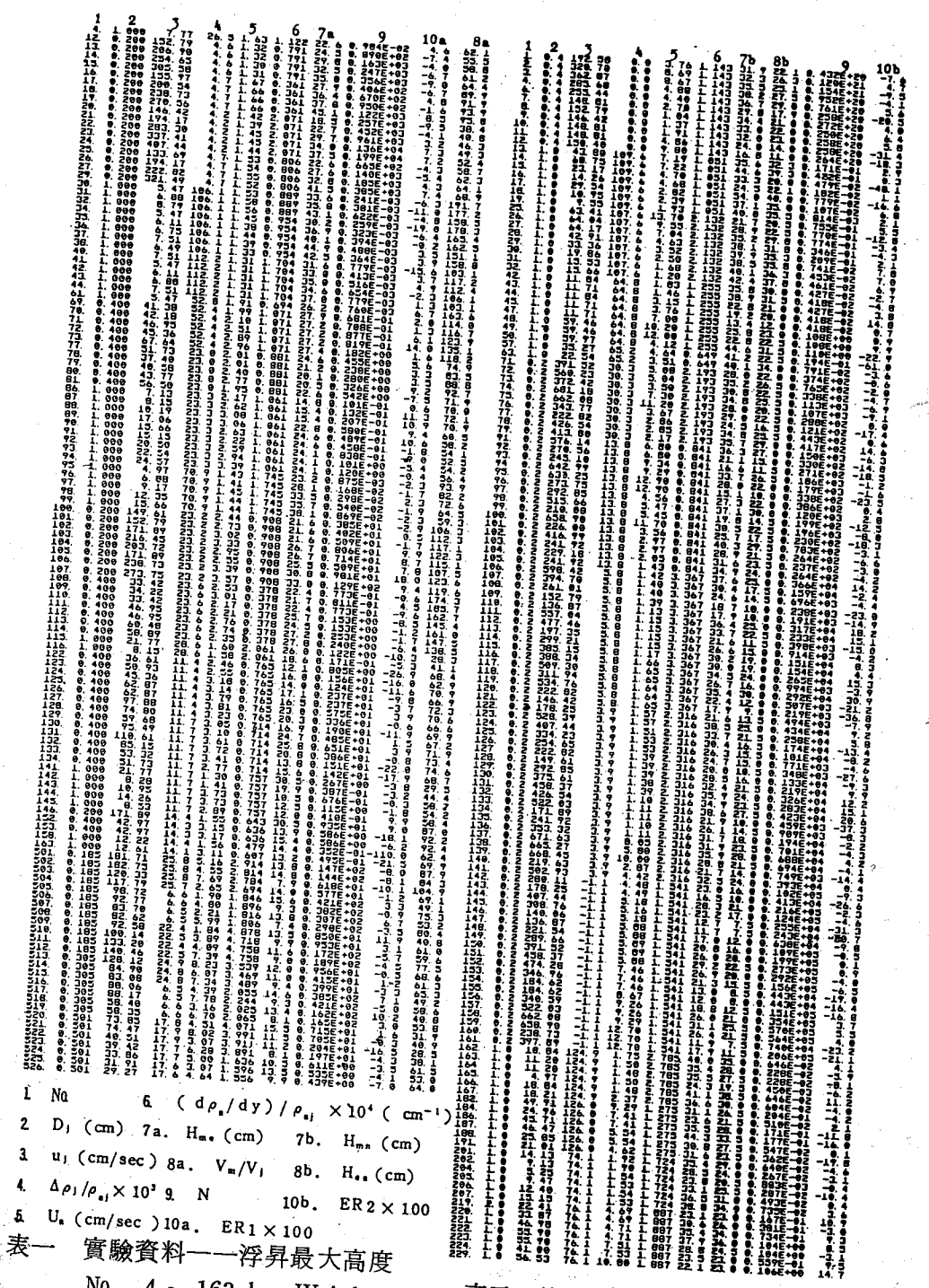

1 No.
2 D_j (cm)
3 u_j (cm/sec)
4 $\Delta\rho_j/\rho_{aj} \times 10^3$
5 U_a (cm/sec)
6 $(d\rho_a/dy)/\rho_{aj} \times 10^4$ (cm^{-1})
7a H_{ma} (cm)
7b H_{mn} (cm)
8a V_m/V_j
8b H_{ea} (cm)
9 N
10a ER1 × 100
10b ER2 × 100

表一 實驗資料——浮昇最大高度
No. 4 ~ 163 by Wright [8]
501 ~ 526 by Authors

表二 實驗資料——浮昇平衡高度
No. 1 ~ 229 by Wright [8]

河口及港灣流場傳輸及擴散之數值研究

黃　榮　鑑
中央研究院物理研究所
梁　興　杰
國立臺灣大學土木工程學研究所

摘　要

風力與潮汐在河口及港灣引生之流場傳輸運動及擴散研究，最初僅由水工模型試驗方法以觀測瞭解其現象，近年由於電子計算機之快速發展，由控制流場變化之方程式；在連續方程式、運動方程式及擴散方程式，藉電子計算機之高速計算以進行數值運算。本文即以有限元素法進行流場之動力模式及擴散模式之數值研究，利用葛拉金近似（ Galerkins approximation ）將垂直積分後之控制方程式轉換爲有限元素方程式，由對時間之積分求解時變微分代數式，以建立二維動力及擴散模式。將模式用以求解一維波方程式，由數值結果與解析解之比較以檢驗模式之準確性，驗證結果顯示結果甚佳。

壹、前　言

河口及港灣爲河川與海洋之連接水域，上游所携帶之一切物質與流量都經此排放外海，該處水體因受潮汐、風、地形及上游流量之影響，使得流場之傳輸與擴散現象變得相當複雜。瞭解河口及港灣之流場流態以及污染質排放在該區域造成之濃度分佈，對於污染之防制及環境水域之保護將有直接之幫助。

一般而言，河口及港灣之流場傳輸及擴散的研究方法有三：現場觀測、水工模型試驗以及數值模擬。以上三種方法各有其特性及重要性。現場觀測爲就原場進行觀測及調查，所得結果最爲眞實，唯費用甚鉅且難獲完整之結果。水工模擬試驗能於實驗室觀測流場與擴散之現象，對於性向之結果能提供良好之參考，惟水工模型對原場之模擬有其一定之限制，很難由實驗結果對原場之特性變化獲得定量之模擬。數值模擬是由控制其物理量變化之制御方程式，藉數值解析及計算以求解其物理量之變化。近年來由於電子計算機之快速發展，許多先前無法求解的問題，如今都能利用電子計算機之高速計算而求解，其中應用最爲廣泛的爲有限差分法[1]與有限元素法[2][3]。

Lin & Leendertse[4][5]，Simons[6]等曾先後以有限差分法探討港灣受潮汐與風及湖泊受風作用下之流場傳輸流況，由於其數值模式中所用未定係數很多，計算龐大

，對於計算時間相當費時。Wang & Connor[7]，Leimhuhler[8]及管[9]曾利用權重殘餘法之有限元素法探討港灣流場之傳輸及擴散問題，惟未曾考慮地形變化、內部剪應力等因子之影響。有限差分法與有限元素法之數值計算各有其優劣利弊，一般都認爲對於複雜邊界的處理，有限元素法較有限差分法爲佳。

河口及港灣內水體由於受潮汐、風、上游入流量地形及邊界等因素之影響，其流場之變化極爲複雜。本文爲利用有限元素法之葛拉金近似（Galerkin's approximation）由控制流場之連續方程式、運動方程式及污染質擴散方程式，垂直積分後之三維方程式轉換爲有限元素方程式，並對控制方程式中各項予以定量計算，和改進對時間積分之技巧及對邊界條件之處理，以使數值分析結果更趨精確與穩定。

貳、基本方程式

河口及港灣受潮汐、風力以及河流流量排入之影響，其流場及濃度分佈的變化可由連續方程式、運動方程式及濃度擴散方程式來描述，這些方程式爲：

$$\frac{\partial u}{\partial x}+\frac{\partial v}{\partial y}+\frac{\partial w}{\partial z}=0 \qquad \cdots\cdots(1)$$

$$\frac{\partial u}{\partial t}+u\frac{\partial u}{\partial x}+v\frac{\partial u}{\partial y}+w\frac{\partial u}{\partial z}-fv=-\frac{1}{\rho}\frac{\partial p}{\partial x}+\frac{\partial \tau_{xx}}{\partial x}+\frac{\partial \tau_{yx}}{\partial y}+\frac{\partial \tau_{zx}}{\partial z} \qquad \cdots\cdots(2)$$

$$\frac{\partial v}{\partial t}+u\frac{\partial v}{\partial x}+v\frac{\partial v}{\partial y}+w\frac{\partial v}{\partial z}+fu=-\frac{1}{\rho}\frac{\partial p}{\partial y}+\frac{\partial \tau_{xy}}{\partial x}+\frac{\partial \tau_{yy}}{\partial y}+\frac{\partial \tau_{zy}}{\partial z} \qquad \cdots\cdots(3)$$

$$\frac{\partial p}{\partial z}=-\rho g \qquad \cdots\cdots(4)$$

$$\frac{\partial c}{\partial t}+u\frac{\partial c}{\partial x}+v\frac{\partial c}{\partial y}+w\frac{\partial c}{\partial z}=\varepsilon_{xx}\frac{\partial^2 c}{\partial x^2}+\frac{\partial}{\partial y}\left(\varepsilon_{yy}\frac{\partial c}{\partial y}\right)+\frac{\partial}{\partial z}\left(\varepsilon_{zz}\frac{\partial c}{\partial z}\right) \qquad \cdots(5)$$

式中，（u,v,w,）爲（x,y,z）方向所對應之流速分量，τ_{ij} 爲剪應力張量之分量，$f=2w_f\sin\phi$，爲地球自轉參數，w_f 爲地球自轉之角速度，ϕ 爲緯度度數。

由於潮汐影響的水面波動爲長波，因此流場可以淺域視之，亦即對於水深方向爲完全混合之水域，可藉垂直向之積分，使三維問題簡化爲二維問題。將上述方程式(1)、(2)、(3)及(4)取垂直向由$-h$至η積分，可得：

$$\frac{\partial H}{\partial t}+\frac{\partial q_x}{\partial x}+\frac{\partial q_y}{\partial y}=0 \qquad \cdots\cdots(6)$$

$$\frac{\partial q_x}{\partial t}+\frac{\partial}{\partial x}\left(\int_{-h}^{\eta}u^2dz\right)+\frac{\partial}{\partial y}\left(\int_{-h}^{\eta}uvdz\right)-fq_y+\frac{\partial}{\partial x}(F_p-F_{xx})-\frac{\partial F_{yx}}{\partial y}$$

$$-\frac{1}{\rho_0}(\tau_{zx}^s-\tau_{zx}^b)-\frac{1}{\rho_0}p^s\frac{\partial H}{\partial x}-g\eta\frac{\partial h}{\partial x}=0 \qquad \cdots\cdots(7)$$

$$\frac{\partial q_y}{\partial t}+\frac{\partial}{\partial x}\left(\int_{-h}^{\eta}uvdz\right)+\frac{\partial}{\partial y}\left(\int_{-h}^{\eta}v^2dz\right)+fq_x-\frac{\partial F_{xy}}{\partial x}+\frac{\partial}{\partial y}(F_p-F_{yy})$$

$$-\frac{1}{\rho_0}(\tau_{zy}^s-\tau_{zy}^b)-\frac{1}{\rho_0}p^s\frac{\partial H}{\partial y}-g\eta\frac{\partial h}{\partial y}=0 \qquad \cdots\cdots(8)$$

式中水面剪應力，τ^s 及底床剪應力，τ^b 分別表示爲：

$$\tau_{zx}^s=\rho_a c_D U_{10}^2\sin\theta \quad , \quad \tau_{zy}^s=\rho_a c_D U_{10}^2\cos\theta$$

及

$$\tau_{zx}^b=\rho_0 c_f(q_x^2+q_y^2)^{1/2}q_x/H^2$$

$$\tau_{zy}^b=\rho_0 c_f(q_x^2+q_y^2)^{1/2}q_y/H^2$$

ρ_a 及 ρ_0 分別爲空氣和水之密度，U_{10} 爲水面上10公尺處之風速，c_D 及 c_f 分別爲空氣阻方係數和底床摩擦係數，θ 爲風向與y方向之夾角，$H=h+\eta$ 爲總水深。

F_{ij} 爲內部剪應力（internal stresses，依據普蘭特混合理論（Prandtl mixing-length theory）可表示如下：

$$F_{ij}=E_{ij}\left(\frac{\partial q_i}{\partial x_j}+\frac{\partial q_j}{\partial x_i}\right) \quad , \quad i,j=1,2$$

$q_x=\int_{-h}^{\eta}udz$ 及 $q_y=\int_{-h}^{\eta}vdz$ 分別表示x－及y－向之單位寬度流量。

擴散方程式(5)經對垂直方向積分後可簡化爲：

$$\frac{\partial c}{\partial t}+\frac{\partial}{\partial x}(\bar{U}\bar{C})+\frac{\partial}{\partial y}(\bar{V}\bar{C})=-\frac{\partial Q_x}{\partial x}-\frac{\partial Q_y}{\partial y} \qquad \cdots\cdots(9)$$

式中 $C=\rho\bar{C}H$，$\bar{U}$，$\bar{V}$ 及 $\bar{C}$ 分別爲垂直之平均物理量。

$$Q_x=-\rho_0 H\left(K_{xx}\frac{\partial\bar{C}}{\partial x}+K_{yx}\frac{\partial\bar{C}}{\partial y}\right)$$

$$Q_y=-\rho_0 H\left(K_{xy}\frac{\partial\bar{C}}{\partial x}+K_{yy}\frac{\partial\bar{C}}{\partial y}\right) \qquad \cdots\cdots(10)$$

K_{ij} 爲擴散係數。

方程式(6)、(7)、(8)及(9)爲控制流場內物理變量H，q_x，q_y 及C之制御方程式，給予流場之適當起始條件及邊界條件即可藉數值方法得到閉合型式解。

流場中之邊界分爲兩類：一爲固定邊界（land boundary），S_q。另一爲開口邊界（ocean boundary），S_f。固定邊界 S_q 上之正交方向流量 q_n 與切線方向流量 q_s 可分別表示爲：

$$q_n=\alpha_{nx}q_x+\alpha_{ny}q_y=q_n^*$$

$$q_s=-\alpha_{ny}q_x+\alpha_{nx}q_y=q_s^* \qquad \cdots\cdots(11)$$

式中，$\alpha_{nx}=\cos(n,x)$ 及 $\alpha_{ny}=\cos(n,y)$ 分別爲方向餘弦。在開口邊界 S_f，由於水位變動而引生之外力亦可以下二式表示之：

$$F_{nn}=\alpha_{nx}F_{nx}+\alpha_{ny}F_{ny}=F_{nn}^*$$

$$F_{ns}=-\alpha_{ny}F_{nx}+\alpha_{nx}F_{ny}=F_{ns}^* \qquad \cdots\cdots(12)$$

域內各點之起始條件可以下式表示，即

$$(H, q_x, q_y, C) = (H_0, q_{x0}, q_{y0}, C_0) \quad \text{當 } t = 0 \qquad \cdots\cdots (13)$$

參、有限元素法

有限元素法是一種求解微分方程式近似解的數值方法，它的基本概念是將整個區域連體視爲子區域元素之組合，做爲流場解析的模擬。在每一個子區域內之連續場性可以用一假設函數來表示，利用變分原理（variable principles）或權重殘餘法（weighting residual）將控制方程式轉換爲該區域之有限元素方程式，再對每個子區域疊加組成大域系統（global system）之微分或代數方程式，利用起始條件及邊界條件，則待解各變數在每一節點之函數值可由此系統方程式求得。

如子區域之元素爲三角形，則元素中各變數可表示如下：

$$\begin{aligned} q_x &= \xi_1 q_{x1}^e + \xi_2 q_{x2}^e + \xi_3 q_{x3}^e \\ q_y &= \xi_1 q_{y1}^e + \xi_2 q_{y2}^e + \xi_3 q_{y3}^e \\ H &= \xi_1 H_1^e + \xi_2 H_2^e + \xi_3 H_3^e \\ C &= \xi_1 C_1^e + \xi_2 C_2^e + \xi_3 C_3^e \end{aligned} \qquad \cdots\cdots (14)$$

式中 ξ_1，ξ_2，ξ_3 爲單位化元素座標，其與 x－y 座標之關係爲：

$$\xi_i = \frac{1}{2A}(c_i + b_i x + a_i y), \quad i = 1, 2, 3 \qquad \cdots\cdots (15)$$

及

$$a_i = x_k - x_j$$
$$b_i = y_j - y_k$$
$$c_i = x_j y_k - x_k y_j$$
$$A = \frac{1}{2}(b_1 a_2 - b_2 a_1)$$

利用葛拉金近似（Galerkins approximation）取形狀函數爲權重函數，將方程式(6)～(9)就每一元素子區域積分並疊加後，經整理得系統方程式：

$$[M_H][\dot{H}] = [P_H] \qquad \cdots\cdots (16)$$
$$[M_{qx}][\dot{q}_x] = [P_{qx}] \qquad \cdots\cdots (17)$$
$$[M_{qy}][\dot{q}_y] = [P_{qy}] \qquad \cdots\cdots (18)$$
$$[M_c][\dot{C}] = [P_c] \qquad \cdots\cdots (19)$$

式中，$[M_H]$，$[M_{qx}]$，$[M_{qy}]$ 及 $[M_c]$ 爲相對於各變數之係數矩陣，$[P]$ 爲柱狀矩陣。

方程式(16)、(17)、(18)及(19)爲時變微分方程式，求解得從設定之起始條件對時間積分。Roache[1] 及 Wang[7] 曾比較不同時間技巧在有限差分法及有限元素法之應用，其中以二次顯性模式（two-step explicit scheme）較佳，不但精確穩定且時間間距 Δt 可較長。二次顯性法的理論與 Lax-Wendroff 有限差分法是相似的。二次顯性法是以兩次一階微分近似直接求得時變函數，即：

$$f\left(t + \frac{\Delta t}{2}\right) = f(t) + \frac{\Delta t}{2} f(t)$$

$$f(t + \Delta t) = f(t) + \Delta t\, f\left(t + \frac{\Delta t}{2}\right) \qquad \cdots\cdots (20)$$

應用二次顯示法求解方程式(16)、(17)、(18)及(19)式之步驟爲：

第一步驟：

$$[\bar{M}_H][H^{n+1/2}] = [M_H][H^n] - \frac{\Delta t}{2}[P_H^n] \qquad \cdots\cdots (21)$$

$$[\bar{M}_{qx}][q^{n+1/2}] = [M_{qx}][q_x^n] - \frac{\Delta t}{2}[P_{qx}^n] \qquad \cdots\cdots (22)$$

$$[\bar{M}_{qy}][q^{n+1/2}] = [M_{qy}][q_y^n] - \frac{\Delta t}{2}[P_{qy}^n] \qquad \cdots\cdots (23)$$

$$[\bar{M}_C][C^{n+1/2}] = [M_C][C^n] - \frac{\Delta t}{2}[P_C^n] \qquad \cdots\cdots (24)$$

第二步驟：

$$[\bar{M}_H][H^{n+1}] = [M_H][H^n] - \Delta t[P_H^{n+1/2}] \qquad \cdots\cdots (25)$$
$$[\bar{M}_{qx}][q^{n+1}] = [M_{qx}][q_x^n] - \Delta t[P_{qx}^{n+1/2}] \qquad \cdots\cdots (26)$$
$$[\bar{M}_{qy}][q^{n+1}] = [M_{qy}][q_y^n] - \Delta t[P_{qy}^{n+1/2}] \qquad \cdots\cdots (27)$$
$$[\bar{M}_C][C^{n+1}] = [M_C][C^{n+1}] - \Delta t[P_C^{n+1/2}] \qquad \cdots\cdots (28)$$

以上諸式中，n，$n+1/2$ 及 $n+1$ 分別爲第 n，第 $n+1/2$ 及第 $n+1$ 時段之值。$[\bar{M}_H]$ 等爲加入邊界條件調整後之矩陣。經由電腦程式及運算，在不同時段之流場中物理變量 H，q_x，q_y 及 C 即可求得其數值解。

肆、結果與討論

爲檢驗模式運算之準確性，利用前述之有限元素法數值模式以探討等水深矩形渠道內之駐立波（standing wave）運動情形，其控制方程式爲：

$$\frac{\partial^2 u}{\partial t^2} = gh\frac{\partial^2 u}{\partial x^2} \qquad \cdots\cdots (29)$$

$$\frac{\partial^2 \eta}{\partial t^2} = gh\frac{\partial^2 \eta}{\partial x^2} \qquad \cdots\cdots (30)$$

如圖(一)(a)所示，假設渠道之長度爲 L，$x = 0$ 處爲開口端，其水面受正弦波 $\eta_0 = a\sin(2\pi/T)t$ 作用，a 爲振幅，T 爲週期。在 $x = L$ 處爲封閉端，其正交方向之流量爲零，即 $u = 0$ 或 $\partial\eta/\partial x = 0$，利用分離變數法可得其解析解爲：

$$u(x,t) = -\frac{a\sqrt{gh}}{h\cos\left(\frac{2\pi}{T}\frac{L}{\sqrt{gh}}\right)}\sin\left[\frac{2\pi}{T}\frac{L}{\sqrt{gh}}\left(\frac{x}{L} - 1\right)\right]\cos\frac{2\pi}{T}t \qquad (31)$$

$$\eta(x,t)=\frac{a}{\cos\left(\frac{2\pi}{T}\frac{L}{\sqrt{gh}}\right)}\cos\left[\frac{2\pi}{T}\frac{L}{\sqrt{gh}}\left(\frac{x}{L}-1\right)\right]\sin\frac{2\pi}{T}t \quad (32)$$

有限元素法之平面分割如圖㈠(b)所示，在三個固定邊界使其正交方向流量爲零。由方程式(21)、(22)、(23)及(25)、(26)、(27)之數值解可獲得駐立波在渠道中之運動情形。圖㈡及圖㈢所示分別爲數值解與解析解在 x＝L 處及 x＝0 處之水位及流速變化之比較。表一及表二爲渠道中各點在不同時段時之比較。比較結果顯示，在兩個週期內，最大誤差與最大值之比不超過 1％，結果相當良好。

爲使上述之數值模式之應用一般化，用以探討不規則地形與形狀之港灣受潮汐、入流量及風等作用下之流場運動情形。港灣之地形及形狀示如圖㈣，入流量爲每秒 100m³，風速爲 10 knot（約 5.05 m／sec），潮汐之水位變化在開口處爲 $\eta_0=a\sin 2\pi/T\ t$，取 a＝0.2 公尺，T＝2 小時。

元素之分割示如圖，以 t＝0 時靜止流場爲起始條件，取 $E_{xx}=E_{yy}=400\ cm^2/sec$，$E_{yx}=E_{xy}=200\ cm^2/sec$，$C_f=0.0036$。上述條件經模式計算結果如下：

1. 節點 7 和 67 二點水位與 y 一向流速之變化如圖㈤(a)、(b)所示，流場傳輸呈週期性運動。
2. 在不同時間之速度場變化如圖㈥(a)、(b)、(c)、(d)所示。
3. 圖㈦(a)、(b)、(c)及(d)所示爲在不同時間流場相對應之流速及等濃度線分佈情形。
4. 數值演算收斂很快，約經過一個週期，流場之變化即趨恒定（stationary）。

伍、結　論

1. 二維數值模式用以一維波方程式之檢定，其數值解與解析解之比較結果甚佳，對於應用於完全混合水體之模擬應可得到良好結果。
2. 二次顯性法對時間之積分可以取至二階微分近似，又可避免非線性項之疊代運算，其結果較一階線性近似準確，且可節省計算機之計算時間。
3. 起始條件與模式之精確及穩定有關，若起始條件設定合理，將易收斂，否則易造成數值運算之不穩定，一般的原則是避免造成梯度變化太大。
4. 由於摩擦的作用，潮汐之傳輸有衰減的現象，越上游受上游入流量的影響越大，受潮汐的影響越小。
5. 應用本文之二維數值模式以預估潮汐作用下污染質之擴散，其結果趨勢相當合理。

參考文獻

1. Roache, P. J., Computational Fluid Dynamics, Hermosa, 1972.
2. Zienkiewicz, O. C., The Finite Element Method, McGraw-Hill, New York, 1977.

3. Gallagher, R. H. et al., Finite Elements in Fluids, 3 Volumes, Wiley-Interscience Publication, 1979.
4. Liu, S. K. & J. J. Leendertse, A Three-dimensional model for estuaries and coastal seas, The Rand Cooperation, R-2405-NOAA, Sep. 1979.
5. Lin, S. K. & J. J. Leenderstse, Multi-dimensional numerical modeling of estuaries and coastal seas, The Rand Cooperation, 1978.
6. Simons, T. J., Development of three-dimensional numerical model of the great lakes, Proceedings 15th Conference on Great Lakes Research, 1972.
7. Leimkuhler, W. F., A two-dimensional finite element dispersion model, Thesis for the degree of civil Engineering, MIT, Sep. 1974.
8. Wang, J. D. & J. J. Connor, Mathematical modeling of near coastal circulation, Tech. Report No. 200, R. M. Parsons Laboratory for Water Resource and Hydrodynamics, MIT, April, 1975.
9. 管秩豐，有限元素法在河口潮汐的傳送應用，國立台灣大學土木工程研究所碩士論文，中華民國七十年六月。

表一　數值計算水位與解析解之比較

X \ t	3T/4	5T/4	7T/4	9T/4	11T/4	Exact
0	-0.1	0.1	-0.1	0.1	-0.1	+0.1
50	-0.1028	0.1005	-0.1027	0.1025	-0.1027	0.1026
100	-0.1047	0.1042	-0.1045	0.1042	-0.1046	0.1044
150	-0.1057	0.1053	-0.1055	0.1052	-0.1057	0.1055
200	-0.1063	0.1056	-0.1061	0.1056	-0.1062	0.1059

表二　數值計算流速與解析解之比較

x \ t	T/2	T	3T/2	2T	5T/2	Exact
0	-0.05466	0.05446	-0.05431	0.05417	-0.05431	0.05440
50	-0.04125	0.04117	-0.04086	0.04096	-0.04087	0.04114
100	-0.02781	0.02772	-0.02751	0.02749	-0.02749	0.02759
150	-0.01388	0.01383	-0.01375	0.01370	-0.01381	0.01384
200	0.00	0.0	0.0	0.0	0.0	0.0

河口及港灣流場傳輸及擴散之數值研究

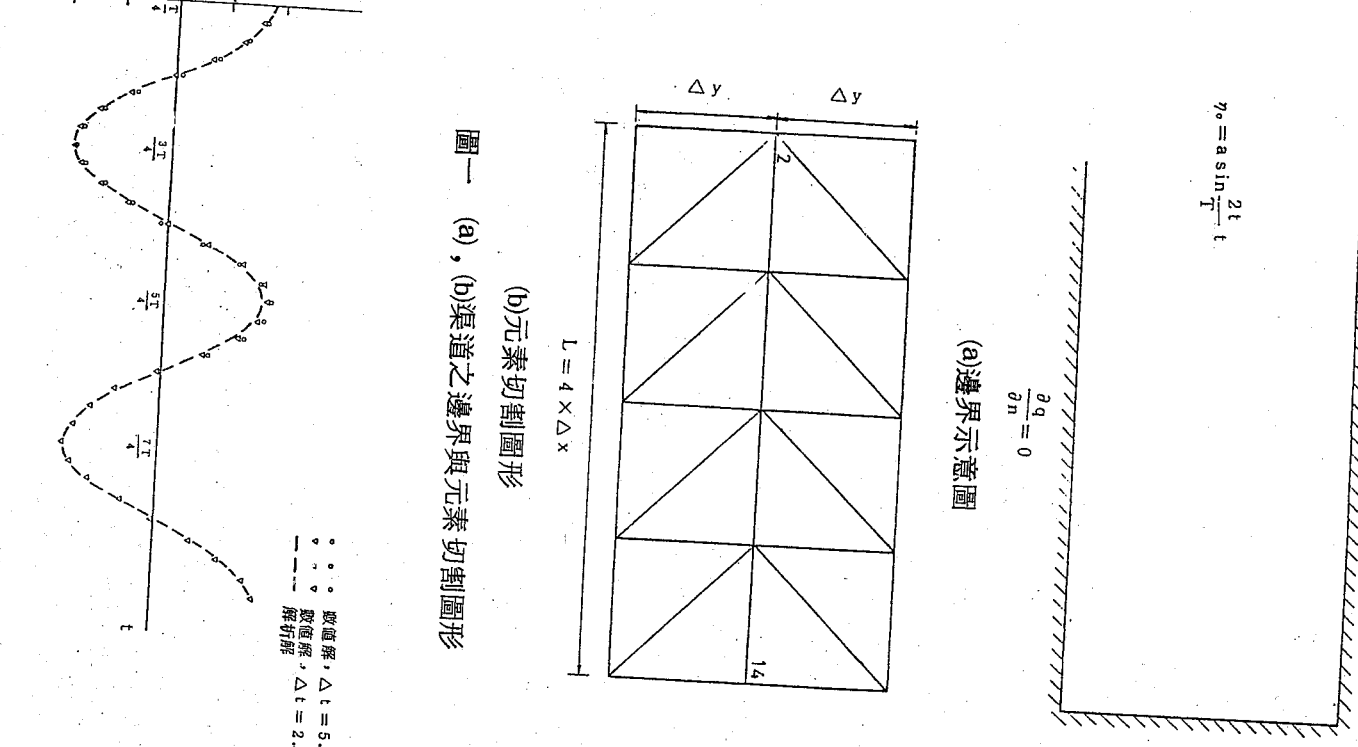

(a)邊界示意圖

(b)元素切割圖形

圖一　(a)，(b)渠道之邊界與元素切割圖形

圖二　x = L 處（節點 14）水位之變化情形

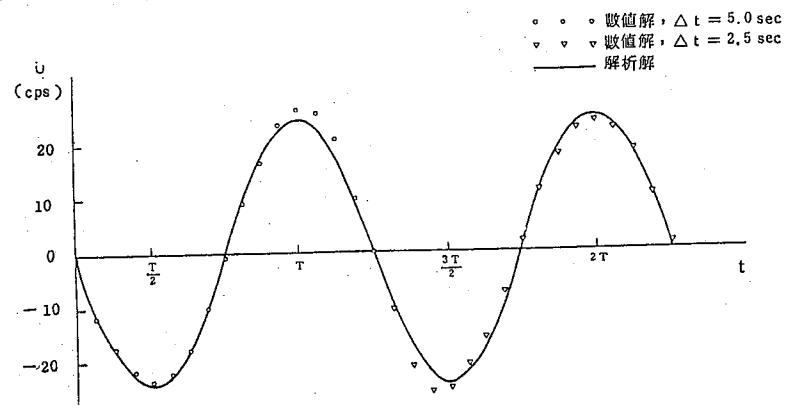

圖三　x = 0 處（節點 2 ）流速之變化情形

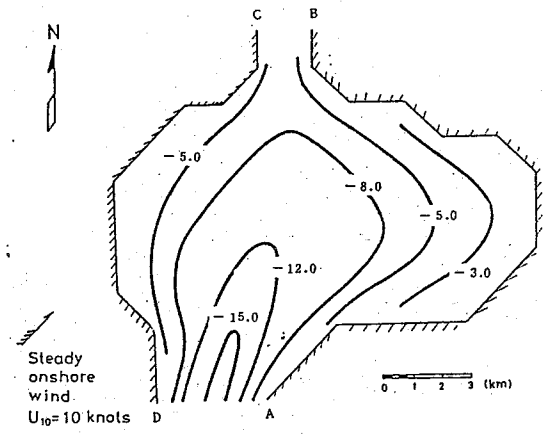

圖四(a)　地形變化之示意圖

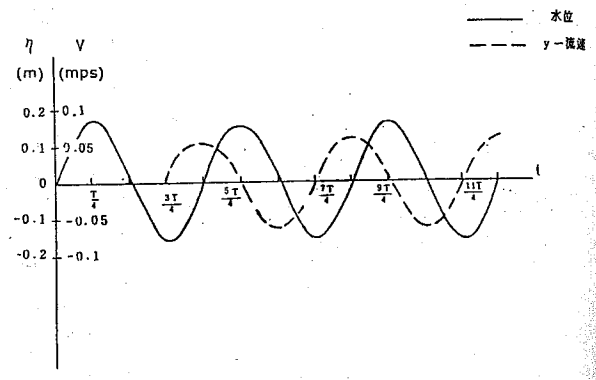

圖五(a)　節點 7 水位與 y－流速之變化圖形

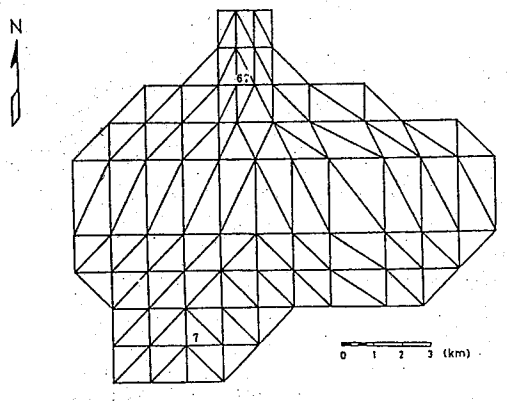

圖四(b)　元素切割示意圖

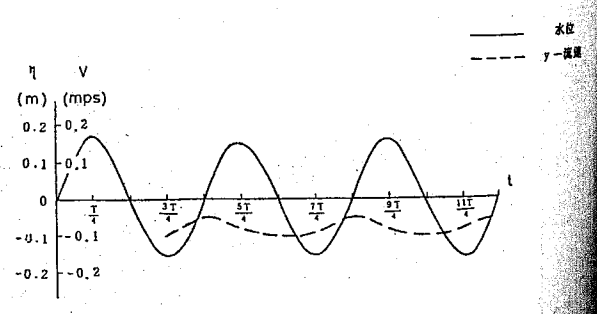

圖五(b)　節點 67 水位與 y－流速之變化圖形

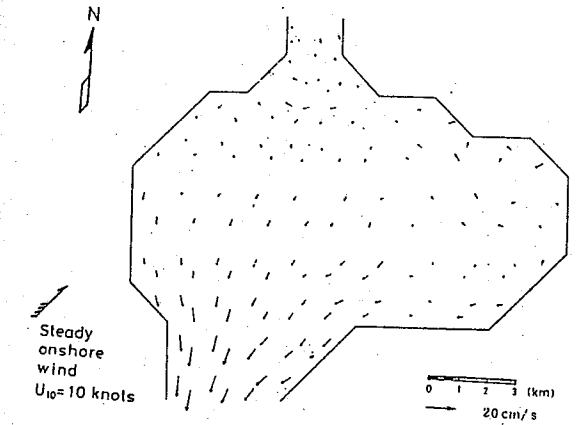

圖六(a)　t = 4.5 小時之速度場

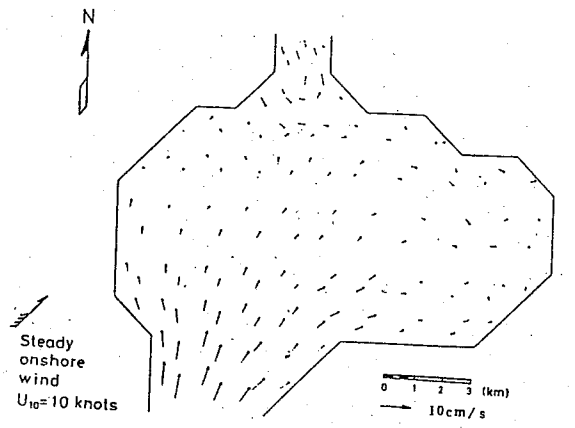

圖六(c)　t = 5.5 小時之速度場

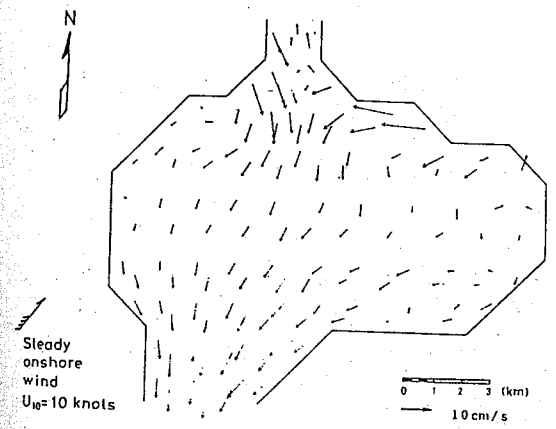

圖六(b)　t = 5.0 小時之速度場

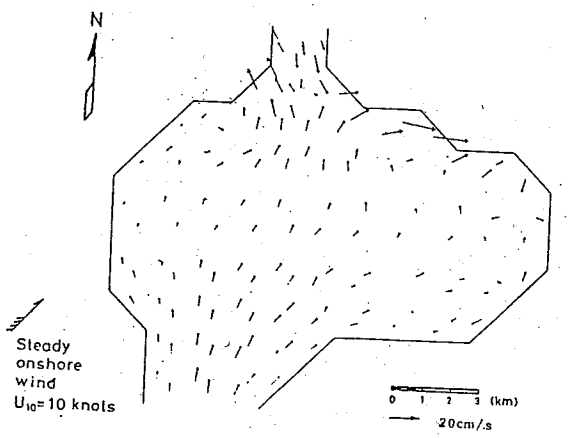

圖六(d)　t = 6.0 小時之速度場

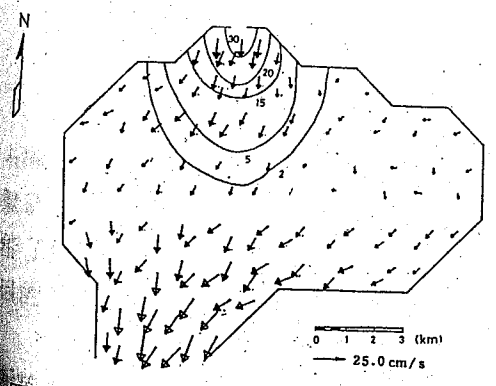

圖七(a)　t = 4.0 小時之等濃度線

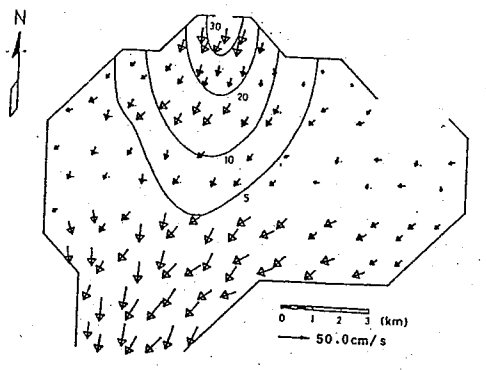

圖七(b)　t = 8.0 小時之等濃度線

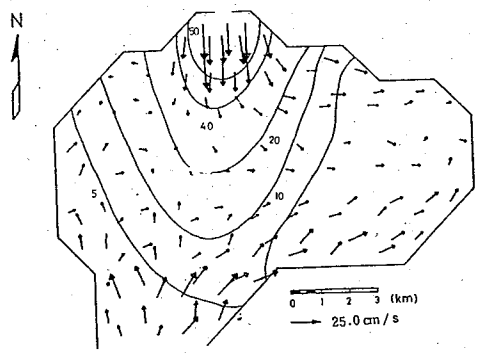

圖七(c)　t = 10.0 小時之等濃度線

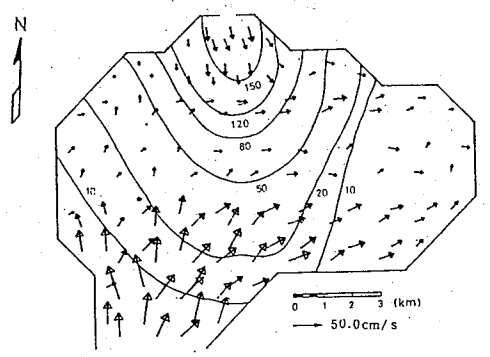

圖七(d)　t = 12.0 小時之等濃度線

大氣擴散參數時間序列預報之研究

梁　文　傑
中央研究院物理研究所
國立臺灣大學機械工程學系

張　瑞　宗
國立臺灣大學環境工程研究所

摘　要

本文是以各擴散參數小時平均值的逐時變化資料爲對象，來分析並建立各參數小時平均值的自迴歸積分移動平均（ ARIMA ）預報模式，以了解各擴散參數的小時變化。

研究結果顯示，此模式能對各大氣擴散參數如風向、風速、大氣穩定度、溫度的變化提供良好且可行的預報，對於週期性與季節性變化的情況，此模式亦能有效的掌握。對未來24小時（一天）的預報，文中以四組數據作個案研究，結果顯示，風向平均誤差爲25度，而大氣穩定度預報則準確性高，風速的平均預報誤差約爲0.45 公尺／秒，溫度的預報誤差則小於 1 ℃。

此研究可供區域性各擴散參數建立預報模式的參考，以預求未來短期內諸參數可能存有的擴散不利情況，儘早做適當的防制，以避免空氣品質的惡化。

壹、引　言

空氣品質是環境品質的重要指標，而空氣品質的好壞與氣象、氣候及地形狀況息息相關。由於因素甚多，使得空氣污染防治策略變得複雜。這些因素包括風向、風速、大氣穩定度（ Atmospheric Stability ）、溫度、太陽輻射（ Solar Radiation ）等。如能了解上述參數的變化，對於空氣污染的防治可得事半功倍的效果。因此本文最主要的目的，即爲對擴散參數在未來短期內的變化做一通盤的了解。

大氣擴散參數中，本文選定大氣穩定度、風向、風速及溫度進行研究，因爲穩定度對於大氣的擴散能力（即擴散係數）影響極大，風向與風速爲決定排放源（污染源）污染物質傳播的方向與速度，而溫度則會因影響煙囪排放的有效高度（Effective height），進一步影響到地面的濃度[1]。如能掌握上述四參數未來的變化，有助於求取其他有關的物理量，進而得知空氣污染擴散的大要。

空氣污染濃度的預報（即一般的擴散模式），通常是利用流體力學的制御方程式（

包括能量方程式），把當時風向、風速、大氣穩定度等氣象因素及污染源的分佈與排放量等資料全盤考慮，以推算下一時間濃度的分佈情形，然而因各種資料的取得受到經費與人力等現實因素的限制，再加上大氣紊流（Turbulence）過於複雜，所得的結果將不可能太密集且準確，必會有某種程度上的誤差，但儘管對局部性變化無法準確把握，就全面性的變化趨勢而言仍然提供了極爲有益的資訊。

本文鑑於擴散模式對局部性變化的掌握有其欠缺，乃另採途徑，直接以偵測站所得的資料，加以分析，利用統計方法，找出適合該區域各擴散參數的預報模式，因資料皆在該地實測，可使擴散模式中各參數的考慮更能反應出當地當時的實況及未來的變化，這些參數預測值應用於擴散模式或直接利用統計方法預測污染狀況，必能更有效的把握局部性變化，補一般大氣擴散模式的不足。

大氣擴散參數變化甚大，其預報雖十分困難，然由前人的研究可發現[2][3][4]以統計預報模式建立的各參數預報模式，如線性迴歸（Linear Regression）、複迴歸（Multi-Regression）及模式輸出統計法（Model Output Statistics）等，效果十分良好。

BOX與Jenkins[5]更於1970年提出時間序列分析法，依各種觀測物理量時間序列的特性，建立不同的隨機時序數學模式（Statistic Model），並應用所建立的隨機模式作預測。此隨機模式包括自迴歸（Auto-Regression簡稱AR）、積分（Integral簡稱I）與移動平均（Moving Average簡稱MA）三部分，故簡稱爲ARIMA，因其爲處理單一變數的問題，所以是單一變數ARIMA（Univariate ARIMA）的時間序列統計模式。此方法已被廣泛的應用在工程、水文、氣象、經濟、商業及自然科學的決策分析、控制研究及定量預測，其進一步的推廣應用是可預期的。本研究即嘗試以ARIMA對諸大氣擴散參數包括風向、風速、大氣穩定度及溫度做時序分析，並建立其預報模式。

貳、基本統計模式理論

一、基本定義

對一物理量做一等時距的連續量測，則量測所得的數列叫做時間序列，而時間序列的分析法，是以統計方法分析。由觀測所得的時間序列，如果它的分配機率，不因時間的移動而改變，稱爲嚴格穩定（Strictly Stationary），若此時序的前二階矩（Moment），不因時間的移動而改變，則稱爲二次穩定（Second-Order Stationary），但若所得的序列係非穩定性（Non-Stationary），則需藉數次的差分，以得新的穩定性時間序列。

一般說來一組時間序列，經由BOX與Jenkins氏所建議的方法，可以建立一個包含有三部分的隨機時間模式，包括自迴歸（AR）、積分（I）與移動平均（MA），其中積分（I）的部分，是當該序列爲非穩定性時才有，所以對一組穩定性的時間序列，它的預報模式將只包括自迴歸與移動平均（ARMA）兩個部分，非穩定性的時間序列，則藉差分的過程，使其穩定，然後再求其ARMA模式，最後合成ARIMA的模式。

二、模式的建立

ARIMA的基本觀念在於一物理量的過去觀測值Z_t，可由一線性隨機模式來代表，該物理量未來的變化，可藉此模式有限個過去觀測值與有限個過去擾動值的權重和來預測。AR（p）模式可寫成：

$$\tilde{Z}_t=\phi_1\tilde{Z}_{t-1}+\phi_2\tilde{Z}_{t-2}+\cdots+\phi_p\tilde{Z}_{t-p}+a_t, \quad \cdots\cdots(1)$$

此處$\tilde{Z}_t=Z_t-\mu$，μ爲觀測物理量的平均值，ϕ_1，$\phi_2\cdots\cdots\phi_p$爲AR（p）模式的p項參數，而$\{a_t\}$數列爲擾動（Shocks），統計上假設此擾動數列爲常態分配（Normal Distribution），其期望值（Expect Value）爲零，變異數（Variance）爲σ_a^2此數列的隨機變數（Random Variable），a_t，$a_{t-1}\cdots a_{t-p}$又稱爲白噪音（White Noise）。

若定義函數$\phi(B)$爲$(1-\phi_1B-\phi_2B^2-\cdots-\phi_pB^p)$，式中B爲後移運算子（Backshift Operator），即B^mZ_t爲Z_{t-m}，則(1)式可改寫爲：

$$\phi(B)\tilde{Z}_t=a_t, \quad \cdots\cdots(2)$$

而MA（q）模式可寫成：

$$\tilde{Z}_t=a_t-\theta_1a_{t-1}-\theta_2a_{t-2}-\cdots-\theta_qa_{t-q}, \quad \cdots\cdots(3)$$

式中θ_1，θ_2，$\cdots\theta_q$爲MA（q）模式的q項參數，a_t，a_{t-1}，$\cdots a_{t-q}$係白噪音。

若定義$\theta(B)$爲$(1-\theta_1B-\theta_2B^2-\cdots-\theta_qB^q)$則上式可寫成：

$$\tilde{Z}_t=\theta(B)a_t, \quad \cdots\cdots(4)$$

綜合(1)～(4)，ARMA（p,q）模式可寫成：

$$\tilde{Z}_t=\phi_1\tilde{Z}_{t-1}+\phi_2\tilde{Z}_{t-2}+\cdots+\phi_p\tilde{Z}_{t-p}+a_t-\theta_1a_{t-1}-\theta_2a_{t-2}-\cdots-\theta_qa_{t-q}$$

或簡寫成 $\cdots\cdots(5)$

$$\phi(B)\tilde{Z}_t=\theta(B)a_t, \quad \cdots\cdots(6)$$

上式適用於時間序列在一統計上的穩定狀況，即觀測數列的機率分配不因時間改變，實際上甚多時間序列傾向於非穩定性，此時則可用下式代表（即ARIMA（p·d·q）模式）：

$$\phi(B)\nabla^dZ_t=\theta(B)a_t, \quad \cdots\cdots(7)$$

上式中∇^d爲$(1-B)^d$，∇^d運算子的功用係將一非穩定性的時間序列Z_t，取d次差分後轉換爲穩定的時間序列。如對(6)式方程式兩邊取期望值，則因白噪音a_t的平均值爲零，我們發現對平均值不爲零的時間序列，需要先減去其平均值μ，以後我們就以$\tilde{Z}_t$代表$Z_t-\mu$。

由Jenkins與Watts[6]的理論ARMA（p,q）模式的變異數可寫爲：

$$\mathrm{Var}(Z_t)=\sigma_a^2\int_{-\frac{T}{2}}^{\frac{T}{2}}\left|\sum_{\alpha=0}^{q}\theta_\alpha e^{-i2\pi\omega\alpha}\right|^2\Big/\left|\sum_{j=0}^{p}\phi_je^{-i2\pi\omega Tj}\right|^2 d\omega, \quad \cdots\cdots(8)$$

式中T爲所取觀測值的總時間長度，ω是頻率（Frequency），σ_a是a_t的變異數。如分子部分的多項式θ_α，（$\alpha=0\cdots\cdots q$）的項數有限，則(8)式會收斂（Converge）

，但分母部份可表示爲（ $1-\phi_j \times e^{-i2\pi\omega T})^{mj}$ 的乘積，其中mj 是第 j 個因子的地方，(8)式的變異數在 $|\phi_j|<1$ 時會收斂，而(2)式方程式的根爲 $\frac{1}{\phi_j}$（ j = 1，2，…，p ），這意味著 $\phi(B)=0$ 的根必須在單位圓的外面，才會使變異數收斂，這就是穩定性的條件。例如對ARMA（1，0）模式：

$$(1-\phi_1 B)\tilde{Z}_t = a_t$$

則

$$\tilde{Z}_t = \phi_1 \tilde{Z}_{t-1} + a_t$$
$$\tilde{Z}_{t+1} = \phi_1^2 \tilde{Z}_{t-1} + \phi_1 a_t + a_{t+1}$$
$$\tilde{Z}_{t+2} = \phi_1^3 \tilde{Z}_{t-1} + \phi_1^2 a_t + \phi_1 a_{t+1} + a_{t+2}$$

以此類推，當 $|\phi_1|>1$ 時，則現在的值對愈遠的將來影響反而愈大，此不合理，而當 $|\phi_1|=1$ 時，則其影響力保持定值，不因時間而消退，即具有累積的作用，此時會產生不穩定的序列，所以穩定性的要求使 $\phi(B)=0$ 的解都必須位於單位圓外。

雖然穩定性對ARMA（p，q）的移動平均部分 θ_α 沒有什麼限制，但它仍必須滿足可逆性（ Invertibility ）的要求，這乃是爲了要使時間序列符合實際的物理現象。例如考慮ARMA（0，1）的情形：

$$\tilde{Z}_t = (1-\theta_1 B)a_t$$

則

$$a_t = (1-\theta_1 B)^{-1}\tilde{Z}_t$$
$$= (1+\theta_1 B+\theta_1^2 B^2+\cdots+\theta_1^k B^k)(1-\theta_1^{k+1}B^{k+1})^{-1}\tilde{Z}_t$$

所以

$$\tilde{Z}_t = -\theta_1\tilde{Z}_{t-1}-\theta_1^2\tilde{Z}_{t-2}-\cdots-\theta^k\tilde{Z}_{t-k}+a_t-\theta_1^{k+1}\tilde{Z}_{t-k+1}$$

若 $|\theta_1|>1$ 則現在的 Z_t 會受到 Z_{t-k} 的影響，k 隨時間的增加而增大，意即愈久遠以前的事件，對現在的情況影響愈大，此與一般現象不合，所以若 $\theta(B)$ 寫成（ $1-\theta_\alpha B)^{m_\alpha}$ 的乘積，其中 m_α 是 $\theta(B)$ 的第 α 根的次數，則 $|\theta_\alpha|<1$，（ $\alpha=1$，… q ），使得該時序可逆，也就是說，可逆的要求使得 $\theta(B)=0$ 的根都必須在單位圓的外面。

討論過穩定性與可逆性的問題後，將着手建立合適的模式。建立模式的過程如圖(一)所示，可概述如下：

1. 利用統計方法鑑定（ Identification ）模式。
2. 由已有的觀測序列來估計（ Estimation ）模式中未知的參數值。
3. 診斷檢驗（ Diagnostic Checking ）此模式是否適當，是否能正確代表觀測的時間序列，並符合精簡原則。
4. 如果模式適當則可用於分析預報，如果模式不適當，則重複進行第 1 至第 3 的步驟，直到尋獲適當的模式爲止。

作時間序列分析時，我們必須算出該序列遲滯 k 的自相關函數（ Autocorrelation Function，簡稱ACF ）及遲滯 k 的部份自相關函數（ Partial Autocorrelation

Function，簡稱PACF），求法詳述於後。但以上各值是由有限長度的序列所求出，並不全然就是理論上實際的值，有時在理論值消失後仍然可能出現相當大的估計值，所以我們需要一個判別方法來指出那些值不爲零，我們取ACF、PACF的標準離差（ Standard deviation ），作爲判斷的依據，如果理論值爲零，而估計值呈常態分佈，則估計值的絕大值大於一倍標準離差的可能性爲三分之一，大於兩倍標準離差的可能性只有二十分之一，所以我們把估計值大於兩倍離差者皆視爲理論值不爲零。

Bartlett[7] 證明ACF的標準離差爲：

$$\sigma[\gamma_k] \simeq \frac{1}{n^{1/2}}\left[1+\sum_{i=1}^{q}\gamma_i^2\right]^{1/2},\quad k>q$$

此處 γ_i 爲遲滯 i 的ACF。另外Quenouill[8] 證明了 PACF 估計標準離差爲：

$$\sigma[\phi_{kk}] = \frac{1}{n^{1/2}},\quad K>P$$

利用 ACF 及 PACF 的標準離差我們可找到理論值不爲零的 ACF 及 PACF，由其分佈的情形，可推論判斷出可能的 ARMA（p，q）模式。

三、模式的分類

(一)非季節性模式

對於穩定的非季節性模式，可用下列原則判斷：

1. 若ACF逐漸消失（ tail off ）而PACF在 $K\le P$ 時顯著，$K>P$ 時不顯著，此時爲 AR（p）模式，即：

$$\tilde{Z}_t = \phi_1\tilde{Z}_{t-1}+\phi_2\tilde{Z}_{t-2}+\cdots+\phi_p\tilde{Z}_{t-p}+a_t$$

或

$$\phi(B)\tilde{Z}_t = a_t$$

2. 若PACF逐漸消失而ACF 在 $K\le q$ 時顯著，$K>q$ 不顯著，則此模式爲MA（q）即：

$$\tilde{Z}_t = a_t-\theta_1 a_{t-1}-\cdots-\theta_q a_{t-q}$$

或可寫爲

$$\tilde{Z}_t = \theta(B)a_t$$

3. 若ACF於遲滯 q − p + 1 時間始呈現指數（ Exponential ）及阻尼正弦波（ Damped Sin Wave ），混合型消退，PACF亦呈現此現象，則此時適用模式爲ARMA（p，q）即：

$$\tilde{Z}_t = a_t-\theta_1 a_{t-1}-\theta_2 a_{t-2}-\cdots-\theta_q a_{t-q}+\phi_1\tilde{Z}_{t-1}+\phi_2\tilde{Z}_{t-2}$$
$$+\cdots+\phi_p\tilde{Z}_{t-p}$$

或可寫成

$$\phi(B)\tilde{Z}_t = \theta(B)a_t$$

然有時可能會發現ACF及 PACF 並沒有如上述的現象而沒有很快的消退，此時意味著可能是一非穩定性的序列。對非穩定的時間序列要經過數次的差分產生穩定性的新時序 W_t（ $W_t=\nabla^d Z_t$，d = 0，1，2，…），此處 $\nabla^d=(1-B)^d$，而 d 爲使 W_t 成爲

穩定的最小差分數，一般不大於 2 。而對於 W_t 我們就可利用前面所述的方法，得其合適的 ARMA（p，q）：

$$\phi(B)W_t = \theta(B)a_t,$$

再把 $W_t = \nabla^d Z_t$ 代入則得一完整的 ARIMA（p，d，q）模式：

$$\phi(B)\nabla^d Z_t = \theta(B)a_t$$

㈡季節性的模式（ Seasonal Model ）

當時間序列具有週期性變化時，其 ACF 及 PACF 也會有週期出現，無法用簡單的差分來消除，此時就要採用季節性模式，此模式分爲兩部份。

1. 週期性的部份

若時間序列具有週期 S ，可把相隔 S的 Z_t 運用前面所說過的方法來求取 ARIMA 模式，即：

$$(1-\phi_1^* B^S - \phi_2^* B^{2S} - \cdots - \phi_{p_1}^* B^{p_1 S})(1-B^S)^{d_1} Z_t$$
$$= (1-\theta_1^* B^S - \theta_2^* B^{2S} - \cdots - \theta_{q_1}^* B^{q_1 S})\rho_t \quad \cdots\cdots(9)$$

上式中 ρ_t 爲另一組時間序列，一般而言 ρ_t 不是白噪音，所以對於 ρ_t 我們仍需作如下操作。

2. 非週期性部份

⑼式中的 ρ_t 可以上述的非季節性時間序列加以判斷，而得一合適的 ARIMA（p，d，q）模式：

$$(1-\phi_1 B - \phi_2 B^2 - \cdots - \phi_p B^p)(1-B)^d \rho_t$$
$$= (1-\theta_1 B - \cdots - \theta_q B^q)a_t \quad \cdots\cdots(10)$$

把週期性及非週期性兩部分⑼及⑽式綜合起來，就得通用的相乘季節性模式（ General Multiplicative Seasonal Model ）：

$$\phi_p(B)(1-B^d)\phi_{p1}^*(B^S)(1-B^S)^{d_1} Z_t$$
$$= \theta_q(B)\theta_{q1}^*(B^S)a_t \quad \cdots\cdots(11)$$

其中

$$\phi_p(B) = (1-\phi_1 B - \cdots - \phi_p B^p)$$
$$\theta_q(B) = (1-\theta_1 B - \cdots - \theta_q B^q)$$
$$\phi_{p1}^*(B^S) = (1-\phi_1^* B^S - \cdots - \phi_{p1}^* B^{p_1 S})$$
$$\theta_{q1}^*(B^S) = (1-\theta_1^* B^S - \cdots - \theta_{q1}^* B^{q_1 S})$$

我們稱此爲（p，d，q）×（ p_1 ， d_1 ， q_1 ）s 的季節性 ARIMA模式。

我們可由理論利用圖表或公式先找出各參數 ϕ ， θ ， ϕ^* 及 θ^* 的起始值（Starting Values ），代入模式中可得一組同樣時間的預測值，我們稱其爲起始擬合（ Original Fitting ）Z_{tf} ，由 Z_{tf} 與 Z_t 的差得到一個殘差的平方和，利用非線性最小平方差法（ Non-Linear Least Square Error Method ），經過數次的迭代（ Iterations ），使殘差平方和爲最小的參數值，即爲所求的參數值。迭代的次數由我們所選的起始值與所要求的精度所決定。

求出各種參數值後，須做模式的診斷檢驗（ Diagnostic Checking ），以便對模式

的適性（ Goodness of Fit ）作診斷，以瞭解所求得的模式是否能最佳的代表觀測數列。第一個檢驗方法爲過度配合（ Overfitting ），在所求得的模式兩側各加一項，倘若原來的模式恰當，則會顯示加上去的項是多餘的，然此法並不表示所得模式爲最佳模式。另一方法是看 a_t 是否白噪音，首先把 a_t 的ACF算出，則因估計的殘差與 a_t 的實際餘差有如下的關係：

$$a_t = a_t + O\cdot\left(\frac{1}{\sqrt{N}}\right)$$

所以若有一個以上的 ACF 明顯的大於兩倍的 $\frac{1}{\sqrt{N}}$ 則考慮修改模式。

最後還要做殘差自相關總體鑑定，若在 k 項後的 a_t 的 ACF 可以忽略且令 $n = N - d - Sd_1$ ，定義下面的量 Q：

$$Q = n\sum_{k=1}^{k}\rho_k^2(a_t)$$

Q值可用來和 χ^2（K－P－d）比較，此處 χ^2 爲Chi-Square 分配，可取 90 %或 95 %。信賴區間來比較，而對 a_t 作一總體檢驗，看是否爲白噪音，若模式不太恰當，則可用殘差的 ACF 來修正。倘若在診斷模式後並未發現模式有不宜之處，則該模式可用來預報。

四、預報的原理

預報的方法是把ARIMA模式展開，若 $Z_t(\ell)$ 表示在時間 t 時預報 $t+\ell$ 時間的值，則對式中各項可用下面的值代入該模式中：

$$[Z_{t-j}] = E[Z_{t-j}] = Z_{t-j}\ ,\ j = 0,1,2$$
$$[Z_{t+j}] = E[Z_{t+j}] = Z_t(j)\ ,\ j = 1,2$$
$$[a_{t-j}] = E[a_{t-j}] = a_{t-j} = Z_{t-j} - Z_{t-j-1}\ ,\ j = 0,1,2$$
$$[a_{t+j}] = E[a_{t+j}] = 0\ ,\ j = 1,2$$

換句話說，若該值爲已發生事件，則用已知值代入，若該值尚未發生則代入期望值，如此一來，我們不僅可在時間 t 作預測，且隨時可因新資料的獲得而做即時預報（Updating Forecasting ），其方法爲首先我們定義無窮級數：

$$\Psi(B) = \sum_{j=1}^{\infty}\Psi_j B^j$$

令 $Z_t = \Psi(B)a_t$

則 $\varphi(B)Z_t = \theta(B)a_t$

$\varphi(B) = \phi(B)\Delta^d$

故 $\varphi(B)\Psi(B) = \theta(B)$

把多項式展開，比較兩邊係數可得：

$$\Psi_1 = \Psi_1 - \theta_1$$
$$\Psi_2 = \varphi_1\Psi_1 + \varphi_2 - \theta_2$$
$$\vdots \quad \vdots \quad \vdots \quad \vdots$$
$$\Psi_j = \varphi_1\Psi_{j-1} + \cdots + \varphi_{p+d}\Psi_{j-p-d} - \theta_j$$

此處 $\Psi_0 = 1$，對 $j < 0$ 之項 $\Psi_j = 0$，且 $j > q$ 時 $\theta_j = 0$，最後可得：

$$\Psi_j = \varphi_1\Psi_{j-1} + \varphi_2\Psi_{j-2} + \cdots + \varphi_{p+d}\Psi_{j-p-d}, \quad j > q$$

又因

$$Z_{t+1}(\ell) = \Psi_\ell a_{t+1} + \Psi_{\ell+1}a_t + \Psi_{\ell+2}a_{t-1} + \cdots\cdots$$
$$Z_t(\ell+1) = \Psi_{\ell+1}a_t + \Psi_{\ell+2}a_{t-1} + \cdots\cdots$$

所以

$$Z_{t+1}(\ell) = Z_t(\ell+1) + \Psi_\ell a_{t+1}$$

故隨時間的進行，每一個新發生的值都可以立刻用來得到一最新的預測。

五、基本資料的算法

對於一組 N 個的時間序列 Z_t 其平均值 μ 及變異數（Variance）σ_z^2 分別爲：

$$\mu = \left[\sum_{i=1}^{N} Z_t\right] / N$$

$$\sigma_z^2 = \left[\sum_{i=1}^{N} (Z_t - \mu)^2\right] / N$$

算出 μ 及 σ_z^2 後可接著計算遲滯 k 的自協變量數（Autocovariance）γ_k 及遲滯 k 自相關函數（ACF）ρ_k：

$$\gamma_k = E[(Z_t - \mu)(Z_{t+k} - \mu)]$$
$$\rho_k = \gamma_k / \gamma_0$$

此處 $E[Z_t]$ 爲統計上的求取期望值，顯然 $\gamma_0 = \sigma_z^2$，而 $\rho_0 = 1$。

得到自相關函數後，我們仍需計算部分自相關函數（PACF）ϕ_{kk}，其表示法爲：

$$\phi_{kk} = \frac{\begin{vmatrix} 1 & \rho_1 & \cdots & \rho_{k-2} & \rho_1 \\ \rho_1 & 1 & \cdots & \rho_{k-3} & \rho_2 \\ \vdots & \vdots & & \vdots & \vdots \\ \rho_{k-1} & \rho_{k-2} & \cdots & \rho_1 & 1 \end{vmatrix}}{\begin{vmatrix} 1 & \rho_1 & \cdots & \rho_{k-1} \\ \rho_1 & 1 & \cdots & \rho_{k-2} \\ \vdots & \vdots & & \vdots \\ \rho_{k-1} & \rho_{k-2} & \cdots & 1 \end{vmatrix}} \qquad \cdots\cdots(12)$$

由上式知 PACF 可由 ACF 而求得：

$$\text{PACF}(1) = \text{ACF}(1) = \rho_1$$
$$\text{PACF}(2) = \frac{\text{ACF}(2) - [\text{ACF}(1)]^2}{1 - [\text{ACF}(1)]^2} = \frac{\rho_2 - \rho_1^2}{1 - \rho_1^2}$$
$$\text{PACF}(3) = \frac{-2\,\text{ACF}(1)\,\text{ACF}(2) - [\text{ACF}(1)]^2\text{ACF}(3)}{1 + 2[\text{ACF}(1)]^2\text{ACF}(2) - [\text{ACF}(2)]^2 - [\text{ACF}(1)]^2}$$
$$= \frac{-2\rho_1\rho_2 - \rho_1^2\rho_3}{1 + 2\rho_1^2\rho_2 - \rho_2^2 - \rho_1^2}$$

六、模式的判斷

(一) AR (P) 模式的特性

AR (P) 的模式可展開如下：

$$\tilde{Z}_t = \phi_1\tilde{Z}_{t-1} + \phi_2\tilde{Z}_{t-2} + \cdots + \phi_p\tilde{Z}_{t-p} + a_t$$

兩邊同乘 Z_{t-k} 再取期望值可得：

$$\gamma_k = \phi_1\gamma_{k-1} + \phi_2\gamma_{k-2} + \cdots + \phi_p\gamma_{k-p} \qquad k > 0$$

兩邊同除 γ_0 則上式變爲：

$$\rho_k = \phi_1\rho_{k-1} + \phi_2\rho_{k-2} + \cdots + \phi_p\rho_{k-p} \qquad k > 0$$

或可寫成 $\phi(B)\rho_k = 0$，此處 $\phi(B) = 1 - \phi_1 B - \cdots - \phi_p B^p$ 而 B 爲對 k 作用而不是 t，若：

$$\phi(B) = \prod_{i=1}^{p}(1 - G_i B)$$

此處 G_1^{-1}，$G_2^{-1}\cdots\cdots G_p^{-1}$ 爲 $\phi(B) = 0$ 的根，則：

$$\rho_k = A_1G_1^k + A_2G_2^k + \cdots + A_pG_p^k$$

穩定性的條件要求 $|G_i| < 1$，假設 $\phi(B)$ 的根是分開（distinct）不連在一起，則：

1. G_i 是實數時，隨著 k 的增加 $A_iG_i^k$ 會呈指數衰減而衰減至零。
2. 若 G_i，G_j 爲成對的共軛複數，則它們會構成如下式的關係式：

$$d^k\sin(2\pi f k + F)$$

而使自相關函數成正弦阻尼波衰退。

再看 AR (P) 的 PACF，設此 AR 模式的次數爲 k，而 ϕ_{kj} 爲其第 j 個的係數，則 ϕ_{kk} 爲最後一個係數，所以由式

$$\rho_j = \phi_{k1}\rho_{j-1} + \cdots + \phi_{k(k-1)}\rho_{j-k+1} + \phi_{kk}\rho_{j-k} \qquad j = 1, 2\cdots k$$

就產生了 Yule-Walker 方程式：

$$\begin{vmatrix} 1 & \rho_1 & \rho_2 \cdots \rho_{k-1} \\ \rho_1 & 1 & \rho_1 \cdots \rho_{k-2} \\ \vdots & \vdots & \vdots \\ \rho_{k-1} & \rho_{k-2} & 1 \end{vmatrix} \begin{vmatrix} \phi_{k1} \\ \phi_{k2} \\ \vdots \\ \phi_{kk} \end{vmatrix} = \begin{vmatrix} \rho_1 \\ \rho_2 \\ \vdots \\ \rho_k \end{vmatrix}$$

所以有式(12)的表示法。

對於AR（P）而言，當k小於或等於ρ時，PACF、ϕ_{kk}會大於零，而在$k>\rho$時則會變成零。

㈡MA（q）模式的特性

MA（q）的模式可寫成：

$$\tilde{Z}_t = a_t - \theta_1 a_{t-1} - \cdots - \theta_q a_{t-q}$$

所以

$$\gamma_k = E[(a_t - \theta_1 a_{t-1} - \cdots - \theta_q a_{t-q})(a_{t-k} - \theta_1 a_{t-k-1} - \cdots - \theta_q a_{t-k-q})]$$

故

$$\gamma_0 = (1 + \theta_1^2 + \theta_2^2 + \cdots + \theta_q^2)\sigma_a^2$$

$$\gamma_k = \begin{cases} (-\theta_k + \theta_1\theta_{k+1} + \theta_2\theta_{k+2} + \cdots + \theta_{q-k}\theta_q)\sigma_a^2 & k = 1, 2, \cdots, q \\ 0 & k > q \end{cases}$$

所以

$$\rho_k = \begin{cases} -\theta_k + \theta_1\theta_{k+1} + \cdots + \theta_{q-k}\theta_q & k = 1, 2, \cdots, q \\ 0 & k > q \end{cases}$$

因此MA（q）的ACF在遲滯k大於q之後會變爲零。MA（q）的ϕ_{kk}除了在$q=1$時

$$\phi_{kk} = -\phi_{1k}(1 - \theta_1^2)/(1 - \theta_1^{2(k+1)})$$

呈現阻尼指數消退外，其他在$q \geq 2$時較複雜，但仍漸漸的消退，所以對MA（q）的判斷主要在依據ACF。

㈢ARMA（p，q）的特性

把ARMA（p，q）的模式展開成：

$$\tilde{Z}_t = \phi_1\tilde{Z}_{t-1} + \cdots + \phi_p\tilde{Z}_{t-p} + a_t - \theta_1 a_{t-1} - \cdots - \theta_q a_{t-q}$$

兩邊乘以Z_{t-k}再取期望值得：

$$\gamma_k = \phi_1\gamma_{k-1} + \cdots + \phi_p\gamma_{k-p} + \gamma_{za}(k) - \theta_1\gamma_{za}(k-1) - \cdots - \theta_q\gamma_{za}(k-q) \quad \cdots\cdots(13)$$

此處$\gamma_{za}(k) = E[Z_{t-k}a_t]$

所以：

$$\gamma_{za}(k) = 0 \quad \text{當 } k > 0$$

$$\gamma_{za}(k) \neq 0 \quad \text{當 } k \leq 0$$

當$k \geq q+1$時：

$$\gamma_k = \phi_1\gamma_{k-1} + \phi_2\gamma_{k-2} + \cdots + \phi_p\gamma_{k-p} \qquad k \geq q+1$$

同除γ_0後得：

$$\rho_k = \phi_1\rho_{k-1} + \phi_2\rho_{k-2} + \cdots + \phi_p\rho_{k-p} \qquad k \geq q+1$$

或可寫成$\phi(B)\rho_k = 0$。

所以ARMA（p，q）的ACF，ρ_1，ρ_2，…ρ_q由式(13)來決定，而此q個AC

，可用來算$k \geq q+1$時，$\phi(B)\rho_k = 0$的ACF，若$q-p<0$則ACF，ρ_j，$j=0$，1，2，會有混合的阻尼指數或阻尼正弦波。若$q-p \geq 0$則ρ_0，ρ_1，…，ρ_{q-p}，此$q-p+1$個起始的ACF，並不表示上述的一般型態，如此可用來鑑別ARMA（p，q）的型式，至於ARMA（p，q）的PACF，則會向無窮遠延伸，它最後會表現出純MA（q）的PACF型式，呈現出阻尼指數和（或）阻尼正弦波。

參、氣象資料分析

一、概　述

本文研究對象爲風向、風速、大氣穩定度與溫度。資料來源爲中央研究院物理研究所於民國71年秋季（10至12月）在南港工職所設的氣象觀測站測定的結果。一般習慣將風向劃分爲十六個方位，本文因研究的目的不同，所取的數據爲每小時平均風向的實測角度。風速採每小時風速的平均值，以公尺／秒表示。一般環境空氣品質模式中的穩定度，係依照Pasiquill(12)與Gifford(13)法，由日照、雲量與風速等觀測值而推算（簡稱P—G分類法），本文係依據Stoner(14)氏的分類法，以水平風向的標準偏差角σ_θ決定大氣穩定度，並將之分爲六級，根據Stoner氏建議，當風速過小時，大氣穩定度以P—G分類法較佳。本文並參考Mitchell和Timbre(15)氏的建議，考慮大氣穩定度的夜間修正。所謂夜間係指日落前一小時至日出後一小時，本文中設定爲下午六時至上午七時，氣溫也是取小時平均值，以℃表示。

二、氣象資料來源

㈠測站位置區域概述

由中央氣象局台北測站所得台北市各氣象要素的平均值，可看出風向於春秋多三季多爲東北季風（出現機會約70％左右），平均風速約爲2～3 m／sec。本研究所設的氣象測站，位於南港區南港工職行政大樓的四樓頂，其感應器高出樓頂約六公尺，即測站離地面的高度約18公尺左右，四周尚稱空曠，唯左方200公尺處有台北市垃圾堆積場，高度約30公尺。300公尺外有小丘陵存在，二者尚不致對測站構成顯著的影響。測站附近大多爲2或4樓的磚瓦房或鋼筋混凝土房，除西南方100公尺處的南港區公所爲十層建築物外，並沒有較高的建築物。

㈡測站使用儀器說明

測站使用的氣象觀測爲微電腦資料處理系統A—10，而記錄資料包括風向、風速、溫度及風向的變異量（即σ_θ）。各氣象因子先經感應器（Sensor），再經訊號調整器（Processor）轉換成爲線性電壓後，進入資料處理機（data logger）作資料分析與處理，經過處理的資料數據，由印刷機印於紙帶上，同時以磁帶記錄機記錄於磁帶上。

此處所用的風速與風向感應器，較一般氣象觀測者所用的精密，風速感應器的起動風僅需0.28 m／s，而一般則在0.6～1.0 m／s。可測得的風速範圍從0～45 m／s亦較一般氣象儀器爲寬，其風力訊號的轉換，係利用光電感應產生方波（脈波），不

同於一般發電式，前者爲一數字形式訊號，精確度與線性程度均較後者類比訊號者佳。風向感應器其起動風速亦爲0.28m／ s，用線圈感應發電，而非一般碳粉電阻感應，故解析力較高。溫度感應器係白金電偶式，其感應範圍從－30 ℃到 50 ℃，在此範圍內線性誤差小於 5 %。

訊號調整器調整各感應器測量的結果，使輸出成爲線性電壓訊號，處理過程是將各個不同位準（ level ）的輸入訊號，放大爲同一位準的輸出訊號，其輸出訊號及所代表的觀測量如下表：

因　子	輸　出（伏　特）	觀　測　值
風　向	0—5	0—360°
風　速	0—5	0—45 m／ s
溫　度	1.785—4.863	0—46.83 ℃

各感應器均爲瞬間訊號，其密度與精確度均高，爲能處理大量資料，本系統選用資料微處理機代替人爲處理。所用者爲 Acurox 的 Auto-data Ten-10 ，具各種算術運作能力，其處理訊號能力每秒35筆（ channel ），可接受 0 — 10 伏特的輸入訊號，有 4 K的儲存能力，除系統本身所用部分，尚有 1000 筆的日容量。輸入的電壓訊號進入微電腦，首先作單元換算，即爲將電腦轉換爲觀測物理量，然後各量依研究需要，計算一定時間內的平均值、最大值、最小值及標準偏差，依序存入微電腦內，經正式操作每分鐘可得 1000 個觀測值。輸出爲每十分鐘的風向最大、最小、平均值與標準偏差，及每小時的風速和溫度的平均值。

資料微處理機，本身有印刷機（ Printer ）一部，可記錄輸出結果，本系統爲使資料處理更爲迅速，另加二個卡式磁帶記錄器，直接記錄於磁帶上，再利用此磁帶直接進入電腦系統，以提高精確度，所用磁帶如坊間所見的卡式帶，攜帶方便，其儲存能力每面約 6000 筆資料，約可供記錄完整的六天資料。

三、研究步驟

由測站取得的氣象參數觀測資料其流程如圖二所示，因計算機容量的每組數據約爲 216 個小時平均值的時序，除溫度與風速以所得數據的時間序列直接建立各別的預報模式外，風向及大氣穩定度的數據，皆先經過處理。風向以向量型式建立預報模式，取風向平均角度的正弦（ Sine ）值及餘弦（ Cosine ）值形成爲 U 、V 的兩個分量，即將一時序分解爲二個長度相同的新時序U及V，而建立其各別的預報模式，本文將水平風向的標準偏差值做如下的處理：

處　理　前	處　理　後
$40 > \sigma_\theta \geq 30$	$\sigma_\theta = 22.5 + \sigma$
$50 > \sigma_\theta \geq 40$	$\sigma_\theta = 22.5 + 2\sigma$
$60 > \sigma_\theta \geq 50$	$\sigma_\theta = 22.5 + 3\sigma$
$\sigma_\theta \geq 60$	$\sigma_\theta = 22.5 + 4\sigma$

表中σ爲原資料的標準偏差值。

本研究使用的統計預報模式爲 Box and Jenkins 的時序預報模式，建立模式的流程如圖㈠所示。

風向及大氣穩定度的模式預報值，需經轉換成所要的結果。由U（ Sine ）及 V（ Cosine ）各別預報模式所得的預報值，取 $\theta = \tan^{-1}\frac{V}{U}$ ，可得對應的角度預報值，其象限的決定則需由U及V的正負號來決定。大氣穩定度預報所得數據需依表二的分類，轉換成穩定度級數。

四、結果與討論

本文主要探討空氣污染擴散參數包括風向、風速、大氣穩定度與溫度，其時序預報模式的可行性。本文取四組數據，每組皆由連續216小時（ 9 天）的小時平均值所組成，爲了解各參數在同一季的變化，數據時間皆屬秋季。四組數據時間爲 1982 年 10 月 1 日至 10 月 9 日（ A組）、 10 月 21 日至 10 月 29 日（ B組）、 11 月 7 日至 11 月 15 日（ C組）、 12 月 11 日至 12 月 19 日（ D組）。

一、統計預報模式

將各組中各參數的時序，利用前述統計理論，經鑑定、參數值估計及各項檢驗後，可得所求的預報模式，其流程見圖㈠。其 ACF 及 PACF 依前述的模式鑑定法，可判定模式的型式，再利用非線性最小平方差，估計出各模式的參數值。20個模式殘差遲滯（ lag ）1 至 36 的 ACF ，其值皆小於二倍標準偏差，與二倍標準偏差的比較參照圖十九，顯示此二十個預報模式皆合要求。自由度（ Degree of Freedom ）爲 30 的 Chi-square 值分別爲：

$$\chi^2_{30}\ (95\%) = 43.8$$
$$\chi^2_{30}\ (90\%) = 40.3$$
$$\chi^2_{30}\ (50\%) = 34.8$$
$$\chi^2_{30}\ (10\%) = 20.6$$
$$\chi^2_{30}\ (5\ \%) = 18.5$$

Q值爲殘差自相關總體檢定的依據，其定義爲：

$$Q = n \sum_{k=1}^{k} \rho_k^2\ (a_t)$$

當Q值愈小時，總體檢驗顯示出殘差與白噪音越相似，20個模式計算所得的Q值（參照表二），皆小於 χ^2_{30}（ 90 %），大部分在 χ^2_{30}（ 50 %）與 χ^2_{30}（ 10 ）之間，顯示所得的諸模式，皆能有效的代表該時序。圖三至圖十八是殘差時序對其標準偏差的累積機率分佈圖，這些圖顯示擬合（ Original Fitting ）的情形及其誤差的分佈情形。

二、各擴散參數連續小時變化的預報模式

㈠風　　向

風向U（Sine）及V（Cosine）的四組預報模式爲：

$$A:\begin{cases} U(\sin):(1-0.4275B-0.2755B^2+0.1364B^6)(Z_t-0.5924)=a_t \\ V(\cos):(1-0.4262B-0.1434B^3)(Z_t-0.4901)=(1+0.06485B^5+0.1253B^{26})a_t \end{cases}$$

$$B:\begin{cases} U(\sin):(1-B)Z_t=(1-0.6881B+0.1121B^7-0.1469B^{13}-0.1995B^{19}+0.035B^{20})a_t \\ V(\cos):(1-0.4112B-0.0544B^2-0.2055B^3-0.06736B^{13})(Z_t-0.3539)=(1-0.0839B^6)a_t \end{cases}$$

$$C:\begin{cases} U(\sin):(1-0.341B-0.1861B^2-0.1117B^5-0.07383B^8)(Z_t-0.651)=(1-0.04684B^3+0.1168B^6)a_t \\ V(\cos):(1-0.1034B-0.1147B^{11})(Z_t-0.3224) \\ \qquad =(1+0.1602B+0.2362B^2+0.2126B^3)a_t \end{cases}$$

$$D:\begin{cases} U(\sin):(1-0.6275B+0.0238B^6)(Z_t-0.7223) \\ \qquad =(1+0.2241B^3-0.1253B^7)a_t \\ V(\cos):(1-0.4053B-0.01276B^2-0.3389B^3-0.08769B^7)(Z_t-0.3998)=(1+0.03166B^3)a_t \end{cases}$$

實際數據與模式擬合值，皆由 $\theta=\tan^{-1}\frac{U}{V}$ 判定角度，再由U及V的正負判定象限以決定所要的角度，由擬合值與實際值之差所得的殘差時序（角度表示），其個別與總體檢定見圖十九與表二，殘差的累積機率分佈見圖三至圖六。

預報模式不具週期性，資料長度僅九天，故trend不明顯，所選取的資料同爲秋季，所以季節性的考慮亦可忽略。四組模式的階數及類型頗有差異，或是因風向本身變異程度頗大，或是因所取的資料太短。應用時需隨時修正模式，才能更吻合實際的情況。

㈡風　速

由ARIMA所建立的各組風速預報模式爲：

$$A:(1-0.0281B^6+0.1142B^{12})(Z_t-0.9327)=(1+0.4235B^6+0.2493B^{26})a_t$$

$$B:(1+0.06104B+0.1721B^{18}-0.1938B^{21})(1-B)Z_t=(1-0.3065B)a_t$$

$$C:(1-0.7578B+0.04903B^{11})(Z_t-0.7545)=a_t$$

$$D:(1-0.3554B-0.1441B^2)(Z_t-1.164)=a_t$$

實際數據與模式擬合值的差所得的殘差時序，其自相關個別及總體檢定見圖十九與表二，殘差的累積機率分佈見圖七至圖十。雖同爲東北季風，或因風速變異太大，或因所取數據太短，四組風速預報模式差異頗大。

㈢大氣穩定度

經第三章處理過的四組時序所建立的預報模式爲：

$$A:(1-0.1827B+0.0664B^2-0.0613B^3)(1-B)Z_t=(1-0.8902B)a_t$$

$$B:(1-0.2902B-0.312B^2+0.05326B^5)(Z_t-20.1)=(1+0.1646B^6)a_t$$

$$C:(1-0.5194B)(Z_t-22.71)=(1-0.1663B+0.02728B^4+0.116B^6-0.116B^6-0.1295B^{34})a_t$$

$$D:(1-0.0774B-0.0901B^5-0.1447B^6)(Z_t-22.21)=(1+0.249B+0.1004B^5-0.122B^{18}-0.1449B^{35})a_t$$

各組實際數據與預報模式擬合值所得的殘差時序，其自相關個別及總體檢定見圖十九與表二，其殘差的累積機率分佈見圖十一至十四。由Mitchell[16]氏的報告知，大氣穩定度的分類方式有數種，本文採 σ_θ 來分類是因爲：

1. σ_θ 可直接以數值表示，時序處理時較爲簡便。
2. 可直接以 σ_θ 之值判定穩定度等級，較其他分類法客觀，在氣象動力學上亦較具意義
3. σ_θ 的資料易於儲存及使用，以往使用較少，乃因資料獲得的不易，現因微處理器（Micro-processor）的進步，使此不利條件消失，則 σ_θ 應用的推廣是可預期的。

㈣溫　度

四組數據所建立的小時平均值預報模式爲：

$$A:(1-0.1793B+0.0177B^6+0.1191B^{13})(Z_t-25.19)=(1+0.346B^6+0.3778B^{13}+0.4409B^{19})a_t$$

$$B:(1-0.09897B+0.00266B^8-0.009B^{24})a_t=(1-0.6526B^{24})a_t$$

$$C:(1-0.969B-0.08775B^2+0.1327B^3)(Z_t-20.93)=(1+0.1191B^{23}+0.281B^{24}+0.1749B^{25})a_t$$

$$D:(1-0.01273B-0.00253B^2-0.00322B^3-0.00205B^4)(1-B)Z_t=(1-0.9222B)a_t$$

原始數據與預測模式擬合值的差值所得的殘差時序，其殘差時序自相關的總體及個別檢定見圖十九與表二，殘差的累積機率分佈見圖十五至圖十八。胡氏[17]曾以ARIMA做溫度預報，然其着眼點爲月平均溫度，而本文重點則爲小時變化。

四組數據中，除第四組外，其餘三組因寒潮的關係，小時值出現突變及跳動等不穩定現象，使得模式的擬合誤差達6.8 ℃。而除B組外，其餘各組模式週期性並不顯著。

三、預報模式特性

建立預報模式的目的在於了解空氣污染擴散參數對於未來短時間的變化。將上述所建立的20個預報模式，對各擴散參數進行未來24小時的預報，其結果列於表三至表十四，表中包括預報值與實際值的差異，絕對值平均誤差（Absolute Mean Error）及誤差的標準偏差。表十五則表示四組數據大氣穩定度的預報級數與實際級數的差異（以穩定度的級數表示）。

一般而言，各預報模式的階數增高，其參數值逐漸變小，但亦有甚多情況並不如此，於模式中亦有階數高達35者，此實爲一35階的微分方程式，但不爲零的參數個數並不多，亦即大部分的高階頂皆不顯著，所得的模式低階頂佔優勢，即時序最後幾個數據值，對未來預報值的影響最大。

㈠風　　向

表三至表六顯示絕對值平均誤差A組爲12.4°，B組爲68.1°，C組爲16.0°，D組爲10.3°，即B組外，其他三組所建立的預報模式，大致尚可吻合實際的變化情形。B組模式的預報會與實際情況有如此大的差異，乃由於在盛行東北季風的秋冬季，預報時間出現明顯的西南風或西北風，而此風向於建立模式的原始資料中，其出現機率尚不足百分之十，且以不規則的型態出現，由殘差的累積機率分佈圖（圖三至圖六），即可看出模式擬合時，對這些特殊值（西南風或西北風），即無法有效的掌握，因而其殘差有高達170°情況，另一原因則爲當時風速爲微風狀態（見表八），風向變化特別大。反觀A、C、D三組，因其預報時間的風向大體不脫東北季風的範圍，預報效果好，平均誤差約12.5°。

㈡風　　速

表七至表十顯示四組的平均誤差約0.4公尺／秒，因有許多靜風存在（風速＜0.5公尺／秒），使得預報模式即使即時預報（Updating Forecasting，見表十六、十七），亦無法有效的使誤差減少。

㈢大氣穩定度

表十五顯示模式預報所得的穩定度級數與實際穩定度級數常相吻合（約佔59％），而差一級者約佔30％（皆已考慮夜間的修正）。以前文獻中尚乏有關大氣穩定度的預報，本文首次嘗試，盼望以後做更多的探討與改進。

㈣溫　　度

表十一至十四顯示未來24小時預報的平均誤差除B組外，約爲0.6℃，B組的平均誤差約3℃，比較實際值與預報值（見表十二）可看出，預報的前8小時其平均誤差約爲0.4℃，8小時後有突變產生，此突變的高溫，於建立模式的原數據中，出現的機率過小而不規則，有賴即時預報來修正。將B組數據做即時預報，其結果列於表十八，從新輸入12個新的觀測值，作未來12小時預報，發現即時預報使原先的5.1℃誤差值降至1.9℃，其預報效果的改進十分顯然，各組參數預報模式的預報結果見表十九。

表二十顯示，殘差時序的標準偏差σ_{at}遠較原時序的標準偏差σ_{zt}爲小。風向、風速及大氣穩定度三參數的σ_{at}值仍大，雖然殘差時序經由診斷檢驗顯示爲白噪音，但其分佈範圍甚廣，顯示其預報的誤差尚大。

對各大氣參數建立AR（24）高階模式的結果與上文之ARMA 預報模式的比較見表二十一，表中顯示於擬合時AR（24）高階模式較原預報模式爲佳，顯示由BOX與Jenkins所建議的ARIMA模式建立法未必能得到最佳的時序預報模式，此或係ACF與PACF的採樣值與眞值頗有出入，或是ARMA混合模式的型式判斷不甚理想所致。

由於受小型電腦PDP-11容量的限制，本文僅取9天的各參數小時平均值做時序分

析，所建立的預報模式統計代表性略顯不足，如用大型電腦，取更長的數據來建立各參數的預報模式，將可得到更具代表性的結果。

伍、結論與建議

本文以Box and Jenkins所發展出的ARIMA時序分析法，來建立空氣污染擴散參數中的風向、風速、大氣穩定度與溫度的預報模式。結果顯示，此時序預報模式，對空氣污染擴散參數能提供良好的預報，此客觀的定量預報，對於溫度的突變情況，亦能利用即時預報法，做立即的修正。此時序預報法可推廣應用至下列範疇：

1. 建立空氣污染相關參數的預報模式，供大污染源廢氣排放控制的參考。
2. 由多數測站的參數及污染濃度預報資料，利用佳化評估理論[18]，而建立地區的空氣污染物質濃度的預報模式。

由於風向與風速的變異頗大，欲得良好的預報成果尚待作更多的研究與探討，以下爲將來研究的可行方向：

1. 將風向、風速等空氣污染擴散參數於頻率域，利用波譜分量（spectrum scale decomposition）分成幾個不同頻率域的時序，分別建立合適的ARIMA模式。
2. 以複變數ARIMA（Multi-ARIMA）建立這些參數的預報模式。
3. 利用辨別分析（Discriminant analysis）[19]先對原數據作詳細的分析，了解未來可能發生突變的機率，再分別考慮適合的統計預報模式。
4. 以高階AR(P)的模式作初步擬合，再將結果之殘差時序作ARMA。

參考文獻

1. John, S. I., Scheme For Estimating Dispersion Parameters As A Function of Release Height, U. S. Ehvironmental Protection Agency, EPA-600/4-79-069, 1979.
2. William, H.K. and F. Lewis, Computer Forecasting of Maximum and Minimum Temperatures, Journal of Applied Meteorology, Vol. 9, 350-359, 1970.
3. Russo, J. A., Jr., I. Enger and E. L. Sorenson, A Statistical Approach to the Short-Period Prediction of Surface Winds, J. Appl. Meteor., Vol. 3, 126-131. 1963.
4. Carter, G. M., Automated Prediction of Surface Wind From Numerical Model Output, Monthly Weather Review, Vol.103, 866-873, 1975.
5. Box, G. E. P. and G. M. Jenkins, Time Series Analysis Forecasting and Control, Holden-Day, San Francisco, 575p, 1976.
6. Jenkins, G. and G. Watts, Spectra Analysis and Its Applications, Holden Day, San Francisco, 523p, 1968.
7. Bartlett, M.S., On the Theoretical Specification of Sampling Properties of Autocorrelated Time Series, Journal Rayal Stal. Soc., B8, Vol.27, 1946.
8. Quenouille, M.H., Approximate Tests of Correlation in Time Series, Jour. Rayal Stal. Soc., B11, Vol. 68, 1949.

9. Turner, D. B., Workbook of Atmospheric Diffusion Estimates, Nat. Air Pollution Control Agency, Cincinnati, Ohio, 84p, 1970.
10. 蔡豐智，梁文傑，台北市二氧化硫時序預報模式之研究，中央研究院物理研究所集刊，第十卷，第 173～210 頁，1980。
11. KO, S. D., Surface Wind Field and Precipitation Activity over Taiwan in Meiyu Season, Annual Report of Institute of Physics, Academia Sinica, Vol. 4, 301-322. 1975.
12. Pasiquill, F., Atmospheric Diffusion John Wiley and Sons, New York, 429p, 1974.
13. Gifford, F. A., Use Routine Meteorological Observation for Estimating Atmospheric Dispersion, Nuclear Safety, Vol.2, 47-51, 1961.
14. Stoner, R. R., Procedures for Reduction of Meteorological data. Environmental Safegard Division, NUS. Corporation, NUS-757, 30p, 1971.
15. KAU, W.S., Lee, H. N. and Kao, S. K.A., Statistical Model for Wind Predication at a Mountain and valley Station Near Anderson Greek, California, J. Appl. Meteor., Vol. 21, 18-21, 1981.
16. Mitchell, A. E. Jr., A Comparison of Short-term Dispersion Estimates Resulting from Various Atmospheric Stability Classification Methods, Atmospheric Environmental, Vol. 16, No. 4, 765-773, 1982.
17. 胡仲英，應用 ARIMA 模式對台北市月平均溫度與降水量的分析與預報，氣象學報，二十三卷，第三期，第 15～16 頁，1977。
18. 梁文傑，空氣污染評估的佳化理論，中央研究院物理研究所集刊，第 8 卷，第 223～258 頁，1979。
19. Lin, G. Y., Oxidant Prediction By Discriminant Analysis in the South Coast Air Basin of California, Atmospheric Environmental, Vol. 16, No. 1, 135-143, 1982.
20. Mitchell, A. E. Jr. and Timbre K.O., Atmospheric Stability Class from Horizontal Wind Fluctuation, Paper 79-29.2 Air Pollution Control Association Annual Meeting, Cincinnati, OH. 1979.

表一　各組數據的說明：各組數據以小時平均值表示收集數據長度 9 天（連續 216 個小時）

組別	數據收集時間	數據內容	單位
A	71 年 10 月 1 日至 10 月 9 日	風向	度
		風速	公尺／秒
		大氣穩定度	度
		溫度	℃
B	71 年 10 月 21 日至 10 月 29 日	風向	度
		風速	公尺／秒
		大氣穩定度	度
		溫度	℃
C	71 年 11 月 7 日至 11 月 15 日	風向	度
		風速	公尺／秒
		大氣穩定度	度
		溫度	℃
D	71 年 12 月 11 日至 12 月 19 日	風向	度
		風速	公尺／秒
		大氣穩定度	度
		溫度	℃

表二　(A)爲各自由度之 χ_α 值，(B)爲二十個殘差時序自相關總體檢定，表中四組數據同表一，Q 爲殘差時序的自相關函數（遲滯 1 至 36）計算所得的 $\chi^2_{0.05}$ 值，括弧內爲自由度。

(A)

自由度 \ χ^2_α 值	$\alpha = 0.05$	$\alpha = 0.025$	$\alpha = 0.01$
28	41.5	44.5	48.3
29	42.6	45.7	49.6
30	43.8	46.9	50.9
40	55.8	59.3	63.6

(B)

組別	擴散參數	Q	組別	擴散參數	Q
A	風向（U）	19.36(32)	C	風向（U）	19.35(29)
A	風向（V）	20.73(31)	C	風向（V）	23.58(30)
A	風速	25.50(32)	C	風速	23.71(33)
A	大氣穩定度	21.71(31)	C	大氣穩定度	30.53(30)
A	溫度	18.62(29)	C	溫度	15.06(29)
B	風向（U）	31.36(31)	D	風向（U）	18.19(31)
B	風向（V）	20.79(20)	D	風向（V）	22.74(30)
B	風速	19.31(32)	D	風速	14.48(33)
B	大氣穩定度	27.06(31)	D	大氣穩定度	16.23(28)
B	溫度	22.70(32)	D	溫度	25.85(32)

表三　71年10月1日至9日風向數據的預報結果，單位爲度。預報值爲所建立風向預報模式，未來24小時預報結果，實際值爲當時風向的觀測值。

未來時間（小時）	預報值	實際值	誤差
1	56.6	56.0	0.6
2	60.1	51.0	9.1
3	53.0	73.0	-20.0
4	51.8	70.0	-18.2
5	47.4	32.0	15.4
6	46.0	58.0	-12.0
7	46.2	31.0	15.0
8	46.6	56.0	-9.4
9	46.5	32.0	14.5
10	47.8	76.0	-28.2
11	50.5	89.0	-38.5
12	50.0	59.0	-9.0
13	53.7	45.0	8.7
14	53.9	36.0	17.9
15	51.2	32.0	91.2
16	50.0	34.0	16.0
17	59.4	34.0	15.0
18	49.3	45.0	4.3
19	49.2	38.0	11.2
20	39.1	50.0	-0.9
21	49.1	48.0	1.1
22	49.1	45.0	4.1
23	49.1	55.0	-5.9
24	49.1	47.0	2.1

絕對值平均誤差＝ 12.38 標準偏差＝ 15.19

表四　71年10月21日至29日風向數據的預報結果，單位爲度，餘參照表三。

未來時間（小時）	預報值	實際值	誤差
1	74.7	85.0	-10.3
2	73.7	84.0	-10.3
3	72.0	75.0	-2.6
4	70.6	78.0	-7.4
5	70.0	115.0	-44.4
6	68.8	94.0	-25.2
7	69.2	87.0	-17.8
8	67.8	104.0	-36.2
9	67.1	231.0	-163.9
10	68.7	271.0	-157.7
11	67.4	260.0	-167.0
12	67.2	201.0	-133.8
13	67.7	242.0	-174.3
14	67.3	279.0	-148.3
15	66.9	286.0	-140.9
16	66.7	281.0	-145.7
17	66.6	36.0	30.6
18	66.5	57.0	9.5
19	66.5	47.0	19.5
20	66.5	112.0	-45.5
21	66.5	81.0	-14.5
22	66.5	107.0	-40.5
23	66.5	25.0	41.5
24	66.5	113.0	-46.5

絕對值平均誤差＝ 68.08 標準偏差＝ 70.50

表五　71年11月7日至15日風向數據的預報結果，單位爲度，餘參照表三。

未來時間（小時）	預報值	實際值	誤差
1	68.3	71.0	-2.7
2	64.6	106.0	-41.4
3	61.9	46.0	15.9
4	65.4	84.0	-18.6
5	66.4	75.0	-8.6
6	66.2	61.0	5.2
7	70.1	108.0	-37.9
8	66.0	81.0	-15.0
9	69.0	98.0	-29.0
10	68.3	100.0	-31.7
11	63.7	70.0	-6.3
12	65.3	79.0	-13.7
13	64.9	90.0	-25.1
14	64.3	83.0	-18.7
15	64.4	83.0	-18.6
16	63.9	35.0	28.9
17	63.8	74.0	-10.2
18	63.9	51.0	12.8
19	63.7	64.0	-0.3
20	63.7	63.0	0.7
21	63.7	102.0	-38.3
22	63.7	63.0	0.7
23	63.7	63.0	0.7
24	63.7	66.0	-2.3

絕對值平均誤差＝ 15.97 標準偏差＝ 17.53

表六　71年12月11日至19日風向數據的預報結果。單位爲度，餘參照表三。

未來時間（小時）	預報值	實際值	誤差
1	78.7	83.0	-4.3
2	76.9	84.0	-7.1
3	77.1	87.0	-9.9
4	72.9	49.0	23.9
5	71.9	66.0	5.9
6	71.6	70.0	1.6
7	70.2	74.0	-3.8
8	69.5	56.0	13.5
9	69.7	87.0	-17.3
10	69.3	89.0	-19.7
11	69.0	65.0	4.0
12	68.3	48.0	20.3
13	67.8	48.0	19.8
14	67.0	52.0	15.0
15	63.4	49.0	14.4
16	62.0	57.0	5.0
17	61.4	49.0	12.4
18	61.2	77.0	-15.8
19	61.2	61.0	0.2
20	61.1	59.0	2.1
21	61.0	74.0	-13.0
22	61.0	74.0	-13.0
23	61.0	60.0	1.0
24	61.0	51.0	10.0

絕對值平均誤差＝ 10.25 標準偏差＝ 12.14

表七　71年10月1日至9日風速數據的預報結果。單位爲公尺／秒，餘參照表三。

未來時間（小時）	預報值	實際值	誤差
1	1.56	1.00	0.56
2	1.25	1.14	0.11
3	0.85	0.75	0.10
4	0.68	0.92	-0.24
5	0.59	1.27	-0.68
6	0.57	1.30	-0.73
7	0.84	1.03	-0.19
8	0.90	0.70	0.20
9	0.82	1.44	-0.42
10	0.84	0.95	-0.11
11	0.96	0.92	0.04
12	0.99	0.65	0.34
13	0.87	1.38	-0.51
14	0.88	2.29	-1.41
15	0.93	2.26	-1.33
16	0.93	2.11	-1.18
17	0.93	2.61	-1.68
18	0.93	2.21	-1.28
19	0.93	1.94	-1.01
20	0.93	1.85	-0.92
21	0.93	1.48	-0.55
22	0.93	1.28	-0.35
23	0.93	0.80	0.13
24.0	0.93	1.30	-0.37

絕對值平均誤差＝ 0.61 標準偏差＝ 0.60

表八　71年10月21日至29日風速數據的預報結果，單位爲公尺／秒，餘參照表三。

未來時間（小時）	預報值	實際值	誤差
1	0.67	0.47	0.20
2	0.63	1.28	-0.65
3	0.65	0.90	-0.25
4	0.65	0.51	0.14
5	0.84	0.17	0.67
6	0.96	0.02	0.94
7	1.03	0.11	0.92
8	1.07	0.02	1.05
9	1.09	0.02	1.07
10	1.10	0.11	0.99
11	1.11	0.72	0.39
12	1.11	0.60	0.51
13	1.12	0.87	0.25
14	1.12	1.33	-0.21
15	1.12	1.97	-0.85
16	1.12	1.57	-0.45
17	1.12	1.14	-0.02
18	1.12	0.80	0.32
19	1.12	0.14	0.98
20	1.12	0.17	0.95
21	1.12	0.17	0.95
22	1.12	0.18	0.94
23	1.12	0.24	0.88
24	1.12	0.03	1.09

絕對值平均誤差＝ 0.65 標準偏差＝ 0.59

表九　71年11月7日至15日風速數據的預報結果，單位爲公尺／秒，餘參照表三。

未來時間（小時）	預報值	實際值	誤差
1	1.38	1.03	0.35
2	1.22	0.77	0.45
3	1.10	0.51	0.59
4	1.00	0.93	0.07
5	0.92	0.87	0.05
6	0.86	0.43	0.43
7	0.83	0.62	0.21
8	0.80	0.38	0.42
9	0.78	0.54	0.24
10	0.78	0.53	0.25
11	0.74	0.75	-0.01
12	0.71	0.69	0.02
13	0.70	1.18	-0.48
14	0.69	1.52	-0.83
15	0.71	1.55	-0.84
16	0.72	1.33	-0.61
17	0.73	1.81	-1.08
18	0.73	1.02	-0.29
19	0.73	1.10	-0.36
20	0.74	0.86	-0.12
21	0.75	0.81	-0.06
22	0.75	1.31	-0.56
23	0.75	0.13	0.62
24	0.75	1.27	-0.52

絕對值平均誤差＝ 0.39 標準偏差＝ 0.47

表十　71年12月11日至19日風速數據的預報結果，單位爲公尺／秒，餘參照表三。

未來時間（小時）	預報值	實際值	誤差
1	1.28	1.33	-0.05
2	1.24	1.14	0.09
3	1.21	1.52	-0.31
4	1.19	1.17	0.02
5	1.18	1.69	-0.51
6	1.17	0.66	0.51
7	1.17	0.46	0.71
8	1.17	1.06	0.11
9	1.17	0.78	0.38
10	1.17	1.64	-0.47
11	1.16	1.19	-0.03
12	1.16	1.37	-0.21
13	1.16	2.07	-0.91
14	1.16	1.58	-0.42
15	1.16	1.86	-0.70
16	1.16	1.70	-0.54
17	1.16	1.45	-0.29
18	1.16	1.09	0.07
19	1.16	1.10	0.06
20	1.16	1.55	-0.39
21	1.16	0.88	0.28
22	1.16	1.43	-0.27
23	1.16	1.42	-0.26
24	1.16	0.77	0.39

絕對值平均誤差＝ 0.33 標準偏差＝ 0.39

表十一　71年10月1日至9日溫度數據的預報結果，單位爲℃，餘參照表三。

未來時間（小時）	預報值	實際值	誤差
11	24.2	24.3	-0.1
2	24.1	23.9	0.2
3	23.8	23.6	0.2
4	23.7	23.6	0.1
5	24.1	23.8	0.3
6	23.9	23.2	0.7
7	23.5	23.5	0.0
8	23.5	23.7	-0.2
9	23.3	23.7	-0.4
10	23.1	23.6	-0.5
11	22.9	23.5	-0.6
12	23.1	23.6	-0.5
13	23.9	23.8	0.1
14	24.9	24.0	0.9
15	25.2	24.0	1.2
16	25.4	24.1	1.3
17	26.7	24.1	2.6
18	26.8	24.1	2.7
19	26.9	24.2	2.7
20	26.9	24.2	2.7
21	26.9	24.2	2.7
22	26.3	24.3	2.0
23	25.3	24.3	1.0
24	24.4	24.3	0.1

絕對值平均誤差＝ 0.99 標準偏差＝ 1.14

表十二　71年10月21日至29日溫度數據的預報結果，單位爲℃，餘參照表三。

未來時間（小時）	預報值	實際值	誤差
1	23.1	23.2	-0.1
2	22.8	23.2	-0.4
3	22.3	23.4	-1.1
4	22.1	23.0	-0.9
5	22.0	22.7	-0.7
6	21.8	22.2	-0.4
7	21.9	21.9	0.0
8	22.0	22.0	0.0
9	23.3	24.0	-0.7
10	25.0	26.0	-1.0
11	25.9	27.8	-1.9
12	27.0	30.1	-3.1
13	26.9	31.8	-4.9
14	26.6	31.2	-4.6
15	25.3	30.6	-5.3
16	24.2	29.8	-5.6
17	23.0	28.8	-5.8
18	22.0	26.6	-4.6
19	20.9	25.4	-4.5
20	20.0	24.7	-4.7
21	19.0	23.9	-4.9
22	18.1	23.3	-5.2
23	17.3	23.0	-5.7
24	16.5	22.4	-5.9

絕對值平均誤差＝ 3.00 標準偏差＝ 2.25

表十三　71年11月7日至15日溫度數據的預報結果，單位爲℃，餘參照表三。

未來時間（小時）	預報值	實際值	誤差
1	19.2	19.0	0.2
2	19.3	19.1	0.2
3	19.5	19.7	-0.2
4	19.6	19.4	0.2
5	19.8	19.6	0.2
6	20.1	20.2	-0.1
7	20.2	19.7	0.5
8	19.5	19.8	-0.3
9	18.5	19.5	-1.0
10	17.8	19.0	-1.2
11	17.6	18.9	-1.3
12	17.7	18.7	-1.0
13	18.0	18.6	-0.6
14	18.1	18.6	-0.5
15	18.2	18.6	-0.4
16	18.3	18.4	-0.1
17	18.4	18.5	-0.1
18	18.5	18.4	0.1
19	18.6	18.1	0.5
20	18.6	18.1	0.5
21	18.7	18.4	0.3
22	18.8	18.6	0.2
23	18.8	18.8	0.0
24	18.9	18.9	0.0

絕對值平均誤差＝ 0.40 標準偏差＝ 0.52

表十四　71年12月11日至19日溫度數據的預報結果，單位爲℃，餘參照表三。

未來時間（小時）	預報值	實際值	誤差
1	15.1	15.3	-0.2
2	15.1	15.4	-0.3
3	15.1	15.1	0.0
4	15.1	15.6	-0.5
5	15.1	16.4	-1.3
6	15.1	16.0	-0.9
7	15.1	16.1	-1.0
8	15.1	15.8	-0.7
9	15.1	16.0	-0.9
10	15.1	15.8	-0.7
11	15.1	16.2	-1.1
12	15.1	17.4	-2.3
13	15.1	18.1	-3.0
14	15.1	17.4	-2.3
15	15.1	15.9	-0.8
16	15.3	16.3	-1.0
17	15.3	16.5	-1.0
18	15.7	16.0	-0.3
19	15.9	16.0	-0.1
20	16.1	16.0	0.1
21	16.3	16.0	0.3
22	16.5	16.1	0.4
23	16.7	15.9	0.8
24	16.9	15.8	1.1

絕對值平均誤差＝ 0.88 標準偏差＝ 0.94

表十五　四組穩定度數據未來24小時預報結果。A與B級穩定度間級數差爲1，A與F級穩定度間級數差爲5。

收集數據時間	未來時間（小時）	1	2	3	4	5	6	7	8	9	10	11	12	13	14	15	16	17	18	19	20	21	22	23	24
71.10. 1. 至10. 9.	預報級數	F	F	F	F	F	F	F	B	B	B	B	B	B	B	B	B	A	F	F	F	F	F	F	F
	實際級數	F	E	F	F	F	E	E	B	B	C	B	B	B	B	B	B	B	F	F	F	F	F	F	E
	級數差	0	1	0	0	0	1	1	0	0	1	0	0	0	0	0	0	1	0	0	0	0	0	0	1
71.10.21. 至10.29.	預報級數	E	F	F	F	F	F	F	B	B	B	B	B	B	B	B	B	B	F	F	F	F	F	F	F
	實際級數	F	F	F	F	F	F	E	A	B	C	B	C	C	B	B	B	B	F	E	F	E	E	E	E
	級數差	1	0	0	0	0	0	1	1	0	1	0	1	1	0	0	0	0	0	1	0	1	1	1	1
71.11. 7. 至11.15.	預報級數	F	F	F	F	F	F	F	B	A	A	B	B	B	B	A	A	A	F	F	F	F	F	F	F
	實際級數	E	F	F	E	F	F	F	B	C	A	C	C	D	D	D	C	C	E	E	E	D	E	E	E
	級數差	1	0	0	1	0	0	0	0	2	0	1	1	2	2	3	2	2	1	1	1	0	1	1	1
71.12.11. 至12.19.	預報級數	F	F	F	F	F	F	F	B	A	B	B	B	A	A	B	B	B	F	F	F	F	F	F	F
	實際級數	F	F	F	F	F	F	F	A	B	B	B	B	B	A	B	B	B	F	F	F	F	F	F	F
	級數差	0	0	0	0	0	0	0	1	1	0	0	0	1	0	0	0	0	0	0	0	0	0	0	0

表十六　71年10月1日至9日風速數據即時預報的結果，單位爲公尺／秒。表中預報值爲表七原預報模式預報值中的後18個值，即時預報值爲將表七實際值中的前6個值輸入，做未來18小時的即時預報。

原預報值	即時預報值	實際值	原預報誤差	即時預報誤差
0.84	0.93	1.03	-0.19	-0.10
0.90	0.93	0.70	0.20	0.23
0.92	0.93	1.44	-0.52	-0.51
0.84	0.93	0.95	-0.11	-0.02
0.96	0.94	0.92	0.04	0.02
0.99	0.94	0.65	0.34	0.29
0.87	0.94	1.38	-0.51	-0.44
0.88	0.92	2.29	-1.41	-1.37
0.93	0.95	2.26	-1.33	-1.31
0.93	0.92	2.11	-1.18	-1.19
0.93	0.87	2.61	-1.68	-1.74
0.93	0.91	2.21	-1.28	-1.30
0.93	0.90	1.94	-1.01	-1.04
0.93	0.95	1.85	-0.92	-0.92
0.93	1.02	1.48	-0.55	-0.46
0.92	1.02	1.28	-0.35	-0.26
0.93	0.93	0.80	0.13	0.13
0.93	0.93	0.30	-0.37	-0.37
絕對值平均誤差			0.6733	0.6489

表十七　71年12月11日至19日風速數據即時預報的結果，單位爲公尺／秒。表中原預報值爲表十原預報模式預報值中的後19個值，即時預報值爲將表十實際值中的前5個數值輸入，作未來19小時的即時預報。

原預報值	即時預報值	實際值	原預報誤差	即時預報誤差
1.17	1.36	0.66	0.51	0.70
1.17	1.31	0.46	0.71	0.85
1.17	1.25	1.06	0.11	0.19
1.17	1.22	0.79	0.38	0.43
1.17	1.20	1.64	-0.47	-0.44
1.16	1.18	1.19	-0.03	-0.01
1.16	1.18	1.37	-0.21	-0.19
1.16	1.17	2.07	-0.91	-0.90
1.16	1.17	1.58	-0.42	-0.41
1.16	1.17	1.86	-0.70	-0.69
1.16	1.17	1.70	-0.54	-0.53
1.16	1.16	1.45	-0.29	-0.29
1.16	1.16	1.09	0.07	0.07
1.16	1.16	1.10	0.06	0.06
1.16	1.16	1.55	-0.39	-0.39
1.16	1.16	0.88	0.28	0.28
1.16	1.16	1.43	-0.27	-0.27
1.16	1.16	1.42	-0.26	-0.26
1.16	1.16	0.77	0.39	0.39
絕對值平均誤差			0.3684	0.3668

表十八　71年10月21日至29日溫度數據即時預報的結果，單位爲℃。表中原預報值爲表十二原預報模式預報值中的後12個值，即時預報值爲將表十二實際值中的前12個數值輸入，做未來12小時的即時預報，而表中實際值則爲表十二實際值中的後12個值爲預報值比較的依據。

原預報值	即時預報值	實際值	原預報誤差	即時預報誤差
26.9	29.8	31.8	-4.9	-2.0
26.6	29.5	31.2	-4.6	-1.7
25.3	29.3	30.6	-5.3	-1.3
24.2	28.8	29.8	-5.6	-1.0
23.0	28.1	28.8	-5.8	-0.8
22.0	28.0	26.6	-4.6	1.4
20.9	27.7	25.4	-4.5	2.3
20.9	27.6	24.7	-4.7	2.9
19.0	27.3	23.9	-4.9	3.4
18.1	26.8	23.3	-5.2	3.5
12.3	25.0	23.0	-5.7	2.0
16.5	23.2	22.4	-5.9	0.8
絕對值平均誤差				

表十九　各組參數預報結果表。四組數據同表一，表中預報誤差爲各組各參數24小時預報數值與實際數值差的標準偏差，四組平均誤差爲同一大氣參數四組數據預報誤差的平均值。

參數		預報誤差	四組平均誤差
風向	A	15.2°	28.8°
	B	70.5°	
	C	17.5°	
	D	12.1°	
風速	A	0.60 公尺／秒	0.51 公尺／秒
	B	0.59 公尺／秒	
	C	0.47 公尺／秒	
	D	0.39 公尺／秒	
大氣穩定度	A	＜1 級	＜1 級
	B	＜1 級	
	C	≒1 級	
	D	＜1 級	
溫度	A	1.14 ℃	1.21 ℃
	B	2.55 ℃	
	C	0.52 ℃	
	D	0.94 ℃	

表二十　原時序與殘差時序標準偏差之比較。四組數據同表一，σ_{zt}爲原時序Z_t的標準偏差，σ_{at}爲殘差時序a_t的標準偏差。

		σ_{zt}（樣本母體）	σ_{at}（殘差）
風向	A	68.2°	30.5°
	B	55.6°	35.7°
	C	70.3°	46.8°
	D	58.9°	28.7°
風速	A	0.72 公尺／秒	0.51 公尺／秒
	B	0.66 公尺／秒	0.33 公尺／秒
	C	0.63 公尺／秒	0.41 公尺／秒
	D	0.86 公尺／秒	0.43 公尺／秒
大氣穩定度	A	13.1°	5.7°
	B	9.0°	4.6°
	C	11.2°	7.1°
	D	8.6°	5.8°
溫度	A	2.64 ℃	0.91 ℃
	B	3.48 ℃	0.64 ℃
	C	4.87 ℃	0.85 ℃
	D	2.55 ℃	0.41 ℃

表二十一　原模式與AR（24）模式殘差時序的比較。四組數據同表一。表中原模式之σ_{at}爲原預報模式擬合後所得的殘差時序a_t的標準偏差，AR（24）模式之σ_{at}爲AR(24)高階模式擬合後所得殘差時序的標準偏差，表中最大殘差值爲各殘差時序的最大值。

		模式型式	σ_{at}	最大殘差值
風向	B	原模式	35.7°	156°
		AR（24）模式	26.5°	149°
	C	原模式	46.8°	175.5°
		AR（24）模式	33.4°	162°
風速	A	原模式	0.51 公尺／秒	2.62 公尺／秒
		AR（24）模式	0.38 公尺／秒	1.78 公尺／秒
	B	原模式	0.33 公尺／秒	1.14 公尺／秒
		AR（24）模式	0.34 公尺／秒	1.17 公尺／秒
	C	原模式	0.41 公尺／秒	2.05 公尺／秒
		AR（24）模式	0.39 公尺／秒	1.98 公尺／秒
	D	原模式	0.43 公尺／秒	2.36 公尺／秒
		AR（24）模式	0.36 公尺／秒	1.46 公尺／秒
溫度	A	原模式	0.91 ℃	6.80 ℃
		AR（24）模式	0.86 ℃	6.36 ℃
	B	原模式	0.64 ℃	2.73 ℃
		AR（24）模式	0.61 ℃	2.62 ℃
	C	原模式	0.85 ℃	4.49 ℃
		AR（24）模式	0.79 ℃	4.27 ℃
	D	原模式	0.41 ℃	2.26 ℃
		AR（24）模式	0.41 ℃	2.01 ℃

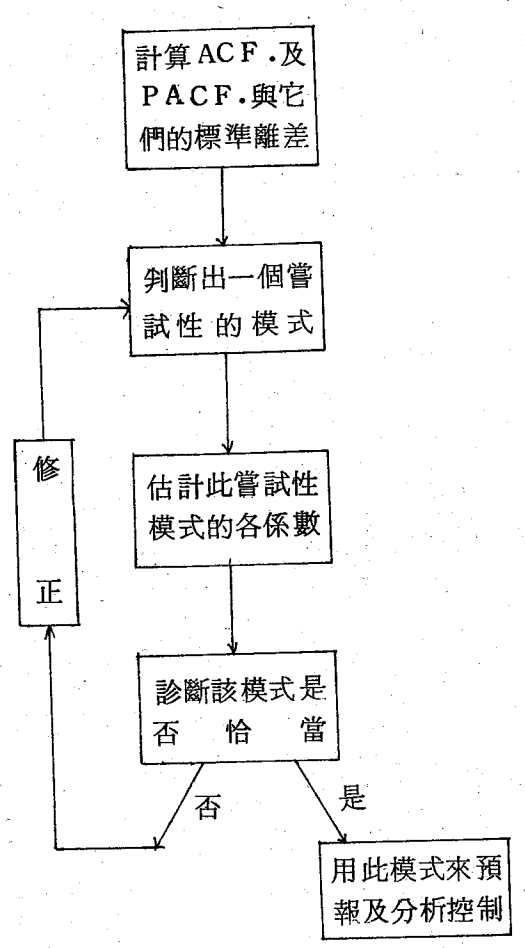

圖一　建立合適的ARIMA 模式的各個步驟

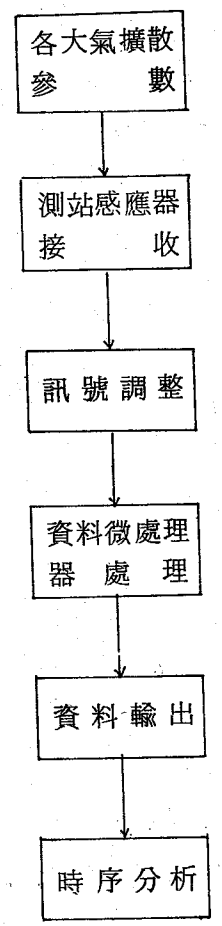

圖二　資料取得的流程

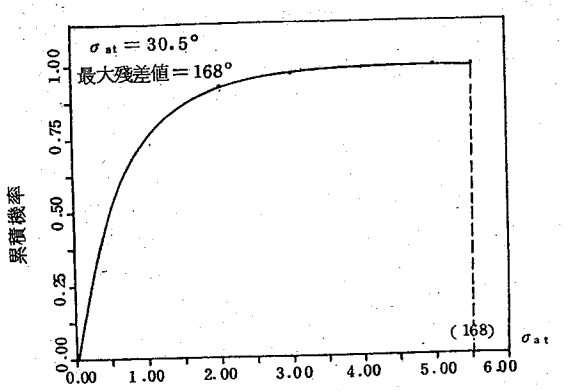

圖三　71年10月1日至9日風向數據殘差時序的累積機率分佈圖表中風向殘差時序爲上述收集時間風向實測值與同時間預報模式擬合值間之差值所組成的時序，σ_{at}參照表二十。

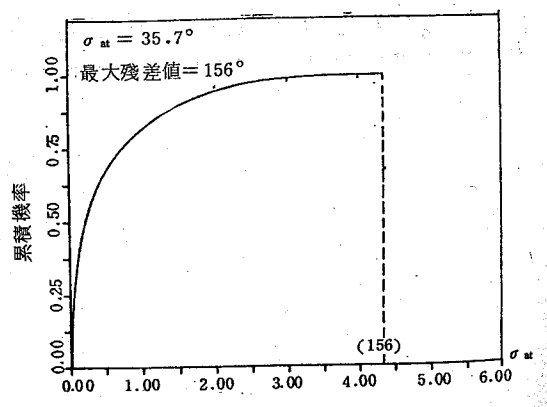

圖四　71年10月21日至29日風向數據殘差時序的累積機率分佈圖，餘同圖三。

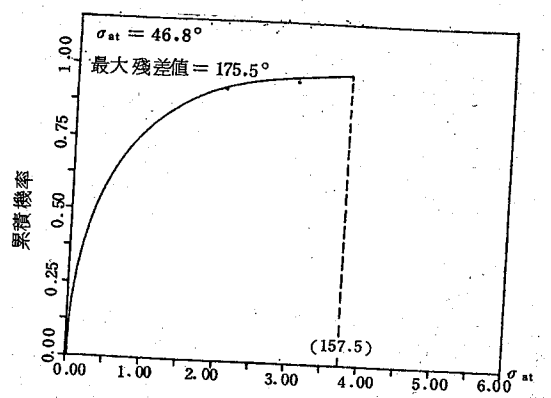

圖五　71年11月7日至15日風向數據殘差時序的累積機率分佈圖餘同圖三。

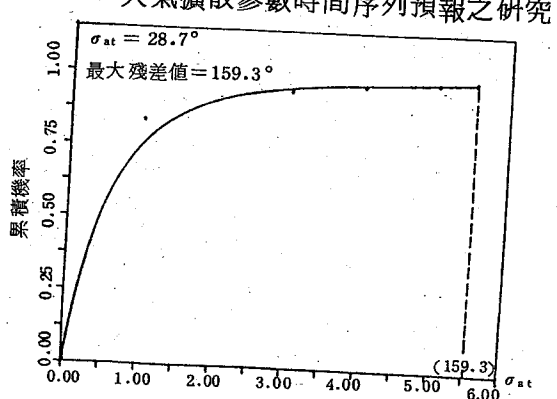

圖六　71年12月11日至19日風向數據殘差時序的累積機率分佈圖餘同圖三。

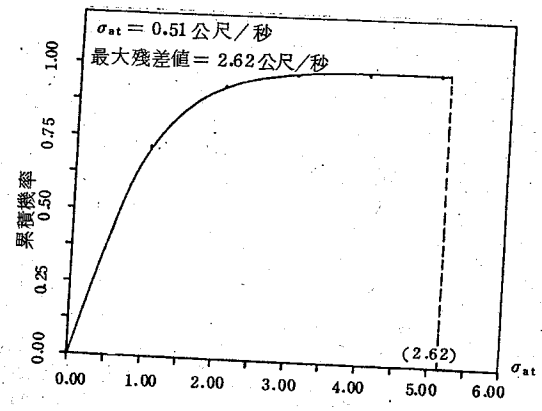

圖七　71年10月1日至9日風速數據殘差時序的累積機率分佈圖餘同圖三。

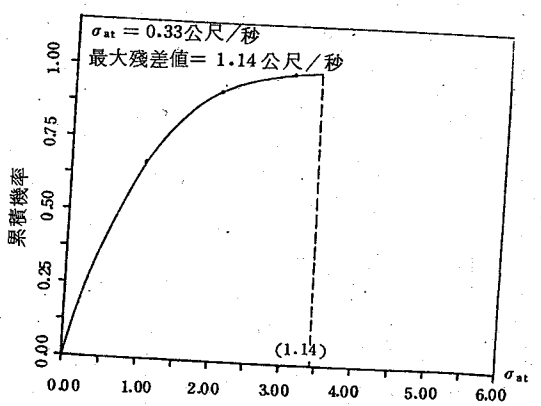

圖八　71年10月21日至29日風速數據殘差時序的累積機率分佈圖餘同圖三。

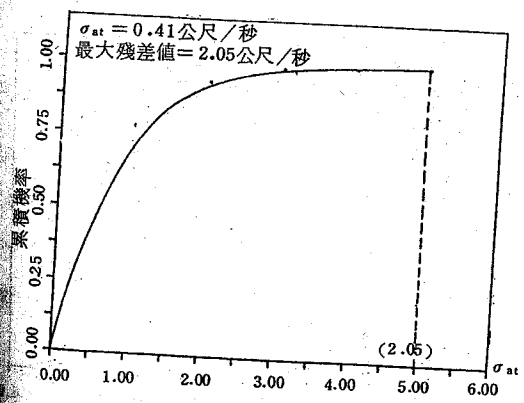

圖九　71年11月7日至15日風速數據殘差時序的累積機率分佈圖餘同圖三。

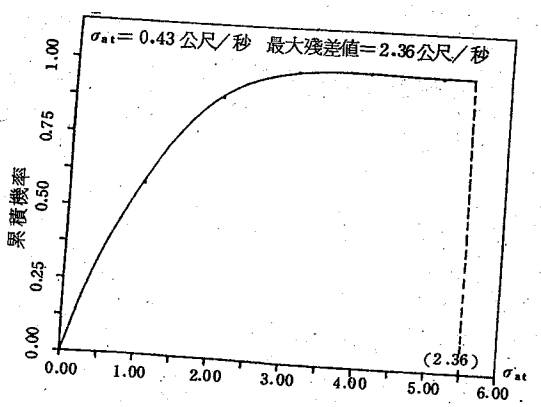

圖十　71年12月11日至19日風速數據殘差時序的累積機率分佈圖餘同圖三。

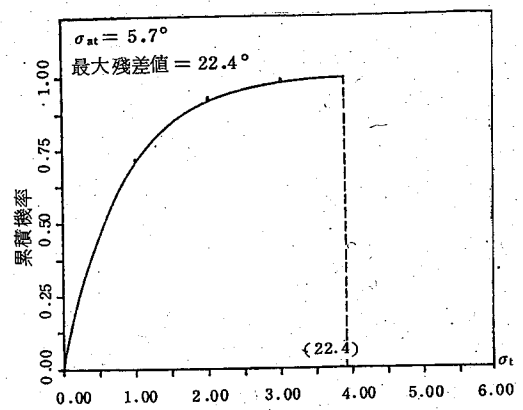

圖十一　71 年 10 月 1 日至 9 日大氣穩定度數據殘差時序的累積機率分佈圖，餘同圖三。

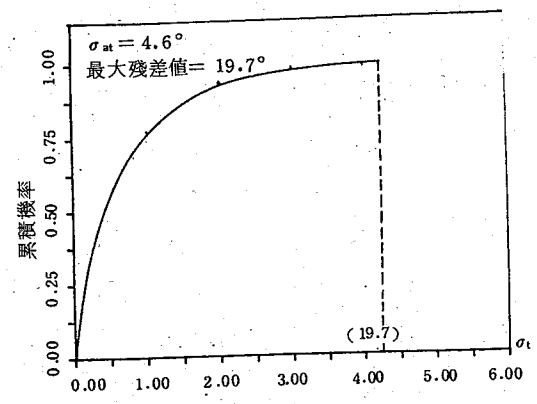

圖十二　71 年 10 月 21 日至 29 日大氣穩定度數據殘差時序的累積機率分佈圖，餘同圖三。

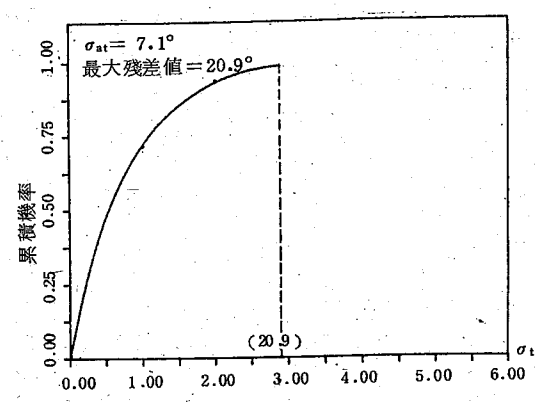

圖十三　71年 11 月 7 日至 15 日大氣穩定度數據殘差時序的累積機率分佈圖，餘同圖三。

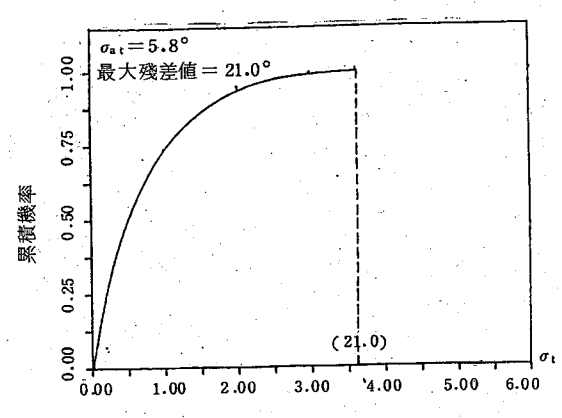

圖十四　71 年 12 月 11 日至 19 日大氣穩定度數據殘差時序的累積機率分佈圖，餘同圖三。

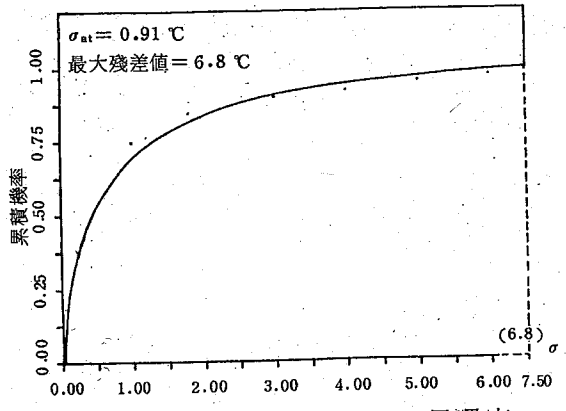

圖十五　71年 10 月 1 日至 9 日溫度數據殘差時序的累積機率分佈圖，餘同圖三。

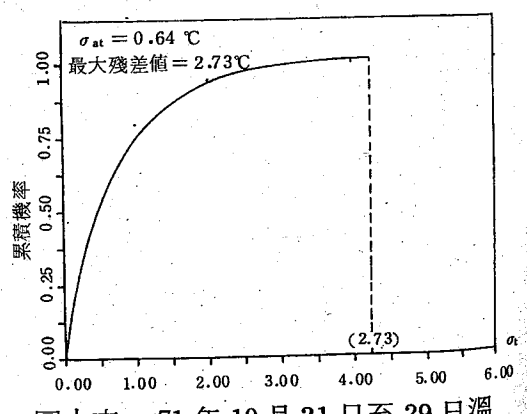

圖十六　71 年 10 月 21 日至 29 日溫度數據殘差時序的累積機率分佈圖，餘同圖三。

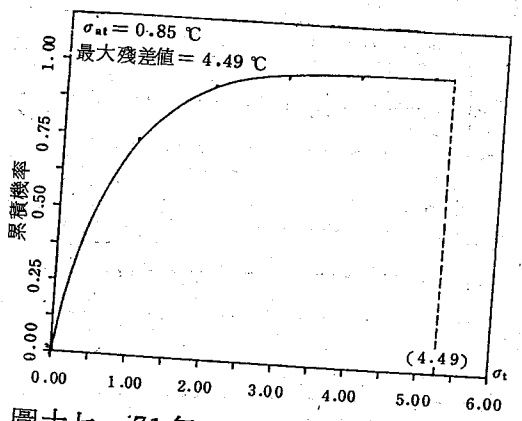

圖十七　71年11月7日至15日溫度數據殘差時序的累積機率分佈圖，餘同圖三。

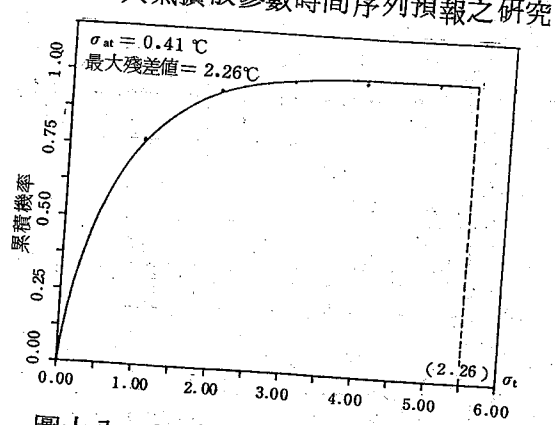

圖十八　71年 12 月 11 日至 19 日溫度數據殘差時序的累積機率分佈圖，餘同圖三。

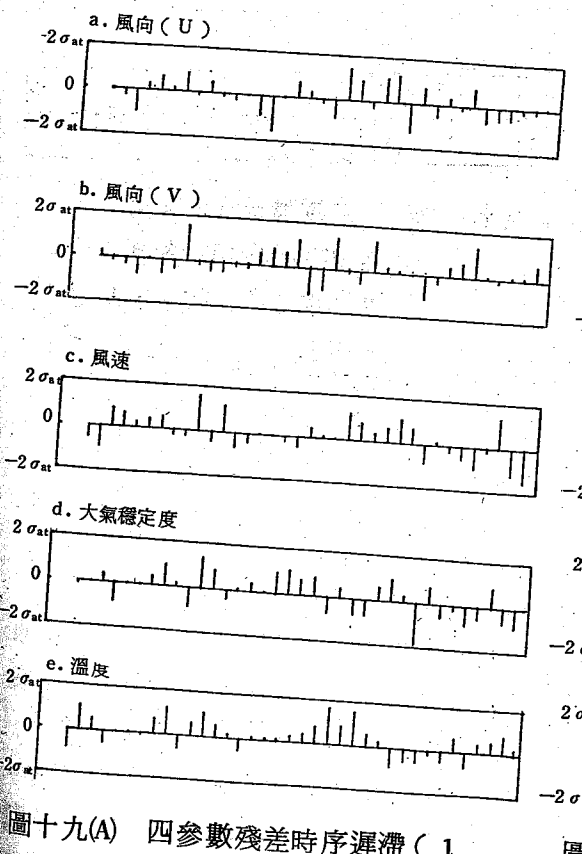

圖十九(A)　四參數殘差時序遲滯（1至36）的自相關對其二倍標準偏差值比較圖，餘參照表二十。

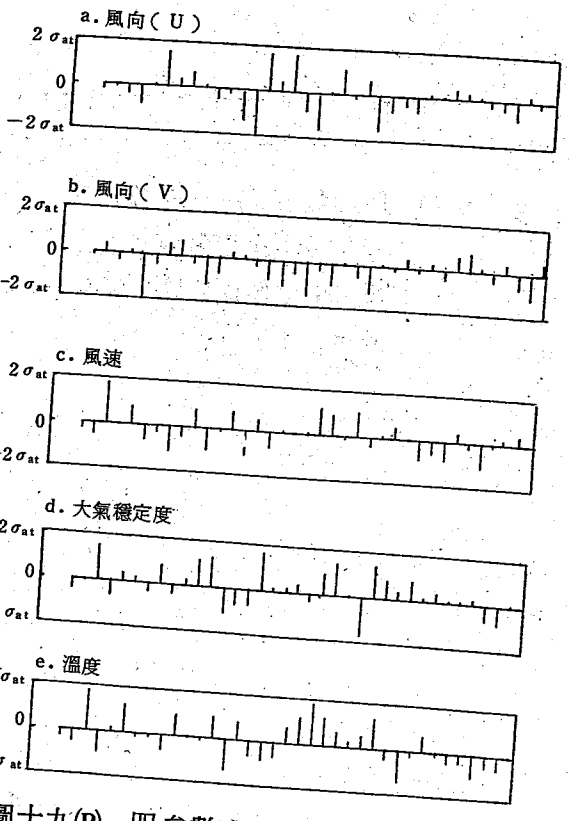

圖十九(B)　四參數殘差時序遲滯（1至36）的自相關對其二倍標準偏差值比較圖，餘參照表二十。

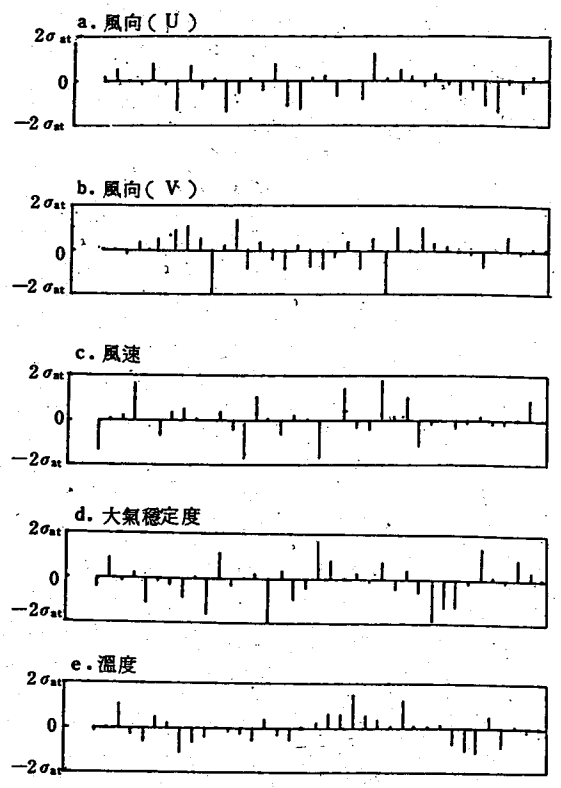

圖十九(C)　四參數殘差時序遲滯（1至36）的自相關對其二倍標準偏差值比較圖，餘參照表二十。

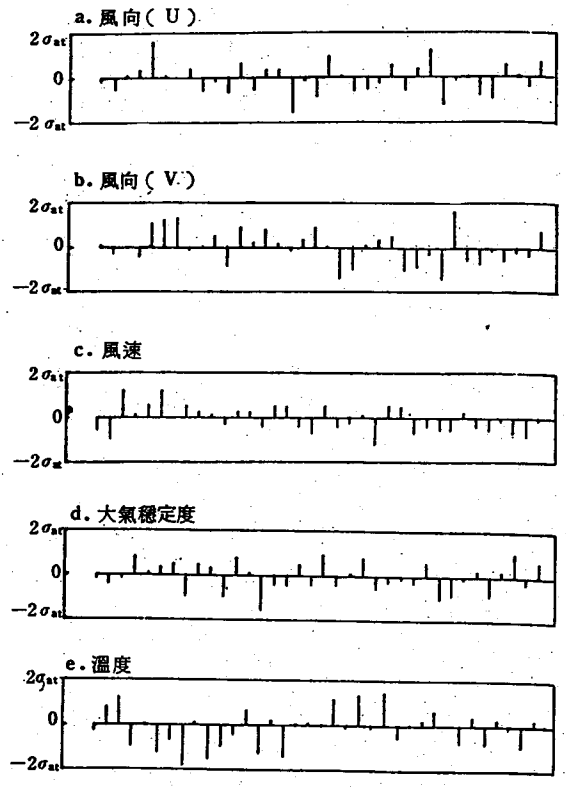

圖十九(D)　四參數殘差時序遲滯（1至36）的自相關對其二倍標準偏差值比較圖，餘參照表二十。

線源光化學污染物擴散模式之原理與應用

梁　文　傑
中央研究院物理研究所
國立臺灣大學機械工程學系
華　梅　英
國立臺灣大學環境工程研究所

摘　要

本研究是應用大氣擴散模式，將擴散空間分割成許多含有等量污染物質的巢空間，由於污染物的擴散，此巢空間也隨之變大，並依風向往下風處傳送，在傳送過程中，巢內產生光化學作用，使污染物濃度改變。此模式涉及數個至數十個光化學反應的聯解，就數學觀點而言，爲數個至數十個常微分方程式的聯解。

本研究自現有文獻選擇四組較具代表性的光化學反應方程式組，應用在實際大氣擴散上，並利用現場實際測定值與理論結果相較，以評估此線源光化學反應模式在台灣地區的可行性。

經由模式計算結果顯示，近距離沿下風方向，O_3、PAN和ALD 濃度會因化學作用而增加，其餘污染物濃度則減少，但無論污染物在擴散之初，濃度隨距離增加或減少，到某一距離後終會因擴散作用而遞減，與實際的污染物擴散情形相同。

壹、引　言

台灣地區人口密度高居世界第二位，工業急速發展，交通日益繁忙。道路的闢建與車輛數的增加，固然帶給人們莫大的便利，但就環境保護的立場，有必要對其可能造成的空氣污染問題加以研究，以供有關防治對策之參考。

空氣品質的改進，預防往往較防治更具效果，此時，數學模式扮演著極重要的角色，因爲它能預估某些情況下可能發生的情形。所以儘管空氣污染模式的發展，尚未達到完全的地步，但是它們在空氣品質的鑑定、預估及防治上仍然能提供許多有益的資訊。一般空氣污染模式，具有理論和經驗混合的特性，理論告訴我們方程式型式，經驗提供這些方程式中某些係數值，如化學反應速率和紊流擴散係數等。我們代入經驗數值，並以實測數據予以校正。經常一個特定的係數需要經過多次的更正，但無論如何，數學模式唯有經過實測數據的證實，才具有實用價值。

由於煙柱擴散問題相當複雜，無法用簡單的模式概括氣象、地形及污染源等所有因

素。當我們研究由單一污染源的擴散問題，經常不包括化學反應、落塵及生物吸收等作用。許多煙流擴散的研究上，大氣擴散參數僅依地區風速和穩定度而異。以高斯煙流擴散爲例，一次污染物濃度和垂直及水平方向擴散係數有關，並且依距離的增加呈現指數性的衰減。線源可視爲由無窮多個點源所組成，只是在濃度的計算上得加入積分的概念，其擴散特性和點污染源相似。一般而言，公路線源因汽車排氣不考慮浮場力的作用，污染物一經排出，能在很短的距離內和大氣混合，因此在接近排放源處的擴散型態和點源排放有些許出入。

光化學反應，和光的照射有關，低層大氣中所接受的可見光和紫外光，除直接來自太陽外，還有大氣散射以及地球表面的反射。其輻射强度的決定包括，太陽直接照射在大氣外層的强度、天頂角（ Zenith Angle ）、自然散射量、大氣散射或吸收性，以及地區的特性等。一般光化學污染物是指化學性轉變半衰期在數小時之內，如碳氫化物中丙烯、丁烯，以及臭氧等。其採樣分析和模式建立與惰性污染物有明顯差異。

以往的研究中，Wanta 與 Lowry[1] 對影響惰性污染物擴散情況的各種氣象條件，做過綜合性的整理。Graedel 等人[2] 研究都市對流層中光化學動力情形，合併化學動力，污染物的時間變化、陽光通量、空氣流和反應體積等因素，結果發現 NO-NO_3-O_3 間的反應，受自由基的影響較大，而自由基主要由乙醛經光分解後而得。Atkinson 等人[3] 爲配合使用大氣光化學空氣品質模擬模式，曾將部分反應機構更新，得知當 NO濃度比 1 ppb 大時，可大量減少反應方程式，而不會發生嚴重影響。1975 年 EPA [4] 刊行公路線源模式使用指針（ User's Guide ），介紹線源惰性污染物擴散模式的建立和使用方法。Dabberdt 等人[5] 研究在各種不同道路結構時，惰性污染物的擴散情形。Friendlander 與 Seinfeld[6] 嘗試使光化學煙霧於體積可膨脹反應器內發生反應。O'Brien 等人[7] 做過反應性污污物不同階段紊亂混合的研究。Steven 與 Philip 等學者[8][9][10] 在光化學煙霧擴散模式方面，由模式建立時方程式的選擇，各係數值的求取，至模式的驗證有一系列的探討。Eschenroeder 等人[11]也同樣有針對線源光化學模式的研究，考慮不同化學反應的影響。國內，有黃賢誠[12]將巢式擴散模式（ cell medel ），應用於光化學污染物擴散情形，此模式將空間分割爲許多含同量污染物的巢空間，隨著污染物的擴散，此巢空間亦隨之變大，並隨風速向下風方向傳送，在傳送過程中，巢內光化學性污染物與巢外加入之污染物起光化學作用，因而改變濃度。

本研究擬合併 Eschenroeder 及 EPA 公路線源模式，並將國內現有黃賢誠的光化學擴散模式加以改進，在污染擴散方面，線源和風向間的夾角可爲任意角度，巢的分格在下風向的長度，可隨濃度之遞減而增大，線源長度由無限線源改爲有限線源，並考慮線源的實際彎曲及不同强度線源的情況，改進近距離污染物的擴散模擬。在光化學反應方面，選擇四組做爲嘗試，比較化學反應的結果。由於國內在光化學污染方面的研究，多直接引用國外資料或數據，研究成果不能直接提供國內污染防治之用。本研究以台灣高速公路桃園至中壢段，作爲模式應用與探討對象，除從事模式的改良外，並利用實測數據求取模式中之參數。模式計算結果亦經實測數據證實。

貳、模式基本理論

一基本理論

在模擬光化學污染物時，最基本的目的，就是要描述一系列的非惰性污染物在大氣紊流中所呈現的結果。由於煙流擴散問題相當複雜，再加上化學反應的參與，使模式的建立必須綜合多項理論。

(一)基本污染擴散模式

假設在流體中含有 n 種污染物，則各污染物的濃度必須滿足擴散方程式[8]

$$\frac{\partial C_i}{\partial t}+\frac{\partial}{\partial x}(uC_i)+\frac{\partial}{\partial y}(vC_i)+\frac{\partial}{\partial z}(wC_i)$$

$$=D_i\left(\frac{\partial^2 C_i}{\partial x^2}+\frac{\partial^2 C_i}{\partial y^2}+\frac{\partial^2 C_i}{\partial z^2}\right)+R_i(C_1,\cdots,C_n,T)+$$

$$S_i(x,y,z,t)\qquad i=1,2,\cdots\cdots,n \qquad \cdots\cdots\cdots\cdots\cdots\cdots(1)$$

其中 u、v、w 爲紊流中三維度空間的風速分量，D_i 爲分子擴散係數，S_i 表排放源的排放率，T爲溫度，R_i 爲由化學反應所產生的污染物變化率，$R_i=R_i(\overline{C}_1+C_1',\overline{C}_2+C_2',\cdots,\overline{C}_n+C_n',T)$ 。在大多數包含化學反應的流體動力問題中，必須考慮質量、動量和能量方程式的聯立解，但是在研究空氣污染上，由於污染濃度極低，一般假定污染物不會影響氣象狀況。假設和紊流擴散比較之下，分子擴散可以忽略不計，且習慣上將風速 u 以 $\overline{u}+u'$表示，同理 $v=\overline{v}+v'$ 、$w=\overline{w}+w'$，代入(1)中，則反應污染物平均濃度變化爲

$$\frac{\partial \overline{C}_i}{\partial t}+\frac{\partial}{\partial x}(\overline{u}\overline{C}_i)+\frac{\partial}{\partial y}(\overline{v}\overline{C}_i)+\frac{\partial}{\partial z}(\overline{w}\overline{C}_i)+\frac{\partial}{\partial x}(\overline{u'C_i'})$$

$$+\frac{\partial}{\partial y}(\overline{v'C_i'})+\frac{\partial}{\partial z}(\overline{w'C_i'})$$

$$=R_i(\overline{C_1+C_1',\ C_2+C_2',\cdots,C_n+C_n',T})+S_i(x,y,z,t)$$

$$\cdots\cdots\cdots\cdots\cdots\cdots(2)$$

此處 $C_i=\overline{C}_i+C_i'$，$\overline{C}_i'=0$，並且溫度的變動予以忽略。(2)式中因爲 $\overline{u'C_i'}$，$\overline{v'C_i'}$，$\overline{w'C_i'}$ 等未知而無法直接求解。根據理論[13]

$$\overline{u'C_i'}=-K_{xx}\frac{\partial \overline{C}_i}{\partial x}\quad,\quad \overline{v'C_i'}=-K_{yy}\frac{\partial \overline{C}_i}{\partial y}\quad,$$

$$\overline{w'C_i'}=-K_{zz}\frac{\partial \overline{C}_i}{\partial z}$$

$$\cdots\cdots\cdots\cdots\cdots\cdots(3)$$

並假設平均反應速率極近於平均濃度的反應速率[14]，即

$$\overline{R_i(C_1+C_1',C_2+C_2',\cdots,C_n+C_n',T)}$$

$$\cong R_i(\overline{C}_1,\overline{C}_2,\cdots,\overline{C}_n,T) \qquad \cdots\cdots\cdots\cdots\cdots\cdots(4)$$

將(3)，(4)式代入(2)式得

$$\frac{\partial \bar{C}_i}{\partial t}+\frac{\partial}{\partial x}(\bar{u}\bar{C}_i)+\frac{\partial}{\partial y}(\bar{v}\bar{C}_i)+\frac{\partial}{\partial z}(\bar{w}\bar{C}_i)$$
$$=\frac{\partial}{\partial x}\left(K_{xx}\frac{\partial \bar{C}_i}{\partial x}\right)+\frac{\partial}{\partial y}\left(K_{yy}\frac{\partial \bar{C}_i}{\partial y}\right)+\frac{\partial}{\partial z}\left(K_{zz}\frac{\partial \bar{C}_i}{\partial z}\right)+$$
$$R_i(\bar{C}_1,\bar{C}_2,\cdots,\bar{C}_n,T)+S_i(x,y,z,t) \quad \cdots\cdots(5)$$

因爲本研究中所使用的時間、空間尺度，均大於單一顆粒運動的時間、空間尺度，因此(5)式能有效的代表大氣傳送和化學反應作用[15]。

二高斯模式

假設x軸與風向垂直，且x、y、z爲相互垂直的三度空間笛卡爾座標系統，則$\bar{u}=\bar{U}$，$\bar{v}=\bar{w}=0$。在x方向的紊亂擴散速率遠小於風所造成的對流擴散速率，即

$$\frac{\partial}{\partial x}\left(K_{xx}\frac{\partial \bar{C}_i}{\partial x}\right)\ll \bar{u}\frac{\partial \bar{C}_i}{\partial x}$$

若不考慮化學反應R_i，污染物由一穩定狀態（Steady state）且强度Q之點源（point source）連續放入風速爲常數並沿x軸吹向的大氣中。根據邊界條件[13]

$$\bar{C}_i=\frac{Q_i}{\bar{U}}\delta(x)\delta(y)\delta(z-h)$$

$$\frac{\partial \bar{C}_i}{\partial z}=0 \qquad z=0,\ x>0 \quad (\text{地面全反射})$$

$$\bar{C}_i=0 \qquad x,\ z\to\infty \quad y\to\pm\infty$$

$$\bar{U}\int_0^{\infty}\int_{-\infty}^{+\infty}\bar{C}_i\,dy\,dz=Q_i$$

則(5)式的解爲[16]

$$\bar{C}_i=\frac{Q_i}{2\pi\sigma_y\sigma_z\bar{U}}\exp\left(-\frac{y^2}{2\sigma_y^2}\right)\left[\exp\left(-\frac{(z+h)^2}{2\sigma_y^2}\right)+\exp\left(-\frac{(z-h)^2}{2\sigma_z^2}\right)\right] \quad \cdots\cdots(6)$$

其中σ_y、σ_z爲y、z方向的濃度擴散標準偏差[4][17]。

若將道路視爲由多點源所組成的定長度線源（Statistical base Finiteline Source），線源和風向的夾角爲θ，x軸沿風向而設，每單位長度線源放出污染强度爲Q_{Li}（參看圖一）。則由一定長線源對接收點（x_R,y_R,z_R）所產生的濃度爲

$$C_i(x,y,z)=\int_{x_L}^{x_u}\frac{Q_{Li}}{2\pi\bar{U}\sigma_y\sigma_z\cos\theta}\exp\left[-\frac{((x_0-x')\tan\theta)^2}{2\sigma_y^2}\right]\cdot$$

$$\left[\exp\left(-\frac{(Z+h)^2}{2\sigma_z^2}\right)+\exp\left(-\frac{(Z-h)^2}{2\sigma_z^2}\right)\right]dX' \quad (\theta\neq 90^\circ) \quad \cdots\cdots(7)$$

Z表示接收點離地面的高度。x_L表示線源對接收點有影響的下方x座標值。x_U表示線源對接收點有影響的上方x座標值。或

$$C_i(x,y,z)=\int_{Y_L}^{Y_u}\frac{Q_{Li}}{2\pi\bar{U}\sigma_y\sigma_z}\exp\left[-\frac{(y'-y_0)^2}{2\sigma_y^2}\right]\cdot$$
$$\left[\exp\left(-\frac{(Z+h)^2}{2\sigma_y^2}\right)+\exp\left(-\frac{(Z-h)^2}{2\sigma_z^2}\right)\right]dy' \quad (\theta=90^\circ) \quad \cdots\cdots(8)$$

此處h是表示排放源離地面的高度。y_L表示線源對接收點有影響的下方y座標值。y_u表示線源對接收點有影響的上方y座標值。對於線源濃度污染，經常以地面上的污染濃度最值得重視，因此，只要令Z＝0所求得的，即爲地面濃度（Ground-Level Concentration），可分別由下二式得之：

$$C_i(x,y,o)=\int_{x_L}^{x_u}\frac{Q_{Li}}{\pi\bar{U}\sigma_y\sigma_z\cos\theta}\exp\left[-\frac{((x_0-x')\tan\theta)^2}{2\sigma_y^2}+\frac{(h)^2}{2\sigma_z^2}\right]dx'$$
$$(\theta\neq 90^\circ) \quad \cdots\cdots(9)$$

或

$$C_i(x,y,0)=\int_{Y_L}^{Y_u}\frac{Q_{Li}}{\pi\bar{U}\sigma_y\sigma_z}\exp\left[-\frac{(y'-y_0)^2}{2\sigma_y^2}+\frac{(h)^2}{2\sigma_z^2}\right]dy' \quad (\theta=90^\circ) \quad \cdots\cdots(10)$$

很顯然的，污染物會在垂直於風向的方向上擴散。但是高斯煙柱模式至少有三項不得忽視的缺點，使它在應用於一般移散模式時受到限制。這三項缺點爲：

(1)無法適當說明經過一段時間後，污染物在大氣中的有效累積情形。

(2)在大空間尺度時，對於長範圍（long-range）作用下，紊亂擴散比起移流擴散將成爲微不足道。

(3)無法說明因各種化學反應存在時，各種污染物間的交互作用。

爲了解決高斯煙柱模式的不足，於是箱模式理論便應運而生[13]。

三箱模式

最早的箱模式理論是由Smith[18]所提出，用以說明非穩定（unsteady）污染物在都市中的累積效應。基本上，它是假設污染物在箱中迅速且均質（homogeneous）的混合。箱的體積是由都市的表面積和混合層高度而決定，然後將箱空間中的均勻（uniform）污染物，以一常微分方程式來表示濃度的變化情形，這時濃度會受移流、化學反

應和降雨的影響而改變。此均質混合的假設，有效解決了箱中紊流混合的問題，但是却無法顧及垂直方向濃度分佈的實際情形，如此將會造成較大誤差。針對這項缺點，Reiquam[19]、Seinfeld 和Mac Cracken et. al. 等人士提出了更進一步的箱模式，那就是把空間劃分成許許多多的小箱子，來解決不同濃度的分佈問題。其基本假設爲：

①污染物一旦進入箱中，能迅速且均勻的混合。

②箱中污染物濃度爲排放進入、移流和化學反應間的變數。

③忽略壁間的擴散作用。

箱模式的發展，彌補了高斯煙柱模式的不足，但是如何選擇合理的箱體積才能確實表示出擴散和化學反應的作用呢？

四可變體積分佈反應器理論（ VVBR ）[6]

所謂VVBR 理論（ Variable Volume Batch Reactor ），簡單的說就是假想將污染質放在體積能變化的反應器內，由擴散作用所引起污染質濃度的減小，可利用反應器體積作相對程度的擴大來模擬，而污染物的化學反應，就可視爲在此逐漸膨脹的虛構反應器內進行。假使暫時不考慮化學反應時，根據質量不滅定律：

$$C_i = \frac{AQ_i}{\bar{z}^3}$$

其中Q_i 爲 i 種污染物的排放量，A爲常數，$\bar{z}$ 爲反應器的長度，將隨時間的增加而增大，相反的，濃度C_i 將隨$\bar{z}$ 的增大而減小。這種觀念極具價值，但是它在求取反應器的體積變化與擴散速率間關係時，並沒有成功。不過VVBR的觀念却導致了環理論（ Ring Concept ）的產生[20]。

五環理論

環理論是由點源的煙柱擴散而發展出來的，將排放煙柱的橫截面上，劃分成許多的同心圓或橢圓，每二條分隔線間所圍成的區域，即爲每一環的面積。此面積大小分隔的決定，是將此橫截面的污染質作等量的分配，換句話說，於每一環中的污染質，其量相當於其他各環的污染量。因爲排放濃度在每一橫截面上，並不呈均勻狀態，而是以高斯分佈爲主，濃度的擴散以主軸最高，因此所區分出每環的面積並不相同。面積的大小，和所欲區分的環數N有關，與離排放源 x 軸的距離和 y 、 z 方向的擴散係數也有關。對於地面上的線源，則以 z 軸作爲每格的基本，利用 X－Y 平面，將 z 方向劃分成許多平行區間（ 見圖二 ），每一區間中，含有等量污染質。

環理論有幾項基本的假設：

1. 在每個環中污染物濃度相同。
2. 劃分等量污染質的區域時，是不考慮化學反應的情況下。
3. 因各環面積不同，相連兩環濃度爲不連續。
4. 當 x 增加時，因擴散作用而使環面積相對的擴大。

綜合環理論和箱模式的特性而導出推廣環理論的擴散模式[6]。

六推廣環理論的擴散模式

根據箱模式把擴散空間分格成許多小格子，每個小格子體積依 x 軸距離的增長而加大，此即推廣環理論。它充分表現了擴散的特性。對於線源，每一格的體積，除了 z 方向污染量分層外，y 方向因爲相同排放强度線源，通常以單位長度做爲區分，x 方向則視需要或誤差限度而定。則每單位長度層區域所含有污染物總量（ $\theta = 90°$ 時 ）爲

$$\int_{z_{ns-1}}^{z_{ns}} \bar{U}\,\bar{C}_i\,dz = \frac{Q_{Li}}{N} \qquad \cdots\cdots(12)$$

其中N表示總共區分的層數，Z_{ns} 表示第 ns 層的高度，Q_{Li} 表單位長度的線源排放强度。將式(8)代入(12)得

$$\int_{z_{ns-1}}^{z_{ns}} \bar{U} \int_{Y_L}^{Y_u} \frac{Q_{Li}}{2\pi\bar{U}\sigma_y\sigma_z} \exp\left[-\frac{(y')^2}{2\sigma_y^2}\right] \cdot \left[\exp\left(-\frac{(Z+h)^2}{2\sigma_y^2}\right) + \exp\left(-\frac{(Z-h)^2}{2\sigma_y^2}\right)\right] dy'dz = \frac{Q_{Li}}{N} \qquad \cdots\cdots(13)$$

同理，當 $\theta \neq 90°$ 時，每單位長度層區域含有污染物量爲：

$$\int_{z_{ns-1}}^{z_{ns}} \overline{U C_i}\,dz = \frac{Q_{Li}}{N\sin\theta} \qquad \cdots\cdots(14)$$

將式(7)代入(14)得

$$\int_{z_{ns-1}}^{z_{ns}} \bar{U} \int_{x_L}^{x_U} \frac{Q_{Li}}{2\pi\bar{U}\sigma_y\sigma_z\cos\theta} \exp\left[-\frac{((X_0 - X')\tan\theta)^2}{2\sigma_y^2}\right] \cdot \left[\exp\left(-\frac{(Z+h)^2}{2\sigma_z^2}\right) + \exp\left(-\frac{(Z-h)^2}{2\sigma_z^2}\right)\right] dx'dz = \frac{Q_{Li}}{N\sin\theta} \qquad \cdots\cdots(15)$$

在(12)～(15)式中 $\int_{z_{ns-1}}^{z_{ns}} \bar{U}\,dZ$ 的值，即爲每格的體積。層區域的區分由地表開始（ $Z_0 = 0$ ），式(13)、(15)可分別寫成：

$\theta = 90°$

$$\int_0^{Z_1} \left\{ \int_{Y_L}^{Y_u} \frac{1}{2\pi\bar{U}\sigma_y\sigma_z} \exp\left[-\frac{(y')^2}{2\sigma_y^2}\right] \cdot \left[\exp\left(-\frac{(z+h)^2}{2\sigma_y^2}\right) + \exp\left(-\frac{(Z-h)^2}{2\sigma_z^2}\right)\right] \cdot dy' \right\} dz = \frac{1}{N} \qquad \cdots\cdots(16)$$

$\theta \neq 90°$

$$\int_0^{Z_1} \bar{U} \left\{ \int_{x_L}^{x_U} \frac{1}{2\pi\bar{U}\sigma_y\sigma_z\cos\theta} \exp\left[-\frac{((X_0 - X')\tan\theta)^2}{2\sigma_y^2}\right] \cdot \right.$$

$$\left[\exp\left(-\frac{(Z+h)^2}{2\sigma_z^2}\right)+\exp\left(-\frac{(Z-h)^2}{2\sigma_z^2}\right)\right]\cdot dX'\Big\}dz$$

$$=\frac{1}{N\sin\theta} \qquad \cdots\cdots(17)$$

理論上由(16)、(17)兩式，可積分而解得 Z_1 的值，Z_1 值解出後，利用 $\int_0^{Z_1}\bar{U}\,dz$ 能求出連接地面的第一格其體積大小。將 z 軸分成許多高度極小的區域代入式(7)或式(8)中，算出各高度的濃度，再將各濃度乘以本身所代表極小區間的體積，可求出每極小區間中污染物的含有量，然後由下向上依序累加，直到所欲分得的 Q_{Li}/N（$\theta=90°$）或 $Q_{Li}/N\cdot\sin\theta$（$\theta\neq 90°$）爲止，如此次第累加，將可得到各層的高度。因濃度依 X 軸的延長而減小，在不同 x 點所得到的層高不同，且隨 x 軸增大而增大。其所涵蓋的體積，視爲 X－Z 二方向圍成的梯形和單位 Y 所構成的範圍，見圖三。其式如下：

$$V=\left[\left(Z^j_{ns}-Z^j_{ns-1}\right)+\left(Z^{j-1}_{ns}-Z^{j-1}_{ns-1}\right)\right]\times\left(X_j-X_{j-1}\right)/2 \qquad \cdots\cdots(18)$$

j 表 x 方向的分格代號

至此，由擴散所造成的影響，已由體積的變化取而代之。並且大氣中已存在的污染物，也可以和煙柱混合後，加入其中反應(7)(21)。這就是巢理論的基礎(12)。

七、巢理論

除了環理論的一些假設條件外，巢理論中必有二點基本假設：

1. 大氣中本身污染物能均勻分佈，並且能和煙柱中的污染物接觸，而以相同的速率進行化學反應。
2. 凡是參與化學反應的污染物，不論是否爲排放源所排放的，皆列入考慮。

大氣污染物儘管能與煙柱污染物紊亂混合，而進行化學反應，但是大氣污染物却沒有擴散因素的介入，因此這二種不同來源的污染質，在觀念上，仍然需要加以區分。也就是說，各個巢格子內部的化學反應，由大氣和煙柱的污染物同時參與，但是因爲大氣污染物的濃度並不擴散，故在巢與巢的交界處，應不斷地有大氣污染物補充。

對於固定的第 ns 區，$D^j_{i,ns}(X)$ 表示第 j 巢在 x 位置（$X_{j-1}\leq X\leq X_j$）所含有第 i 種污染物的總量，$C_{i,ns,b}$ 表示在 X 處 i 種污染物的濃度，則在 j－1 巢交界處（$X=X_{j-1}$），$D^{j-1}_{i,ns}(t_{j-1})$ 與 $D^j_{i,ns}(t_{j-1})$ 的關係爲：（參看圖四）

$$D^j_{i,ns}(t_{j-1})=D^{j-1}_{i,ns}(t_{j-1})+w\times C_{i,ns,b,x_{j-1}}\times\left(V_{ns,j}-V_{ns,j-1}\right) \qquad \cdots\cdots(19)$$

而 $D^j_{i,ns}(X)$ 的起始值爲：

$$D^j_{i,ns}(t_0)=\left(C_{i,ns,o}+WC_{i,ns,b,o}\right)\times V_{ns,1} \qquad \cdots\cdots(20)$$

其中 W 表示排放源與大氣混合程度的參數，（$0\leq W\leq 1$）。$V_{ns,j}$ 表第 j 巢的體積，

$C_{i,ns,j}$ 表示在 X_j 處的濃度值。則 $D^j_{i,ns}(X)$ 在 j 盒內因化學反應所引起的變化，可以由下式求得：

$$\frac{dD^j_{i,ns}(X)}{dt}=V_{ns,j}R_i \qquad \cdots\cdots(21)$$

$$C_{i,ns,t,j}=\frac{D^j_{i,ns}(X)}{V_{ns,j}}+(1-W)C_{i,ns,b,j} \qquad \cdots\cdots(22)$$

$C_{i,ns,t,j}$ 爲 ns 區域中，大氣與煙柱的污染總濃度。當 W＝0 時，巢理論將簡化爲推廣環理論。

在模式的建立過程中，巢體體積的計算，和光化學反應作用，被視爲二種完全獨立的過程。擴散所造成濃度減少的特性，用相對的體積增大來表示，已在前面敍述過，至於化學反應的計算也將於下節作一說明。

八、化學反應的計算(22)

以表一爲例，這一系列的反應中，各污染物濃度隨時間而變化，因此可以將各污染物的濃度變化寫成系列聯立常微分方程式：

$$\frac{dC_{NO_2}}{dt}=-P_1+P_3+P_6-P_8$$

$$\frac{dC_{NO}}{dt}=P_1-P_3-P_6$$

$$\frac{dC_{O_3}}{dt}=P_2-P_3-P_5+0.5P_7$$

$$\frac{dC_{O_2}}{dt}=-P_2+P_3-P_7$$

$$\frac{dC_{C_4H_8}}{dt}=-P_4-P_5$$

$$\frac{dC_{RCO_X}}{dt}=2.5P_4+2.5P_5-P_6-P_7-P_8$$

$$\frac{dC_{ALD}}{dt}=0.12P_4+0.12P_5$$

$$\frac{dC_{PAN}}{dt}=0.67P_8$$

其中 $P_1=\alpha_1C_{NO_2}$，$P_2=\alpha_2C_OC_{O_2}C_M$，$P_3=\alpha_3C_{O_3}C_{NO}$，$P_4=\alpha_4C_OC_{C_4H_8}$，$P_5=\alpha_5C_{O_3}C_{C_4H_8}$，$P_6=\alpha_6C_{RCO_X}C_{NO}$，$P_7=\alpha_7C_{RCO_X}C_{O_2}$，$P_8=\alpha_8C_{RCO_X}C_{NO_2}$，

α 爲化學反應速率 ……(24)

這最重要的 NO_2，NO，O_3 光化學反應循環中(23)(24)

$$NO_2 + h\nu \xrightarrow{1} NO + O$$
$$O + O_2 + M \xrightarrow{2} O_3 + M \qquad \cdots\cdots(25)$$
$$O_3 + NO \xrightarrow{3} NO_2 + O_2$$

$$\frac{dC_O}{dt} = K_1 C_{NO_2} - K_2 C_O C_{O_2} C_M \qquad \cdots\cdots(26)$$

若將(26)式的等號右方做數值上的估計，其值將非常趨近於 0，在物理意義上，反應 1 中氧原子的產生和反應 2 中氧原子的消耗量幾乎相等，因此習慣上將氧原子的濃度視爲定值，不隨時間而變，此稱爲穩定近似（ Steady-State Approximation ）。

同樣的在此處的光化學反應模式中，也採用穩定近似的假設：

$$\frac{dC_O}{dt} = P_1 - P_2 - P_4 = 0$$

即
$$C_O = \frac{\alpha_1 C_{NO_2}}{\alpha_2 C_{O_2} C_M + \alpha_4 C_{C_4H_8}}$$

在每一巢體積中氧原子的濃度不隨時間而變化。但巢與巢的比較，氧原子濃度則未必相同。

利用數值方法，求解聯立方程式[23]，可得到各種污染物經化學反應後的濃度。

九、模式的建立

模式的建立分爲二部份，第一部分求出巢體積。此巢體積隨著距離的增加而增加，將擴散濃度減小的特性，以巢體增大來代表。第二部分考慮巢內的化學反應。每個巢體視爲獨立的作用空間，化學反應在其中進行，污染物間濃度相互影響發生變化。

巢體積的計算，由於線源對接收點的影響範圍有限，式(7)、(8)中 X_L ，X_U 及 Y_L ，Y_U 的決定是以接收點向線源展開上下各 22.5° 的延伸線交點爲範圍。當線源和風向間夾角 θ 小於 22.5° 時，延伸線和線源將不會相交，使線源積分由負無窮大至 X_U 或 Y_U，爲減少計算上的困擾，當夾角小於或等於 30° 時，影響範圍下方 X_L 即以 30° 時計算的 X_L 長度爲主。選擇影響範圍之後，因式(13)或(15)的計算過於複雜，無法直接由數值方法求出 Z_{ns} 高度，所以自 $Z = 0$ 開始，先將 z 方向空間劃分成更細小的層區，計算每一層區的污染物量，再以式(14)或(12)判斷，累加各小層區污染物量，直到 Q_{Li}/N 或 $Q_{Li}/N \cdot \sin\theta$ 爲止的 Z 高度即爲 Z_1 ，依次類推求 $Z_2 \cdots Z_{ns}$ 高。層區高度求出後，以式(18)作爲基本計算各巢體積。式(13)、(15)中 σ_y 、σ_z 表示污染物在和風向呈直交的水平、垂直濃度擴散的標準偏差，其值和下風距離 x 有關，此處根據 P－G 曲線求取。污染物濃度以高斯求積法計算（ Gaussian Quaduature ）[24]，先將積分式做變數轉換，使積分區間成爲 -1 到 $+1$，然後在其中選定適當的節點，予以加權計算，此法既簡單又準確，但是當積分區間逐漸增長時，所取的節點數必須相對增加，否則誤差值將會跟著加大，表七爲各種穩定度情況下，節點數 n 和距離的關係。

模式中將空間劃分成許多小格，由於將連續空間改爲不連續空間，其中可能會引起相當的誤差。對於 $j-1$ 巢，當 $x = x_{j-1}$ 時(22)式成爲：

$$C^{j-1}_{i,ns,t} = \frac{D^{j-1}_{i,ns}(x_{j-1})}{\bar{V}_{ns,j-1}} + (1-W) \times C^{j-1}_{i,ns,b} \qquad \cdots\cdots(27)$$

對於 j 巢，當 $x = x_{j-1}$ 時(22)式成爲：

$$C^{j}_{i,ns,t} = \frac{D^{j}_{i,ns}(x_{j-1})}{\bar{V}_{ns,i}} + (1-W) \times C^{j-1}_{i,ns,b} \qquad \cdots\cdots(28)$$

理論上，同樣在 $x = x_{j-1}$ 處(27)應等於(28)，但實際上將二式相減得：

$$\triangle C^{j}_{i,t,ns} = \frac{D^{j}_{i,ns}(x_{j-1})}{\bar{V}_{ns,j}} - \frac{D^{j-1}_{i,ns}(x_{j-1})}{\bar{V}_{ns,j-1}} \qquad \cdots\cdots(29)$$

則 $\triangle C^{j}_{i,nn}$ 表示二者的誤差。將式(19)代入上式，則：

$$\triangle C^{j}_{i,t,ns} = \left[\frac{D^{j-1}_{i,ns}(x_{j-1})}{\bar{V}_{ns,j}} + W C^{j-1}_{i,ns,b}\left(1 - \frac{\bar{V}_{ns,j-1}}{\bar{V}_{ns,j}}\right)\right] - \frac{D^{j-1}_{i,ns}(x_{j-1})}{\bar{V}_{ns,j-1}}$$

$$= \left[W C^{j-1}_{i,ns,b} - \frac{D^{j-1}_{i,ns}(x_{j-1})}{\bar{V}_{ns,j-1}}\right]\left(1 - \frac{\bar{V}_{ns,j-1}}{\bar{V}_{ns,j}}\right)$$

$$= C^{j-1}_{i,ns}\left(\frac{\bar{V}_{ns,j-1}}{\bar{V}_{ns,j}} - 1\right) \qquad \cdots\cdots$$

由(30)可知，$\triangle C^{j}_{i,ns,t}$ 直接與 $\bar{V}_{ns,j-1}/\bar{V}_{ns,j}$ 有關，當 $\bar{V}_{ns,j-1} = \bar{V}_{ns,j}$ 時 $\triangle C^{j}_{i,ns,t} = 0$ 因此對相鄰兩巢的體積比，應控制在一定的程度下，以減少誤差。

參、模式的應用

本線源是以台灣南北高速公路爲模擬對象，高速公路由基隆起至高雄端，全長三百七十三點二四公里，道路二旁的地形，自北而南由丘陵起伏漸趨於平坦。爲有效配合模式的特性，選擇了桃園交流道至南中壢交流道間一段直線線源爲模擬，此路段附近以遼濶的田野爲主。在桃園交流道和南中壢交流道間，還有機場交流道、內壢交流道和北中壢交流道。由於中正國際機場的存在，桃園交流道至機場交流道間的車輛流量，很明顯的較機場交流道至南中壢交流道要高，因此本區的線源視爲二段強度不同的排放源。第一段爲桃園交流道至機場交流道間長二公里的區域，第二段爲機場交流道至南中壢交流道間長十點四公里的區域。由於只有在收費站處才有交通流量的記錄，因此第一段的流量以泰山收費站的記錄爲代表，第二段的流量以楊梅收費站的記錄代表。

模式資料的分析必需具有(1)氣象條件。(2)車輛流量。(3)排放因子。氣象條件包括風向、風速、大氣穩定度等，用以求得擴散的特性。大氣穩定度是由風向、風速、天頂角、總雲量、相對濕度、氣溫和露點等資料求得。車輛流量是根據泰山、楊梅收費站的記錄值。由於記錄值只有大客車、大貨車和輕型車三種，因此車輛種類的區分就分爲此三大類，表十爲交通量。排放因子(emission factor)的計算是根據美國環境保護署在1972曆年(calendar)做全國性調查時，加州的統計和計算法[25] 。排放因子是以車輛行一公里或一英哩所放出的污染物質量爲基本單位。因爲採樣時的氣溫不同，採樣點處的平均車速不同[26] ，所以排放因子會有差異，應予分別計算而得。計算時假設100%熱起動(hot start operation)。排放因子又依車種、柴油或汽油引擎而變化，但是限於資料的不足，此處假設輕型車全部爲汽油引擎，大客車和大貨車全部爲柴油引擎。將排放因子求出後(見表十一)，乘以當天車流量，即可得當天的污染物排放總量，在模式計算時線源污染物排放強度是以 $\mu g/sec\text{-}m$ 爲單位輸入，所以得再將每天排放總量除以86400，而得每秒平均排放量，見表五。

事實上汽車排出碳氫化合物的種類多不勝數，各種類的排出量也無法確定，再加上碳氫化合物的氧化過程非常複雜，因此要想得到確切的化學反應機構，是極爲困難的事。假使在模式建立之初，就以大量化學反應式作爲嘗試，將爲十分不智之舉，本研究以較具代表性的反應爲主，選擇四組基本光化學系列反應，分別予以嘗試(見表一～四)[11][3][27]，模式計算流程圖見圖六。

模式計算時的輸入資料：

1. 高斯求積法節點數n，權數，節點值。
2. 穩定度NS，風向和線源夾角 θ，氣溫T，風速U。
3. 總區分層數N。
4. 欲模擬之層號I。
5. 測點和線源的相對座標。
6. 控制巢體積x方向長度的係數 C_s。
7. 二不同強度排放源的比例QC。
8. 蘭吉固達法中的變幅H。
9. 混合係數W。
10. 排放準強度 Q_i。
11. 背景濃度 C_{ib}。
12. 各污染物的分子量。
13. 化學反應速率常數 α。

各種變數的輸入值列於表六。

四、結果與討論

根據數據組Ⅰ～Ⅳ以及光化學反應組PC-1～PC-4的計算機模擬計算得到：圖八

～圖十四爲數據組Ⅰ的計算結果。圖十五～圖二十一爲數據組Ⅱ的計算結果，圖二十二～圖二十八爲數據組Ⅲ的計算結果，圖二十九～圖三十五爲數據組Ⅳ的計算結果。圖形中若標明PC-n則表示第n組光化學反應。

圖七爲各數據組計算體積比較情形，Ⅳ曲線尾端分成編號爲1、2二條是由於有二段不同强度污染源的結果。當X < 620 m，接收點只受中壢—機場交流道間有限線源單一排放强度影響，但 x ≥ 620 m時，線源上端影響接收點的區域已開始涵蓋排放强度較大的桃園交流道—機場交流道的污染源，接收點的濃度較單一排放時爲高，因此層累積至 Q_L/N 或 $Q_L/N \times \sin\theta$ 的高度較低，使體積也略爲偏低。隨著距離繼續增加，較强污染源的影響增大，體積之間的差異也隨著增大。若以不同數據組體積的比較，理論上應與穩定度有直接關係，穩定度代表大氣紊亂狀況，穩定度愈小，亂流作用愈大，污染擴散情況愈好，也就是愈容易擴散。濃度減低，相對的巢體積則因而增大，所以穩定度由A→F，體積應有減少趨勢。圖七爲不同穩定度情況下，體積的變化情形，證明此項推論的正確。本文中計算影響接收點的線源長度，是以接收點向線源展開上下各22.5°的延伸線交接範圍內，假使線源和風向夾角愈小，影響接收點的線源將愈長，模式建立時線源影響的下方長度以夾角30°作爲限制，此假設經計算，當夾角爲25°時，所造成的誤差在十萬分之四以內，當夾角爲23°時，其誤差在十萬分之八以內，因此基於計算上的方便，當夾角小於或等於30°時。影響接收點的線源由原點以下長度以30°時的長度爲代表，將不會造成嚴重影響。

在體積求算過程中，流量值的輸入應屬不必要，因爲流量和濃度值之間呈正比例現象，求出的濃度作用只在於將它累積到流量的N分之一量(N爲Z方向的分格數)。因此可將流量視爲一定值代入。但是當線源車輛流量受地段影響，會有顯著差異而造成不同强度的排放量，這時各流量間的比例關係必需加以研究，因爲擴散的特性將由體積的大小代表之。此種强度不同的線源，在求取接收點濃度時依流量大小分成數段，各別積分之後累加。流量和流量間有一定比例關係，計算時加入一比例常數校正。此種强度比例校正在排放污染物量爲一定或在不起化學反應情形下，將不會產生任何困擾，但在本研究中以光化學反應爲主，而光化學反應爲一連串的反應，不同二路段間各種污染物排放會有不同的比例，究竟流量校正比例常數應如何選取，必需經由大量實測數據值和多次試誤法，來尋找較爲合理的代表。

濃度計算時以高斯積分法(Gaussian Quadrature)作爲線源的積分計算，高斯積分法的缺點在於係數及函數的幅數通常爲無理數。這在手算時會感到困難，若使用電腦計算，則不會受到影響，因此這項缺點在本模式上可以不必考慮。高斯積分法與使用合成牛頓—寇次(Newton-Cotes)法相比較，高斯公式能以較少的計算而獲得較高的準確度，在程式設計上也較爲簡單，所以本模式中即利用此法來做積分的計算。在排放因子中，NO_x 包括NO及 NO_2，於本模式中，二者皆爲排放源污染物，且視爲二種分別考慮的污染物，在 NO_x 中彼此所佔百分數並沒有明確的分析記錄。同樣的，H.C.是表示總碳氫化合物量，其中種類非常多，至於實際含 C_4H_8 或 C_3H_6 的量也沒有完整記錄。綜合這些不定值，在模式輸入值的選取上必須做多次試驗，以取得統計上的價值。

對於光化學反應方程式的選取，最基本的光分解循環爲式㉖的三項反應，其中M爲第三種介質用以吸收反應的能量，在空氣中M物質可能爲 O_2 或 N_2。根據實驗這三項反應作用非常迅速。若是所有光化學反應都能包括在式㉖中此項假設正確的話，則可推知 NO 、NO_2 、O_3 的濃度將爲定值，反應所產生穩定狀態的 O_3 ，濃度爲初始 NO_2的函數。因此由 NO_2 濃度可算出 O_3 的濃度，再因燃燒過程排入大氣中以 NO 爲主，NO_2 量極微，臭氧濃度應該維持在一定限度之內。然而，事實上 O_3 濃度遠大於此限度，因此可以斷定除式㉖之反應外還有其他反應存在使 NO 氧化成 NO_2 時不消耗 O_3 ，造成 O_3 累積成高濃度，而氮氧化物濃度則逐漸降低，正如大氣中所發生的情形一般。這一點由於碳氫化合物的存在而獲得解決。已存在有相當反應性的氧原子，能打擊碳氫化合物，尤其是穩定性較弱的烯屬烴（ olefin ），使雙鍵斷裂爲二，產生自由基（ free radical），此自由基具有高度反應性，能繼續參與其他的反應。這些有機性自由基與 O_2 形成過氧基（ Reroxy radicals ）能釋出一氧原子而使NO氧化爲 NO_2 ，因而干擾了上述所提及的 NO 、NO_2 、O_3 循環。在烯屬烴參與反應時形成另一種基，可能是醛類，因爲醛類爲氧原子與烯系烴反應所產生生成物的一種。過氧基的旁支反應，可能形成硝基過氧乙醯（PAN），這是一種非常强烈的眼睛刺激劑，對植物會造成傷害。硫化物在光化學煙霧中所扮演的角色，尚未能完全了解，因此在此暫時不予考慮。事實上光化學作用的連鎖反應非常多[27][28]，要推測光化學煙霧反應的模式，非常困難，爲了簡化極大數目可能反應，在複雜項目中僅選取速率較快的反應或較具代表性的反應。反應速率常數曾經多位專家在實驗室中研究並發表於報章雜誌上。本模式中第一組光化學反應，是根據A.Q. Eschenroeder et al.[11] 所做的研究，也就是取上面所述最基本又具代表性的反應爲主。因烯屬烴中以直鏈一二丁烯的活性較其他碳氫化合物爲多，因此以 C_4H_8 爲碳氫化合物的代表。第二組反應式中只將 C_4H_8 以 C_3H_6 取而代之，C_3H_6的氧化系統和空氣污染反應系統也十分接近，和 C_4H_8 比較起來 C_3H_6 的氧化速率較慢，PAN 產生量較少。第三、四組光化學反應是以 Seinfeld[22] 書中所選取化學反應組中具代表性的反應式做爲模擬對象。

模式根據上述資料進行計算機模擬，結果繪製成各種曲線，就第Ⅰ組數據結果顯示，經由PC-1，PC-2所計算出濃度沒有太大差異，而經PC-3，PC-4者除ALD 爲前二組的十倍外，其他濃度也差異有限。就Ⅲ所進行將Z空間分成三種層次：100，50 20 比較濃度計算值，結果三者之間並沒有固定關係存在。

縱觀圖形的趨勢。NO_2因原本就以固定量排入大氣中，排入時本身已到達某種濃度，因此儘管NO作用會增加 NO_2 量，但 NO_2 會進行相當快速光分降作用，形成NO，並產生最後污染物PAN ，在增加或減少總量上仍以減少爲多，因此其進入大氣之後呈現指數性衰減。NO分解爲 NO_2 的速度相當快速，假使 NO_2 排放量爲 0，則若干距離後，NO_2 量會累積至某特定高度，這都由於NO的氧化作用，因此NO 本身量會因快速分解而逐漸減少。O_3 如前所述，將NO氧化爲 NO_2 的速率較過氧基氧化速率慢，因此會逐漸累積，但是因爲擴散作用存在，使濃度的累積到達一定程度後，擴散的影響較化學作用要大，因而又有減小的趨勢。其濃度曲線爲起伏狀，先升後降。C_4H_8 因不停被氧原

子撞擊，形成自由基，又沒有其他的作用產生以增高濃度，因此爲一向下減小曲線。ALD和PAN 由於都是反應組的最後產物，所以濃度會逐漸增加，當增加至某一定程度後也因擴散作用而逐漸減小，如同 O_3 一般；但各污染物累積到何種程度才開始減少，依種類和擴散情況而異。

巢體積變化的限制已在前章敘述過，在愈遠離排放源時巢體積愈大，巢體的決定在 x 軸上的尺度可依距離增長而增加，因爲在近排放源處由於體積本身很小，邊長的尺度稍有變化就會造成無法忽略的影響，而依體積的增大，影響程度減小，因此只要在體積變化能允許的範圍內，隨距離增加將 x 方向尺度擴大，可減少部份計算機使用時間，却不會對結果產生影響。

對於式㉓聯立常微分方程式的求解，是利用四階蘭吉固達法計算（ Fourth - order Runge - Kutta Method ）。每一步驟需要計算 f （ x ，y ）四次，本模式選用蘭吉固達法的原因有：①步驟簡單，計算時只要知道前一點（ x_i ，z_i ）即可。②它的誤差與泰勒級數相合，可以 h^p 表示。③過程中不必計算 f （ x_i ，y_i ）的導數值，僅須重複計算函數 f 值即可。

由體積曲線（圖七）第Ⅳ組數據所計算的巢體積在 620 m處呈現略低的趨勢，在濃度計算上則會有較一般略高的結果（如圖二十九～圖三十五）。

伍、結論與建議

本文將巢理論運用於線源污染擴散上而做光化學模式的設計，經實際在中山高速公路上的模擬，結果能與實際量測值配合，因此模式的推估，仍有其價值存在。對高速公路的污染狀況，以 NO_2爲例，國內規定環境空氣品質爲一小時月平均值爲 0.05 ppm ，而量測結果約爲 0.005 ppm較限值低約一個數量級，污染情形尚不嚴重。但依六十八年至六十九年比較，以泰山收費站記錄結果，車輛增加率小型車約爲 10 %，重型客車爲 3.5 %，重型貨車爲 109 %。增加趨勢值得重視，可能造成的污染問題，應注意及早防範。

模式發展過程中，有幾點尚待改進或值得深入探討之處。第一，x 方向濃度必須由近而遠一個巢一個巢計算而得知，假使欲測數十公里遠處某點，將耗費大量時間計算此點之前的濃度，因此如何簡化過程有再研究的必要。第二，z 方向分層的計算，是先區分成更多更小的層區域，再累加至一定量爲止，假使能由計算中直接求出層區域的高度，可節省許多計算機時間。第三，模式中各輸入值，應加以確認。如排放因子、氣象狀況、不同來源强度間的比例值等，若能確定，計算結果的可信度將大爲提高。第四，採樣數目增加。有足夠採樣值才能驗證模式推估的正確性。第五，污染物量測種類增加。使污染物間化學作用得以證實。經過這些改進模式的彈性和價值將大爲增加。

參考文獻

1. Wanta, R. C., "Meteorology and Air Pollution", Chap, 7, in Air Pollution (A. C. Stern, ed.) Vol. I, 2nd ed. Academic Press, New York, (1976).
2. Graedel, T. E., Farrow, L. A., and Weber, T. A., "Kinetic Studies of the Photechemistry of the Urban Troposphere", Atmos. Envir., 10, 1095-1116, (1976).
3. Atkinson, R., Lloyd, A. C., Winges, L. "An Updated Chemical Mechanism for Hydrocarbon/NOx/SO2 Photooxidations Suitable for Inclusion in Atmospheric Simulation Models", Atmos. Environ. 16, No. 6, 1341-1355, (1982).
4. Zimmerman J. R., and Thompson, R. S. "User's Guide for Highway, A Highway Air Pollution Model", EPA-650/4-74-008, (1975).
5. Dabberdt, W. F., Shelar. E., Marimont, D. and Skinner, G., "Analysis, Experimental Studies, and Evaluations of Control Measures for Air Flow and Air Quality on and Near Highways", FHWA-RD-78-179, (1979).
6. Friendlander, S.K., and Seinfeld, J. H., "A Dynamic Model of Photochemical Smog", Envir. Sci. Tech., 3, 1175-1181, (1969).
7. O'Brein, E. E., "Turbulent Mixing of Two Rapidly Reacting Chemical Species", Phys. Fluids, 14, 1326-1331, (1971).
8. Reynolds, S. D., Roth, P. M., and Seinfeld, J. H. "Mathematical Modeling of Photochemical Air Pollution-I. Formulation of the Model", Atmos. Environ, 7, 1033-1061, (1973).
9. Roth, P. M., Roberts, P. J. W., Lin, M., Reynolds, S. D., and Seinfeld, J. H., "Mathematical Modeling of Photochemical Air Pollution-II. A Model and Inventory of Pollutant Emissions", Atmos. Environ. 8, 97-130, (1974).
10. Reynolds, S. D., Liu, M., Hecht, T. A., Roth, P. M., and Seinfeld, J. H., "Mathematical Modeling of Photochemical Air Pollution. III. Evaluation of the Model", Atmos. Envir, 8, 563-596, (1974).
11. Eschenroeder, A. Q., and Martinzs. J. R., "A Modeling Study to Characterize Photochemical Atmospheric Reactions to the Los Angeles Basin Area', General Research Cooperation, EPA-22-69-127, (1969).
12. 黃賢誠，“多目標式計算空氣污染擴散與化學反應濃度之計算機數學模式”，科學發展月刊，7,1,3-20,(1979)。
13. Calder, K. L., "Eddy Diffusion and Evaporation in Flow Over Aerodynamically Smooth and Rough Surfaces: A Treatment Based on Laboratory Laws of Turbulent Flow with Special Reference to Conditions in the Lower Atmosphere", Q. J. Mech. Appl. Math., 2, 153-176, (1949).
14. Hoffert, M. I., "Atmospheric Transport, Dispersion, and Chemical Reactions in Air Pollution: A Review", AIAA J., 10, 377-387, (1977).
15. Lamb, R. G., and Seinfeld, J. H. "Mathematical Modeling of Urban Air Pollution-General Theory", Envir. Sic. Tech. 7, 253-265, (1973).
16. Sutton, O. G., Micrometeorology, McGraw-Hill, New York, (1953).
17. Green, A. E. S., Singhal, R. P., and Venkateswar, R., "Analytic Extensions of the Gaussian Plume Model", JAPCA, 30, No. 7, 773-776, (1980).
18. Smith, M., "The Concentrations and Residence Times of Pollutants in the Atmosphere", Intercience, New York, 155-166., (1961).
19. Reiquam, H., "Sulfur: Simulated Long-Range Transport in the Atmosphere", Science, 170, 318-320, (1976).
20. Freiberg, J., "The Iron Catalyzed Oxidation of SO2 to Acid Sulphate Mist in Dispersing Plumes", Atmos. Environ. 10, 121-130, (1976).
21. Donaldson, C. du P., and Hilst, G. R., "Effect of Inhomogeneous Mixing on Atmospheric Photochemical Reactions", Envir. Sci. Tech. 6, 812-186, (1972).
22. Seinfeld, J. H., Air Pollution: Physical and Chemical Fundamentals, McGraw-Hill, Inc., (1975).
23. McGraw-Hill, A. J. "Chemistry and Physiology of Los Angeles Smog", Ind. Eng. Chem., 44, 1423-1438, (1952).
24. Gerald, C. F., Applied Numerical Analysis, 2nd ed., Addison-Wesley Publishing Company, (1969).
25. "Compilation of Air Pollutant Emission Factors, 3rd ed. EPA. No. AP-42, (1977).
26. 七十一年度高速公路交通動態資料調查報告，高速公路局，(1982)。
27. Cocks, A. T., and Fletcher, I. S., "Possible Effects of Dispersion on the Gas Phase Chemistry of Power Plant Effluents", Atmos. Environ. 16, No. 4, 667-678, (1982).
28. Augustsson, T. R., "The Effects of Isotropic Multiple Scattering and Surface Albedo on the Photochemistry of the Troposhere", Atmos. Environ. 16, No. 6, 1373-1380, (1982).

表一　第一組光學化學反應（PC-1）

此爲最基本的光化學反應式，H.C.是以C_4H_6的狀態排出

編號	反　　應	反應速率常數
1	$NO_2 + h\nu \rightarrow NO + O$	$0.072 \sim 0.05$ min^{-1}
2	$O + O_2 + M \rightarrow O_3 + M$	1.32×10^{-5} $ppm^{-2}min^{-1}$
3	$O_3 + NO \rightarrow NO_2 + O_2$	21.8 $ppm^{-1}min^{-1}$
4	$O + C_4H_8 \rightarrow 2.5RCO_x + 0.12ALD$	1.11×10^{-5} $ppm^{-1}min^{-1}$
5	$O_3 + C_4H_8 \rightarrow 2.5RCO_x + 0.12ALD$	6×10^{-1} $ppm^{-1}min^{-1}$
6	$RCO_x + NO \rightarrow NO_2$	50 $ppm^{-1}min^{-1}$
7	$RCO_x + O_2 \rightarrow 0.5\ O_3$	5×10^{-6} $ppm^{-1}min^{-1}$
8	$RCO_x + NO_2 \rightarrow 0.67$ PAN	6 $ppm^{-1}min^{-1}$

表二　第二組化學反應（PC-2）

假設H.C.是以C_3H_6的形式排出，所造成反應的變化。

編號	反　　應	反應速率常數
1	$NO_2 + h\nu \rightarrow NO + O$	0.4 min^{-1}
2	$O + O_2 + M \rightarrow O_3 + M$	1.32×10^{-5} $ppm^{-2}min^{-1}$
3	$O_3 + NO \rightarrow NO_2 + O_2$	21.8 $ppm^{-1}min^{-1}$
4	$O + C_3H_6 \rightarrow 2.5RCO_X + ALD$	4.97×10^{4} $ppm^{-1}min^{-1}$
5	$O_3 + C_3H_6 \rightarrow 2.5RCO_x + ALD$	1.8×10^{-1} $ppm^{-1}min^{-1}$
6	$RCO_x + NO \rightarrow NO_2$	50 $ppm^{-1}min^{-1}$
7	$RCO_x + O_2 \rightarrow 0.5O_3$	2.3×10^{-5} $ppm^{-1}min^{-1}$
8	$RCO_x + NO_2 \rightarrow 0.67PAN$	6 $ppm^{-1}min^{-1}$

表三　第三組光化學反應（PC-3）。此處存在NO_2和O_3之直接反應，且考慮N_2O_5的形成和對反應過程的影響。

編號	反　　應	反應速率常數
1	$NO_2 + h\nu \rightarrow NO + O$	$0.072 \sim 0.05$ min^{-1}
2	$O + O_2 + M \rightarrow O_3 + M$	1.32×10^{-5} $ppm^{-2}min^{-1}$
3	$O_3 + NO \rightarrow NO_2 + O_2$	21.8 $ppm^{-1}min^{-1}$
4	$O + C_4H_8 \rightarrow 2.5RCO_x + 0.12ALD$	1.11×10^{5} $ppm^{-1}min^{-1}$
5	$O_3 + C_4H_8 \rightarrow 2.5RCO_X + 0.12ALD$	6×10^{-1} $ppm^{-1}min^{-1}$
6	$RCO_X + NO \rightarrow NO_2$	50 $ppm^{-1}min^{-1}$
7	$RCO_X + O_2 \rightarrow 0.5O_3$	5×10^{-6} $ppm^{-1}min^{-1}$
8	$RCO_X + NO_2 \rightarrow 0.67PAN$	6 $ppm^{-1}min^{-1}$
9	$NO_2 + O_3 \rightarrow NO_3$	5.017×10^{-2} $ppm^{-1}min^{-1}$
10	$NO + NO_3 \rightarrow N_2O_5$	2640 $ppm^{-1}min^{-1}$
11	$N_2O_5 \rightarrow NO_2 + NO_3$	5.847 $ppm^{-1}min^{-1}$
12	$NO_3 + NO \rightarrow 2NO_2$	2.8×10^{5} $ppm^{-1}min^{-1}$

表四　第四組光化學反應（PC-4）。同表三但忽略N_2O_5的作用。

編號	反　　應	反應速率常數
1	$NO_2 + h\nu \rightarrow NO + O$	$0.072 \sim 0.05$ min^{-5}
2	$O + O_2 + M \rightarrow O_3 + M$	1.32×10^{-5} $ppm^{-2}min^{-1}$
3	$O_3 + NO \rightarrow NO_2 + O_2$	21.8 $ppm^{-1}min^{-1}$
4	$O + C_4H_8 \rightarrow 2.5RCO_X + 0.12ALD$	1.11×10^{5} $ppm^{-1}min^{-1}$
5	$O_3 + C_4H_8 \rightarrow 2.5RCO_X + 0.12ALD$	6×10^{-1} $ppm^{-1}min^{-1}$
6	$RCO_X + NO \rightarrow NO_2$	50 $ppm^{-1}min^{-1}$
7	$RCO_X + O_2 \rightarrow 0.5O_3$	5×10^{-6} $ppm^{-1}min^{-1}$
8	$RCO_X + NO_2 \rightarrow 0.67PAN$	6 $ppm^{-1}min^{-1}$
9	$NO_2 + O_3 \rightarrow NO_3$	5.017×10^{-2} $ppm^{-1}min^{-1}$
10	$NO_3 + NO \rightarrow 2NO_2$	2.8×10^{5} $ppm^{-1}min^{-1}$

表五　桃園交流道至機場交流道及機場交流道中至中壢交流道間高速公路污染物排放量（單位$\mu g/m\text{-}sec$）。

	2月22日		4月15日		4月16日	
	H.C.	NO_X	H.C.	NO_X	C.H.	NO_X
泰山	2,200	4,106	1,730	5,240	2,250	5,120
楊梅	-	-	1,133	4,310	1,570	4,290

表六　模式計算時的輸入資料（取表九中第4、5、6、8四組）。

項目 \ 組別		I	II	III	IV
高斯積分法選取點數	n	8	12	20	20
穩定度	NS	2	3	5	4
風向與線源夾角	θ	30	60	30	30
氣　溫	T	29	28	27	20
風　速	U	9	9	7	8
巢體長度控制係數	C_s	0.05	0.05	0.05	0.05
不同污染强度比例值	QC	1.2	1.2	1.2	1.2
蘭吉固達法增加係數	H	0.0025	0.0025	0.0025	0.0025
污染源與背景污染物混合係數	W	1	1	1	1
NO_2排放量	Q_{NO2}	300	700	300	300
NO排放量	Q_{NO}	1,200	2,000	1,200	1,000
H.C.排放量	$Q_{H\ C}$	400	400	400	450

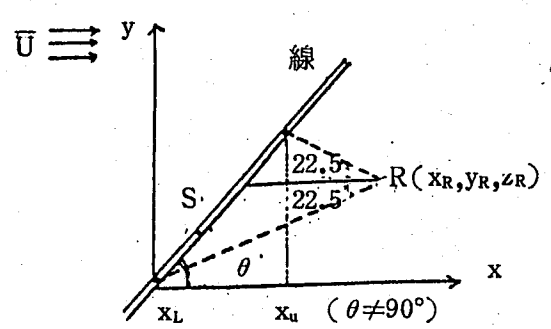

圖一　線源和風向夾角爲 θ（$\theta \neq 90°$），影響接收點的線源投影於 x 軸的長度爲 $x_L x_U$ 線段 R（x_R, y_R, z_R）爲接收點。S（$x^1, y^1, 0$）爲有限線源中任意點。

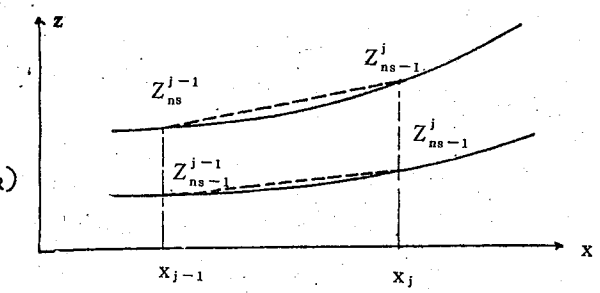

圖三　第 ns 個巢體積在 t_{j-1} 至 t_j 時爲 x－z 上的梯形面積（Z^{j-1}_{ns-1} Z^{j}_{ns-1} Z^{j}_{ns} Z^{j-1}_{ns}）和單位 y 長所圍成的範圍。

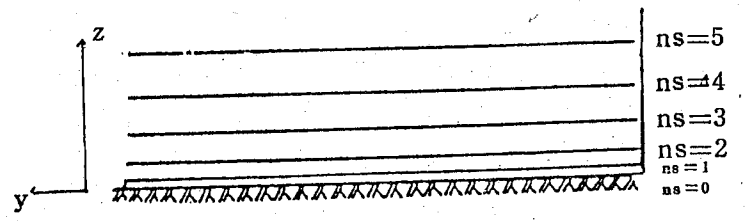

圖二　線源排放，與風向垂直的橫截面面上分成等污染物量的層區域

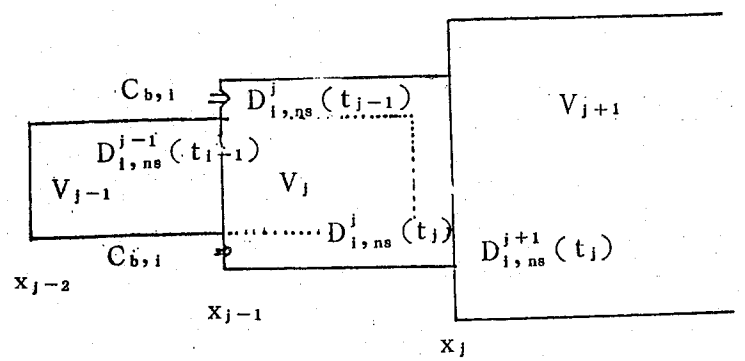

圖四　巢與巢的交界處二端，理論上污染物量會相同，但因背景濃度的加入，使結果並不相同。V_j 表示在 t 時之巢體積。$C_{b,i}$ 爲第 i 種污染物之背景濃度。x_j 爲 t_j 時之 x 軸向位置點。$D^{j}_{i,ns}(t_j)$ 和 $D^{j+1}_{i,ns}(t_j)$ 分別表示在 x_j 點區分成的左右二巢中接近 x_j 處，第 i 種污染物在第 ns 層區中的污染物總量。

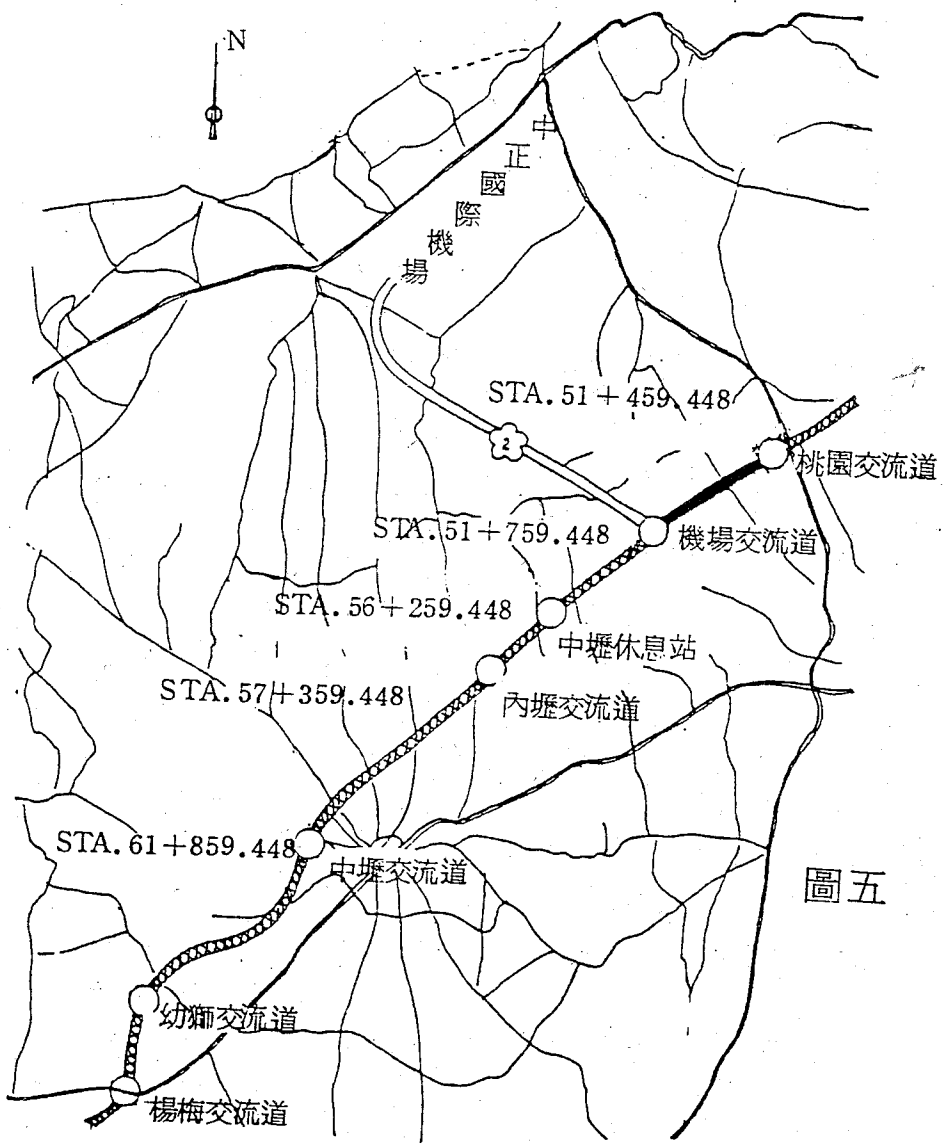

圖五

圖五　高速公路桃園交流道至楊梅交流道平面圖。此段可視爲直線線源，因排放强度不同，以機場交流道劃分成二段强度源。

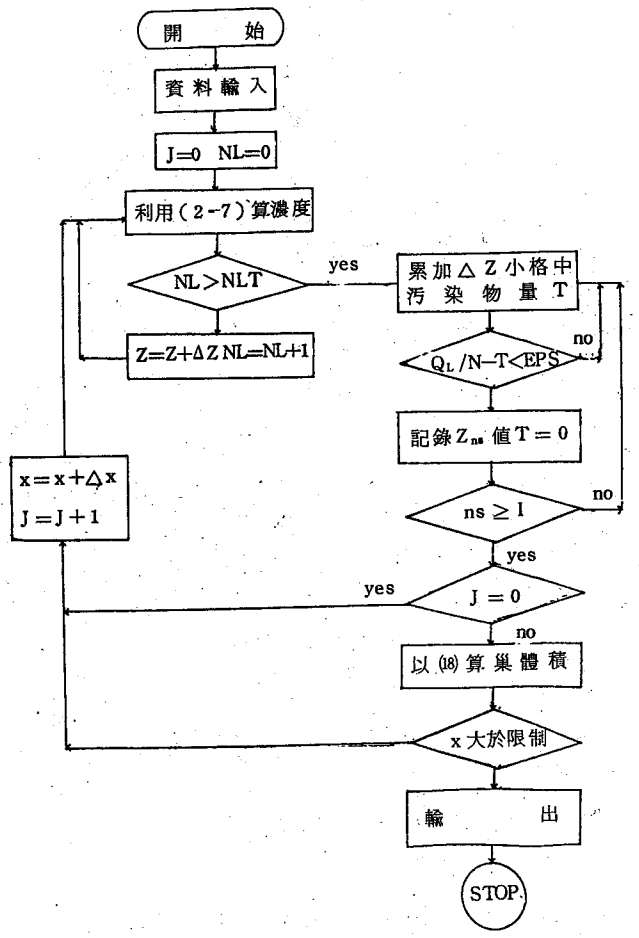

圖六 (a)體積計算流程圖

*NLT為預定計算的極小區域總數，EPS為誤差容許限度，I為欲模擬的層號，Z_{ns}為層ns 頂離地面高度，J為x方向分格數，△Z為Z方向之增加量。

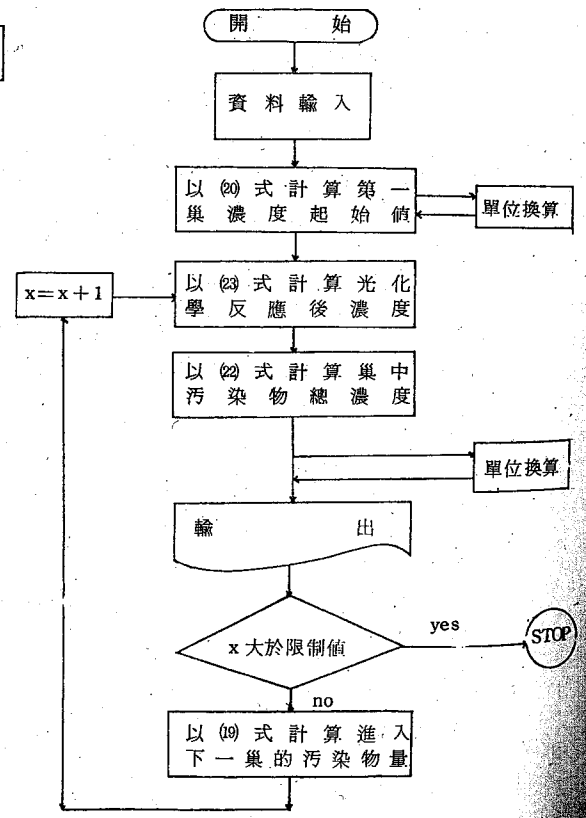

圖六 (b)進行光化學反應流程圖

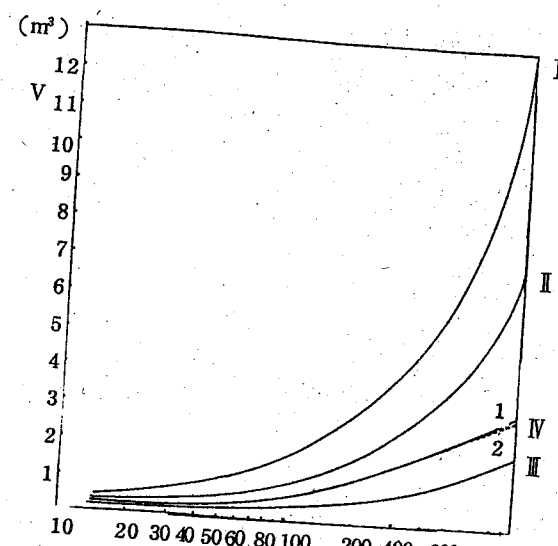

圖七 各數據組所計算巢體積和距離的關係。I為穩定度B級線源與風向之夾角30°。Ⅱ為C級穩定度，夾角60°。Ⅲ為E級穩定度，夾角30°。Ⅳ為D級穩定度，夾角30°。Ⅳ中實線表單一強度線源結果，虛線表620 m處起受強度較強線源加入影響，使濃度增加，體積減少。體積都由近而遠漸次增加。

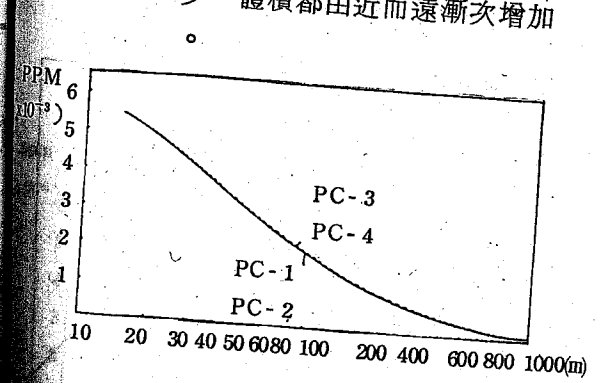

圖八 模式計算個案（見表九）第一組情況下，NO_2濃度隨距離變化的情形。實線表第一、二組光化學反應濃度變化情形，虛線表第三、四組情形。

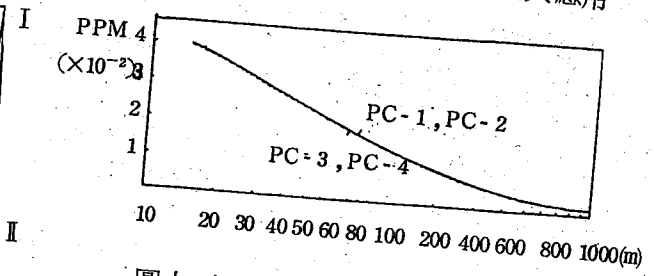

圖九 同圖十七唯係NO 濃度。採樣值和模式計算值間有4%的誤差。光化反應組1，2較3，4計算結果略大。

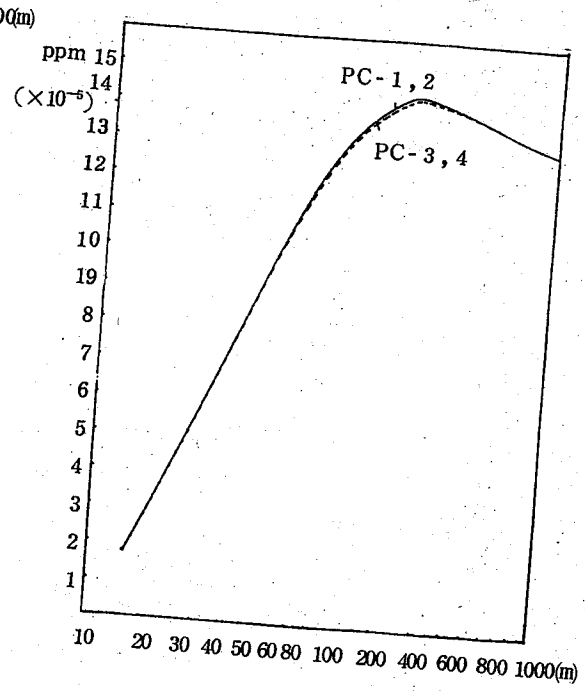

圖十 同圖十七唯係O_3 濃度。在220公尺遠處產生最大值後開始下降。光化學反應1，2組較3，4組在最大值附近，濃度稍大。

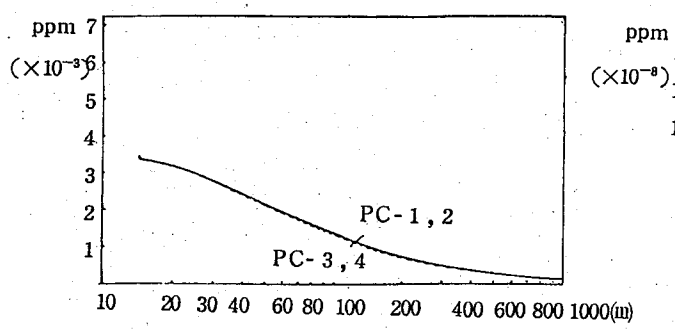

圖十一　同圖十七唯係C_4H_8 濃度。光化反應組 1，2較 3，4 計算濃度稍大。

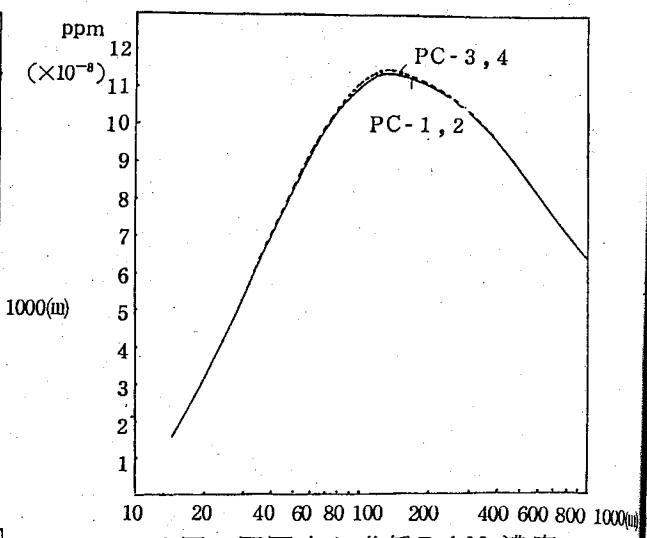

圖十四　同圖十七唯係PAN 濃度。約在 120 m處產生最大值，光化反應組 1，2 比 3，4 略小。

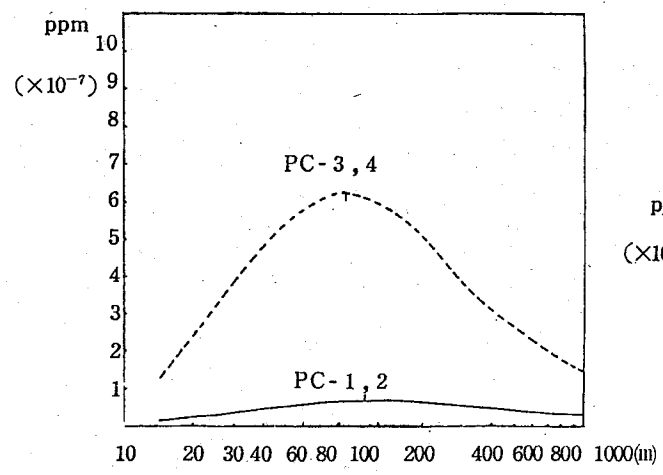

圖十二　同圖十七唯係ALD 濃度。光化反應組 1，2 約比 3，4 濃度小近一個數量級。前者最大濃度約在 130 m處。後者最大濃度約在 90m處。

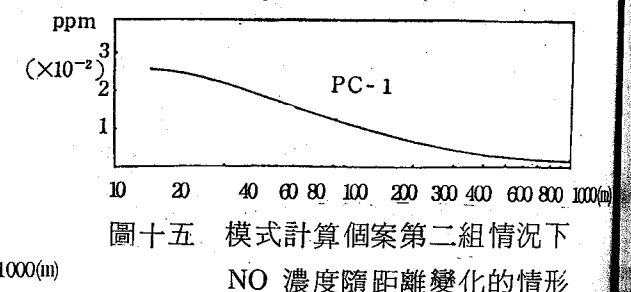

圖十五　模式計算個案第二組情況下 NO 濃度隨距離變化的情形（Ⅱ）。

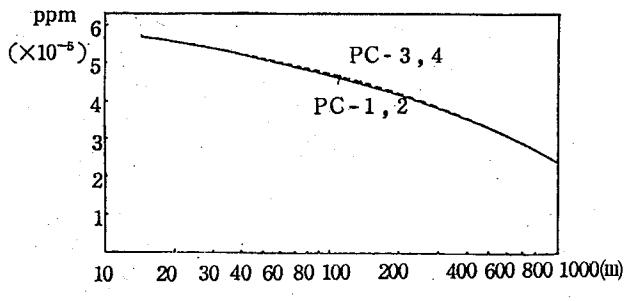

圖十三　同圖十七唯係RCO_X 濃度。光化反應組 1，2 比 3，4 略小。

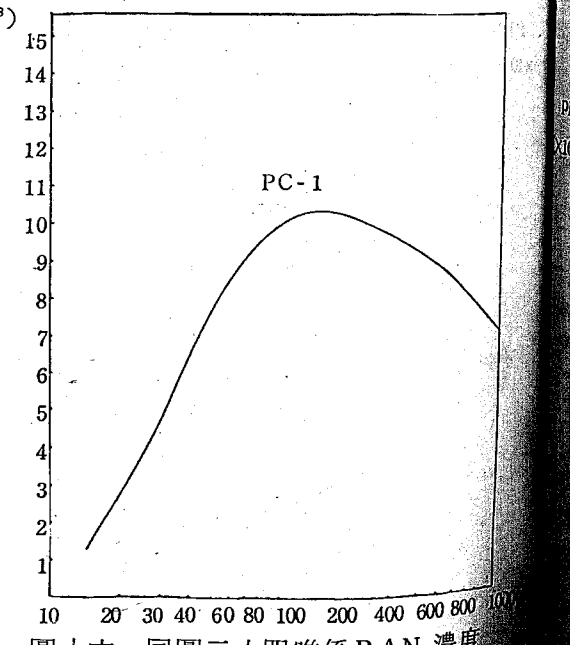

圖十六　同圖二十四唯係PAN 濃度。約在 160 m處產生最大值

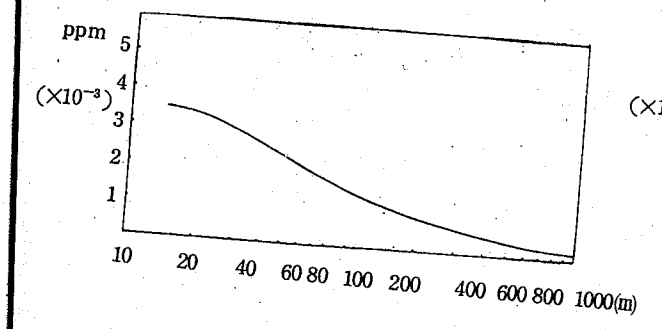

圖十七　同圖二十四唯係C_4H_8 濃度

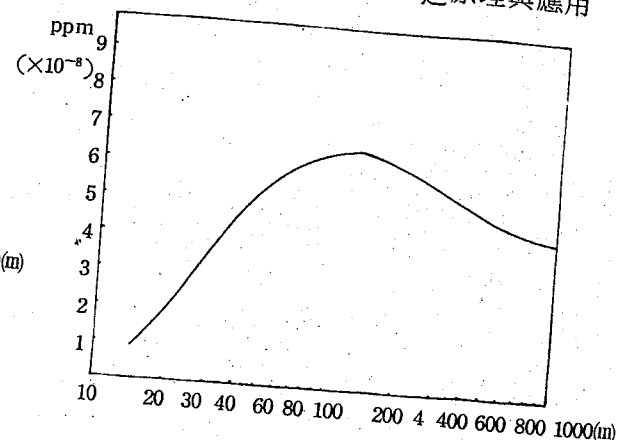

圖二十　同圖二十四唯係ALD 濃度。約在 120 m處產生最大值

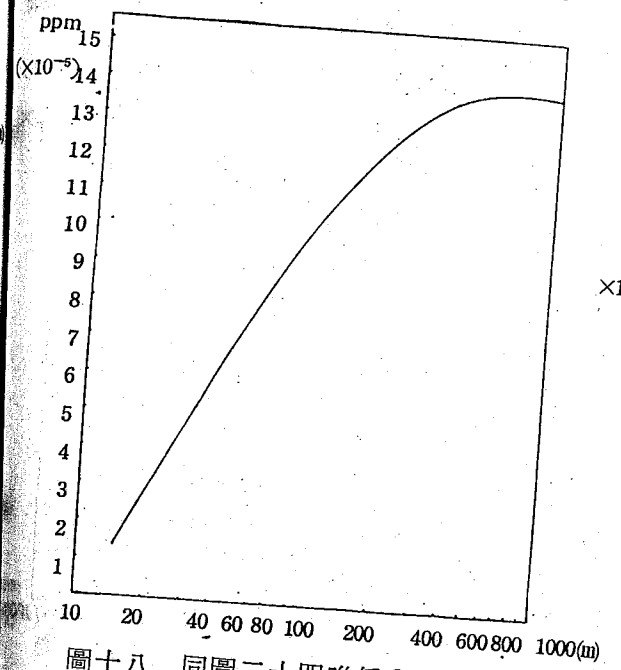

圖十八　同圖二十四唯係O_3 濃度，約在 650 m處產生最大值。

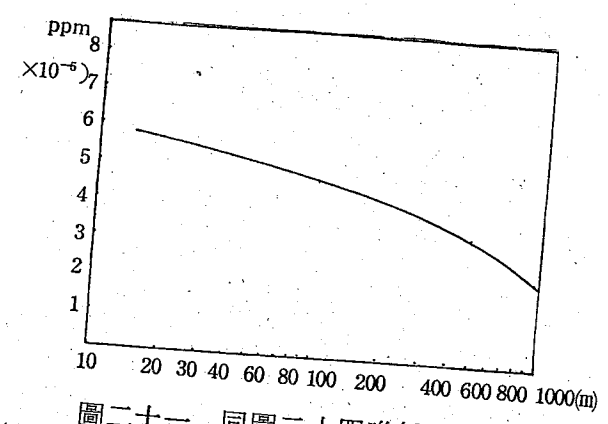

圖二十一　同圖二十四唯係RCO_X 濃度

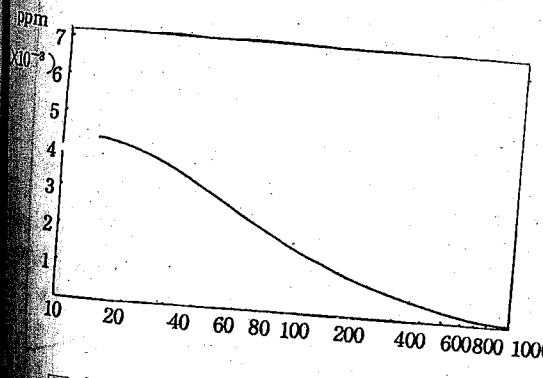

圖十九　同圖二十四唯係NO_2 濃度。採樣值與計算值間差約在12%之內。

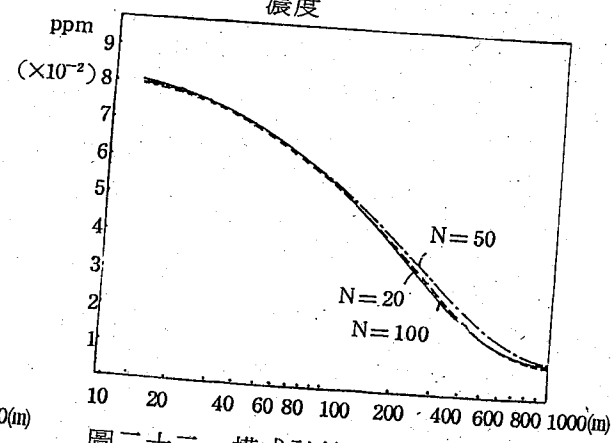

圖二十二　模式計算個案第三組情況下NO 濃度隨距離變化的情形。採樣點和計算點在層區間分 100 格時非常接近。N表層區間分格數。

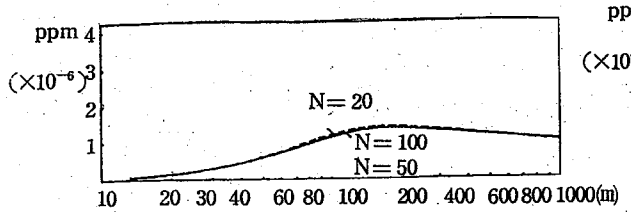

圖二十三　同圖三十一唯係ALD 濃度，約在 180 m處發生最大值。

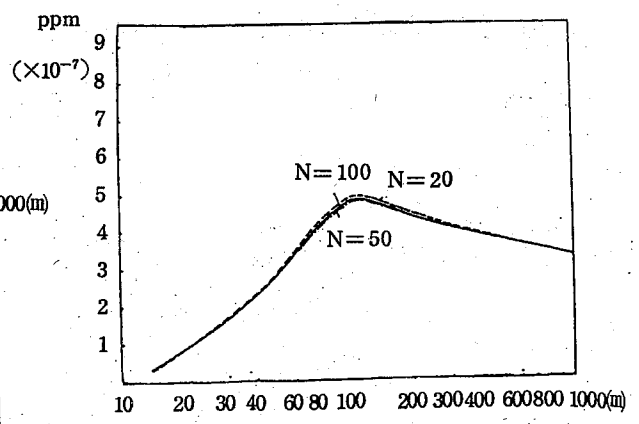

圖二十六　同圖三十一唯係PAN 濃度。約在 110 ～ 120 m附近產生最大值。N＝20者最大濃度處附近較其他二者略高。

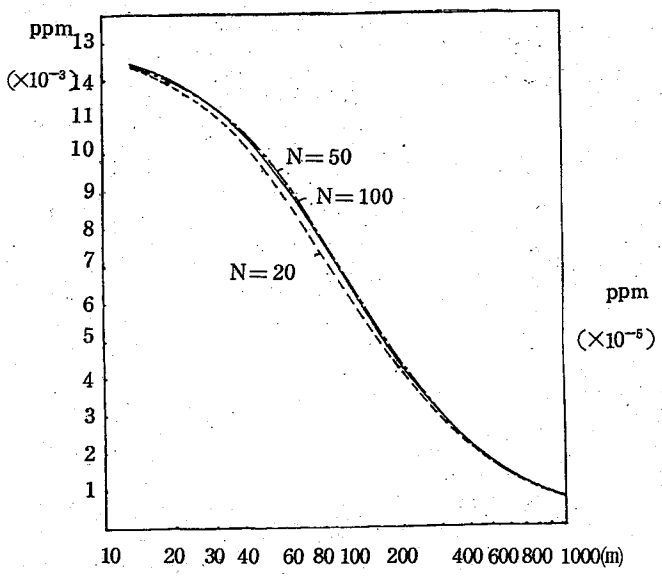

圖二十四　同圖三十一唯係NO 濃度。N＝20者較其他二者計算濃度值較小。

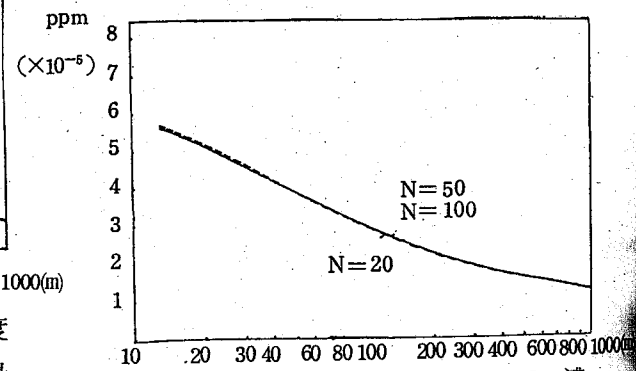

圖二十七　同圖三十一唯係RCOx 濃度。三者計算值相近。

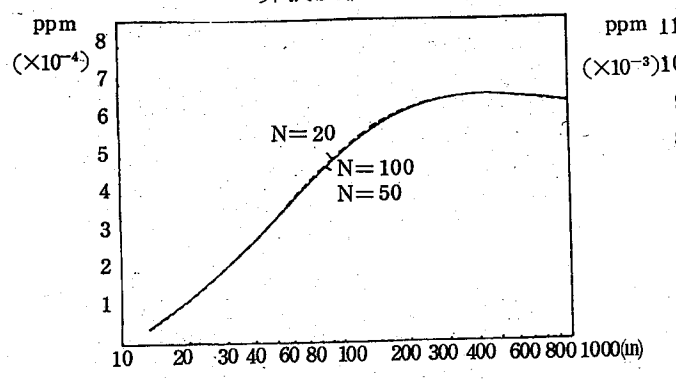

圖二十五　同圖三十一唯係 O_3 濃度。最大濃度值約在 400 m處。N＝50和 100 計算出濃度相差極微。虛線爲N＝20者計算之濃度。

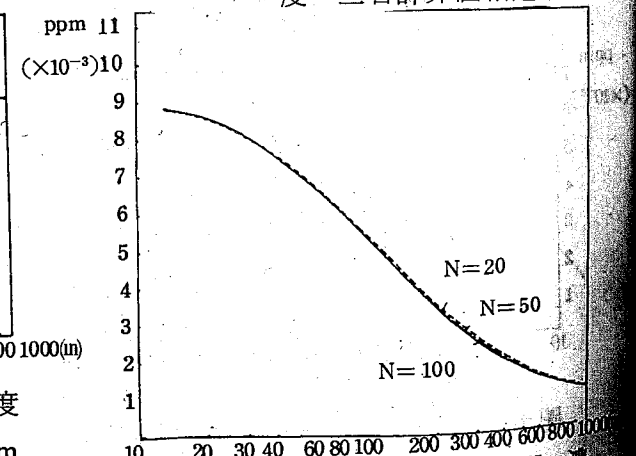

圖二十八　同圖三十一唯係 C_4H_8 濃度。N＝50和N＝100計算值極相近，在 150 m至 600 m間才稍有區別。

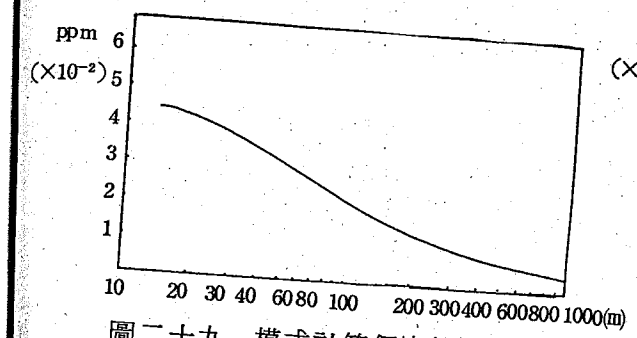

圖二十九　模式計算個案第四組情況下NO 濃度隨距離變化的情形。

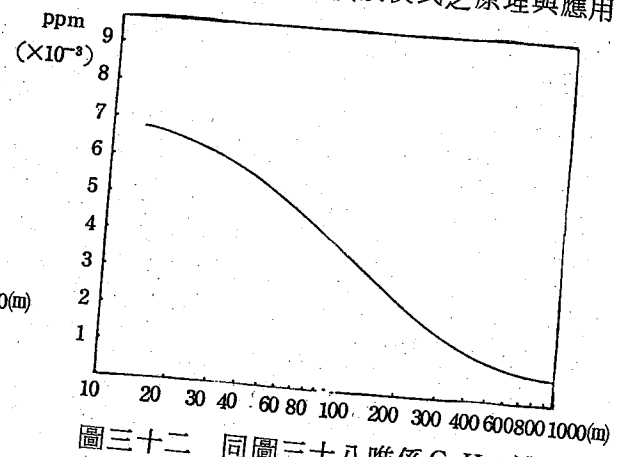

圖三十二　同圖三十八唯係 C_4H_8 濃度。

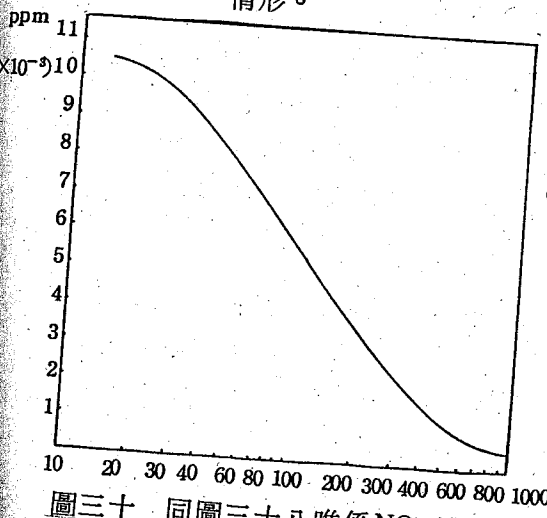

圖三十　同圖三十八唯係 NO_2 濃度

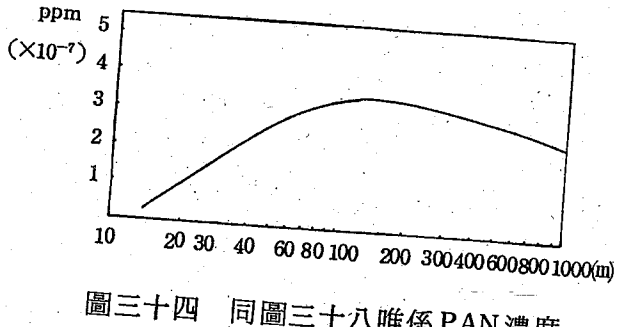

圖三十四　同圖三十八唯係PAN濃度

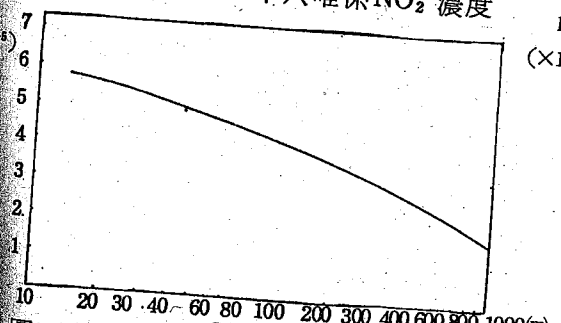

圖三十一　同圖三十八唯係 RCO_X 濃度。

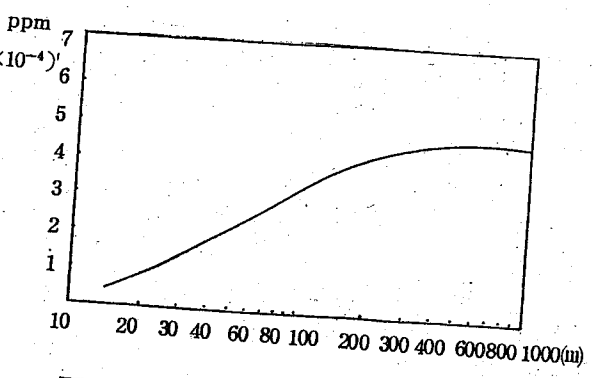

圖三十五　同圖三十八唯係 O_3 濃度

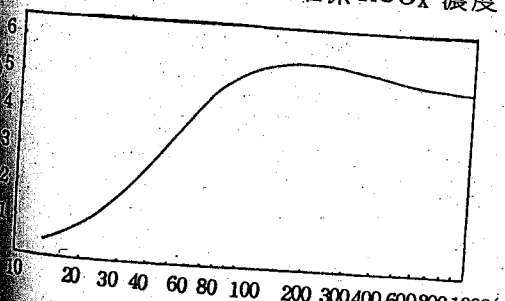

圖三十三　同圖三十八唯係ALD濃度

大氣自界層風洞之規劃與設計研究

大氣物理及流體力學組同仁

摘　要

本研究計劃之目的在研究大氣邊界層的紊流現象以風洞流體實驗可行性之探討，並進行規劃與設計研究。歐美國爲同等目的設計之風洞包括，美國克羅拉多州立大學流體與擴散實驗室（ FDDL ）之氣象風洞（ Meteorological Wind Tunnel ）與環境風洞（ Environmental Wind Tunnel ）。美國環境保護署（ EPA ）風洞實驗室之環境風洞，加拿大西溫特里（ Western Ontario ）大學之邊界層風洞實驗室設備。另外日本筑波科學園區亦設有同類型之風洞設備二～三組（分屬於日本國立公害研究所及產業資源研究所）。該類型風洞設備之主要特徵爲風洞試驗段的長度約爲其截面尺度的10～20倍，用以維持穩定之紊流邊界層，使得風洞內之紊流邊界層完全相似於大氣邊界層中近地之慣性次層（該慣性次層之氣象學俗名爲大氣近地層）。另外之特徵爲風洞內設置熱交換器，以維持垂直方向密度層變之流體。

中研院物理所籌建中之風洞主要之實驗問題包括：

(1)大氣近地層風力對建築結構物影響之研究，以配合國科會防災科技研究。

(2)複雜地形地物之紊流擴散現象研究。

(3)受小尺度地形影響之氣流現象研究。

(4)雷諾數與福祿數（或李查遜數）變化條件下之基本紊流現象研究。

爲達到上述主要之研究問題特徵之要求，籌建中之風洞之試驗段長60英呎（ 18.5 公尺），寬10英呎（ 3.048 公尺），高 7 英呎（ 2.13 公尺）。另外試驗段之高度可以變化，以調整流軸向壓力梯度。風洞之基本結構爲開放吸入式風洞，進口收縮比爲 4 ： 1 。試驗段內風速變化範圍爲 3～65英呎／秒（ 1～20m／sec ）。動力系統採用直流變速 200Hp馬達，帶動十六槳軸流式風扇（ axial fan ）。在試驗段內設置三個實驗轉盤，以配合不同之實驗問題。而試驗段之主要建造材料爲夾板，以便因應將來實驗之須求而變更。

壹、前　言

人類大部份之起居活動皆發生於地表附近，因此受近地表數百公尺高度以下之大氣流場强烈之影響。此流場可稱之爲大氣邊界層，乃是地表與高空大氣作動量，熱量和質量交換的主要場所。人類生活環境之品質與此大氣邊界層之特性有密不可分之關係，其中尤其以(1)建築物及結構之風力負荷及抗風設計，(2)大氣擴散之質量輸送及污染控制，(3)風能之利用，(4)局部區域性風場研究與風力行爲管制，四者與邊界層各個因子變化有直接之關聯。Cermak〔1〕指出此類問題之研究必須綜合流體力學，空氣動力學，氣象學，結構學之知識，而可稱之爲風力工程學（Wind Engineering）。在美國，The Office of Emergency Preparedness〔2〕之報告指出，過去50年來由於風災造成之經濟損失，每年平均約1億美元。Sander〔3〕估計於1963～1970年之間，暴風現象使年平均損失超過5億美元，並導致1667人死亡，18,285人受傷。在台灣每年夏季颱風襲擊，威力之强大，對建設、農作物破壞之嚴重，亦使人談颱變色。但台灣地區人口日增，其分佈亦日廣，將來向空中及風力條件不適合居住之環境發展，乃是必然之趨向。故風災損失之統計數字預計仍然會繼續增加。

今日，由於新建材之使用及新設計觀念之進步，得以造出更高、更龐大、重量更輕之建築物。但却使其機械阻尼（mechanical damping）不易平衡所承受之風力負荷。加上玻璃之廣泛使用，建築物之抗風設計不僅要考慮避免結構上之全盤性破壞，亦要減少脆弱部份之局部性損害。相同地，大氣層調整生態環境之能力已不足以應付人類產生之空氣污染。因此研究風力輸送現像使污染物集中度合乎人類生存之標準，亦是刻不容緩之工作。風力能源之利用是近年來替代能源開發之重點。唯有了解風場之特性才能作最有效地廠址選擇及效益評估。此外，局部區域性之風力行爲控制對於機場飛機之飛行安全，行人所受之風力擾動，社區之通風等問題非常重要。適當設計之風力行爲控制設備，積極地安排建築物位置及防風林，皆可使這些不利之條件獲得合理之改善。

研究風力工程學可利用三種方法，(1)流體力學之理論解析及數學模擬，(2)現場之實際測計，(3)實驗室內之風洞模擬。然而Corrsin〔4〕推測要解隨機起始條件（random initial conditions）之芮維爾－史脫克（Navier-Stokes）方程式，大約需要10^{18}位元（bit）之電腦記憶容量。因此即使是最新之電腦，其記憶體容量及速度仍不足以記錄紊流流場所產生大數量之渦漩（eddies）特徵。因此數學模擬僅能提供定性之參考。大氣邊界層之實際測計，無論在人力、物力，及時間上皆耗費甚大，有緩不濟急之勢，故最有效之法乃採用大氣風洞模擬實驗。且因風洞實驗流場可複製（reproductivity），控制性良好，故Houghton and Carruthers〔5〕，Davenport〔6〕，Cermak〔7〕等皆建議應用大氣風洞實驗模擬風力影響爲風力工程研究不可或缺之方法。

利用風洞研究流體力學之基本現象雖然非常普遍，然而國內已往所使用者大都屬於航空研究用風洞。其試驗段流場爲層流型態（laminar flow）且平均速度和溫度相當均勻。爲避免側壁邊界層之增厚，或形成紊流邊界層，故其試驗段長度與截面特徵寬度之比通常爲1～5，其模型尺寸不大，故試驗段截面亦相當小。而大氣邊界層風洞則不然，爲要實際模擬大氣近地層（surface layer）之高雷諾數（Reynolds number，超過10^7以上）剪力流場（shear flow），容納大面積之地形地物模型，故其試驗段截面積須較大。且試驗段長度與截面特徵寬度之比通常爲10～15，以維持紊流邊界層之發展及模擬上游地面邊界條件之相似性。因此，一般航空用之風洞特徵上和大氣邊界層風洞有極大之分野，也無法用來研究風力工程之問題。環顧國內已有之風洞設備，皆屬於航空或教學用風洞。中央研究院物理研究所流體力學組籌造大氣邊界層風洞之目的，即彌補國內在此方面研究之空白。本研究計劃即針對風洞實驗室之設立進行規劃與設計研究。

貳、理論根據

1 大氣邊界層之特性：

地球表面接受太陽輻射量的不一致造成壓力不平衡乃是形成風之基本原因。此外，由於地球的自轉，雲層之覆蓋，雨水之凝結，地表溫度及粗糙度之差異，地形變化等非線性因素和大氣流場之交互作用，使風之特性變化莫測。因此只能利用紊流統計法來描述風場現象。一般而言，由地表至1000公尺高度之間的大氣運動是屬於紊流邊界層型態，而稱之爲行星邊界層（planetary boundary layer）。山岳或丘陵背面流場的分離，颱風，狂飆（hurricanes）及龍捲風都有可能破壞此種邊界層結構。而在500公尺高度以上時，表面阻力（surface drag force）對空氣流之影響可忽略，且流場壓力梯度和地球自轉科氏力（Coriolis force）幾乎平衡，風向平行於等壓線（isobars），此時稱之爲地轉風（geostrophic wind）而自地表到500公尺高度之流場，Cermak〔8〕稱爲大氣邊界層。而由地表至150公尺高度之間大氣，其紊流動量、熱量及質量之傳遞速率隨地表之特性而不同，稱之爲大氣近地層。大部份風力工程問題皆發生於大氣近地層，故模擬此層之種種現象，即是大氣邊界層風洞之主要目的。Lettau〔9〕認爲行星邊界層之運動方程式可寫成

$$f(V-V_g)-\frac{\partial}{\partial z}<u'W'>=0 \tag{2.1}$$

$$f(U_g-U)-\frac{\partial}{\partial z}<v'W'>=0 \tag{2.2}$$

利用渦漩黏滯係數（eddy viscosity）K_M可將雷諾應力和平均速度表成：

$$<u'W'>=-K_M\frac{\partial U}{\partial z} \tag{2.3}$$

$$<v'W'>=-K_M\frac{\partial V}{\partial z} \tag{2.4}$$

而利用尺度長度（scale length）L_M 及混和長度（mixing length）可將 K_M 寫成

$$K_M = \ell^2(z)\left[\left(\frac{\partial U}{\partial z}\right)^2+\left(\frac{\partial V}{\partial z}\right)^2\right]^{1/2} \tag{2.5}$$

$$\frac{\ell(z)}{L_M} = \frac{0.4\,z/L_M}{1+4\,(z/L_M)^{5/4}} \tag{2.6}$$

$$\text{而 } L_M = 0.0736\,u_*/f \tag{2.7}$$

由此可獲得兩個無因次函數

$$U/u_* = F_1(fz/u_*,\ U_g/fz_0) \tag{2.8}$$

$$V/u_* = F_2(fz/u_*,\ U_g/fz_0) \tag{2.9}$$

此時 f 爲科氏參數（Coriolis Parameter）

V 爲 y 方向之平均速度，v′爲 y 方向速度變動（velocity fluctuation）

U 爲 x 方向之平均速度，u′爲 y 方向速度變動

$(\ )_g$ 爲在地轉風高度之值

u_* 爲摩擦速度（friction velocity）

z_0 爲地面粗糙長度（Surface Roughness length）。

由此可看出羅士培數（Rossby number $R_0 = U_g/fz_0$）固定時，無因次速度 U/u_* 及 V/u_* 乃是無因次高度 fz/u_* 之函數。

風力工程學之應用範圍最主要分成兩部分，即溫度層變現像與嚴重影響風力效應之邊界層區域。當考慮風力對建築物的影響效應時，最重要乃是獲得强風狀態下之邊界層特性。此時强風會加强流場混和之效果，而摧毀溫度層變之現像。然而研究區域性空氣污染或都市地區大氣質量輸送問題，則需要微風邊界層之資料。此時近地層之溫度層變會影響紊流場之混和作用。

强風狀態下之邊界層平均風速之垂直分佈可用次方律（power law）來描述

$$U/U_g = (Z/Z_g)^{1/n} \tag{2.10}$$

Houghton and Carruthers〔5〕認爲 1/n 值和地表粗糙度 z_0 及採樣時所取平均時間之長短有關。

欲模擬大氣流場之行爲，則不僅其速度分佈，其陣風强度及頻率亦須顧及。因流場之紊流强度乃是使建築物發生動力移動（dynamic movement）及流場分離、再密合（re-attach）之決定因素。Fichtl and McVehil〔10〕顯示在李查遜數（Richardson number）爲零時，近地層之紊流動能頻譜有下列之關係式

$$\frac{n\,S(n)}{u_*^2} = \text{const.}\left(\frac{nz}{U(z)}\right)^{-2/3} \tag{2.11}$$

此時 n 爲頻率，S(n)爲縱軸向頻譜（longitudinal spectrum）由此可看出紊流强度與高度變化之關係。

在大氣近地層，Monin and Obukhov〔11〕認爲具有均勻粗糙度、溫度及熱通量之表面，利用流場統計法可推測平行此表面之平面具有平面同質性（planar-homogeneity）

。此時影響流場結構之因子爲流體密度 ρ，表面剪應力 τ_0，表面熱通量 H_0，穩定參數 g/T，及突出邊界層之高度 z。將這些變數之無因次組合可得到大氣近地層之速度、溫度及長度尺度。

摩擦速度 $u_* = (\tau_0/\rho)^{1/2}$

摩擦溫度（friction temperature）$T_* = -H_0/(\rho C_p K' u_*)$ (2.12)

Monin-Obukhov 長度 $L = -u_*^3/[(K'g/T)H_0/\rho C_p]$ (2.13)

此時 K′爲 Kármán 常數 (2.14)

C_p 爲常壓之比熱

g 爲重力加速度

T 爲平均溫度。

無因次之風剪應力（wind shear）$(K'z/u_*)(\partial U/\partial z)$ 和溫度梯度 $(z/T_*)(\partial T/\partial z)$ 可用 (z/L) 之函數來代表。

$$U(z)-U(z_{ref}) = \frac{u_*}{K}\left[\ell n(z/z_{ref})+B_u(z-z_{ref})/L\right] \tag{2.15}$$

$$T(z)-T(z_{ref}) = T_*\left[\ell n(z/z_{ref})+B_T(z-z_{ref})/L\right] \tag{2.16}$$

而垂直速度變動之標準差爲

$$\frac{<W'^2>^{1/2}}{u_*} = \phi_1(z/L) \tag{2.17}$$

此時 B_U，B_T 皆爲成層穩定度 Z/L 之函數。

當雷諾數非常大時，Kolmogorov〔12〕認爲速度黏滯係數 ν 和紊流能量消散率 ϵ 控制高波數（high-wave-number）之紊流頻譜。其相對之速度及長度尺度分別爲 $(\nu\epsilon)^{1/4}$ 及 $(\nu^3/\epsilon)^{1/4}$。此時一維（one-dimension）之長軸向頻譜應爲

$$[(u'^2)E_u(K)]/(\epsilon\nu^5)^{1/4} = \phi_2[K(\nu^3/\epsilon)^{1/4}] \tag{2.18}$$

K 爲波數

E_u 爲長軸向之能量頻譜

以上(2.10)式至(2.18)式，皆是比照風洞模擬流場與大氣邊界層特性之良好指標。爲達成這些相似性之要求，Hunt and Fernholz〔13〕，Nee, Szewczyk and Yang〔14〕，Snyder〔15〕與 Cermak〔8, 16〕等文討論不同性質的風力工程學問題須要考慮之風洞設計因素。

2 風洞模擬之相似律

應用風洞進行模擬之流體力學原理包括：(1)幾何相似性，(2)動力相似性，(3)熱力相似性，與(4)起始及邊界條件相似性。由無因次的流體力學基本方程式：

$$\frac{\partial U_i^*}{\partial t^*}+U_j^*\frac{\partial U_i^*}{\partial X_j^*}+R_0^{-1}\,2\,\epsilon_{ijk}\Omega^* U^* = -\frac{\partial P^*}{\partial X_i^*}-R_1\theta^*\delta_{i3}+R_E^{-1}\frac{\partial^2 U_i^*}{\partial X_j^* \partial X_j^*} \tag{2.19}$$

$$\frac{\partial U_i^*}{\partial X_i^*} = 0 \tag{2.20}$$

$$\frac{\partial \theta^*}{\partial t^*}+U_j^*\frac{\partial \theta^*}{\partial X_j^*}=\frac{1}{P_r}\frac{1}{R_E}\frac{\partial^2\theta^*}{\partial X_j^*\partial X_j^*}+\frac{E_c}{R_E}\Phi^* \qquad (2.21)$$

$$R_o\ (\text{Rossby No.})=\frac{U_o}{\Omega_o L_o}$$

$$R_i\ (\text{Richardson No.})=g\frac{\triangle T_o\ L_o}{T_o\ \ U_o^2}$$

$$R_E\ (\text{Reynolds No.})=\frac{U_o L_o}{\nu}$$

$$P_r\ (\text{Prandtl No.})=\frac{\nu}{K/\rho_o C_p}$$

$$E_c\ (\text{Eckert No.})=\frac{U_o^2}{C_p\triangle T}$$

在上面無因次過程中

U_o ：流場之特徵速度尺度。
L_o/U_o ：流場特徵時間尺度。
ρU_o^2 ：流場之特徵壓力尺度。
L_o ：流場之特徵尺度。
$\triangle T_o$ ：流場之特徵溫度差。
g ：重力加速度。
Ω_o ：地球轉動座標之特徵角速度。
ν ：流體之運動黏滯係數。
K ：流體之導熱係數。
C_p ：空氣之定壓熱容。
Φ ：爲流體之焦耳加熱。

由方程式(2.19)～(2.21)可以看出，實際流場變化與風洞內之模擬流場之相似性要求爲：

(1)模型各方向之比例縮尺相同，滿足流體連續性。

(2)動力之相似性要求羅士培數、李查遜數、與雷諾數與實際流場情況相同。

(3)熱力之相似性要求普朗特數與艾卡數與實際流場情況相同。

在實際應用風洞進行模擬實驗時，上述之相似性要求不可能全部達到，因此設計實驗應依問題之特性，權衡輕重，考慮重要之相似性要求。Snyder〔15〕主張在嚴格要求下，如果應用非旋轉風洞模擬大氣邊界層現象時，模擬對象之水平尺度不可超過5公里。在這種情況下，羅士培數$R_o>10$，科氏力的效應可不予考慮。Cermak等〔17〕在較鬆的條件下，主張水平尺度小於150公里之大氣邊界層現象可以不考慮科氏力的效應。另外大氣邊界層屬於密度層變之流體(density stratified flow)，其特徵李查遜數在正負1之間，代表成層穩定或成層不穩定之流動狀態。因此浮揚力(buoyancy force)在大氣邊界層現象有其絕對之重要性。但是在研究防風問題時，主要之興趣對

象爲強風情況下地形或建築結構物與流體之交互作用，此時李查遜數趨近於零，故可應用一般之環境風洞(無加溫裝置)來模擬流體現象〔7〕。對於熱力相似性的要求，如果風洞內之空氣接近常溫與大氣壓，則普朗特數與實際大氣現象相同。另外艾卡數代表流體黏滯力之摩擦加熱作用。在低次音速流動情況下，這種黏滯力之焦耳加熱作用可以忽略〔1，7〕。

綜合上述對於流體模擬實驗相似性的要求，我們尚未討論雷諾數相似性的要求。一般言之，大氣邊界層之特徵雷諾數高達10^8以上，因此要求風洞內之雷諾數與實際情況相同幾無可能。所幸，目前對紊流現象之瞭解，紊流在高雷諾數具有雷諾數相似性之特徵(Reynolds number similarity)〔18〕，亦即當雷諾數超過某臨界值時，紊流結構之特徵不受雷諾數大小的影響。依照Kolmogorov的理論，當雷諾數夠大時，紊流頻譜(power spectrum)即有慣性次階(inertial subrange)的特徵出現，因此紊流的無因次頻譜(以Kolmogorov之紊流微尺度參數來常化)呈相似性。由很多的實驗數據顯示〔1，19〕。風洞內紊流邊界層之頻譜經常化後與實際大氣邊界層之紊流頻譜呈完全之相似性。而一般風洞內的雷諾數約比實際大氣邊界層之雷諾數要小二個數量級以上。這個事實說明，當風洞內之雷諾數達到臨界值以上時，大氣邊界層內的紊流結構可以應用環境風洞進行模擬。紊流結構的相似性，對於研究紊流振動對於結構物的影響具有重大的關係。另外研究紊流擴現像時亦須紊流頻譜之相似〔20〕。

由實驗結果〔8，15〕等顯示，風洞內的臨界雷諾數約爲10^4左右，這個條件決定風洞的模型縮尺比例，紊流邊界層的厚度與風洞試驗段的長度。

由上述雷諾數所影響的紊流邊界層特性，我們可以決定風洞內模型的縮尺比例，即

$$\frac{(R_E)_P}{(R_E)_M}\leq 10^4$$

可以得到 (2.22)

$$U_M L_M \geq 10^{-4} U_P L_P \qquad (2.23)$$

$(R_E)_P$ ：實體之雷諾數。
$(R_E)_M$ ：模型之雷諾數。
U_P ：實際情況之流速。
L_P ：實際情況之尺度。
U_M ：風洞內之流速。
L_M ：風洞內模型之尺度。

在應用(2.21)與(2.22)式時，假設風洞內模型屬於空氣動力之鈍型物(Bluff Body)，否則模型表面之滯性次層(viscous sublayer)受雷諾數的影響很大。

模型實驗之初始與邊界條件相似性要求迫近流易(approaching flow)與實際狀態相似。亦即

(1)迫近流場之平均流速分佈呈指數率分佈(logrithmic wind profile)。

(2)迫近流場內雷諾應力(Reynolds stress)與紊流動能分佈與大氣邊界層相似。

⑶迫近流場內之動能頻譜（ Power spectrum ）與實際狀態相似。

爲達到上述模擬的條件，風洞試驗段須有足夠的長度及適當的表面粗糙度（ Surface roughness ），以維持穩定之紊流邊界層。

參、大氣環境風洞基本設計

設計考慮因素：

環境風洞設備之主要實驗目的包括：

⑴大氣紊流邊界層之模擬。

⑵風力對於建築結構物的影響。

⑶大氣紊流邊界層之擴散現象。

⑷複雜地形對氣流之影響，風力能源開發之研究。

基於上述實驗目的考慮，環境風洞之基本特性爲發生（ generation ）及維持一穩定之紊流邊界層。爲達到上述的，風洞各項特性的決定，分述如后：

1. 風洞試驗段高度與寬度的決定：

由於試驗段高度影響模擬之紊流邊界層厚度。一般研究風力對於建築結構物之影響時，實體之高度約爲 100 ～ 200 公尺，如果模型之縮尺爲 1/200 ～ 1/500 ，風速的縮尺爲$\frac{1}{2}\sim\frac{1}{3}$，則風洞內模型之特徵雷諾數可以超過 10^5。在這種狀況下，風洞內求出之風阻係數（ $C_f=\triangle P/\frac{1}{2}\rho U^2$ ）較不受雷諾數大小的影響（ Reynolds number independency ）。故試驗風力對建築結構物之影響時，風洞內紊流邊界層之厚度須在 100 公分以上，而試驗段的高度須超過 150 公分以上。

試驗段寬度的決定，主要考慮模型放置於風洞內之阻檔效應（ Blockage effect ），及側壁邊界層的影響。一般風洞模擬實驗的指標原則爲模型面積之阻檔率（Blockage ratio ）以不超過 10 % 爲原則。另外試驗段的寬度亦影響試驗轉盤（ turntable ）的直徑。相對於模型之不同方向之迫近氣流（ approaching flow ），可以轉動試驗轉盤觀測模型物下游流場的變化。基於上述的考慮及各種可能的實驗狀況，環境風洞試驗段的高度決定爲 7 英呎（ 2133.6 mm ），寬度爲 10 英呎（ 3048 mm ）。

2. 試驗段長度的決定：

試驗段的長度爲影響紊流邊界層厚度與穩定性的主要因素。根據 Cermak 等人〔17〕，與 Counihan〔 21 〕的實驗研究，風洞內紊流邊界層可以由自然成長的方式或應用人工紊流發生器（ Vortex generator ）方式，模擬相似於大氣近地邊界層的流場（ Atmospheric surface boundary layer ）。於風洞底面加置粗糙元素之自然成長之紊流邊界層厚度在下游 10 公尺處約爲 50 公分以上。以渦流發生器置於試驗段入口，並於底面加置粗糙元素之紊流邊界層可達 100 公分以上，唯人工形成之邊界層約須 6 ～ 8 倍之邊界層厚度之下游距離形成穩定之邊界層（ Pertaka and Cermak ，〔 22 〕）。從風洞之實驗目的探討，一般紊流擴散實驗之模型比例縮尺以 1/500 ～ 1/1000 爲宜，

故風洞內模擬之邊界層厚度在 50 公分以上即可達到目的，但擴散實驗需要較長之下游距離，故以紊流擴散實驗實驗考慮風洞試驗段的長度以 10 ～ 15 公尺爲宜。一般風力對建築結構物影響的實驗，模型比例縮尺約爲 1/200 左右 ，以增高模型之雷諾數（ 10^5 ～ 10^6 ）。

在這種情況下，風洞內紊流邊界層的厚度約須 100 ～ 150 公分，須要 15 公尺以上長度的試驗段來維持穩定的邊界層，綜合以上的考慮，另外爲增加風洞實驗目的的多元性，決定風洞試驗段的長度爲 18.5 公尺（ 60.7 英呎 ）。

3. 風洞之動力與循環系：

一般低速風洞之動力與循環系有兩種型態：

㈠閉路循環系（ closed-circuit type ），㈡開放式風洞（ open-circuit type ）（ Pope and Harper ，〔 23 〕）。一般而言，閉路循環式風洞，能量效率高，但初始建造費用高。另外應用風洞進行紊流擴散現象模擬時皆須採用追踪劑（ tracer gas ）的技術來分析擴散現象，因此閉路式的風洞會累積追踪劑的濃度，引起實驗技術的困難。從初始造價與實驗目的考慮決定中研院物理所之大氣環境風洞爲開放式風洞（ open-circuit type wind tunnel ）。開放式風洞，因動力風扇（ fan ）與試驗段相對位置可分成㈠吸入式風洞（ suction type wind tunnel ）與㈡吹送式風洞（ blowing type wind tunnel ）。吹送式之風洞，風扇置於試驗段的上游，風扇的作用爲風洞管路之增壓站，整個試驗段之空氣之靜壓與大氣壓相同，故試驗段氣密（ air tight ）的問題不須考慮。但是風扇運動產生之螺狀渦流不易控制，影響試驗段氣流的均勻與穩定性。相反吸入式風洞之試驗段須有良好的氣密性，但風扇葉片的尾流作用可以不必控制。以吸入式安排之風洞，其整流段可以簡化（相對於吹送式）。總體考慮結果，中研院物理所風洞決定爲單向吸入式風洞（ open-circuit suction type ），整個風洞分爲三個單元，㈠進口整流收縮段，㈡試驗段，㈢風扇動力段。其空氣動力設計容後再述。

4. 風洞試驗段風速範圍之決定：

研究局部小地形或建築結構物對氣流之影響（或交互作用）時，風洞內主要量度的參數爲壓差係數 C_P，

$$C_P=\frac{\triangle P}{\frac{1}{2}\rho U_0^2} \qquad (3.1)$$

對於一般空氣動力鈍形物，壓差係數在雷諾數超過 10^4 時，趨近常數值，其值不隨著雷諾數的增大而變化。以 1/200 縮尺的模型，在風洞內的尺寸大約爲 50 ～ 100 公分 ，因此當風洞內的平均流速超過 2 m/ sec 時，模型的雷諾數即可超過 10^4 之臨界值。但在這種風速情況下，流場之靜壓差值約爲 10^{-1} 毫米水柱高 ，量度十分困難，一般之壓力感應器（ pressure transducer ）亦會受到風扇或周界噪音的影響，增高感應器的噪訊比（ noise to signal ratio ）。因此在量度壓差係數 C_P 時，爲降低噪訊比，風洞內操作風速 U_0 須提高至 10 ～ 15 m / sec 以上（ Personal communication with Prof. J.E.Cermak ）。爲了這個目的風洞設計之最大風速定爲每秒 20 公尺。〔註〕

另一方面爲了將來風洞從事密度變流（ density stratified flow ）現象之研究，例如熱噴流（ thermal plume ）現象，爲了維持福祿數（ Froude number ）或李查遜數的相似性，必須降低風洞試驗段內之風速至 1 ～ 2 m／sec 。基於上述二種考慮，風洞試驗段內之平均風速設計爲 1 ～ 20m／ sec ，連續可調整形式。

5. 試驗段流向靜壓差調整：

大氣邊界層流場，其於壓力梯度力主要由科氏力所平衡，沿風向的壓力梯度遠小於 10^{-4} dyne／cm^3 。反之，在風洞試驗段內，由於摩擦損耗，壓力梯度可達 10^{-1} dyne／cm^3 以上。更有甚者，由於模型引起流向截面積的改變，造成之壓差影響模擬相似性。由於上述的考慮，環境風洞之試驗段內須具備流向靜壓差調整裝置。規劃中之環境風洞試驗段之上壁可以調整其高度，其範圍爲 200 公分至 250 公分。

〔註〕：試驗段內之噪音強度以 80 分貝估計，產生之空氣壓力變差值爲 ± 2 dyne／cm^2 ，如氣流靜壓變化提升至 ± 100 dyne／cm^2 則噪訊比可降至 1／100 以下，此時風洞試驗段內之操作風速須提升至 15 ～ 20 m／ sec 。

肆、大氣環境風洞之進口整流設計

1. 風洞試驗段進口紊流強度控制：

吸入式風洞，空氣經由進口段內之紊流控制組合，包括蜂巢孔與整流細網，使紊流的強度降低，再經收縮段，可使流速均勻。下面討論蜂巢孔、整流細網與收縮段對於風洞內紊流強度的控制作用。

(1)蜂巢孔（ honey-cone ）的作用

一般蜂巢孔的管徑約爲數公分到十公分左右，因此其特徵雷諾數約爲數千以上（約爲 10^4 以上），經過蜂巢孔的氣流會以紊流的形態發生，唯其紊流的尺度約與蜂巢大小相當。且在蜂巢孔後的紊流接近等向性紊流（ isotropic turbuleuce ）。對於等向性紊流消散作用（ dissipation ）的理論可以根據 Taylor 之預測〔 24 〕：

$$\frac{U}{u'}=\frac{5x}{A^2M}+B \tag{4.1}$$

U：代表通過蜂巢孔之平均流速。

u′：代表紊流之平均異差值（ rms value ）。

M：代表蜂巢孔之尺寸。

x：代表離開蜂巢孔之下游距離。

A：爲一萬有常數（ universal constant ）。

B：常數，隨蜂巢孔之幾何形狀而異。

由英國 NPL（ National Physical Lab. ）Simmons 與 Salter 氏之實驗數據，孔徑在一英吋左右之蜂巢孔後之等向性紊流強度之變化可依據下式計算。

$$\frac{U}{u'}\doteq 1.30\frac{x}{M}+5.5 \tag{4.2}$$

(2)整流細網的作用

依據 Schubaner, Spangenberg 與 Klenbanoff 〔 25 〕等之研究，整流細網之特徵雷諾數須維持在 40 以下，$\frac{Ud}{\nu}<40$ 。通過整流細網後之紊流與前述之等向性紊流不同。整流細網後之紊流已屬於流體黏滯力直接作用之紊流（ turbulence in dissipation range ）。由 Dryden 與 Abbott 〔 26 〕之實驗數據，通過整流細網前後之紊流強度可以應用下式估計：

$$\left(\frac{u'}{U}\right)_{\substack{\text{with}\\ \text{screen}}}=\frac{1}{(1+k_s)^{n/2}}\left(\frac{u'}{U}\right)_{\substack{\text{without}\\ \text{screen}}} \tag{4.3}$$

n：整流細網的層數

$k_s=\triangle P / \frac{1}{2}\rho U^2$ ，爲整流細網的壓降係數。

ρ：空氣密度

$\triangle P$：通過細網前後之靜壓差。

一般設計之經驗建議風洞內的整流細網的壓降係數須避免採用超過 3 之細網。由於織網的不均勻的影響，太密的細網會使得風洞內平均流的均勻性破壞。故一般設計時採用 k_s 值較小之網，而抑制紊流的效果，可由多層細網來增强它的整流作用。

(3)收縮段對於紊流的抑制作用

收縮段對於不同方向之紊流渦旋會產生不同的作用。在估計收縮段的作用時，我們假設進入收縮段時之紊流屬於等向性紊流。如果 C 代表收縮段前後之截面積比，則沿流方向（ streamwise ）的紊流因渦度的擠壓作用（ vortex shrinking effect ）會減弱 C 倍，另外橫向（ transverse ）的紊流因渦度的抽拉作用（ vortex stretching effect ）增强$\sqrt{C}$倍（ Tennekes and Lumley ，〔 27 〕）。以公式表示

$$\frac{u'_{t_2}}{u'_{t_1}}=\sqrt{C} \tag{4.4}$$

$$\frac{u'_{l_2}}{u'_{l_1}}=\frac{1}{C} \tag{4.5}$$

u'_l ：streamwise 方向之紊流强度。

u'_t ：transverse 方向之紊流强度。

1 ：代表收縮段前之位置。

2 ：代表收縮段之位置。

則經過收縮段後之紊流強度可以導出爲

$$\frac{2u'^2_{t_2}+u'^2_{l_2}}{U_2^2}=\frac{2Cu'^2_{t_1}+\frac{1}{C^2}u'^2_{l_1}}{C^2U_1^2} \tag{4.6}$$

由 $u'^2_2=2u'^2_{t_2}+u'^2_{l_2}$ (4.7)

$u'^2_1=2u'^2_{t_1}+u'^2_{l_1}$ (4.8)

則 $\frac{u_2'}{U_2} = \sqrt{\frac{1}{3}\left(\frac{2}{c}+\frac{1}{c^4}\right)}\frac{u_1'}{U_1}$ (4.9)

應用(4.9)式估計收縮段對紊流強度作用時，並未考慮流體黏滯力之消散作用。

2 大氣環境風洞試驗段進口之紊流強度估計

(1)蜂巢孔設計規格

爲避免產生通過蜂巢孔後之大尺度渦流；蜂巢孔的長度與其直徑之比約須六倍至八倍（Bradshaw and Pankhurst，〔28〕）。籌建中風洞之進口因置於戶外，爲避免激流（surge flow）的發生，蜂巢孔（或蜂巢管）的長度與直徑比定爲10。

- 材料：PVC管。
- 直徑3公分，管壁厚度0.2公分，管長30公分。

(2)整流細網設計規格

- 材料：不銹鋼細絲。
- 網織：每英吋18方格織。
- 網絲直徑：0.011英吋。

(3)進口整流段收縮比，4：1。

應用前述之理論估計方法及蜂巢管，整流細網及收縮比之規格，籌建中風洞之紊流強度估計值列於下表。

試驗段風速 (m/s)	1.0	5.0	10.0	15.0	20.0	說明
進口段風速 (m/s)	0.25	1.25	2.5	3.75	5.0	
細網雷諾數	4.36	21.8	43.6	65.5	87.3	
k_s值	1.3	1.2	1.1	1.0	0.9	
蜂巢孔後紊流	5.4 %	5.4 %	5.4 %	5.4 %	5.4 %	下游30公分處
四層細網後紊流	1.02 %	1.12 %	1.22 %	1.35 %	1.49 %	
試驗段紊流	0.42 %	0.46 %	0.50 %	0.55 %	0.61 %	

註：k_s值參照Pope及Harper〔23〕。

伍、大氣環境風洞之規格與構造

㈠風洞整體構造說明：

大氣環境風洞爲一開放吸入式之風洞（open-circuit suction type）。其結構體包括進口整流段，收縮段，試驗段，與動力段，及風洞本體之支架。風洞本體之佈置，參閱圖一、圖二與圖三。風洞各段的內容說明如下：

1 進口整流段：內容包括

(a) Inlet Bell。

(b)蜂巢管及蜂巢管固定鐵絲網。

(c)四層整流細網。

(d)整流網與蜂巢管之清潔孔，該孔可以容許長柄吸塵器伸進蜂巢與細網內部進行維護清潔工作。

2 收縮段：

收縮段連結進口段與試驗段。該段斜面之彎輻主要以二個三次方程式曲線相接而成。在板金設計時須避免斜率的轉折點。

3 試驗段：

試驗段主要爲夾板結構構成，其上壁可以調整其高度位置，使得氣流通過試驗段時稍呈發散（divergent），以動壓彌補靜壓之摩擦損失，維持試驗段內流向之壓力梯度爲零的狀況（實際上壓力梯度小於 10^{-3} dyne/cm^3）。該上壁調整裝置的設計可參閱圖四。

試驗段內部設置感應器之三度空間活動機構，該儀器支架的位置可由風洞外之儀表遙控其位置。儀器支架調整位置的準確度小於2～3 mm。

另外試驗段內部亦考慮照明，實驗轉盤及照相孔的設計。

4 動力段：

動力段主要包括：

(1)動力段進口收縮管，承接試驗段長方形出口至風扇之圓形進口。

(2)風扇組合，內容包含風扇葉子轉子，軸承，整流片及傳動皮帶。

(3)風扇出口擴散管。

(4)動力段本體與動力馬達（置於風扇外側）之基座。

在動力段進口收縮管上設置人孔以備工作人員進入做風扇葉片調整工作。另外在上部設置照明設備。在設計動力段基座時考慮馬達及風扇振動的防止。動力段與風洞本體亦採分開結構之設計，附止振動之傳遞。

㈡風洞材料及尺寸規格：

1 進口整流段

對於蜂巢孔、整流細網、安全粗網及風扇葉片組之管流之壓降計算，則採用壓降係數之經驗公式

$$K=\frac{\triangle p}{\frac{1}{2}\rho u^2} \qquad (6.4)$$

在該式中 u 爲通過裝置之平均流速。

㈡最大壓降與風洞所需最大馬力計算：

由於摩擦與壓降損耗與風洞內，風速的平方成正比，故最大壓降與最大需要馬力可由風洞試驗段內最大風速情況估計。

(1)最大流量

$V_{max}=2.13\times3.048\times20\ m/sec$

$=129.8\ m^3/sec$

$=275.6\times10^3$ cubic feet per min.（CFM）

(2)空氣密度，ρ

在 25 °C，一大氣壓情況

$\rho=1.205\times10^{-3}\ gm/cm^3$

(3)空氣運動黏滯係數，ν（常溫，常壓狀態）。

$\nu=1.6\times10^{-5}\ m^2/sec$

(4)動壓（velocity pressure），P_v

①進口段　$u=5\ m/sec$

$P_v=150.6\ dyne/cm^2$

②收縮段

平均流速　$u=12.5\ m/sec$

$P_v=941.4\ dyne/cm^2$

③試驗段

平均流速　$u=20\ m/sec$

$P_v=2410\ dyne/cm^2$

③動力段之收縮管

平均流速　$u=36.4\ m/sec$

$P_v=7994\ dyne/cm^2$

(5)相當直徑，D_e

①進口段　$D_e=5.019\ m$

②收縮段　$D_e=4.1\ m$

③試驗段　$D_e=2.5\ m$

④動力段收縮管　$D_e=2.3\ m$

(6)摩擦係數，f

①進口段

$R_E=1.57\times10^6$

$\frac{\varepsilon}{D_e}=0.00001$　（commercial steel）relative roughness

$f=0.012$

②收縮段

$R_E=1.92\times10^6$

$\frac{\varepsilon}{D_e}=0.0001$　（commercial steel）

$f=0.01$

③試驗段

$R_E=3.1\times10^6$

$\frac{\varepsilon}{D_e}=0.005$　（木材與風洞內之粗糙元素）

$f=0.019$

④動力段收縮管

$R_E=4.0\times10^6$

$\frac{\varepsilon}{D_e}=0.00002$　（commerical steel）

$f=0.011$

(7)壓降係數，K

①蜂巢孔　$K=0.3$

②蜂巢孔前後之保護粗網　$K=0.2\times2=0.4$

③整流細網四層　$K=4\times0.9=3.6$

④安全網　$K=0.2$

⑤風扇組合　$K=0.075$　（由風扇原廠提供）。

(8)壓降，$\triangle p$

①進口段　$L=2\ m$，

$\triangle p=0.72\ dyne/cm^2$

②收縮段　$L=4\ m$，

$\triangle p=9.18\ dyne/cm^2$

③整流組合，包括蜂巢孔、細網與粗網

$\triangle p=647.6\ dyne/cm^2$

④試驗段　$L=18\ m$

$\triangle p=329.69\ dyne/cm^2$

⑤安全網

$\triangle p=482.0\ dyne/cm^2$

⑥風扇組合　$P_v=7994.8\ dyne/cm^2$

授 J: A. Peterka教授，及李文槐先生；對於風洞之特性規劃提供重要之建議。美國 Aerolab 公司陳兆梅博士，清華大學動力機械系巢慶成教授，台大機械系黃博治教授對於風洞動力段風扇與動力馬達之選擇亦提供寶貴之資料與建議。美國環境保護署（EPA），環境風洞實驗室Dr. W. H. Snyder 對於試驗段內儀器活動支架，及擴散實驗之儀器設備，提供了寶貴之規劃設計資料。中鼎工程公司設備設計部廖運焜經理及盧增輝先生對於風洞之結構及操作機構之設計，讓我們構想中之風洞變成可以施工製造之詳圖，尤其是盧增輝先生備極辛勞，對於風洞施工之每一步驟都詳細之檢查，確定其品質。我們都致以最大之敬意與謝意。中央研究院物理研究所所長林爾康先生對於風洞實驗室之設立，極力之支持與鼓勵，特此表示謝意。

參考資料

1. Cermak, J. E. 1975, "Applications of Fluid Mechanics to Wind Engineering - A Freeman Scholar Lecture" Trans. of the ASME, J. of Fluids Eng., Vol. 97, pp.9-38.
2. Disaster Preparedness, Report to the Congress, Office of Emergency Preparedness, U. S. Government Printing Office, 3 Vols., Jan. 1972.
3. Sander, F. 1971, "Toward Defining Human Needs: How Does the Atmosphere Hurt Us?" Bulletin of the American Meteorology Society, Vol. 52, pp.446-449.
4. Corrsin, S. 1961, "Turbulent Flow", Amer. Sci. 49, pp.300-325.
5. Houghton, E. L. and Carruther, N. B. 1976 "Wind Effects of Buildings and Structures", John Wiley & Sons, New York, p.243.
6. Davenport, A. G. 1967, "The Treatment of Wind Loading on Tall Buildings", Proc. of Symposium on Tall Buildings, Univ. of Southampton, Apr. 1966.
7. Cermak, J. E. 1976, "Aerodynamics of Buildings", Annual Review of Fluid Mechanics, Vol.8, pp.75-106.
8. Cermak, J. E. 1981, "Wind Tunnel Design, for Physical Modeling of Atmospheric Boundary Layers", J. of the Engineering Mechanics Division, ASCE, Vol. 107, No. EM3, pp.623-642.
9. Lettau, H. H. 1962, "Theoretical Wind Spirals in the Boundary Layer of a Barotropic Atmosphere", Beitr, Phys. Atmos., Vol. 35, pp.195-212.
10. Fichtl, G. H. and McVehil, G. F. 1970, "Longitudinal and Lateral Spectra of Turbulence in the Atmospheric Boundary Layer of the Kennedy Space Centor", J. Appl. Meteorol., 9, pp.51-63.
11. Monin, A. S. and Obukhov, A.M. 1954, "Basic Laws of Turbulent Mixing in the Ground Layer of the Atmosphere", Trudy Geofizs. Inst. An. SSSR, 2. No. 24, pp.163-187.
12. Kolmogorov, A. N. 1941, "The Local Structure of Turbulence in Incompressible Viscous Fluid for very Large Regnolds Number", Doklady AN SSSR, Vol. 30, No. 4, pp.299-303.
13. Hunt, J. C. R. and Fernholz, H. 1975, "Wind-Tunnel Simulation of the Atmospheric Boundary: A Report on Euromech 50", J. Fluid Mechanics., Vol. 70, Part 3, pp.543-559.
14. Nee, V. W., Szewczyk, A. A. and Yang, K.T. 1975, "Atmospheric Wind Tunnels - A Survey", ND-TR-WT-1, Oct., Univ. of Notre Dame ID.
15. Snyder, W. H. 1972, "Similarity Criteria for the Application of Fluid Models to the Study of Air Pollution Meteorology", Boundary Layer Meteorolgy, 3, pp.113-134.
16. Cermak, J.E. 1971, "Laboratory Simulation of the Atmospheric Boundary Layer", AIAA Journal, Vol. 9, No. 9, pp.1746-1754.
17. Cermak, J. E., Sandborn, V. A., Plate, E. J., Binder, G. H., Chuang, H., Meroney, R. N., and Ito, S., 1966 "Simulation of Atmospheric Motion by Wind Tunnel Flow", Report to Army under Contract DA-AMC-28-043-G20, Colo. State University.
18. Townsend, A.A., 1956: "The Structure of Turbulent Shear Flow", Cambridge University Press, p.315.
19. Jensen, M., 1958: "The Model-Law for Phenomena in a Natural Wind", Ingenioren Int., Ed. 2, No. 4,
20. Pasquill, F., 1974: "Atmospheric Diffusion", Second Ed., Ellis Horwood Publisher, Chichestor, p.429.
21. Counihan, J., 1973: "Simulation of an Adiabatic Urban Boundary Layer in a Wind Tunnel", Atmos. Environment, Vol. 7, pp.673-689.
22. Peterka, J. A., and Cermak, J. E., 1974: "Simulation of Atmospheric Flows in Short Wind Tunnel Test Section", FDDL, CER73-74 JAP-JEC32, Colo. State University, p.52.
23. Pope, A., and Harper, J.J., 1966: "Low-Speed Wind Tunnel Testing", John Wiley and Sons, New York, p.457.
24. Taylor, G. I., 1935:"Statistical Theory of Turbulence", Part I and II, Proc. Roy. Soc. A.
25. Schubauer, G. B., W. G. Spangenberg, and P. S. Klebanoff, 1950 "Aerodynamic Characteristics of Damping Screen", TN2001, NACA.
26. Drydon, H.L. and I.H. Abbott, 1950: "The Design of Low-Turbulence Wind Tunnel", NACA, Report, 940.
27. Tennekes, H. and J. L. Lumley, 1972: "A First Course in Turbulence", MIT Press. p.300.
28. Bradshaw, P. and R.C. Pankhurct, 1962: "The Design of Low-Speed Wind Tunnels", NPL-ARC 24041.

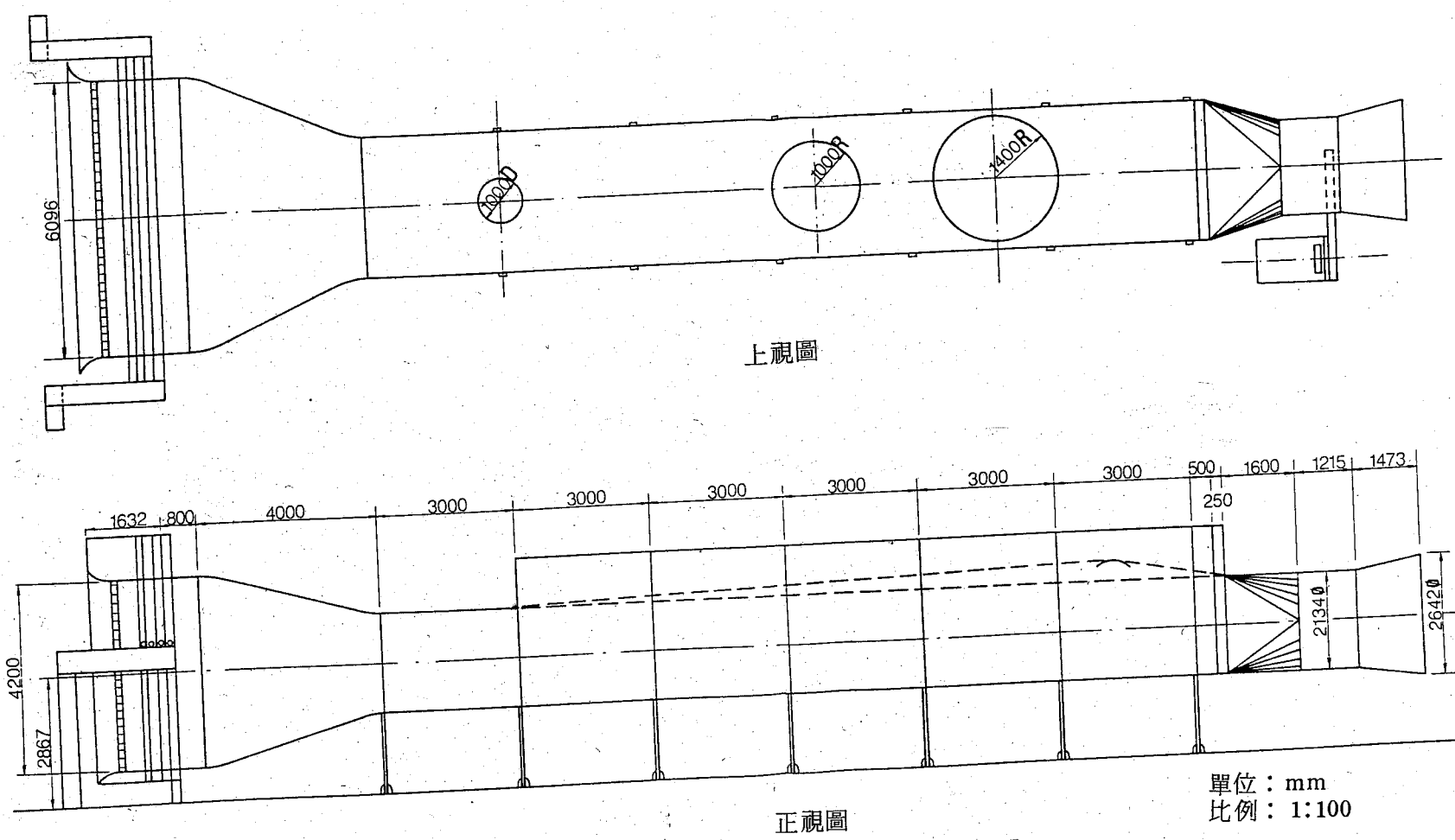

圖一、 大氣環境風洞上視圖與正視圖

No. 說明	No. 說明
1 保護網	7 試驗轉盤
2 蜂巢管	8 可調高度頂板
3 整流網	9 安全網
4 整流收縮段	10 風扇收縮管
5 收縮段	11 軸流風扇
6 試驗段	12 擴散管

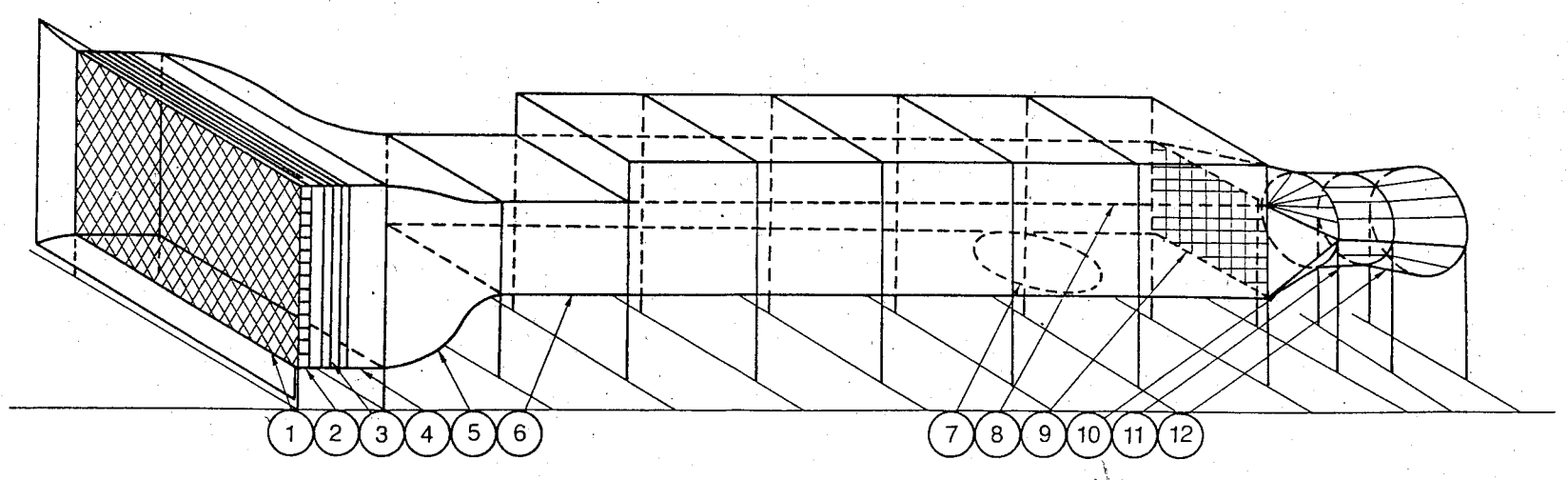

圖二、 大氣環境風洞立體圖

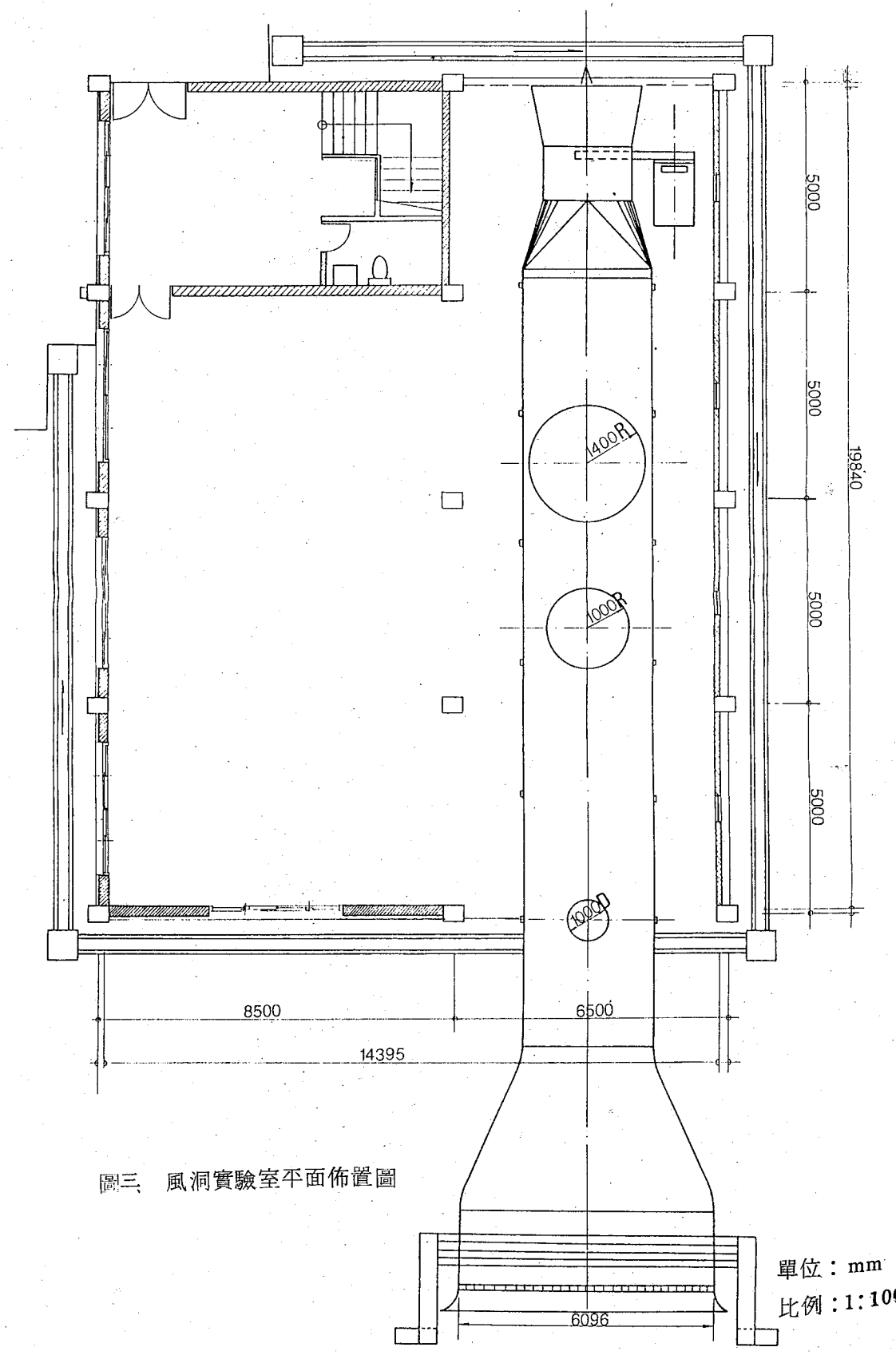

圖三、 風洞實驗室平面佈置圖

單位：mm
比例：1:100

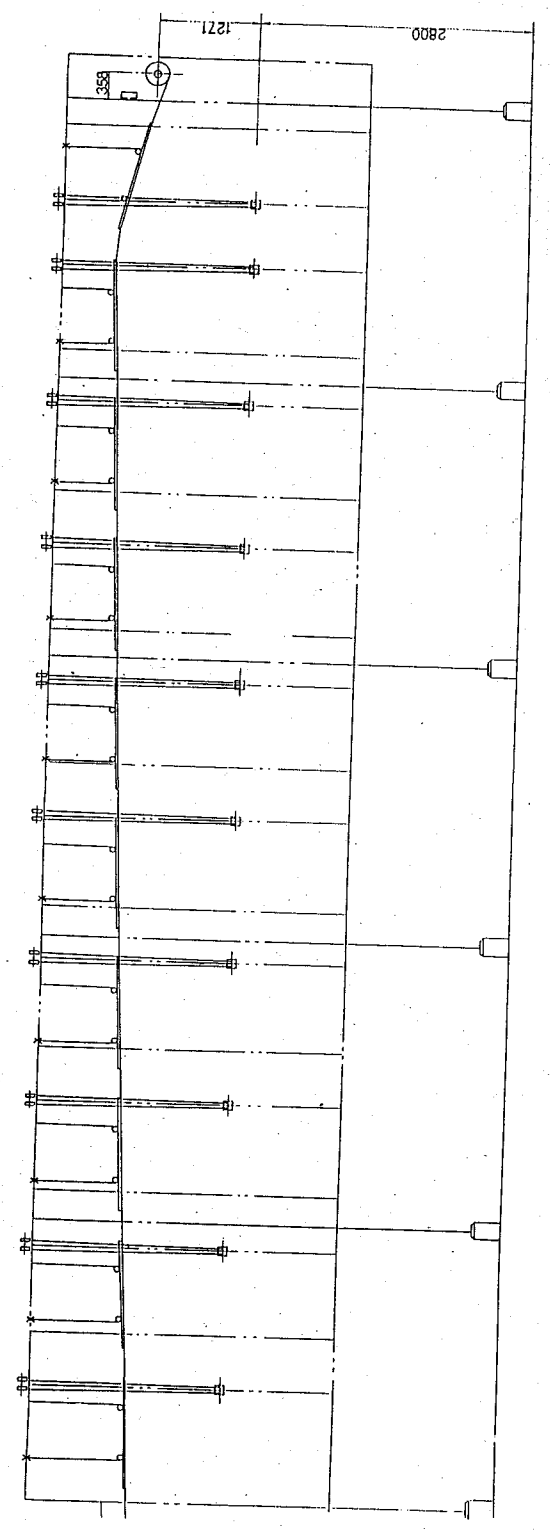

單位：mm
比例：1:45

圖四之一，風洞試驗段流軸向壓力調整裝置（側視圖）

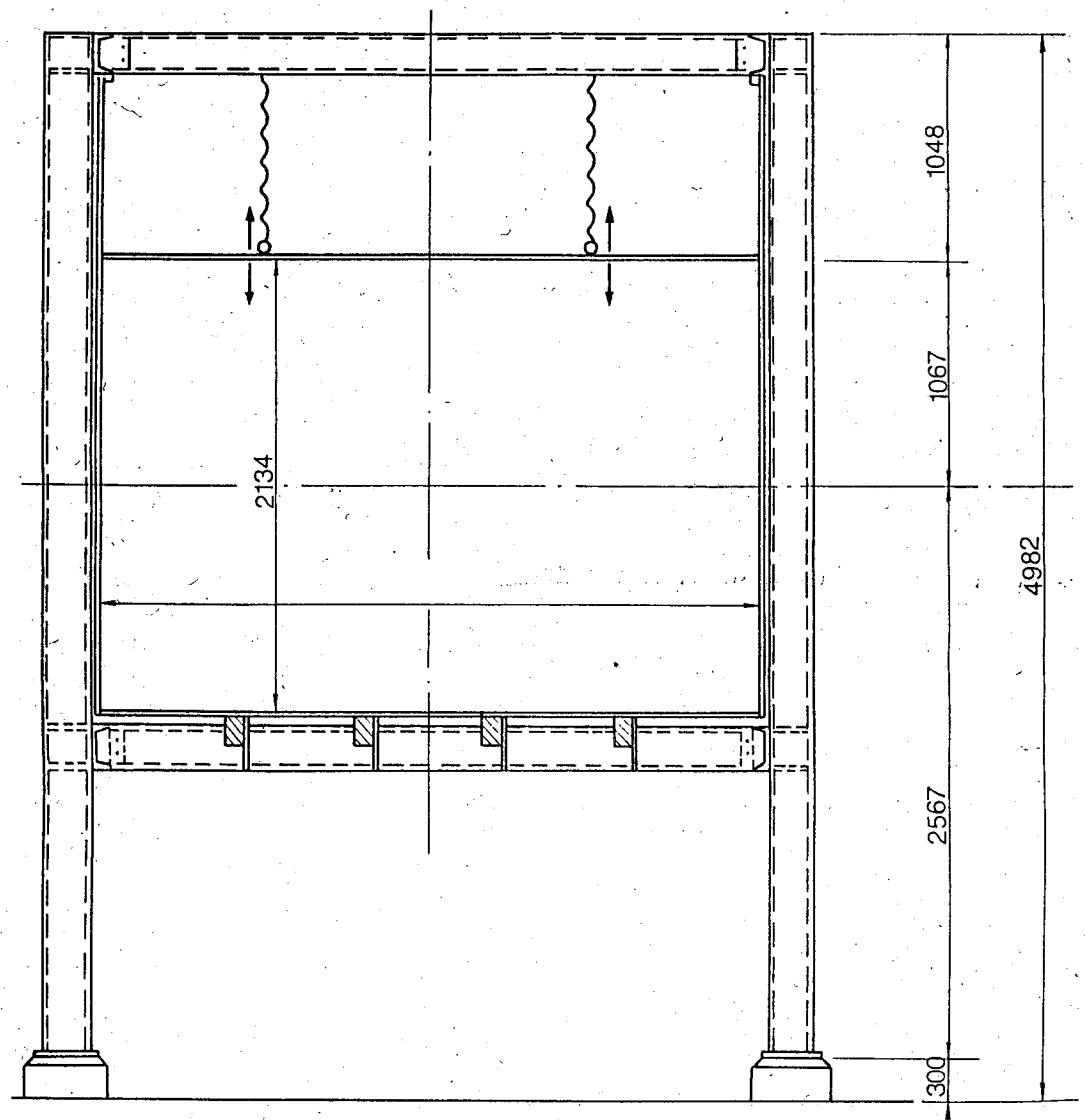

圖四之二，風洞試驗段流軸向壓力調整裝置（剖面圖）比例：1:30
單位：mm

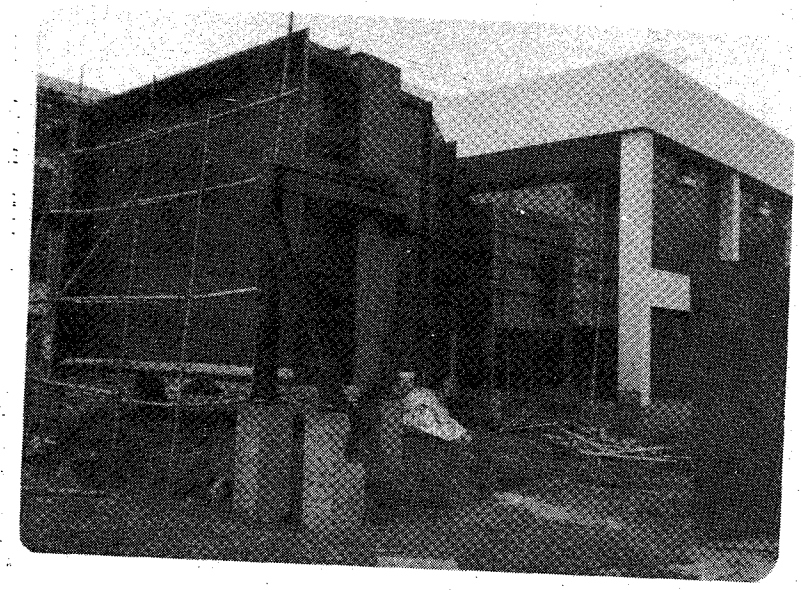

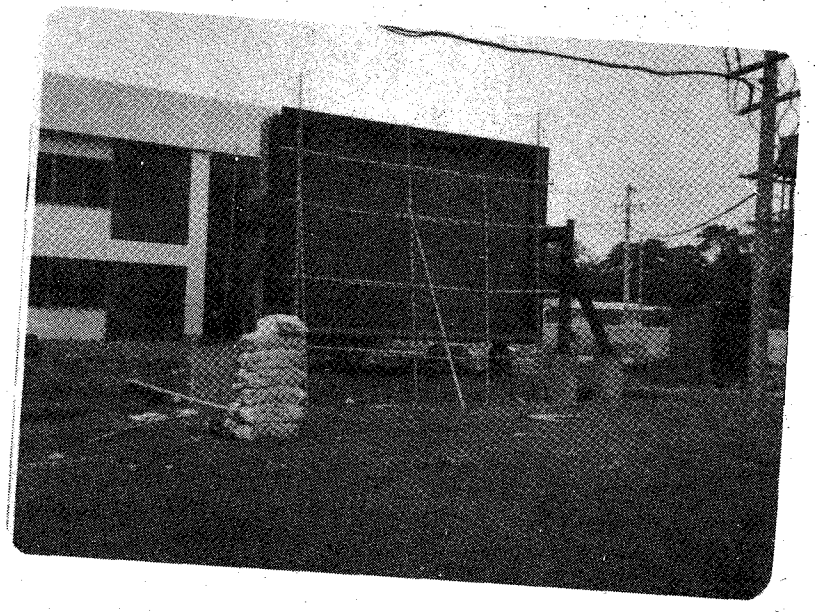

風洞進口收縮段

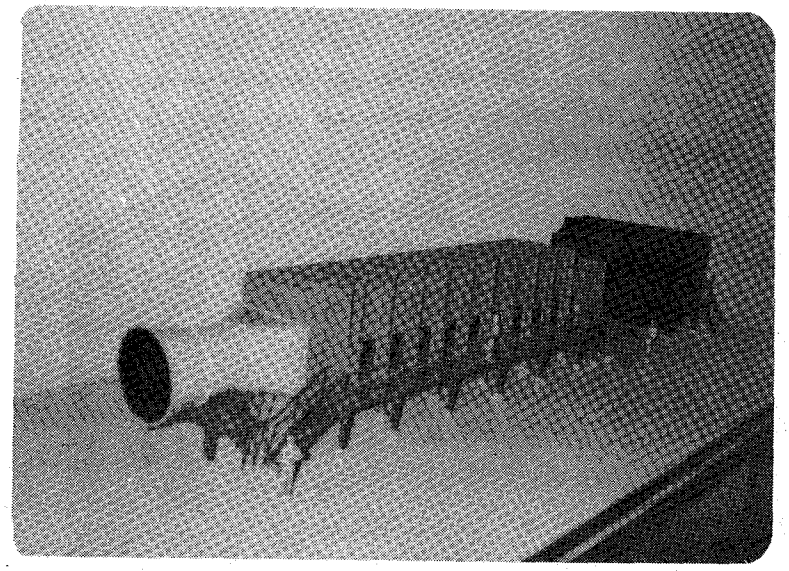

大氣環境風洞實體三十分之一模型

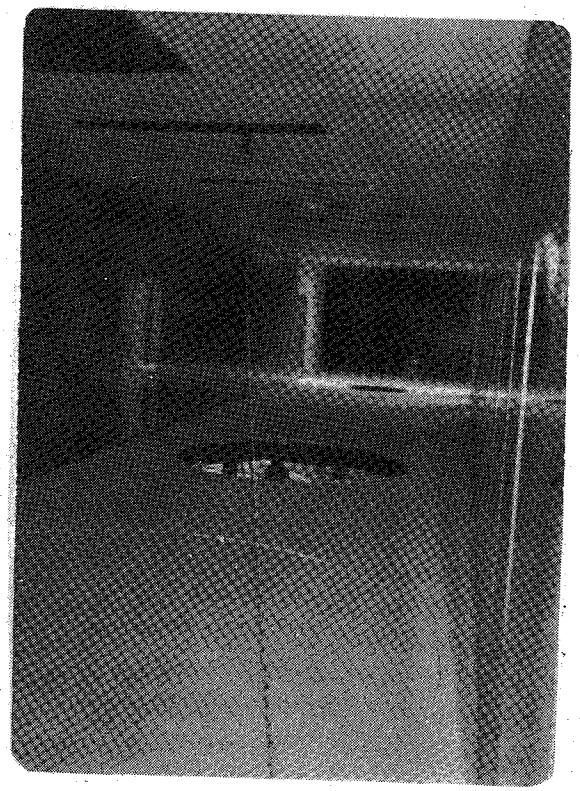

風洞試驗段內部

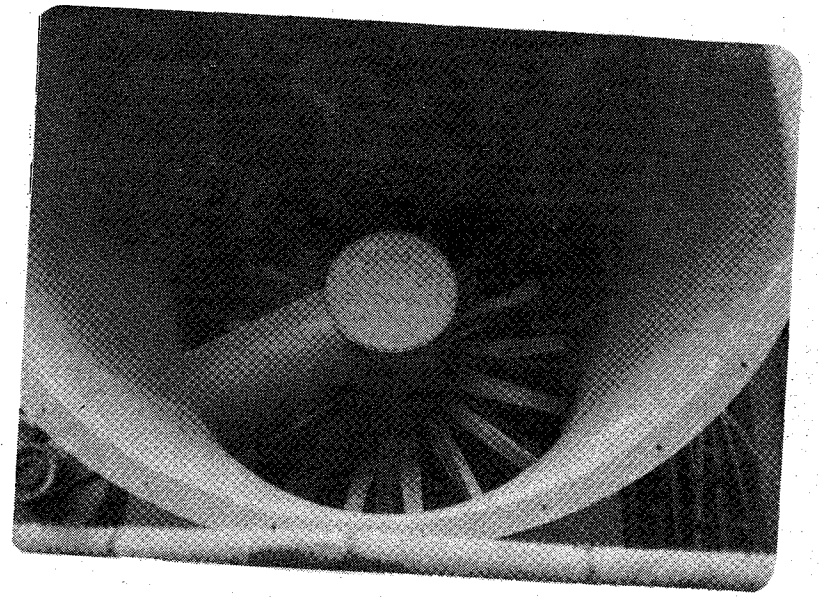

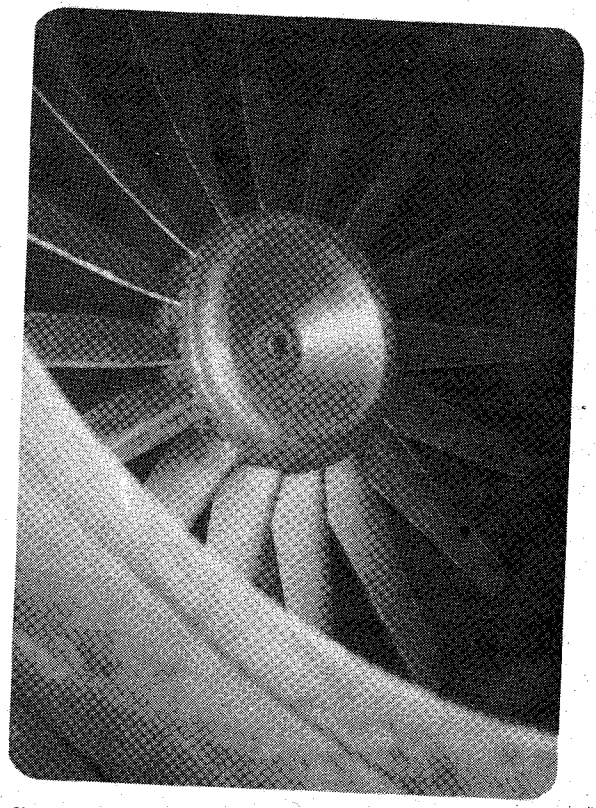

風洞動力段軸流式風扇（JOY AXIVANE FAN）

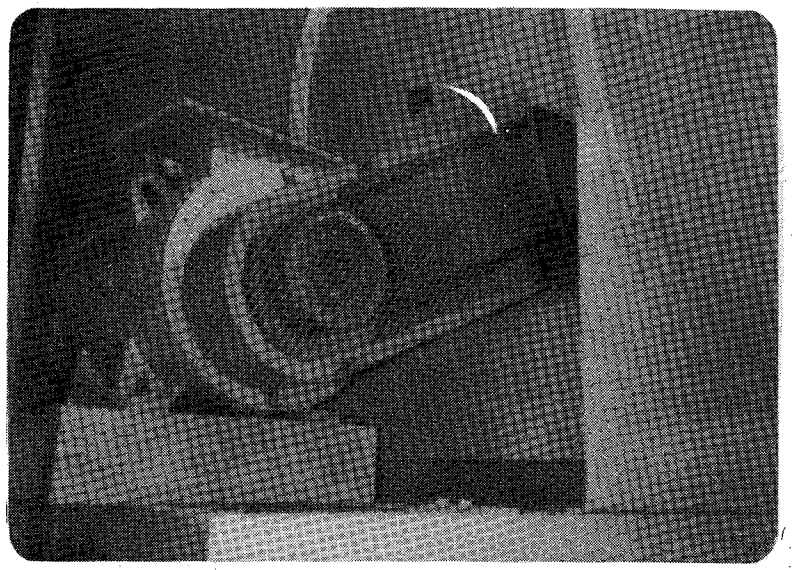

風洞動力段 200HP 直流變速馬達

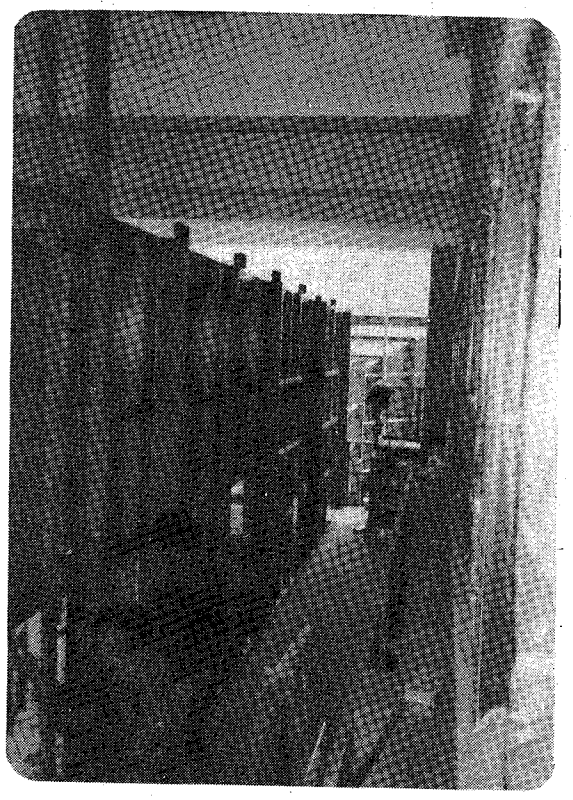

風洞施工過程

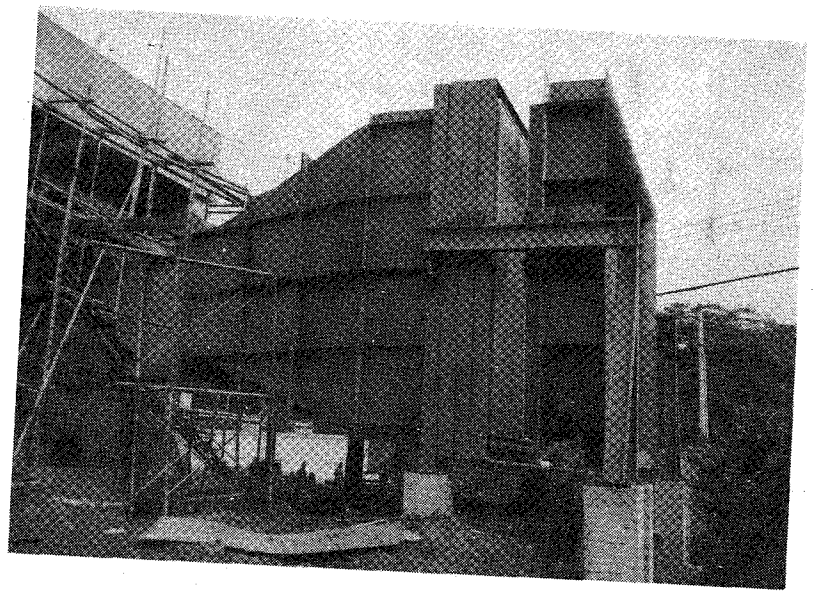

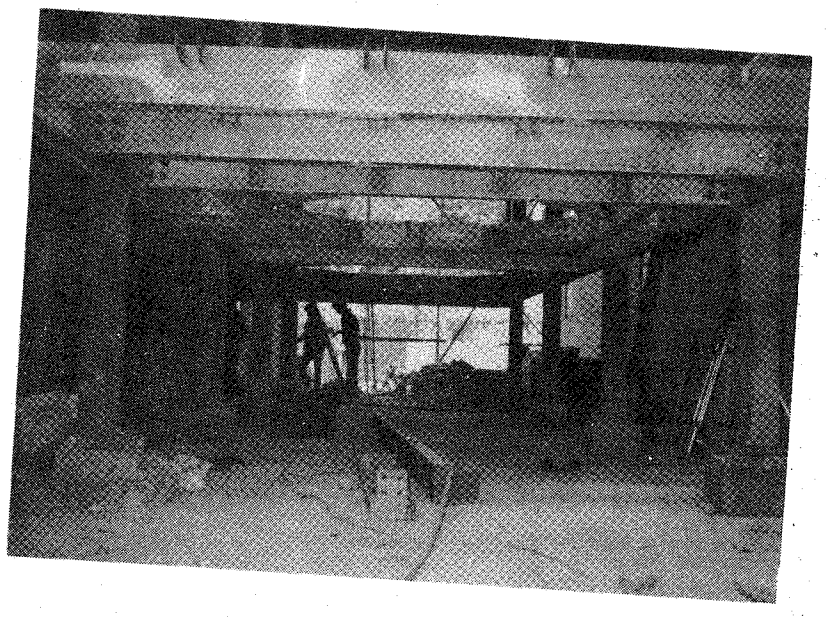

風洞施工過程

Annual Report of the Institute of Physics, Academia Sinica, Vol. 13, 1983

AN EXACT RENORMALIZATION GROUP TRANSFORMATION AND PROPERTIES OF POSITIVE SYMMETRY MATRICES

Chin-Kun Hu

Institute of Physics, Academia Sinica

Nankang, Taipei, Taiwan, R. O. C.

A positive symmetric m x m matrix P can be interpreted as the transfer matrix for an one-dimensional array of particles which have m-discrete energy levels and the most general nearest neighbor interactions. It is shown that $P' = P^2$ can be considered as exact renormalization group (RG) transformation applied on such one-dimensional system which does not have any phase transitions for $T > 0$. The exact RG transformation can be iterated to reach the high temperature fixed point. From the known asymptotic behaviour of RG transformations near the high temperature fixed point, we can derive and have a physical picture of properties of P^{2^n} as $n \to \infty$, which can also be derived directly from the matrix theory. We also show that the fixed point of the RG transformations can be obtained directly from the eigenvector corresponding to the largest eigenvalue of P. The formulation is applied to the spin-1/2 Ising model as an illustration.

Published in Chinese J. Phys. (Taipei), Vol. 21, No. 3, 4 (1983).

PERCOLATION, CLUSTERS, AND PHASE TRANSITIONS IN SPIN MODELS

Chin-Kun Hu

Institute of Physics, Academia Sinica

Nankang, Taipei, Taiwan, R. O. C.

The phase transition in the Ising model and the percolation transition in the lattice percolation model have many common characteristics, which have motivated researchers to explore whether the former is a percolation transition of a correlated percolation model. Previous attempts to draw such connection have been either unsuccessful or dissatisfactory. Considering each lattice site with an Ising spin occupied and the nearest-neighbor (NN) coupling between occupied sites as a bond with a bond probability p depending on the NN coupling constant J and the temperature T, we formally show that the partition function of the Ising model is the generating function of a bond-correlated percolation model (BCPM) with a bond probability $p = 1 - \exp(-2J/kT)$. The BCPM has the Ising critical temperature and exponents, including ν, ν', η, β, α, α' and γ (perhaps also γ'). From the connection between the Ising model and the BCPM, we also derive and hence give geometrical meaning of the finite-size scaling and broadening at first-order phase transitions of the Ising model. Our approach may easily be extended to many spin models and give geometrical meaning to other properties of spin models.

To be published in Physical Review B1, Vol. 29 (1984).

SITE-BOND-CORRELATED PERCOLATION AND A SUBLATTICE DILUTE POTTS MODEL AT FINITE TEMPERATURES

Chin-Kun Hu

Institute of Physics, Academia Sinica

Nankang, Taipei, Taiwan, R. O. C.

It is shown that the partition function of a sublattice dilute q-state Potts model (SDQPM) for even positive integer q at finite temperatures is the generating function of a site-bond-correlated percolation model (SBCPM) which favors subgraphs with larger numbers of disconnected finite clusters. The phase diagrams for the SBCPM are obtained from the corresponding phase diagrams for the SDQPM. A device is introduced to establish the connection between the SDQPM for $q \to 1$ and a site-bond (random) percolation model (SBPM). The results of this work contain those of some previous papers as special cases.

To be published in Physical Review B1, Vol.29 (1984).

CORRELATED PERCOLATION AND THE PHASE TRANSITIONS IN ISING-LIKE SPIN MODELS*

Chin-Kun Hu
Institute of Physics
Academia Sinica
Nankang, Taipei, R. O. C.

Considering each lattice site with a spin occupied and the lattice site without a spin unoccupied, we could formally show that the partition functions of many Ising-like spin models are the generating functions of correlated percolation models. Each correlated percolation model has the same critical properties as the corresponding spin model. From such connections, we could physically understand many properties of spin models. In this paper, we first formally show that the partition function of the q-state Potts model (QPM) is the generating function of a q-state bond-correlated percolation model (QBCPM) which has the same critical point and exponents as those of the QPM. From this connection, we propose a geometrical conditon of phase transitions and give geometrical reasons for the variation of the critical exponent α with q, the changeover from second-order to first-order phase transition as q increases, and the finite-size scaling and broadening at thermal and magnetic first-order phase transitions. Similar analyses for other spin models will be presented in other papers.

---

*Presented at Symposium on Condensed Matter Physics, November 25-26, 1983 at Institute of Physics, Academia Sinica, Taipei, Taiwan, R. O. C.

CORRELATED PERCOLATION AND THE PROPERTY OF MATTER*

Chinn-Kun Hu
Institute of Physics,
Academia Sinica
Nankang, Taipei, R. O. C.

Many physical systems may be represented by spin models. Using the method of the previous paper, we formally show that the partition functions of many spin models corresponding to physical systems are the generating functions of correlated percolation models. From such connections, we could physically understand many properties of matter, such as the unusual behavior of superooled water, sol-gel phase transition, etc.

---

*Presented at Symposium on Condensed Matter Physics, November 25-26, 1983 at Institute of Physics, Academia Sinica, Taipei, Taiwan, R. O. C.

Annual Report of the Institute of Physics, Academia Sinica, Vol. 13, 1983

MAGNETIC STATES OBSERVED IN HIGH-RESOLUTION (p, n) EXPERIMENTS

H. Orihara and C. D. Zafiratos

Cyclotron and Radioisotope Center,

Tohoku University, Sendai 980, Japan

S. Nishihara, K. Furukawa, M. Kabasawa and T. Nakagawa

Department of Physics, Faculty of Science,

Tohoku University, Sendai 980, Japan

K. Maeda

College of General Education, Tohoku University,

Sendai 980, Japan

K. Miura

Tohoku Institute of Technology,

Nagamachi-Koeji, Sendai 982, Japan

G. C. Kiang

Institute of Physics, Academia Sinica,

Taipei, 115, R. O. C.

H. Ohnuma

Department of Physics, Tokyo Institue of Technology,

Oh-okayama, Tokyo 152, Japan

A study of magnetic (unnatural-parity) states observed in charge-exchange (p, n) experiments is presented. The (p, n) reactions on ^{12}C, ^{14}C, ^{16}C, ^{24}Mg and ^{28}Si have been investigated at $E_p = 35$ MeV by means of time-of-flight technique. In the first half of this report, feasibility of analyses for the low-energy (p, n) data with use of the proposed realistic nucleon-nucleon interactions is discussed. In the next half analyses for angular distributions of the differential cross section for the transitions of the spin-isospin type such as from 0^+ to 0^-, 2^-, 4^- and 6^- states are presented.

---

*Proceedings of the 1983 RCNP International Symposium on Light Ion Reaction Mechanism, Osaka Japan, Research Center for Nuclear Physics, Osake University.

Annual Report of the Institute of Physics, Academia Sinica, Vol. 13, 1983

EXCITATION OF GIANT GAMOW-TELLER RESONANCES IN THE REACTION $^{140}Ce(p, n)\,^{140}Pr$

H. Orihara, G. C. Kiang

Cyclotron and Radioisotope Center,

Tohoku University, Sendai 980, Japan

S. Nishihara, T. Murakami, T. Nakagawa, K. Furukawa

Department of Physics, Faculty of Science,

Tohoku University, Sendai 980, Japan

K. Maeda

College of General Education,

Tohoku University, Sendai 980, Japan

K. Miura

Tohoku Institute of Technology,

Nagamachi-Koeji, Sendai 982, Japan

S. Adachi

Institute for Nuclear Study, University of Tokyo,

Tanashi, Tokyo 188, Japan

H. Ohnuma

Department of Physics, Tokyo Institute of Technology,

Oh-okayama, Meguro, Tokyo 152, Japan

Two broad peaks were observed at $E_x = 6.5$ and 12.1 MeV in the (p, n) reaction on ^{140}Ce at $E_p = 38$ MeV. They are interpreted as the $T = T_0 - 1$ Gamow-Teller resonances (GTR). A self-consistent TDA model with a Skymre type interaction predicts such a splitting of teh $T = T_0 - 1$ GTR, and reproduces the relative energies and strengths of the components. Experimental results are also compared with a recent RPA calculation which includes Δ—hole excitations.

---

*On leave from the Institute of Physics, Academia Sinica, Taipei, Taiwan, R. O. C.

Published in Physics Letters 118B, 283 (1982).

LOW-TEMPERATURE HEAT CAPACITIES OF SrF2 AND OTHER FLUORIDE COMPOUNDS

Lawrence T. Ho

Institute of Physics, Academia Sinica,

Taipei, Taiwan, R. O. C.

D. P. Dandekar

U. S. Army Materials and Mechanics Research Center,

Watertown, Massachusetts 02172

James C. Ho

Physics Department, Wichita State University,

Wichita, Kansas 67208

Heat-capacity measurements between 2 and 22 K have been made on SrF_2, yielding a limiting value of Debye temperature $\theta_D(0) = 385$ K. A brief review is then given, for various fluoride compounds XF_2 (X = Ba, Ca, Cd, Mn, Pb and Sr), on the general agreement between their $\theta_D(0)$ values as determined from calorimetric measurements and those from elastic-constant measurements, as well as on the general trend of deviations of their lattice heat capacity from a simple Debye behavior.

Published in Phys. Rev. B27, 3881, (1983).

EXCITATION SPECTRA OF GROUP II IMPURITIES IN Ge: Ge(Mg^o), Ge(Be^o) and Ge(Be^-)

L. T. Ho

Academia Sinica, Taipei, R. O. C.

J. W. Cross and A. K. Ramdas

Purdue University, Indiana, U. S. A.

R. Sauer

University of Stuttgart, Stuttgart, Germany

E. E. Haller

University of California, Berkeley, U. S.A.

Magnesium diffused into germanium behaves as an acceptor. The high resolution far infrared absorption spectrum of Ge(Mg^o) reveals a Lyman spectrum characteristic of a neutral double acceptor[2] with the G, D, C, B, A″, A′, and A lines at 31.22, 32.97, 33.72, 34.34, 34.69, 34.88, and 35.15 meV respectively, in turn yielding an ionization energy of 35.85 meV. The excitation spectrum of Ge(Be^o) examined under the high resolution shows that all the excitation lines have additional structure. We ascribe this to the $\{\Gamma_8 \times \Gamma_8\} = \Gamma_1 + \Gamma_3 + \Gamma_5$ ground state structure of a double acceptor. Excitation lines with spacing four times that of Ge(Be^o) have been observed in samples with compensating donors; we ascribe them to Ge(Be^-). When this compensation is large, broadenings and asymmetries characteristic of the Stark effect due to charged centers are observed.

Published in Bulletin of the American Physical Society Vol. 28, 339 (1983).

THE BEHAVIOR OF MAGNESIUM IMPURITIES IN GERMANIUM

L. T. Ho.

Institute of Physics Academia Sinica

Nankang, Taipei, Taiwan, R. O. C.

A solid solubility of the order of 10^{16} atoms/cm^3 has been found for magnesium impurities in germanium by the diffusion technique. Unlike being an interstitial donor in silicon[1], electrical measurement indicates that magnesium enters germanium lattice substitutionally and behaves like an acceptor[2]. The infrared absorption spectrum of magnesium impurities in germanium shows excited states similar to those of group III and other group II acceptors. Contrary to the believe that the depth of the acceptor level within the same group increases as the row number in the periodic table increases, magnesium is found to be a deeper impurity in germanium than zinc.

---

1. L. T. Ho and A. K. Ramads, Phys. Rev. B5, 462 (1972).
2. L. T. Ho. Appl. Phys. Lett. 35, 409 (1979).

Presented at Asia Pacific Physics Conference, Singapore, June, 1983.

DEVIATIONS FROM MATTHIESSEN'S RULE IN THE NICKEL-CHROMIUM SYSTEM*

Y. D. Yao

Institute of Physics, Academia Sinica

Taipei, Taiwan, R. O. C.

S. Arajs

Department of Physics, Clarkson College of Technology

Potsdam, N. Y. U. S. A.

E. E. Anderson

The University of Alabama in Huntsville

Huntsville, Alabama, U. S. A.

The deviations from Matthiessen's rule are studied between 4 and 300 K for Ni-Cr alloys containing Cr up to 27 at %. For Ni-Cr alloys with Cr concentration smaller than about 5 at %, the deviations from Matthiessen's rule of the resistivity can be explained by a two-current model. However, this model is not valid for Ni-Cr alloys with Cr concentration larger than about 11 at %.

---

*Published in Phys. Stst. Sol. (a) 79, 327 (1983).

FERROMAGNETIC MULTIFILAMENTARY Fe AND Ni WIRES WITH HIGH COERCIVE FIELDS PRODUCED BY POWDER METALLURGY PROCESSING*

Y. D. Yao

Institute of Physics, Academia Sinica,

Taipei, Taiwan, R. O. C.

S. Foner

Francis Bitter National Magnet Laboratory,

Massachusetts Institute of Technology, Cambridge

Massachusetts, 02139, U. S. A.

Powder metallurgy processed multifilamentary Cu-Fe, Cu-Ni, and Nb-Ni ferromagnetic composite wires were fabricated with a relatively high coercive field H_c at room temperature. Compacts of Cu-36 wt. % Fe, Cu-36 wt.% Ni, and Nb-36 wt.% Ni powders were reduced in cross section to produce ferromagnetic multifilamentary materials. Nominal areal reduction ratios of 10^8 for Cu-36 wt.% Fe and 10^4 for Nb-36 wt.% Ni and Cu-36 wt.% Ni resulted in values of $H_c \sim 195$ Oe, 95 Oe, and 77 Oe, respectively. A final 300°C anneal of the Cu-36 wt.% Fe composite gave $H_c \sim 460$ Oe. The average ferromagnetic fiber diameters are estimated to be 100 - 1000 A for the Fe fibers and are about 1 μm for the Ni fibers.

---

*Published in Appl. Phys. Lett. 43, 697 (1983).

島狀銻薄膜的非晶體與晶形相變

梁　乃　崇

中央研究院物理研究所

摘　要

島狀銻薄膜的非晶形與晶形相變可用拉曼散射觀察到，銻島的表面積與其體積之比（S／V）愈大愈難結成晶體，島狀銻薄膜的平均厚度與其等效結晶活化能大約成反比，平均厚度爲 200 Å 時，其等效結晶活化能爲 0.75 eV；20 Å 時爲10eV，由實驗結果推斷，銻的表面結晶活化能應在 10 eV 以上。

RAMAN SCATTERING FROM WEDGE-SHAPE Sb FILMS ON Ag FILMS

N. T. Liang

Institute of Physics, Academia Sinica

Nankang, Taipei, R. O. c.

T. T. Chen and Shou-Yih Wang

Department of Physics, National Tsing-Hua University

Hsinchu, Taiwan, R. O. C.

The resonance Raman scattering from an Sb wedge of variable effective thickness with underlayer or overlayer Ag has been studied. On the Sb wedge there was found a boundary line below which the wedge was Sb islands while above which the wedge was continuous. The normalized Raman signal from the Sb wedge was found to become enlarged in the island region whereas to become reduced in the continuous reg ion when a Ag island film was added as underlayer or overlayer.

Published in Chinese J. Phys. (Taipei), Vol. 21, No. 3, 4, (1983).

RESONANCE RAMAN SCATTERING FROM CRYSTAL VIOLET DEPOSITED ON ROUGH Ag FILMS

Y. C. Chou

Department of Physics, National Tsing Hua University

Hsinchu, Taiwan 300, R. O. C.

N. T. Liang

Institute of Physics, Academia Sinica

Nankang, Taipei, R. O. C.

The observed thickness dependence and excitation profiles of the surface enhanced resonance Raman scattering (SERRS) from crystal violet (CV) on Ag films demonstrated the importance of surface roughness and chemical effects. A tentative argument based on the overlap between the molecular resonance and the excitable surface resonances could reasonably explain the observed excitation profiles.

To be published in Chinese J. Phys. (Taipei), Vol.21, submitted for publiscation.

LATTICE VIBRATIONS OF CRYSTALLINE TITANIUM AND TIN TETRACHLORIDES

W. S. Tse

Institute of Physics, Academia Sinica,

Taipei, Taiwan (115), R. O. C.

C. C. Chen

Department of Physics, Soochow University

Taipei, Taiwan (111), R. O. C.

H. Chang

Department of Chemistry, National Tsing Hua University,

Hsinchu, Taiwan (300), R. O. C.

N. T. Liang

Institute of Physics, Academia Sinica,

Taipei, Taiwan (115), R. O. C.

The vibrational spectra of polycrystalline samples of titanium and tin tetrachlorides at 80 K have been investigated by Raman spectroscopic techniques. In the intramolecular region, isotopic and crystalline field splittings are observed, in substantial agreement with earlier work. In the lattice region, ten of the twelve Raman-active lattice modes are observed. A simple model is suggested and used to distinguish the low-frequency lattice translational from librational modes.

To be published in Journal of Raman Spectroscopy (1984).

ON THE STABILITY, SWITCHING VOLTAGE AND TRANSIENT ON-CHARACTERISTICS OF AMORPHOUS THIN FILMS

Chun Chiang

Institute of Physics Academia Sinica,

Nankang, Taipei, Taiwan, R. O. C.

By proposing that two types of reversible configurations co-existing in the film, that the ratio of two configurations is determined by current according to the law of mass action and the electronic energy transfer, that the difference of configurations may be due to phase, bonding state, filament formation, valence alternation pair, etc., mathematical equations can be derived to explain the threshold switching, the time dependence of the threshold voltage, transient ON characteristics and the non-linearity of the conductance.

Published in Physics Letters 99A, 453 (1983).

A DYNAMIC EQUATION FOR SWITCHING IN AMORPHONS THIN FILMS

Chun Chiang
Institute of Physics Academia Sinica,
Nankang, Taipei, Taiwan, R. O. C.

Base on Chiang's previous theory of threshold switching in amorphous thin films, a dynamic switching equation is formulated for the first time; numerical calculation of this equation shows that it can predict the experimental results very well. It is also pointed out that the differentiation of delay time and switching time may be misleading theoretically and it is proposed to use instead the smooth switching time, during which no appreciable change is observed and the drastic switching time during which appreciable change is observed.

To be published in Physica Status Solidi (a) (1984).

THE EXCITATION PROPERTIES OF NERVE MEMBERANES

Chun Chiang
Institute of Physics, Academia Sinica,
Nankang, Taipei, Taiwan, R. O. C.

With the assumption of coupling between the membrane dipoles and the phonons, it is possible to explain sodium activation, sodium inactivation, potassium activation with time delay, the nerve action potential, after-potential oscillation and gating currents in a coherent way. While it is possible that some polishing and modification may be needed in the future, it seems at present that this theory is able to explain a large amount of data satisfactorily.

Published in Neural Membranes, Edited by Grace Y. Sun, Nicolas Bazan, Jan-Yen Wu, Guiseppe Porcellati, and Albert Y. Sun. (The Humana Press, 1983).

Annual Report of the Institute of Physics, Academia Sinica, Vol. 13, 1983

A STUDY OF THE PLANETARY BOUNDARY LAYER WITH HIGHER-ORDER CLOSURE MODEL

Len-Fu W. Chang

Institute of Physics, Arademia Sinica,

Nankang, Taipei, Taiwan, R. O. C.

In this study, the continuous evolution of a convective planetary boundary layer (PBL) is simulated by turbulence higher-order-closure model. The closure assumptions include the return-to-isotropy effect proposed by Rotta (1951), the universal theory about turbulence dissipation by Kolmogoroff (1941), and the down-the-gradient transport analogy relating thirdmoment quantities to second-moment quantities.

Statistics of turbulence in a convective PBL simulated by model are compared with experimental data. The detailed turbulence structure predicted by model is reasonably well.

As inferred from the simulation study, a convective PBL can be conceived as comprising three layers; the surface layer, the well-mixed layer, and the turbulent inversion layer. Below the turbulent inversion layer, ensemble mean profiles of a convective PBL reveal similarity, regardless of the baroclinic geostrophic shear. This is due to the existence of two distinct time scales associated with geostrophic forcing and convective turbulence mixing. The geostrophic shear is not effective in changing the ensemble mean profiles, because of its long-time scale process compared to convective turbuelent mixing. Finally, the turbulent inversion layer serves as the matching layer which connects the mixing layer from below to the free atmosphere above, both dynamically and thermodynamically.

To be published in Proceeding of the National Science Council of the Republic of China, Vol. 8, No. 2, (1984).

本文主要討論應用紊流高階收合模式研究對流性大氣邊界層的變化。紊流收合模式的主要假設爲紊流回復等向性效應(Rotta,1951)，紊流動能滯耗效應(Kolmogoroft, 1941)，及第三階與第二階紊流統計量間之逆梯度傳遞性效應。

從模式模擬之紊流邊界層各種總集平均量與實驗觀測數據比較相當一致。進一步的檢討模擬結果可以發現，對流性大氣邊界層可以定性上分成三層：近地層、混合層與紊流逆溫層。在紊流逆溫層以下之總集平均速度與位溫變化呈高度之相似性，而地轉風切變對該種相似性沒有影響。本文另以定性理論分析，發現地轉風切變屬於長時間(在中緯度爲 3 ～ 6 小時)之效應，而紊流對流混合作用屬於短時間之效應(數分鐘)。模式研究結果印證這種推論。在整個對流邊界層與自由大氣層接合過程中，紊流逆溫層之熱力與動力作用不可忽略。

AUTHOR INDEX

本集刊每年出版一次

非　賣　品

中　央　研　究　院

物　理　研　究　所　集　刊

第　十　三　卷

發行人：林　　爾　　康

編輯者：中央研究院物理研究所集刊編輯委員會

出版者：中央研究院物理研究所　　臺北市南港區

印刷者：萬　達　打　字　印　刷　有　限　公　司

電　話：三　九　四　〇　七　一　八

中　華　民　國　七　十　二　年　十　二　月　出　版

ANNUAL REPORT
of
THE INSTITUTE OF PHYSICS
ACADEMIA SINICA

VOLUME 13 DECEMBER 1983

THE INSTITUTE OF PHYSICS, ACADEMIA SINICA
TAIPEI, TAIWAN, REPUBLIC OF CHINA

中央研究院物理研究所集刊

發 行 人 (Publisher)
林 爾 康 (E. K. Lin)

執行編輯 (Executive Editor)
胡 進 錕 (C.-K. Hu)

The Annual Report is published annually by the Institute of Physics, Academia Sinica, Taipei, Taiwan 115, Republic of china.

中央研究院物理研究所集刊

第十三卷

中央研究院物理研究所印行

CONTENTS 目 錄

ARTICLES

FLUID MECHANICS AND ATMOSPHERIC PHYSICS

ABSTRACT

THEORETICAL PHYSICS

NUCLEAR PHYSICS

SOLID STATE PHYSICS AND BIOPHYSICS

FLUID MECHANICS AND ATMOSPHERIC PHYSICS

ERRATA

Ta-You Wu: A NOTE ON EINSTEIN'S RELATION OF TRANSITION PROBABILITIES

On page 1, "." should be put after Equations (1) and (5); "," should be put after line 9, and Equations (3) and (4).

On page 2, "," should be put after Equation (8); "N'_m" of Equation (9) should be replaced by "N_m".

A NOTE ON EINSTEIN'S RELATION OF TRANSITION PROBABILITIES

Ta-You Wu

Academia Sinica, Taipei

In Einstein's theory of Planck's formula (1917), the basic relation is

$$N_n B^m_{\uparrow n} \phi_\nu = N_m B^m_{\downarrow n} \phi_\nu + N_m A^m_{\downarrow n} \tag{1}$$

On using the Boltzmann theorem

$$N_m = N_n e^{-\beta(E_m - E_n)} \tag{2}$$

and the condition that

$$\lim_{\beta h \nu \to 0} \phi_\nu = \frac{8\pi\nu^2}{c^3} kT$$

one arrives at

$$B^m_{\uparrow n} = B^m_{\downarrow n} \tag{3}$$

$$A^m_{\downarrow n} = \frac{8\pi h\nu^3}{c^3} B^m_{\downarrow n} \tag{4}$$

and

$$\phi_\nu = \frac{8\pi h\nu^3}{c^3} \frac{1}{e^{\beta h\nu} - 1} \tag{5}$$

The purpose of the present note is to point out that when the system of particles obey the Bose-Einstein or the Fermi-Dirac statistics, the relation (2) must be modified accordingly. It is well known that

$$\frac{N_n}{N} = \frac{1}{e^{-\gamma + \beta E_n} - a}, \qquad a = \begin{Bmatrix} 1 \\ 0 \\ -1 \end{Bmatrix} \quad \text{for} \begin{Bmatrix} \text{B.E.} \\ \text{Boltzmann} \\ \text{F.D.} \end{Bmatrix} \tag{6}$$

It can be shown then the relation (1) in general becomes*

$$N_n B^m_{\uparrow n} \phi_\nu = N_m B^m_{\downarrow n} \phi_\nu + N_m A^m_{\downarrow n} \left(1 + a \frac{N_n}{N}\right) \tag{7}$$

where

$$a\,\frac{N_o}{N} = \left\{ \begin{array}{c} \dfrac{1}{e^{-\gamma+\beta E_n}-1} \\ 0 \\ -\dfrac{1}{e^{-\gamma+\beta E_n}+1} \end{array} \right\} \text{for} \left\{ \begin{array}{l} \text{B.E.} \\ \text{Boltzmann} \\ \text{F.D.} \end{array} \right\} \text{system} \qquad (8)$$

and relations (3), (4), (5) remain valid.

The meaning of the $a\,\frac{N_n}{N}$ in (7) is clear. For the F. D. case, when $N_n = 0$, the transition rate of $m \longrightarrow n$ is $N_m A_n^m$. When $N_n \neq 0$, the Pauli principle reduces this rate by $\frac{N_n}{N}$. For the B. E. case, the transition rate of $m \longrightarrow n$ is enhanced by $\frac{N_n}{N}$. For the Boltzmann case the transition probability for $m \longrightarrow n$ is independent of N_n. This is in accord with Brillouin's derivation of (6).

* The relation (1) should in fact be replaced by

$$N_n B_n^m \left(1 + a\,\frac{N_m}{N}\right) \phi_\nu = N_m B_n^m \left(1 + a\,\frac{N_n}{N}\right) \phi_\nu + N_m' A_n^m \left(1 + a\,\frac{N_n}{N}\right), \qquad (9)$$

the argument being that given in the end paragraph. But in view of $B_n^m = B_n^m$ (3), this relation (9) reduces to (7).

Introducing statistical weights g_m, g_n for states m, n does not change the result above.

PHENOMENOLOGICAL RENORMALIZATION GROUP APPROACH TO PHASE TRANSITIONS

Chin-Kun Hu

Institute of Physics, Academia Sinica

Nankang, Taipei, Taiwan, R. O. C.

P. Kleban

Department of Physics and Astronomy and

Laboratory for Surface Science and Technology

University of Maine at Orono

Orono, Maine 04469, U. S. A.

A phenomenological renormalization group (PRG) transformation is formulated based on the idea that the renormalization group (RG) transformation can be considered as a process of replacing the original system by another one with fewer degrees of freedom but having the same or approximately the same free energy. As in Nightingale's PRG theory, only the inverse temperature (β) or external field (h) conjugate to the order parameter of the system is allowed to vary in the PRG transformation. It is found that the susceptibility diverges proportional to the number of particles in the system at first order transitions. The behavior of the correction to such finite-size scaling is also discussed. As a demostration, this formulation is applied to the two-dimensional Ising model and it is found that its susceptibility has the expected behavior. Some theoretical problems related to our formulation are also discussed.

I. INTRODUCTION

The calculation of the macroscopic properties of thermodynamic systems, such as phase diagrams and critical parameters, from given interactions between constituent particles of the systems, is one of the central problems of statistical mechanics. Before 1971, the methods used in such calculations included mean field theory[1], diagonization of the transfer matrix[2, 3], series expansion[4], and Monte-Carlo simulation[5] Each of these methods has certain advantages and disadvantages. For the two-dimensional Ising model with nearest neighbor (nn) interaction only, one can diagonize[2] the transfer matrix for an arbitrary number of spins to obtain the exact free energy, and hence specific heat, critical point etc., of the system. But for Ising models with more complicated interactions or

in higher space dimensions, one can diagonize only transfer matrices for small finite numbers of column or surface spins. Thus one can not calculate very accurate critical points and exponents which are manifestation of interactions among infinite number of particles with different length scales in given space dimensions. The Monte-Carlo simulation and mean field method have similar difficulties when dealing with systems at critical points. On the other hand, although the series expansion method[4] becomes very complicated when applied to high order term calculations and systems with complicated interactions, it does produce some reliable critical parameters for certain model systems[4].

In the first half decade of the 1960's, both experimental and theoretical results indicate that the critical exponents satisfy certain equalities which motivated Widom[6] in 1965 to introduce the scaling hypothesis for the free energy of a system near its critical point. In 1966. Kadanoff[7] presented a heuristic argument, called the Kadanoff construction, that provides intuitive support for the scaling hypothesis. The Kadanoff construction was eventually mathematically realized as a systematic calculation procedure when Wilson[8] introduced the renormalization group (RG) method to statistical physics. In the RG calculations of physical quantities, the contributions from different length scales are taken into acccunt and the qualitatively correct and even quantitatively accurate results can thus be obtained[9].

In the first few years after 1971, people usually carried out RG transformation in momentum space. In recent years, more attention has been paid to the position space renormalization group (PSRG) transformation. One of the reasons for this change is that lattice-gas models of certain experimentally available physical or chemical absorption systems on surfaces correspond to certain spin models[10] and the calculation of phase diagrams for such spin models is possible using PSRG methods. The PSRG methods often employed are the Niemeijer-van Leeuwen method[11], Kadanoff's variational approximation[12, 13], and Migdal-Kadanoff approximation[14,15]. Each of these methods also has certain virtues and limitations. The Niemeijer-van Leeuwen method is based on the assignment of block spin (i.e. transformed spin variable) to a certain number of site spins according to the majority rule in a system with a finite number of site spins. The complexity of the calculation increases

exponentially with the number of site spins in a given RG transformation. In Kadanoff et al.'s lower bound variational approximation[12, 13] only spins in the same primitive unit cell of the lattice can have nonzero couplings. The RG transformation in the Migdal-Kadanoff[14, 15] approximation is very simple, but this method is applicable directly to models with the nn interactions only. These limitations greatly reduce the possibility of direct application of the methods[11-15] to lattice-gas models for certain physically realizable systems. Besides such limitations. systematic errors of the PSRG methods just mentioned can easily reach 5 - 20%, and there is apparently no easy systematic way to reduce such errors.

In 1976, Nightingale[16] proposed a phenomenological renormalization group theory for second order phase transitions based on the finite-size scaling of the correlation length at second order phase transition temperatures. In this theory, the ratios among the coupling constants for the spins of the transformed and the original systems are assumed to be the same and only the inverse temperature(β) and magnetic field(h , coupling with order parameter) can be adjusted to satisfy the finite-size scaling of the correlation length ξ_n for simi-infinite n x ∞ spin systems, where n is the number of spins in a column. ξ_n can be calculated frcm the largest (λ_1) and second largest (λ_2) eigenvalues of the transfer matrix for n column spins as $\xi_n = 1/\ln(\lambda_1/\lambda_2)$. This method can be applied to spin models with complicated couplings among spins. The accuracy of such calculations can be increased easily by increasing n. Thus this is a very powerful method for calculating critical points and indices at second order phase transitions. However, this method can not be applied generally to locate first order phase transition points and thus can not be used to calculate the complete phase diagrams for many experimentally interesting systems.

The purpose of this paper is to formulate a phenomenological renormalization group (PRG) theory which has the advantages of Nightingale's theory and can also be systematically applied to first order phase transitions. The basic idea of our approach had been reported in 1981 American Physical Society march meeting[17] and also in a short paper[18]. Our approach, which will be reported in section 2, proceeds directly from previous PSRG developments and Nightingale's theory and

is based on the following ideas: (1) the RG transformation can be considered as a systematic way to replace the original system by a system with fewer degrees of freedom but having the same or approximately the same free energy; the ratios among the coupling constants for the spins of the transformed and the original systems are assumed to be the same and only β or h is adjusted to satisfy the requirement that the transformed and the original systems have the same or approximately the same free energy, (2) the RG transformation becomes more and more accurate when the fraction of the degrees of freedom subtracted each time in succesive RG transformations becomes less and less, (3) if there is a first or second order phase transition at $\beta = \beta_c$, $h = h_c$, then (β_c , h_c) is a fixed point of the RG transformation.

Based on the above ideas, we derive a scaling relation for the susceptibility at the fixed points of large systems, where the scaling power is a maximum at first order transitions. We will also discuss corrections to such scaling relations in finite systems. In the formulation of Sect. II, some of the assumptions made in the previous paper[18] are either not necessary or more comprehensible from a unified physical picture. The connection with traditional RG transformations[11-15] is also more clear. In Sect. III, we apply our formulation to the two-dimensional Ising model and find that the susceptibility has the expected behaviour. In Sect. IV, some theoretical problems related to our theory are discussed. A brief conclusion is given in Sect. V.

II. GENERAL FORMULATION

Our formulation is based on the following interpretation of the RG transformation. Let us take the application of the Niemeijer-van Leeuwen method[11] to the two-dimensional spin model on a square lattice as an example:

(2.1) Interpretation of a Conventional RG Transformation.

Suppose we have Ising spins, $s_1, \cdots\cdots s_N$, on a two-dimensional square lattice as shown in Fig.1 with interaction Hamiltonian $H (s_1, \cdots\cdots s_N)$. In the following, we shall use s(i, j) to denote spin s at coordinate (i, j). Some examples of s spin coordinates are shown in Fig. 1. To define a Niemeijer-van Leeuwen RG transformation, we define cell spins, $t_1, \cdots\cdots t_{N'}$, (N' = N/4),

on the lattice with doubled lattice constant also shown in Fig.1. We will use t(i, j) to denote a spin t on a lattice point, [i, j] where i and j are integers and " [ ] " indicates that t spins are on a lattice with doubled lattice constant. The purpose of the RG transformation is to find an effective Hamiltonian $H'(t_1, \cdots\cdots t_{N'})$ for the cell spins which has the same or approximately the same free energy as that calculated from $H (s_1, \cdots\cdots s_N)$. However, this is not an easy problem for $N \to \infty$. To make the calculation possible, one breaks the whole lattice into small 4 x 4 blocks of site spins as indicated by broken lines in Fig. 1. The broken lines break all coupling between site spins on different 4 x 4 blocks, e.g. s(2, 1) with s(1, 0), s(2, 0), and s(3, 0). To restore partially the loss of energy caused by the broken lines, one imposes a periodic boundary condition for each block of 4 x 4 site spins, e.g. the couplings between s(2, 1) and s(1, 0), s(2, 0), and s(3, 0) are replaced by the couplings between s(2, 1) and s(1, 4), s(2, 4), and s(3, 4). We thus have a block potential, e.g. v(s(1, 1) .....s(4, 4)) $\equiv v (s_1, \cdots\cdots s_{16})$, for each block of 4 x 4 site spins. From $v (s_1, \cdots\cdots s_{16})$, it is quite straightforward to calculate the block potential $v'(t[1 , 1] , \cdots\cdots t [2 , 2]) \equiv v'(t_1, \cdots\cdots t_4)$ for cell spins:

$$\exp (v'(t_1, \cdots\cdots , t_4) = \sum_{s_1, \cdots\cdots s_{16}} \exp (v (s_1, \cdots\cdots s_{16}) + T (t_1, \cdots\cdots t_4 ; s_1, \cdots\cdots s_{16})), \qquad (1)$$

where $T(t_1, \cdots\cdots t_4 ; s_1, \cdots\cdots s_{16})$ satisfies:

$$\sum_{t_1, \cdots\cdots t_4} \exp (T (t_1, \cdots\cdots t_4 ; s_1, \cdots\cdots s_{16})) = 1 \qquad (2)$$

to ensure that $v'(t_1, \cdots\cdots t_4)$ and $v(s_1, \cdots\cdots s_{16})$ have the same free energy. $v'(t_1, \cdots\cdots t_4)$ can be expanded as a summation of the invariant functions of $t_1, \cdots\cdots t_4$ with the coupling constants as expansion coeficients, which include the configuration independent constant C_o' . C_o' can also be calculated from the equation:

$$C_o' = \sum_{t_1, \cdots\cdots t_4} v'(t_1, \cdots\cdots t_4)/NCF, \qquad (3)$$

where NCF is the total number of configurations for $t_1, \cdots\cdots t_4$. The coupling constants except C_o' can be put together as a vector K'. It is then assumed that

the t spins within a block and the t spins in the neighboring blocks have the same coupling constant, e.g. the nearest neighbor coupling between t(1, 0) and t(1, 1) is the same as the nearest neighbor coupling between t(1, 1) and t(1, 2). We thus arrived at the Hamiltonian $H'(t_1, \cdots\cdots t_{N'})$ for cell spins with $\vec{K}'$ as the coupling constant vector. Let f(K) and f(K') denote the free energy per spin calculated from Hamiltonian with K and K' as coupling constant respectively, then

$$f(\vec{K}) \cong (f(\vec{K}') + K_0'(\vec{K}))/L^2 \qquad (4)$$

where L = 2 is the scale factor, $K_0' = C_0'/4$ is the background energy per cell spin for the transformed system. Equation (4) is only approximately, rather than exactly true, because the RG transformation of (1) only gives the approximate free energy for the transformed system. We can carry out the next step of RG transformation by breaking the lattice for $t_1, \cdots\cdots t_{N'}$, into 4 x 4 blocks of spins as indicated by the solid line in Fig. 1 and then proceeding in the same way as before. Such RG transformations can be carried out step by step until a fixed point is reached, where the free energy for the remaining degrees of freedom can be easily calculated. Thus Niemeijer-van Leeuwen's RG transformation[11] can be considered as a process of replacing original systems by other systems with fewer degrees of freedom, which have approximately the same free energy as the original system. We can also give a similar interpretation to the Migdal-Kadanoff[14, 15] and Kadanoff et al's[12, 13] lower bound RG transformation, where the free energy of the transformed system is a lower bound to the free energy of the original system. From this interpretation, it is easy to understand that there are appreciable errors in such RG transformations, because a large fraction of coupling bonds among spins are broken (in Niemeijer-van Leeuwen's method) or removed (in Migdal-Kadanoff approximation and Kadanoff et al's lower bound RG transformation) in each RG transformation. On the other hand, if only a small fraction of the bonds are broken in each RG transformation, more accurate results can be obtained. This is one of our basic motivations for the phenomenological RG transformation.

(2.2) Phenomenological RG Transformation.

For the purpose of easy presentation and comparison with prior methods, we formulate the phenomenological RG(PRG) transformation for spin models on a two-dimensional square lattice. This formulation can obviously be extended to three-

dimensions and other lattices.

As in the previous case, suppose we have Ising spins $s_1, \cdots\cdots s_N$ on a two-dimensional square lattice as shown in Fig. 2 with interaction Hamiltonian $H(s_1, \cdots\cdots s_N)$. The spins can have more complicated couplings than those in the previous case. We shall use s(i, j) to denote the spin on lattice point (i, j), where i and j are integers. To define a PRG transformation, we divide the lattice into n x m blocks of site spins as indicated by broken lines in Fig. 2. The broken lines break all coupling between site spins on different n x m blocks of site spins, e.g. s(n, 2) with s(n+1, 1), s(n+1, 2), and s(n+1, 3). To compensate for the loss of energy caused by broken lines, we impose periodic boundary condition for site spins on n x m blocks, e. g. the coupling between s(n, 2) and s(n+1, 1), s(n+1, 2), and s(n+1, 3) are replaced by couplings between s(n, 2) and s(1, 1), s(1, 2), and s(1, 3) respectively. We thus have an interaction potential $v(s(1, 1), \ldots s(n, m)) \equiv v(s; n, m)$ for nm site spins. The free energy of the nm site spins with the block potential v(s; n, m) can be calculated and is denoted by F(n, m; β , h), where β is the inverse temperature and h is an external field coupling with the order parameter. Now we define n'm' spin variables t(1, 1),... t(n', m') inside each nm block of site spins, where $1 < n/n' = m/m' = L$ = linear scale factor and t(1, 1), ... t(n', m') assume the same spin components as s (e.g., if s = $\pm$ 1, then t=$\pm$1). We also assume that the t spins couple in the same way as the s spins (including periodic boundary condition). Their block potential for a given configuration is denoted by v'(t(1, 1), ... t(n', m')$\equiv$v'(t; n', m'). As in the case of Niemeijer-van Leeuwen's RG transformation, we can establish the RG transformation by the requirement that the free energy calculated from v'(t';n', m') should be the same as that calculated from v(s; n, m). One possible way to realize this requirement is to introduce a generating function T(t(1, 1), ... t(n', m'); s(1, 1), ... s(n, m)) $\equiv$ T(t; s) which satisfies the normalization condition:

$$\sum_{(\,\,)\ s(1,1),\cdots,s(n,m)} \exp(v(s;n,m)+T(t;s)) = 1 , \qquad (5)$$

and v'(t; n', m') is related to v(s; n, m) by the transformation:

$$\exp(v'(t;n',m')) = \sum_{s(1,1),\cdots s(n,m)} \exp(v(s;n,m) + T(t;s)) . \qquad (6)$$

Eqs. (5) and (6) ensure that the free energy calculated from v'(t; n', m') is the same as that calculated from v(s; n, m) as is the case for (1) and (2). As in an ordinary RG transformation, v'(t; n', m') also contains a configuration independent constant C_o (n, m, n', m', β , h) which can be calculated from the equation:

$$C_o'(n,m,n',m',\beta,h)=\sum_{t(1,1),\ldots t(n',m')} v'(t;n',m')/NCF, \quad (7)$$

where NCF is the number of terms in the configuration summation of (7). It is easy to show that

$$\frac{\partial^2}{\partial h^2} C_o'(n,m,n',m',\beta,h)\geq 0, \quad (8)$$

$$\frac{\partial^2}{\partial \beta^2} C_o'(n,m,n',m',\beta,h)\geq 0. \quad (9)$$

Equations (8) and (9) will be used later in the discussion of the scaling behavior of magnetic susceptibility and specific heat at phase transition points. C_o' of (7) can be considered as a background energy of the t spin system arising from elimination of some degrees of freedom in the original s spin system. Thus C_o' becomes less and less important as $\frac{nm}{n'm'} \to 1^+$ and n, m, n', and m' tend to large numbers.

For the large values of n, m, n', and m', where the RG transformation is expected to be more accurate, it is difficult to carry out the transformation of (6) in practice. Thus we take the configuration sum over t(1, 1), ... t(n', m') on both sides of (6) and have the equation:

$$F(n,m;\beta,h)=F(n',m';\beta',h')+C_o'(n,m,n',m',\beta,h), \quad (10)$$

where F(n, m,; β , h) and C_o' (n, m, n', m', β , h) are defined above and F(n', m'; β' , h') is the free energy calculated from the configuration dependent part of v(t; n', m') (i.e. exclude the contribution from C_o'). We will use (10) as our PRG transformation equation.

Now dividing (10) by nm, we have:

$$f(n,m;\beta,h)=L^{-d}[f(n',m';\beta',h')+K_o'(n,m,n',m',\beta,h)]. \quad (11)$$

Here d=space dimensions, f(n, m; β , h) = F(n, m; β , h)/nm, f(n', m'; β' , h') = F(n', m'; β' , h')/n'm', and K_o' (n, m, n', m', β , h) = C_o (n, m, n', m', β , h)/n'm'. Eq. (11) is the PRG transformation for the transformed variables

β' , h', and K_o' . In later discussions, we will consider the RG transformation only in a particular direction perpendicular to the β or h axis in the (β , h) plane, e.g. we fix β (or h) and change h(or β) only. For the moment, suppose we know β' and h' for the transformed system. We then use β' and h' as coupling parameters for the infinite t spins system whose free energy per spin is denoted by f(β' , h'). f(β' , h') satisfies approximately the equation:

$$f(\beta,h)\cong L^{-d}[f(\beta',h')+K_o'(n,m,n',m',\beta,h)], \quad (12)$$

where f(β , h) is the free energy per spin of the original infinite s spin system. The difference between (11) and (12) should be noted; the former is the PRG transformation equation for β' or h', similar to (1) in an ordinary RG transformation, while (12) is the approximate equation for the free energy per spin of the infinite system, similar to (4) in an ordinary RG transformation.

Now we fix $\beta' = \beta$ and allow h' to change in (11) and (12) then take the derivative of (12) with respect to h to obtain the equation:

$$M(\beta,h)=L^{-d}[(\frac{\partial h'}{\partial h})M(\beta,h')+\frac{\partial}{\partial h}K_{o,h}'(n,m,n',m',\beta,h)], \quad (13)$$

where the subscript h has been included in $K_{o,h}'$ to indicate that only h is allowed to vary in the PRG transformation. Suppose the original Hamiltonian $H(s_1,\ldots s_N)$ is an even function of $s_1,\ldots s_N$ at h = 0. Then the second term on the right-hand side of (13) is zero at h = 0. In this case if

$$\Delta M(\beta,0)=M(\beta,0^+)-M(\beta,0^-)\neq 0, \quad (14)$$

we have

$$(\frac{\partial h'}{\partial h})=L^d. \quad (15)$$

This is the condition of the first order transition considered by B. Nienhuis and M. Nauenberg[19]. Now we fix $\beta' = \beta$ and take the second derivative of (11) with respect to h at h = 0 and have:

$$\chi(n,m,\beta,h)=L^{-d}(\frac{\partial h'}{\partial h})^2\chi(n',m';\beta,h')$$
$$+L^{-d}[\frac{\partial}{\partial h}(\frac{\partial h'}{\partial h})M(n',m';\beta,h')$$
$$+\frac{\partial^2}{\partial h^2}K_{o,h}'(n,m,n',m',\beta,h)], \quad (16)$$

Since h' is an odd function of h, the second term on the right-hand side is zero at h = 0. As n, m, n' and m' $\to\infty$ and nm/n'm' $\to 1^+$, the first term on the right-hand side of (16) becomes singular at phase transition points, but the last term is still regular or much less singular than the first term, which will be discussed further in section (4.4). Thus we can neglect the last term and have:

$$\chi(n, m, \beta, 0) = L^d \chi(n', m', \beta, 0), \qquad (17)$$

where (15) for a first order transition at h = 0 has been used. For large but finite n, m, n', and m', (17) can be considered as an approximate equation of finite-size scaling at a first order transition. At the second order transition, we have[9]:

$$\left(\frac{\partial h'}{\partial h}\right) = L^{d-\beta/\nu}. \qquad (18)$$

Following a similar procedure and argument to derive (17), we have:

$$\chi(n, m, \beta, 0) = L^{d-2\beta/\nu}\chi(n', m', \beta, 0), \qquad (19)$$

at second order transitions for large n, m, n', and m'. Since $\beta/\nu > 0$, we conclude from (17) and (19) that χ (n, m, β, 0) increases with n and m most rapidly at a first order transition. This can be used as a criterion to locate the first order transition point. For this purpose, we define the function:

$$\begin{aligned}\Delta\chi(n, m, n', m', \beta, h) &= \chi(n, m, \beta, h) - L^d\chi(n', m', \beta, h') \\ &= \left(L^{-d}\left(\frac{\partial h'}{\partial h}\right)^2 - L^d\right)\chi(n', m', \beta, h') \\ &+ L^{-d}\left[\frac{\partial}{\partial h}\left(\frac{\partial h'}{\partial h}\right)M(n', m', \beta, h')\right. \\ &\left. + \frac{\partial^2}{\partial h^2}K'_o(n, m, n', m', \beta, h)\right]. \qquad (20a)\end{aligned}$$

From (8), (17), (19), (20a), and the statement following (16), it is obvous that for large but finite n, m, n', and m',

$$\Delta\chi(n, m, n', m', \beta, h = 0) \geq 0 \qquad (20b)$$

at first order transition points, and

$$\Delta\chi(n, m, n', m', \beta, h = 0) < 0 \qquad (20c)$$

at second order transition points or points where there is no transition. Thus if we plot $\Delta\chi$ (n, m, n', m', β, h) as a function of h at a first order transition temperature, there will be a region of positive sign near h = 0 even for quite large (but finite) n, m, n', and m'. This behavior can be used to identify the region of first order transitions (see next section for an example).

Now we fix h' = h = 0 and allow β' to change in (11) and (12). The first derivation of (12) with respect to β and the second derivative of (11) with respect to β are given by:

$$U(\beta, 0) = L^{-d}\left[\left(\frac{\partial\beta'}{\partial\beta}\right)U(\beta', 0) + \frac{\partial}{\partial\beta}K'_{o,\beta}(n, m, n', m', \beta, 0)\right], \qquad (21)$$

$$\begin{aligned}&C(n, m, \beta, 0) \\ &= L^{-d}\left(\frac{\partial\beta'}{\partial\beta}\right)^2 C(n', m', \beta', 0)(\beta/\beta')^2 + L^{-d}\left[\beta^2\frac{\partial}{\partial\beta}\left(\frac{\partial\beta'}{\partial\beta}\right)U(n', m', \beta', 0)\right. \\ &\left. + \beta^2\frac{\partial^2}{\partial\beta^2}K'_{o,\beta}(n, m, n', m', \beta', 0)\right], \qquad (22)\end{aligned}$$

where $U(\beta, 0) = \frac{\partial}{\partial\beta}f(\beta, 0)$, $U(\beta', 0) = \frac{\partial}{\partial\beta'}f(\beta', 0)$,

$C(n, m, \beta, 0) = \beta^2\frac{\partial^2}{\partial\beta^2}f(n, m, \beta, 0)$, $C(n', m', \beta', 0) = \beta'^2\frac{\partial^2}{\partial\beta'^2}f(n', m', \beta', 0)$. If β_c is a fixed point of (11) at h = 0 and

$$U(\beta_c, 0) = U(\beta + \varepsilon, 0) - U(\beta - \varepsilon, 0) \neq 0 \qquad (23)$$

for positive $\varepsilon \to 0^+$, then it follows from (21) that:

$$\frac{\partial\beta'}{\partial\beta} = L^d \qquad (24)$$

at the first order transition temperature β_c. At a second order phase transition temperature, we have[9]:

$$\frac{\partial\beta'}{\partial\beta} = L^{(d/\nu - \alpha)}. \qquad (25)$$

As n, m, n', and m' $\to\infty$ and nm/n'm' $\to 1^+$, the first term on the left-hand side of (22) become singular at phase transition points, but the last two terms are still regular or much lesser singular than the first term, which will be discussed

further in section (4.4); thus we can neglect the last two terms and have:

$$C(n, m, \beta_c, 0) = L^d C(n', m', \beta_c, 0) \qquad (26)$$

at first order transition points and

$$C(n, m, \beta_c, 0) = L^{d(\alpha/(2-\alpha))} C(n', m', \beta_c, 0) \qquad (27)$$

at second order phase transition points. Since α for second order phase transitions is generally less than 1, we concluded from (26) and (27) that C increases with n and m mostly rapidly at first order transition points. This can also be used as a criterion to locate the first order transition point. If it happens that $\frac{\partial}{\partial \beta'} \frac{\partial \beta'}{\partial \beta} = 0$ in (22), which is not always true, then following the argument given before for $\Delta\chi$ of (20), we expect that $\Delta C(n, m, \beta, 0) = C(n, m, \beta, 0) - L^d C(n', m', \beta, 0)$ will show a region of positive sign around the first order transition points. Thus in this case, we can locate a first transition temperature from the behavior of ΔC.

III. AN EXAMPLE : SPIN-1/2 ISING MODEL

Now we will apply the formulation of section 2 to the Ising model on a square lattice with the nearest neighbor (nn) interaction to demonstrate that (20) can actually be used to locate the region of first order transitions. The Hamiltonian for the Ising model is given by:

$$\beta H = -K \sum_{(ij)} \sigma_i \sigma_j - h \sum_i \sigma_i \qquad (28)$$

where the first and the second summations extend over all nn bonds and sites of the lattice, respectively; σ_i , $\sigma_j = \pm 1$. The model of (28) on a square lattice has a second order transition at h = 0, $T_c = K_c^{-1} = (0.44068....)^{-1}$, and a line of first order transitions for h = 0, $T < T_c$. When we apply (20) to locate the region of first order transitions for fixed n and n', and varied m and m', we expect to get more and more accurate results by increasing m and m', because the fractions of broken bonds decrease as m and m' increase. In the limit $m \to \infty$, $m' \to \infty$: We get the best result for fixed n and n'. In the limit $m \to \infty$, the magnetization per spin for the n x ∞ system is given by:

$$M(n, \infty, K, h) = \frac{1}{n} \langle \psi_0 | \sum_{i=1}^{n} \sigma_i | \psi_0 \rangle , \qquad (29)$$

where ψ_0 is the eigenvector corresponding to the largest eigenvalue λ_0 of the transfer matrix R for the n column spins of the n x ∞ system. An efficient procedure to find λ_0 and ψ_0 for R can be found in Nightingale's paper[16]. The magnetic susceptibility per spin for the n x ∞ system $\chi(n, \infty, K, h)$ can be calculated from $M(n, \infty, K, h)$ by numerical differentiation. For very small h, we have:

$$\chi(n, \infty, K, 0) = M(n, \infty, K, h) / h , \qquad (30)$$

because $M(n, \infty, K, h = 0) = 0$ for the semi-infinite system. For given K, h, and n, we choose n' = n - 1 and calculate the quantities:

$$\Delta\chi(n, \infty, K, h) = \chi(n, \infty, K, h) - \left(\frac{n}{n-1}\right)^d \times \chi(n-1, \infty, K, h) , \qquad (31)$$

for very small h. The behaviour of $\Delta\chi / n^2$ as a function of K is shown in Fig. 3 for n = 5, 8, and 10. From Fig. 3, we may conclude that (20) can actually be used to locate the region of the first order transitions accurately.

IV. DISCUSSION

Some theoretical problems related to our formulation of Sect. II are discussed as follows:

(4.1) If there is a line of first order transition with a discontinous order parameter for $T < T_c$ and there is a second order transition at $T = T_c$ (e.g. two-dimensional Ising mo-el), then $\frac{\partial h'}{\partial h}$ equals L^d for $T < T_c$ and $L^{d-\beta\nu}$ at $T_c = T_c$. It seems that this is an unpleasant feature in our theory, because $\frac{\partial h'}{\partial h}$ appears to be a discontinuous function of T at $T = T_c$. However, the above result follows from the fact that we keep β fixed during PRG transformation and systems at different T or β should be considered as distinct because they can not transform from one into another. Thus we can not consider $\frac{\partial h'}{\partial h}$ as a function

of T in our treatment. Here we give a physical meaning to our PRG transformation with fixed T. A RG transformation can be considered as viewing the system from different length scales or at different distances from the system. If we apply a very small magnetic field h on a system at $T < T_c$, then there is a net magnetization in the direction of h. However, if we view the system on the microscopic scale, the spins of the system still flip quickly between up and down states. If we go away from the system, that corresponds with the situation after RG transformation, the spins of the system appear to be more rigid. If T of the system is allowed to vary in RG transformation, then one can interpret the situation by saying that the system is at $T' < T$, i.e. RG transformation transforms the system from T to $T' < T$. However, in our PRG transformation, T is fixed and one can interpret the situation (spins are more rigid.) by saying that a larger external magnetic field h' is applied to the system. By fixing T in PRG transformation, we force h = 0 for any T to be a fixed point in PRG transformation and thus have the result $\frac{\partial h'}{\partial h} = L^d$ at first order transtion temperatures.

(4.2) It has been pointed out[20] that the calculation of the spontaneous magnetization of the two-dimensional Ising model by C. N. Yang[21] and also E. W. Montroll, R. B. Potts, and J. C. Ward[22] is in fact a calculation of $(\chi_N / N)^{1/2}$ for $N \to \infty$. Thus $\chi_N \propto N$ when $T < T_c$. This holds for periodic boundary conditions, for which zero field susceptibility per spin χ_N may be written as a sum of N two-spin correlation function $< s_i \, s_j >$, since the magnetization m_N vanished identically. This result may be extended to some other Ising models with periodic boundary condition. These results are consident with our derivations of Sect. II.

(4.3) In the exact results mentioned above, the periodic boundary condition is crucial for the result that $\chi_N \propto N$. In the formulation of Sect. II, we also use the periodic boundary condition for n x m and n' x m' blocks of site and cell spins respectively. Such periodic boundary conditions follow naturally in our formulation, because we use the extra coupling arising from the periodic boundary condition to compensate for the loss of energy due to the breaking of bonds between different blocks of spins. However, our formulation also allows the free

boundary condition, but we expect that it will give less acurate result, e.g. in the location of first order transition region by using (20).

(4.4) In the derivation of (17), (19), (26), and (27) it has been said that the first term on the left-hand side of (16) and (22) is most singular and dominate the behavior of χ and C as n, m, n', and m' $\to \infty$ and nm/n'm' $\to 1^+$. It is reasonable to expect that this is indeed the case, because χ and C are associated with n'm' degrees of freedom and $\frac{\partial^2}{\partial h^2} K'_{o,h}$ and $\frac{\partial^2}{\partial \beta^2} K'_{o,\beta}$, are associated with nm-n'm' degrees of freedom, which is much smaller than n'm' in the limit nm/n'm' $\to 1^+$.

(4.5) It has been suggested by R. B. Griffiths, P. A. Pearce[23], and T. W. Burkhardt[24] that some RG transformations in the thermodynamic limit might be singular. However, in our formulation of Sect. II, only an infinitesimal fraction of the degrees of freedom are removed in the PRG transformation, a situation similar to the case of the exact RG transformation by Hilhorst et al.[25], and we don't actually take the thermodynamic limit (we just take the limit of large but finite n, m, n', and m'), it is reasonable to expect that our PRG transformation is also regular and free from the singularity of the free energy of the thermodynamic system.

(4.6) Recently, the result $\chi_N \propto N$ has been obtained by Fisher and Berker[26], Blöte and Nightingale[27], and Hu[28] using other methods. However, in such treatments there is no result concerning the correction to scaling at first order transitions (see (20b)).

(4.7) In the derivation of (17), (19), (20), (26), and (27), we don't actually solve the PRG transformation equation but only use certain reasonable properties of the transformation (e.g. the existence of T in (5) and (6)), similar situations are not rare in other branches of physics. For example, in the field theory of elementary particle physics, the PCT (parity, charge conjugation, and time reversal) symmetry is not obtained from the solution of the field equation but derived from certain properties of the field[29].

V. CONCLUSION

We have used a phenomenological renormalization group transformation to derive the finite-size scaling at first order phase transitions including the behavior of the correction term. We demonstrate in the simple Ising model that these results can be used to locate the region of first order transitions accurately. It is expected that the same technique can be applied to locate the rigion of first order phase transitions for other spin models where the exact solution is not available.

VI. ACKNOWLEDGEMENT

We are indebted to Professors R. B. Griffiths, W. -D. Chen, J. P. Valleau, S. G. Whittington, and A. J. Guttmann for useful discussions on the paper. The work was supported by the Office of Naval Research, USA, when the first draft of the paper was completed. One of the auther (C. K. Hu) was supported by the National Science Council of the Republic of China when the final version of the paper was completed.

REFERENCES

(1) H. E. Stanley, Introduction to Phase Transitions and Critical Phenomena. Oxford University Press, New York/Oxford, 1971, p.79.

(2) L. Onsager, Phys. Rev. 65, 117(1944).

(3) L. K. Runnels, in Phase Transitions and Critical Phenomena V.2 edited by C. Domb and M. S. Green. Academic Press, London/New York, 1972, p.305.

(4) C. Domb and M. S. Green (editors), Phase Transitions and Critical Phenomena V.3. .Academic Press, London/New York, 1974.

(5) K. Binder (editor), Monte-Carlo Methods in Statistical Physics. Springer-Verlag, Berlin/New York, 1979.

(6) B. Widom, J. Chem. Phys. 43, 3892 and 3898 (1965).

(7) L. P. Kadanoff, Physics 2, 263 (1966).

(8) K G. Wilson, Phys. Rev. B4, 3174, 3184 (1971).

(9) S. K. Ma, Modern Theory of Critical Phenomena. W. A. Benjamin, Inc., London, 1976.

(10) M. N. Barber, Phys. Reports 59, 375 (1980).

(11) a. T. Niemeijer & J. M. J. van Leeuwen Phys. Rev. Lett. 31, 1412 (1973), and Physica (Utrecht) 71, 17 (1974).

b. M. Nauenberg & B. Nienhuis, Phys. Rev. Letts 33, 944, 1598 (1974).

(12) L. P. Kadanoff, A. Houghton, and M. C. Yalabik, J. Stat. Phys. 14, 171 (1976).

(13) C.-K. Hu and P. Kleban, J. Comp. Phys. 43, 289 (1981).

(14) A. A. Migdal, Sov. Phys. JETP 42, 743 (1976).

(15) L. P. Kadanoff, Ann. Phys. (N. Y.) 100, 359 (1976).

(16) M. P. Nightingale, Physica 83A, 561 (1976); Phys. Lett. 59A, 486 (1977); Proc. Kon. Ned. Akad. Wet. Series B. 82, 235, 245, 269 (1979).

(17) C.-K. Hu and P. Kleban, Bull. Am. Phys. Soc. 26, 241 (1981).

(18) P. Kleban and C.-K. Hu, Bull. Am. Phys. Soc. 27, 92, 325 (1982).

(19) B. Nienhuis and M. Nauenberg, Phys. Rev. Lett 35, 477 (1975).

(20) T. D. Schultz, D. C. Mattis and E. Lieb, Rev. Mod. Phys. 38, 856 (1964).

(21) C. N. Yang, Phys. Rev. 85, 808 (1952).

(22) E. W. Montroll, R. B. Potts, and J. C. Ward, J. Math. Phys. 4, 308 (1963).

(23) R. B. Griffiths and P. A. Pearce, Phys. Rev. Lett. 41, 917 (1978); J. Stat. Phys. 20, 499 (1979).

(24) T. W. Burkhardt, Phys. Rev. Lett. 43, 1629 (1979).

(25) H. J. Hilhort, M. Schick. and J. M. J. van Leeuwen, Phys. Rev. B19, 2479 (1979); H. J. F. Knops and H. J. Hilhorst, Phys. Rev. B19, 3689 (1979).

(26) M. E. Fisher and A. N. Berker, Phys. Rev. 26, 2507 (1982).

(27) H. W. Blöte and M. P. Nightingale, Physica 112A, 405 (1982).

(28) C.-K. Hu, Phys. Rev. B1, Vol. 29, April (1984).

(29) R. F. Streater and A. S. Wightman, PCT, Spin and Statistics, and All That. W. A. Benjamin, Inc., New York, 1964.

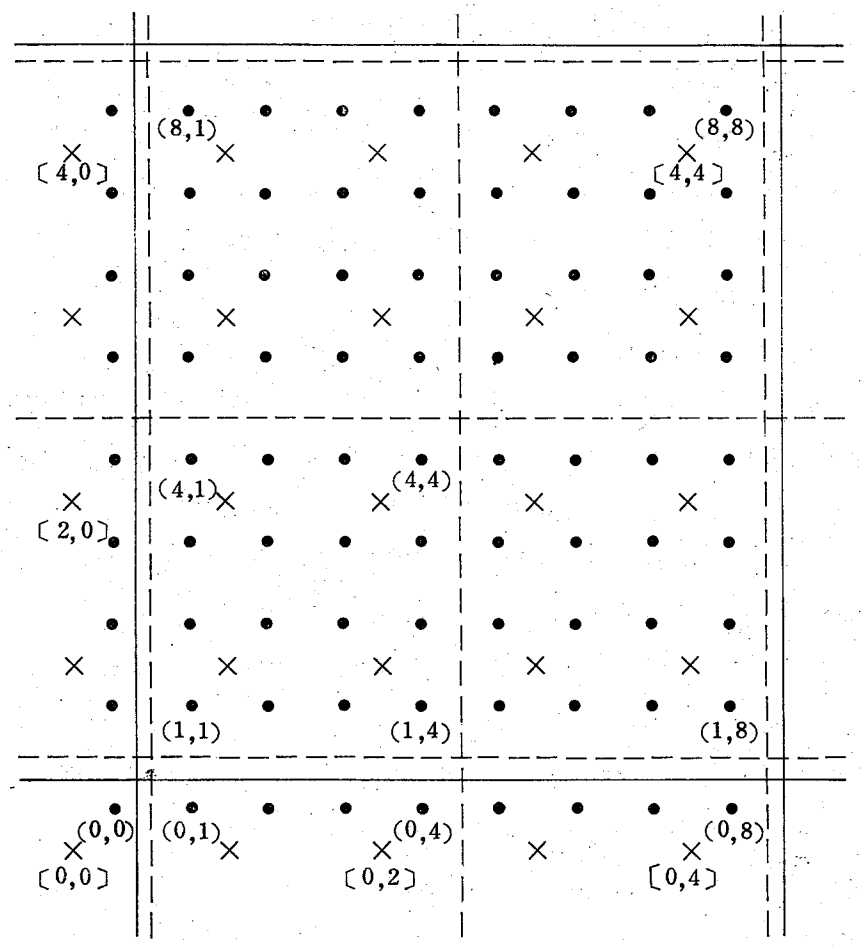

Fig. 1. Lattices and coordinates for the original spins $s_1,....s_N$ (•) and the transformed spins $t_1,....t_{N'}$(x) of the RG transformation. The coordinates for s and t spin are denoted by (i, j) and [k, l] respectively, where i, j, k and l are integers and the unit for [k, l] is double that for (i, j). Note that the origin for (i, j) and [k, l] are different. Some examples of (i, j) and [k, l] are shown in the diagram. In the RG Transformation, the site spins are divided into 4 x 4 blocks as indicated by the dotted lines. The 16 site spins(s) inside each block are transforme into 4 cell spins(t) by equation (1). For detail, see section (2.1).

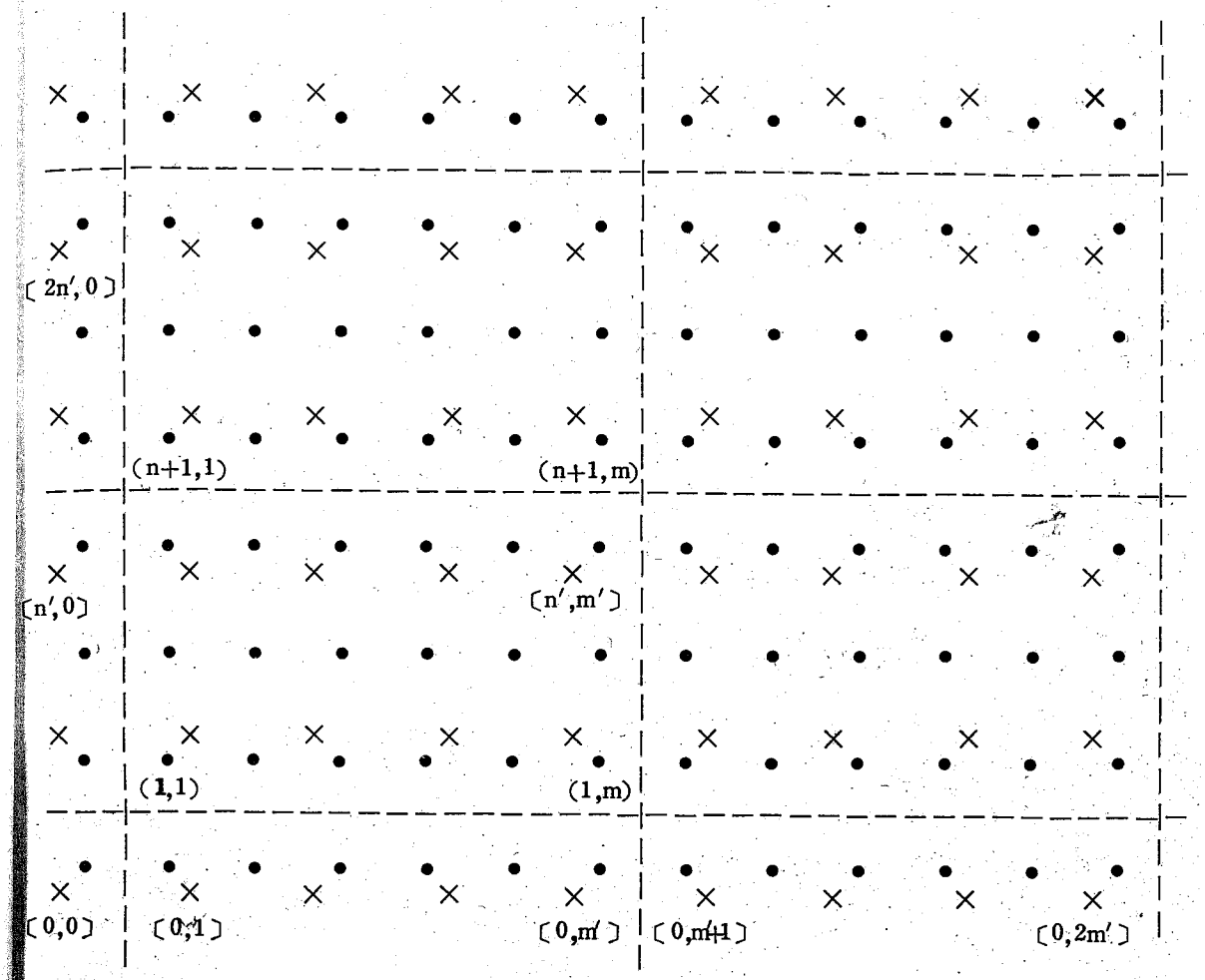

Fig. 2. Lattices and coordinates for the original spins $s_1,....s_N$ (•) and the transformed spins $t_1,....t_{N'}$(x) of the PRG transformation. The coordinates for s and t spin are denoted by (i, j) and [k, l] respectively, where i, j, k and l are integers and the unit for [k, l] is double that for (i, j). Note that the origin for (i, j) and [k, l] are different. Some examples of (i, j) and [k, l] are shown in the diagram. In the PRG transformation, the site spins $s_1,....s_N$ are divided into n x m blocks as indicated by the dotted lines. The mn site spins(s) inside each block are transformed into m'n' cell spins(t) by equation (6) or (11), where m/m'=n/n'=L=linear scale factor. For detail, see section (2.2). In this figure m=6, n=3, m'=4, n'=2 and L=1.5.

whose cell potential have 90^o rotation symmetry but do not have the permutation symmetry. They extended the MKVM to the two-parameter case, i.e. p_1 and p_2 are determined by minimizing the single cell free energy, and applied the method to calculate the critical points for the Baxter model[8] with several sets of coupling constants. Were Huang and Shih's two-parameter modified Kadanoff variation method justifiable, then to calculate derivatives of the free energy for the two-dimensional square-lattice Ising model with 90^o rotation symmetry, one should extend Hu and Kleban's method[5] from one parameter to two parameters. The latter is expected to be much more complicated than the former. In this note, we will prove that when applied to square-lattice Ising models with 90^o rotation symmetry, the RG transformation in the two-parameter modified Kadanoff variational method breaks the 90^o rotation symmetry if $|p_1| \neq |p_2|$. Since the transformed systems are expected to have the same symmetry properties as the original system, it is inappropriate to apply the two-parameter method to the spin model with 90^o rotation symmetry, e.g. the Baxter model. Hu and Kleban's method[5] with only one variational parameter is still appropriate for the square-lattice Ising models with 90^o rotation symmetry.

The most general form of the cell potential for the square-lattice Ising models with 90^o rotation symmetry and up-down symmetry may be written as[5]:

$$\nu(\sigma_1,\sigma_2,\sigma_3,\sigma_4) = K_o + K_{nn}(\sigma_1\sigma_2 + \sigma_2\sigma_3 + \sigma_3\sigma_4 + \sigma_4\sigma_1) + K_{nnn}(\sigma_1\sigma_3 + \sigma_2\sigma_4) + K_4\sigma_1\sigma_2\sigma_3\sigma_4 . \quad (1)$$

Here K_o , K_{nn} , K_{nnn} and K_4 denote a constant, nearest-neighbour (nn), next-nearest-neighbour (nnn), and four-spin interactions, respectively, $\sigma_1,\sigma_2,\sigma_3$, and σ_4 are four spins located clock-wise on a typical unit cell as shown in Fig. 1 and $\sigma = \pm 1$. It follows from equation (1) that:

$$\nu(1,1,1,1) = \nu(-1,-1,-1,-1) , \quad (2)$$

$$\begin{aligned}&\nu(1,1,1,-1)=\nu(1,1,-1,1)=\nu(1,-1,1,1)\\ &=\nu(-1,1,1,1)=\nu(-1,-1,-1,1)=\nu(-1,-1,1-1)\\ &=\nu(-1,1,-1,-1)=\nu(1,-1,-1,-1) , \end{aligned} \quad (3)$$

$$\begin{aligned}&\nu(1,1,-1,-1)=\nu(1,-1,-1,1)\\ &=\nu(-1,-1,1,1)=\nu(-1,1,1,-1) , \end{aligned} \quad (4)$$

$$\nu(1,-1,1,-1)=\nu(-1,1,-1,1) . \quad (5)$$

Thus there are four independent cell potentials, say $\nu(1,1,1,1)$, $\nu(1,1,1,-1)$, $\nu(1,1,-1,-1)$ and $\nu(1,-1,1,-1)$, which are linerar functions[5] of four independent parameters in equation (1).

Using the two-parameter form of the generating function given by equation (5) of Ref. (7), the RG transformation from the original cell potentials $\nu(\sigma_1,\sigma_2,\sigma_3,\sigma_4)$ to the transformed cell potentials $\nu(\mu_1,\mu_2,\mu_3,\mu_4)$ may be written as:

$$\begin{aligned}&\exp[\nu'(\mu_1,\mu_2,\mu_3,\mu_4)]\\ &= \sum_{\sigma_1\sigma_2\sigma_3\sigma_4} \exp[4\nu(\sigma_1,\sigma_2,\sigma_3,\sigma_4) + p_1(\mu_1\sigma_1 + \mu_3\sigma_3) + p_2(\mu_2\sigma_2 + \mu_4\sigma_4)] \,/\, \{\exp[p_1(\sigma_1+\sigma_3) + p_2(\sigma_2+\sigma_4)]\\ &+ \exp[-p_1(\sigma_1+\sigma_3) - p_2(\sigma_2+\sigma_4)]\} , \end{aligned} \quad (6)$$

where μ_1, μ_2, μ_3 and μ_4 are four spins located clockwise on a typical unit cell of the transformed system as shown in Fig. 1 and $\mu = \pm 1$

If the cell potentials $\nu'(\mu_1,\mu_2,\mu_3,\mu_4)$ have the same symmetry properties as the original systems, then $\nu'(\mu_1,\mu_2,\mu_3,\mu_4)$ must satisfy equations (2) to (5). On the other hand, to show that $\nu'(\mu_1,\mu_2,\mu_3,\mu_4)$ do not have the same symmetry properties as the original system, one only needs to show that cell potentials $\nu'(\mu_1,\mu_2,\mu_3,\mu_4)$ do not satisfy certain equality in equations (2) to (5).

It follows from equation (6) that:

$$\begin{aligned}\exp[\nu'(1,1,1,-1)] &= \frac{\cosh 2p_1}{\cosh 2(p_1+p_2)} Z_1^4 + (2\cosh 2p_2 + \frac{2}{\cosh 2p_2}) Z_2^4 + 2\cosh 2p_2 Z_3^4\\ &+ \frac{\cosh 2p_1}{\cosh 2(p_1-p_2)} Z_4^4 , \end{aligned} \quad (7)$$

and

$$\exp\left[\nu'(1,1,-1,1)\right]=\frac{\cosh 2p_2}{\cosh 2(p_1+p_2)}Z_1^4 + \left(2\cosh 2p_1+\frac{2}{\cosh 2p_1}\right)Z_2^4 + 2\cosh 2p_1\, Z_3^4 + \frac{\cosh 2p_2}{\cosh 2(p_1-p_2)}Z_1^4 \qquad (8)$$

where

$$Z_1 = e^{\nu(1,1,1,1)}, \qquad (9)$$

$$Z_2 = e^{\nu(1,1,1,-1)}, \qquad (10)$$

$$Z_3 = e^{\nu(1,1,-1,-1)}, \qquad (11)$$

and

$$Z_4 = e^{\nu(1,-1,1,-1)}. \qquad (12)$$

When $p_2 = p_1$ or $p_2 = -p_1$, we have $\nu'(1, 1, 1, -1) = \nu'(1, 1, -1, 1)$. Since Z_1, Z_2, Z_3, and Z_4 are independent parameters, when

$$|p_1| \neq |p_2| \qquad (13)$$

we have

$$\nu'(1,1,1,-1) \neq \nu(1,1,-1,1), \qquad (14)$$

i.e. the cell potentials $\nu'(\mu_1,\mu_2,\mu_3,\mu_4)$ do not have the 90^0 rotation symmetry.

For the Baxter model[8], K_{nn} of equation (1) should be zero and we have:

$$\nu(1,1,1,1) = \nu(1,-1,1,-1) \qquad (15)$$

and

$$Z_1 = Z_4 . \qquad (16)$$

When Z_1 and Z_4 of equations (7) and (8) satisfy the equality of equation (16), we still have equation (14) if equation (13) is still true.

In conclusion, we have shown that the two-parameter RG transformation[7] could not preserve the 90^0 rotation symmetry of the square-lattice Ising model when $|p_1| \neq |p_2|$. Therefore, it is inappropriate to apply this method to the square-lattice Ising model with 90^0 rotation symmetry, e.g. the Baxter model.

ACKNOWLEDGEMENT

The author thanks Professors Y. -M. Shih and W. -D. Chen for useful discussions. This work was supported by the National Science Council of the Republic of China under Grant No. NSC73-0204-M001-03.

REFERENCES

(1) L. P. Kadanoff, A. Houghton, and M. C. Yalabik, J. Statist, Phys. 14, 171 (1976).

(2) S. L. Katz and J. D. Gunton, Phys. Rev. B 16, 2163 (1977).

(3) Y. M. Shih, et al., Phys. Rev. B 19, 529 (1979).

(4) M. N. Barber, J. Comput. Phys. 34, 414 (1980).

(5) C. -K. Hu and P. Kleban, J. Comput. Phys. 43, 289 (1981).

(6) C. -K. Hu and P. Kleban, Phys. Rev. B 25, 6760 (1982).

(7) H. -M. Huang and Y. -M. Shih, Phys. Lett. 89 A, 257 (1982).

(8) R. J. Baxter, Ann. Phys. (NY) 70, 193 (1972).

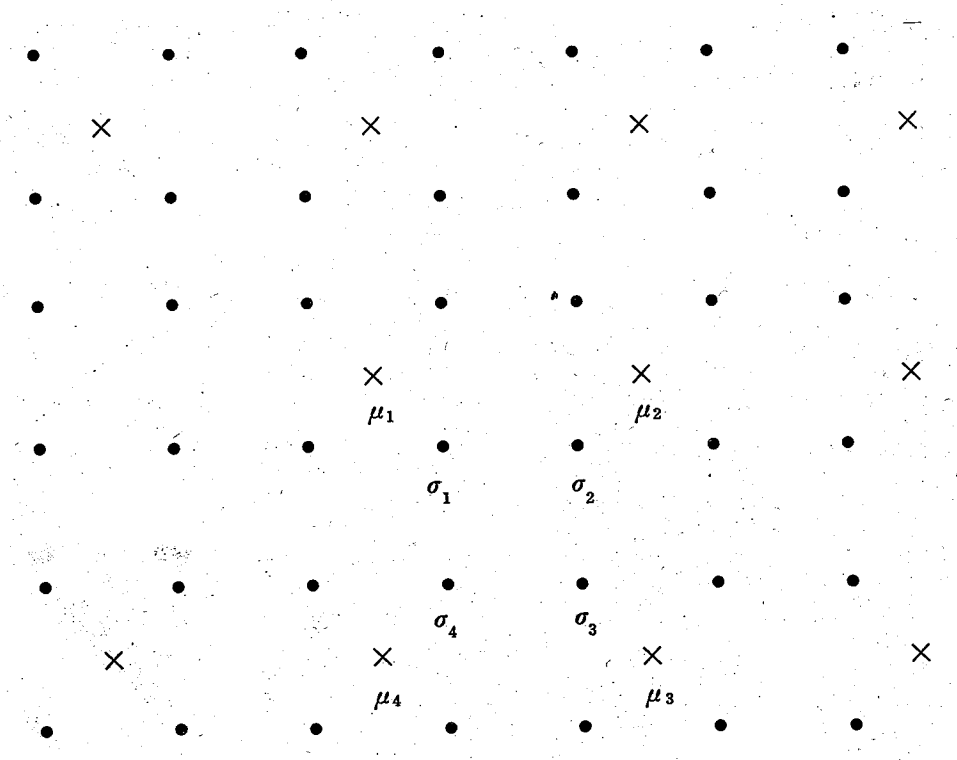

Fig. 1. The original σ -spin system (•) and the transformed μ -spin system (X) on square lattices. Note that the lattice constant of the latter is twice that of the former.

GAMMA TRANSITIONS IN ^{124}Te FOLLOWING THE BETA DECAY OF ^{124}Sb*

D. Wang, E. K. Lin, G. C. Jon and C. W. Wang
Institute of Physics, Academia Sinica
Nankang, Taipei, Taiwan, R. O. C.

The γ -radiation following the beta decay of 60.2d ^{124}Sb from thermal neutron capture in ^{123}Sb has been investigated with a Ge(Li) detector and a Ge(Li)-NaI(T ℓ) coincidence spectrometer. A total of 38 γ -rays was observed and the directional correlation has been measured for the 1248.6 keV → 602.6 keV → 0, 1325.6 keV → 602.6 keV → 0, 2293.9 keV → 602.6 keV → 0 and 2693.8 keV → 602.6 keV → 0 cascades. The energies, intensities and the multipole mixing ratios of the γ -rays in ^{124}Te have been deduced. The populated levels of ^{124}Te were identified up to 2.775 MeV. A previously unreported γ -transition was observed between levels at 2521 keV and 1958.1 keV.

1. INTRODUCTION

In recent years considerable attention has been devoted to the nuclear spectroscopy by decay scheme studies. The population of levels in ^{124}Te following the radiocative decays has been the topic of many investigations by Grabowski et al[1], Baker et al[2], Behar et al[3], Meyer et al[4], and Auer et al[5] from the decay of ^{124}Sb, and by Ragaini et al[6] from the decay of ^{124}I. The results have been comprehensively compiled by Ledered and Shirley[7] in "Table of Isotope", which have established the presence of numerous excited states of ^{124}Te up to ~ 3 MeV excitation. In particular, the lower excited states below 2091.5 keV have been extensively investigated, they exhibit somewhat vibrational pattern in nature. It is believed that the vibrational model with a pairing-plus-quadrupole force and coupling of the core to the shell model states of the two protons outside the closed shell[8] would be the most successful to describe the low-lying level scheme of ^{124}Te. However, the structure of the higher excited states of ^{124}Te are not well established. Several I^π assignments remain uncertain. Experimentally, there appeares some inconsistencies in the directional correction data for the casecade transitions from the higher excited levels, and discrepancies with the theoretical

* Supported by the National Science Council, Republic of China.

model exist. It seems necessary to require more experimental information for further studies.

The experimental works of the thermal neutron capture reaction on heavy nuclei with use of high resolution Ge(Li) detector in this laboratory have been extensively investigated to study the nuclear level scheme for several years. It is purpose of the present investigation on the beta decay of ^{124}Sb to provide additional experimental information on the level scheme of ^{124}Te and to confirm I^{π} assignments by observation of $\gamma - \gamma$ coincidence and directional correlations. Emphasis has been made in the present work to investigate the γ-rays which represent the transition between levels above 1249 keV in ^{124}Te.

2. EXPERIMENTAL METHOD

Radioactive sources of ^{124}Sb were obtained through the thermal neutron capture reaction in ^{123}Sb by the irradiation of 1 mg isotropically enriched sample powder (98.23% in ^{123}Sb and 1.77% in ^{121}Sb) with thermal neutron flux of about 5 x 10^{11} n-cm^{-2}-sec^{-1} for 10 hours in the reactor of national Tsinghua University. The sample was irradiated in a sealed capsules. After irradiation, the sample was taken out from reactor and was allowed for cooling in a period of 30 days, since the half life of the ^{124}Sb and ^{122}Sb activities is known to be 60.2d and 2.8d, respectively. The small amounts of ^{121}Sb impurity admixture in the sample apparently cause no interference in the present measurement of γ-rays from the beta decay of ^{124}Sb.

The experiments were based on conventional measurements carried out in nuclear spectroscopy with radiative sources. Singles spectra of γ-rays were taken mainly with a 43-cm^3 coaxial ORTEC Ge(Li) detector and standard low-noise amplifiers. The data were accumulated in a Camberra 4096-channel analyzer. To measure coincidence a Ge(Li)-Na(Tℓ) spectrometer was applied. A block diagram of electronic circuit used in the coincidence measurement is given in Fig. 1. The Ge(Li) detector was kept fixed, while the NaI(Tℓ) scintillation detector was allowed to rotate an angle as desired. The detailed description of the apparatus and methods of data treatment is given in previous papers.

3. RESULTS AND ANALYSIS

A. Singles γ-ray spectrum

Singles γ-ray spectra of ^{124}Te from beta decay of ^{124}Sb as viewed with Ge(LI) detector is presented in Figs. 2-5. Typical resolution obtained in the present measurement was 2.8 keV (FWHM) for ^{60}Co 1333 keV peak. Fig. 2 shows the γ-ray spectrum in the low-energy portion (240 keV - 740 keV). The higher energy portion of the γ-ray spectrum is shown in Figs. 3-5. A total of 48 γ-rays was observed. The γ-ray at 602.6 keV is seen to be quite intensive. Peaks due to ^{124}Te are seen up to 2182.3 keV. Among 48 peaks, thirty-eight were identified belonging to the energy levels in ^{124}Te by using half-life decay testing method; while seven of the others at 241.8 keV, 251.7 keV, 583.2 keV, 911.5 keV, 1461.0 keV, 1765.0 keV, and 2205.7 keV were arised from natural background, and the rest at 669.1 keV, 1069.0 keV, and 1180.0 keV are attributed to pair production. For all 38 γ-rays, the corresponding transitions in ^{124}Te were identified. The γ-ray appeared at 563.9 keV was found to represent a new transition between the 2521.5 keV and 1958.1 keV levels in ^{124}Te, it was not previously reported.

The energies of γ-rays observed in Figs. 2-5, the relative intensities and the classification of the 38 transitions between levels of ^{124}Te are listed in Table 1, where the available information on the energies of γ-rays from previous work is also listed in the third column for comparison.

The energy and efficiency calibration were derived from standard γ-ray sources. Also, the known energies of photo peaks arised from natural background measured at the same time as shown in the singles spectrum were used in the calibration. Photo peak efficiencies for the Ge(Li) detector were determined by using standard gamma sources with conventional method. From the first least square fit in the calibration, the relation between γ-ray energy and number of channel c was obtained as E(keV) = 0.705c + 82.2.

Energies of the observed γ-rays were then accurately determined as given in the second column of Table 1. It is seen that the determined energies agree very with previous measurement.

branching ratios for many transition lines were determined in the present

investigation. Table 2 shows the determined branching ratios for transitions from the 2293.9 keV, 2039.2 keV, 1958.1 keV, and 1325.6 keV levels in ^{124}Te. Our results were found in agreement with previous work[7] within 50%.

B. $\gamma-\gamma$ coincidence measurements

A 3" x 3" NaI(Tℓ) scintillator was used as the gating detector for Ge(Li)-NaI(Tℓ) coincidence measurements, and standard fast-slow coincidence was employed with resolving time of $\sim$ 5 ns. The coincidence measurements were carried out with a proper gate set over the 602.6 keV, which corresponds to the energy of γ-ray emitted in the transition from the first excited state to ground state of ^{124}Te. The energy interval selected by this gating may contain contributions arised from the 602.6 keV, 632.5 keV, 646.0 keV and 722.9 keV radiations.

Typical γ-ray coincidence spectra are shown in Fig. 6. It is seen that a total of 16 rays was observed in the coincidence spectra. Of these 16 γ-rays, six arise from the higher excited states of ^{124}Te in a cascade transition to the first excited state (2^+) at 602.6 keV and then to the ground state; four represent the cascade transitions arising from higher excited states of ^{124}Te to the second excited state (4^+) at 1248.6 keV; and three are attributed to the cascade transitions from higher excited states of ^{124}Te to the third excited state (2^+) at 1325.6 keV. The results of the coincidence measurements are summarized in Tables 3 and 4.

Relative intersities for the γ-rays appeared in the coincidence spectra have been calculated. Their values are relatively comparable to those of the corresponding γ-rays appeared in the singles γ-ray spectra, except the one at 968.3 keV which is seen to have comparably larger intensity appeared in the singles spectra because of contribution of the γ-ray at 969.2 keV from background ^{208}Ac.

C. Directional Correlation Measurement

Directional correlation measurements were carried out with an attempt to study the cascade transitions in ^{124}Te arising from higher excited states to the first excited state at 602.6 keV and then to the ground state. We set gating over the 602.6 keV as in the case of the coincidence measurement. Data were taken at angles θ = 90°, 105°, 120°, 135°, 165° and 180° for four cascades 1248.6 keV $\rightarrow$ 602.6 keV $\rightarrow$ 0, 1325.6 keV $\rightarrow$ 602.6 keV $\rightarrow$ 0, 2293.9 keV $\rightarrow$ 602.6 keV - 0, and 2693.8 keV $\rightarrow$ 602.6 keV $\rightarrow$ 0. The observed photo-peak areas were fitted to a linear combination

of Lagendre polynominal $P_L(\theta)$ by a CYBER 172 computer.

It has been shown that at a given angle the correlation function $W(\theta)$ for γ-cascade $I_a(L_1,L_1')I_b(L_2,L_2')I_c$ between three levels I_a, I_b, I_c of an even-even nucleus could be simply expressed[9] as follows:

$$W(\theta) = A_0 + A_2P_2(\theta) + A_4P_4(\theta)$$

where correlation coefficients A_L are defined in terms of the multipole mixing ratio δ of Krane and Steffen[10]. Referring to the first transition in the cascade, δ is given by

$$\delta = \langle I_a \,||\, L_1+1 \,||\, I_b\rangle / \langle I_a \,||\, L_1 \,||\, I_b\rangle$$

For the cascade transitions investigated, the cascade mode is $I_a(L_1,L_1+1)\,2^+(2,0)0^+$, anisotropy $A(\delta)$ is given in terms of coefficients A_2 and A_4

$$A(\delta) = \frac{\frac{3}{2}A_2 + \frac{5}{8}A_4}{1 - \frac{1}{2}A_2 + \frac{3}{8}A_4}$$

We have written a computer program for correlation coefficients A_L and anisotropy $A(\delta)$ for different I_a, and L_1, and from the calculated A_L we then extract the multipole mixing ratio.

Experimentally we obtain coefficient A_2^{exp} and A_4^{exp} from the least square fit to the measured correlation function $W(\theta)$. Figs 7 and 8 show the correlation functions and decay scheme from cascades 1248.6 keV $\rightarrow$ 602.6 keV $\rightarrow$ 0, 1325.6 keV $\rightarrow$ 602.6 keV $\rightarrow$ 0, 2293.9 keV $\rightarrow$ 602.6 keV $\rightarrow$ 0, and 2693.8 keV $\rightarrow$ 602.6 keV $\rightarrow$ 0. The dot represents the measured values of the correlation function $W(\theta)$. With the experimental data at 90° and 180°, we obtain anisotropy

$$A^{exp}(\delta) = \frac{W(180°) - W(90°)}{W(90°)}$$

The results on the measured coefficients A_2^{exp} and A_4^{exp}, and anisotropy $A^{exp}(\delta)$ are listed in Table 5 and compared with the calculated values. The agreement is seen to be satisfactory.

4. SUMMARY AND DISCUSSION

In the obtained coincidence spectra we identified many two γ-rays in the

cascade transitions between energy levels of ^{124}Te, the decay scheme of ^{124}Te between levels up to 2775.1 keV is established as shown in Fig. 9. It is seen that there are a large number of transitions feeding the first 2^+ level at 602.6 keV. Our result is in good agreement with most earlier investigations(7).

The three lowest excited states of ^{124}Te are well known to be 0^+, 2^+, and 4^+ respectively as described by the hydrodynamical vibrational mode(11). In the present work, we established 13 levels above the 1248.6 keV 4^+ level. Ref. 5 indicates the presence of one level at 2710.6 keV. No supporting evidence was found for this level in the present work. We observed a γ-ray at 563.9 keV, which represents a new transition between the 2521.5 keV and 1958.1 keV levels and is proposed to be associat with M3/E2 mode.

Among 13 levels identified, the levels at 1325.6 keV, 2039.2 keV, and 2091.5 keV were all assigned(7) to be 2^+; the level at 1958.1 keV has been carefully investigated by Behar et al(3) and their measurements on the directional correlations and polarization-directional corrections have determined a unique spin assignment of 4^+ for the 1958.1 keV level; and the level at 2293.9 keV was known(7) to be 3^-; while the I^π assignment of the other levels at 2182.5 keV, 2225.0 keV, 2322.9 keV, 2483.4 keV and 2521.5 keV were all uncertain. From analysis of data obtained in the directional correlation measurements for the 646-603, 723-603, 1691-603, and 2091-603 cascades in the present work, we obtain evidence for the I^π assignment of levels at 1248.6 ke 1325.6 keV, 2293.9 keV and 2693.8 keV to be 4^+, 2^+, 3^- and 3^-, respectively.

Table 6 and Fig. 7 summarize results of the directional correlation measurements for the above mentioned cascades. For the 646-604 and 2091-603 cascades the values o A_L coefficients and δ are consistent, respectively, with a 4^+-2^+-0^+ spin sequence of a nearly pure E2 character, and with a 3^--2^+-0^+ spin sequence of a nearly E1 chara This supports the spin and parity assignment 4^+ for the 1248.6 keV level and 3^- for the 2693.8 keV level. Our directional correlation results for the 723-603 and 1691-603 cascades agree, respectively a 2^+-2^+-0^+ spin sequence of a probable E2 multipola with M1 admixture (δ = -3.5 for the 723 keV transition), and a 3^--2^+-0^+ spin sequence of a probable E1 multipolarity with M2 admixture (δ = -0.05 for the 1691 ke transition). We have evidence that the 1325.6 keV and 2293.9 keV levels are 2^+ and 3^- respectively. The δ -values determined in the present work for the mixing ratio

of above four cascades agree quite well with the obtained in the work of Baker et al(2).

In conclusion, the structure of ^{124}Te nucleus is very complex. It is believed that the results of this work offer evidences concerning some highly excited states of ^{124}Te and provide useful experimental information for the detailed theoretical description of the nucleus ^{124}Te.

ACKNOWLEDGEMENT

We are grateful to Mr. G. C. Kiang for his suggestions and discussion as well as assitance in the initial phase of the experiment, and to the Institute of Nuclear Engineering, National Tsinghua University for providing assistance in the irradiation of samples.

REFERENCES

(1) Z. W. Grabowskik K. S. Krane and R. M. Steffen, Phys. Rev. 3C, 1649 (1971).
(2) K. B. Baker, J. H. Hamilton, A. V. Ramayya and G. Highland, Nucl. Phys. A186, 493 (1972).
(3) M. Behar, G. Garcia Bermudez, A. Filevich and M. C. Cambiaggio, Phys. Rev. 12C, 767 (1976).
(4) R. A. Meyer, W. B. Walters and R. C. Razaini, Nucl. Phys. A127, 959 (1969).
(5) I. P. Auer, J. J. Reidy and M. L. Wiedenbeck, Nucl. Phys. A124, 199 (1969).
(6) R. C. Ragaini, W. B. Walters, A. A. Noyes, and R. A. Meyer, Phys. Rev. 187, 1721 (1969).
(7) C. Michael Lederer and Vriginia S. Shirley, Table of Isotopes (7th ed.), John Wiley & Sons, Inc. New York.
(8) E. Degrieck and G. Vanden Berghe, Nucl. Phys. 141 (1974).
(9) M. E. Rose, Phys. Rev. 93, 477 (1954).
(10) K. S. Krane and R. M. Steffen, Phys. Rev. C2, 724 (1970).
(11) A. Bohr and B. R. Mottelson, Mat. Tys, Dan. Vid. Selsk. 27, No. 16 (1963).

Table 1 Energies, intensities, and classifications of the transitions in ^{124}Te

Peak No.	Energy		Relative Intensity	Classification
	Present Work	Ref. 7		
1	241.8±0.3		0.696±0.009	From Ra-226
2	336.0±0.3	335.8	1.012±0.009	2293.9 1958.1
3	351.7±0.3		0.592±0.007	From Ra-226
4	370.9±0.4	370.4	0.393±0.006	2693.8 2322.9
5	400.2±0.4	400.0	1.073±0.009	2793.8 2293.9
6	443.9±0.2	443.99	1.445±0.011	2483.4 2039.2
7	468.9±0.4	468.6	0.551±0.007	2693.8 2225.0
8	511.0			
9	525.3±0.2	525.5	0.903±0.009	2483.4 1958.1
10	563.9±0.2		0.543±0.007	2521.5 1958.1
11	583.2±0.3		0.524±0.007	From Tℓ-208
12	602.6	602.72	602.550±0.23	602.6 g.s.
13	632.5±0.2	632.4	0.555±0.007	1958.1 1325.6
14	646.0	645.82	42.784±0.060	1248.6 602.6
15	669.1		4.900±0.020	From 1691.2(D)
16	709.6±0.2	709.31	3.417±0.017	1958.1 1248.6
17	713.7±0.3	713.82	5.133±0.021	2039.2 1325.6
18	722.9±0.2	722.78	53.788±0.067	1325.6 602.6
19	735.6±0.4	735.8	0.670±0.008	2693.8 1958.1
20	790.8±0.3	790.8	3.235±0.017	2039.2 1248.6
21	817.1±0.2	816.8	0.251±0.005	2775.1 1958.1
22	856.1±0.3	856.9	0.061±0.002	2182.5 1325.6
23	899.2±0.5	899.8	0.060±0.002	2225.0 1325.6
24	911.5		0.332±0.005	From Ac-228
25	968.3±0.3	968.2	7.227±0.025	2293.9 1325.6
26	976.5±0.3	976.4	0.094±0.003	2225.0 1248.6
27	1045.3±0.3	1045.24	6.419±0.023	2293.9 1248.6
28	1069.0		1.047±0.009	From 2091.3 (D)
29	1180.0		2.359±0.014	From 1691.2 (S)
30	1325.8±0.2	1325.5	4.146±0.019	1325.6 g.s.
31	1355.5±0.2	1355.2	2.693±0.015	1958.1 602.6
32	1368.2±0.4	1368.2	6.014±0.023	2693.8 1325.6
33	1376.0	1376.0	0.602±0.007	2701.6 1325.6
34	1436.8±0.3	1436.7	2.784±0.015	2039.2 602.6
35	1445.1±0.4	1445.2	0.487±0.006	2693.8 1248.6
36	1461.0		1.552±0.011	From K-40
37	1489.1±0.3	1489.0	1.451±0.011	2091.5 602.6
38	1526.5±0.2	1526.3	1.033±0.009	2775.1 1248.6
39	1579.9±0.3	1579.9	0.951±0.009	2182.5 602.6
40	1622.6±0.3	1622.4	0.063±0.002	2225.0 602.6
41	1691.2±0.3	1691.2	100.000±0.092	2293.9 602.6
42	1720.3		0.197±0.004	2322.9 602.6
43	1765.0		0.101±0.003	From Ra-226
44	1918.8±0.2	1918.6	0.088±0.003	2521.5 602.6
45	2038.9±0.3	2039.3	0.116±0.003	2039.2 g.s.
46	2091.3±0.4	2091.0	9.071±0.027	2693.8 602.6
47	2182.3±0.3	2182.6	0.054±0.002	2182.5 g.s.
48	2205.7		0.018±0.001	From Ra-226

Table 2 Branching ratios for transitions from the 2293.9keV, 2039.2 keV, 1958.1 keV, and 1325.6 keV levels in ^{124}Te.

Level energy (keV)	γ-energy (keV)	Branching ratio	
		Present Work	Ref. 7
2293.9	336.0	0.196±0.002	0.079
	968.3	2.740±0.01	1.84
	1045.3	2.490±0.01	1.85
	1691.2	49.000±0.045	49.00
2039.2	713.7	1.310±0.007	2.40
	790.8	0.880±0.004	0.75
	1436.8	1.020±0.007	1.02
	2038.9	0.050±0.001	0.061
1325.6	722.9	13.460±0.015	11.3
	1325.8	1.420±0.006	1.42
1958.1	632.5	0.130±0.003	0.16
	709.6	0.850±0.004	1.43
	1355.5	0.930±0.006	0.93

Table 3 Results of the coincidence measurements

Peak No.	Energy (keV)	Relative Intensity	Transition	
			From	to
1	602.6	500.10±3.4	602.6	g.s.
2	646.0	36.89±0.92	1248.6	602.6
3	669.1	5.15±0.34	From 1691.2 (D)	
4	709.6	2.99±0.26	1958.1	1248.6
5	713.7	5.00±0.57	2039.2	1325.6
6	722.9	49.40±1.07	1325.6	602.6
7	790.8	2.83±0.26	2039.2	1248.6
8	968.3	2.50±0.24	2293.9	1325.6
9	1045.3	6.00±0.37	2293.9	1248.6
10	1325.8	2.89±0.10	1325.6	g.s.
11	1355.5	2.86±0.21	1958.1	602.6
12	1368.2	6.12±0.38	2693.8	1325.6
13	1436.8	2.89±0.20	2039.2	602.6
14	1526.5	1.01±0.16	2775.1	1248.6
15	1691.2	100.00±1.50	2293.9	602.6
16	2091.3	9.41±0.47	2693.8	602.6

Table 5 Results on the measured angular correlation coefficients and anisotropy

Transition	Expermental			Calculated
	A_2	A_4	Anisotropy	Anisotropy
$1249(I_1) \rightarrow 603(2^+) \rightarrow 0(0^+)$	0.100 ± 0.012	0.0081 ± 0.013	0.181 ± 0.095	0.167
$1326(I_1) \rightarrow 603(2^+) \rightarrow 0(0^+)$	0.148 ± 0.025	0.2800 ± 0.030	0.336 ± 0.090	0.386
$2294(I_1) \rightarrow 603(2^+) \rightarrow 0(0^+)$	-0.031 ± 0.016	-0.0002 ± 0.019	-0.013 ± 0.055	-0.046
$2694(I_1) \rightarrow 603(2^+) \rightarrow 0(0^+)$	-0.071 ± 0.021	0 ± 0.035	-0.089 ± 0.176	-0.103

Table 6 Summary of the directional correlation measurements

Transition	Experimental		χ^2	Calculated values					Reference 2	
	A_2	A_4		I_1	L_1	A_2	A_4	δ_1	A_2	A_4
$1249(I_1) \rightarrow 603(2^+) \rightarrow 0(0^+)$	0.100	0.0081	0.174	4	2	0.102	0.0091	0	0.095	0.003
	± 0.012	± 0.013							± 0.001	± 0.011
$1326(I_1) \rightarrow 603(2^+) \rightarrow 0(0^+)$	0.148	0.280	1.48	2	1	0.142	0.302	$-3.5^{a)}$	0.136	0.270
	± 0.025	± 0.030							± 0.009	± 0.015
$2294(I_1) \rightarrow 603(2^+) \rightarrow 0(0^+)$	-0.031	-0.0002	1.716	3	1	-0.0309	-0.0002	$-0.05^{b)}$	-0.068	-0.011
	± 0.016	± 0.019							± 0.005	± 0.011
$2694(I_1) \rightarrow 603(2^+ \rightarrow 0(0^+)$	-0.071	0	0.913	3	1	-0.0714	0	0	-0.067	-0.038
	0.021	0.035							± 0.012	± 0.018

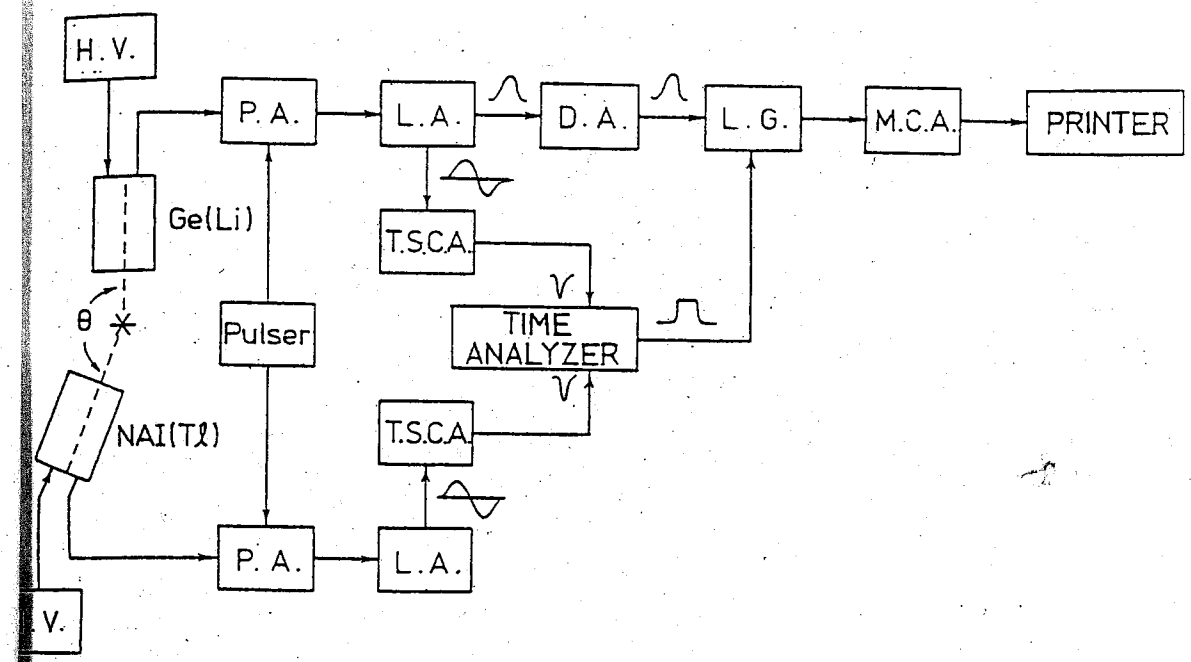

Fig. 1. Block diagram of electronics used in the coincidence measurement.

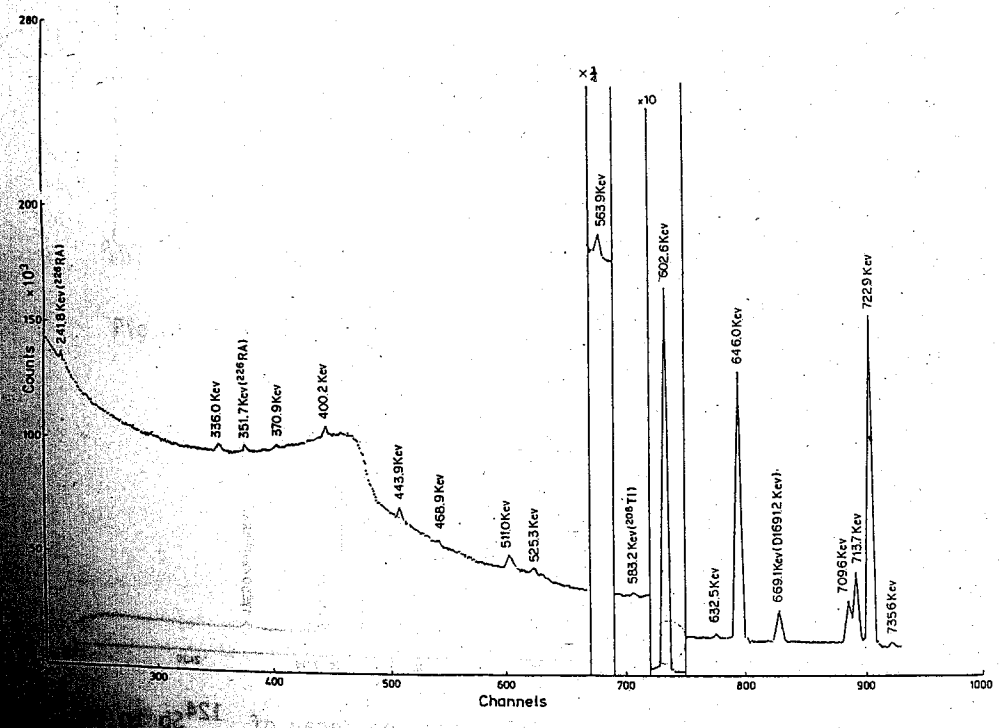

Gamma-ray singles spectrum following the decay of ^{124}Sb in the energy range of 240-740 keV.

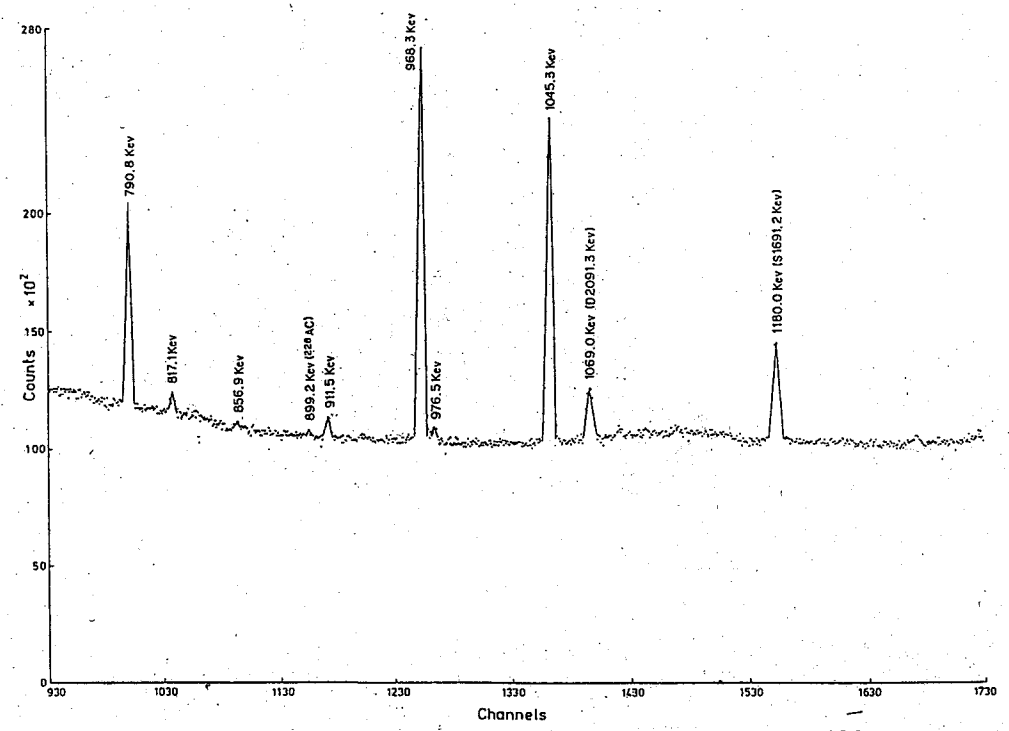

Fig. 3. Gamma-ray singles spectrum following the decay of ^{124}Sb in the energy range 740-1320 keV.

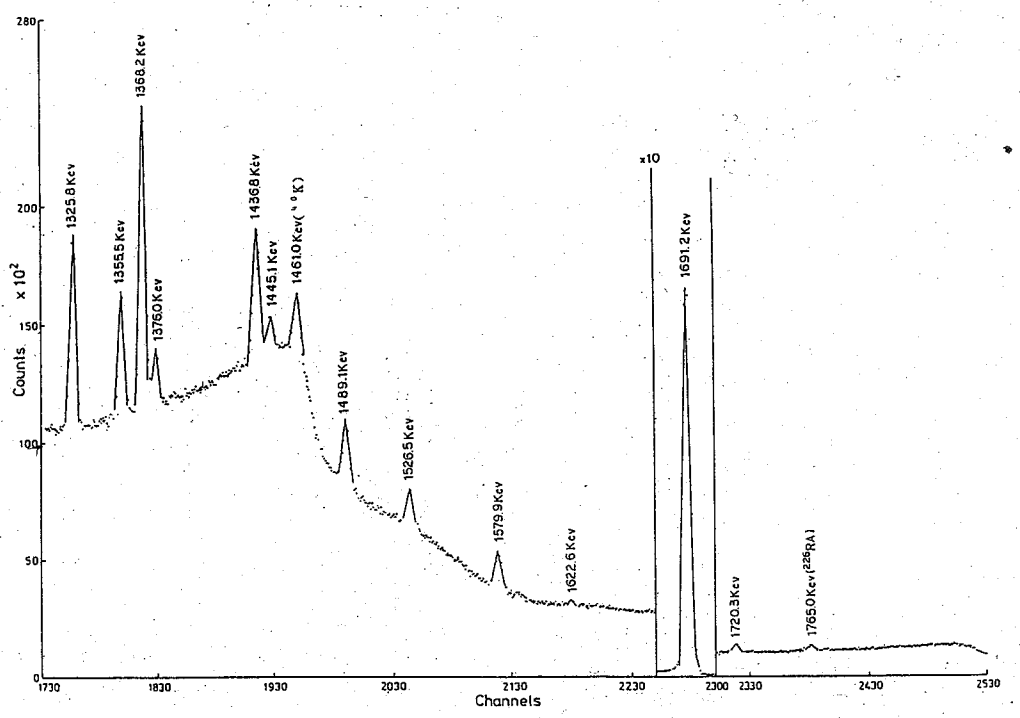

Fig. 4. Gamma-ray singles spectrum following the decay of ^{124}Sb in the energy range of 1320-1890 keV.

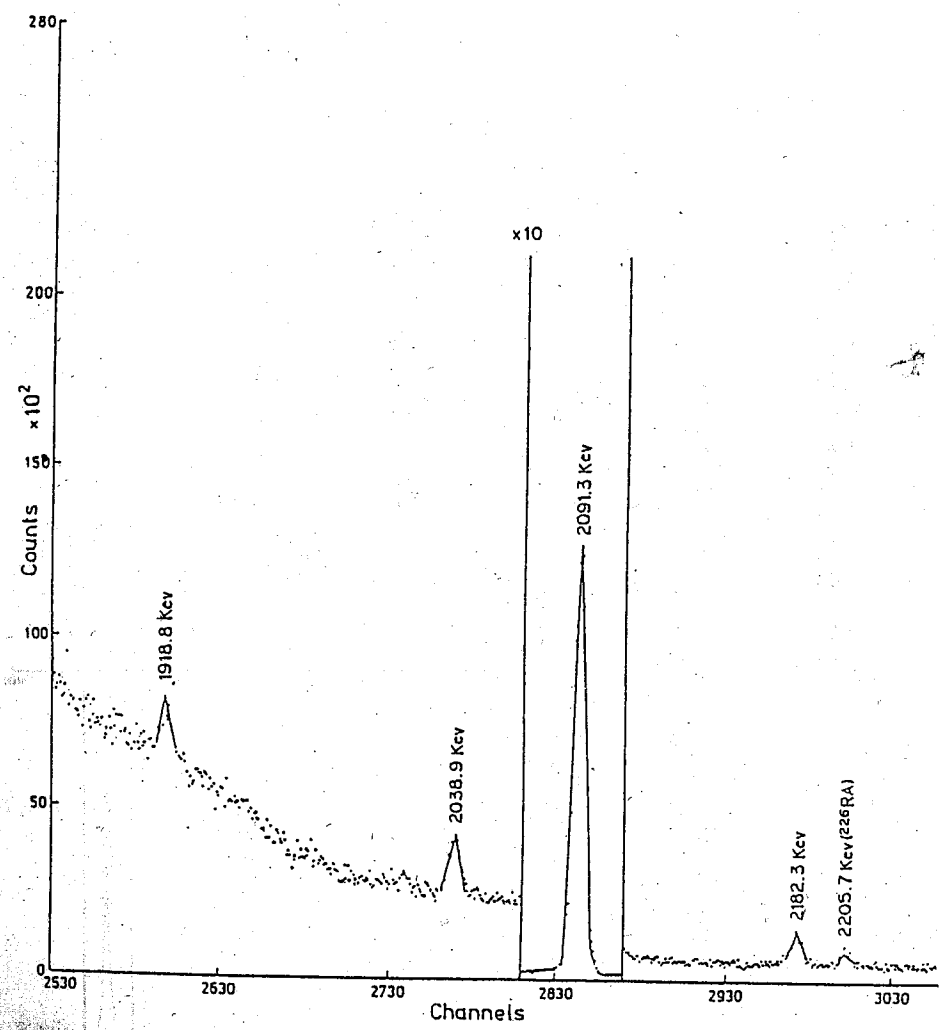

Fig. 5. Gamma-ray singles spectrum following the decay of ^{124}Sb in the energy range of 1890-2230 keV.

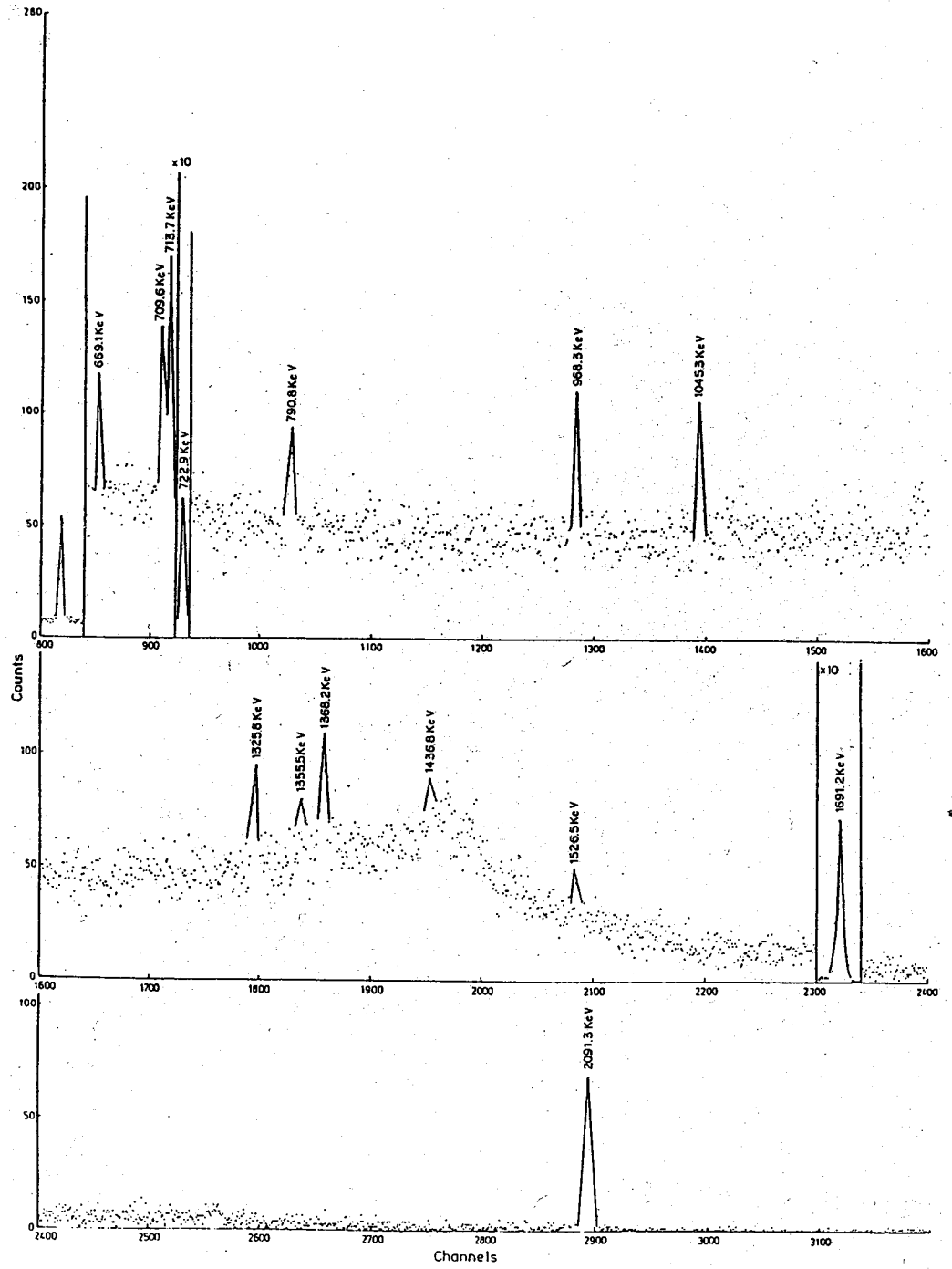

Fig. 6. Gamma-ray coincidence spectrum gated at 602.6 keV.

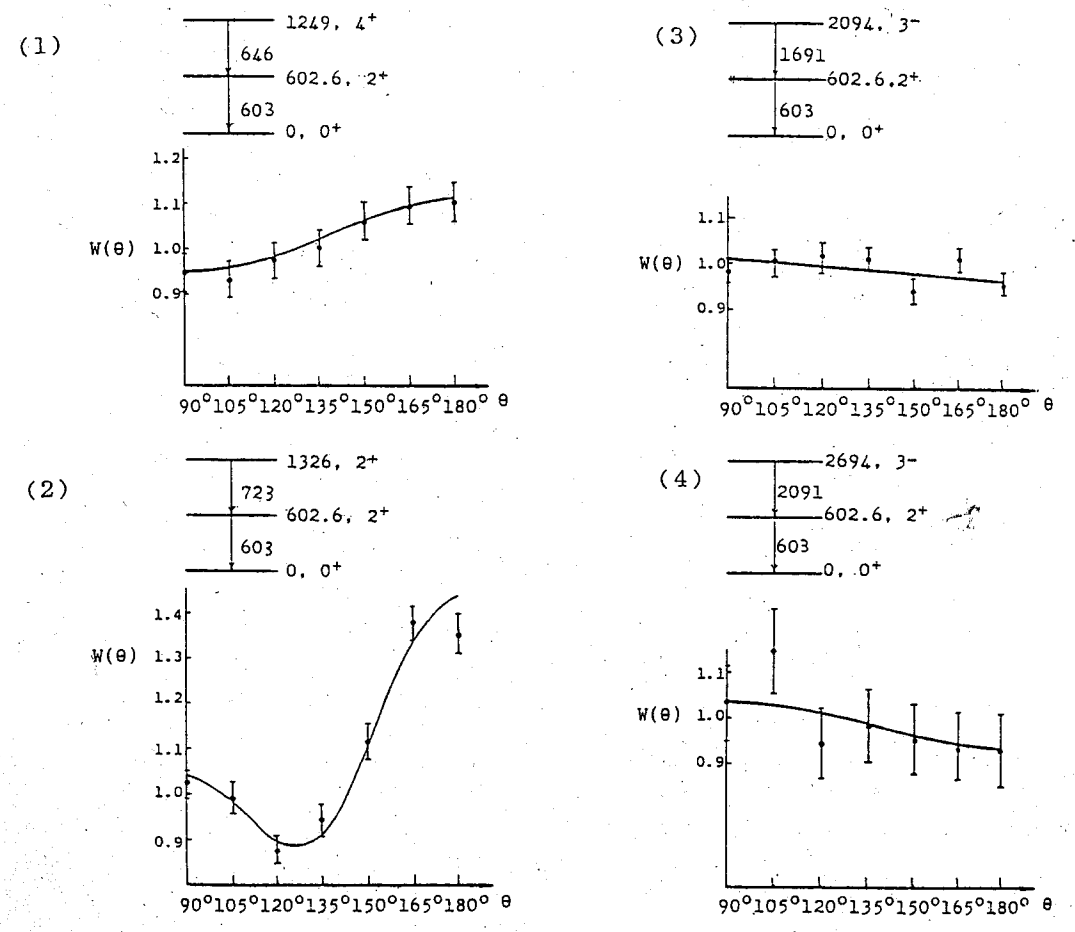

Fig.7. The fitted angular correlation function and the experimental data of (1) 646-603 cascade, (2) 723-603 cascade, (3) 1691-603 cascade, (4) 2091-603 cascadem.

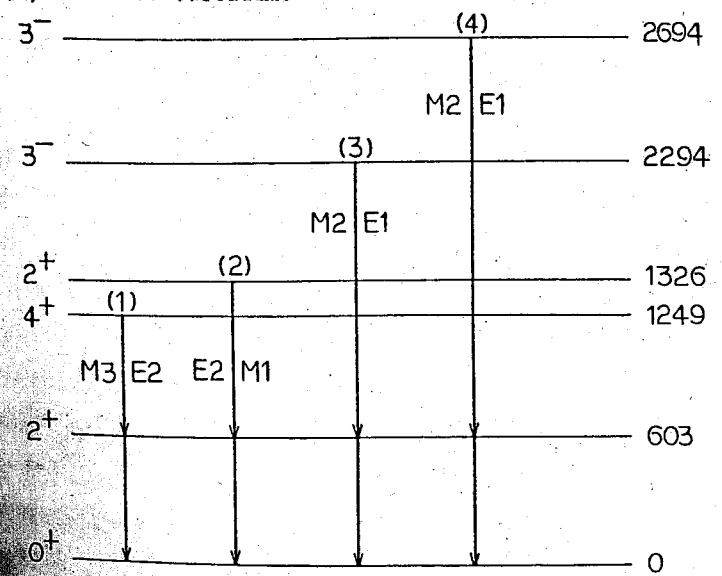

Fig. 8. The ^{124}Te decay scheme from (1) 646-603, (2) 723 -603, (3) 1691-603 and (4) 2091-603 cascades.

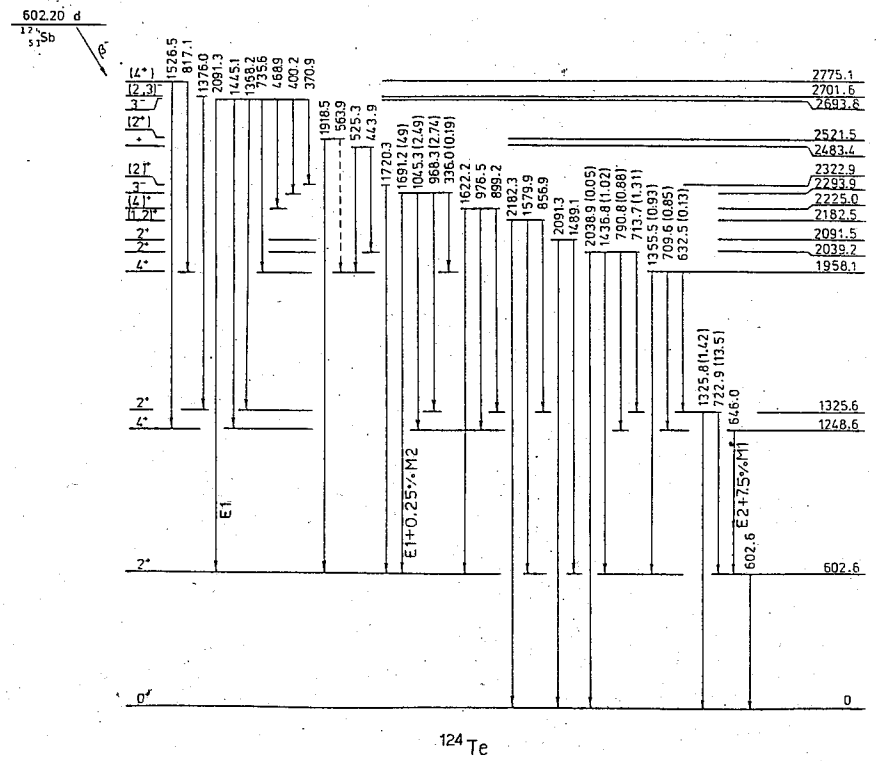

Fig. 9. The decay scheme of ^{124}Te.

本所新建大樓伽瑪背景之分析

王　　定

仲　　慶

摘　要

利用本所原子核小組73c.c HpGe 伽瑪線偵測器量取本所新建大樓三個不同房間之伽瑪背景，可發現有51條伽瑪射線，此51條伽瑪線經分析及確定分別由八個不同放射源所放出，除 ^{40}K 核種外，^{208}Tl，^{212}Bi，^{212}Pb，^{228}Ac來自釷系，^{214}Bi，^{214}Pb，^{224}Ra 來自鈾系。比較分析此三處伽瑪背景，對相同能量而不同房間瑪伽射線間之相對強度其差別不超過15%，其次利用HpGe偵測器對不同能量伽瑪射線之效率關係計算本所大樓伽瑪背景劑量約爲 0.3 9 ± 0.06 毫倫琴／週，遠較一般保健物理所定有關生物反應之許可劑量爲低。

壹、緒　言

宇宙射線及地表所存在之天然放射性核種是伽瑪背景的主要來源。此微量伽瑪背景對人體之影響，到目前爲止還所知有限。一般建築物內伽瑪背景主要來源爲建築材料內之天然放射性核種，主要爲釷（Th）系、鈾（U）系與鉀－40（^{40}K）核種[1]。由於宇宙射線大部份被阻擋於屋外，因此一般室內伽瑪背景劑量較室外爲低[2][3]。對於一般伽瑪放射性或原子核物理實驗室，此微量之伽瑪背景會造成量度伽瑪線譜上之若干嚴重干擾，因此一般伽瑪放射性或原子核物理實驗室均將伽瑪背景之認定及量度作爲必要之工作之一，以免其影響實驗結果之分析。

本所新建大樓於本年(73)七月完成，爲求對原子核實驗室及大樓內其他實驗室之伽瑪背景有一普遍之瞭解，本實驗利用本所原子核小組現有之 73 cc. HpGe 伽瑪偵測器，量度大樓內三個不同房間之伽瑪背景，分析比較此三處伽瑪背景不同能量伽瑪射線間之相對強度，並與已知原舊大樓有關伽瑪背景之資料做一比較，由HPGe 偵測器對不同伽瑪射線之不同效率，計算伽瑪背景之劑量，並列表說明其生物效應之微小。

貳、實驗分析與結果

本實驗利用HPGe高分解力偵測器量取伽瑪背景線譜，此偵測器對 ^{60}Co 1332.47 Kev 伽瑪射線之分解力爲 2.8 KeV，並利用 Canberra Series 80 型多頻道分析儀記錄實驗數據，實驗分三個不同房間量取伽瑪背景線譜。

A室：114 號原子核實驗室

B室：113 號原子核實驗室

C室：大廳

每一室量取伽瑪背景線譜之時間均爲 24 小時。

分析此三室伽瑪背景線譜，均可發現 51 條伽瑪射線，將A室之伽瑪線譜繪於圖一，圖一中括弧內之同位素表示此條伽瑪射線之來源核種，圖一中 238.63 KeV，241.98 KeV 與 1588.3 KeV，1593.3 KeV兩組伽瑪射線係由於偵測器之分解力有限而無法完全分開，將此三組伽瑪線譜，以 1460.75 KeV 伽瑪射線之强度定爲 100 單位，校正每組伽瑪射線間之相對强度，與 1979 年所刋登本所舊大樓有關伽瑪背景之資料[4]作一比較，列於表一，表一中伽瑪射線能量係根據 1978 年所收集 " Table of Isotope " 一書[5]所錄，相對强度之誤差係統計誤差，由表一中來源一欄共可發現八種伽瑪背景來源核種，其中 ^{208}Tl，^{212}Bi，^{212}Pb，^{228}Ac 四核種來自釷系，^{214}Bi，^{214}Pb，^{226}Ra 三核種來自鈾系，表一中所列本所舊大樓資料其伽瑪射線僅發現 18 條，係由於量取伽瑪背景時間不足之故。

由表一中比較A，B，C三室同能量伽瑪射線間之相對强度，發現其差別最多不超過 25 %，比較A，B，C三室有關 1460.95 Kev 伽瑪射線相對强度之比爲 1 : 0.938 : 0.925，以此比值校正A，B，C三室同能量伽瑪射線間之相對强度，取 17 條强度較强之伽瑪射線列於表二，表二中相對强度之誤差亦係統計誤差，由表二可發現A，B，C三室間實際伽瑪背景强度之差別不超過 15 %。

其次假設伽瑪背景線源對圓柱狀偵測器晶體（Crystel）面是均勻的劑量分佈[1]，由 73 cc.HPGe 偵測器對伽瑪光子之效率關係[6]，

$$\ln(EFF) = -0.37(\ln E)^2 + 4.27(\ln E) - 14.4 \quad \cdots\cdots(1)$$

EFF：效率　　E：伽瑪射線能量

計算A室伽瑪背景劑量爲 0.39 毫倫琴 / 週，根據A，B，C三室伽瑪背景相對强度之差別不超過 15 %，故可得本所新建大樓伽瑪背景劑量約爲 0.39 ± 0.06 毫倫琴 / 週，將 1972 年所著 " 保健物理 " 一書[7]有關放射線劑量法與生物反應列於表三，由表三可看出本所大樓內之伽瑪背景劑量距 0.3 倫琴 / 週之許可劑低約 10^{-3} 倍。

參考文獻

(1)熊建華、張賜元著，核子科學，第十九卷，第四期，223 頁（民國七十一年十二月）。

(2) Wayne M. Lowder, Ascher Segall, and William J. Condon, Environmental Radiation Survey in Northern New England, In The Natural Radiation Environment (J. A. S. Adams and A. M. Lowder, Eds.), p.907. Univ. of Chicago Press, Chicago, 1964.

(3) Cecil Pinkerton, William Y. Chen, R. G. Hutchins, and Ralph E. Schrohenloher, Background Radioactivity Monitoring of a Pilot Study Community in Washington Country, Maryland. In The Natural Radiation Environment (J. A. S. Adams and A. M. Lowder, Eds.), p.919, Univ. of Chicago Press, Chicago, 1964.

(4)江紀成等著，中央研究院物理研究所集刋第九卷，31 頁（民國六十八年）

(5) C. Michael Ledever and Virginia S. Shirley, Table of Isotopes (7th ed.), John Wiley & Sons, Inc. New York.

(6)本所原子核組實驗所收集之有關 73 c.c. HPGe偵測器對不同能量伽瑪射線效率資料。

(7)D. J. Rees 著，黃則夫譯，保健物理，228 頁，民國六十一年出版。

表一：新大樓與舊大樓伽瑪背景强度之比較

伽瑪射線能量 (KeV)	相對强度 新建大樓 A室	B室	C室	舊大樓	來源
186.18	7.75 ± 0.08	7.97 ± 0.10	8.49 ± 0.19		^{226}Ra
209.3	5.09 ± 0.06	5.39 ± 0.09	5.26 ± 0.15		^{228}Ac
241.98(238.63)	87.87 ± 0.26	84.48 ± 0.32	89.66 ± 0.61	72.19	^{214}Pb(^{212}Pb)
270.2	6.23 ± 0.07	6.14 ± 0.09	6.43 ± 0.16		^{228}Ac
277.4	3.00 ± 0.05	2.53 ± 0.06	2.66 ± 0.10		^{208}Tl
295.21	19.30 ± 0.12	19.78 ± 0.15	20.24 ± 0.29	36.43	^{214}Pb
300.11	5.00 ± 0.06	5.22 ± 0.08	5.52 ± 0.15		^{212}Pb
327.6	3.91 ± 0.05	4.38 ± 0.07	4.16 ± 0.14		^{228}Ac
338.3	15.83 ± 0.11	15.27 ± 0.14	15.20 ± 0.25	17.16	^{228}Ac
351.92	34.27 ± 0.16	37.19 ± 0.21	36.24 ± 0.39	36.43	^{214}Pb
409.8	1.76 ± 0.04	1.98 ± 0.04	1.83 ± 0.09		^{228}Ac
463.0	5.52 ± 0.06	5.74 ± 0.08	5.09 ± 0.15		^{228}Ac
510.72	17.65 ± 0.11	16.87 ± 0.14	18.80 ± 0.28	29.96	^{208}Tl
562.6	0.86 ± 0.03	0.94 ± 0.03	0.90 ± 0.06		^{228}Ac
583.14	34.62 ± 0.16	33.74 ± 0.21	32.61 ± 0.36	33.65	^{208}Tl
609.31	32.85 ± 0.16	33.65 ± 0.21	36.55 ± 0.39	30.86	^{214}Bi
665.45	1.22 ± 0.03	0.92 ± 0.03	0.98 ± 0.06		^{214}Bi
727.3	7.40 ± 0.07	6.96 ± 0.09	7.71 ± 0.18	11.30	^{212}Bi
768.36	3.87 ± 0.05	3.81 ± 0.06	3.99 ± 0.13		^{214}Bi
786.0	1.78 ± 0.04	2.01 ± 0.05	2.09 ± 0.08		^{214}Pb
795.0	3.74 ± 0.05	4.23 ± 0.07	4.26 ± 0.13		^{228}Ac
806.17	0.73 ± 0.02	0.91 ± 0.03	0.88 ± 0.06		^{214}Bi
835.6	1.06 ± 0.03	0.89 ± 0.03	0.85 ± 0.06	6.31	^{228}Ac
839.2	0.66 ± 0.02	0.72 ± 0.03	0.79 ± 0.06		^{214}Pb
860.4	4.59 ± 0.06	4.55 ± 0.08	4.35 ± 0.13	7.42	^{208}Tl
911.1	24.53 ± 0.14	23.18 ± 0.17	22.85 ± 0.31	18.89	^{228}Ac
934.06	2.00 ± 0.04	2.11 ± 0.05	1.98 ± 0.08		^{214}Bi
968.8	18.79 ± 0.12	18.13 ± 0.15	18.85 ± 0.28	17.24	^{228}Ac
1120.29	8.78 ± 0.08	8.52 ± 0.10	9.11 ± 0.20	7.00	^{214}Bi
1155.19	1.34 ± 0.03	1.31 ± 0.04	1.24 ± 0.07		^{214}Bi
1238.11	4.79 ± 0.06	4.67 ± 0.08	4.81 ± 0.14	3.88	^{214}Bi
1280.96	0.62 ± 0.02	0.78 ± 0.02	0.58 ± 0.05		^{214}Bi
1377.67	1.85 ± 0.04	1.97 ± 0.05	1.63 ± 0.08		^{214}Bi
1407.98	1.25 ± 0.03	1.42 ± 0.04	1.03 ± 0.07		^{214}Bi
1460.75	100	100	100	100	^{40}K
1496.2	0.42 ± 0.02	0.62 ± 0.03	0.54 ± 0.05		^{228}Ac
1509.23	0.95 ± 0.03	1.08 ± 0.04	1.06 ± 0.07		^{214}Bi
1588.3(1593.3)	6.33 ± 0.07	7.11 ± 0.10	7.12 ± 0.17		^{228}Ac(^{208}TlD)
1620.6	0.86 ± 0.03	0.92 ± 0.03	0.90 ± 0.06		^{212}Bi
1630.7	0.94 ± 0.03	1.19 ± 0.04	1.14 ± 0.07		^{228}Ac
1661.3	0.69 ± 0.02	0.84 ± 0.03	0.83 ± 0.06		^{214}Bi
1729.6	1.23 ± 0.03	1.49 ± 0.04	1.47 ± 0.08		^{214}Bi
1764.51	7.55 ± 0.07	7.79 ± 0.10	8.29 ± 0.18	8.84	^{214}Bi
1847.42	1.10 ± 0.03	1.11 ± 0.04	0.98 ± 0.06		^{214}Bi
2103.3	3.53 ± 0.05	3.79 ± 0.07	3.63 ± 0.12	5.21	^{208}Tl S
2118.55	0.49 ± 0.02	0.59 ± 0.03	0.48 ± 0.05		^{214}Bi
2204.21	1.99 ± 0.04	2.24 ± 0.05	2.38 ± 0.10		^{214}Bi
2447.8	0.63 ± 0.02	0.77 ± 0.03	0.83 ± 0.06		^{214}Bi
2614.5	21.43 ± 0.13	22.25 ± 0.17	22.82 ± 0.23		^{208}Tl

表二：A，B，C三室同能量伽瑪背景强度之比較

來源	伽瑪射線能量 (KeV)	相對强度 A室	B室	C室
^{40}K	1460.75	1 ± 0.003	0.938 ± 0,003	0.925 ± 0.006
^{208}Tl	583.14	1 ± 0.005	0.914 ± 0.006	0.871 ± 0.010
	2614.5	1 ± 0.006	0.974 ± 0.007	0.985 ± 0.011
^{212}Bi	727.3	1 ± 0.010	0.882 ± 0.012	0.964 ± 0.023
^{212}Pb	300.11	1 ± 0.012	0.979 ± 0.015	1.021 ± 0.025
^{214}Bi	609.31	1 ± 0.005	0.961 ± 0.006	1.029 ± 0.011
	1120.29	1 ± 0.009	0.910 ± 0.011	0.960 ± 0.021
^{214}Pb	295.21	1 ± 0.006	0.961 ± 0.008	0.970 ± 0.013
	351.92	1 ± 0.005	1.018 ± 0.006	0.978 ± 0.011
^{226}Ra	186.18	1 ± 0.010	0.965 ± 0.012	1.013 ± 0.022
^{228}Ac	209.3	1 ± 0.012	0.993 ± 0.016	0.956 ± 0.027
	270.2	1 ± 0.011	0.924 ± 0.013	0.955 ± 0.024
	338.3	1 ± 0.007	0.905 ± 0.008	0.888 ± 0.014
	463.0	1 ± 0.012	0.975 ± 0.014	0.853 ± 0.025
	911.1	1 ± 0.006	0.886 ± 0.007	0.862 ± 0.011
	968.8	1 ± 0.006	0.905 ± 0.007	0.928 ± 0.013
	1588.3	1 ± 0.012	1.054 ± 0.015	1.040 ± 0.025

表三　放射線劑量法與生物反應

劑量法 劑量，（倫琴）	劑量率	照射情況*	生物反應
0.3	每週	T	可能沒有（許可劑量）
1	每日（年計）	T	白血球減少症
1.5	每週	L	可能沒有（手及手指的許可劑量）
25	單次劑量	L	瘤細胞內的染色體破裂（組織培養）
50-100	累積的小劑量	L	基因突變使得自生率每代增加二倍。
60	單次劑量	L	磷酸活性退化
200	單次劑量	T	噁心
300	單次劑量	L	100kV 的紅斑劑量（小範圍）
300-500	單次劑量	T	男性的 LD_{50}（50 %致死量）
300-600	單次劑量	L（卵巢）	女性絕育
400	單次劑量	L	可逆性脫毛
400-500	10-50 γ/日	T	臨床復原
500	單次劑量	L	200kV 的紅斑劑量（小範圍）
600-800	單次劑量	L（睪丸）	男性絕育
600-900	300γ/日或小劑量		放射線內障
1000	單次劑量	L	鐳的紅斑劑量
1000-1500	200-300γ/日	L	骶阻滯
1000-2500	200-300γ/日	L	顯著的放射性敏感癌反應
1500	200-300γ/日	L（卵巢）	卵巢截除（女性）
1500-2000	200-300γ/日	L	唾腺功能停止
1800-2000	200-300γ/日	L（胃）	胃酸缺乏
2000	單次劑量	L	2MeV 的紅斑劑量
2000-3000	200-300γ/日	L（腎臟）	放射線胃炎
2500-6000	200-300γ/日	L	中等放射線敏感癌反應
2700-3000	單次劑量	L	溼性脫皮，但皮膚會復原：100kV 放射線（小範圍）
3600-5000	200-300γ/日	L	皮膚極限（單門靜脈，200kV，5×5 厘米範圍）
4000-5000	200-300γ/日	L	神經組織極限
5000-6000	200-300γ/日	L	胃腸道極限
5000-7000	200-300γ/日	L	溼性脫皮，但皮膚會復原（單門靜脈 2000 至 3000 kV 放射線，10 × 10 厘米範圍）
～50000	10-100γ/日	L	生癌

*T＝total body（全身）；L＝local（局部）。
＋此處使用的劑量率單位γ/日＝倫琴/日。

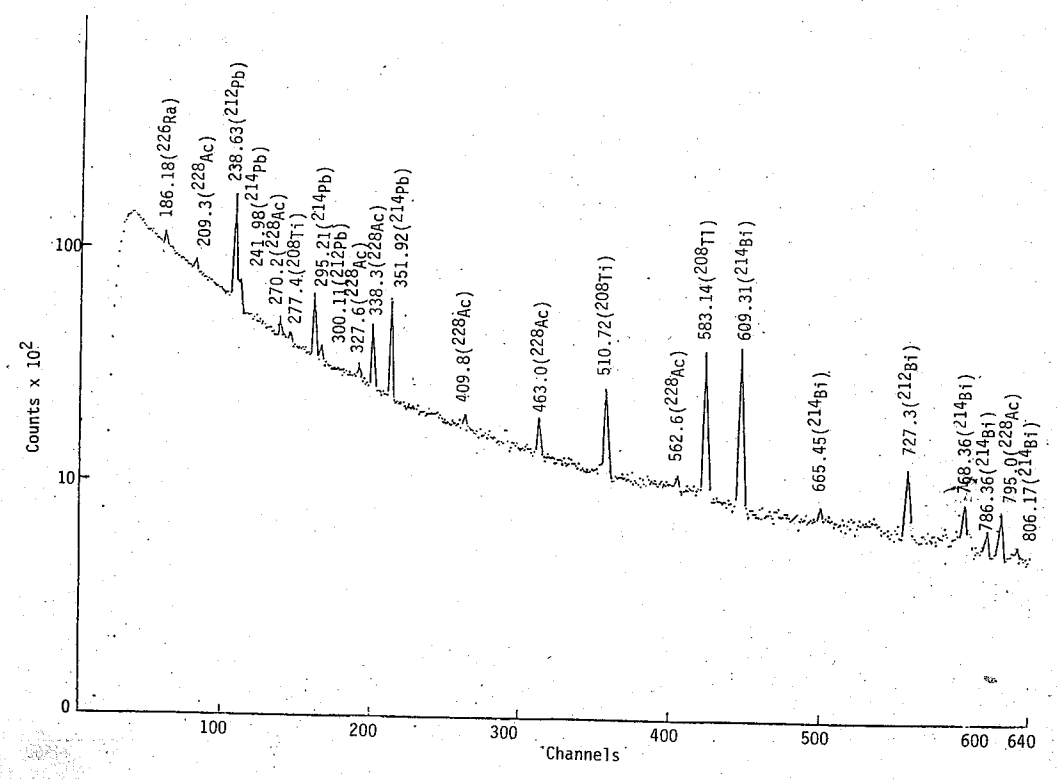

圖一　A室伽瑪背景線譜（180 KeV- 810 KeV）

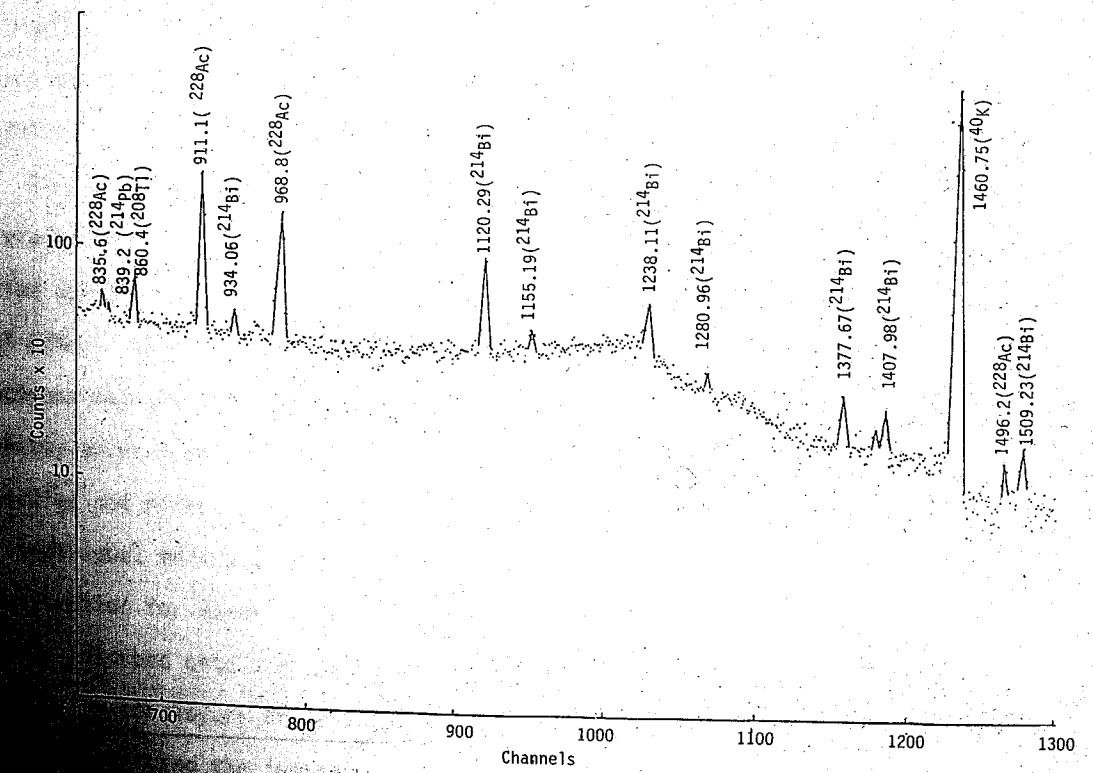

圖一　A室伽瑪背景線譜（810 KeV- 1520 KeV）

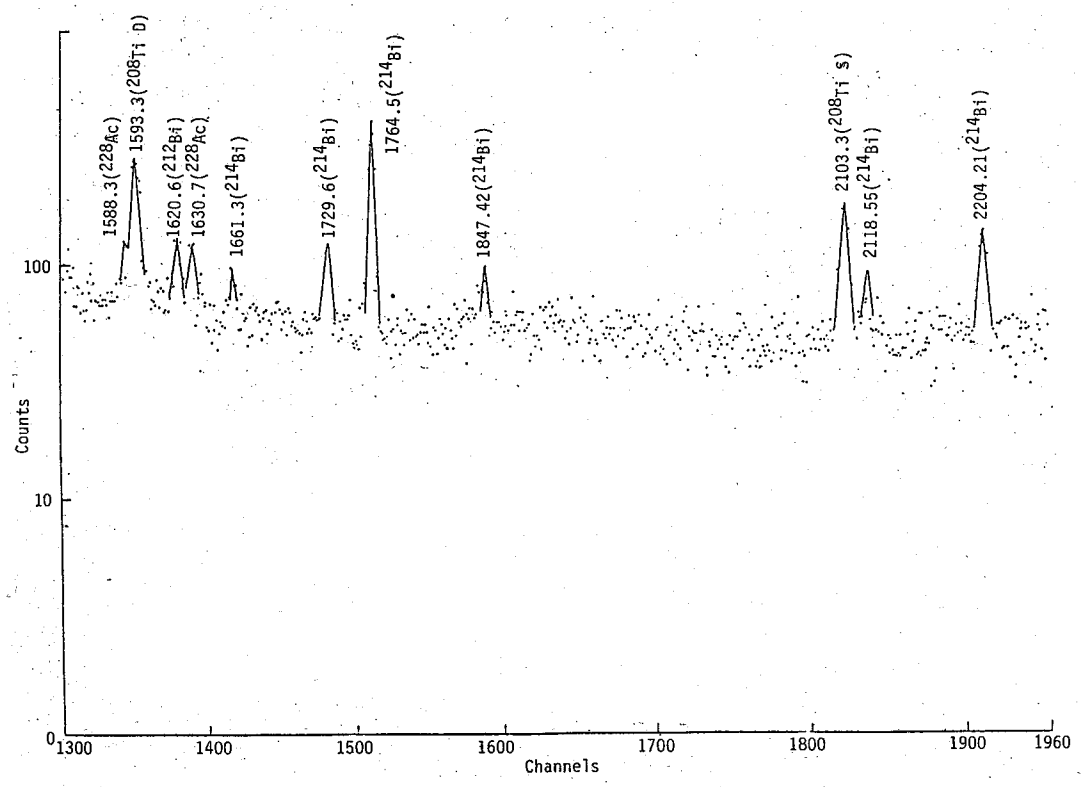

圖一　A室伽瑪背景線譜（1520 KeV - 2230 KeV ）

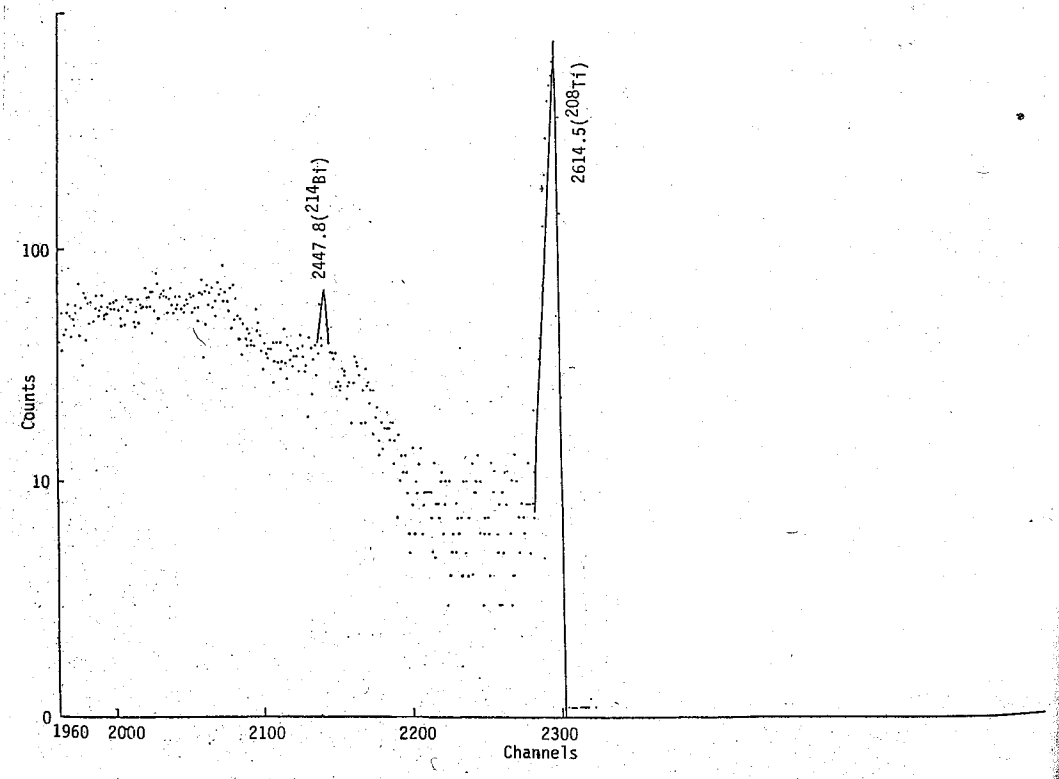

圖一　A室伽瑪背景線譜（2230 KeV - 2620 KeV ）

A NEW THEORY OF SURFACE ENHANCED RAMAN SCATTERING

Chun Chiang

Institute of Physics Academia Sinica

Nankang, Taipei, Taiwan, R. O. C.

It is proposed that the π electrons of p-orbitals in the adsorbed melecules may delocalize via the metal, thus the electrons excited by the photon impacted on the molecule may not only provoke Raman scattering in that particular molecule, but may also delocalize to other molecules and provoke Raman scattering in other molecules. This increases the effective cross section and leads to the enhancement of the Raman scattering. Many data may be explained with the present theory.

Since the discoverty of intensive Raman line of pyridine molecules adsorbed on the silver electrode (1), intensive effort has been directed to elucidate this surface enhanced Raman scattering (SERS). Many theories have been proposed for its explanation, see for example reference (2, 3), no theory seems to have been accepted overwhelmingly. Here we would like to propose a simple mechanism for its explanation.

When molecules are adsorbed onto the metal such as Ag, Au, Cu, etc., if the molecules have the lone pair electrons or π electrons, these electrons may delocalize and transmit through the metal medium so that they may interact and influence each other. When these electrons in a single molecule are excited, the excited electrons may transmit to other molecules via metal as well. Thus not only the directly excited molecule will contribute to the Raman intensity, other adsorbed molecules not directly excited may also contribute to the Raman intensity, namely, individual molecules become effectively a "giant molecule" and the effective cross section for Raman scattering is increased. Since large amount of molecules adsorbed onto the metal, thus an intensity enhancement factor of 10^6 may be monolayers of molecules adsorbed. Also, the metal surface provides an ing the photons, which can also excite the electrons. These excited grate to the adsorbed molecules and contribute to the Raman singnals,

leading to SERS. The proposal that the electrons are delocalized in the system also predicts that the polarizability of the molecules is increased, since ample electrons can be supplied in response to any change of field or environments. This also contribute to the SERS.

The exact interaction between the adsorbed molecules and metal may vary case by case, the π electrons of the molecules may form a π complex with the metal or the lone pair of the molecule may donate a bond to the metal or the electrons may turnel through the barrier. However, as long as the electrons can delocalize in the molecule and migrate or tunel to the metal, and in turn, the carriers in metal may also migrate or turnel to the adsorbed molecules, the SERS will be exhibited. For this reason, the best molecules showing this SERS are those with π electron double bond, especially those with conjugated double bond.

For effective communication of electrons between adsorbed molecules and metal, the surface properties, especially, the surface charge, will play an important role. The residue charges on the surface can attract the molecules, and facilate the electronic delocalization of electron between the molecules and the metal, thus electronically processed surface shows SERS. The electrons may also deposit on top of the metal surface curvature, this is also the reason why irregular surface shows larger enhancement of Raman signals.

The present theory relies on the delocalization of electrons among various molecules adsorbed. Thus the recent discovery (14, 15) that the SERS may be due to the carbonized non-crystalline phase between the pyridine and the metal can be easily incorporated within this theory, since the carbonized phase can also provide a means for the delocalization of electrons.

This simple theory may explain or predict many other experimental data as follows:

1. Since it is the π electron of the double bond which delocalizes and comunicates within the system, the SERS effect will be stronger for the vibration mode of the atoms having the π electrons. Thus the double bond or triple bond strechi will show strong enhancement, whereas the C-H vibration in the same molecule show litter enhancement. Also, CH_4 and C_2H_6 should not show SERS. These a indeed observed (4, 5).

2. Since the delocalized electrons can migrate freely to various location, the energy fluctuation would be larger. Also, due to the interaction among the molecules and between the molecule and the metal, the energy state will be broadened and SERS spectrum will be broadened as indeed observed by Moskovits and DiLella (4, 5). Metiu and Palk have suggested the possibility of coupling of the molecular vibration to the electronic degrees of freedom of the matal (6), but no dotail has been given yet. From another point of view, the photons in a single adsorbed molecule is trapped in that single molecule, thus its life time is longer, whereas, the photons in "giant molecule" can transport to other site and makes transition there, the increased possibility of transition makes the life time smaller. Concequently, the SERS spectrum will be broadened. That the electron transition in adsorbed molecules will display shorter lifetimes and lower energies has been reviewed befoere (8), the present theory emphisizes further the interaction among the adsorbed molecules as a source of broadening.
3. It is observed that for several layers of alkene molecules adsorbed on metal, besides a very enhanced, broadened and shifted peck, there is also a weaker, unbroadened, unshifted peck located at the same frequency as in polycrystaline material (5). The very much enhanced, shifted peck may be explained by the conjugated "giant molecule"; the delocalization of electrons in double bond will lessen the double bond character and the double bond vibration frequency will be shifted to the lower value. The unshifted pack may be explained as due to the local field such as image field effect (9, 10) or surface plasmon effect (4), which may not only acting at the first lager, but acting at second or third layer as well. These effects are weaker and may not necessarily cause broadening of frequency shifting.

According to the present theory, the larger is the size of the metal substrate, the more is the molecules adsorbed, and the more enhancement is the scattering. However, it should note that the larger is the size of the metal, the more po- will be the dissipation of the excited electrons in the bulk of the Thus there is an optimum size for which the SERS will be the maximum. (7) have found that the films which show the largest Raman signals of isolated islands of approximatly 200-400A dimensions. Taking

the surface area as 5×10^5 Å^2 and the attached molecule area as 10 Å^2 the number of adsorbed molecules is 5×10^4 and this is approxcimatly the SERS enhancement factor. The possibility that the energy of the excited delocalized electrons may also be dissipated in the metal matrix explains the fact that the background Raman continum intensity is also increased.

5. If the photons or excited electrons involve in other optical process such as luminescence or absorption, then this luminescence or absorption should also be enhanced. This is indeed observed (11, 12, 13).

In Conclusion, by proposing that the electrons in the adsorbed molecules may delocalize so that all the individual moleules may effectively becomes a "giant molecule", the SERS may be explained. Many data may be explained with this idea.

REFERENCES

(1) M. Fleischmann, P. J. Hendra, A. J. McQuillan, Chem. Phys. Lett. 26, 123 (1974).

(2) T. E. Furtak, J. Reyes, Surf. Sci. 93, 351 (1980).

(3) R. K. Chang, T. E. Furtak, Ed. Surface Enhanced Raman Scattering, Plenum, New York (1982).

(4) M. Moskovits and D. P. DiLella, Chem. Phys. Lett. 73, 500 (1980).

(5) M. Moskovits and D. P. DiLella, in Surface Enhanced Raman Scattering, Ed. Chang, Furtak, Plenum, New York pp.243 (1982).

(6) H. Metiu and E. Palke, J. Chem. Phys, 69, 2574 (1978).

(7) J. G. Bergman, D. S. Chemla, P. F. Liao, A. M. Glass, A. Pinczuk, R. M. Hart and D. H. Olson, Opt. Lett, 6, 33 (1981).

(8) R. R. Chance, A. Prock and Sibley in: Advances in Chemical Physics, Vol. 37, Eds. I. Prigogine and S. Rice (1978) p.1.

(9) F. W. King, R. P. Van Duyne and G. C. Schatz, J. Chem. Phys, 69, 4472 (1978).

(10) S. Efrima and H. Metiu, Chem. Phys. Letters 60, 59 (1978).

(11) G. Ritchie, E. Burstein and R. B. Stephens, Bull. Am. Phys. Soc. 26, 359 (198

(12) A. Hartstein, J. R. Kirtley, and J. G. Tsang, Phys. Rev. Lett. 45, 201 (1980)

(13) A. M. Glass, P. F. Liao, J. G. Bergman and D. A. Olson, Opt. Lett, 5, 368 (19

(14) R. P. Cooney, M. W. Howard, M. R. Mahoney and T. P. Mernagh, Chem. Phys. Let 79, 459 (1981).

(15) T. P. Mernagh and R. P. Cooney, J. Raman Spectroscopy, 14, 138 (1983).

ATOMIC AND ELECTRONIC PROCESSES OF SWITCHING IN AMORPHOUS THIN FILMS*

Chun Chiang

Institute of Physics Academia Sinica

Nankang, Taipei, Taiwan, R. O. C.

It is proposed that the conversion of C_3° from C_2° leads to the switching. Since C_3° has more connection points, the conductivity of C_3° is higher and large current favours the C_3° species; thus increasing the current increas the C_3° density and less voltage is needed to sustain the same amount of current. This explains the S shaped negative resistance. The concept is simple and the mathematics for quantitative calculation is manageable.

Switching in amorphous thin films is an important phenomenon. Despite its intensive research[1] its explaination is still a controversy.

Recently, Kastner et. al.[2] propose an important concept of valence alteration pair (VAP) to explain the properties of Chalcogenide amorphous thin films. Using this concept, Petersen and Adler[6] propose that if certain minimum amount of valence alternational pairs are present, the Mott transition may be initiated by carrier generation induced by field to form the C_3° band by the reaction $C_3^+ + e^- \rightarrow$ C_2° or $C_1^- + e^+ \rightarrow C_3^\circ$, thus producing the high conductivity state; below a critical VAP density, no switching can occur. The carrier density in the ON state is independent of the VAP density, however, the current in ON state increases with filament size. Also, Adler et. al.,[3] propose that the field-induced carrier generation can neutralize the charge traps(C_3^+, C_1^-), when all the traps are filled carriers can transit the sample with an enhanced mobility andthe generation power required to keep the traps filled is reduced. The carrier is dependent on electrode (no interband generation) and the filment growth with area to maintain constant current density. Since both of these models depends on the carrier generation by field induction, it seems that S shaped negative conductance may not be one of these mechanism.

---

* Physics Letters, 1984.

The purpose of this letter is to propose another mechanism, which utilizes the concept of VAP in another form. The mechanism proposed is the current mediated conversion of C_2° and C_3°, where C_2° and C_3° represent the chalcogenide elements with two bonds and three bonds respectively. In the normal state, C_2° is the lowest neutral state, however, two neighboring C_2° may interact such that C_3° are formed

$$2\,C_2^\circ \rightleftarrows 2\,C_3^\circ\,(e^*) \qquad (1a)$$

where the star indicates that the neutral C_3° has an electron in high energy state (antibonding state in this case). This electron may further transport to other low energy site such as the dangling bond and release the energy

$$2\,C_3^\circ\,(e^*) \rightarrow 2\,C_3^+ + 2\,e + \text{energy} \qquad (1b)$$

Two neighboring C_2° may also react to form one C_3° and one dangling bond such as

$$2\,C_2^\circ \rightleftarrows C_3^\circ\,(e^*) + C_1^\circ \qquad (2a)$$

The high energy state electron also can transport to C_1° and release the energy

$$C_3^\circ\,(e^*) + C_1^\circ \rightarrow C_3^+ + C_1^- + \text{energy} \qquad (2b)$$

Eqs. (1) and (2) may also be expressed in a diagramatic way in Fig. 1.

In the normal film in OFF state, there are certain number of C_2° elements with bond strain or being too much crowded, so that Eq. (1) proceeds to the right and energy is released. Also there are certain number of atoms located far away in the forming process such that dangling bonds are formed, namely,

$$C_2^\circ \rightarrow 2\,C_1^\circ \qquad (3)$$

Since there are equal probability for the atoms to be displaced too crowdly or too loosely, thus equal number of C_3^+ and C_1^- will be formed from Eqs. (1) and (3). Eq. (2) also produces equal number of C_3^+ and C_1^-. The electrons in C_3^+, C_1^- and C_2° in OFF state are all paired, thus this can explain the observed data that no EPR signals are observed in chalcogenide film.

If passing current through the film, the electrons in C_1^- is excited to the excited state or conduction band, Eqs. (1b) and (2b) are essentially reversed; namely, energy is provided such that electron is excited into the high energy anti-bonding state C_3°. Since C_3° lattice has more connection points with other species this is the low resistance path and electrons will choose C_3° lattice as the conducting path. If no C_3° path is available, the electron has to pass through lattice via hopping process and the local energy will be higher and this is the

preferable path. As more current passing through the film, the C_3° lattice will be used up and more current has to use the C_2° species as conducting path. However, since a large excitation energy is needed for the electron to be excited into the conduction band and since C_2° species have less connection points, its conductivity is less; thus, by passing equal amount of current through the film, the local energy via the path of C_2° lattice is higher than that via the path of C_3° lattice. For this reasons, the film prefers the C_3° lattice and the C_2° species will be transformed to C_3° species according to Eq. (1a) or (2a) and depending on the environment of neighboring atoms. This kind of transformation may be termed current mediated structure transformation. This idea may be put in an equation as

$$F(I) + 2C_2^\circ \rightleftarrows G(I) + 2C_3^\circ \qquad (4)$$

where F(I) and G(I) represent the energy produced when current passing through C_2° lattice or C_3° lattice respectively. Since the electron in C_3° species is in excited state already and also its resistivity is less, thus $G(I) < F(I)$, and higher current favours the C_3° species and Eq. (4) proceeds to the right. Furthermore, a film with more C_3° species will have less resistivity and less voltage drop, thus increasing the current will increase the C_3° species and decrease the voltage drop. When most of the C_2° species have been transformed to C_3° species, then increasing the current will increase the voltage drop again. This mechanism explains the S shaped negative conductance satisfactorily. Note that in this transformation process, only electronic bonding is changing and not much atomic displacement is involved, thus the process can be very fast. If relatively large atom displacement is involved, then permenent change may occure such as in memory process or the forming process.

In a film the high energy stress occurs near the boundary between C_2° and C_3° species, the C_2° near the C_3° has high tendency to transform to C_3°, thus C_3° will [illegible] nucleus and a conducting filament will be formed before the switching starts. [illegible] initiation of switching process, the filament will grow in size with current [illegible] transformed to C_3° around the C_3° filament and the voltage will drop. [illegible] state consistes mostly the C_2° and equal number of C_3^+ and C_1^-; the [illegible] consistes mostly the C_3° species; in the S shaped negative conductance [illegible] consists a mixture of C_2° and C_3°. The properties of ON and OFF [illegible] in following table:

State	ON State	Off State	Mixed State
Species	C_3°	C_2° , C_3^+, C_1^-	C_3° , C_2°
Excitation Energy	Little or non (electron in anti-bonding orbital)	Large (from lone pair to conduction band)	Medium
Carriers	More	Less	Medium
Connection Network	Three connection points	Two connection points in average	Medium
Conductivity	Large	Small	Medium
dI/dV	Positive	Positive	Negative

Chiang[4, 5] previously has formulated a quantitative switching theory by proposing two configurations co-exist in the film. The theory was able to explain many experimental data such as delay time, triensient ON characteristics, etc.. The present communication provides the specific details about the species of the configuations. These configurations are also consistant with the other properties such as no EPR signal is observed and the conductivity is of $e^{-E/KT}$ type. The major difference between this theory and those proposed by Adler et al[3] and Peterson and Adler[2] is that the present theory depends on the conversion of C_2° to C_3° , the excitation and traping of C_3^+ and C_1^- determine only the conduction in OFF state but may contribute very little to the switching process. On the other hand, those by Adler et al and Peterson and Adler depend on a fixed minimum amount of C_3^+ and C_1^- pairs present in the OFF state, below which no switching can occur; the number of the pairs is not changed, however, the excitation of C_3^+ and C_1^- species or the conversion of C_3° from C_3^+ and C_1^- , not from C_2° , leads to switching. Also in the present theory, the growth of filament size determines the S shaped negative conductance, and it is a mixture state of C_3° and C_2° ; however, the other theory conjecture on the growth of filament size with the current in the ON state and it is not quite clear how does the S shaped negative conductance occur.

In conclusion, a structure conversion induced by current is proposed, the concept is simple and the mathematics is managable and it is able to explain many experimental data.

REFERENCES

1) D. Adler, H. Henisch, N. Mott, Rev. Mod. Phys. 50, 209 (1978).

2) M. Kastner, D. Adler, and H. Fritzsche, Phys. Rev. Lett. 37, 1504 (1976).

3) D. Adler, M. S. Shur, M. Silver, S. R. Ovshinsky, J. Appl. Phys. 51(b), 3289 (1980).

4) C. Chiang, Phys, Stat. Sol. (a) 54, 735 (1979).

5) C. Chiang, Sol. Stat. Comm. 39, 111 (1981).

6) K. E. Petersen and D. Adler, J. Appl. Phys. 50, 5065 (1979).

FIGURE LEGEND

Fig. 1. (a) A diagramatic representation of Eq. (1a).
(b) A diagramatic representation of Eq. (2a). The lone pair is represented by two dots and the & represents the electron in high energy anti-bonding state.

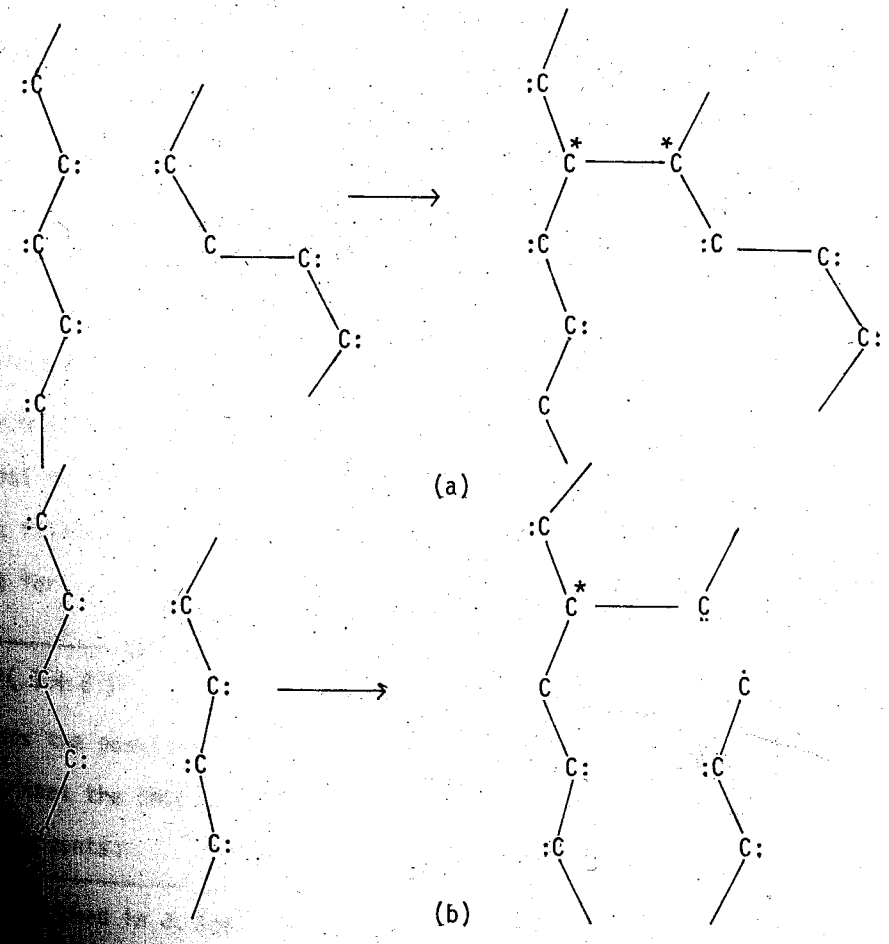

ON TRAPPING AND SWITCHING IN SEMICONDUCTORS: A COMMENT*

Chun Chiang
Institute of Physics Academia Sinica
Nankang, Taipei, Taiwan, R. O. C.

Adler et al. propose that field-induced filling of traps may lead to S shaped negative differential conductance, and using the existance of two solutions of electron concentration for a given applied field as evidence for it. We comment on the conditions for this existance of two solutions and its significance to the SNDC

Intensive effort has been directed to the elucidation of switching mechanism of amorphous thin films. Recently, Adler et al[1] have proposed that the field-induced filling of positively and negatively charged traps may lead to S shaped negative differential conductance (SNDC). Using the hypotheses that the field induced generation rate of electron hole pair is equal to the rate of electronic filling to the acceptor or the rate of hole filling to the negative traps, they derived the following equations

$$P/N|_{\pm} = \frac{1}{2}(\lambda^{-1} - 1 - \xi) \pm \{[\frac{1}{2}(\lambda^{-1} - 1 - \xi)]^2 - \xi\}^{\frac{1}{2}} \qquad (1)$$

and

$$N = [N_0 + \lambda(1 \mp P/N)]/[1 - (P/N)] \qquad (2)$$

where P or N is proportional to the concentration of holes or electrons, λ is proportional to field, N_0 is a constant and ξ is the ratio of the rate of electronic filling to the rate of the hole filling to the traps. From this, they claim that for

$$\frac{1}{2(1+\xi)} \leqq \lambda \leqq \frac{1}{[1+\xi^{\frac{1}{2}}]^2} \qquad (3)$$

exists the possibility of two solutions for P or N at a given λ, thus ing that the SNDC characteristics is present. We like, however, to make comments:

---

shed in J. Appl. Phys. (1984).

1. According to their mathematical derivation, the condition for the existance of two possible solutions for P or N should be

$$\frac{1}{2(1+\xi)} < \lambda < \frac{1}{[1+\xi^{\frac{1}{2}}]^2}, \quad \xi < 1 \tag{4}$$

Namely, the equal signs in Eq. (3) should be droped and the condition that $\xi < 1$ should be imposed. Fig. 1 (a) or 1(b) is a plot of Eq. (2) with ξ = 5 or 0.5 respectively, it can be seen that two positive solutions do not exist in Fig. 1(a). Note that two negative solutions exist for $0.083 < \lambda < 0.095$ but physically is not possible. Fig. 1(b) indicates that two positive solutions exist for $0.33 < \lambda < 0.34$. There are solutions existing in other region of λ, however N or P is either negative or imaginary and is physically impossible, thus it is not ploted in the diagram.

2. There are certain regions where no solution exists, indicating that the mechanism breaks dawn and is unrealistic, thus cast serious doubts of the validity of their mechanism.

3. Adler et al[1] claim that the existance of two possible solutions for a given λ indicates that the SNDC characteristic is present; however, the existance of two possible solutions only indicate that the NDC characteristic is present and is not sufficient to explain the whole story of SNDC. To fully explain the SNDC, it is required to demonstrate that three possible solutions should exist for a given λ, rather than two (as shown in their Fig. 8). A switching equation for amorphous thin films with three possible solutions for a given value of field has been derived[2], also, this equation has solution for all region of field and seems to have beteer ability to elucidate the switching mechanism.

REFERENCES

(1) D. Adler, M. S. Shur, M. Silver, S. R. Ovshinsky, J. Appl. Phys. 51, (6), 328 (1980).

(2) C. Chiang, Physica Status Solidi (a) 54, 735 (1979).

FIGURE LEGEND

Fig. 1. Plot of equation (2) with N_o = 0.07. For 1(a), ξ = 5, for 1(b), ξ =0.5.

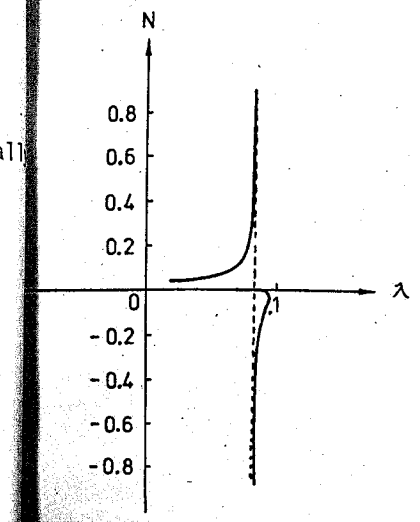

Fig. 1(a)

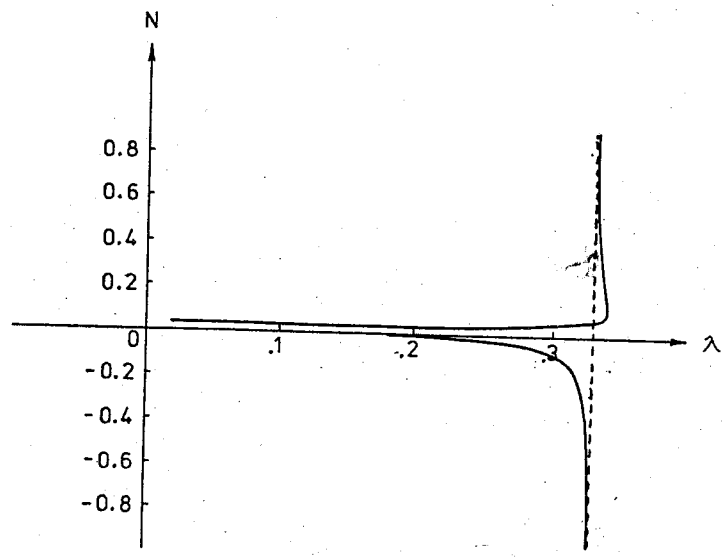

Fig. 1(b)

LONG-WAVELENGTH LATTICE VIBRATIONS OF CRYSTALLINE HCl AND HBr

Chia-Nan Chang (1), and Wan-Sun Tse(2)

Department of Electronic Engineering and Technology,

National Taiwan Institute of Technology(1) and Institute

of Physics, Academia Sinica, Nankang, Taipei, Taiwan, R. O. C. (2)

Lattice dynamics calculations of crystalline orthorhomic HCl and HBr in phase III are studied by using the Born-Von Karman model with seven interactomic force constants which is capable of giving good agreement between the observed and calculated zone centre ($\vec{q} \simeq 0$) frequencies. The calculated results show that the forces between atoms in different chains and different planes are much weaker than those between nearest neighbors in the same linear chain.

1. INTRODUCTION

Solid HCl and HBr are isomorphic molecular crystals which has been the subject of several experimental and throretical studies[1-7]. They both have three solid phases[1]. In phase I and II, the hydrogen atoms are disorded and the unit cell has 4 molecules. In the low temperature phase III, the hydrogens are fully ordered and the crystal structure is ordered orthorhombic with space group C_{2v}^{12} ($Bb2_1m$) The molecules form planar zig-zag hydrogenbonded chains, with two molecules in the primitive unit cell on sites of Cs symmetry. The three-dimensional structure of these zig-zag chains is shown in figure 1.

Based on a group theoretical analysis[2], the lattice and stretching vibrations for $q = 0$ of these crystals are classified into twelve non-degenerate normal modes in accordance with their symmetries. There are three translational ($A_1 + B_1 + A_2$) four librational modes ($A_1 + B_1 + A_2 + B_2$) corresponding to the external ons of rigid molecules. In addition, there are also two stretching modes $+ B_1$) . The A_1 mode is the in-plane vibration of the two molecules cell and is totally symmetric. The B_1 mode is the antisymmetric hich alternate molecules are exactly out of phase.

s been two major methods of long-wavelength lattice dynamics calculation

of crystalline HCl and HBr. The first one[3], using the Buckingham exp-six potential considers the angular force of bonds indirectly by placing a point charge on each at of the bonds and is complex in calculation. The second one[4], using the Born-Von Karman harmonic potential, neglects all the forces between the atoms in different zig-zag chains and is not physically appealing. In this paper, a simple three dimensional model is proposed. This model takes into account the atomic forces between atoms of adjacent zig-zag chains and considers the angular forces of bonds directly. The parameters of this model are adjusted to attempt to interpret those normal modes of vibrations obtained from spectroscopic techniques[1-2].

In section2, the model of the long-wavelength lattice dynamics calculation of a crystal is developed and then the parameters of the model adopted are explained. In section 3, the calculated results and discussions are presented.

2. THEORY AND MODEL ADOPTED

As a result of thermal fluctuations, each atom in a crystal is displaced from its equilibrium position by a small amount $\vec{u}\begin{pmatrix}\mu\\ \ell\\ k\end{pmatrix}$ where $\vec{u}\begin{pmatrix}\mu\\ \ell\\ k\end{pmatrix}$ represents the displacement of the ℓ^{th} atom of the k^{th} kind in the μ^{th} cell of the crystal. In the Born-Von Karman's approximation of harmonic force between atoms in a crystal, the equations of motion for each atom of the crystal are

$$M_k \ddot{u}_\alpha \begin{pmatrix}\mu\\ \ell\\ k\end{pmatrix} = - \sum_{\mu',\ell',k',\beta} \phi_{\alpha\beta} \begin{pmatrix}\mu & \mu'\\ \ell & \ell'\\ k\ ; & k'\end{pmatrix} u_\beta \begin{pmatrix}\mu'\\ \ell'\\ k'\end{pmatrix} \tag{1}$$

where $\phi_{\alpha\beta}\begin{pmatrix}\mu & \mu'\\ \ell & \ell'\\ k\ ; & k'\end{pmatrix}$ is the negative of the force exerted in the α-direction on the atom $\begin{pmatrix}\mu\\ \ell\\ k\end{pmatrix}$ when atom $\begin{pmatrix}\mu'\\ \ell'\\ k'\end{pmatrix}$ is displaced a unit distance in the β-direction all other atoms being kept at their equilibrium position.

As usual, we choose the displacement $u\begin{pmatrix}\mu\\ \ell\\ k\end{pmatrix}$ in a travelling-wave form of wavevector $\vec{q}$ with its corresponding amplitude independent of the cell (μ)[8][9]. In the long wavelength limit ($\vec{q} = 0$) and for nontrivial solutions of the various amplitudes in each unit cell, we can obtain the following secular equation for the crystal as

$$\left| D_{\alpha\beta}\begin{pmatrix}\mu & \mu'\\ \ell & \ell'\\ k\ ; & k'\end{pmatrix} - \omega^2\, \delta_{\alpha\beta}\, \delta_{\ell\ell'} \delta_{kk'} \right| = 0 \tag{2}$$

where $D_{\alpha\beta}\begin{pmatrix}\mu & \mu'\\ \ell & \ell'\\ k\ ; & k'\end{pmatrix} = (M_k M_{k'})^{-1/2} \sum_{\beta,\ell',k'} \phi_{\alpha\beta}\begin{pmatrix}\mu & \mu'\\ \ell & \ell'\\ k\ ; & k'\end{pmatrix}$ is an element of the long wavelength mass reduced dynamical matrix D.

The eigenvalues of the dynamical matrix D are the squared frequencies of the phonons, ω^2, and the matrix which diagonalised D is the matrix of phonon eigenvectors. The problem of obtaining the phonon frequencies and eigenvectors at long wavelength limit then consists of constructing D and diagonalising it.

In this three-dimensional interacting model, the interaction of H...H, H...Cl and H...Br between adjacent zig-zag chains in different planes were assummed to be negligible due to the lighter mass of hydrogen, while the range of interactions of Cl...Cl and Br... Br were limited to their first nearest neighbors with the central force constant ξ[9]. The model is outlined in Figure 2, and all the force constants are shown. The range of interaction of each hydrogen atom and halogen atom is limited to its fourth-nearest neighbors in each planar zig-zag chain structure. Assuming central force constants between one atom to the other atoms are taken to its first to fourth nearest neighbors only (represented respectively as α, β, λ and γ) and the axially symmetric angular force constants[10] are taken to its first and second nearest neighbors (represented respectively as δ_2 and δ_1), the dynamical matrix interaction for those four atoms (2 molecules of HCl or HBr) in one unit cell can be obtained as following (expressed in dyadic forms):

$$\phi\begin{pmatrix}1 & 1\\ 1\ ;\ 1\\ H & N\end{pmatrix}=\phi\begin{pmatrix}1 & 1\\ 1\ ;\ 1\\ N & H\end{pmatrix}=-[(\hat{i}\hat{i}+\hat{k}\hat{k})\delta_2+\hat{j}\hat{j}(\alpha)],$$

$$\phi\begin{pmatrix}1 & 1\\ 1\ ;\ 2\\ H & N\end{pmatrix}=\phi\begin{pmatrix}1 & 1\\ 2\ ;\ 1\\ N & H\end{pmatrix}=-[(\hat{i}\hat{i}+\hat{k}\hat{k})\delta_1+\hat{j}\hat{j}(\beta)],$$

$$\phi\begin{pmatrix}1 & 1\\ 1\ ;\ 2\\ H & H\end{pmatrix}=\phi\begin{pmatrix}1 & 1\\ 2\ ;\ 1\\ H & H\end{pmatrix}$$

$$=-\left(\frac{\gamma}{P}\right)[\hat{i}\hat{i}(a^2+b^2)\cos^2\theta+\hat{j}\hat{j}(x)-(\hat{i}\hat{j}+\hat{j}\hat{i})(W)]$$

$$\phi\begin{pmatrix}1 & 2\\ 1\ ;\ 2\\ H & N\end{pmatrix}=\phi\begin{pmatrix}1 & -2\\ 2\ ;\ 1\\ N & H\end{pmatrix}$$

$$=-[\hat{i}\hat{i}\left(\frac{\varepsilon}{Q}\right)(a+b)^2\cos^2\theta+\hat{j}\hat{j}\left(\frac{\varepsilon}{Q}\right)(V^2)-(\hat{i}\hat{j}+\hat{j}\hat{i})\left(\frac{\varepsilon}{Q}\right)(V)(a+b)\cos\theta]$$

$$\phi\begin{pmatrix}1 & 1\\ 2\ ;\ 2\\ H & N\end{pmatrix}=\phi\begin{pmatrix}1 & 1\\ 2\ ;\ 2\\ N & H\end{pmatrix}$$

$$=-[\hat{i}\hat{i}(\alpha\cos^2\theta+\delta_2\sin^2\theta)+\hat{j}\hat{j}(\alpha\sin^2\theta+\delta_2\cos^2\theta)+\hat{k}\hat{k}(\delta_2)],$$

$$\phi\begin{pmatrix}1 & \pm 3\\ 1\ ;\ 2\\ N & N\end{pmatrix}=\phi\begin{pmatrix}1 & \pm 5\\ 2\ ;\ 1\\ N & N\end{pmatrix}=-\frac{\xi}{S}[\hat{i}\hat{i}(d^2\sin^2\frac{\phi}{2})+\hat{j}\hat{j}(T^2)+\hat{k}\hat{k}(c^2)$$

$$-(\hat{i}\hat{j}+\hat{j}\hat{i})(T)(d\sin\phi)\pm(\hat{i}\hat{k}+\hat{k}\hat{i})(c)(d\sin\phi)\pm(\hat{j}\hat{k}+\hat{k}\hat{j})(c)(T)],$$

$$\phi\begin{pmatrix}1 & -2\\ 2\ ;\ 1\\ H & N\end{pmatrix}=\phi\begin{pmatrix}1 & +2\\ 1\ ;\ 2\\ N & H\end{pmatrix}=-[\hat{i}\hat{i}(\beta\cos^2\theta+\delta_1\sin^2\theta)+\hat{j}\hat{j}(\beta\sin^2\theta$$

$$+\delta_1\cos^2\theta)+\hat{k}\hat{k}(\delta_1)-(\hat{i}\hat{j}+\hat{j}\hat{i})(\tfrac{1}{2})(\beta-\delta_1)\sin 2\theta]$$

$$\phi\begin{pmatrix}1 & \pm 6\\ 2\ ;\ 1\\ N & N\end{pmatrix}=\phi\begin{pmatrix}1 & \pm 4\\ 1\ ;\ 2\\ N & N\end{pmatrix}=-\frac{\xi}{S}[\hat{i}\hat{i}(Y^2)+\hat{j}\hat{j}(Z^2)+\hat{k}\hat{k}(c^2)$$

$$-(\hat{i}\hat{j}+\hat{j}\hat{i})(Y)(Z)\pm(\hat{i}\hat{k}+\hat{k}\hat{i})(c)(Y)\pm(\hat{j}\hat{k}+\hat{k}\hat{j})(c)(Z)] \quad (3)$$

where $P=a^2+b^2+2ab\sin\theta$

$Q=(a+b)^2+2a(a+b)\sin^2\theta+a^2$

$R=d^2+b^2-2bd\sin\theta+c^2$

$S=d^2+(a+b)^2+c^2-2d(a+b)\cos(\frac{\phi}{2})$

$T=(a+b)-d\cos(\frac{\phi}{2})$

$V=a+(a+b)\sin\theta$, $W=2ab\cos\theta+\frac{1}{2}(a^2+b^2)\sin 2\theta$

$U=(a+b)+a\sin\theta$

$X=(a^2+b^2)(1+\sin^2\theta)+4ab\sin\theta$

$Y=(a+b)\cos\theta-d\sin(\frac{\phi}{2})$

$Z=(a+b)\sin\theta+d\cos(\frac{\phi}{2})$

$\theta=\phi-90°$

Each element $\phi_{\alpha\beta}\begin{pmatrix}\mu & \mu'\\ \ell & \ell'\\ k\ ;\ k'\end{pmatrix}$ of the dynamical matrix $\phi\begin{pmatrix}\mu & \mu'\\ \ell & \ell'\\ k\ ;\ k'\end{pmatrix}$ in Eq. (3) were calculated by the following formula[10]

$$\phi_{\alpha\beta}\begin{pmatrix}\mu & \mu'\\ \ell & \ell'\\ k\ ;\ k'\end{pmatrix}=-\{(\phi_r-\phi_t)\frac{[x_\alpha\begin{pmatrix}\mu'\\ \ell'\\ k'\end{pmatrix}-x_\alpha\begin{pmatrix}\mu\\ \ell\\ k\end{pmatrix}][x_\beta\begin{pmatrix}\mu'\\ \ell'\\ k'\end{pmatrix}-x_\beta\begin{pmatrix}\mu\\ \ell\\ k\end{pmatrix}]}{R^2}+\phi_t\delta_{\alpha\beta}\}$$

where ϕ_r and ϕ_t are respectively the central force constant and the axially symmetric force constant (if it exists) between atoms $\begin{pmatrix}\mu\\ \ell\\ k\end{pmatrix}$ and $\begin{pmatrix}\mu'\\ \ell'\\ k'\end{pmatrix}$, and R the distance between these two atoms, and $x_\alpha\begin{pmatrix}\mu\\ \ell\\ k\end{pmatrix}$ and $x_\beta\begin{pmatrix}\mu'\\ \ell'\\ k'\end{pmatrix}$ are the coordinates of these two atoms in the α direction and β direction respectively (α, β = x, y, z). The structural properties of the phase III crystals are listed in Table 1.

The condition that the value of the force on each atom is invariant under a rigid body translation of the crystal, we have the following condition of force constants[9],

$$\phi_{\alpha\beta}\begin{pmatrix}\mu & \mu\\ \ell & \ell\\ k\ ; & k\end{pmatrix}=-\sum_{\substack{\mu\neq\mu'\\ \ell\neq\ell'\\ k\neq k'}}\phi_{\alpha\beta}\begin{pmatrix}\mu & \mu'\\ \ell & \ell'\\ k\ ; & k'\end{pmatrix} \tag{4}$$

This equation is important in the construction of Eq. (2).

3. RESULTS AND DISCUSSIONS

The equations of motion for the four atoms in the x, y and z direction, relating the seven interacting constants, established a 12 x 12 dynamical matrix as discussed in previous section. The force constants were then adjusted to give optimum agreement between the observed[2] and the calculated frequencies. All the calculations and fittings were performed on a VAX 11/780 computer using the Jacobi rotation method. The optimized values of the force constants and the results of the calculations as compared with the experimental values are summarized in Table 2. The assignment of the symmetry of each mode was made by studying the transformation properties of the eigenvectors of the dynamical matrix and by comparison between the calculated values and the experimental values.

From Table 2, it is seen that not only the calculated two in-plane translational mode frepmencies (A_1+B_1) are in good agreement with those from experiments, but also the calculated low frequency out-of-plane A_2 translational mode is also in good match with the observed values due to fact that in this three-dimensional model inter-planar forces are included. This is a much better result compared with previous two-dimensional model calculation on solid HCl ($28.5cm^{-1}$ compared with $61cm^{-1}$) and solid HBr ($18cm^{-1}$ compared with $45cm^{-1}$). The two stretching (A_1+B_1) modes are also very well fitted. However, the overall agreement between the calculated and observed librational frequencies is less than satisfactory. The larger errors of the librational modes may be caused by the electric moments in crystalline HCl and HBr[3][7], which bring into play long-range electrostatic forces between the atoms and limit the accuracy of this harmonic model. Note that the pure translational modes are not identically equal to zero because of the round off errors produced during the diagonalization procedure. (In the construction of Eq. (2), the conditions of equilibrium of the pure translational modes have been taken into account by using Eq. (4)).

The comparsions of the directions of the force components due to various force constants with that of vibrational modes reveal three interesting facts. (1) α and β are closely related to the eigenfrequencies of the two stretching modes A_1 & B_1 (2) γ and ϵ determine mostly the eigenfrequencies of the in-plane modes $B_1(T)$, $A_1(T)$ & $B_1(L)$, but the splitting of these frequencies are determined by ξ, δ_1 and δ_2. (3) The eigenfrequencies of the three out-of-plane modes $A_2(T)$, $A_2(L)$ & $B_2(L)$ are determined wholly by ξ , δ_1 are δ_2 , since only forces of these three force constants have force components along the z-direction.

It can be found that the angular force constants δ_1 and δ_2 have the vibrational effect of deforming the angle ϕ between the bonds, and are important in getting satisfactory explanations of the observed results. A pure central force model, with zero values of δ_2 and δ_1 and two additional interplanar force constants was also analyzed and found to be unable to give a reasonable fitting between the calculated and observed eigenfrequencies and eigenvectors. This fact indicates that the binding force of molecular bond and hydrogen bond are both central and noncentral in character.

The model adopted in these calculations of crystalline HCl and HBr shows good overall fitting between the observed and calculated frequencies. The average deviation for solid HCl is 9.1% while that for solid HBr is 6.0%. These deviations are smaller than the corresponding values of the planar model that were proposed by Chang et al recently[4]. A comparsion between the optimized values of all force constants shows that the force between atoms in different chains and different planes are much smaller than those between nearest neighbors in the same chain. It seems that this three dimensional model is reasonably successful in the long-wavelength lattice dynamics calculations of crystalline HCl and HBr in their low temperature phase.

4. REFERENCES

[2] [illegible]esel and B. H. Torrie, Can. J. Phys. 55, 592 (1977).

[3] [illegible]n and A. Anderson, Chem. Phys. Lett. 17. 104 (1972).

[4] [illegible]out and J. W. Leech, Solid State Phys. 7, 3245 (1974).

(4) C. N. Chang, W. S. Tse, and L. Chang, Chin, J. Phys. 25, No. 1, 21 (1983).

(5) M. Ito, M. Suzuki and T. Yokoyama, J. Chem. Phys. 50, 2949 (1969).

(6) R. Savcie and A. Anderson, J. Chem. Phys. 40, No.2, 548 (1966).

(7)D. E. Stogryn and A. P. Stogyrn, Molec. Phys. 11, 371 (1966).

(8) G. S. Pawley, Phys. Stat. Sol. (b) 49, 475 (1972).

(9) A. A. Maradudin, E. W. Montroll, G. M. Weiss and I. P. Ipatova. The Theory of Lattice Dynamics in the Harmonic Approximation. 2-nd edn. p.14, Academic press. (1971).

(10) N. Wakabayashi and R. M. Nicklow, Neutron Scattering and Lattice Dynamics of Material with Layered Structures. p.413 Addision-Wesly Publishing. (1979).

Table 1. Structural properties of the phase III crystal[c]

	HCl	HBr
Molecular bond length a(Å)	1.275	1.414
Hydrogen bond length b(Å)	2.413	2.513
Distance between two adjacent planes of zig-zag chains: c(Å)	2.900[a]	3.040[b]
Half distance between two adjacent chains in the same plane d(A)	2.558	2.790
Angle between the molecular bond and the hydrogen bond ϕ ($\theta = \phi - 90°$)	93°31'	91°48'

(a) estimated values from Ref. (5).

(b) estimated values from Ref. (6).

(c) The values of a,b,d and ϕ of the crystals are from Refs. (4), (5) and (6).

Table 2. Calculated frequencies and force constant for solid HCl and HBr in phase III (cm^{-1})

Assignment		HCl Obs[2](18K)	HCl Calc. (this work)	HBr Obs[2](18K)	HBr calc. (this work)
A_1	Acoustic	0	0.076	0	0.108
B_1	Acoustic	0	0.705	0	0.949
B_2	Acoustic	0	0.753	0	0.984
A_2	(o/p)T	61	66.01	45.0	45.85
A_1	(i/p)T	88.5	84.40	61.0	60.124
B_1	(i/p)T	114	110.4	75.5	76.94
A_2	(o/p)L	141.5	198.7	147	189.4
B_2	(o/p)L	223	201.2	207	190.4
A_1	(i/p)L	336	320.2	297	282.71
B_1	(i/p)L	409	449.3	376	394.39
A_1	(i/p)S	2697	2699.9	2395	2393.2
B_1	(i/p)S	2741.5	2720	2431	2410.2

Optimized force constants: (in units of 10^5 dyne/cm).

HCl		HBr	
α	: 413500	α	: 327500
β	: 7320	β	: 8350
γ	: 3700	γ	: 2720
ε	: 3580	ε	: 2550
ξ	: 1180	ξ	: 1340
δ_1	: 780	δ_1	: 680
δ_2	: 1560	δ_2	: 1450

out of plane; i/p in plane; L, libration; T, translation; S, streching.

Figure 1. The three-dimensional structure of phase III solid HCl and HBr. The symbols H_ℓ^μ and N_ℓ^μ represent the ℓ^{th} hydrogen atom and the ℓ^{th} halogen atom respectively in the μ^{th} primitive unit cell of the crystal. N represent Cl or Br atom.

Figure 2. Force constants of phase III solid HCl and HBr adopted in the calculation described in this paper.

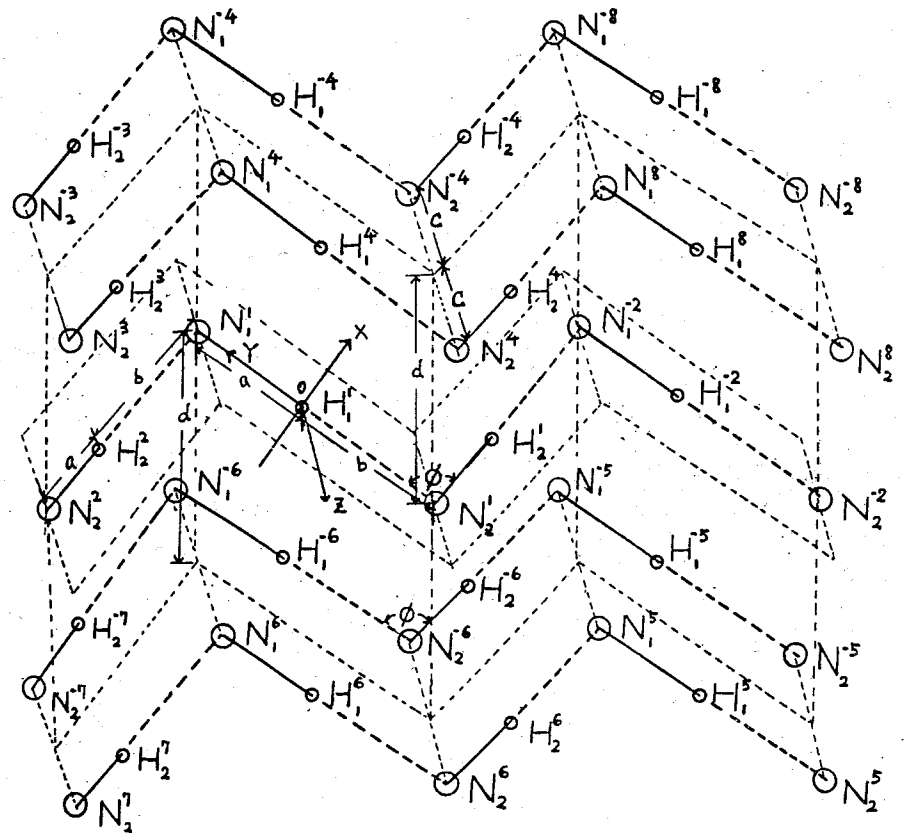

Fig. 1.

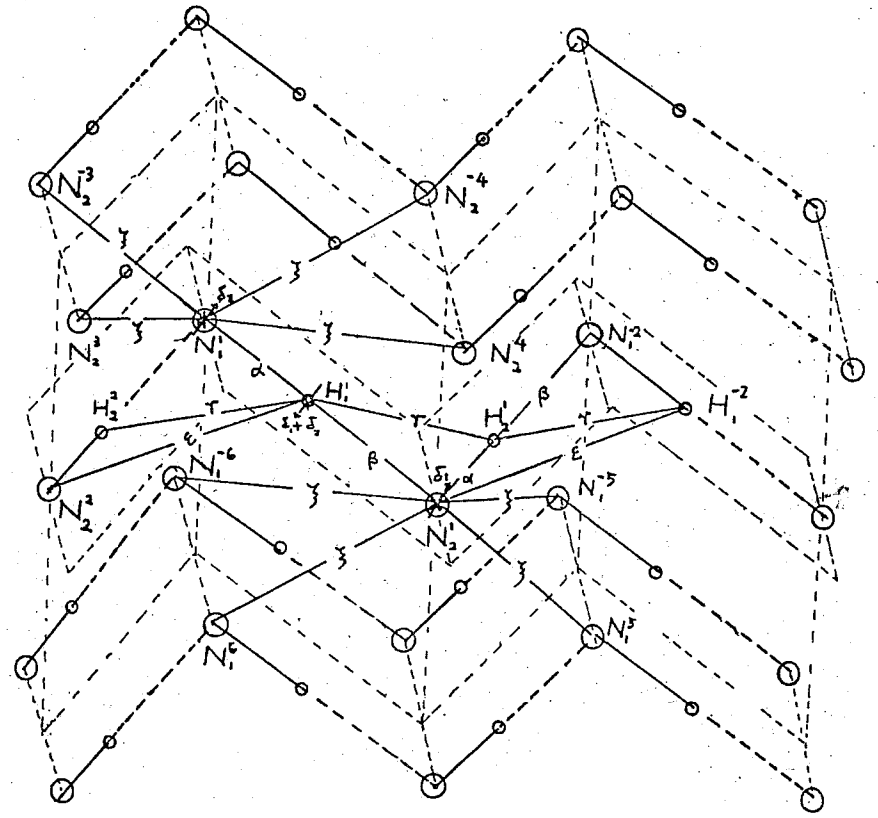

Fig. 2.

RAMAN SPECTRA OF CRYSTALLINE SILICON AND GERMANIUM TETRACHLORIDES

W. S. Tse and C. C. Chen[1]

Institute of Physics, Academia Sinica,

Nankang, Taipei, Taiwan (115), R. O. C.

Laser Raman spectra of polycrystalline samples of silicon and germanium tetrachlorides have been observed for the lattice and intramolecular vibrational regions at 80K. Comparisons are made with the spectra of known crystalline $TiCl_4$, and the observed peaks of $GeCl_4$ are classified into translational and librational model. Classification scheme: 78.

The Raman spectra of these molecular tetrachlorides in the liquid state has been studied previously (1, 2), but there has been no systematic study of these tetrachlorides in the solid state including external and internal vibrations. The Raman spectra of polycrystalline $SiCl_4$ and $GeCl_4$ in the internal mode region have been recorded by clark and Hunter (3). In this letter we report a comprehensive study of the high resolution Raman spectra of the tetrachlorides of silicon and germanium as polycrystalline films at 80K including both internal and external vibrations.

The Raman spectra were excited by the 5145 Å line of 200-400mW from a Spectra Physics 170-00 argon ion laser using a standard 90° scattering configuration. The scattered light was dispersed by a Spex 1401 double monochromator and was detected by an EMI 9558 QA photomultiplier which was cooled down to -20°C. Photon-electron pulses were then processed through the SSR 1120 amplifier/discriminator and then converted into analog signal by the SSR 1105 photon counter/data converted console. The low temperature sample cell was a Pyrex made double layer dewar and was discussed in a previous paper (4). Frequencies reported here were estimated to be accurate within ±1 cm⁻¹ for sharp features.

The lattice spectra of both samples at 80K are shown in Figure 1 and the

[1] Department of Physics, Soochow University, Taipei, Taiwan (111), R. O. C.

peak positions are listed in Table 1. The low frequency Raman spectra of these two crystals have not been reported except some preliminary results was obtained by one of us (5). Complete X-ray data are available for titanium tetrachloride (6) at 241K and tin tetrachloride (6, 7) at 234K which have the tin tetrabromide structure (6, 7) with the monoclinic space group $P2_1/c$ and Z=4. No Structural data is availabl for crystalline silicon and germanium tetrachlorides but it is believed that $SiCl_4$ and $GeCl_4$ crystals could be the same structures as $TiCl_4$ and $SnCl_4$ (6). The group theoretical analysis based on the known crystal structure of $TiCl_4$ predicts six Raman active librational modes and also six Raman active translational modes (4). In previous paper (4) it has been shown that the lattice spectra of $TiCl_4$ and $SnCl_4$ are similar to each other in peak shapes and relative intensities because these two crystals have similar structures. It is the aim of this work to study and compare the nature of the lattice modes with the hope that they will provide some information about the crystal structures of the two unknown samples of $GeCl_4$ and $SiCl_4$ and try to classify the lattice modes.

From Figure 1, there are obvious similarities between the results of the Raman spectra of $GeCl_4$ and $TiCl_4$ both in spectral band shapes and relative intensities except the corresponding weak features are absent in $GeCl_4$ spectrum. This shows that the crystal structure of $TiCl_4$ and $GeCl_4$ may be similar to each other. In solid $TiCl_4$ spectrum the lattice modes consist of ten peaks and a simple model (4) shows that the lattice modes are classified into translational and librational motions. The basic assumption of such simple model says that to determine a first approximation to the lattice frequencies, we consider the intermolecular interactions between the molecules in $TiCl_4$ and $GeCl_4$ may be identical provided that crystalline $TiCl_4$ and $GeCl_4$ have similar structure and also their lattice dimensions are nearly the same. Since the crystalline $SnCl_4$ and $TiCl_4$ have the same structure and also their lattice dimensions are nearly the same (4), and that the molecular weight of $GeCl_4$ and the intramolecular bond length r_{Ge-Cl} are more closely related to $TiCl_4$ than $SnCl_4$. Hence lattice dimensions of $GeCl_4$ and $TiCl_4$ may nearly the same when they form isostructural crystals.

The molecules can perform translational or librational motions at a lattice site in the crystal. The frequencies are calculated from the following two simp

expressions:

$$\nu_T = \frac{1}{2\pi}\sqrt{\frac{K_T}{M}}$$

$$\nu_L = \frac{1}{2\pi}\sqrt{\frac{K_L}{I}}$$

where K_T and K_L are the relevant force constants and in this case we will assume them nearly the same in both samples because of the identical intermolecular interactions. Applying the above simple idea we have

$$\nu_T \propto \frac{1}{\sqrt{M}} \quad \text{and} \quad \nu_L \propto \frac{1}{r_{X-Cl}}$$

Where r_{X-Cl} is the intramolecular bond length and M is the total molecular mass. The frequency ratios $\nu(TiCl_4)/\nu(GeCl_4)$ are obtained by pairing off the observed peaks in $TiCl_4$ and $GeCl_4$ spectra according to their relative intensities and relative spectral band shapes as shown in Table 2. The theoretical ratio for the translational modes is 1.063, while that for the librational modes is 0.952. From Table 2, we note that the three lowest lattice modes all have values close to 1.063 and hence are mostly translational motion in nature. The next four higher frequency peaks have the ratio values close to 0.952 and therefore these peaks may be associated with librational motions. On the other hand, the lattice spectrum of crystalline $SiCl_4$ is different from the spectrum of $TiCl_4$ and $GeCl_4$ in relative intensities and spectral band shapes so that we cannot apply the above simple model to distinguish which are translational or librational modes. Therefore, its structure may be different from $TiCl_4$ and $GeCl_4$.

Raman spectra of the internal modes of these two crystals were also recorded [illegible] The regions of all four fundamentals have been examined and that the [illegible] and crystal splittings have also been observed. However, the results are [illegible]ubstantially different from those of Clark and Hunter (3) except the intensity [illegible] the $\nu_1(A_1)$ mode components of $SiCl_4$. The splitting of the $\nu_1(A_1)$ [illegible] into five bands is isotopic in origin arising from the two isotopes [illegible] Five tetrachloride species occur with abundances: $X^{35}Cl_4$ (32.54%), $X^{35}Cl_2{}^{37}Cl_2$ (20.5%), $X^{35}Cl^{37}Cl_3$ (4.43%) and $X^{37}Cl_4$ [illegible]ording to Clark and Hunter (3) the intensity of the $Si^{35}Cl_4$

band and that of $Si^{35}Cl_3{}^{37}Cl$ at liquid nitrogen temperature is nearly the same. However, for our polycrystalline sample, we found that the observed ratio close to the calcualted abundance ratio (0.772). The other observed splittings (isotopic and crystalline field splittings) in the intramolecular vibrational regions are similar to Clark and Hunter's (3) work and so will not be discussed here.

The authors would like to thank Dr. H. Chang and N. T. Liang for fruitful discussions.

REFERENCES

(1) K. Nakamoto, Infrared Spectra of Inorganic and Cordination Compounds, (Wiley, New York 1970).

(2) R. J. H. Clark and C. J. Willis, Inorg, Chem, 10(1971) 28.

(3) R. J. H. Clark and B. K. Hunter, J. Chem. Soc., 15A(1971) 2999.

(4) W. S. Tse, C. C. Chen, H. Chang and N. T. Liang, J. Raman Spectro., (Accepted for Publication).

(5) W. S. Tse, Ph. D. Thesis, (University of Waterlo 1980).

(6) P. Brand and H. Sachmann, Z. Anorg, Chem., 321 (1963) 269.

(7) P. Brand and H. Sachmann, Acta. Cryst., 16(1963) 446.

FIGURE CAPTIONS

Figure 1. The lattice Raman spectra of Crystalline $GeCl_4$ and $SiCl_4$ at 80K. The asterisk (*) indicates a plasma line. Spectral resolution is 1 cm^{-1}. The inserted figure is the spectrum of crystalline $TiCl_4$ (4).

Table 1. The lattice frequencies of crystalline $GeCl_4$ and $SiCl_4$ at 80K.

Frequency (cm^{-1})	
$GeCl_4$	$SiCl_4$
25.0	25.0
33.5	30.0
40.0	33.0
49.0	36.0
51.0	40.0
54.5	46.0
68.0	55.0

Table 2. Comparison of the lattice frequencies of $GeCl_4$ measured in this work with $TiCl_4$ frequencies at 80K (4).

$\sqrt{M(GeCl_4)/M(TiCl_4)} = \sqrt{214.4/189.71} = 1.063$ (T)

$r(GeCl_4)/r(TiCl_4) = 2.08/2.185 = 0.952$ (L)

Frequency (cm^{-1})		$\frac{\nu(TiCl_4)}{\nu(GeCl_4)}$	Assignment
$TiCl_4$	$GeCl_4$		
25.3	25.0	1.012	T
35.1	33.5	1.047	T
42.0	40.0	1.050	T
48.3	49.0	0.985	L
51.0	51.0	1.000	L
54.8	54.5	1.005	L
65.5	68.0	0.805	L

T = translational mode.

L = librational mode.

$M(GeCl_4)$ = total mass of $GeCl_4$

$M(TiCl_4)$ = total mass of $TiCl_4$

$r(GeCl_4)$ = bond length between Ge and Cl atoms.

$r(TiCl_4)$ = bond length between Ti and Cl atoms.

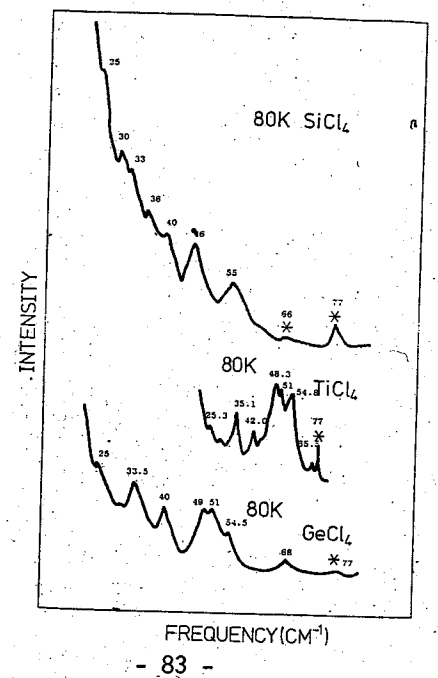

EFFECT OF HALOPERIDOL AND NOMIFENSINE ON THE DOPAMINE AUTO-REGULATION IN RAT

W. K. Wang, L. S. Jenq, T. L. Hsu and Y. Chiang

Biophysics Laboratory, Institute of Physics,

Academia Sinica Taipei,

Taiwan, 115, R. O. C.

Haloperidol [1-3] has long been identified as an antagonist to dopamine postsynaptically. Some study[4-5] on synaptosomal preparation also showed that it antagonize the inhibitory effect of apomorphine which has been characterized as a dopamine agonist that preferentially bind presynaptic dopamine receptor[6,7]. However, we found that haloperidol would not antagonize dopamine auto-inhibition. It's inhibitory effect and dopamine auto-inhibition were additive. This suggests that we might need to refine our terminology and separate the presynaptic and postsynaptic effect of drugs.

Spragu-Dawley rat (180-230 g) were killed by decapitation. The corpus striatum was dissected on ice and homogenized in 10 Vols. 0.32 M sucrose using teflon pestle tissue homogenizer. After centrifigation at 1000g for 15 min, 50 $\mu\ell$ aliquots of the synaptosome-containing supernatant were incubated with 150 $\mu\ell$ physiological medium as described before[(8)], only some NaH_2PO_4 were replaced by $NaHCO_3$ to give final pH of 7.4 after equilibration with 95%. O_2 - 5% CO_2 at 37°C. Dopamine (DA) and haloperidol (HD) were added to the incubation medium with 10 $\mu\ell$ 0.1 M phosphorous buffer pH 7.4 as carrier. DA formation was calculated from the $^{14}CO_2$ output from [1—^{14}C] tyrosine, averaged over 50 minutes of incubation to 120 minutes of incubation. The rate of dopamine synthesis was about of that at pH = 6.6. We shifted to this pH because it is a more physiological

10^{-5} M added to the incubation mixture reduced $^{14}CO_2$ release to 76.2±1.8% from 5 preparation) of its normal rate.

10^{-6} M reduced the $^{14}CO_2$ release to 89.8±1.9% (mean±S.D. from 5 the normal rate, HD at 10^{-7} M had no significant effect.

CO_2 released from the preparation with HD and DA compare to the one with HD alone were summerized in Table 1. The presentce of HD doesn't change the auto-inhibition effect of DA. Only the one with HD (10^{-5}) and DA (10^{-6}) seemed to have some blocking effect. Fig. 1 showed some of these data.

The HD alone acted like DA, it behaved like a agonist presynaptically. It did not antagonize DA auto-inhibition either. This was not the some as that of apomorph whose inhibitory effect can be blocked by HD. Actually this may be the reason why HD is such a strong DA blocking agent[9], it blocked DA effects post-synaptically as well as inhibited DA synthesis presynaptically. From these results, we also see that the traditional way to define agonist and antagonist should be refined to separate the presynaptic and postsynaptic effect. The most effective blocking agonist will be the one like haloperidol, it worked as agonist presynaptically and as antagonist postsynaptically. While the most effective stimulating agent will be the one which does the reverse.

We thank Janssen Pharmaceutica for sending pure-haloperidol.

Table I. $\frac{^{14}CO_2 \text{ release (DA+HD)}}{^{14}CO_2 \text{ release HD}}$

Concentration of DA / Concentration of HD	10^{-5} M	10^{-6} M
10^{-5} M	38.6 ± 6.53 (4)	95.0 ± 2.33 (4)
10^{-6} M	42.6 ± 6.48 (6)	89.3 ± 3.78 (5)
10^{-7} M	37.9 ± 2.82 (5)	91.5 ± 1.79 (5)
0	40.1 ± 7.93 (4)	89.7 ± 3.50 (8)

DA : Dopamine HD: Haloperidol,

the data present as Mean ± S. D. (No of experiments)

REFERENCES

(1) Clement-Cormirer, Y. C., Kebabian, J. W., Petzold, G. L. & Greengard, P., Proc. Natn, Acad. Sci. U. S. A. 71, 1113-1117 (1974).

(2) Miller, R. J., Horn, A. S. & Iversen, L. L., Molec Pharmac 10, 759-766, (1974).

(3) Bochaert, J. Tassin, J. P., Thierry, A. M., Glowinski, J., & Premont, J., Brain Res. 232, 391-400 (1977).

(4) Christiansen J. & Squires, R. J. Pharm., Pharmac. 26, 367-369 (1974).

(5) Iversen, L. L., Rogawski, M. A., Miller, R. J., Molec. Pharmac. 12, 251-262 (1976).

(6) Nagy, J. I., Lee, T., Seeman, P. and Fibiger, H. C., Nature 274, 278-281 (1978).

(7) Raiteri, M., Cervoni, A. M., Carmine, R. O., Levi, G., Nature 274, 706-708 (1978).

(8) Wang, W. K., Chiang, Y., Jenq, L. S., Chen, N. K., Nature 296, 354 (1982).

(9) Staurton, D. A., Magistretti, P. J., Koob, G. F., Shoemaker, W. J., & Bloom, F. E., Nature 299, 72-74 (1982).

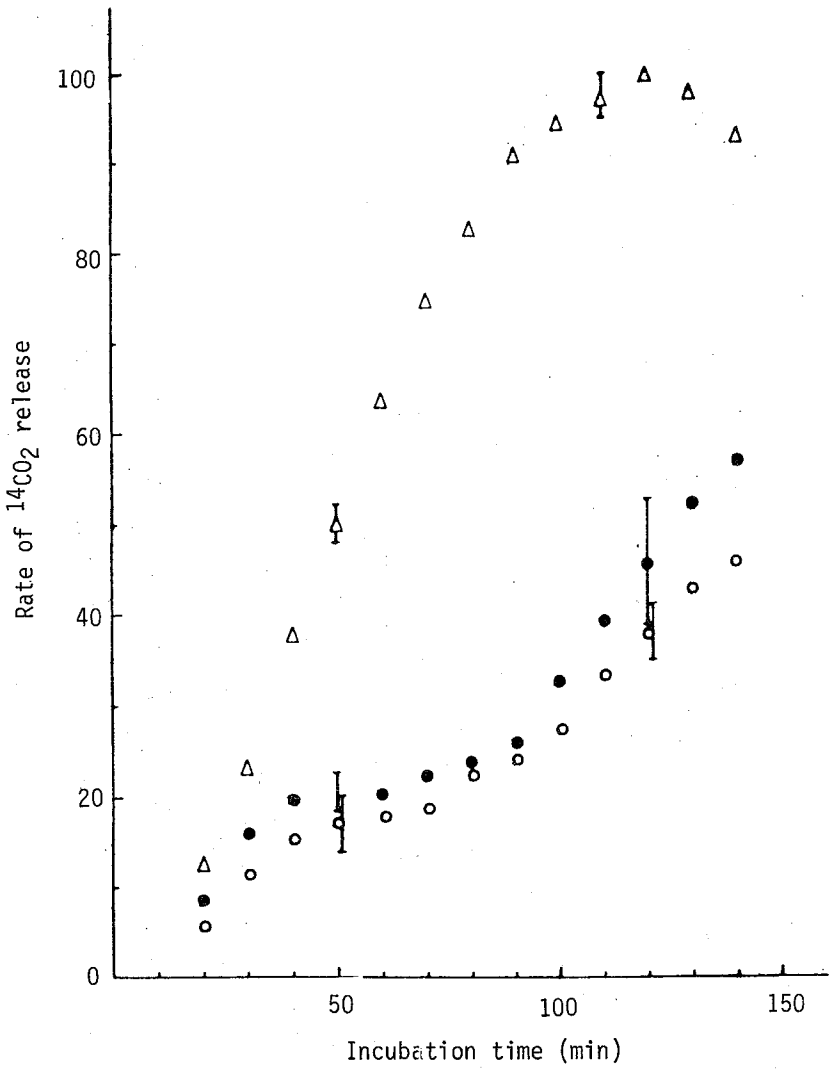

Fig. 1. Rate of $^{14}CO_2$ release from labelled tyrosine plotted against incubation time, error bar shown are standard deviation (mean ± S. D. for six preparations). Dopamine at 1 x 10^{-5} M added to the preparation (●) strongly inhibited dopamine synthesis. Haloperidol at 1 x 10^{-6} M together with dopamine at 1 x 10^{-5} M (o) further inhibited dopamine biosynthesis, Δ , control.

A VARIATIONAL-KINEMATICAL MODEL FOR FLOW OVER COMPLEX TERRAIN

Len-Fu W. Chang, Robert R. Hwang, Shwu-Ching Lin
Institute of Physics,
Academia Sinica, Nankang,
Taipei, Taiwan, R. O. C.

A variety of wind measurement systems may exist over region characterized with complex topography. These various systems include the mandatory rawindsound observation and the surface wind measurement. These observed wind field is inherent with different kinds of error, including resolution ability and vertical extend of measuring. Furthermore, topography effect may limit their representability. In this study, a variational-kinematical algorithm is adopted with mass continuity and topography as the constraints for analysis of wind flow over complex terrain. Case study is performed with flow over northern part of Taiwan.

I. INTRODUCTION

The analyses of wind and/or flow pattern over the region characterized by complex terrain are important procedure for many different applications. The wind energy survey over a specific region needs long term wind statistics at several locations where the adequate wind observations are not available. On the orther hand, estimation of the air pollutants and/or radioactive materials transport and dispersion for the purpose of environmental control, also requires the wind-flow pattern analysis. In general, a veriety of wind measurement systems may exist in a specific region. These various wind data sources include the rawindsound observations, surface wind observations, or some special pilot-balloom observations. These different measurement systems may be inherent with different kinds of error, different resolution ability, furthermore, the terrain may impose the limitation for their spacial representability. Thus, the intorpolation techanique is not suitable to obtain wind information at locations without direct observations.

In this paper, we devise a variational-kinematical algorithm to analyze the wind-flow pattern over complex terrain.

KINEMATICAL-VARIATIONAL ANALYSIS ALGORITHM

The analysis of flow pattern over a region of complex terrain is achieved by the variational method (Sasaki, 1958; 1970 a, b) with the kinematic (mass continuity and terrain boundary conditions) relationships as the constraint. For different purporses, Sherman (1978), and Dickerson (1978) formulated the variational algorithms to analyze the flow field over the complex terrain. Although, their approach to the problem differes slightly, both require the initial guess of vertical velocity in the computational domain. This kind of approach may cause uncertainty inherent in the calculated variance. However, this drawback may be adjusted through the using of different weighting factors for horisontal wind components and the vertical wind component in the models of Sherman and Dickerson. Furthermore, the performance of variational analysis depends very much upon the prescribed model depth within which mass balance is assumed to be maintained. Recently, Endlich et. al. (1982) have modified Sherman's algorithm, utilizing terrain following coordinate system and different laws for wind profiles. In the following, we proceed to develop a new variational analysing scheme, and through case studies to exame the performance of proporsed scheme.

For most applications, terrain following coordinate defined as

$$\hat{Z} = Z - E(x, y), \tag{1}$$

is convinent to incorporate into the analysing scheme. Here, the terrain elevation above the sea-level is denoted by E(x, y). The Boussinesq incompressible fluid continuity equation can be expressed as

$$\frac{\partial u}{\partial x} + \frac{\partial v}{\partial y} + \frac{\partial \hat{w}}{\partial \hat{z}} = 0 , \tag{2}$$

where $d\hat{z}/dt = \hat{w}$ The variational algorithm based on minimizing the variance between observed wind and analyzed wind can be formulated as

$$J = \iiint [\frac{1}{2}(u - u_0)^2 + \frac{1}{2}(v - v_0)^2 + \lambda (\frac{\partial u}{\partial x} + \frac{\partial v}{\partial y} + \frac{\partial \hat{w}}{\partial \hat{z}})] dx dy d\hat{z}, \tag{3}$$

In (3), λ is the so-called Lagrangian multiplier, and continuity equation (2) is imposed as the constraint condition. The direct interpolating wind components at each grid point are denoted by u_0 and v_0, respectively. The stationary condition of (3) yields the Euler-Lagrange equations:

$$u = u_0 + \frac{\partial \lambda}{\partial x} , \tag{4}$$

$$v = v_0 + \frac{\partial \lambda}{\partial x} , \tag{5}$$

$$\frac{\partial \lambda}{\partial z} = 0 \quad , \text{ and} \tag{6}$$

$$\frac{\partial u}{\partial x} + \frac{\partial v}{\partial y} + \frac{\partial \hat{w}}{\partial \hat{z}} = 0 , \tag{7}$$

Equation (4) - (7) are subjected to the natural boundary condition,

$$\iiint [\frac{\partial}{\partial x}(\lambda \delta u) + \frac{\partial}{\partial y}(\lambda \delta v) + \frac{\partial}{\partial \hat{z}}(\lambda \delta \hat{w})] dx dy d\hat{z} = 0, \tag{8}$$

derived from the variational problem. The condition (8) implied that at the lateral boundary we may adjust the horizontal wind components to satisfy the mass continuity relationship; while at the upper and lower boundary, the vertical velocity component $\hat{w}$ must be specified. The Physical lower boundary condition is

$$\hat{w} = 0 , \quad \text{at} \quad \hat{z} = 0 \tag{9}$$

At the upper boundary ($\hat{z}$ = H), we may assume that the prevailing flow is not disturbed by the surface inhomogeneity, such that the prevailing flow above H is quasi-horizontal; then

$$\hat{w} = -\vec{v}(H) \cdot \nabla E \tag{10}$$

After some manipulation of (4) - (10), it yields the analyzing equation for our problem,

$$\frac{\partial^2 \lambda}{\partial x^2} + \frac{\partial^2 \lambda}{\partial y^2} = -\frac{1}{H}\int_0^H (\frac{\partial u_0}{\partial x} + \frac{\partial v_0}{\partial y}) dz - \frac{1}{H}[\vec{v_0}(H) + \nabla \lambda] \cdot \nabla E , \tag{11}$$

KINEMATICAL-VARIATIONAL ANALYSIS ALGORITHM

The analysis of flow pattern over a region of complex terrain is achieved by the variational method (Sasaki, 1958; 1970 a, b) with the kinematic (mass continuity and terrain boundary conditions) relationships as the constraint. For different purporses, Sherman (1978), and Dickerson (1978) formulated the variational algorithms to analyze the flow field over the complex terrain. Although, their approach to the problem differes slightly, both require the initial guess of vertical velocity in the computational domain. This kind of approach may cause uncertainty inherent in the calculated variance. However, this drawback may be adjusted through the using of different weighting factors for horisontal wind components and the vertical wind component in the models of Sherman and Dickerson. Furthermore, the performance of variational analysis depends very much upon the prescribed model depth within which mass balance is assumed to be maintained. Recently, Endlich et. al. (1982) have modified Sherman's algorithm, utilizing terrain following coordinate system and different laws for wind profiles. In the following, we proceed to develop a new variational analysing scheme, and through case studies to exame the performance of proporsed scheme.

For most applications, terrain following coordinate defined as

$$\hat{Z} = Z - E(x, y), \tag{1}$$

is convinent to incorporate into the analysing scheme. Here, the terrain elevation above the sea-level is denoted by E(x, y). The Boussinesq incompressible fluid continuity equation can be expressed as

$$\frac{\partial u}{\partial x} + \frac{\partial v}{\partial y} + \frac{\partial \hat{w}}{\partial \hat{z}} = 0 , \tag{2}$$

where $d\hat{z}/dt = \hat{w}$ The variational algorithm based on minimizing the variance between observed wind and analyzed wind can be formulated as

$$J = \iiint [\frac{1}{2}(u - u_0)^2 + \frac{1}{2}(v - v_0)^2 + \lambda (\frac{\partial u}{\partial x} + \frac{\partial v}{\partial y} + \frac{\partial \hat{w}}{\partial \hat{z}})] \, dx dy d\hat{z}, \tag{3}$$

In (3), λ is the so-called Lagrangian multiplier, and continuity equation (2) is imposed as the constraint condition. The direct interpolating wind components at each grid point are denoted by u_0 and v_0, respectively. The stationary condition of (3) yields the Euler-Lagrange equations:

$$u = u_0 + \frac{\partial \lambda}{\partial x} , \tag{4}$$

$$v = v_0 + \frac{\partial \lambda}{\partial x} , \tag{5}$$

$$\frac{\partial \lambda}{\partial z} = 0 \quad , \text{ and} \tag{6}$$

$$\frac{\partial u}{\partial x} + \frac{\partial v}{\partial y} + \frac{\partial \hat{w}}{\partial \hat{z}} = 0 , \tag{7}$$

Equation (4) - (7) are subjected to the natural boundary condition,

$$\iiint [\frac{\partial}{\partial x}(\lambda \delta u) + \frac{\partial}{\partial y}(\lambda \delta v) + \frac{\partial}{\partial \hat{z}}(\lambda \delta \hat{w})] dx dy d\hat{z} = 0, \tag{8}$$

derived from the variational problem. The condition (8) implied that at the lateral boundary we may adjust the horizontal wind components to satisfy the mass continuity relationship; while at the upper and lower boundary, the vertical velocity component $\hat{w}$ must be specified. The Physical lower boundary condition is

$$\hat{w} = 0 , \quad \text{at} \quad \hat{z} = 0 \tag{9}$$

At the upper boundary ($\hat{z}$ = H), we may assume that the prevailing flow is not disturbed by the surface inhomogeneity, such that the prevailing flow above H is quasi-horizontal; then

$$\hat{w} = -\vec{v}(H) \cdot \nabla E \tag{10}$$

After some manipulation of (4) - (10), it yields the analyzing equation for our problem,

$$\frac{\partial^2 \lambda}{\partial x^2} + \frac{\partial^2 \lambda}{\partial y^2} = -\frac{1}{H}\int_0^H (\frac{\partial u_0}{\partial x} + \frac{\partial v_0}{\partial y}) dz - \frac{1}{H}[\vec{v_0}(H) + \nabla \lambda] \cdot \nabla E , \tag{11}$$

with the imposed lateral boundary condition,

$$\lambda = 0 \qquad (12)$$

ANALYSIS PROCEDURE AND RESULTS

The domain of wind flow analysis is shown in Figure 1. A rectangular grid system, with horizontal grid distance of 4 Km, is used to represent the flow field. The vertical grids are unevenly spaced, at 10, 50, 100, 200, 400, 600, 800, 1000 meters above the ground. The terrain elevation E(x, y) is shown in Figure 1, and is digitized at each grid point to served as the input data of the model. For verification of the model and adjustment of the optimum model height, H, ten different cases are tested. During the the testing run of the model, surface wind observations from twelve stations and one rawindsound report have been used as the input data. Under two hundred meters altitude above the ground, vertical wind profile of 1/7th power law is used to extrapolate the surface wind data upward. While above the two hundred meters altitude, homogeneous wind flow from the rawindsound report is used. The objective analysis scheme by Barnes (1973) is used to interpolated observed wind data to each grid points. The filtering characteristics inherent in Barnes scheme can be selected by choosing different parameters in interpolation algorithm. In this study, due to the sparsity of observing stations, the radius of influence of the interpolation scheme is choosed about 10 grid point distance (the 63% response function value), as shown by Figure 2. The content of the ten testing cases is listed in Table 1. In these cases, significantly different flow patterns are intentively selected to represent the typical winter and summer wind fields over northorn Taiwan. In summer season, surface heating causes strong local circulation embedding in the relatively weak prevailing flow. While, in winter season, wind flow pattern is controled largely by northest monson and the local terrain. The performance of the variational-kinematical model is checked through these case study.

From equation (11), it can be seen that the prescribed model depth, H, influences the performance of the model a great deal. Since, by (10), it is assumed that the prevailing flow over the complex terrain area becomes undisturbed and quasi-

horizontal flow without singnificant vertical motion at the level H. An objective prccedure to determine H is as follows, Define

$$H = \alpha \, E_{rms} \, , \qquad (13)$$

where

$$K^2_{rms} = \frac{1}{G-1} \sum_{i=1}^{G} E_i^2 \, , \qquad (14)$$

The rcot mean square value of terrain elevation over the analyzing area (the model domain) is denoted by E_{rms}, and is defined by (14). In (14), the total number of grid points is denoted as G, for the testing cases, G = 31 x 20. Over the model domain, the value of Krms is 526 meter. The optimun value of H is determined via variation of the value of α, such that the mean square value, σ^2, between analyzed winds, u_c, v_c, and the observed winds, u_o and v_o, is minimum. That is

$$\sigma^2 = \frac{1}{N-1} \sum_{i=1}^{N} [(u_c - u_o)_i^2 + (v_c - v_o)_i^2] \, , \qquad (15)$$

where, N is equal to ten (number of cases) multipling by twelve (the number of observing stations). The results from testing runs are shown in Figure 3. For the value of α between 1.6 to 2.6, the values of root mean square deviation σ^2 are about the same. This is corresponding to the values of H between 850 meters to 1360 meters. Beyond this range, the error increases tremendously. For this reason, we prescribed the model depth, H, to be 1000 meter. This happens to be coincidence with the typical depth of the planetary boundary layer. The numerical solution of (11) is via the typical over-relaxation method for Helmholtz type partial differential equation. However, the arrangement of grid points for wind components and the Lagrange multiplier, λ must be staggered according to Sasaki et. al. (1978).

The typical winter time surface flow patterns are shown in Fig. 4 - Fig. 11. The observed surface winds at twelve stations are shown in Fig. 4, Fig. 7, Fig. 10, and Fig. 12, respectively, for four out of the ten selected cases. In winter time, when east China-continental high pressure system moving eastward, northern Taiwan experiences northeartern to southeastern prevailing winds. Fig. 5 shows the analyze

surface wind flow pattern, this is obtained by observations from 12 surface stations. It can be seen that notheastern prevailing flow is deflected by the major mountain ridge of Taiwan island. While, in the Taipei valley, the wind direction becomed eastern, and the wind speed is relatively slow. In order to check the performance of the wind analyzing model, we delete two wind reports at Taipei station (station 692) and Keelung Station (station 694) as the input data to the model. The result is shown in Fig. 6. Comparison between Fig. 5 and Fig. 6, it can be seen the model is capable in revealing the wind condition at data sparse area, when the flow is largely controlled by terrain forcing. Fig. 10 to Fig. 13 show similar prevailing flow condition (judging from the reports from the station located at northeast offshore of Taiwan island), but difference in time. In summer (shown, in Fig. 12 and 13), due to stong surface heating the high land areas become the major confluence flow centers, while the Taipei valley endures low wind speed and diffulent flow condition. This situation is not prominent in winter.

The verification of the model is judged by the percentage error by comparing the reported winds at Taipei station and Keelung Station with the model anlayzed winds, while these two station's reports are deleted from the input data. The error, DEV, is defined as

$$DEV = \frac{\sum_{i=1}^{N} [(u_c - u_o)_i^2 + (v_c - v_o)_i^2]}{\sum_{i=1}^{N} [u_o^2 + v_c^2]_i} \qquad (16)$$

In (16), since there are ten different case studies, and two deleting stations, the number of N is 20. From the testing runs of the model, the DEV value is found to be 18.69%.

CONCLUSION

The proposed variation-kinematical model for analyzing wind characteristics at data sparse area has been checked for flow patterns at northern Taiwan island. In this study, it has been found that the performance of the model is sensitive to the prescribed depth of model domain. Since, this is the key factor affecting the

assumption of mass balance of flow field over complex terrain. We proporsed that the model depth should proportion to the root-mean-squre value of terrain elevation over the analyzing domain. By intentively, deleting reports from two observing stations as the imput, it is found that the interpolation ability of wind characteristics at data sparse area from the model calculation is quite well, the percentage error as defined by (16) is about 18%.

From this study, we are confident that this wind analyzing model is capable in serving as a preliminary tool in the wind energy survey problem or mesoscale transport of air pollutants in complex terrain area like northern Taiwan island.

REFERENCES

(1) Barnes, S. L., 1973: Mesoscale Objective Map Analysis Using Weighted Time-series Observation. NOAA Tech. Memo., ERL-NSSL-62.

(2) Dickerson, M. H., 1978: MASCON - A Mass Consistent Atmospheric Flux Model for Regions with Complex Terrain. J. Appl. Meteor., 17, 241-253.

(3) Endlich, R. M., F. L. Ludwig, C. M. Bhumeralker, and M. A. Estorque, 1982: A Diagnostic Model for Estimating Winds at Potential Sites for Wind Turbines, J. Appl. Meteor., 21, 1441-1454.

(4) Sasaki, Y., 1958: An Objective Analysis Based on the Variational Method. J. Meteor. Soc. Japan, 36, 77-88.

(5) _____, 1970a: Some Basic Formalisms in Numerical Variational Analysis. Mon. Wea. Rev., 98, 875-883.

(6) _____, 1970b: Numerical Variational Analysis Formulated under the Constraints Determined by Long-wave Equations and Low-pass Filter, Mon. Wea. Rev., 98, 8 884-898.

_____, P. S. Ray, J. S. Goerss, and P. Soliz, 1978: Inconsistent Finite Differencing Errors in the Variational Adjustment of Horizontal Wind Component, Meteor. Soc. Japn, 57, 88-92.

Sherman, C. A., 1978: A Mass-consistent Model for Wind Fields over Complex Terrain, J. Appl. Meteor., 17, 312-319.

Table 1. Content of Case Studies

Case No.	Time	Prevailing Wind*
1	1983, 1, 30; 14LT	N, 10 m/sec
2	1983, 1, 30; 23LT	NE, 12 m/sec
3	1983, 1, 31, 17LT	E, 10 m/sec
4	1983, 2, 1; 08LT	SW, 5 m/sec
5	1983, 2, 1; 14LT	SSE,10 m/sec
6	1983, 2, 1; 23LT	NE, 3 m/sec
7	1982, 7, 8; 23LT	SSW, 3 m/sec
8	1982, 7, 9; 02LT	2, 6 m/sec
9	1982, 7, 9; 11LT	SE, 5 m/sec
10	1982, 7, 9; 20LT	SSE, 3 m/sec

*Prevailing winds are indicated by surface wind reports at Pon-chia-yu island about 300 Km northest of Taipei.

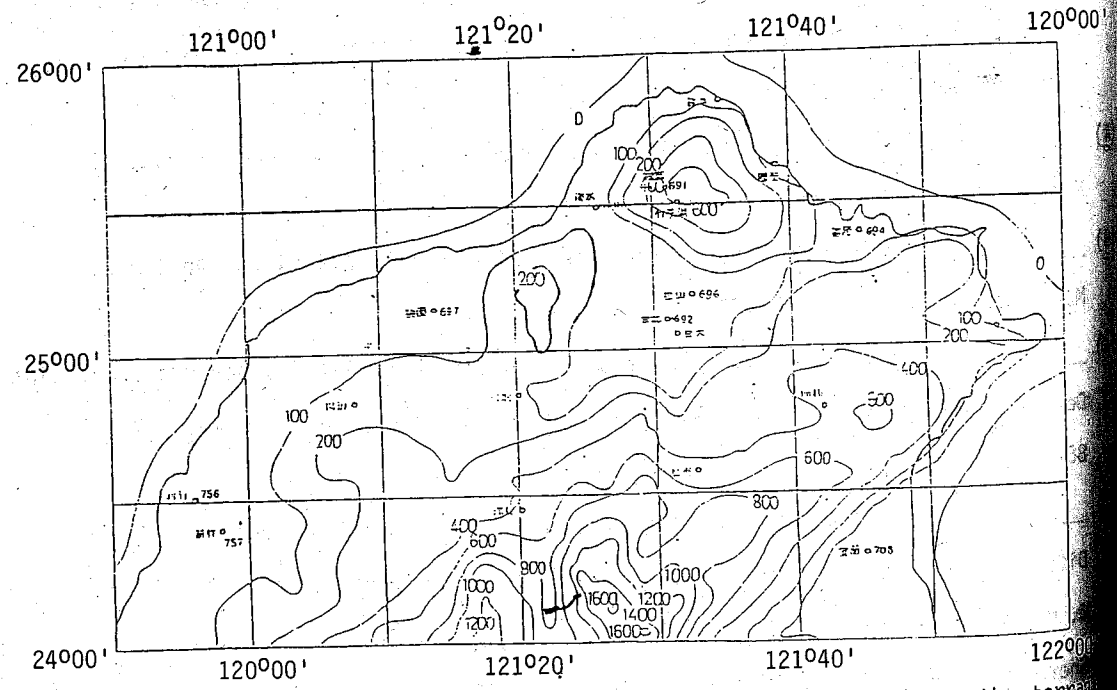

Fig. 1. The topography of Northern Taiwan, The contour-lines indicate the terra elevation above the sea-level (in meters).

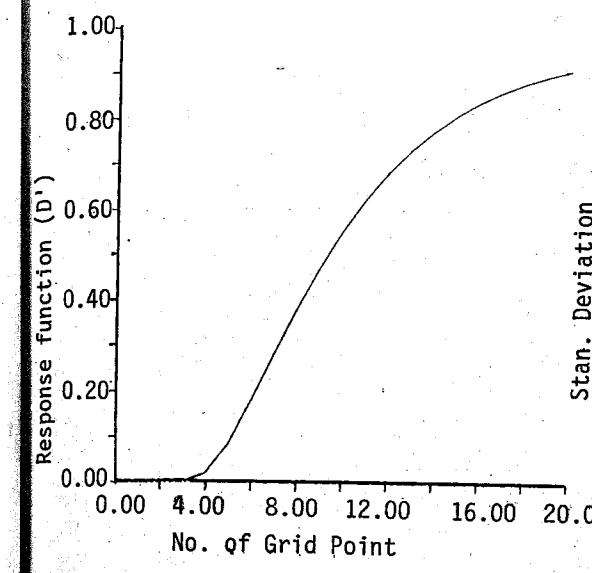

Fig.2. The response function of the objective analysis scheme (Barns scheme). The distance between grid points in 4.Km.

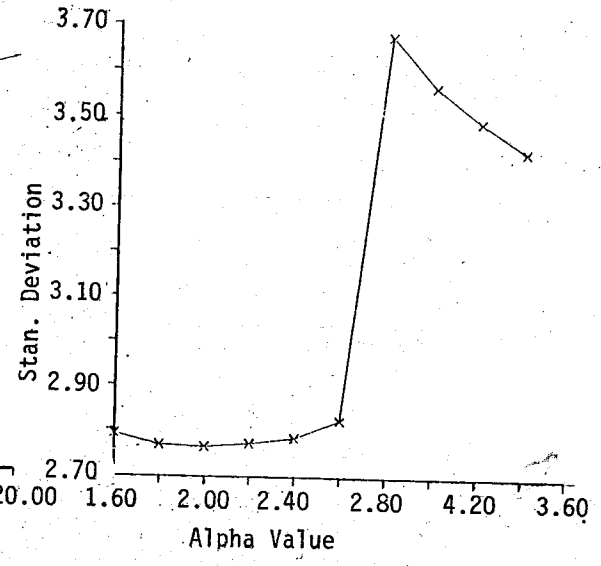

Fig.3. The relation defined by (13), (14) and (15).

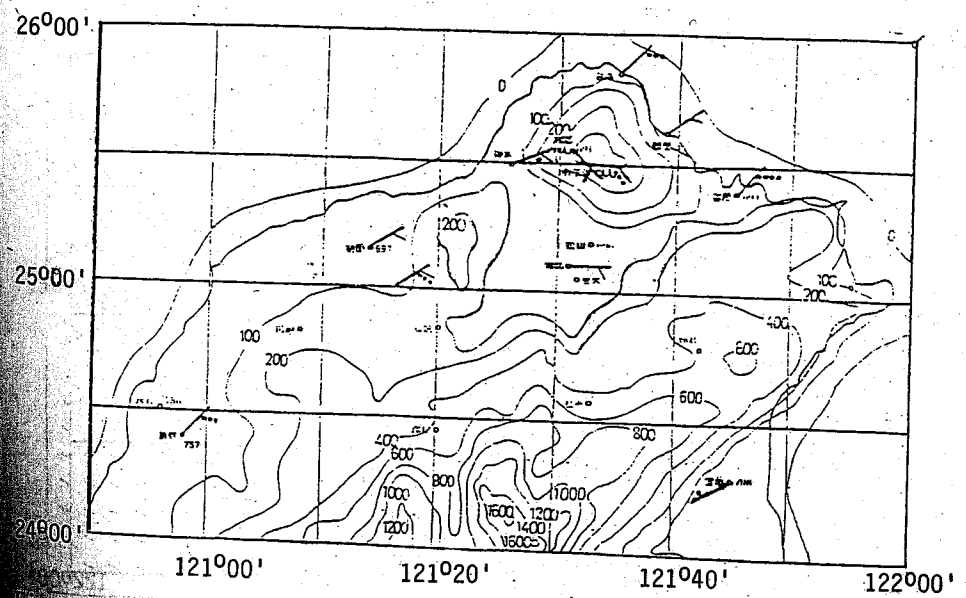

Fig. 4. The observed surface winds of case 2. A full-bar represents 10 m/sec, half-bar for 5 m/sec, and dot for 1 m/sec.

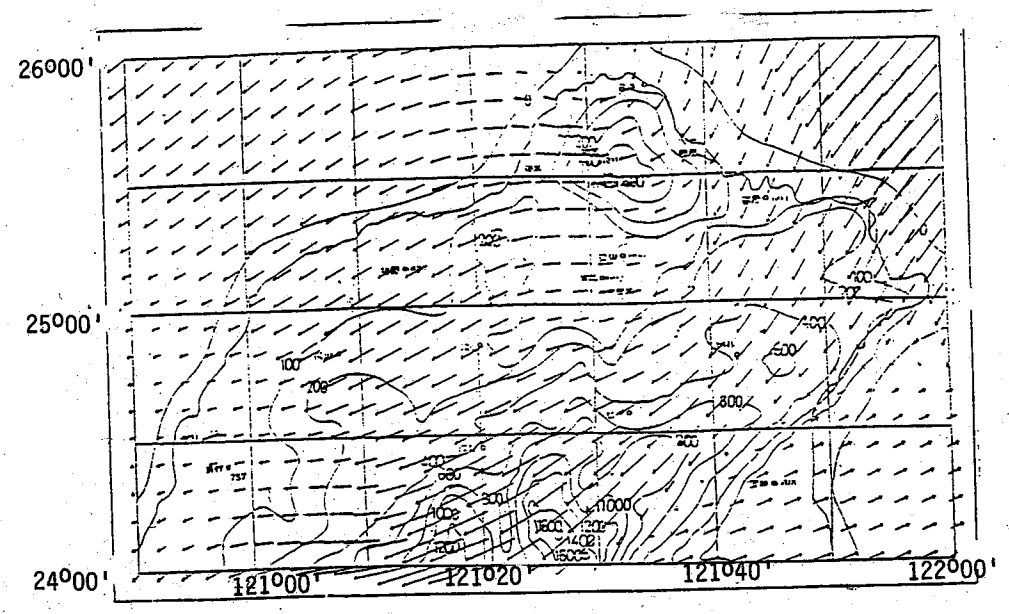

Fig. 5. The analyed surface wind pattern for case 2, in this analysis, 12 surface wind reports are used as the input data.

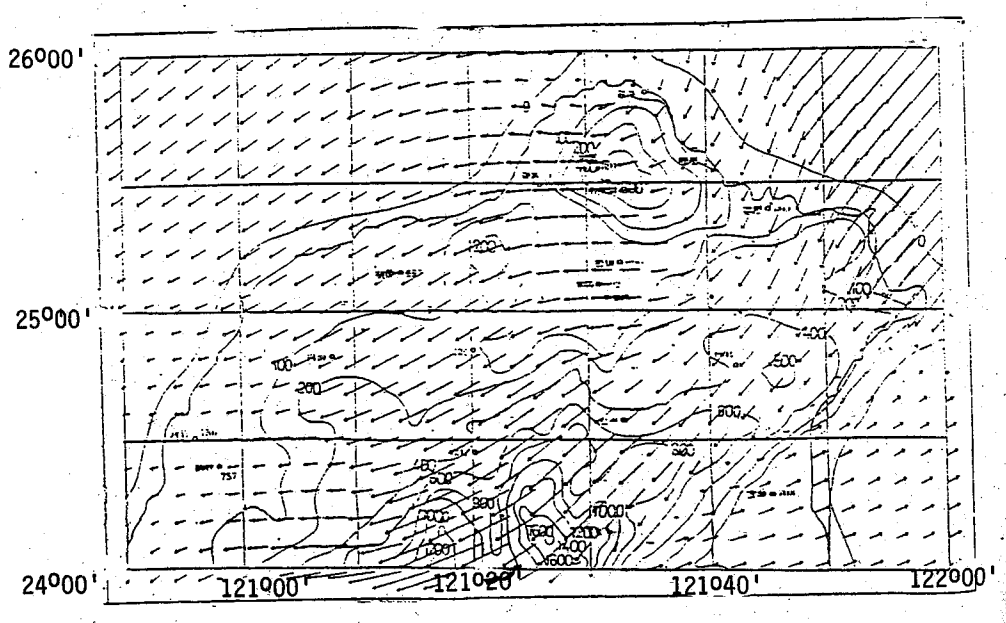

Fig. 6. Same Fig. 5, Except wind reports at Taipei (Station No. 692), Keelung (Station No. 694) are omitted in the input data.

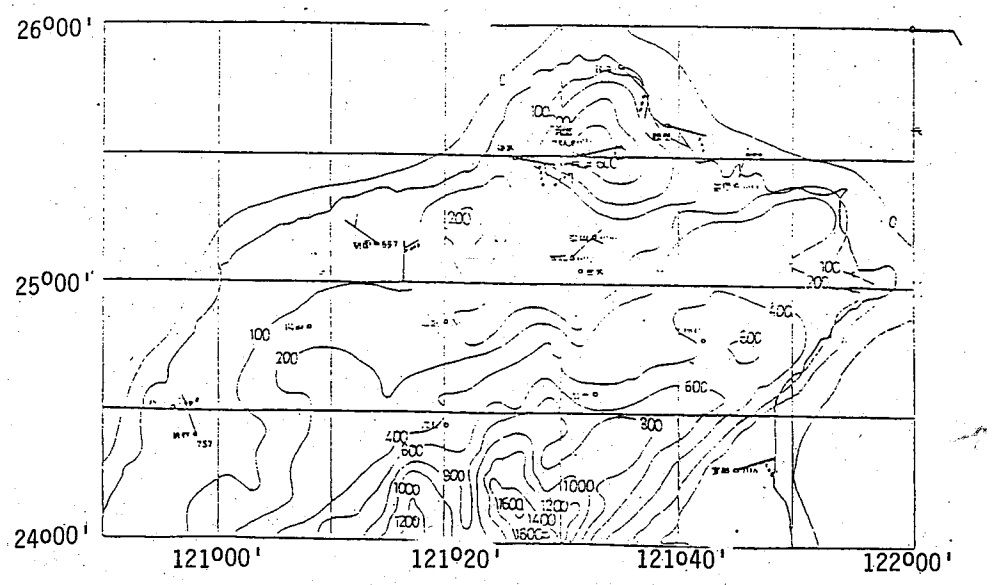

Fig. 7. The observed surface winds of case 3.

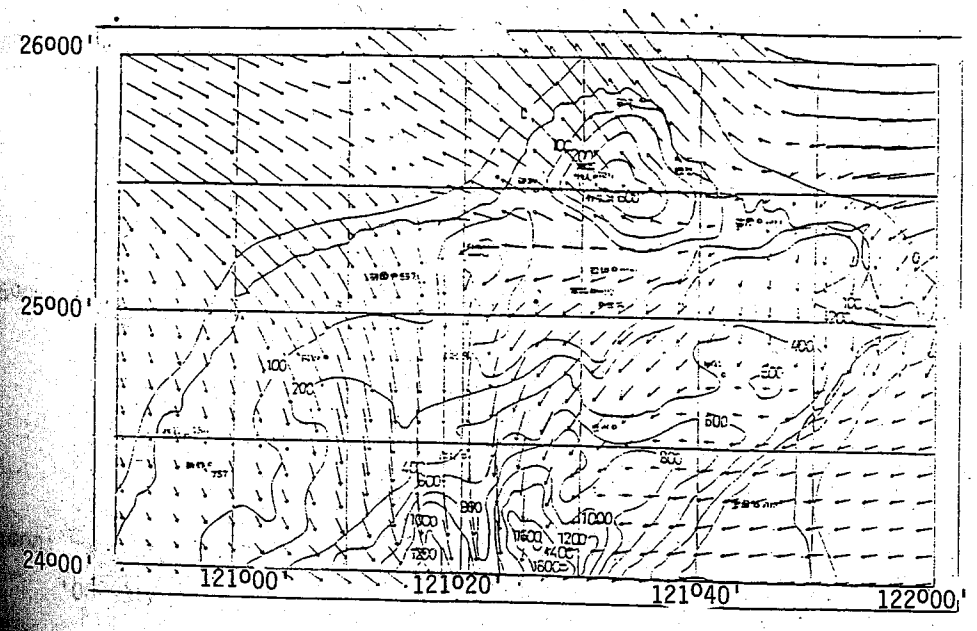

Fig. 8. The analyzed surface wind pattern for case 3. There is a total of 12 surface wind reports are used as the input data.

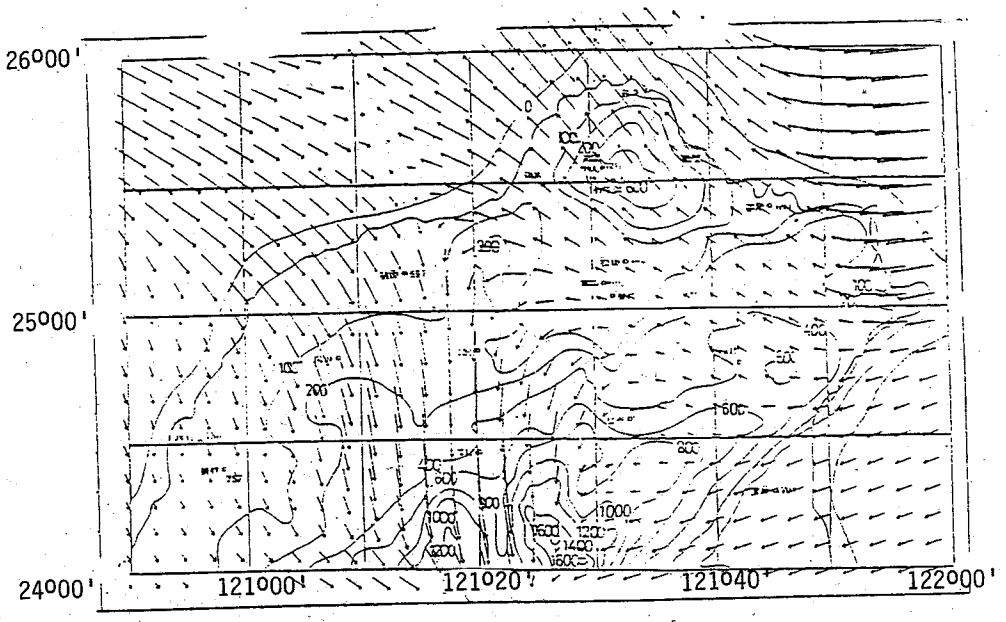

Fig. 9. Same as Fig. 8, except wind report at Taipei and Keelung are omitted in the input data.

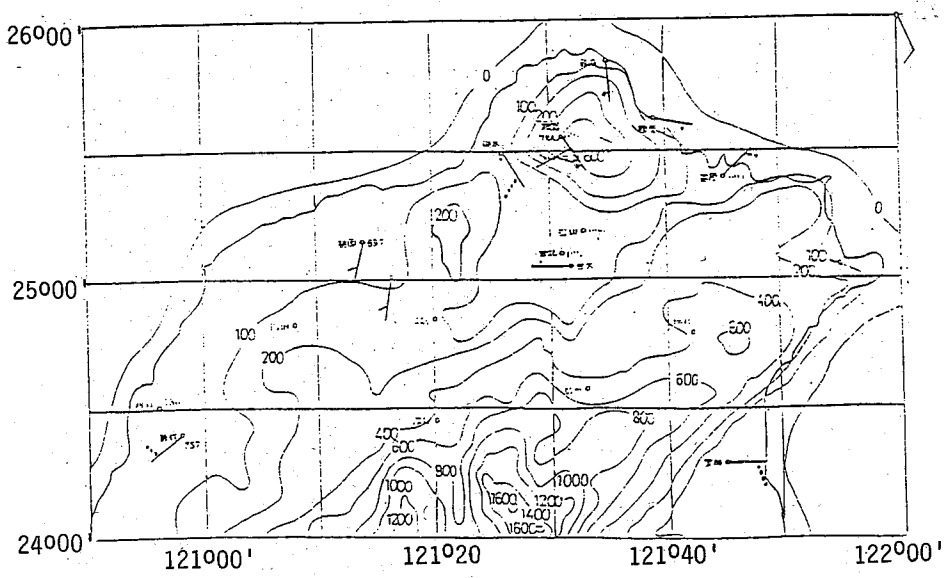

Fig. 10. Observed surface wind for case 5.

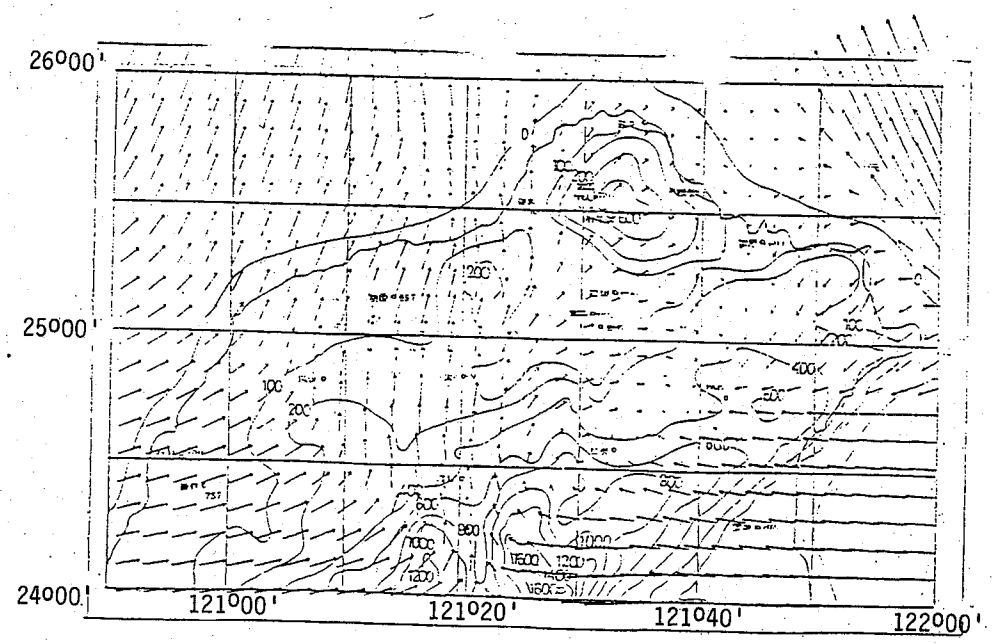

Fig. 11. The analyzed surface wind pattern for case 5.

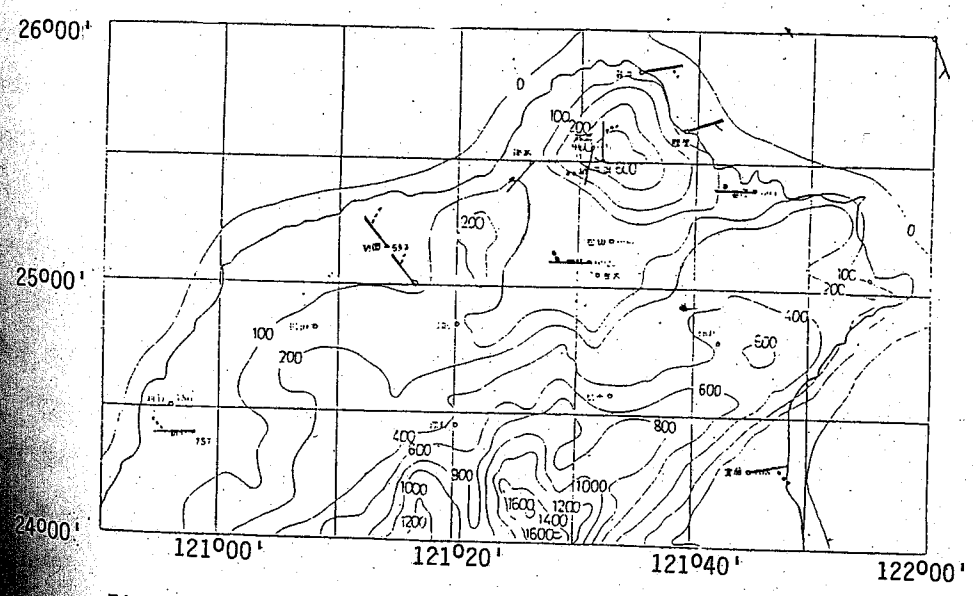

Fig. 12. The observed surface winds for case 9.

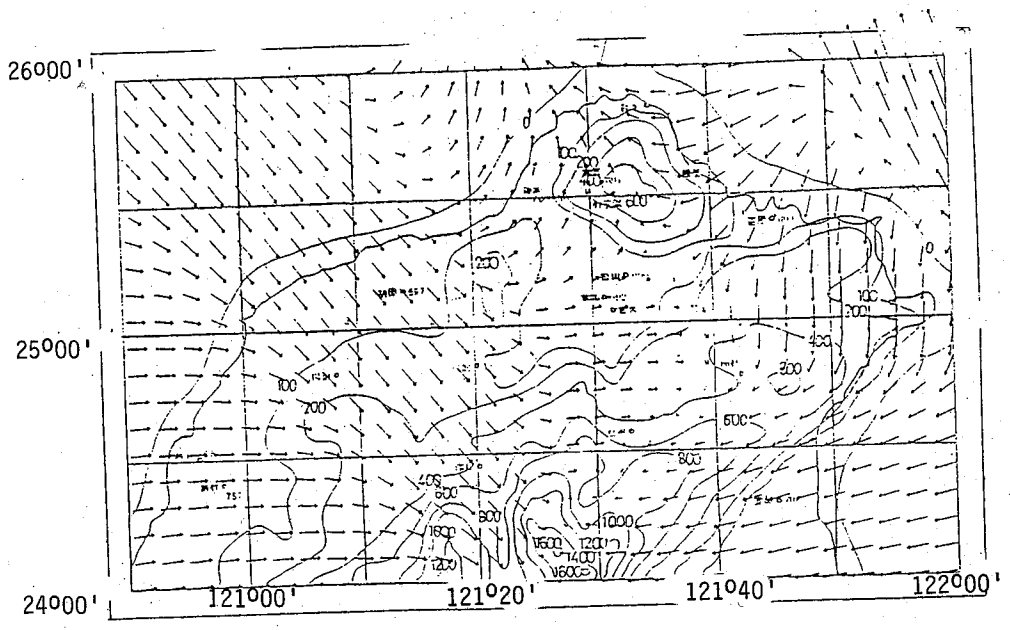

Fig. 13. The analyzed surface wind pattern for case 9.

THEORETICAL STUDY OF ROCKET EXHAUST PLUMES
PART I: CHARACTERISTICS METHOD

L. C. Chien, C. T. Wang, W. J. Liang and F. L. Chen
Institute of Physics
Academia Sinica, Nankang,
Taipei, Taiwan, R. O. C.

The method of characteristics has been developed to investigate the underexpanded rocket exhaust plumes. According to the plume structure, the computational procedures are set up similar to the formation process of actual flow. The method are employed on solving the plumes of two standard nozzles under different conditions and the plume of Thor missile exhausts into supersonic ambient flow. The results are compared with the existing solutions. For an object comparison, furthermore, the results got by finite difference method are devoted to calculating the same plumes stated previously. It is found that the results obtained with these two different numerical simulations are in good agreement.

INTRODUCTION

The rocket exhaust gases from highly underexpanded nozzles operating in low pressure condition results in large billowing plumes. Figure 1 shows a typical underexpanded rocket exhaust plume from a single-engine missile. Between the jet shock and the air shock, there is a turbulent mixing layer in which the air mixes with the exhaust flow. The air shock is the outer limit of the region in which the exhaust flow influences the air flow while the jet shock is the inner limit. Consequently, the flow in the region bounded by the jet shock and Mach disc is identical to the flow that would result when exhausting into vacuum.

Recent interest in rocket exhaust plumes has been stimulated by many design problems that arised when the exhaust gas left nozzle. For example, problems involving the effects of the plume impinging on the other vehicles, ground surface, and even on it own vehicle have received considerable attention. Still another case of great concern is the severe attenuation of communication signals between a space vehicle and ground control caused by the presence of free electrons in the plume. Other problems caused by large billowing plumes, such as the easy-detection of due to infared radiation exited from plume, cannot be avoid avoided but to

understand the plumes.

The method of characteristics are first used to calculate plume flowfiled. In the method characteristics solution, the flow at the lip of nozzle is expanded through a Prandtl-Meyer expansion fan to the pressure calculated at the dividing streamline. After the exhaust flow passes through the expansion region, it is turned by the dividing causing characteristics of the same family to coalesce and form the jet shock. The jet shock is of increasing strength as it moves downstream and, thereafter, decreases when it reaches the maximum diameter. One of the classical reports applying the method of characteristics of calculate plumes is by Love et al (1). However, in this report the so-called "fold-back" method employing in characteristics net results that the calculatings are valid only in the region near exit surface. This simplification has been eliminated by Andrew et al (2). And the resulting plume flowfield has been experimentally verified by Vick et al (3). There are some other investigators, Cassanoval et al (4) and Reis et al (5), are devoted to applying the method of characteristics on plume flowfield.

In addition to the method of characteristics technique for compating inviscid plume flowfields, Boyton and Thomson (6) have recently devised a Lagrangian finite-difference technique which can be applied to the solution of inviscid as well as viscous plume flowfield. Their technique has been extended by incorporating chemical non-equilibrium and turbulent transport capability into the analysis by Tannehill (7). This method will be discussed in detail in part II of this subject.

Both the method of characteristics and the Lagrangian finite-difference technique require a considerable amount of effort and computer time. This has prompted several investigators to dévelop approximate method which can be quickly applied to problem of determining the gross plume structure. They are, such as, Albini (8), and Hubbard (9). These approximate methods are able to determine the geometry of the plume shape, jet shock location, and internal pressure distribution.

However, the characteristics method, still, is a highly efficient technique for calculating the inviscid supersonic flow.

In the present paper, the authors developed a method of characteristics which the numerical calculating procedures are set up in similar to the formation process of actual flow. It is devoted to calculating the inviscid, rotational plume flowfield. The results obtained are, then, employed on comparison with the existing solutions.

GOVERNING EQUATIONS

In this section the equations necessary for computing the supersonic flowfield on a rocket exhaust plume are presented. The equations are applicable to both viscous and inviscid flowfield, and the flowfield including non-equilibrium chemical reactions if the proper terms are retained.

According to the derivation of Edelman and Weilerstein (10), the general equations for steady flow of a reacting mixture of perfect gases are:

Global continuity equations:

$$\nabla \cdot \rho \overline{V} = 0 \tag{1}$$

Species continuity equations:

$$\nabla \cdot \rho C_i \overline{V} = \rho \dot{W}_i - \nabla \cdot \overline{J}_i \tag{2}$$

Momentum equations:

$$\nabla \cdot [(\rho \overline{V})\overline{V}] = -\nabla P + \nabla \cdot \overline{\overline{\tau}} \tag{3}$$

Energy equations:

$$\nabla \cdot \rho \overline{V} H = \nabla \cdot (\overline{\overline{\tau}} \cdot \overline{V}) - \nabla \cdot \overline{Q} - \nabla \cdot \sum_{i=1}^{N} h_i J_i \tag{4}$$

Equation of state:

$$P = \rho \overline{R} T \sum_{i=1}^{N} \frac{C_i}{M_i} \tag{5}$$

where H is the total enthalpy, subscript i represnets the ith species from a total N.

In these equations, the viscous shearing stress $\overline{\overline{\tau}}$ is given for a Newtonian fluid and the heat transfer term Q can be evaluated by Fourier law. The diffusional mass flux term $\overline{J}_i$ can be applied by Fick's law (11). Accordingly, the species production term $\dot{W}_i$ represents the production rate of the ith species from the system of chemical reactions can be given by the classical Arrhenius law (12).

In order to simplify the above equations, some assumptions will be employed on the plume flowfield. In the high altitude, the assumption of frozen flow can be employed everywhere in the plume flowfield (13). Also, due to the results got by Tanne-

hill (7), it is shown that the reacting processes influent the plume slightly. So that the mass production term, $\dot{W}_i$, is neglected here; similarly, the mass diffusion term, $\dot{J}_j$ can be ignored due to the transition to turbulent is delayed. So that, the species continuity equation (2) would not be considered; and the species number N is equal to one. This simplification avoids the complex iteration in computational procedure. Furthermore, at high altutide the viscosity of the flowfield is small due to the ambient low pressure. Then, the viscous terms in equations (3) and (4) are negligible. Finally, assuming there is no heat transfer in the plume flowfield, the heat transfer term $\vec{Q}$ is equal to zero. The subject, depends on the assumptions made above, appears to be a steady, inviscid and frozen flowfield problem.

The flow in the plume will be taken as isentropic along the streamline. That would lose no generality because the existance of the gradient in entropy and stagnation entropy normal to the streamline makes the flow rotational in the flowfield. It satisfies the physical phenomena that the flow is rotational after the ambient flow passes through bow shock uniformly. Accordingly, the governing equations become:

Global continuity equations (6)

$$\nabla \cdot (\rho \overline{V}) = 0$$

Momentum equations: (7)

$$\nabla \cdot [(\rho \vec{V}) \vec{V}] + \nabla \rho = 0$$

Energy equations: (8)

$$\nabla \cdot (\rho \vec{V} H) = 0$$

Equation of state: (9)

$$P = \rho \overline{R} T$$

For an isentropic flow along the streamline, the energy equation may be replaced by speed of sound equation (14): (10)

$$\nabla \cdot (\vec{V} P) - a^2 \nabla \cdot (\vec{V} \rho) = 0$$

Taking the plume as a two-dimensional flowfield, equations (6), (7) and (10) can be transformed into characteristics and compability equations as follows:

Characteristic equations: (11)

$$(\frac{dy}{dx})_0 = x_0 = \frac{v}{u}$$

$$(\frac{dy}{dx})_\pm = x_\pm = \tan (\theta \pm \alpha) \quad (12)$$

Compability equations:

$$\rho \overline{V} \, d \overline{V} + dp = 0 \quad (13)$$

$$dp - a^2 d\rho = 0 \quad (14)$$

$$\frac{\sqrt{M^2 - 1}}{\rho \overline{V}^2} d\rho_\pm \pm d\theta_\pm + \zeta \left[\frac{\sin\theta \; dx_\pm}{yM \cos (\theta \pm \alpha)} \right] = 0 \quad (15)$$

where $\zeta = 0$ for planar flow, and $\zeta = 1$ for axisymmetric flow. The index +, - and 0 denoted C_+, C_- and C_0 characteristic curves, respectively.

These equations are sloved to determine the location and physical properties of the points through which the characteristics pass. Together with the oblique shock equations (14), they described the plume flowfield completely.

NUMERICAL PROCEDURE

The supersonic flow exhausted from the nozzle of rocket into ambient low pressure flowfield caused rapidly expansion near the nozzle lips. Originated from the lips, the expansion waves spread over in the flowfield comprised the Prandtl-Meyer expansion fan. Between the exhaust surface and the Prandtl-Meyer expansion fan, there locates a unifrom region, i.e., Mach cone. In this region, the physical properties are almost keep constant (for circular nozzle only). The characteristic lines which penetrate through the prandtl-Meyer expansion fan are the expansion waves. These waves, then, reflect from the plume boundary with becoming compression ones. The jet shock is formed by the coalescence of these reflected compressive waves. As moving downstream, a normal shock forms due to the increases of pressure ration between the flowfield of plume and ambient. If the ambient flow is supersonic, an oblique shock will happen outside of the plume boundary.

The calculating procedures of the method of characteristics used here would be developed similar to that of actual flow. A segment of typical characteristics network is shown in Figure (2). The calculation started from the exit surface. From the exit surface, lots of characteristic lines with different family exited and formed a characteristics network in Mach cone. The outerest characteristic line of

Mach cone is called Leading Characteristic Line (L. C. Line). Many expansive characteristics spread outward from L. C. Line in the prandtl-Meyer expansion region. In whole flowfield, there exist right-running characteristic lines C_- and left-running characteristic line C_+ . The expansion waves belong to the right-running characteristic line C_- . On the other hand, the left-running characteristic lines across the expansion region would reflect from the plume boundary with becoming compressive waves. These compressive characteristic lines coalesced and formed the jet shock. The computation continued with truncating one of the coalesced characteristics and the other one still moved downward.

The program is developed with the calculation procedure stated as above. It can analyze planner or axisymmetric flow. The Prandtl-Meyer expansion fan is set up so that the right-running expansion waves are uniformly spread. This is done by making the pressure difference between two near waves decrease as pressure decreases. If an error occurs in an arithmetic subrouting (THERMO), a new point is insert in the previous right-running line, and the current line is recalculated. This action is displayed in the output flowfield may be truncated along a left-running wave reflected from the axis under user control. This reduced the computer time considerably. It is also found that the characteristics net needs to be fine for the distored region.

RESULTS AND DISCUSSION

The method of characteristics developed in this paper is employed in solving inviscid plumes exhausted by rocket under difference pressure ratios and exit conditions. The results are compared with the existing solution of irrotational flow and the finite-difference solutions.

The primary parameters which influence exhaust plume profile are exit Mach number M_j , nozzle lip angle θ_N , specific heat ratio γ and the ratio between exit pressure P_j and ambient pressure $P\infty$. To investigate the physical phenomena affected by these four parameters, the program is devoted to solving the plume flowfield under various conditions due to changing those parameters. First, the effect of exit Mach number is observed (Figure 3). Five plumes' profiles are shown for different M_j = 1.5 (0.5) 3.5. The shape inflated as decreased Mach number. It

because the faster the exit flow, the less the influence by ambient flow pressure. On the upper-left corner in figure 3 showed the relationship between M_j and plume radius under different pressure ratios. It found that the influence of M_j increased as pressure ratio increased. Likewise, the effect of pressure ratio is observed in the same way (Figure 4). The high pressure ratio causes the inflection of plume shape. Furthermore, different lip angle influents the plume shape greatly (Figure 5). The exit flow expands dominately as lip angle becomes large. The specific heat ratio of the gas of the exit flow also has a considerable influence on the plume shape (Figure 6). High value of γ denotes the gas absorbed more energy with increasing one degree of absolute temperatue. So that, the higher γ caused large velocity of exit flow under same difference of temperature. That is the reason why the higher value of γ induces the small diameter of plume.

After analyzing the physical phenomena found that the results are resonable, the program is devoted to solving plumes of two standard nozzles, conical and circular nozzle, under three different conditions to compare with the existing solutions (Table I). The initial turning angle will be solved firstly. The flow angle through which the flow will expand is the difference between the Prandtl-Meyer expansion angles corresponding to the jet-boundary Mach number and exit Mach number. It is

$$\alpha_N = \nu_1 + \nu_N + \theta_N \tag{16}$$

where α_N is the turning angle υ_1 and ν_N are the Prandtl-Meyer expansion angle with respect to the boundary and exit Mach number, respectively. And θ_N is the lip angle as stated before. The calculated results under different pressure ratios of the two nozzles are compared with those obtained by Andrews et al (10) nicely (Figure 7). The method of characteristics can predict the flow near the exit surface well although may be under different calculation procedures.

Various plumes' shapes which are obtained under three different conditions of nozzle I and nozzle II (Figure 8 and 9). The results would compare with those got Andrew et al (10) which are evaluated in the irrotational flowfield. It is found the plumes with rotational flow are fatter than the plumes with irrotational Physically, uniform flow pass through bow shock will induce the flow to be onal. Furthermore, it needs iteration in calculation process for rotational ecause there are three characteristic lines pass through one node. But it is

not for the irrotational flow because there are only two characteristic lines for one node. This causes the numerical error which will propagate downstream and reduce that the solution is unacceptable in the downstream flowfield. Figure 10 is the plume exhausted by nozzle II under pressure ratio equals to 23800, i.e., almost under the vacuum ambient condition. In this figure, one can inspect obviously the coalescence of the reflected compressive waves which forms the jet shock. There are 40 right-running characteristic lines in the Prandtl-Meyer expansion fan. The characteristics net in the Mach cone is too crowded to show here. The propagate of Mach waves in the flowfield is one of the features of the characteristics method. This can be observed in Figure 10 easily.

On the nodes of characteristics net, there are some physical properties, such as pressure, temperature and Mach number, which are solved previously. In Figures 11, 12 and 13, the distributions of pressure, temperature and Mach number for nozzle I under case 1 are shown with the iso-valued curves. Observing the pressure distribution, there exists a pressure jump near the plume boundary. That is the result caused by jet shock. Again, it is found that the isobars formed close regions near the axis and expanded outward gradually with decreasing values. Contractly, the influence of ambient conditions propagates inward step by step. That is why the region far away from boundary is called "undisturbed region". On the upper-left corner, the Prandtl-Meyer expansion fan is shown with the pressure decreased outward rapidly. Similary, the undisturbed region can also be found in the distribution of temperature and Mach number. In these figures, there exist unreasonable bubble that is caused by coarse characteristics net in the flowfield. The uniform region, Mach cone, can be inspected by the value of first iso-valued curve on each figure equals to the exit condition. In addition, one can find that the temperature and pressure decreased as move downstream. This is induced by the ambient low pressure and temperature flowfield. On the other hand, for isentropic flow the decreasing of temperature causes the increasing Mach number. These properties developed downstream in this way until a normal shock happened. Behind the normal shock, called Mach disc, the flow becomes subsonic (not shown here).

The plumes obtained before are under the still ambient flow condition. For investigating the influent of ambient supersonic flow, the plumes of Thor missile

which exhausted into a supersonic flowfield are calculated with the method of characteristics developed in the paper. The results are compared with those obtained by Tannehill (7) (Figure 14 and 15). The plume shape obtained by the method of characteristics are fatter than the result of Tannehill obtained by Lagrangian finite-difference method. Furthermore, the pressure distribution along surface A in Figure 14 is compared in Figure 15. Care must be taken here that the data of Tannehill shown in Figure 15 are enlarged ten times in scale. Because the origin data shown by Tannehill are obviously unreasonable because they are too small for the exit condition. By adjusting in this way as Figure 15, the data of this paper and Tannehill before jet shock are compared nicely. But it is not for the data in jet shock layer. The detailed discussion of these distored results can be found in Chen (15).

For making an objectly comparison of the results got by the method of characteristics developed in this paper, the authors follows the Lagrangian finite-difference method developed by Boyton and Thomson (6) with some modifications to calculate the plume stated above. The detailed procedures and results are to be published as the second part of this study about rocket exhaust plumes. Here, this developed method under modifications made by the authors is employed on solving the plume exhaust by Thor missile to make an object comparison between the results of method of characteristics and Tannehill. In Figures 16, 17 and 18 are shown the comparisons got by these two different numerical approaches. The plume shapes got by method of characteristics and Lagrangian finite-difference method are almost matched each other. The pressure distributions along surface A in Figure 16 have also the results in good agreement. In addition, the temperature distributions along surface A are almost in the same result (Figure 18). The matched results got by two different numerical approaches proved the reliability of method of characteristics developed in this paper. As the disagreement data of Tannehill, the authors thought it as the wrong values of plume conditions given in his paper.

To predict the location of Mach disc, the pressure distribution downstream of shock is shown in Figure 19. The Mach disc happened at the location where the ssure down tream of the jet shock reaches a minimum (16). The location obtained sima and Radtke is 33 meters downstream from the exit surface. And the press- stribution in Figure 19 reaches a minimum about 35 meters downstream.

Finally, to compare with the experimental data, the curvature of plume boundary near the nozzle lips is investigated here. Under constant exhausted velocity, the curvatures with various pressure ratios are calculated as shown in Figure 20. These results are compared with those got by Love et al (1). As shown in this Figure , for M_j = 2.0, the experimental results (1) is 8.2, theoretical result (1) is 7.6, and the investigated result got here is 7.75.

CONCLUSION

The method of characteristics was developed in investigate the supersonic, inviscid plume under various altitudes with frozen, rotational flowfield. This method was employed on solving two standard nozzles under different cases and the plume of Thor missile exhausted into supersonic ambient flow. This method can predict the plume shape and internal structure of plume flowfield rapidly and accurately.

The computer excution time required to calculate the plume flowfield, which based on 20 nodes on exit surface and 20 pieces of Prandtl-Meyer expansion waves truncated at the 10th waves afterwards, is about 26 seconds for CDC CYBER-74 computer.

REFERENCES

(1) Love, E. S., Grigsby, C. E., Lee, L. P., and Woodling, M. T. Experimental and theoretical studies of axisymmetric free jets. United states National Aeronautics and space Administration Technical Report R-6, 1959.

(2) Andrews, E. H., Jr., Vick, A. R., and Craidon, C. B. Theoretical boundaries and internal characteristics of exhaust plumes from three different supersonic nozzles. United States National Aeronautics and Space Administration Technical Note D-2650. 1965.

(3) Vick, A. R., Andrews, E. H., Jr., Dennard, J. S., and Craidon, C. B. Comparisons of experimental free-jet boundaries with theoretical results obtained with the method of characteristics. United States National Aeronautics and Space Administration Technical Note D-2327. 1964.

(4) Reis, R. J., Aucoin, P. J., and Stechman, R. C. "Predition of Rocket Exhaust

Flowfields." J. Spacecraft, Vol. 7, No. 2, pp.155-159, 1970.

(5) Cassnova, R. A. "Expansion of Jet into a Vacuum", Eleventh International Symposium on Combustion, Univ. of Calif. Berkeley, Calif. 1966.

(6) Boynton, F. P. and Thomson, A. Numerical computation of steady, supersonic two-dimensional gas flow in natural coordinates. Journal of Computational Physics 3:379-398. 1969.

(7) Tannehill, J. C. Numerical computation of intermediate altitude rocket exhaust plumes, including nonequilibrium chemical reactions and diffusion. Ph. D. Thesis, Iown State Univ. Ames, Iowa. 1969.

(8) Albini, F. A. Approximate computation of underexpanded jet structure. American Institute of Aeronautics and Astronautics Journal 3:1535-1537, 1965.

(9) Hubbard, E. W. Approximate calculation of highly underexpanded jets. American Institute of Aeronautics and Astronautics Journal 4:1877-1879, 1966.

NOMENCLATURE

a : Speed of sound, m/sec.

C_i : Mass fraction of species i.

H : Total enthalpy, KJ/Kg.

h_i : Enthalpy of element i, KJ/Kg.

$\bar{J}_i$: Mass diffusion rate of element i.

M : Mach number.

M_j : Molecular weight of element i.

N : Number of element.

p : Pressure, newton/m^2.

q : Heat flow vector, J/sec.

R : Gas constant, Nm/Kg, mole.^oK.

u : Velocity in x direction, m/sec.

v : Velocity in y direction, m/sec.

V : Velocity ($\sqrt{v^2+u^2}$), m/sec.

$\dot{w}_i$: Production rate of species i.

ρ : Density, Kg/m^3.

τ : Stress tensor, Newton/m^2.

υ : Prantle-Meyer expansion angle (degree).

θ : Flow angle (degree).

α : Shock angle (degree).

INDEX

o : Along streamline.

+ : Along left-running characteristics.

- : Along right-running characteristics.

N : On the lips of nozzle.

Table 1. Nozzles exit and operating conditions for this study

		Nozzle I (circular arc)	Nozzle II (conical)	Thor nozzle
M_j		5.35	3.39	2.986
P_j (atm)		7.42×10^{-3}	3.237×10^{-1}	0.617
T_j (°K)		2000	2000	2060
θ_N (degree)		0	19.5	0
r_j (m)		6.464×10^{-2}	1.054×10^{-2}	0.5791
γ		1.24	1.18	1.210
P_∞ (atm)	case 1	7.510×10^{-4}	2.158×10^{-2}	1.3425×10^{-3}
	case 2	3.945×10^{-5}	1.360×10^{-3}	
	case 3	1.372×10^{-6}	1.360×10^{-5}	
T_∞ °K		200	200	266.15
M_∞				5.117
P_j / P_∞	case 1	9.88	15	459.6
	case 2	188.1	238	
	case 3	5410	23800	
Ambient Flow		Still	Still	Supersonic

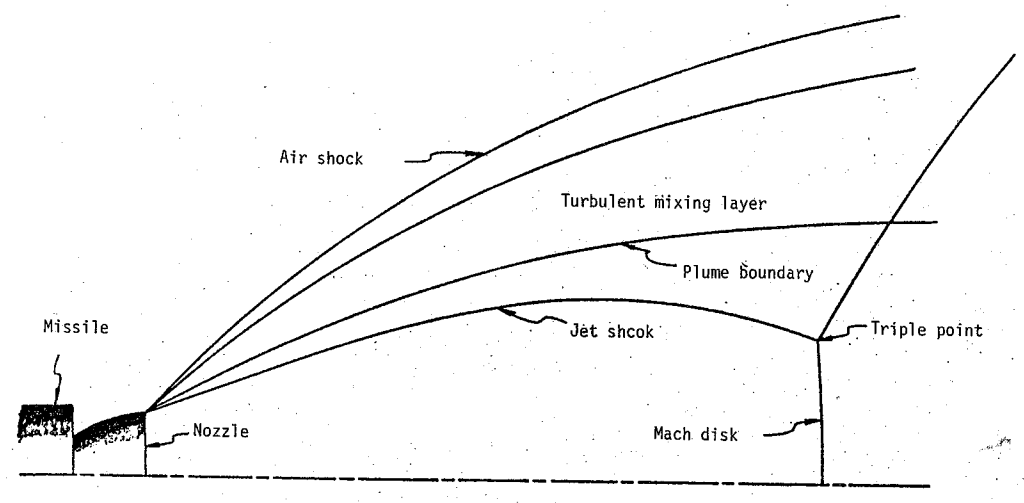

Figure 1. The underexpanded rocket exhausted plume.

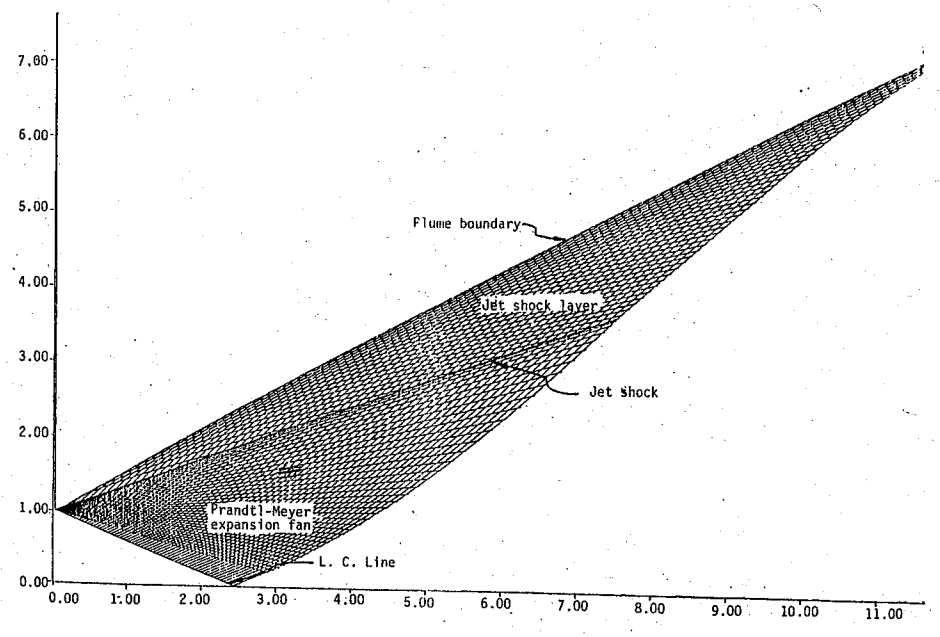

Figure 2. The structure of characteristic net of rocket exhausted plume.

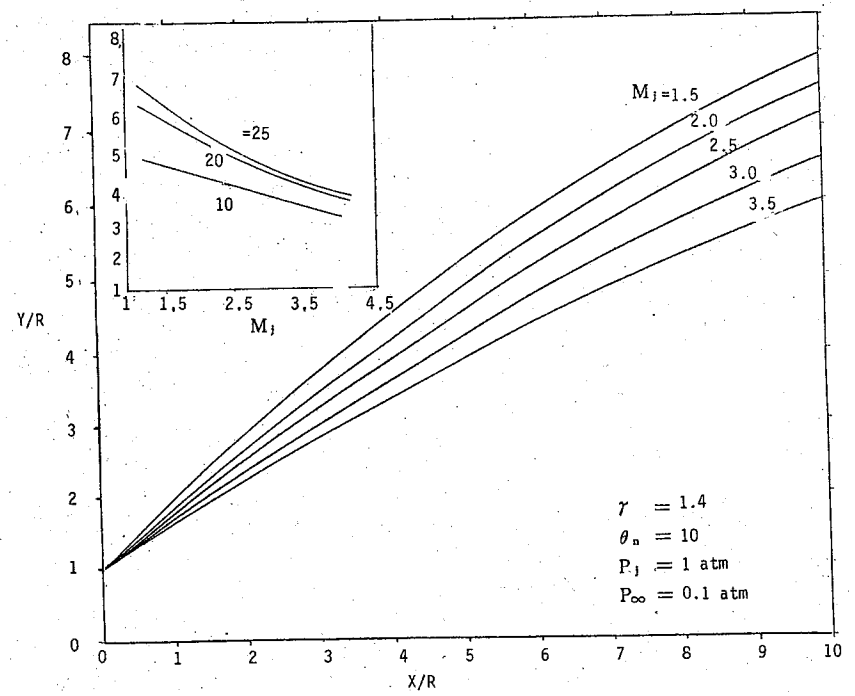

Figure 3. The effect of exiting Mach number on the plume profile. The diagram on the upper left corner shows that the relation between the radius of the plumes on X/R-4 and the exiting Mach number base on different pressure ratio.

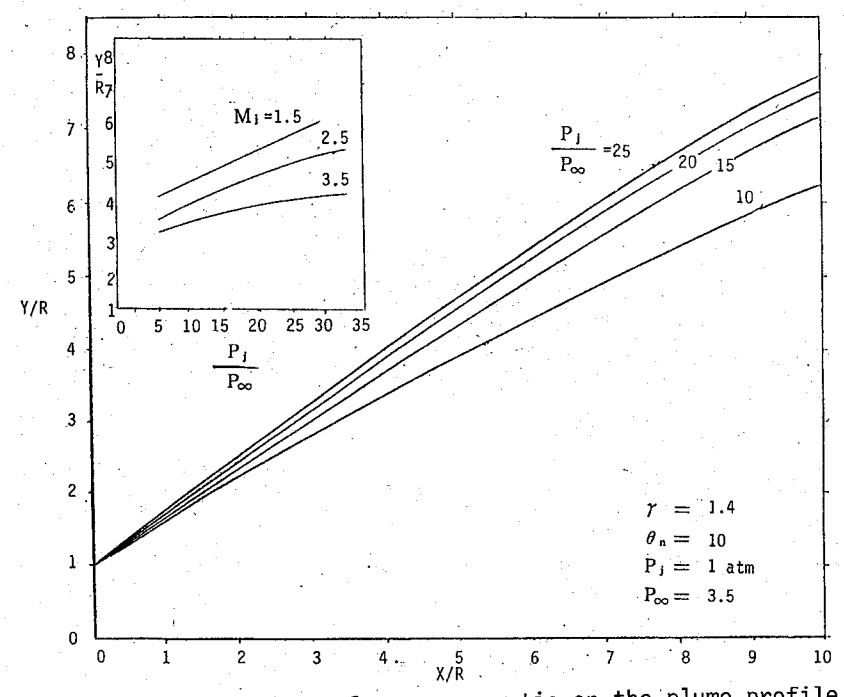

Figure 4. The effect of pressure ratio on the plume profile The diagram on the upper left corner shows that the relation between the radius of the plumes on X/R=4 and the pressure ratio base on different exiting Mach numbers.

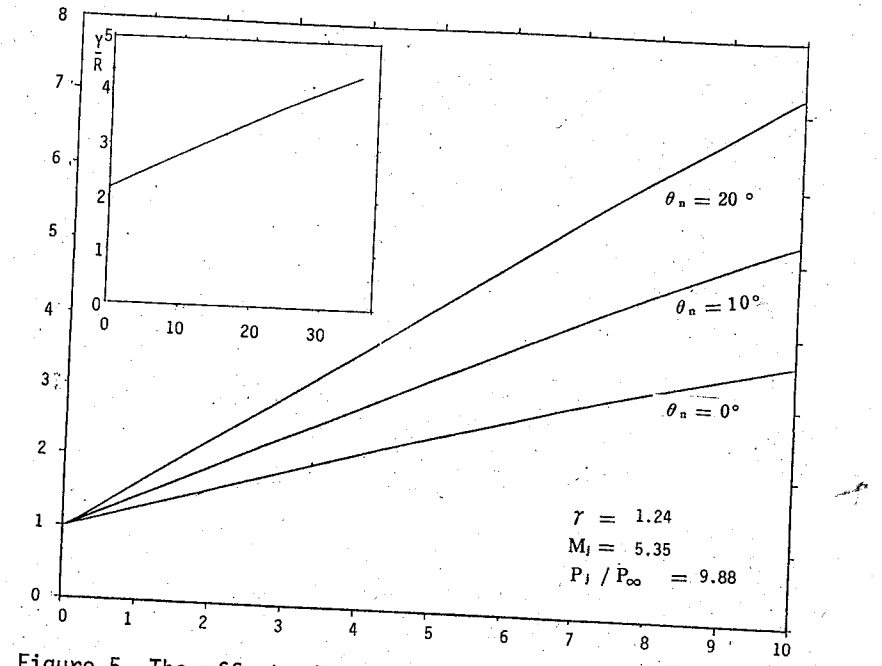

Figure 5. The effect of nozzle lip angle on the plume profile. The diagram on the upper left corner shows that the relation between the radius of the plumes on X/R=5 and the nozzle lip angle.

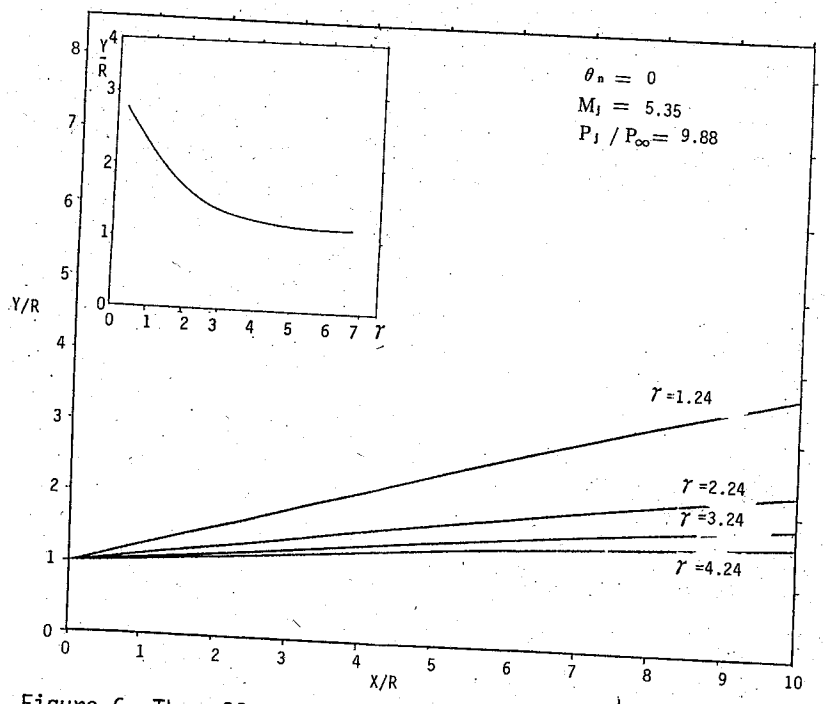

Figure 6. The effect of the ratio of specific heat on the plume profile. The diagram on the upper left corner shows that the relation between the radius of the plumes on X/R=5 and the ratio of specific heat.

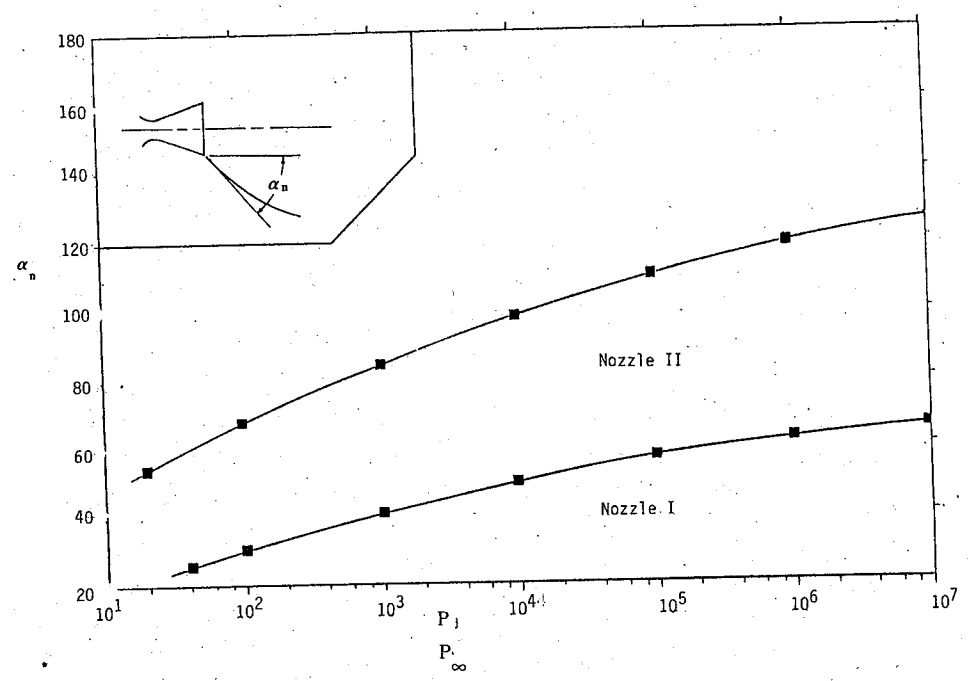

Figure 7. The relation between initial turning angle and the pressure retio. ◪ ;Andrew (1965); — : this study.

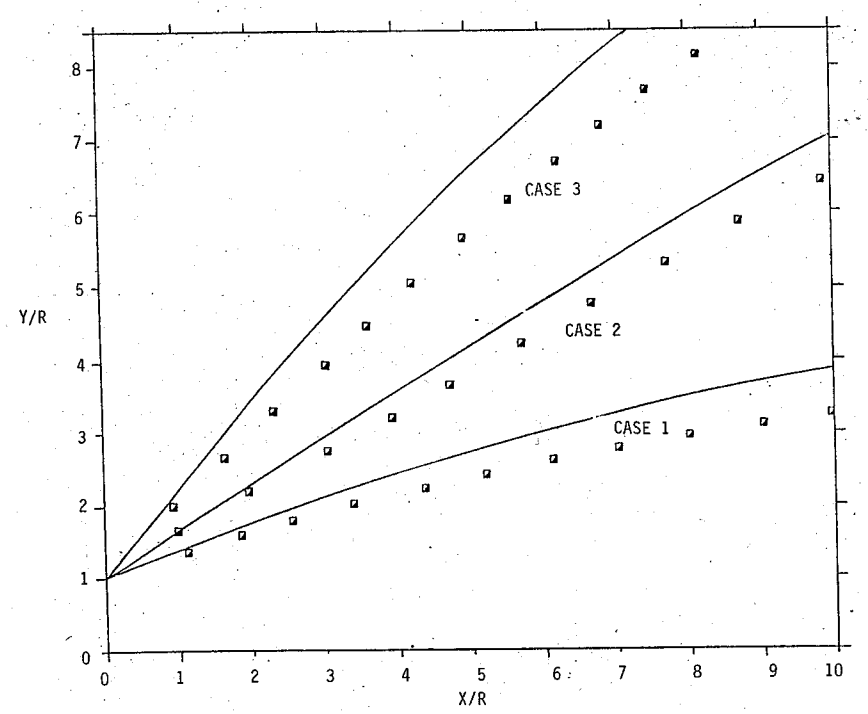

Figure 8. The plume profile of nozzle I under different ambient conditions.
◪: Andrew (1965, irrotational flow); ___: this study (rotational flow).

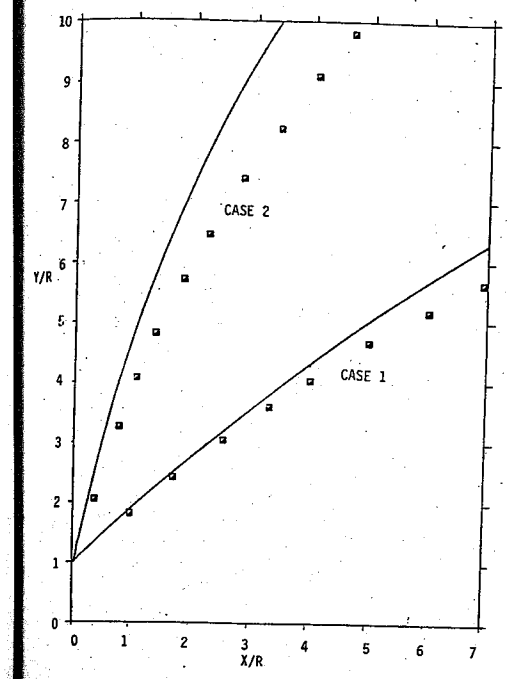

Figure 9. The plume profile of nozzle II under different ambient conditions. ◪: Andrew (1965, irrotational flow); ___: this study (rotational flow).

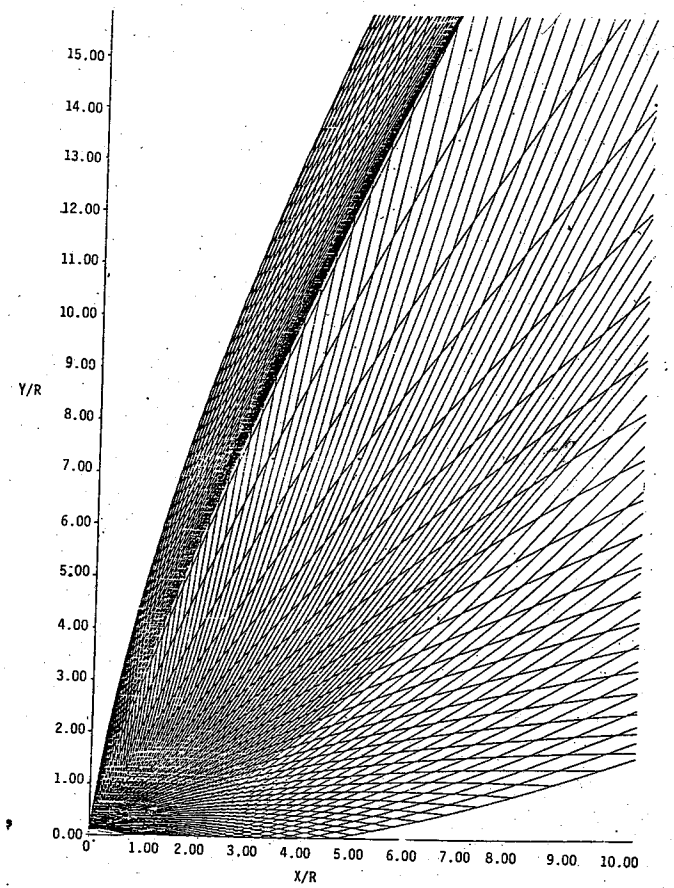

Figure 10. The characteristic net of plume exhausted by nozzle II.

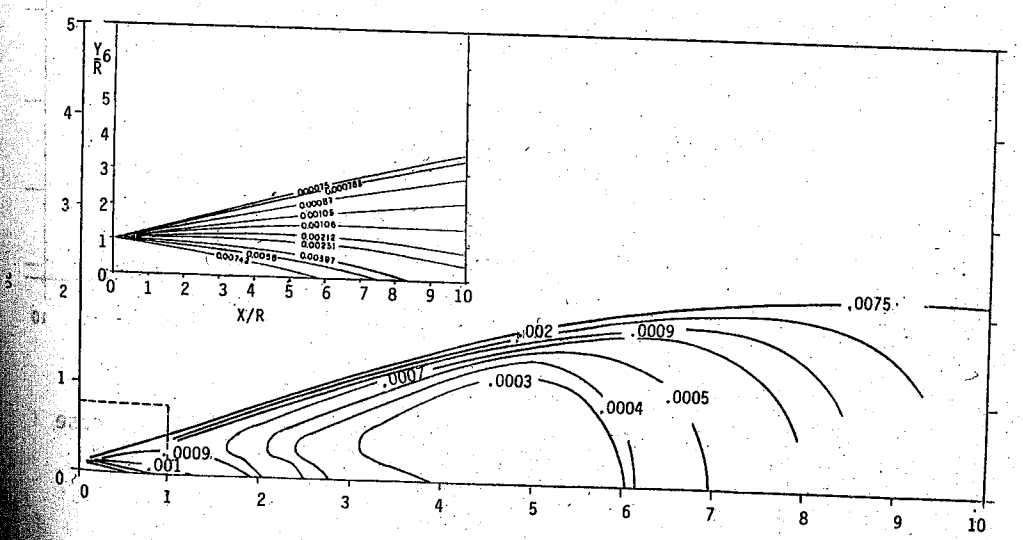

Figure 11. Pressure distribution of plume exhausted by nozzle I, case I, The diagram on the upper left corner is the plume flow field near nozzle in enlarged scale.

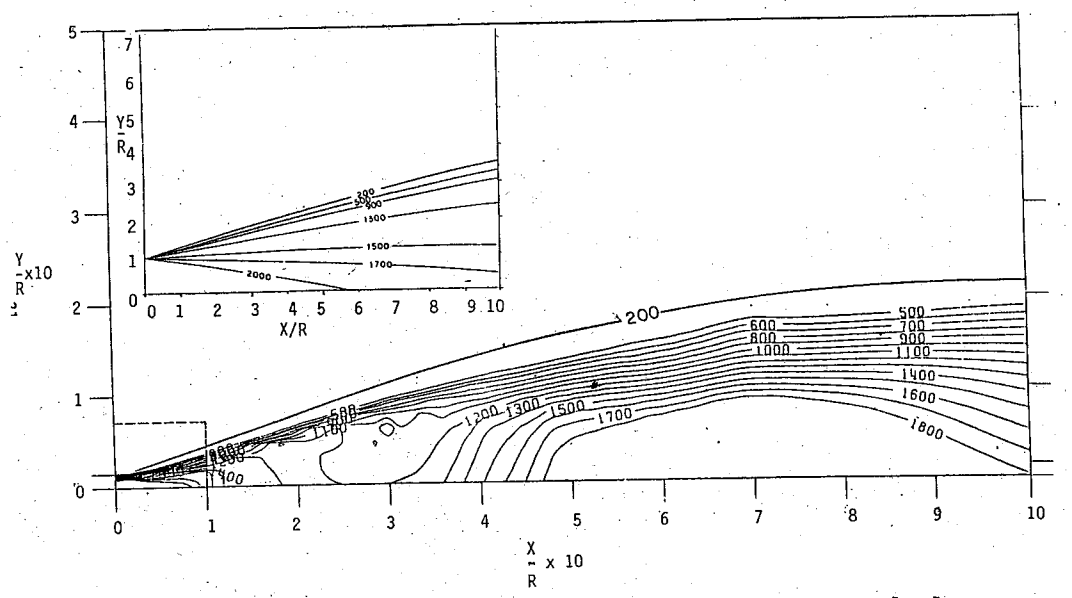

Figure 12. Temperature distribution of plume exhausted by nozzle I, case I. The diagram on the upper left corner is the plume flow field near nozzle in enlarged scale.

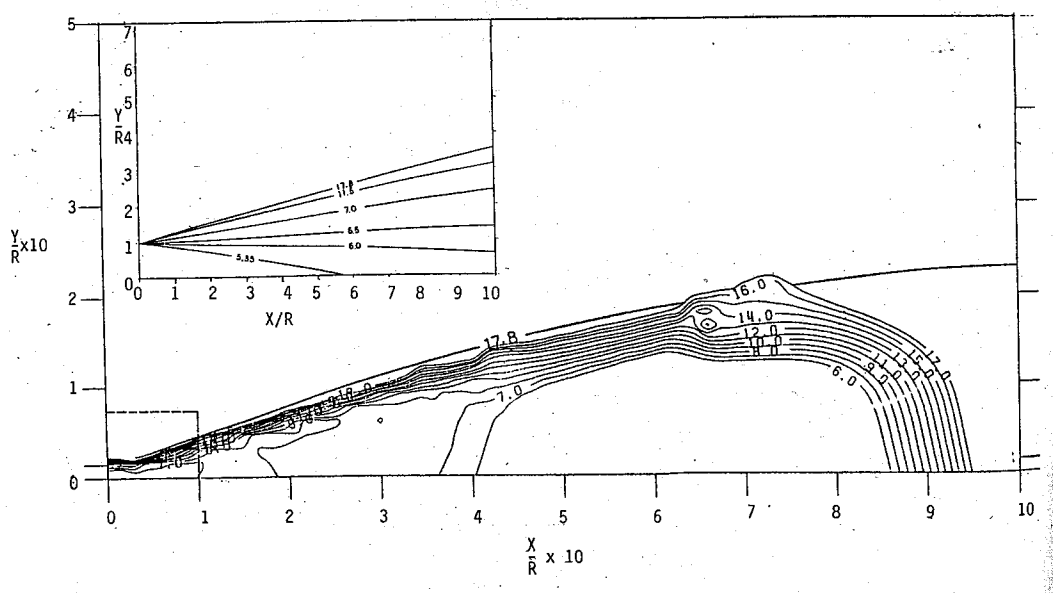

Figure 13. Mach number distribution of plume exhausted by nozzle I, case I. The diagram on the upper left corner is the plume flow field near nozzle in enlarged scale.

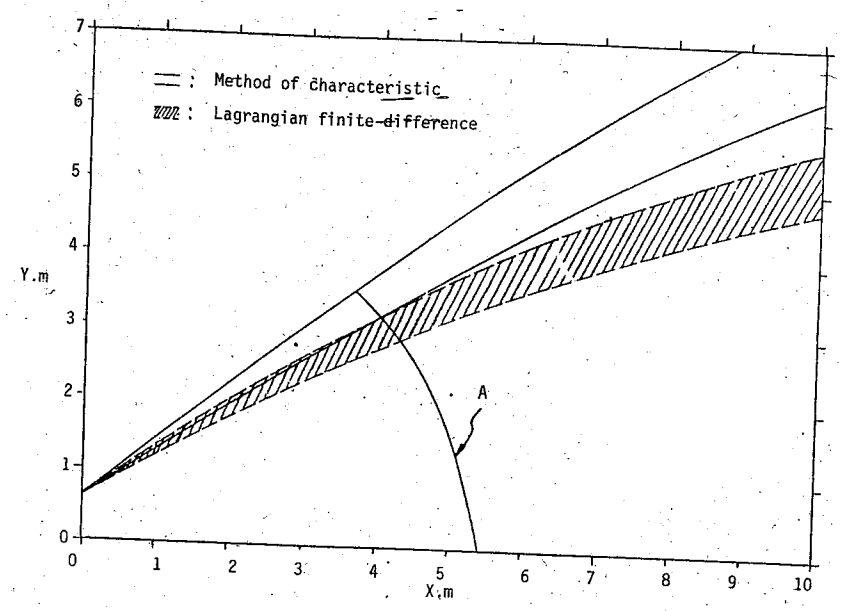

Figure 14. Thor plumes got by method of characteristics and Largrangian finite difference method (Tannehill).

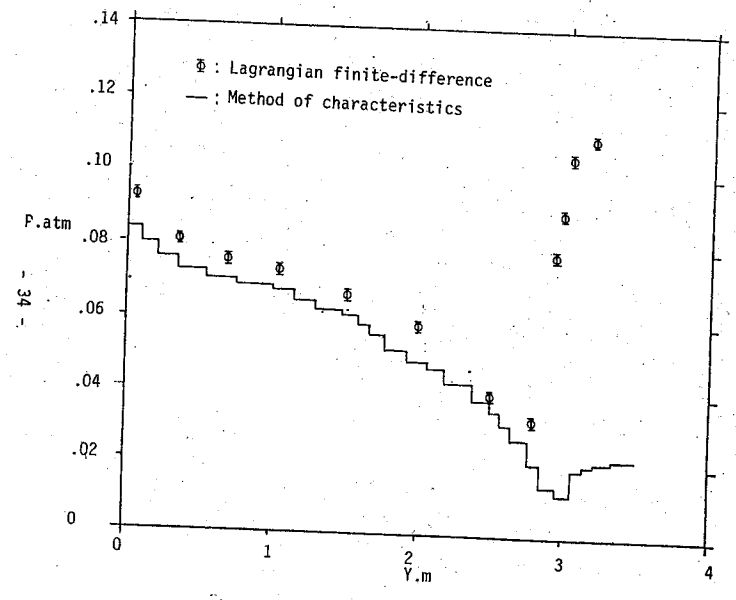

Figure 15. Pressure along surface A in Figure 14.

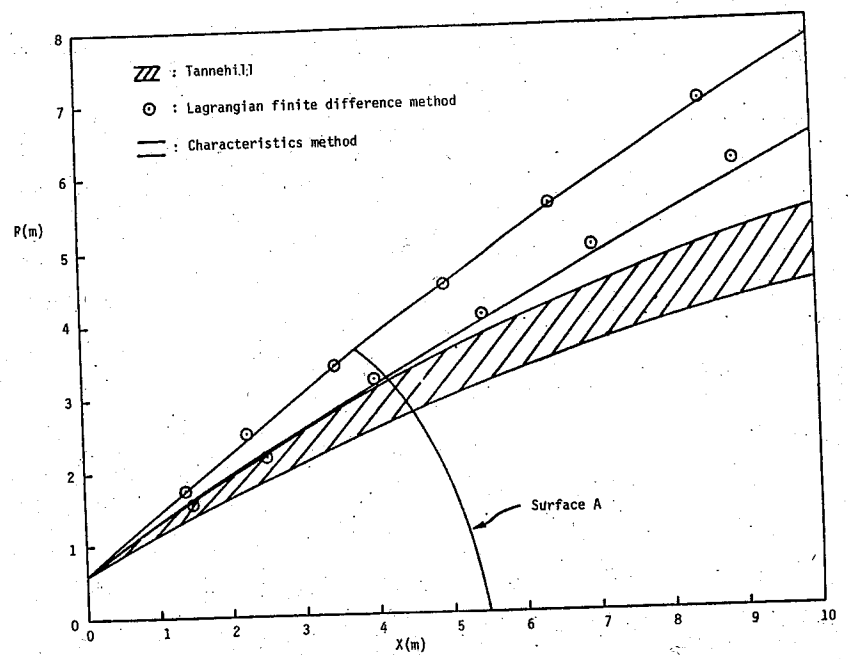

Figure 16. Thor plumes of three results got by different numerical techniques.

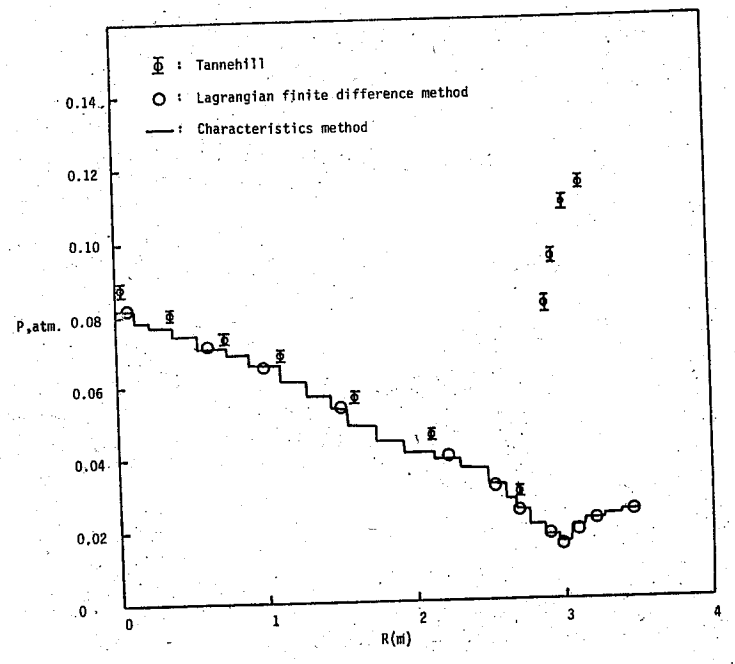

Figure 17. Pressure distributions along surface A in Figure 16 with three different numerical techniques.

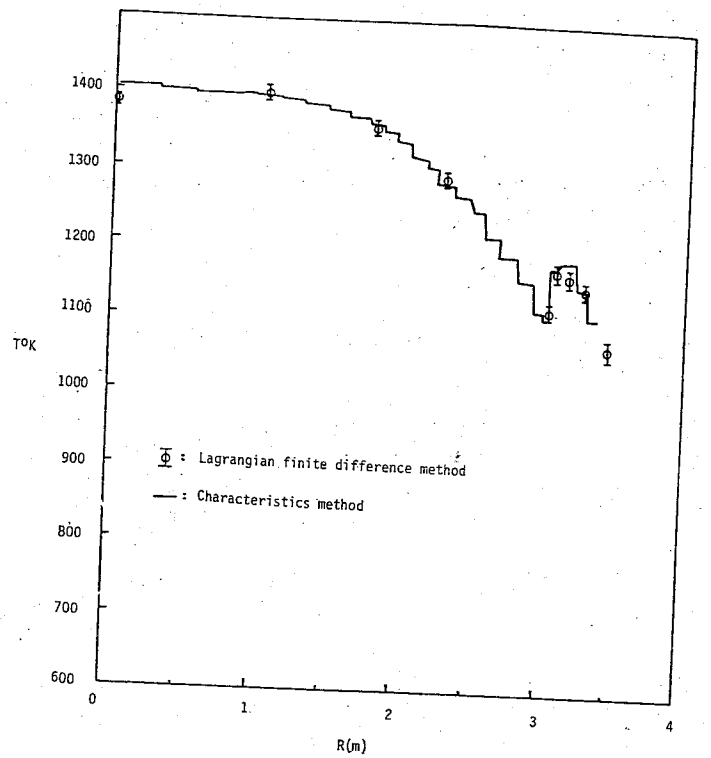

Figure 18. Temprature distributions along surface A in Figure 16 with two different numerical techniques.

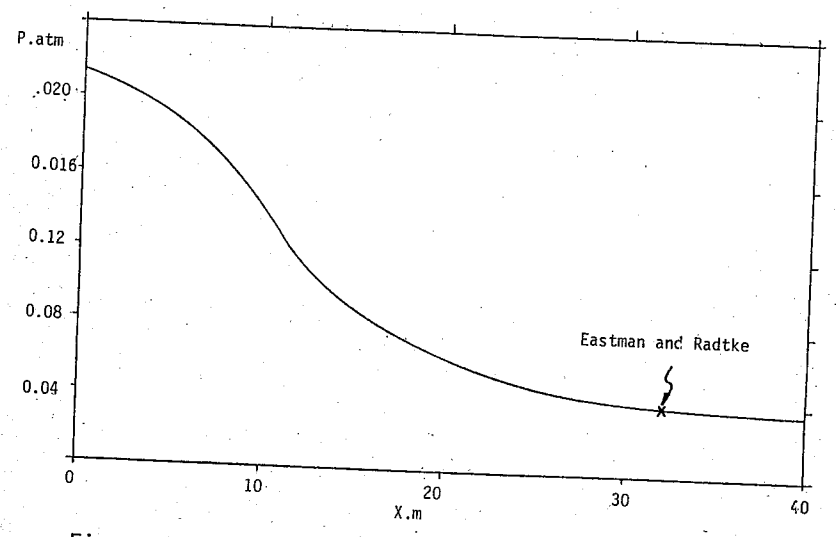

Figure 19. Pressure along jet shock of Thor plume. The location of normal shock is estimated by the method developed by Eastman by Radtke (1962).

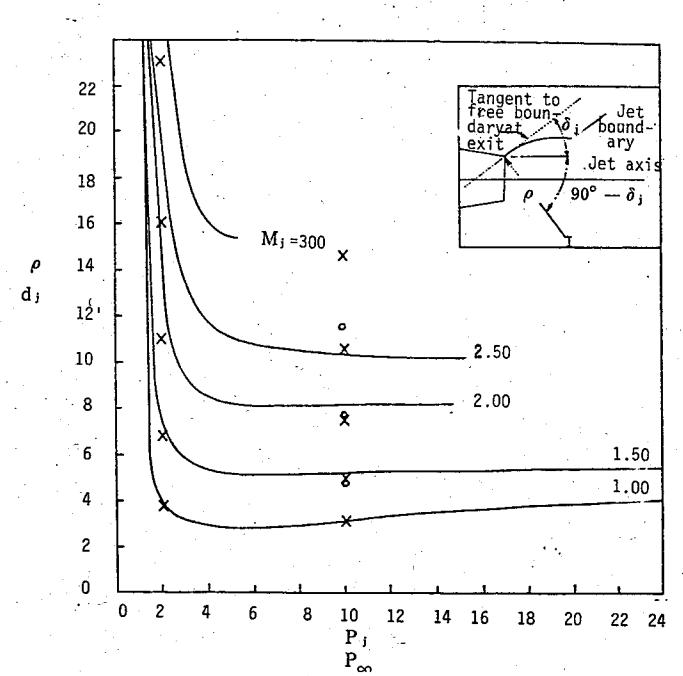

Figure 20. The curvatures of plume boundary at nozzle lip versus to pressure ratio and and Mach number.
—: Love (1); x; characteristics method; o : this study.

THEORETICAL STUDY OF ROCKET EXHAUST PLUMES PART II: FINITE-DIFFERENCE METHOD

L. C. Chien, C. T. Wang, W. J. Liang and F. L. Chen
Institute of Physics
Academia Sinica Nankang,
Taipei, Taiwan, R. O. C.

The rocket exhaust plumes under various altitudes are investigated by finite difference method. This numerical technique operates in the natural coordinates system and marches downstream from a surface of the nozzle exit. By this technique, the flow properties in rocket exhaust plumes are thus calculated and compared with those obtained by method of characteristics. The results obtained by the different numerical techniques are compared and agree excellently.

Finally, the flow properties along the axis and radial direction in the undistrubed region are investigated to aprove the assumption of undisturbed region in the calculating procedure is reasonable.

INTRODUCTION

The Lagrangian finite difference method and the method of characteristics are the two conventional computation methods used in investigating supersonic flow. In the method of characteristics solution, the shock is located by the coalesence of the characteristic lines of same family (1). The flowfield near the nozzle exit can be accurately predicted by the method (2). However, this numerical procedure exhibits computational difficulties for the cases of the low ambient pressure and high exit Mach number. Under these conditions, the characteristics of opposite family will eventually diverge unless the mesh size is refined, and the calculation can't be continued to great distances from the nozzle in an efficient manner.

In addition to the method of characteristics technique for computing inviscid plume flowfields, Boyton and Thomson (3) have recently devised a Lagrangian finite difference technique which can be applied to the solution of inviscid as well as viscous plume flowfields. In this method, the computation procedure was first based on determining the undisturbed, internal inviscid flow by expanding the test gases to a vacuum. Next, the initial locations of the jet shock and divi-

ding streamline are determined. Then, let the region between the jet shock and dividing streamline propagate into the previously calculated undisturbed flows.

Both the method of characteristics and the Lagrangian finite difference method required a considerable amount of effort and computation time. Some approximate methods are developed to predict the gross plume structure (4-6). These inviscid methods are excellent to determined the plume shape, jet shock location, and the internal pressure distribution.

In this study, the Lagrangian finite difference method are employed on solving the inviscid plume flow. The computation procedure was developed by the analysis of Boyton (3) for rocket exhaust plumes under various altitudes. The results obtained by this study are compared with those by method of characteristics (7). Also, the assumptions made for the computation procedure are approved by investigating that the structure of undisturbed region is independent with the boundary condition.

EQUATIONS AND COMPUTATIONAL PROCEDURE

The equations necessary to describe the rocket exhaust plume are shown in part one of this subject (7). For a two-dimensional or axially symmetric flow of an inviscid fluid, in which the gradients of pressure, temperature, and velocity are assumed much smaller in the direction of flow than normal to it, the equations simplified by using an order of magnitude analysis can be written in natural coordinate as follows:

Global continuity:

$$\frac{\partial}{\partial s}(\rho A u) = 0 \tag{1}$$

Streamwise momentum:

$$\rho u \frac{\partial u}{\partial s} + \frac{\partial p}{\partial s} = 0 \tag{2}$$

Normal momentum:

$$\rho u^2 \frac{\partial \theta}{\partial s} + \frac{\partial p}{\partial n} = 0 \tag{3}$$

Energy:

$$\rho u \frac{\partial}{\partial s}\left(h + \frac{1}{2} u^2\right) = 0 \tag{4}$$

State:

$$p = \rho \overline{R} T \tag{5}$$

Here s is the distance along a streamline, n the distance normal to it. These equations are transformed directly by equations (6) to (9) in PART I of this study. In those equations, by setting the normal pressure gradient term equal to zero, the boundary layer equations are obtained. These equations are similar to those derived by Boyton and Thomson (3) if relevant terms are included.

The Lagrangian finite-difference method developed by Boyton and Thomson (3) is employed on solving these equations. The flowfield is divided into a grid system which is composed of streamlines and the orthogonal surface (Figure 1). In the convention, the kth streamtube is bounded on the left by the kth streamline for an observor facing downstream, and the orthogonal surfaces are indexed ℓ. In each streamtube the properties are constant in the orthogonal direction but vary between orthogonal surfaces.

The start the calculation, data along an initial orthogonal surface are required. These data include the flow properties in the streamtubes, the positions, and flow angles of the dividing streamlines. In addition, the boundary conditions on either side of the flow must be specified. The curvature of the kth streamline at the initial ℓth surface is evaluated using normal momentum equation. This procedure is repeated for each streamline so that all streamtube areas, $A_{K,\ell+1}$ at the new surface can be calculated. Then, the remaining conservation equations can be integrated directly along the streamtubes in the usual manner. Each surface is calculated twice. For the second pass, average values between old and new surfaces are used. The computation marches downstream in this manner until the calculation in terminated.

This scheme is explicit and is therefore subject to instabilities unless the step size is limited. The stable step size is given as (3):

$$\delta S \leq \frac{1}{2} \delta n \left[\left(M^2 - 1 \right)^{-\frac{1}{2}} \right]^{-1} \tag{6}$$

The location of grid point at new orthogonal surface can be obtained by stepping downstream a stable stepping distance δS using a circular arc or a straight line to approximate the streamline curvature.

Rewritten in finite-difference form, equations (1) to (5) become:

Global continuity:

$$\dot{m}_k = \rho_{k,\ell}\, u_{k,\ell}\, A_{k,\ell} = \rho_{k,\ell+1}\, u_{k,\ell+1}\, A_{k,\ell+1} \tag{7}$$

Streamwise momentum:

$$\dot{m}_k \left(u_{k,\ell+1} - u_{k,\ell} \right) + \overline{A}_k \left(P_{k,\ell+1} - P_{k,\ell} \right) = 0 \tag{8}$$

Normal momentum:

$$-\left[\frac{\partial \theta}{\partial S}\right]_{k,\ell} = \left[\frac{4\,(2\pi\gamma_{k,\ell})^j}{u_{k,\ell} + u_{k+1,\ell}}\right]\left[\frac{P_{k+1,\ell} - P_{k,\ell}}{\dot{m}_k + \dot{m}_{k+1}}\right] \tag{9}$$

Energy:

$$\dot{m}_k \left(h_{k,\ell+1} - h_{k,\ell} + \frac{1}{2} u^2_{k,\ell+1} - \frac{1}{2} u^2_{k,\ell} \right) = 0 \tag{10}$$

State:

$$P_{k,\ell+1} = \rho_{k,\ell+1}\, \overline{R}\, T_{k,\ell+1} \tag{11}$$

where j is 0 for planar flow, 1 for axisymmetric flow.

With $A_{K,\ell+1}$ calculated as stated before, there are 5 unknow $P_{K,\ell+1}$, $T_{K,\ell+}$, $\rho_{K,\ell+}$, $u_{K,\ell+1}$ and $h_{K,\ell+1}$ can be got by solving equations (7) to (11) simultaneously.

BOUNDARY CONDITIONS

The natural coordinate system employed in this paper allows several different types of boundary conditions to be easily incorporated. First, the symmetry axis can be taken as a streamline. Likewise, dividing streamlines can be used directly if the outside ambient pressure of Newtonian impact pressure is specified

$$P_b = P_\infty + \rho_\infty u^2{}_\infty \sin^2 \left(\theta_b - \theta_\infty \right) \tag{12}$$

Shocks in the flowfield are calculated in a discontinuous way. That is, the undisturbed region is calculated initially by exhausting flow into vacuum and then the shocked region is computed using the shock as a boundary discontinuity which propagates into the previously calculated undisturbed region. The shock angle and conditions downstream of the shock can be obtained by requiring that the shock turn the flow parallel to the nearest streamline being carried in the calculation. The shock angle σ can be determined from (8).

$$\zeta^3 + b\zeta^2 + c\zeta + d = 0 \tag{13}$$

where

$$\zeta = \sin^2\sigma$$

$$b = -\frac{\left(M^2_\infty + 2 \right)}{M^2_\infty} - \sin^2\delta'$$

$$c = \frac{2M^2_\infty + 1}{M^4_\infty} + \left[\frac{(\gamma+1)^2}{M^4_\infty} + \frac{\gamma+1}{M^2_\infty}\right]\gamma \sin\delta' \tag{14}$$

$$d = -\frac{\cos^2\delta'}{M^4_\infty}$$

using the Newton-Raphson method. The pressure and temperature downstream of the shock are then obtained from

$$P_s = P_\infty \left[\frac{2\gamma M^2_\infty \zeta - (\gamma - 1)}{\gamma + 1}\right] \tag{15}$$

and

$$T_s = T_\infty \left[\frac{P_s}{P_\infty}\right] \frac{(\gamma-1)M^2_\infty \zeta + 2}{(\gamma+1)M^2_\infty \zeta} \tag{16}$$

RESULTS AND DISCUSSION

In this section, various comparisons are made between the results obtained using the Lagrangian finite difference method and the method of characteristics of PART I (7). By assuming inviscid and no chemical reaction, the rocket exhaust plumes under various altitudes are calculated. In addition, the exhaust gas are not allowed to mix with the air and the position of dividing streamline is determined by assuming that the pressure acting on the outside of the dividing streamline is the newtonian shocklayer pressure, equation (12).

In computing the nozzle exhaust plume flowfield, the exhaust flow must be first expanded into vacuum. This calculation is necessary in order to describe the region bounded by the jet shock and the Mach disc. This region is called undisturbed region.

Because very low pressures near the nozzle lips will cause the streamtube areas

to increase greatly, a large number of small streamtubes must be placed near the nozzle lip to initiate the calculation. Some of the streamlines and orthogonal surfaces for this expansion are shown in Figure 2. There are 43 initial streamtubes on the exhaust surface. The calculating steps downward uniformly near the initial surface and increases the step distance as goes far away. The pressure and temperature distributions in this vacuum plume are shown in Figure 3 and 4 respectively. It is found that the isobars and isothermal lines are spread out from inner region gradually. In other words, the boundary effect propagates into the flow region step by step and will decay to form the undisturbed region.

The next step is to locate the initial positions of the jet shock and dividing streamline. In the present calculation, the initial jet shock and dividing streamline locations were obtained using the characteristics method program developed in PART I (7). This is a very convenient and accurate method for locating these two locations (Figure 20 in PART I). Once the jet shock is located, the jet shock layer can be calculated letting the jet shock propagate into the previously calculated undisturbed vacuum plume. The flow properties in the jet shock layer far downstream were not very dependent on the initial conditions (8). The location of the dividing streamline and jet shock determined by the method of characteristics and Lagrangian finite difference method are shown in Figure 5 for comparison with satisfactory agreement. The reason for the uncoincidence between the calculated results and the results of Tannehill (9) is explained in PART I in detail. The pressure distribution along surface A in Figure 5 is shown in Figure 6. Also shown is the temperature distribution in Figure 7.

To get more advanced investigate, nozzle exhaust plumes under various altitude are calculated by the method of characteristics and the Lagrangian finite-difference method. Three cases used in PART I are adapted here compare the results of these two numerical techniques (Figure 8). The invicid plumes' profile got by these two numerical techniques are shown excellent agreement in comparison. But there exists obvious unccincidence between these results and those of irrotational flowfield. It is shown here that the more complicate calculation in rotational flowfield in this study results in the more accurate results than those of irrotational flow-

field calculation, which is with less iteration.

The structures of these plume flowfields are also investigated here. Figure 9 to Figure 11 show the pressure, temperature and Mach number distributions along the vertical line at X/R = 5. On these figures, it is found that these properties in the undisturbed region almost coincide each other without any effect due to the boundary variation. Reaching near the boundaries, these properties were induced to conform with the boundary conditions. It is found in these figures the property distributions were departed near the plume boundaries. For investigating the undisturbed region in detail, the property distributions along the axis of the plume were investigated in Figure 12 to 14. Independent with the various ambient conditions, the property distribution of plumes along the axis coincide each other as same as those along vertical line in the undisturbed region. Also shown a phenomenum is that the properties along axis in the Mach cone region. It is the result of the flow exhausted from a circular arc nozzle (2).

CONCLUSION

The Lagrangian Finite Difference Method is employed in investigating the nozzle exhaust plumes. The results are used to compare with those got by method of characteristics developed in PART I of this subject. After study from different point of views, the results got by these two numerical techniques are found in nice comparison. this is due primary to the calculating procedures of these two numerical techniques are developed by physical meaning. Furthermore, the assumptions of the undisturbed region and the shock layer are shown reasonable by the calculated results.

Unfortunately, there is no experimental data to the knowledge of the authors with which the rocket exhaust plumes under various conditions can be compared. This is due to the difficulties in setting up the test apparatus, a rocket nozzle and external air stream.

REFERENCES

(1) Love, E. S., Grigsby, C. E., Lee, L. P., and Woodling, M. T. Experimental and

theoretical studies of axisymmetric free jets. United States National Aeronautics and Space Administration Technical Roport R-6, 1959.

(2) Eastman, D. W. and Radtke, L. P. Two-dimensional or axially symmetric real gas flows by the method of characteristics. Boeing Company Document D2-10599, 1962.

(3) Boynton, F. P. and Thomson, A. Numerical Computation of steady supersonic two-dimensional gas flow in natural coordinates. Journal of Computational Physics 3: 379-398, 1969.

(4) Albini, F. A. Approximate computation of underexpanded jet structure. American Institute of Aeronautics and Astronautics Journal 3: 1535-1537, 1965.

(5) Hubbard, E. W. Approximate calcuation of highly underexpanded jets. American Institute of Aeronautics and Astronautics Journal 4:1877-1879, 1966.

(6) Luce, R. W. and Jarvinen, P. O. An approximate method for predicting plume sizes for nozzle flow into still air. American Institute of Aeronautics and Astronautics Journal 6: 182-183, 1968.

(7) Chien, L. C., C. T. Wang, W. J. Liang and P. L. Chen. Theoretical Study of Rocket Exhaust Plumes. PART I: Characteristics Method Annual Report of Institute of Physics, Academia Sinica Mechanical Engineering. Vol. 13, 1983.

(8) Tannehill, J. C. Numerical Computation of Intermediate Altitude Rocket Exhaust Plumes, Including Nonequilibrium Chemical Reactions and Diffusion. Ph. D. Dissertation, Iowa State University, 1969.

(9) Amer Aeronautical Laboratory. Amer Research Staff. Equations, tables, and charts for compressible flow. United State National Advisory Committee for Aeronautics Report 1135, 1953.

NOMENCLATURE

A : Area of streamtube

h : Enthalpy

M : Mach number

$\dot{m}$: Mass flow rate

n : Coordinate in normal direction

P : Pressure

$\bar{R}$: Gas constant

T : Temperature

s : Coordinate in streamwise direction

S : Stable step size

r : Radius

u : Velocity in streamwise direction

ρ : Density

θ : Flow angle

δ' : Shock deflection angle

γ : Ratio of specific heats

ζ : $\sin^2 \sigma$, equation (13)

σ : Shock angle

INDEX

∞ : Freestream condition

b : Boundary condition

ℓ : Condition in ℓh surface

s : Condition behind shock

j : 0 for plannar flow, 1 for axisymmetric flow

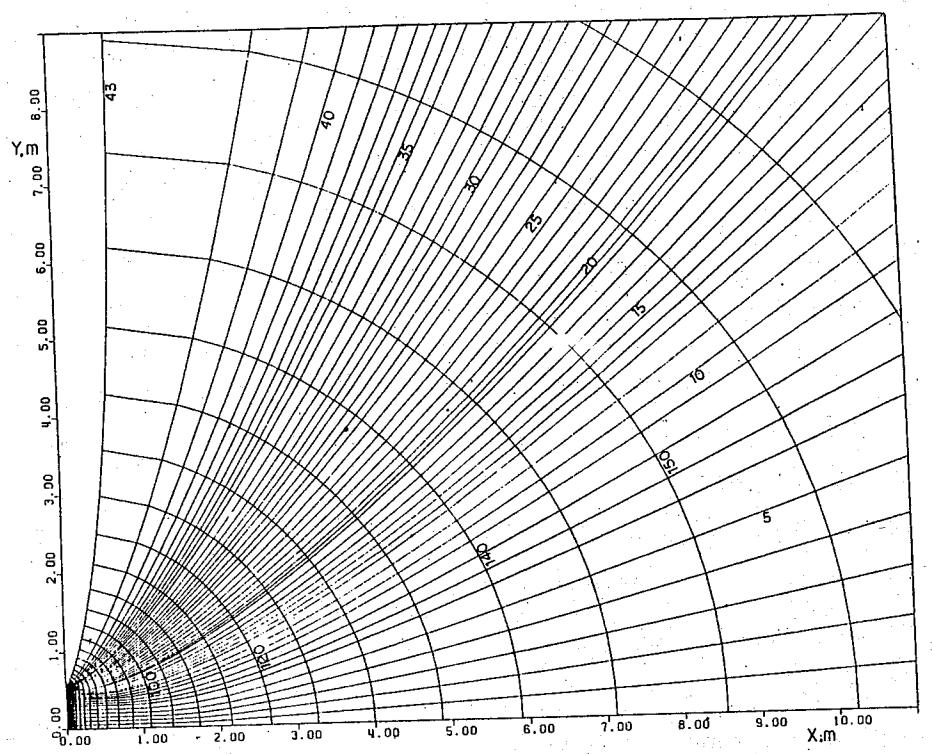

Figure 2. The streamtubes of vaccum plume.

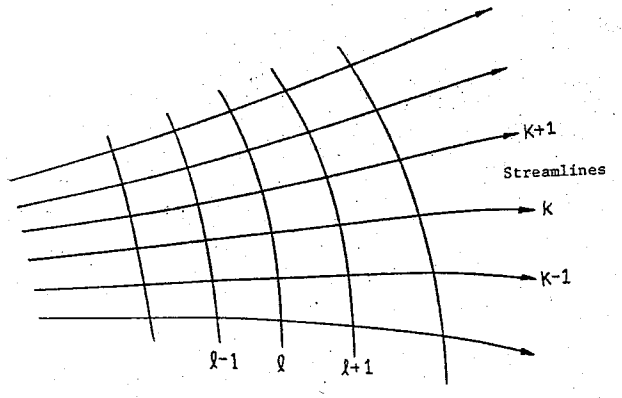

Orthogonal surfaces

Figure 1. Lagrangian finite difference mesh.

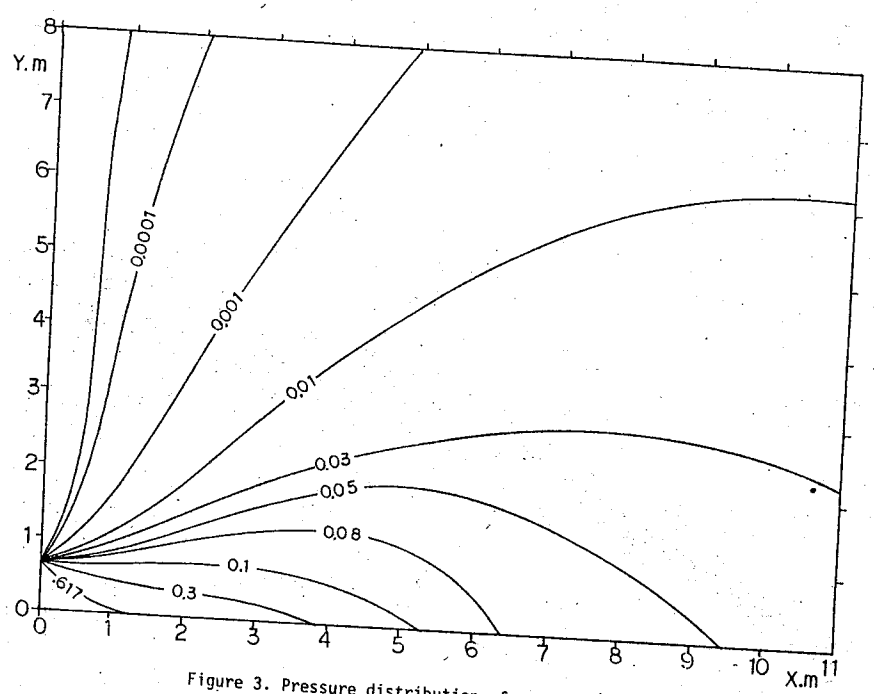

Figure 3. Pressure distribution of vaccum plume (atm).

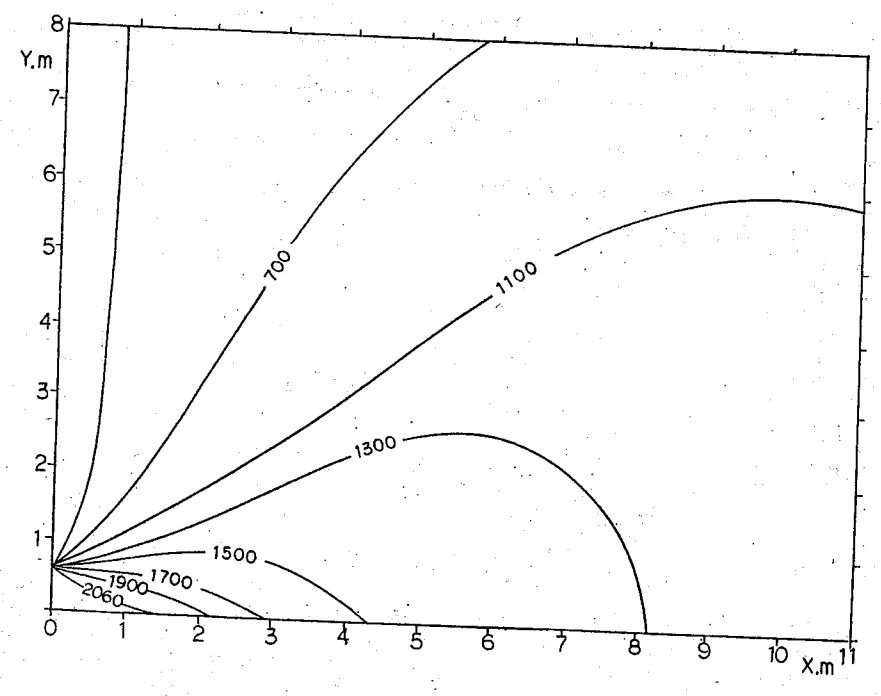

Figure 4. Temperature distribution of vaccum plume (^{o}K).

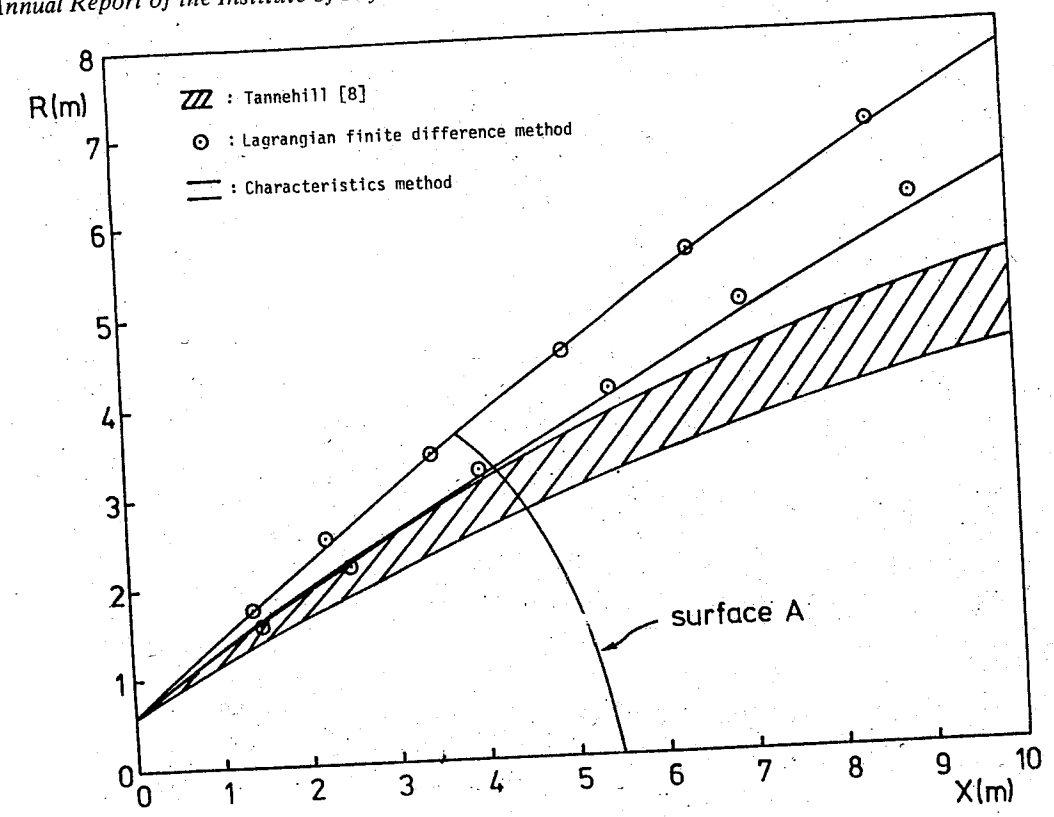

Figure 5. Profiles of Thor exhaust plume. Comparison among the results got by Lagrangian finite difference metnod, characteristics method, and those of Tannehill [8].

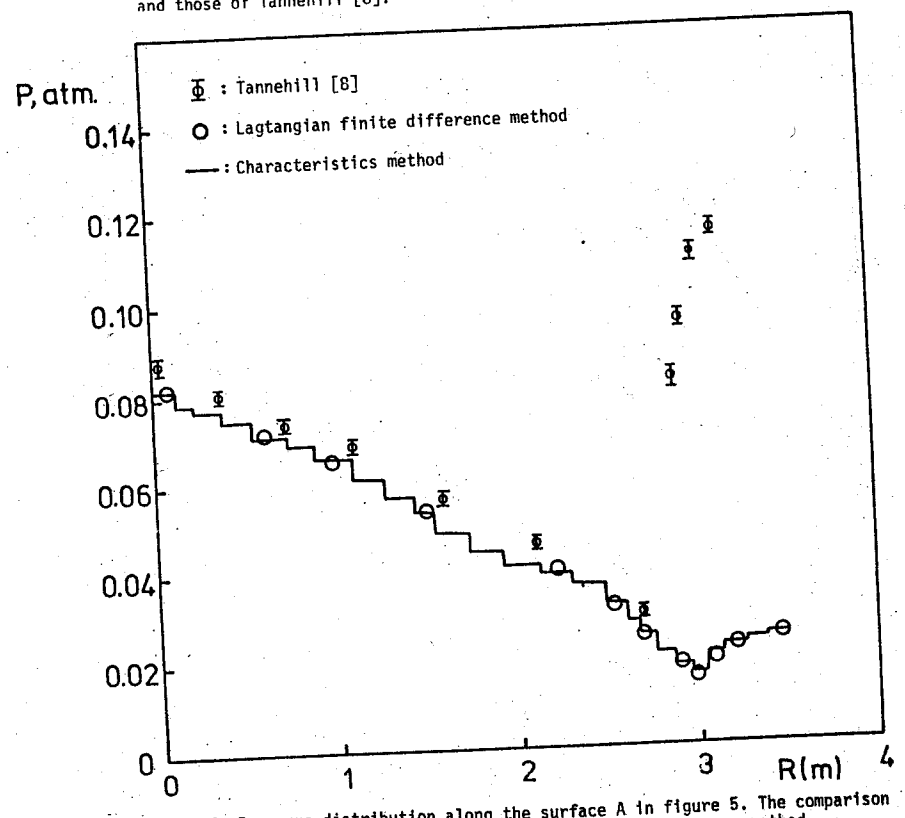

Figure 6. Pressure distribution along the surface A in figure 5. The comparison among the results got by Lagrangian finite difference method, characteristics method, and those of Tannehill [8].

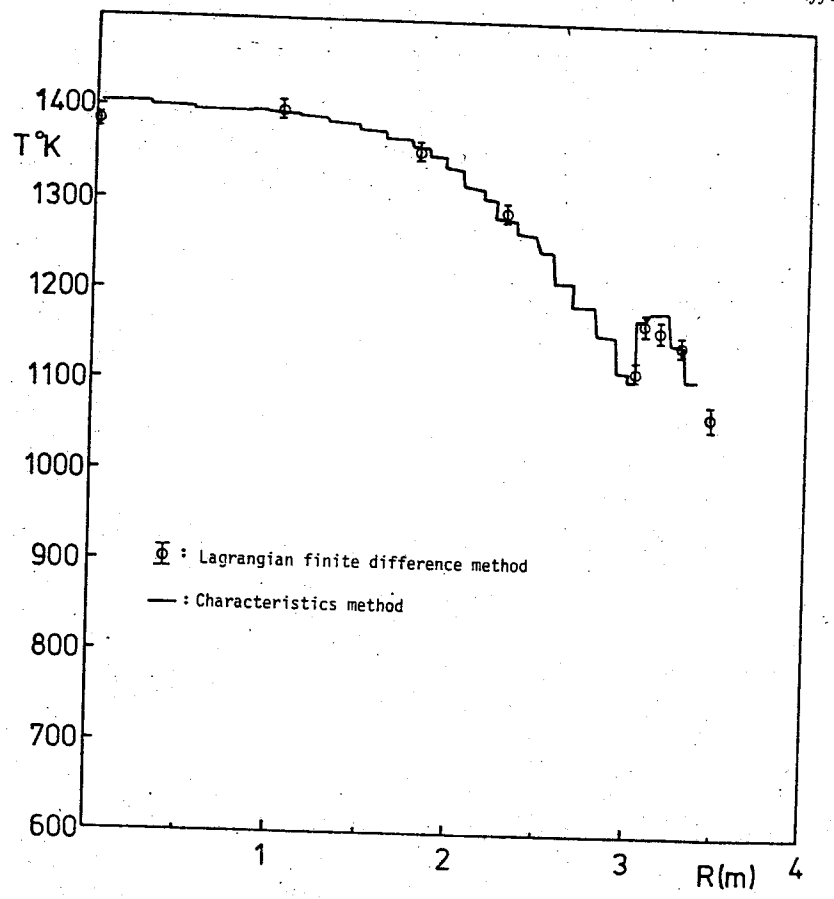

Figure 7. Temperature distribution along surface A in figure 5. The comparison between the results got by Lagrangian finite difference method and characteristic method.

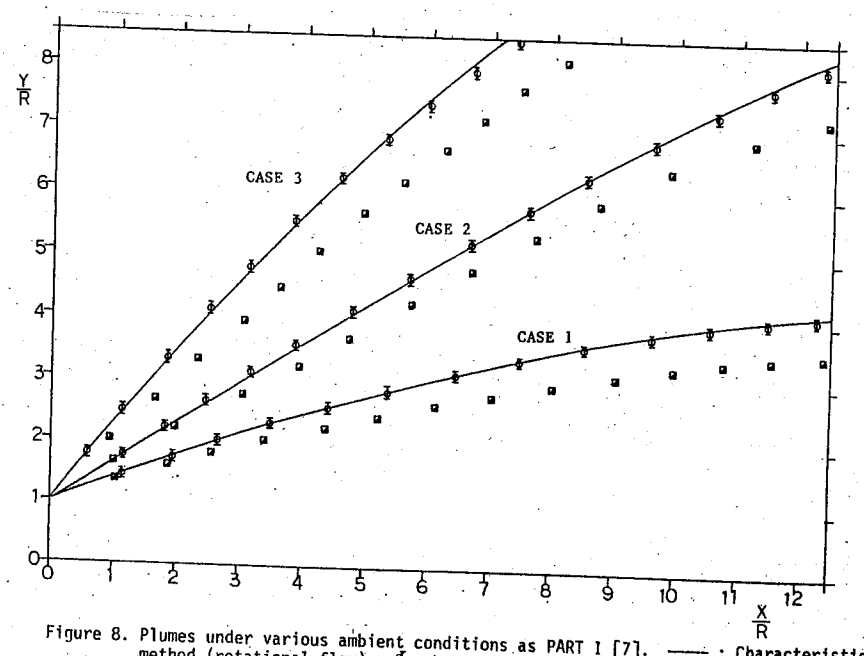

Figure 8. Plumes under various ambient conditions as PART I [7]. —— : Characteristics method (rotational flow); Ø : Lagrangian finite difference method; ◪ : Characteristics method (irrotational flow).

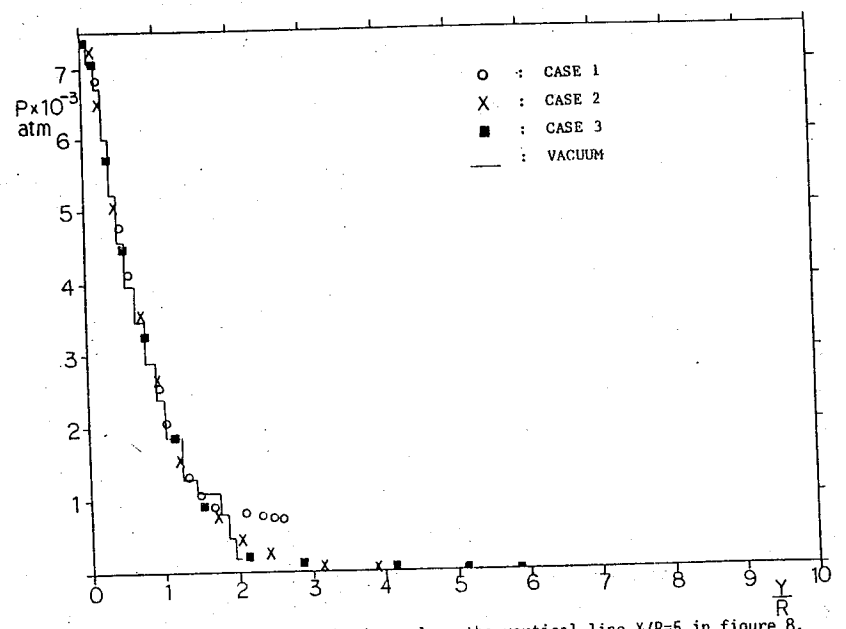

Figure 9. Pressure distributions along the vertical line X/R=5 in figure 8.

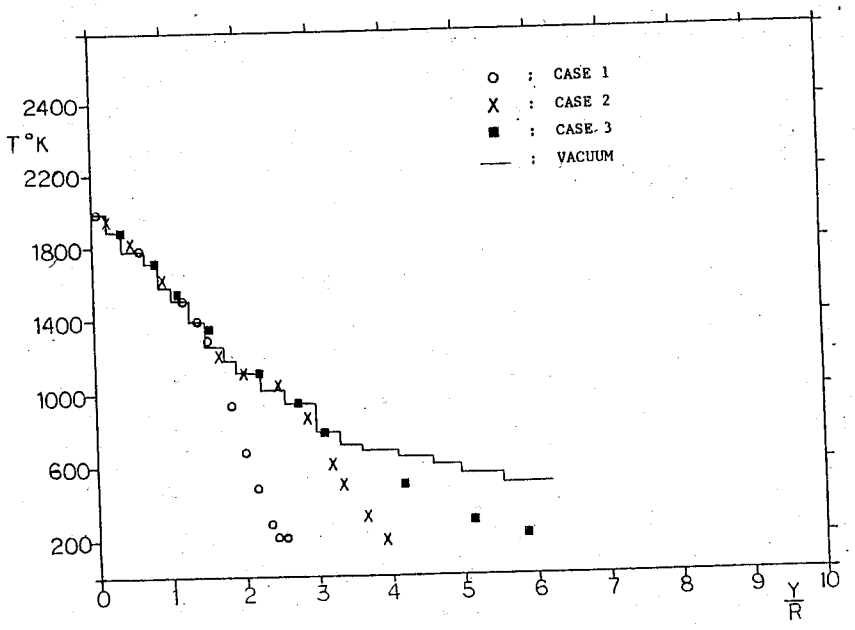

Figure 10. Temperature distributions along the vertical line X/R=5 in figure 8.

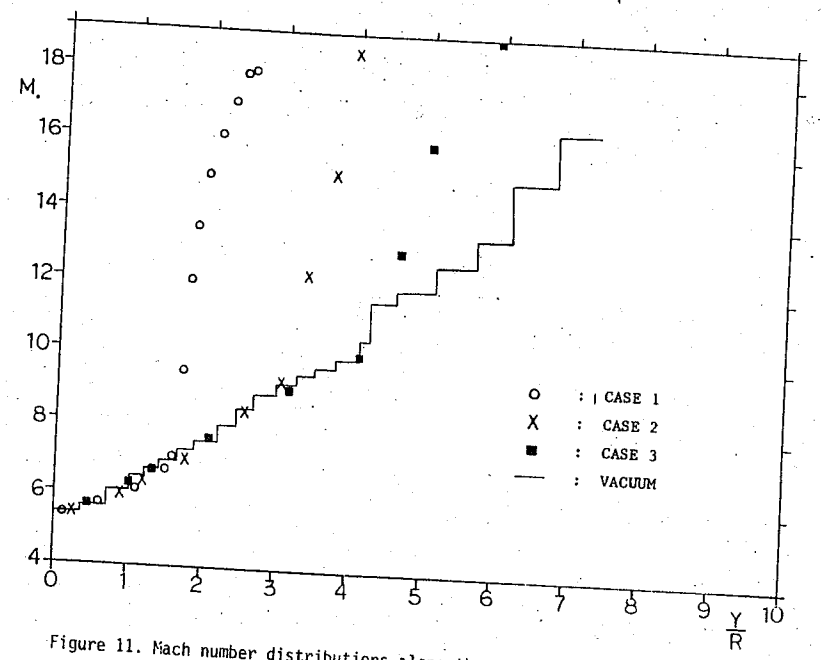

Figure 11. Mach number distributions along the vertical line X/R=5 in figure 8.

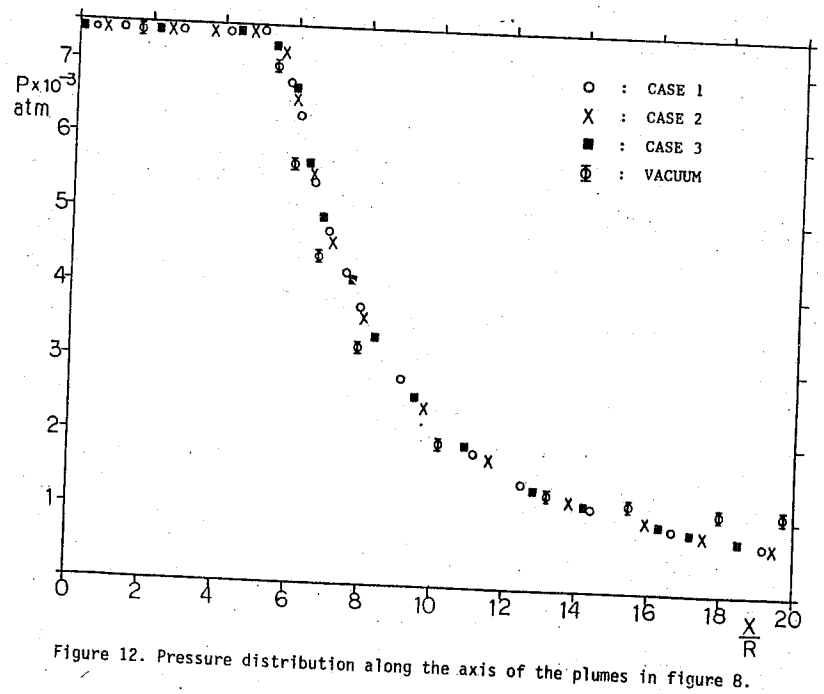

Figure 12. Pressure distribution along the axis of the plumes in figure 8.

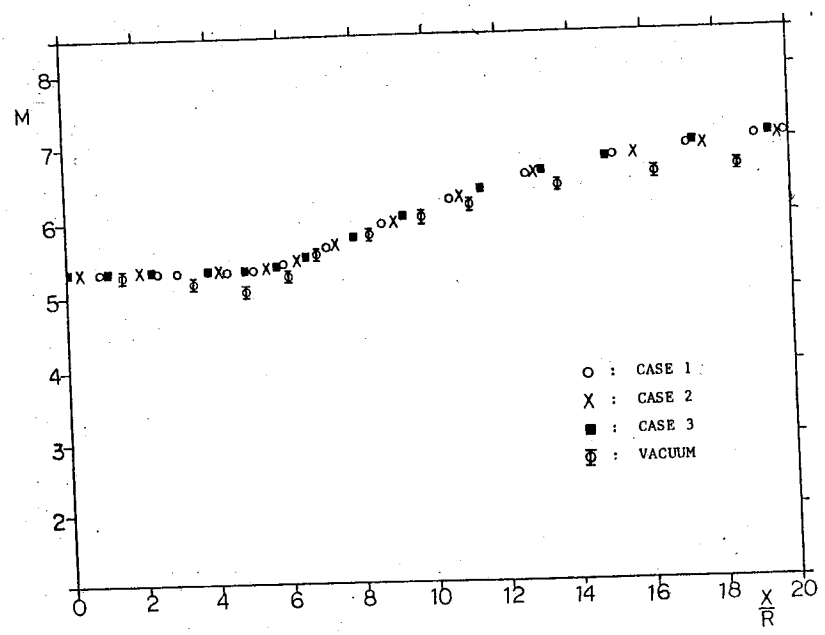

Figure 14. Mach number distributions along the axis of the plumes in figure 8.

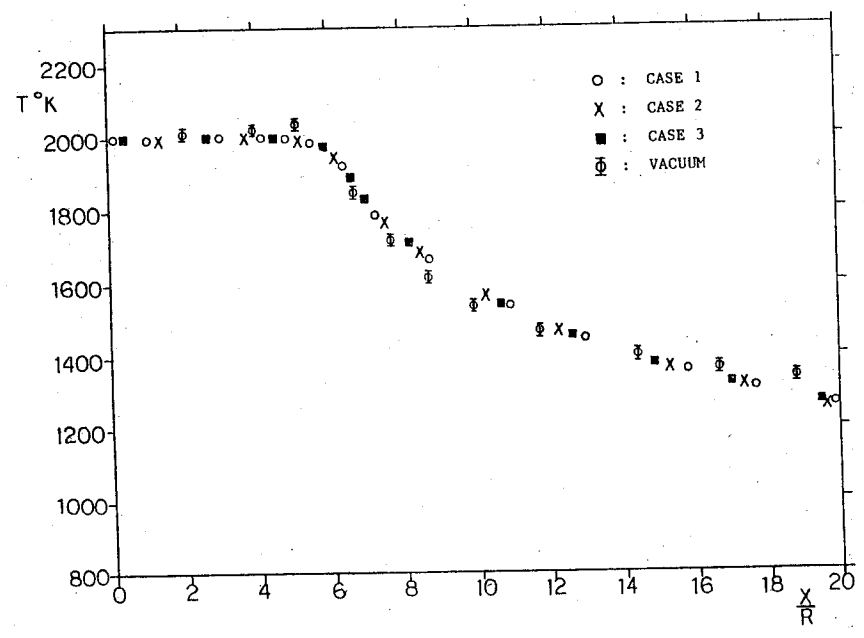

Figure 13. Temperature distribution along the axis of the plumes in figure 8.

THEORETICAL STUDY OF ROCKET EXHAUST PLUMES PART III: VISCOUS EFFECT

L. C. Chien, C. T. Wang, W. J. Liang and F. L. Chen
Institute of Physics
Academia Sinica, Nankang,
Taipei, Taiwan, R. O. C.

Due to the strong interaction between the rocket exhaust plume and the supersonic ambient flow, the viscous effect should not be ignored when the mixing layer become dominate the entire plume flow. The Lagrangian finite-difference scheme is employed here on solving the equations which include viscous terms. To investigate the viscous effect on the plume flow, the Thor plumes are calculated for both laminar and turbulent flows to compare with that for inviscid flow. It is found that the viscous phenomena dominate the plume flow when the shock layer width become as large as the diameter of nozzle exit.

INTRODUCTION

The inviscid calculations described in PART I and II are excellent for predicting the plume shape, jet shock location, and the internal flow structure. However since the air is not allowed to mix with the rocket exhaust flow, the viscous transport effects are totally ignored. The viscous layer due to the mixing of rocket exhaust flow and ambient supersonic flow will increase in size until it completely dominates the entire flowfield. The viscous terms of the governing equations for supersonic plume flowfield will become the same order of magnitude as other terms in those equations when the viscous layer size becomes as large as the diameter of the nozzle exit surface. Under this circumstance, the viscous effect should not be ignored any more.

To consider the strongly viscous transport effect on the plum flow, several investigators (1-3) have used the standard boundary layer equations to represent the mixing layer in the plume. However, when using the boundary layer equations to govern the mixing layer, several problems immediately become apparent. First of all, this representation is valid only in the region near the nozzle exit or far from the nozzle exit where the mixing layer is very thin or fully developed, respectively. The second drawback is that a zero radial pressure gradient is assumed.

This turns out to be a poor approximation for the turbulent mixing layer.

Still, the major drawback in using conventional boundary layer equations to represent the mixing layer in the plume lies in the problem of determining the coupling effects between the two surrounding inviscid flows and the mixing layer. Iteration techniques must be employed which are based on the boundary layer displacement thickness. This makes the computation very difficult.

A scheme developed by Thomson (4) and Boynton (5) used new equations which were derived from the Navier-Stokes equations using an order of magnitude analysis in which the gradients of pressure, temperature, and velocity are assumed much smaller in the direction of flow than in a direction normal to the flow. The resulting equations are somewhat similar to the boundary layer equations but include a normal momentum equation.

Two techniques have been proposed to solve this set of equations. The first technique (6, 7) uses a modified method of characteristics procedure in which viscous forcing terms are used. The second technique is a Lagrangian finite-difference procedure which has been applied by Thomson and Boynton (8) principally to the solution of high altitude rocket exhaust plumes. This procedure is more efficient than the previously mentioned modified method of characteristics procedure because in it the characteristic mesh becomes very compressed at high Mach numbers.

In the Lagrangian finite-difference scheme, the flowfield was described into a grid consisting of streamtubes and the surfaces orthogonal to them. Initially, the vacuum plume was calculated to be the boundary conditions of the following computation. With the initial locations of jet shock and dividing streamling determined by method of characteristics, the viscous layer bounded by jet shock and dividing streamline propagates into the previously calculated undisturbed vacuum plume. The entire viscous layer can be solved without iteration using this method.

Due to complicated structure of the plume flowfield, there exists no scheme which can be employed on solving the entire plume flowfield. A modular approach developed by Dash et al (9) has been implemented permitting variations in the mode of operation to accommodate the changing environment. Via this approach, the model can be operated in modes encompassing those available in all current plume models.

The entire computation procedures are built around the selt-contained plume modules discussed in reference 9.

In the present study, the Lagrangian finite-difference scheme is employed here on solving the viscous mixing layer of the plume flowfield. The governing equations derived by Edelman and Weilerstein (10) which were shown in PART I (11) are solved without considering the concentration diffusion. The larminar transport is assumed initially in order to simplify the derivation. After the final forms of the larminar equations are obtained, they are transformed to their turbulent counterparts. The Thor plume was calculated for both the laminar and turbulent flow to compare with the inviscid plume. The pressure and temperature distributions are also investigated for the viscous effect on the plume.

ANALYTICAL DEVELOPMENT

The general equations for the steady flow of a reacting mixture of perfect gas derived by Edelman and Weilderstein (10) are shown in PART I (11). In the following analysis, laminar transport is assumed initially to simplify the derivation. After the final form of the larminar equations are obtained, they are transformed to their turbulent counterparts by the conventional turbulent boundary layer Theory (12).

The general equations can be rewritten in natural coordinate system by order of magnitude analysis assumed the gradient of pressure, temperature, velocity and species concentrations are substantially smaller in the direction of flow than in a direction normal to the flow. After derived by Tannehill (12) and assumed for the non-reacting flow in this study, these equations became as follow:

Global continuity:

$$\frac{\partial}{\partial s}(\rho A u) = 0 \tag{1}$$

Streamwise momentum:

$$\rho u \frac{\partial u}{\partial s} + \frac{\partial p}{\partial s} = \frac{1}{r j} \frac{\partial}{\partial n}\left[r^{j} \mu \frac{u}{n} \right] \tag{2}$$

Normal momentum:

$$\rho u^2 \frac{\partial \theta}{\partial s} + \frac{\partial p}{\partial n} = 0 \tag{3}$$

Energy:

$$\rho u \frac{\partial H}{\partial s} = \frac{1}{r^j} \frac{\partial}{\partial n} \left[r^j \frac{\mu}{Pr} \frac{\partial H}{\partial n} \right] + \frac{1}{r^j} \frac{\partial}{\partial n} \left[r^j \left(1 - \frac{1}{Pr} \right) \mu u \frac{\partial u}{\partial n} \right] \tag{4}$$

State:

$$P = \rho \bar{R} T \tag{5}$$

where j = 0 is for plannar flow, j = 1 for axisymmitric flow. Equations (1) to (5, are suitable to describe the two-dimensional or axially symmetric flow of a non-reacting, viscous, heat-conducting fluid without considering the mass diffusion. Here, the total enthalpy H is function of temperature and velocity. So that, there are five equations for five unknowns once the streamlines have been located and the streamtube areas defined.

The present equations (1 to 5) can be rewritten for the turbulent flow with the turbulent counterparts replacing the relevant variables. These equations are transformed into turbulent equations by an intuitive argument which uses information gained from convectional turbulent boundary layer theory. According to applying on a turbulent mixing layer, the resulting turbulent boundary layer equations, in terms of time-averaged flow variables, are:

Global continuity:

$$\frac{\partial}{\partial s} (\rho u A) = 0 \tag{6}$$

Streamwise momentum:

$$\rho u \frac{\partial u}{\partial s} + \frac{\partial P}{\partial s} = \frac{1}{r^j} \frac{\partial}{\partial n} \left[r^j \varepsilon_v \frac{\partial u}{\partial n} \right] \tag{7}$$

Normal momentum:

$$\rho u^2 \frac{\partial \theta}{\partial s} + \frac{\partial P}{\partial n} = 0 \tag{8}$$

Energy:

$$\rho u \frac{\partial H}{\partial s} = \frac{1}{r^j} \frac{\partial}{\partial n} \left[r^j \frac{\varepsilon_v}{Pr_t} \frac{\partial H}{\partial n} \right] + \frac{1}{r^j} \frac{\partial}{\partial n} \left[r^j \left(1 - \frac{1}{Pr_t} \right) \varepsilon_v u \frac{\partial u}{\partial n} \right] \tag{9}$$

State;

$$P = \rho \bar{R} T \tag{10}$$

where ε_v and Pr_t are the eddy viscosity and turbulent Prandtl number, respectively. In addition, note that all variables are now time-averaged quantities. For the special case of compressible turbulent mixing most investigators modified the incompressible eddy viscosity expressions of Prandtl (13) either by performing a transformation which relates the compressible flow to an incompressible flow or by including a representive density (14). In present study, the latter form of modification is used in an expression proposed by Edelman and Fortune (15). This expression, which is constant across the width of the mixing layer, is written as

$$\varepsilon_v = \frac{\Delta Y}{C} \left[(\rho u)_{max} - (\rho u)_{min} \right] + 0.0485 \tag{11}$$

where ΔY is the mixing layer width, C is constant. The value of C was set equal to 900 and the turbulent Prandtl number was 1.2 (12) in this study.

The Lagrangian finite-difference method is employed on solving the equations mentioned above which contain both hyperbolic and parabolic types if the flow is supersonic everywhere. The flowfield is divided by the streamlines and the orthogonal surfaces. The calculating procedures are similar to those stated in PART II (16). However, because the flow is considered to be viscous here, the conservation equations cannot be integrated directly along the streamtubes after the new orthogonal surface had been calculated. Consequently, these conservation equations must be solved in finite-difference form. The calculation is arranged so that all momentum, energy lost from one streamtube reappears in the adjancent streamtube. The stable step size for the explicit scheme used here is now set as:

$$\delta s \leq \frac{1}{2} \delta n \left[\frac{1}{Re} + (M^2 - 1)^{-1/2} \right]^{-1} \tag{12}$$

In finite-difference form, these equations become those as shown below after some arrangements from Tannehill (12):

Global continuity:

$$m_k = \rho_{k,l} u_{k,l} A_{k,l} = \rho_{k,l+1} u_{k,l+1} A_{k,l+1} \tag{13}$$

Streamwise momentum:

$$\dot{m}_k(u_{k,l+1}-u_{k,l})+\bar{A}_k(P_{k,l+1}-P_{k,l})=\Delta_k[r_k^j\,\tau_k\,\delta s_k](2\pi)^j \quad (14)$$

Normal momentum:

$$-\left[\frac{\partial\theta}{\partial s}\right]_{k,l}=\left[\frac{4(2\pi r_{k,l})^j}{u_{k,l}+u_{k+1,l}}\right]\left[\frac{P_{k+1,l}-P_{k,l}}{\dot{m}_k+\dot{m}_{k+1}}\right] \quad (15)$$

Energy:

$$\dot{m}_k\left(h_{k,l+1}-h_{k,l}+\frac{1}{2}u^2_{k,l+1}-\frac{1}{2}u^2_{k,l}\right)$$

$$=\Delta_k\left[r_k^j\left(Q_k+\frac{1}{2}\left(u_k^2+u^2_{k,l}\right)\right)^{1/2}\tau_k\right] \quad (16)$$

State:

$$P_{k,l+1}=\rho_{k,l+1}\bar{R}T_{k,l+1} \quad (17)$$

where

$$\bar{\tau}_k=\overline{2(2\pi r)^j u_k\rho_k\mu}\;\overline{\frac{u_{k+1}-u_k}{\dot{m}_{k+1}-\dot{m}_k}} \quad (18)$$

$$\bar{\theta}_k=\overline{2(2\pi r)^j u_k\rho_k}\;\overline{\frac{C_p\mu}{Pr}}\;\overline{\frac{T_{k+1}-T_k}{\dot{m}_{k+1}+\dot{m}_k}} \quad (19)$$

In these equations, the operator Δ_k takes the difference in the bracket quantity across the kth streamtube; the variable with bar indicates the average value of the variable during the step downstream is to be used. The relationship between the enthalpy h and the total enthalpy H is shown below:

$$H=h+\frac{1}{2}u^2 \quad (20)$$

If the eddy viscosity and Turbulent Prandtl number replaced the viscosity and Prandtl number in these finite-difference equations, equations (13) to (19) became the turbulent equations again for the time-averaged variables.

RESULTS AND DISCUSSION

As the plume exhausted into the supersonic flowfield, there happened viscous transport process dominatly on the plume boundary. To consider the viscous effec

the viscous term in equations shown in PART I (11) are included in the computation of this study. Because the viscous transport phenomena is due to the velocity difference between the surpersonic plume flow and supersonic ambient flow, the viscous effect is investigated in the shocklayer only. In this study, both the laminar and turbulent flow are considered to simulate the flow in the shocklayer.

The computating procedures are the same as stated in PART II (16). The plume exhausted into vacuum was first calculated to be the boundary conditions for calculating the shock layer. After that, the initial locations of the jet shock and dividing streamline are calculated by the method of characteristics used in PART I (11). The laminar flow was first taken to simulate the shocklayer flow. In the viscous calculation, the number of streamtubes on the initial surface which situated between the initial locations of jet shock and dividing streamline can be set equal to that used in inviscid case. Usually 5 is the suitable number for the calculation. The number of streamtube will increase as goes downstream. However, since the streamtubes are continually added to the calculation as the shocklayer propagates downstream, the calculation will become repititions and complicated. In addition, the computation time is essentially inversely proportional to the square of the tube width (8). So that, it is necessary to combine tubes from time to time. A new streamtube is added when the mass flux approximates the average of those in the other streamtubes; and the tubes are combined when they are in the similar conditions (8). In the program, there is a parameter which will keep the number of streamtubes not exceed a certain value.

The viscous Thor plumes for both laminar flow and turbulent flow are investigated here and shown in Figure 1 to compare with that for inviscid flow. The locations of the dividing streamline and jet shock near the nozzle exit surface computed by the present viscous calculations were identical to the locations determined in the inviscid calculation. Further downstream from the exit surface, the jet shock and the dividing streamline displace outward slightly from their inviscid locations.

The reason why the viscous effect is dominate in the downstream is that the terms of the viscous terms are the same as other those of terms in the governing

equations when the width of shocklayer grows up to the value of the width of nozzle exit surface. However, physically, the viscous effect causes the increase of the flow velocity in normal direction. In addition, the pressure gradient along the othogonal surface in shocklayer is greater for viscous flow than inviscid flow. See Figure 2. That is why the shocklayer grows fatter as goes downstream.

To investigate the pressure and temperature distributions in the shocklayer, the results got from both the viscous and inviscid calculations along the surface B in Figure 1 are shown in Figure 2 and 3. They are found being coincident except that the gradients in normal direction are larger for the viscous flow. Due to the great convective the temperature gradient in normal direction for turbulent flow is larger than that of either the laminar or the inviscid flow.

As an conclusion, it is found that the viscous effect for the supersonic flow is less dominate than that for the incompressible flow. That is because the convection terms in the governing equations for supersonic flow are in larger order than the viscous terms. However, in the incompressible flow, the convection terms and the viscous terms are almost in the same orders.

CONCLUSION

Viscous calculation is employed on investigating the visous effect on the plume flowfield. The viscous transport process affects the plume dominatly when the mixing layer grows up as the width of the layer is as large as that of nozzle exit. The normal gradients of pressure and temperature in mixing layer are larger for turbulent flow than for larminar flow. Under using the Lagrangian finite-difference scheme, the after-burning process can be included in the calculating procedure. In addition, to investigate the complete plume flow, the analysises of both viscous inviscid and gas/particle interactions are necessary to be involved.

NOMENCLATURE

A : Area of streamtube.

C : Constant in eddy viscosity expression.

C_p : Specific heat.

h : Enthalpy.

H : Total enthalpy.

m : Mass flow rate.

M : Mach number.

n : Coordinate in normal direction.

P : Pressure.

Pr : Prandtl number.

Pr_t : Turbulent Prandtl number.

r : Radius.

$\bar{R}$: Universal gas constant.

Re : Reynolds number.

s : Coordinate in streamwise direction.

T : Temperature.

u : Velocity in streamwise direction.

ΔY : Width of mixing layer.

Δk : Difference across kth streamtube.

δn : Width of streamtube.

δs : Step in streamwise direction.

ε_v : Eddy viscosity.

θ : Flow angle.

μ : Viscosity coefficient.

π : 3.1415926

ρ : Density.

τ : Shear stress.

SUBSCRIPTS

k : Condition in streamtube K.

k+1 : Condition in streamtube K+1.

o : Condition at old surface.

n : Condition at new surface.

Annual Report of the Institute of Physics, Academia Sinica, Vol. 13. 1983.

線源光化學污染物擴散模式之原理與應用勘誤表

圖九至圖十四文字說明中之同圖十七改爲同圖八。

圖十六至圖二十一文字說明中之同圖二十四改爲同圖十五。

圖二十三至圖二十八文字說明中之同圖三十一改爲同圖二十二。

圖三十至圖三十五文字說明中之同圖三十八改爲同圖二十九。

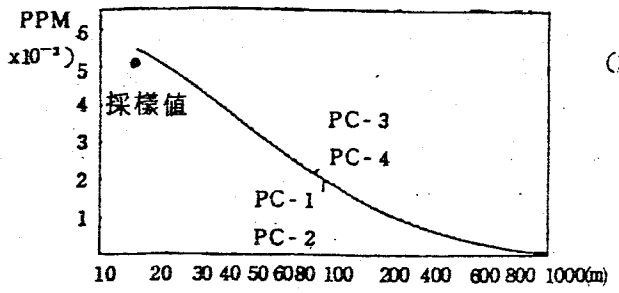

圖八　模式計算個案第一組情況下，NO_2濃度隨距離變化的情形。實線表第一、二組光化學反應濃度變化情形，虛線表第三、四組情形。

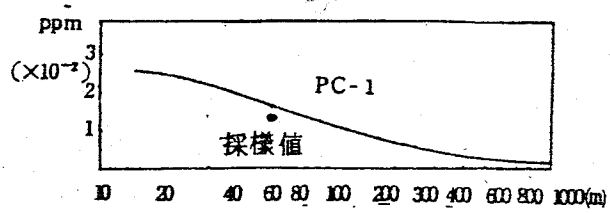

圖十五　模式計算個案第二組情況下NO濃度隨距離變化的情形（Ⅱ）。

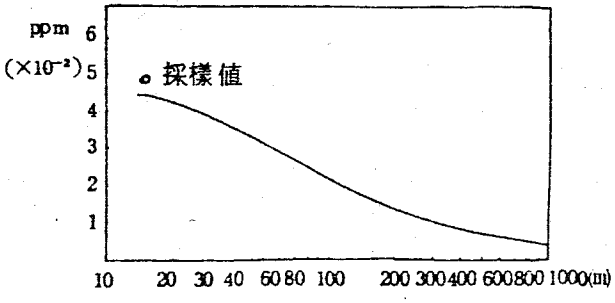

圖二十九　模式計算個案第四組情況下NO濃度隨距離變化的情形。

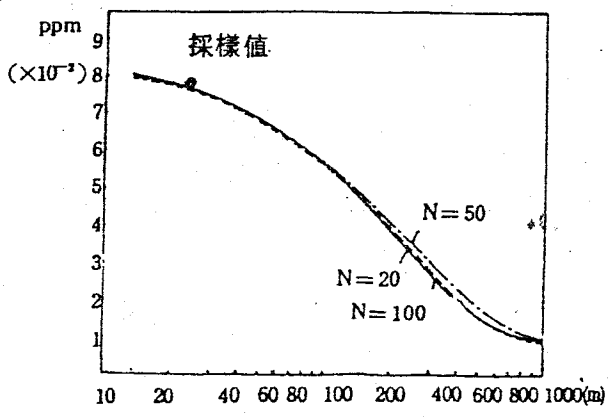

圖二十二　模式計算個案第三組情況下NO濃度隨距離變化的情形。採樣點和計算點在層區間分100格時非常接近。N表層區間分格數。

REFERENCES

(1) Libby, P. A. Theoretical analysis of turbulent mixing of reactive gases with application to supersonic combustion of hydrogen. American Rocket Society Journal 32: 388-396. 1962.

(2) Rczsa, R. B. Preliminary review of turbulent jet-mixing and afterburning in rocket exhaust plumes. Chrysler Corporation Space Division Technical Bulletin AE-64-79, 1964.

(3) Vasiliu, J. Turbulent mixing of a rocket exhaust jet with a supersonic stream including chemical ractions. Journal of the Aerospace Sciences 29:19-28, 1962.

(4) Thomson, J. A. L. High altitude rocket plume structure. General Dynamics Convair Report GD/C-DBE65-023, 1965.

(5) Boynton, F. P. The multitube supersonic flow computer code. Gernal Dynamics Convair Report GDC-DBE67-003, 1967.

(6) Vick, A. R., Cubbate, J. M. and Andrews, E. H., Jr. Rocket exhaust plume problems and some recent related research. Unpublished mimeographed paper presented at a Specialists Meeting on the Fluid Dynamic Aspects of Space Flight, Marseille, France, April 1964. Ames, Iowa; Department of Aerospace Engineering, Iowa State University of Science and Technology. Ca. 1969.

(7) Farmer, R. C., Prozan, R. J., McGimsey, L. R., and Ratliff, A. W. Verification of a mathematical model which represents large, liquid rocket-engine exhaust plumes. American Institute of Aeronautics and Astronautics Paper 66-650. 1966.

(8) Boynton, F. P. and Thomson, A. Numerical Computation of steady, supersonic two-dimensional gas flow in natural coordinates. Journal of Computational Physics 3:379-398. 1969.

(9) Dash, S. M. Pergament, H. S., and Thorpe, R. D. A Modular Approach for the Coupling of Viscous and Inviscid Processes in Exhaust Plume Flows. 17th Aerospace Science Meeting, 79-0150, 1979.

(10) Edelman, R. and Weilerstein, G. Mixing and combustion in supersonic flow with lateral pressure gradient effects. General Applied Science Laboratories,

Inc. Technical Report 636, 1968.

(11) Chien, L. C. and Chen, F. L. Theoretical Study for Rocket Exhaust Plumes. PART I Characteristics Method to be Published on the Journal of Chinese Mechanical Engineering.

(12) Tannehill, J. C. Numerical Computation of Intermediate Altitude Rocket Exhaust Plumes, Including Nonequilibrium Chemical Reactions and Diffusion. Ph. D. dissertation, Iowa State University, 1969.

(13) Schlichting, H. Boundary layer theory. 4th ed. New York, New York, McGraw-Hill Book Company, Inc. 1960.

(14) Eggers, J. M. Velocity profiles and eddy viscosity distributions downstream of a Mach 2.22 nozzle exhausting to quiescent air. United States National Aeronautics and Space Administration Technical Note D-3601, 1966.

(15) Peters, C. E., Peters, T., and Billings, R. B. Mixing and burning of bounded coaxial streams. Arnold Engineering Development Center Technical Report 65-4, 1965.

(16) Chien, L. C., and Chen F. L., Theoretical Study of Rocket Exhaust Plumes. PART II: Finite-Difference Method. To be published on the Journal of Chinese Mechanical Engineering.

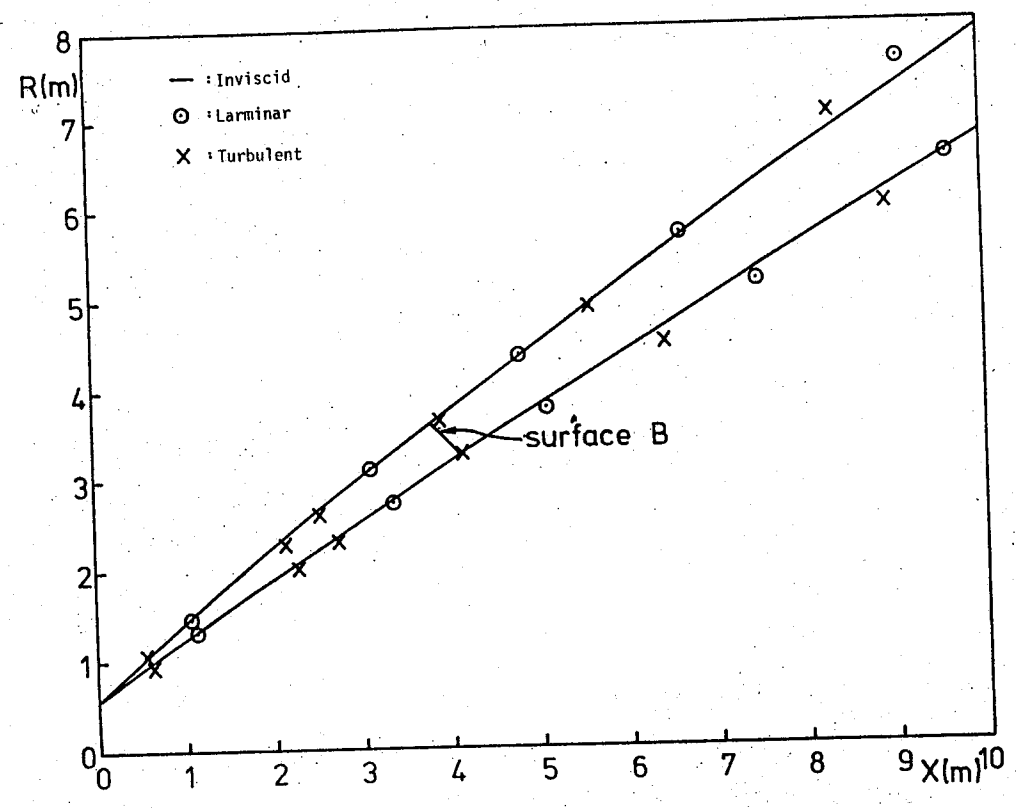

Figure 1. Thor plumes for larminar flow, turbulent flow and inviscid flow.

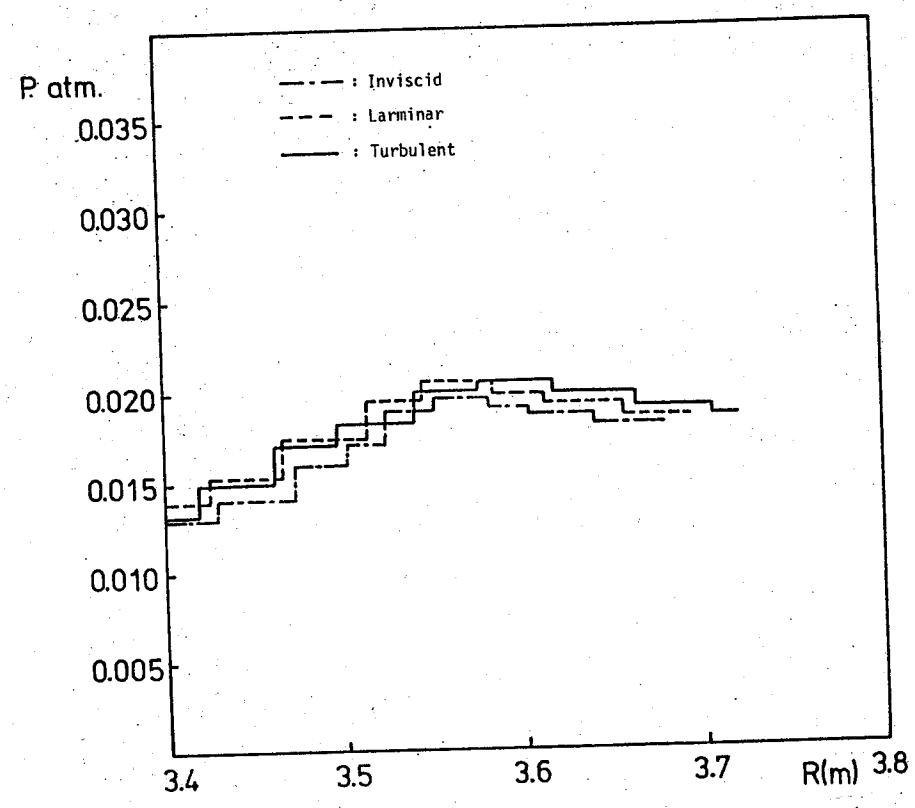

Figure 2. Pressure distributions along the surface B of figure 1.

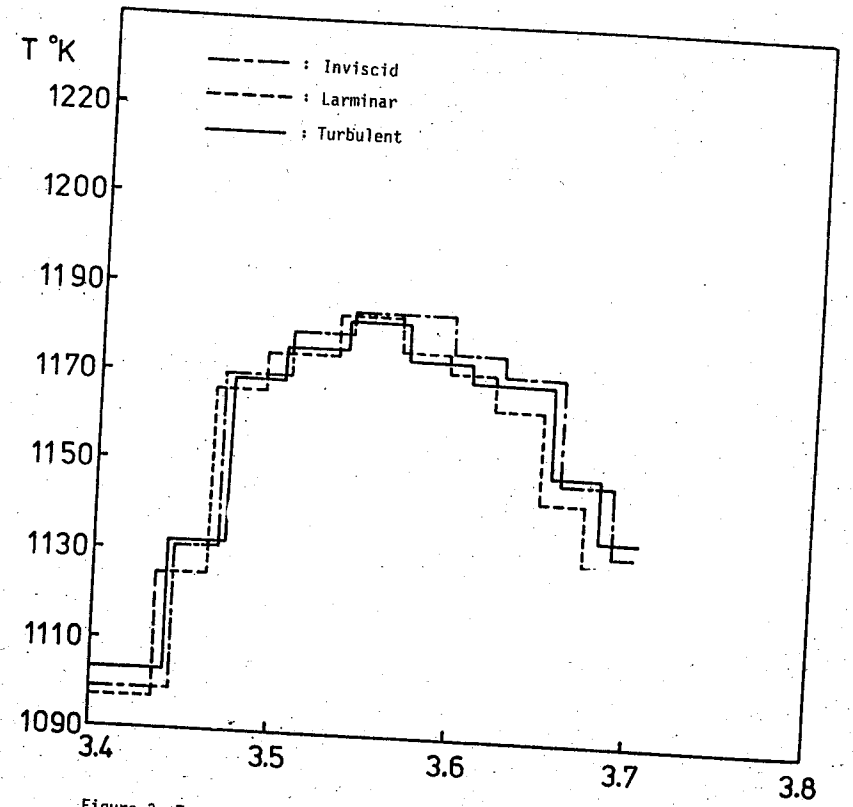

Figure 3. Temperature distributions along the surface B in figure 1.

垂直浮昇射流在流動密度層變水域中之浮昇與混合研究

黃　榮　鑑
中央研究院物理研究所
蔣　德　普
國立台灣大學造船工程研究所

摘　要

本文藉因次分析、數學模式、實驗等程序，探討具橫向流動之密度層變水域裡，垂直入射兼具啓始動量與密度差異射流之浮昇發展特性。

以因次分析方法推導流況參數 $N = GM_j^2 / B_j^2$ 作爲界分射流形態爲浮流、浮昇射流、動量射流之有效參數，且射流體總體性質物理量無因次參數和流況參數N之間，存在一定的函數次方關係式（3—a）～式（3—c）。實驗資料配合斷面積分法建立之數學模式演算，發現Taylor 捲增概念閉合控制方程式之捲增關係式採Abraham 建議但經本文修正之式（8—e）較佳，捲增係數 α_1 射流形態與流況參數N間有一演化趨勢式(9)，模式之可行性就其與實驗間之誤差分佈、軌跡趨勢而言尚稱良好，且在速度比k值相當小（$k < 4$）時仍能適用，顯示模式之優越性；進而以實驗及數學模式演算驗證因次分析推導之無因次函數間次方關係，推求可供海洋放流工程設計參考之簡便公式與圖表。

壹、緒　言

隨著經濟的茁長與生活水準的提昇，都市污水及工業廢水的排除量相對的日與俱增；然而河川涵容能力有限、廢水處理廠擴建速度無法與之配合再加上經濟效益的考慮，致使如何利用廣大海洋水域自然的力量來稀釋淨化污廢水，已成爲各國環境流體力學家們竭力研究的項目之一。海洋放流措施爲經初級或二級處理後之污廢水，以管道輸送至海面下約60公尺深地帶排放，因其與週遭水體間速度、密度差異而相混合，再藉海流帶動逐步擴散；此一過程中污廢水可能浮昇的最大高度、稀釋程度、浮昇平衡位置爲工程師設計海洋放流所面臨之最重要問題；由於放流管排除污廢水之力學特性與浮昇射流流場相似，吾人可藉研究一兼具速度、密度差異之射流，在橫向流動密度層變流場中浮昇發展特性模擬之。

依控制射流體物理量可將發展階段分爲近域、遠域。前者受控於射流體與環境水域

間差異引致之捲增、浮昇效應，爲第一次擴散階段；後者受控於環境水域亂流引致之亂流擴散，爲第二次擴散階段；本文之探討限於前者。

本問題理論解析上有二大機件：捲增及阻力關係式。捲增概念係由Morton, Taylor & Turner 〔 1 〕引入，用以閉合斷面積分法建立之數學模式，Taylor 〔 2 〕繼而假設捲增速度與射流體中心速度成正比，然而在複雜情況下捲增關係式之選定仍是意見紛紜；捲增係數不爲一定值常數而和射流形態有一演化趨勢〔 3 〕，有關浮昇射流在靜止層變水域中之浮昇與混合研究，黃〔18〕等曾作了系列的探討，在橫向流動水域裡因捲增關係式之不同仍未有定論。橫向流動量傳遞於射流體的阻力作用由Fan〔 4 〕、Abrabam 〔 5 〕率先以水流通過圓柱體所受阻力之形式予以考慮，阻力係數經Chan、Lin & Kennedy 〔 6 〕實驗指出在近域裡其與速度比K值有關。實驗方面近年來以Wright之一系列研究〔 7,8,9 〕較爲突出，其以因次分析方法推導若干特性長度配合實驗資料探討射流問題。

本文首先由與問題有關之諸因數著手，經由因次分析提出一界分射流形態之無因次參數、探討在不同射流形態下射流體總體物理量和N之函數次方關係；理論探討上以斷面積分法建立數學模式，藉實驗資料分析捲增關係式之適用性、界定捲增係數、驗證數值模式之可行性，進而檢視因次分析所推論者。

貳、因次分析

因次分析爲一數學程序，係將某一現象有關之因數就因次歸納整理，組合成相當數學模式解答之無因次函數關係式；吾人可藉之與實驗及數學模式相驗證，在適當範圍內其形式簡便可提供工程設計參考。於本問題有關因數可分爲三類，其分別爲：

1. 射流體總體性質物理量：本文探討浮昇最大高度H_m 、浮昇平衡高度H_e、浮昇最高點比質量流率V_m （ 稀釋率可由V_m / V_j 表之 ）。
2. 啟始排放條件：以流率表示下有啟始比質量流率$V_j = R^2 u_j$ 、啟始比動量流率$M_j = u_j V_j$ 、啟始比浮量流率$B_j = (\Delta\rho_j / \rho_{aj}) g V_j$。
3. 環境水域性質：密度層變參數$G = (g / \rho_{aj}) (d\rho_a / dy)$ 、水平流速U_a

諸因數間關係可由下式表示：

$$f (P_i, V_j, M_j, B_j, G, U_a) = 0 \qquad i = 1, 2, 3 \qquad (1-a)$$

式中： $P_1 = H_m$, $P_2 = H_e$, $P_3 = V_m$

又，射流體比質量流率因捲增效應沿發展路徑迅速增加，此一效應係受控於射流體與週遭水體間速度、密度差異，而和啟始比質量流率之相關性甚弱；故V_j 僅在排放口附近有其影響力，於式(1－a) 中其與 P_i 之相關性可予忽略，且就形態而言V_j 已含括於M_j 、B_j二因數內，爲簡化因次分析〔 7, 9, 10 〕將之略去改寫爲：

$$f' (P_i, M_j, B_j, G, U_a) = 0 \qquad i = 1, 2, 3 \qquad (1-b)$$

上式中有五個物理量，具時間、長度二個基本因次，由Buckinghm π－定理知其至多可組成三個無因次參數，分別爲：

$$\left(\frac{H_m B_j^{1/2}}{M_j^{3/4}}, \frac{H_e B_j^{1/2}}{M_j^{3/4}}, \frac{V_m B_j^{1/2}}{M_j^{5/4}} \right) \sim f_{BM} \left(\frac{G M_j^2}{B_j^2}, \frac{U_a M_j^{1/4}}{B_j^{1/2}} \right) \qquad (2-a)$$

定義：流況參數$N = G M_j^2 / B_j^2$ 爲啟始排放條件中動量、浮量二驅動力比值之無因次參數〔 11 〕；若射流啟始驅動力爲浮量主控，此時N之階數相當小（ 如$N \sim 10^{-3}$ ）射流形態趨向於浮流，則式(1－b) 略去M_j 經因次分析得：

$$\left(\frac{H_m G^{3/8}}{B_j^{1/4}}, \frac{H_e G^{3/8}}{B_j^{1/4}}, \frac{V_m G^{5/8}}{B_j^{3/4}} \right) \sim f_B \left(\frac{U_a}{G^{1/8} B_j^{1/4}} \right) \qquad (2-b)$$

反之，若射流啟始驅動力爲動量主控，此時N之階數相當大（ 如$N \sim 10^3$ ）射流形態趨向於動量射流，則式(1－b) 略去B_j 經因次分析得：

$$\left(\frac{H_m G^{1/4}}{M_j^{1/4}}, \frac{H_e G^{1/4}}{M_j^{1/4}}, \frac{V_m G^{1/4}}{M_j^{3/4}} \right) \sim f_M \left(\frac{U_a}{G^{1/4} M_j^{1/4}} \right) \qquad (2-c)$$

式(2－a)、(2－b)、(2－c) 中各無因次參數經適當配比後，可合併寫爲一通式：

$$\left(\frac{H_m B_j^{1/2}}{M_j^{3/4}}, \frac{H_e B_j^{1/2}}{M_j^{3/4}} \right) \sim N^{-3/8} \cdot f'_{HB} \left(\frac{H_m G^{1/2}}{U_a} \right) \qquad \text{浮　流}$$

$$\sim f'_H \left(N, \frac{H_m G^{1/2}}{U_a} \right) \qquad \text{浮昇射流}$$

$$\sim N^{-1/4} \cdot f_{HM} \left(\frac{H_m G^{1/2}}{U_a} \right) \qquad \text{動量射流} \qquad (3-a、b)$$

$$\frac{V_m B_j^{1/2}}{M_j^{5/4}} \sim N^{-5/8} \cdot f_{VB} \left(\frac{V_m G}{U_a^3} \right) \qquad \text{浮　流}$$

$$\sim f_V \left(N, \frac{V_m G}{U_a^3} \right) \qquad \text{浮昇射流}$$

$$\sim N^{-1/4} \cdot f_{VM} \left(\frac{V_m G}{U_a^3} \right) \qquad \text{動量射流} \qquad (3-c)$$

爲檢視射流體總體性質物理量無因次參數和參數N間次方關係是否如上所示，及提供簡單無因次式供海洋放流工程設計參考，以之進行複迴歸分析：

$$\frac{H_m B_j^{1/2}}{M_j^{3/4}} \sim N^p \cdot \left(\frac{H_m G^{1/2}}{U_a} \right)^m \qquad (4-a)$$

$$\frac{H_e B_j^{1/2}}{M_j^{3/4}} \sim N^q \cdot \left(\frac{H_e G^{1/2}}{U_a} \right)^n \qquad (4-b)$$

$$\frac{V_m B_j^{1/2}}{M_j^{5/4}} \sim N^r \cdot \left(\frac{V_m G}{U_a^3} \right)^\ell \qquad (4-c)$$

$p, q \sim -3/8$, $r \sim -5/8$ 浮　流

$\sim [-3/8, -1/4]$, $\sim [-5/8, -1/4]$ 浮昇射流

$\sim -1/4$, $\sim -1/4$ 動量射流 (4－d)

參數次方p、q、r是否如式（4－d）所示，參數次方m、n、ℓ之值爲何，將由實驗及數學模式演算驗證及求得。

叁、數學模式

射流問題之近域模式處理方法可分爲二類。其一爲從Navier-Stokes方程式著手將之以亂流擾動項代入展開，藉假設一亂流模式閉合控制方程式再以數值方法解析，由於高階非線性方程式之複雜性，此種方法缺乏實用性。其二爲在射流體斷面沿軸向速度、密度差具動力相似性假設下，以斷面積分法建立射流體質量、動量、浮量守恆方程式，藉Taylor 捲增概念閉合後得一組一階擬線性常微分方程式，再以數值方法求解（謂之Similarity Solution）；此一數學模式物理意義至爲明顯且易於數值計算，於探討射流總體性質工程觀點上具有實用性，本文循此解析射流問題。

一射流體控制方程式：

射流體之發展（如圖1）自勢心區頂點後已達完全發展之亂流，此時射流體實際斷面爲腎形其內有二個對稱渦性流動（如圖2）；今假設斷面爲圓形、軸向對稱，且渦性流動甚弱可以不計其對射流體發展之影響，則斷面上沿軸向速度、密度差分佈可接受相似性假設處理〔4,12〕，設其可由高斯分佈近似〔1,4,12,13〕表爲：

$$(u-U_a\cos\theta)=(u_c-U_a\cos\theta)\cdot\exp(-r^2/b^2) \qquad (5\text{—a})$$

$$(\rho_a-\rho)=(\rho_{ac}-\rho_c)\cdot\exp(-r^2/\lambda^2b^2)=\Delta\rho_c\cdot\exp(-r^2/\lambda^2b^2) \qquad (5\text{—b})$$

由Boussinesq 假設並定義射流體特性半徑R：射流體斷面上速度u所攜之物理量可分爲二部份，一爲（$u-U_a\cos\theta$）所攜，一爲$U_a\cos\theta$所攜；作爲斷面積分時前者可將式（5－a）、（5－b）代入利用高斯分佈特性計算化簡，後者則需有一適量邊界作爲積分上限方能計算，然而在高斯分佈假設下射流體無邊界（趨近於∞）可言。今假想一半徑爲R之斷面其上速度$\overline{u}$爲均勻分佈，設此一斷面上之比質量流率、比動量流率和（$u-U_a\cos\theta$）所攜者相同，即：

$$\pi R^3\overline{u}=\int_0^\infty(u-U_a\cos\theta)(2\pi r\,dr)$$

$$\pi R^2\overline{u}^2=\int_0^\infty(u-U_a\cos\theta)^2(2\pi r\,dr)$$

解之得$R=\sqrt{2}\,b$，此值含括高斯分佈特性及質量、動量流率均衡之物理意義，據此定義一射流體特性半徑R作爲計算速度$U_a\cos\theta$所攜之物理量。

則通過射流體斷面之比質流率$\overline{V}$、比動量流率M、比浮量流率B，經由式（5－a）、（5－b）計算化簡後爲：

$$V=\int_A u\cdot dA=\pi b^2(u_c+U_a\cos\theta) \qquad (6\text{—a})$$

$$M=\int_A u^2\cdot d_A=\frac{1}{2}\pi b^2(u_c+U_a\cos\theta)^2 \qquad (6\text{—b})$$

$$B=\int_A\frac{\rho_a-\rho}{\rho_{aj}}u\cdot dA=\pi\lambda^2b^2\cdot\frac{\Delta\rho_c}{\rho_{aj}}\cdot\left(U_a\cos\theta+\frac{U_c-U_a\cos\theta}{1+\lambda^2}\right) \qquad (6\text{—c})$$

假設：(1)流況爲定常態、不可壓縮流動、流體黏滯效應不顯著，(2)環境水域亂流引致亂流擴散及射流體縱向延散，遠小於射流體與週遭水體間速度、密度差異捲增所產生之側向混調，(3)地球自轉Coriolis Force 及流軸偏斜向心力等均甚小可予不計；則依質量守恆、動量守恆、浮量守恆、軌跡幾何關係，射流體發展控制方程組可寫如：

質量守恆 $$\frac{d(\overline{V})}{ds}=E \qquad (7\text{—a})$$

動量守恆$\overrightarrow{X}$ $$\frac{d(M\cos\theta)}{ds}=F_e+(e_\theta)\cdot F_D\sin\theta \qquad \begin{matrix}若\,\theta>0\,,e_\theta=1\\ \theta<0\,,e_\theta=-1\end{matrix} \qquad (7\text{—b})$$

$\overrightarrow{Y}$ $$\frac{d(M\sin\theta)}{ds}=-F_b-(e_\theta)\cdot F_D\cos\theta \qquad (7\text{—c})$$

浮量守恆 $$\frac{d(B)}{ds}=V\cdot\left(\frac{d\rho_a}{dy}/\rho_{aj}\right)\cdot\frac{dy}{ds} \qquad (7\text{—d})$$

軌跡幾何 $$\frac{d(\chi)}{ds}=\cos\theta \qquad (7\text{—e})$$

$$\frac{d(y)}{ds}=\sin\theta \qquad (7\text{—f})$$

式中：

捲增量$E=2\pi RV_e$

捲增力$F_e=E\cdot U_a$

阻　力$F_D=C_D\cdot\frac{(U_a\sin\theta)^2}{2}(2R)$

浮　力$F_b=\int_A\frac{\rho_a-\rho}{\rho_{aj}}g\cdot dA=\pi\lambda^2b^2g\cdot\frac{\Delta\rho_c}{\rho_{aj}}$

式（7－a）～（7－f）係一組擬線性常微分方程組，自變數爲s，應變數爲x、y、θ、b、u_c、$\Delta\rho_c/\rho_{aj}$；在決定捲增關係使之閉合及給予適當初值條件後得以數值方法求解，本文以Fourth-Order Runge-Kutta Method 運算之，於電腦程式中設定計算所需精度上，下限控制條件，自動調整演算間距Δs 以節省計算機時間。

二捲增關係式：

閉合斷面積分法建立數學模式之捲增概念係由Morton〔1〕提出，繼之Taylor〔2〕建議：假設捲增速度V_e與射流體軸心速度u_c成正比$V_e=\alpha u_c$，α爲捲增係，其後研究本問題學者大都在此一構架上嘗試適用於不同狀況下之捲增關係式，其中Fox〔3〕、Hirst〔14〕及黃、王〔18〕等藉雷諾應力分佈具動力相似性之假設，出適用於靜止水域（密度層變或均質）之捲增關係式較具解析性，其將α分爲二部，α_1、α_2：

$$V_e=\left(\alpha_1+\frac{\alpha_2\sin\theta}{F_\ell^2}\right)u_c \qquad (8\text{—a})$$

式中： $\alpha_2=\lambda^2(2\lambda^2-1)/(H\lambda^2)$ ， $F_t^2=u_c^2/(gb\cdot\Delta\rho_c/\rho_{aj})$

在密度均勻水域有橫向流動情況下，Abraham〔5〕將捲增關係式表爲：

$$V_e=\alpha_1(u_c-U_a\cos\theta)+\alpha_3(U_a\cos\theta)\cdot\sin\theta \qquad (8-b)$$

綜合式（8－a）、（8－b）可將具橫向流動密度層變水域裡捲增關係式表爲：

$$V_e=(\alpha_1+\alpha_2|\sin\theta|/F_t^2)(u_c-U_a\cos\theta)+\alpha_3(U_a\cos\theta)\cdot|\sin\theta| \qquad (8-c)$$

式中 θ 爲流軸偏斜角度因子，因捲增與路徑角度無關故修正爲 $|\sin\theta|$ 。

密度層變水域裡以式（8－c）捲增關係式閉合控制方程式之數學模式作數值演算時，$\Delta\rho_c$ 隨射流體發展有正、負相間出現之振盪現象（如圖3），F_t^2 爲 $\Delta\rho_c$ 函數將隨之變化，致使捲增量在計算上有向內捲進（正）與向外捲出（負）之別；作者以爲 $\Delta\rho_c$ 隨射流體發展之振盪現象是合理的，但就捲增而言不論是向內捲進抑是向外捲出均爲一混調過程，射流體比質量流率均應沿發展路徑持續增加（可由實驗觀察得知），按此式（8－c）宜加修正爲：

$$V_e=(\alpha_1+\alpha_2|\sin\theta|/|F_t^2|)(u_c-U_a\cos\theta)+\alpha_3(U_a\cos\theta)\cdot|\sin\theta| \qquad (8-d)$$

或爲： $V_e=\alpha_1(u_c-U_a\cos\theta)+\alpha_3(U_a\cos\theta)\cdot|\sin\theta|$ (8－e)

式（8－d）、（8－e）何者爲佳，將藉實驗與數學模式演算驗證之。

三捲增係數：

1. α_1 ：依前人研究〔3〕不爲一定值常數而與射流形態有關，於射流趨向浮流者其值大於射流趨向動量射流者；依前述因次分析流況參數N可視爲界分射流形態有效參數，本文嘗試以之爲界分原則界定之。

2. α_2 ：依前人研究〔14〕$\lambda=1.11$（動量射流）至1.16（浮流）間，當 F_t^2 相當小時此一差異方對捲增量計算有所影響，故逕採 $\lambda=1.16$ ，則 $\alpha_2=0.97$ 。

3. α_3 ：Richards 〔15〕實驗資料指出在密度均勻水域裡其值爲0.5，本文將之延用至密度層變水域裡。

4. C_D ：依Chan,Lin & Kennedy 實驗資料〔6〕，於近域裡 C_D 和速度比 $k=u_j/U_a$ 之分佈如圖四，由其分佈趨勢本文假設當 $k>10$ 時 $C_D\sim0.8$ 。

四初值條件：勢心區頂點各量之推求

1. S_o,θ_o ：採Schatzmann〔16〕實驗迴歸式

$$S_o=(6.2-20.0/k)D_j$$

$$\theta_o=\pi(1.0-1.22/k)/2$$

2. b_o ：假設排放口至勢心區頂點間浮力，阻力變化甚小可予不計，則二者垂直方動量應相同，積分式（7－c）得：

$$b_o=\left(\frac{2.0}{\sin\theta_o}\right)^{1/2}\cdot\frac{u_j}{(u_c+U_a\cos\theta)}\cdot R_j$$

3. u_{co} ：$u_{co}=u_j+U_a\cos\theta_o$

4. $\Delta\rho_{co}/\rho_{aj}$ ：排放口至勢心區頂點間浮量守恆，積分式（7－d）省略微小項次後得：

$$\frac{\Delta\rho_{co}}{\rho_{aj}}=\frac{R_j^2}{\lambda^2 b_o^2}\cdot\frac{u_j}{\frac{u_j}{1+\lambda^2}+U_a\cos\theta}\cdot\frac{\Delta\rho_j}{\rho_{aj}}$$

肆、實　驗

「實驗」對問題之分析是相當重要的，於學理上可界定數學模式中諸係數、驗證模式可行性；更可藉之檢視因次分析推導之無因次函數次方關係是否正確，進而求出相當於數學模式解答之簡便公式與圖表供工程設計參考。本問題所需模擬之環境水域具密度層變又有橫向流動，故應用相對速度原理以「於靜止之密度層變水域裡，有一等速運動垂直排放之射流」模擬之；又爲避免排放口運動過程干擾到水域密度層變，而將排放口安設於水面下適當位置由上往下排放。實驗在一長3.7公尺、寬0.3公尺、深0.3公尺壓克力水槽中進行，實驗方法與步驟〔17,18〕簡述如下：

1 密度層變水域：利用鹽水填加方法，在水槽中每二公分由下而上充填不同鹽量之鹽水14層（如圖5），其過程約需6～7小時；填妥之水域各層密度差異在不受擾動情況下，由於分子擴散作用將漸趨緩和，靜置10～20小時（視層變梯度、室溫而定）後，水域密度將呈線性分佈（如圖6）。

2 相對速度：在水槽上方架設二支平行於水槽二側鋼軌供台車行走，台車上安設由三組滑輪及一組變速馬達組成之傳動系統，利用可變電壓器改變電源電壓（40～110伏特），使台車在不同速度（1.0～8.0公分／秒）下前進；排放口架設於水槽橫斷面中心位置之台車上並伸入水面下適當位置，則由台車帶動可使排放口在水域中依所需速度前進（如圖7）。

3 流場顯現：利用架設於台車上方光箱（箱內面鋪錫紙、1 kw 水銀燈一具），以光箱底面1毫米寬之狹縫將光源集中射出照射在射流體（排放溶液配有染料Rhodamine W.T）中心斷面上，利用射流體與環境水域間明暗程度差異得以攝得其發展軌跡（如圖8）；照相器材爲Nikom、F_2、50 mm 鏡頭、附自動捲片裝置之相機，將之固定於台車側下方隨車前進，拍攝時使用1 LFORD ASA 400 高感光度底片、快門爲一秒、光圈視染料濃度而定在2.8～5.6間。

實驗過程中，最大排放量僅達水域體積之0.003％，其對定常態假設之影響極微可忽略之；本文實驗共計26組，實驗數據如表一編號501～506，攝得射流體軌跡中心位如圖9.1～9.26。

伍、結果與討論

先以實驗結果比較捲增關係式何者爲佳、界定捲增係數、驗證模式可行性，進而以

實驗、數學模式驗證因次分析推導之無因次函數次方關係。

一分別以式（8－c）、（8－d）、（8－e）捲增關係式進行數學模式演算，以演算得軌跡和圖 9.1～9.26 實驗軌跡作比較，結果顯示式（8－d）、（8－e）較式（8－c）爲佳，蓋式（8－c）不滿足射流體應隨其發展路徑不斷增大之物理現象。

二以表一實驗資料中浮昇最大高度爲基準，比較式（8－d）、（8－e）捲增關係式進行數學模式演算所求出 α_1 最佳值（浮昇最大高度演算值最接近實驗值時之 α_1）和流況參數N之關係，結果發現：

1.式（8－e）捲增關係式所求出 α_1 最佳值和N有較佳之相關性。

2.式（8－d）捲增關係式在速度比甚小（$k<5$）時，最大浮昇高度演算值遠小於實驗值，茲以表一編號86實驗資料（$k=3.3$）演算作一說明：

⑴圖 10.1 爲演算軌跡比較：式（8－d）、（8－e）演算得浮昇最大高度分別爲 $3.2D_j$、$14.7D_j$ 而實驗值爲 $14.8D_j$，式（8－d）演算值與實驗值相去甚遠且此不準確性經測試分析知與 α_1、α_3 值大小無關。

⑵圖 10.2 爲捲增量計算比較：於此例中式（8－d）所描述捲增配比爲 $\alpha_2|\sin\theta|/|F_\ell{}^2|\cdot(u_c-U_a\cos\theta)\ll\alpha_1(u_c-U_a\cos\theta)$，$\alpha_3(U_a\cos\theta)\cdot|\sin\theta|$ 此一配比甚不合理；且在射口附近捲增量高達射流體比質量流率之1.7倍，不合理的龐大捲增迅速消彌了射流體週遭水體密度差異的浮昇效應，又射流體動量所具浮昇力遭橫向流動壓制，射流體無法向上浮昇致使演算結果偏低。

據此，作者以式（8－e）作爲閉合控制方程式之捲增關係式。

三因次分析式（2－a）中參數 $U_aM_j{}^{1/2}$，就形態而言與流況參數 $N=GM_j{}^2/B_j{}^2$ 相類似，亦可視爲啟始排放條件動量、浮量＝驅動力比值之無因次參數；但依本文分析結果其與 α_1 之相關性較弱，故本文採 $N=GM_j{}^2/B_j{}^2$ 作爲界分射流形態及選定捲增係數 α_1 之有效參數。所求出 α_1 和N間關係大致爲：

$N\sim[0,1]$	，	$\alpha_1\sim0.053$	， 射流形態～浮　流
$\sim[1,10]$	，	~0.045	， 浮昇射流
$\sim[10,\infty]$	，	~0.034	， 動量射流

四以式（8－e）捲增關係式、式⑼捲增係數 α_1 進行數學模式演算，就軌跡趨勢、射流體浮昇最大（平衡）高度驗證模式可行性，其結果分述如下：

1.軌跡趨勢：演算及實測比較如圖 9.1～9.26，其趨勢及吻合程度尚佳。

2.浮昇最大高度 H_m（實驗資料如表一）：實驗值 H_{me}、計算值 H_{mn} 間誤差 $ER1=(H_{me}-H_{mn})/H_{me}$ 列如表一 10a，其分佈大致爲

$|ER1|<5\%$ 佔 53％ ，$|ER1|<10\%$ 佔 84％

$|ER1|<15\%$ 佔 91％ ，$|ER1|<20\%$ 佔 97％

3.浮昇平衡高度 H_e（實驗資料如表二）：實驗值 H_{ee}、計算值 H_{en} 間誤差 $ER2=(H_{ee}-H_{en})/H_{ee}$ 列如表二 10b，其分佈大致爲

$|ER2|<5\%$ 佔 47％ ，$|ER2|<10\%$ 佔 68％

$|ER2|<15\%$ 佔 80％ ，$|ER2|<20\%$ 佔 90％

就軌跡趨勢、誤差分佈而言模式可行性尚稱良好，且在速度比相當小（$k<4$）時本模式仍能準確預測更顯其優越性。

五以實驗點啟始排放條件因數 M_j、B_j，環境水域性質因數 G、U_a，配合浮昇最大（平衡）高度實驗值 H_{me}（H_{ee}），浮昇最高點比質量流率計算值 V_m（稀釋率 V_m/V_j 列如表一 8a），按式（4－a）、（4－b）、（4－c）作複迴歸分析；結果發現參數次方 m、n、ℓ 等隨射流形態變動範圍很小可以一定值視之，其分別爲 2/5、2/5、－1/5；以 $(H_{me}B_j{}^{1/2}/M_j{}^{3/4})\cdot(H_{me}G^{1/2}/U_a)^{-2/5}\sim N$、$(H_{ee}B_j{}^{1/2}/M_j{}^{3/4})\cdot(H_{ee}G^{1/2}/U_a)^{-2/5}\sim N$ 及 $(V_mB_j{}^{1/2}/M_j{}^{5/4})\cdot(V_mG/U_a{}^3)^{1/5}\sim N$ 在雙對數座標格紙上作圖（如圖 11.1、11.2、11.3）藉之檢視參數N之次方 p、q、r，結果發現其與因次分析推導之式（3－a）、（3－b）、（3－c）相當接近，經整理後得：

$$\frac{H_mB_j{}^{1/2}}{M_j{}^{3/4}}=C_1\cdot N^p\cdot\left(\frac{H_mG^{1/2}}{U_a}\right)^{2/5}\qquad(10\text{－a})$$

$$\frac{H_eB_j{}^{1/2}}{M_j{}^{3/4}}=C_2\cdot N^q\cdot\left(\frac{H_eG^{1/2}}{U_a}\right)^{2/5}\qquad(10\text{－b})$$

$$\frac{V_mB_j{}^{1/2}}{B_j{}^{5/4}}=C_3\cdot N^r\cdot\left(\frac{V_mG}{U_a{}^3}\right)^{-1/5}\qquad(10\text{－c})$$

$N\sim[0,1]$，射流形態～浮　流，$C_1=2.20$，$p=-0.352$〔理論值－0.375〕

$C_2=2.18$　$q=-0.355$〔理論值－0.375〕

$C_3=2.01$　$r=-0.622$〔理論值－0.625〕

$\sim[1,10]$，～浮昇射流，$C_1=2.42$，$p=-0.305$

$C_2=$ —　$q=$ —

$C_3=1.97$　$r=-0.458$

$\sim[10,\infty]$，～動量射量，$C_1=1.77$，$p=-0.272$〔理論值－0.250〕

$C_2=1.93$　$q=-0.260$〔理論值－0.250〕

$C_3=1.04$　$r=-0.272$〔理論值－0.250〕

（10－a）、（10－b）、（10－c）相關係數均在 0.95 以上，在適當範圍內與圖 11.1、11.2、11.3 可供海洋放流工程設計參考。

陸、結　論

本文探討具橫向流動之密度層變水域裡，兼具啟始動量與密度差異射流之混合發展過程由因次分析、數學模式演算、實驗驗證等步驟，獲致結論如下：

在速度密度差具動力相似性假設下，採 Taylor 捲增概念閉合斷面積分法建立射

流體控制方程式之近域數學模式，就射流體總體性質而言其結果是可以接受的。

2. 捲增關係式在有橫向流動水域裡，當 k 值較小時式（ 8 － d ）不適用，採 Abraham 建議經本文修正之式（ 8 － e ）則能有良好的預測。

3. 本文建立之數學模式就軌跡趨勢、浮昇最大（平衡）高度演算，在與實驗比較下模式可行性尚稱良好，且在 $k < 4$ 時仍能適用益顯其優越性。

4. 因次分析推導之流況參數 $N = GM_j^2 / B_j^2$ ，可作爲界分射流形態及選定捲增係數 α_1 之有效參數，其演化情形如式(9)。

5. 實驗及數學模式演算驗證了因次分析方法推導之無因次參數函數間次方關係。式（10—a）、（10—b）、（10—c） 及圖 11.1 ， 11.2 ， 11.3 相當於數學模式解答，其形式簡便在適當範圍裡當對工程設計有所助益。

參考文獻

1. Morton, B., Taylor, G. I. & Turner, J. S., "Turbulent Gravitational Convection from Maintained and Instantaneous Sources," Journal of the Royal Society, London, England, A234, 1956.
2. Taylor, G. I., "Flow Induced by Jets," Journal Aero/Space Science. Vol. 25, 1958.
3. Fox, D. B., "Forced Plume in a Stratified Fluid," Journal of Geophysical Research, Vol. 75, 1970.
4. Fan, L. N., "Turbulent Buoyant Jets into Stratified or Flowing Ambient Fluids," W. M. Keck Laboratory of Hydraulics and Water Resources, Report No. KH-R-15, California Institute of Technology, Pasadena, California. 1967.
5. Abraham, G., "The Flow of Round Buoyant Jets Issuing Vertically into Ambient Fluid Flowing in a Horizontal Direction," Delft Hydraulics Laboratory, Delft, Netherlands, Report No. 81, 1971.
6. Chan, T. L., Lin, J. T. & Kennedy, J. F., "Entrainment and Drag Forces of Deflected Jets," Journal of the Hydraulics Division, ASCE, Vol. 102, 1976.
7. Wright, S. J., "Mean Behavior of Buoyant Jets in a Crossflow," Journal of the Hydraulics Division, ASCE, Vol. 103, 1977.
8. Wright, S. J., "Effects of Ambient Crossflows and Density Stratification on the Characteristic Behavior of Round Turbulent Buoyancy Jets," California Institute of Technology Report No. KH-R-36, 1977.
9. Wright, S. J., Wong, D. T. & Zimmerman, K. E., "Outfall Diffuse Mechanics in Stratified Ambient Fluid," Journal of the Hydraulics Division, ASCE, Vol. 108, 1982.
10. Alavian, V. & Hoopes, J. A. "Thermal Fronts in Heated Water Discharges," Journal of the Hydraulics Division, ASCE, Vol. 108, 1982.
11. Fisher, H. B., et al., Mixing in Inland & Coastal Waters, Academic Press, Inc. New York, 1977.
12. Rouse, H., Yih, C. B. & Humphreys, H. W., "Gravitational Convection from a Boundary Source," Tellus, Vol. 4, 1952.
13. Baumgartuer, D. J., & Trent, D. S., "Ocean Outfall Design Part 1 Liteaature Review and Theoretical Development," United States Department of the Interior Federal Water Quality Administration, 1970.
14; Hirst, E., "Buoyant Jets Discharged to Quiescent Stratified Ambients," Journal of Geophysical Research, Vol. 76, 1971.

15. Richards, J. M., "Experiments on the Motion of Isolated Cylindrical Thermals Through Unstratified Surroundings," International Journal of Air and Water Pollution, Vol. 7, 1963.
16. Schatzmann, M., "Auftriebsstrahlen in Naturlichen Stromungen-Entwicklung eines Mathematischen Modells," Thesis Pressented to Universitat Karlsruhe, in Karlsruhe, Germany, 1967.
17. 黃榮鑑、周文輝、王燦汶，“密度層變流中的擴散及其在海洋放流之應用”國立台灣大學水工試驗所試驗報告第52號，1977。
18. 黃榮鑑、王德忠、蔡西銘，“垂直浮昇射流在靜止密度層變水域中之浮昇與混合研究”，土木水利，十卷三期，37～59頁，1983。
19. 黃榮鑑，“二維密度層變流通過障礙受阻的研究”，中國工程學刊五卷三期，167～177頁，1982。
20. Jirka, G. H. & Fong, L. M., "Vortex Dynamic and Birfurcation of Buoyant Jet in Crossflow," Journal of the Engineering Mechanics Division, ASCE, Vol. 107, 1981.

符號說明

(x, y)	：笛卡爾座標系統	s	：射流體軸心位置
V	：射流體比質量流率	θ	：射流體軸向$\vec{s}$與x軸向$\vec{x}$交角
M	：射流體比動量流率	G	：水域密度層變參數
B	：射流體比浮量流率	U_a	：水域橫向流動速度
E	：捲增量	F_b	：浮　力
V_e	：捲增速度	F_D	：阻　力
F_e	：捲增力	C_D	：阻力係數
F_l	：局部密度福祿數	k	：速度比
R	：射流體特性半徑	N	：流況參數
D_j	：排放口直徑	H	：　體浮昇高度
R_j	：排放口半徑	ρ	：射流體時均密度
u	：射流體時均速度	ρ_a	：環境水域密度
λ	：擴散比	$\Delta\rho$	：同位置之環境水域與射流體間密度度差異
α	：捲增係數，α_1，α_2，α_3	b	：高斯分佈特性半徑
$(\ )_j$	：排放口位置	$[\ ]_e$	：實驗值
$(\ )_m$	：浮昇最高位置	$[\ ]_n$	：數學模式演算值
$(\ )_e$	：浮昇平衡位置	$ER1$	：$ER1 = (H_{me} - H_{mn}) / H_{me}$
$(\ )_o$	：勢心區頂點位置	$ER2$	：$ER2 = (H_{ee} - H_{en}) / H_{ee}$
$(\ )_c$	：射流體軸心位置		

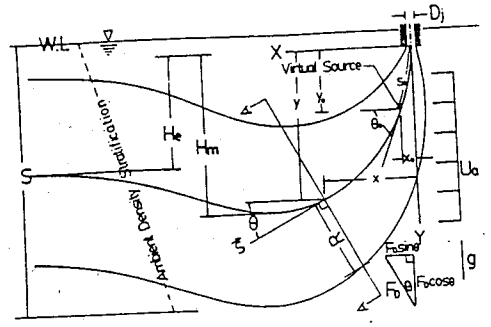

圖 1　射流體發展示意圖

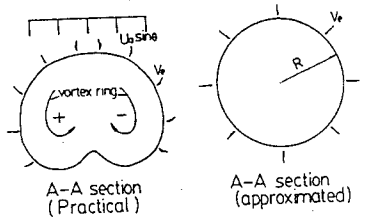

圖 2　射流體橫斷面

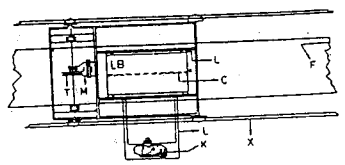

圖 7　實驗設備頂視圖

X：鋼軌
B：電源
M：馬達
V：電壓控制
T：傳動系統
E：排放管線
G：閥門
H：浮盆
I：鐵架
L：連桿
LB：光箱
C：狹縫（１mm）
K：相機
A：１KW水銀燈
F：環境水域水槽
D：鹽水拌合槽
P：鹽水充填管線

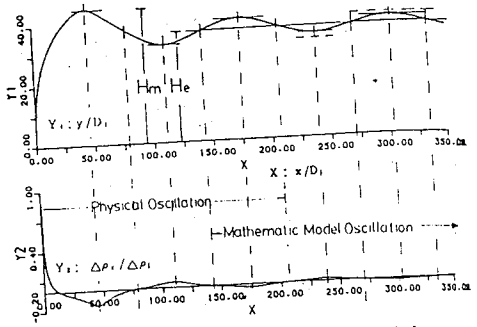

圖 3　密度層變水域振盪現象

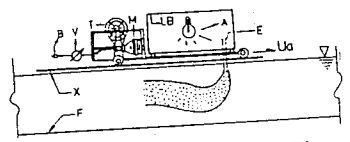

圖 8　實驗設備側視圖

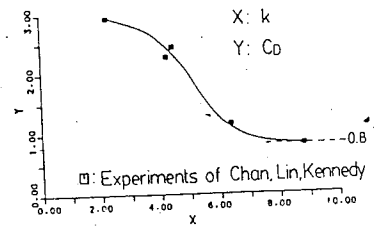

圖 4　阻力係數和速度比關係

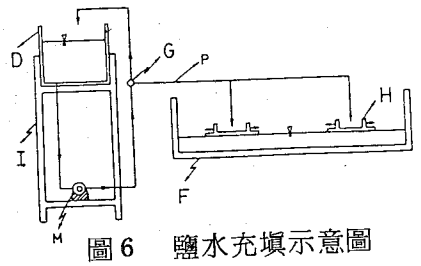

圖 6　鹽水充填示意圖

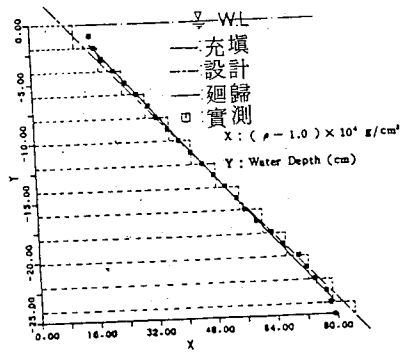

圖 5　環境水域密度層變

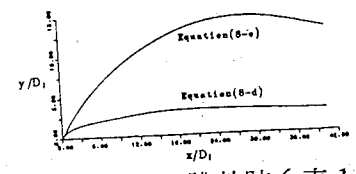

圖 10.1　射流體軌跡（表 1 No. 86）

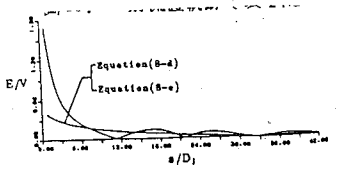

圖 10.2　射流體捲增量（表 1 No. 86）

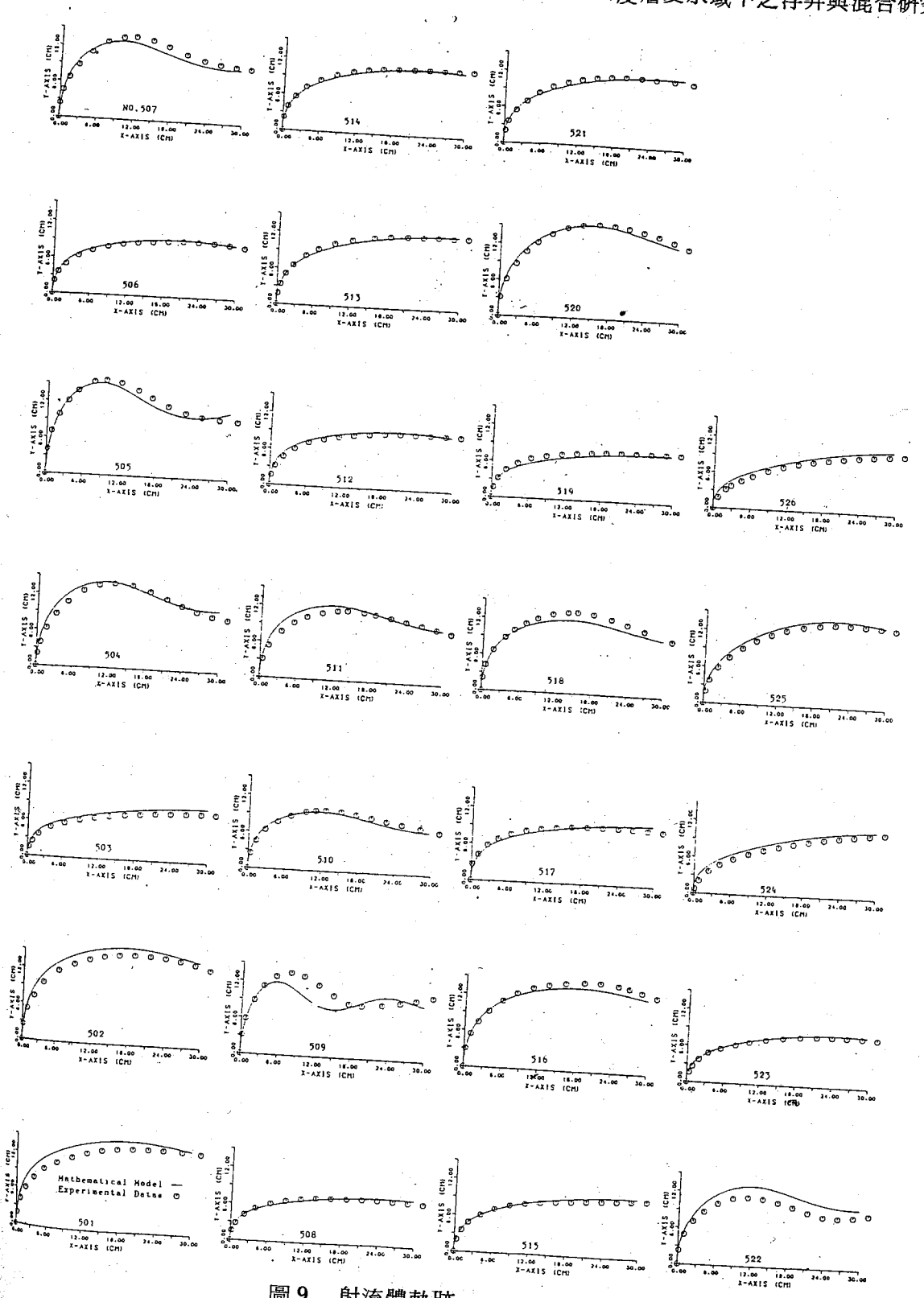

圖 9　射流體軌跡

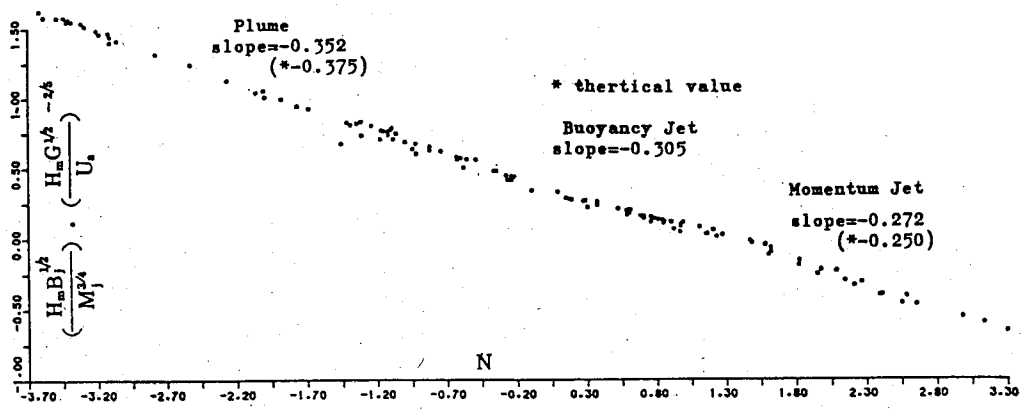

圖 11.1 $\frac{H_m B_j}{M_j^{3/4}} \sim N^p \cdot \left(\frac{H_m G^{1/2}}{U_a}\right)^m \qquad m = 2/5$

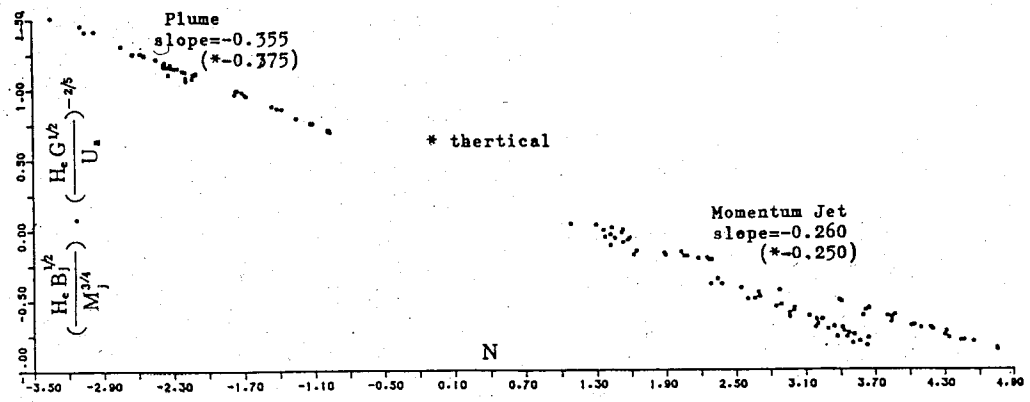

圖 11.2 $\frac{H_e B_j}{M_j^{3/4}} \sim N^q \cdot \left(\frac{H_e G^{1/2}}{U_a}\right)^n \qquad n = 2/5$

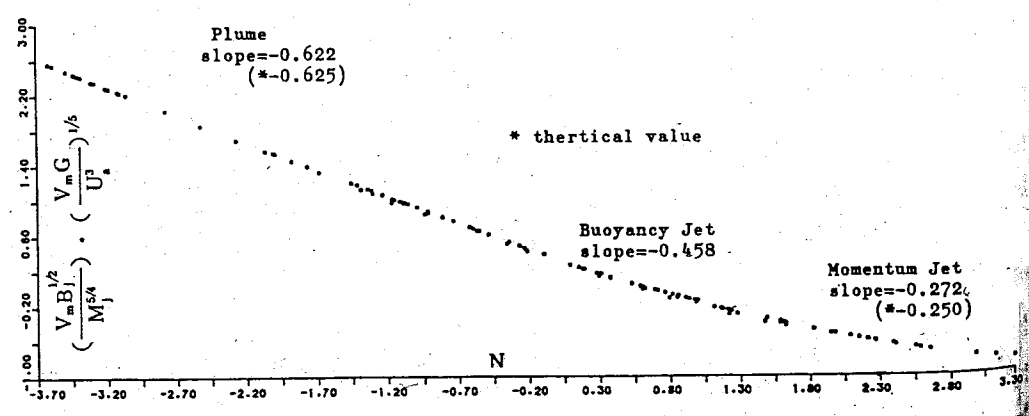

圖 11.3 $\frac{V_m B_j}{M_j^{5/4}} \sim N^r \cdot \left(\frac{V_m G}{U_a^3}\right)^\ell \qquad \ell = -1/5$

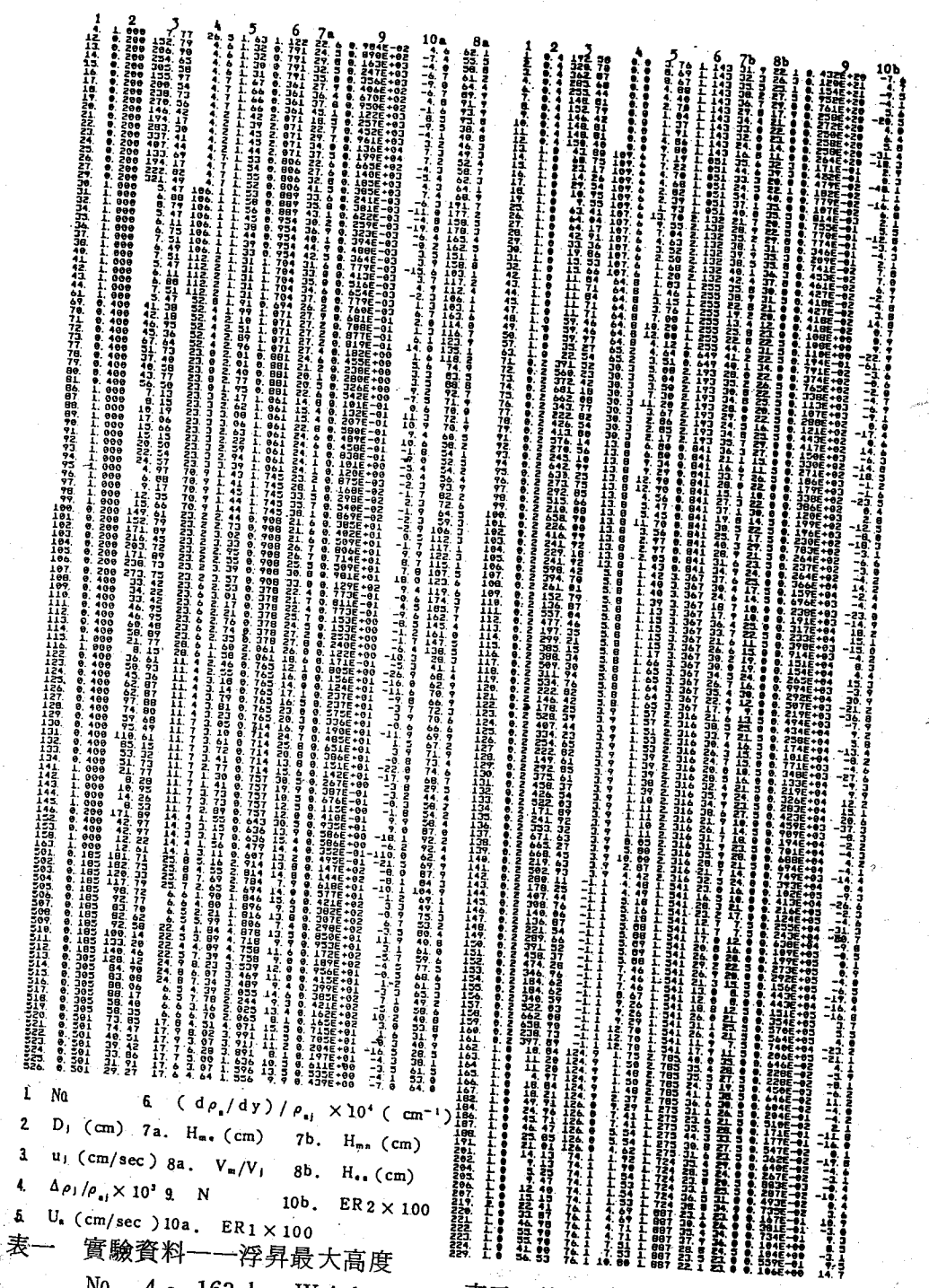

1 No.
2 D_j (cm)
3 u_j (cm/sec)
4 $\Delta\rho_j/\rho_{aj} \times 10^3$
5 U_a (cm/sec)
6 $(d\rho_a/dy)/\rho_{aj} \times 10^4$ (cm^{-1})
7a H_{ma} (cm)
7b H_{mn} (cm)
8a V_m/V_j
8b H_{ea} (cm)
9 N
10a ER1 × 100
10b ER2 × 100

表一 實驗資料——浮昇最大高度
No. 4 ~ 163 by Wright [8]
501 ~ 526 by Authors

表二 實驗資料——浮昇平衡高度
No. 1 ~ 229 by Wright [8]

河口及港灣流場傳輸及擴散之數值研究

黃　榮　鑑
中央研究院物理研究所
梁　興　杰
國立臺灣大學土木工程學研究所

摘　要

風力與潮汐在河口及港灣引生之流場傳輸運動及擴散研究，最初僅由水工模型試驗方法以觀測瞭解其現象，近年由於電子計算機之快速發展，由控制流場變化之方程式；在連續方程式、運動方程式及擴散方程式，藉電子計算機之高速計算以進行數值運算。本文即以有限元素法進行流場之動力模式及擴散模式之數值研究，利用葛拉金近似（ Galerkins approximation ）將垂直積分後之控制方程式轉換爲有限元素方程式，由對時間之積分求解時變微分代數式，以建立二維動力及擴散模式。將模式用以求解一維波方程式，由數值結果與解析解之比較以檢驗模式之準確性，驗證結果顯示結果甚佳。

壹、前　言

河口及港灣爲河川與海洋之連接水域，上游所携帶之一切物質與流量都經此排放外海，該處水體因受潮汐、風、地形及上游流量之影響，使得流場之傳輸與擴散現象變得相當複雜。瞭解河口及港灣之流場流態以及污染質排放在該區域造成之濃度分佈，對於污染之防制及環境水域之保護將有直接之幫助。

一般而言，河口及港灣之流場傳輸及擴散的研究方法有三：現場觀測、水工模型試驗以及數值模擬。以上三種方法各有其特性及重要性。現場觀測爲就原場進行觀測及調查，所得結果最爲眞實，唯費用甚鉅且難獲完整之結果。水工模擬試驗能於實驗室觀測流場與擴散之現象，對於性向之結果能提供良好之參考，惟水工模型對原場之模擬有其一定之限制，很難由實驗結果對原場之特性變化獲得定量之模擬。數值模擬是由控制其物理量變化之制御方程式，藉數值解析及計算以求解其物理量之變化。近年來由於電子計算機之快速發展，許多先前無法求解的問題，如今都能利用電子計算機之高速計算而求解，其中應用最爲廣泛的爲有限差分法[1]與有限元素法[2][3]。

Lin & Leendertse[4][5]，Simons[6]等曾先後以有限差分法探討港灣受潮汐與風及湖泊受風作用下之流場傳輸流況，由於其數值模式中所用未定係數很多，計算龐大

，對於計算時間相當費時。Wang & Connor[7]，Leimhuhler[8]及管[9]曾利用權重殘餘法之有限元素法探討港灣流場之傳輸及擴散問題，惟未曾考慮地形變化、內部剪應力等因子之影響。有限差分法與有限元素法之數值計算各有其優劣利弊，一般都認爲對於複雜邊界的處理，有限元素法較有限差分法爲佳。

河口及港灣內水體由於受潮汐、風、上游入流量地形及邊界等因素之影響，其流場之變化極爲複雜。本文爲利用有限元素法之葛拉金近似（Galerkin's approximation）由控制流場之連續方程式、運動方程式及污染質擴散方程式，垂直積分後之三維方程式轉換爲有限元素方程式，並對控制方程式中各項予以定量計算，和改進對時間積分之技巧及對邊界條件之處理，以使數值分析結果更趨精確與穩定。

貳、基本方程式

河口及港灣受潮汐、風力以及河流流量排入之影響，其流場及濃度分佈的變化可由連續方程式、運動方程式及濃度擴散方程式來描述，這些方程式爲：

$$\frac{\partial u}{\partial x}+\frac{\partial v}{\partial y}+\frac{\partial w}{\partial z}=0 \qquad \cdots\cdots(1)$$

$$\frac{\partial u}{\partial t}+u\frac{\partial u}{\partial x}+v\frac{\partial u}{\partial y}+w\frac{\partial u}{\partial z}-fv=-\frac{1}{\rho}\frac{\partial p}{\partial x}+\frac{\partial \tau_{xx}}{\partial x}+\frac{\partial \tau_{yx}}{\partial y}+\frac{\partial \tau_{zx}}{\partial z} \qquad \cdots\cdots(2)$$

$$\frac{\partial v}{\partial t}+u\frac{\partial v}{\partial x}+v\frac{\partial v}{\partial y}+w\frac{\partial v}{\partial z}+fu=-\frac{1}{\rho}\frac{\partial p}{\partial y}+\frac{\partial \tau_{xy}}{\partial x}+\frac{\partial \tau_{yy}}{\partial y}+\frac{\partial \tau_{zy}}{\partial z} \qquad \cdots\cdots(3)$$

$$\frac{\partial p}{\partial z}=-\rho g \qquad \cdots\cdots(4)$$

$$\frac{\partial c}{\partial t}+u\frac{\partial c}{\partial x}+v\frac{\partial c}{\partial y}+w\frac{\partial c}{\partial z}=\varepsilon_{xx}\frac{\partial^2 c}{\partial x^2}+\frac{\partial}{\partial y}\left(\varepsilon_{yy}\frac{\partial c}{\partial y}\right)+\frac{\partial}{\partial z}\left(\varepsilon_{zz}\frac{\partial c}{\partial z}\right) \qquad \cdots(5)$$

式中，（u,v,w,）爲（x,y,z）方向所對應之流速分量，τ_{ij} 爲剪應力張量之分量，$f=2w_f\sin\phi$，爲地球自轉參數，w_f 爲地球自轉之角速度，ϕ 爲緯度度數。

由於潮汐影響的水面波動爲長波，因此流場可以淺域視之，亦即對於水深方向爲完全混合之水域，可藉垂直向之積分，使三維問題簡化爲二維問題。將上述方程式(1)、(2)、(3)及(4)取垂直向由$-h$至η積分，可得：

$$\frac{\partial H}{\partial t}+\frac{\partial q_x}{\partial x}+\frac{\partial q_y}{\partial y}=0 \qquad \cdots\cdots(6)$$

$$\frac{\partial q_x}{\partial t}+\frac{\partial}{\partial x}\left(\int_{-h}^{\eta}u^2dz\right)+\frac{\partial}{\partial y}\left(\int_{-h}^{\eta}uvdz\right)-fq_y+\frac{\partial}{\partial x}(F_p-F_{xx})-\frac{\partial F_{yx}}{\partial y}$$

$$-\frac{1}{\rho_0}(\tau_{zx}^s-\tau_{zx}^b)-\frac{1}{\rho_0}p^s\frac{\partial H}{\partial x}-g\eta\frac{\partial h}{\partial x}=0 \qquad \cdots\cdots(7)$$

$$\frac{\partial q_y}{\partial t}+\frac{\partial}{\partial x}\left(\int_{-h}^{\eta}uvdz\right)+\frac{\partial}{\partial y}\left(\int_{-h}^{\eta}v^2dz\right)+fq_x-\frac{\partial F_{xy}}{\partial x}+\frac{\partial}{\partial y}(F_p-F_{yy})$$

$$-\frac{1}{\rho_0}(\tau_{zy}^s-\tau_{zy}^b)-\frac{1}{\rho_0}p^s\frac{\partial H}{\partial y}-g\eta\frac{\partial h}{\partial y}=0 \qquad \cdots\cdots(8)$$

式中水面剪應力，τ^s 及底床剪應力，τ^b 分別表示爲：

$$\tau_{zx}^s=\rho_a c_D U_{10}^2\sin\theta \quad , \quad \tau_{zy}^s=\rho_a c_D U_{10}^2\cos\theta$$

及

$$\tau_{zx}^b=\rho_0 c_f(q_x^2+q_y^2)^{1/2}q_x/H^2$$

$$\tau_{zy}^b=\rho_0 c_f(q_x^2+q_y^2)^{1/2}q_y/H^2$$

ρ_a 及 ρ_0 分別爲空氣和水之密度，U_{10} 爲水面上10公尺處之風速，c_D 及 c_f 分別爲空氣阻方係數和底床摩擦係數，θ 爲風向與y方向之夾角，$H=h+\eta$ 爲總水深。

F_{ij} 爲內部剪應力（internal stresses，依據普蘭特混合理論（Prandtl mixing-length theory）可表示如下：

$$F_{ij}=E_{ij}\left(\frac{\partial q_i}{\partial x_j}+\frac{\partial q_j}{\partial x_i}\right) \quad , \quad i,j=1,2$$

$q_x=\int_{-h}^{\eta}udz$ 及 $q_y=\int_{-h}^{\eta}vdz$ 分別表示x－及y－向之單位寬度流量。

擴散方程式(5)經對垂直方向積分後可簡化爲：

$$\frac{\partial c}{\partial t}+\frac{\partial}{\partial x}(\bar{U}\bar{C})+\frac{\partial}{\partial y}(\bar{V}\bar{C})=-\frac{\partial Q_x}{\partial x}-\frac{\partial Q_y}{\partial y} \qquad \cdots\cdots(9)$$

式中 $C=\rho\bar{C}H$，$\bar{U}$，$\bar{V}$ 及 $\bar{C}$ 分別爲垂直之平均物理量。

$$Q_x=-\rho_0 H\left(K_{xx}\frac{\partial\bar{C}}{\partial x}+K_{yx}\frac{\partial\bar{C}}{\partial y}\right)$$

$$Q_y=-\rho_0 H\left(K_{xy}\frac{\partial\bar{C}}{\partial x}+K_{yy}\frac{\partial\bar{C}}{\partial y}\right) \qquad \cdots\cdots(10)$$

K_{ij} 爲擴散係數。

方程式(6)、(7)、(8)及(9)爲控制流場內物理變量H，q_x，q_y 及C之制御方程式，給予流場之適當起始條件及邊界條件即可藉數值方法得到閉合型式解。

流場中之邊界分爲兩類：一爲固定邊界（land boundary），S_q。另一爲開口邊界（ocean boundary），S_f。固定邊界 S_q 上之正交方向流量 q_n 與切線方向流量 q_s 可分別表示爲：

$$q_n=\alpha_{nx}q_x+\alpha_{ny}q_y=q_n^*$$

$$q_s=-\alpha_{ny}q_x+\alpha_{nx}q_y=q_s^* \qquad \cdots\cdots(11)$$

式中，$\alpha_{nx}=\cos(n,x)$ 及 $\alpha_{ny}=\cos(n,y)$ 分別爲方向餘弦。在開口邊界 S_f，由於水位變動而引生之外力亦可以下二式表示之：

$$F_{nn}=\alpha_{nx}F_{nx}+\alpha_{ny}F_{ny}=F_{nn}^*$$

$$F_{ns}=-\alpha_{ny}F_{nx}+\alpha_{nx}F_{ny}=F_{ns}^* \qquad \cdots\cdots(12)$$

域內各點之起始條件可以下式表示，即

$$(H, q_x, q_y, C) = (H_0, q_{x0}, q_{y0}, C_0) \quad \text{當 } t = 0 \qquad \cdots\cdots (13)$$

參、有限元素法

有限元素法是一種求解微分方程式近似解的數值方法，它的基本概念是將整個區域連體視爲子區域元素之組合，做爲流場解析的模擬。在每一個子區域內之連續場性可以用一假設函數來表示，利用變分原理（variable principles）或權重殘餘法（weighting residual）將控制方程式轉換爲該區域之有限元素方程式，再對每個子區域疊加組成大域系統（global system）之微分或代數方程式，利用起始條件及邊界條件，則待解各變數在每一節點之函數值可由此系統方程式求得。

如子區域之元素爲三角形，則元素中各變數可表示如下：

$$\begin{aligned} q_x &= \xi_1 q_{x1}^e + \xi_2 q_{x2}^e + \xi_3 q_{x3}^e \\ q_y &= \xi_1 q_{y1}^e + \xi_2 q_{y2}^e + \xi_3 q_{y3}^e \\ H &= \xi_1 H_1^e + \xi_2 H_2^e + \xi_3 H_3^e \\ C &= \xi_1 C_1^e + \xi_2 C_2^e + \xi_3 C_3^e \end{aligned} \qquad \cdots\cdots (14)$$

式中 ξ_1，ξ_2，ξ_3 爲單位化元素座標，其與 x－y 座標之關係爲：

$$\xi_i = \frac{1}{2A}(c_i + b_i x + a_i y), \quad i = 1, 2, 3 \qquad \cdots\cdots (15)$$

及

$$a_i = x_k - x_j$$
$$b_i = y_j - y_k$$
$$c_i = x_j y_k - x_k y_j$$
$$A = \frac{1}{2}(b_1 a_2 - b_2 a_1)$$

利用葛拉金近似（Galerkins approximation）取形狀函數爲權重函數，將方程式(6)～(9)就每一元素子區域積分並疊加後，經整理得系統方程式：

$$[M_H][\dot{H}] = [P_H] \qquad \cdots\cdots (16)$$
$$[M_{qx}][\dot{q}_x] = [P_{qx}] \qquad \cdots\cdots (17)$$
$$[M_{qy}][\dot{q}_y] = [P_{qy}] \qquad \cdots\cdots (18)$$
$$[M_c][\dot{C}] = [P_c] \qquad \cdots\cdots (19)$$

式中，$[M_H]$，$[M_{qx}]$，$[M_{qy}]$ 及 $[M_c]$ 爲相對於各變數之係數矩陣，$[P]$ 爲柱狀矩陣。

方程式(16)、(17)、(18)及(19)爲時變微分方程式，求解得從設定之起始條件對時間積分。Roache[1] 及 Wang[7] 曾比較不同時間技巧在有限差分法及有限元素法之應用，其中以二次顯性模式（two-step explicit scheme）較佳，不但精確穩定且時間間距 Δt 可較長。二次顯性法的理論與 Lax-Wendroff 有限差分法是相似的。二次顯性法是以兩次一階微分近似直接求得時變函數，即：

$$f\left(t + \frac{\Delta t}{2}\right) = f(t) + \frac{\Delta t}{2} f(t)$$

$$f(t + \Delta t) = f(t) + \Delta t\, f\left(t + \frac{\Delta t}{2}\right) \qquad \cdots\cdots (20)$$

應用二次顯示法求解方程式(16)、(17)、(18)及(19)式之步驟爲：

第一步驟：

$$[\bar{M}_H][H^{n+1/2}] = [M_H][H^n] - \frac{\Delta t}{2}[P_H^n] \qquad \cdots\cdots (21)$$

$$[\bar{M}_{qx}][q^{n+1/2}] = [M_{qx}][q_x^n] - \frac{\Delta t}{2}[P_{qx}^n] \qquad \cdots\cdots (22)$$

$$[\bar{M}_{qy}][q^{n+1/2}] = [M_{qy}][q_y^n] - \frac{\Delta t}{2}[P_{qy}^n] \qquad \cdots\cdots (23)$$

$$[\bar{M}_C][C^{n+1/2}] = [M_C][C^n] - \frac{\Delta t}{2}[P_C^n] \qquad \cdots\cdots (24)$$

第二步驟：

$$[\bar{M}_H][H^{n+1}] = [M_H][H^n] - \Delta t[P_H^{n+1/2}] \qquad \cdots\cdots (25)$$
$$[\bar{M}_{qx}][q^{n+1}] = [M_{qx}][q_x^n] - \Delta t[P_{qx}^{n+1/2}] \qquad \cdots\cdots (26)$$
$$[\bar{M}_{qy}][q^{n+1}] = [M_{qy}][q_y^n] - \Delta t[P_{qy}^{n+1/2}] \qquad \cdots\cdots (27)$$
$$[\bar{M}_C][C^{n+1}] = [M_C][C^{n+1}] - \Delta t[P_C^{n+1/2}] \qquad \cdots\cdots (28)$$

以上諸式中，n，$n+1/2$ 及 $n+1$ 分別爲第 n，第 $n+1/2$ 及第 $n+1$ 時段之值。$[\bar{M}_H]$ 等爲加入邊界條件調整後之矩陣。經由電腦程式及運算，在不同時段之流場中物理變量 H，q_x，q_y 及 C 即可求得其數值解。

肆、結果與討論

爲檢驗模式運算之準確性，利用前述之有限元素法數值模式以探討等水深矩形渠道內之駐立波（standing wave）運動情形，其控制方程式爲：

$$\frac{\partial^2 u}{\partial t^2} = gh\frac{\partial^2 u}{\partial x^2} \qquad \cdots\cdots (29)$$

$$\frac{\partial^2 \eta}{\partial t^2} = gh\frac{\partial^2 \eta}{\partial x^2} \qquad \cdots\cdots (30)$$

如圖(一)(a)所示，假設渠道之長度爲 L，$x = 0$ 處爲開口端，其水面受正弦波 $\eta_0 = a\sin(2\pi/T)t$ 作用，a 爲振幅，T 爲週期。在 $x = L$ 處爲封閉端，其正交方向之流量爲零，即 $u = 0$ 或 $\partial\eta/\partial x = 0$，利用分離變數法可得其解析解爲：

$$u(x,t) = -\frac{a\sqrt{gh}}{h\cos\left(\frac{2\pi}{T}\frac{L}{\sqrt{gh}}\right)}\sin\left[\frac{2\pi}{T}\frac{L}{\sqrt{gh}}\left(\frac{x}{L} - 1\right)\right]\cos\frac{2\pi}{T}t \qquad (31)$$

$$\eta(x,t)=\frac{a}{\cos\left(\frac{2\pi}{T}\frac{L}{\sqrt{gh}}\right)}\cos\left[\frac{2\pi}{T}\frac{L}{\sqrt{gh}}\left(\frac{x}{L}-1\right)\right]\sin\frac{2\pi}{T}t \quad (32)$$

有限元素法之平面分割如圖㈠(b)所示，在三個固定邊界使其正交方向流量爲零。由方程式(21)、(22)、(23)及(25)、(26)、(27)之數值解可獲得駐立波在渠道中之運動情形。圖㈡及圖㈢所示分別爲數值解與解析解在 x＝L 處及 x＝0 處之水位及流速變化之比較。表一及表二爲渠道中各點在不同時段時之比較。比較結果顯示，在兩個週期內，最大誤差與最大值之比不超過 1％，結果相當良好。

爲使上述之數值模式之應用一般化，用以探討不規則地形與形狀之港灣受潮汐、入流量及風等作用下之流場運動情形。港灣之地形及形狀示如圖㈣，入流量爲每秒 100m³，風速爲 10 knot（約 5.05 m／sec），潮汐之水位變化在開口處爲 $\eta_0=a\sin 2\pi/T\ t$，取 a＝0.2 公尺，T＝2 小時。

元素之分割示如圖，以 t＝0 時靜止流場爲起始條件，取 $E_{xx}=E_{yy}=400\ cm^2/sec$，$E_{yx}=E_{xy}=200\ cm^2/sec$，$C_f=0.0036$。上述條件經模式計算結果如下：

1. 節點 7 和 67 二點水位與 y 一向流速之變化如圖㈤(a)、(b)所示，流場傳輸呈週期性運動。
2. 在不同時間之速度場變化如圖㈥(a)、(b)、(c)、(d)所示。
3. 圖㈦(a)、(b)、(c)及(d)所示爲在不同時間流場相對應之流速及等濃度線分佈情形。
4. 數值演算收斂很快，約經過一個週期，流場之變化即趨恒定（stationary）。

伍、結　論

1. 二維數值模式用以一維波方程式之檢定，其數值解與解析解之比較結果甚佳，對於應用於完全混合水體之模擬應可得到良好結果。
2. 二次顯性法對時間之積分可以取至二階微分近似，又可避免非線性項之疊代運算，其結果較一階線性近似準確，且可節省計算機之計算時間。
3. 起始條件與模式之精確及穩定有關，若起始條件設定合理，將易收斂，否則易造成數值運算之不穩定，一般的原則是避免造成梯度變化太大。
4. 由於摩擦的作用，潮汐之傳輸有衰減的現象，越上游受上游入流量的影響越大，受潮汐的影響越小。
5. 應用本文之二維數值模式以預估潮汐作用下污染質之擴散，其結果趨勢相當合理。

參考文獻

1. Roache, P. J., Computational Fluid Dynamics, Hermosa, 1972.
2. Zienkiewicz, O. C., The Finite Element Method, McGraw-Hill, New York, 1977.

3. Gallagher, R. H. et al., Finite Elements in Fluids, 3 Volumes, Wiley-Interscience Publication, 1979.
4. Liu, S. K. & J. J. Leendertse, A Three-dimensional model for estuaries and coastal seas, The Rand Cooperation, R-2405-NOAA, Sep. 1979.
5. Lin, S. K. & J. J. Leenderstse, Multi-dimensional numerical modeling of estuaries and coastal seas, The Rand Cooperation, 1978.
6. Simons, T. J., Development of three-dimensional numerical model of the great lakes, Proceedings 15th Conference on Great Lakes Research, 1972.
7. Leimkuhler, W. F., A two-dimensional finite element dispersion model, Thesis for the degree of civil Engineering, MIT, Sep. 1974.
8. Wang, J. D. & J. J. Connor, Mathematical modeling of near coastal circulation, Tech. Report No. 200, R. M. Parsons Laboratory for Water Resource and Hydrodynamics, MIT, April, 1975.
9. 管秩豐，有限元素法在河口潮汐的傳送應用，國立台灣大學土木工程研究所碩士論文，中華民國七十年六月。

表一　數值計算水位與解析解之比較

X \ t	3T/4	5T/4	7T/4	9T/4	11T/4	Exact
0	-0.1	0.1	-0.1	0.1	-0.1	+0.1
50	-0.1028	0.1005	-0.1027	0.1025	-0.1027	0.1026
100	-0.1047	0.1042	-0.1045	0.1042	-0.1046	0.1044
150	-0.1057	0.1053	-0.1055	0.1052	-0.1057	0.1055
200	-0.1063	0.1056	-0.1061	0.1056	-0.1062	0.1059

表二　數值計算流速與解析解之比較

x \ t	T/2	T	3T/2	2T	5T/2	Exact
0	-0.05466	0.05446	-0.05431	0.05417	-0.05431	0.05440
50	-0.04125	0.04117	-0.04086	0.04096	-0.04087	0.04114
100	-0.02781	0.02772	-0.02751	0.02749	-0.02749	0.02759
150	-0.01388	0.01383	-0.01375	0.01370	-0.01381	0.01384
200	0.00	0.0	0.0	0.0	0.0	0.0

河口及港灣流場傳輸及擴散之數值研究

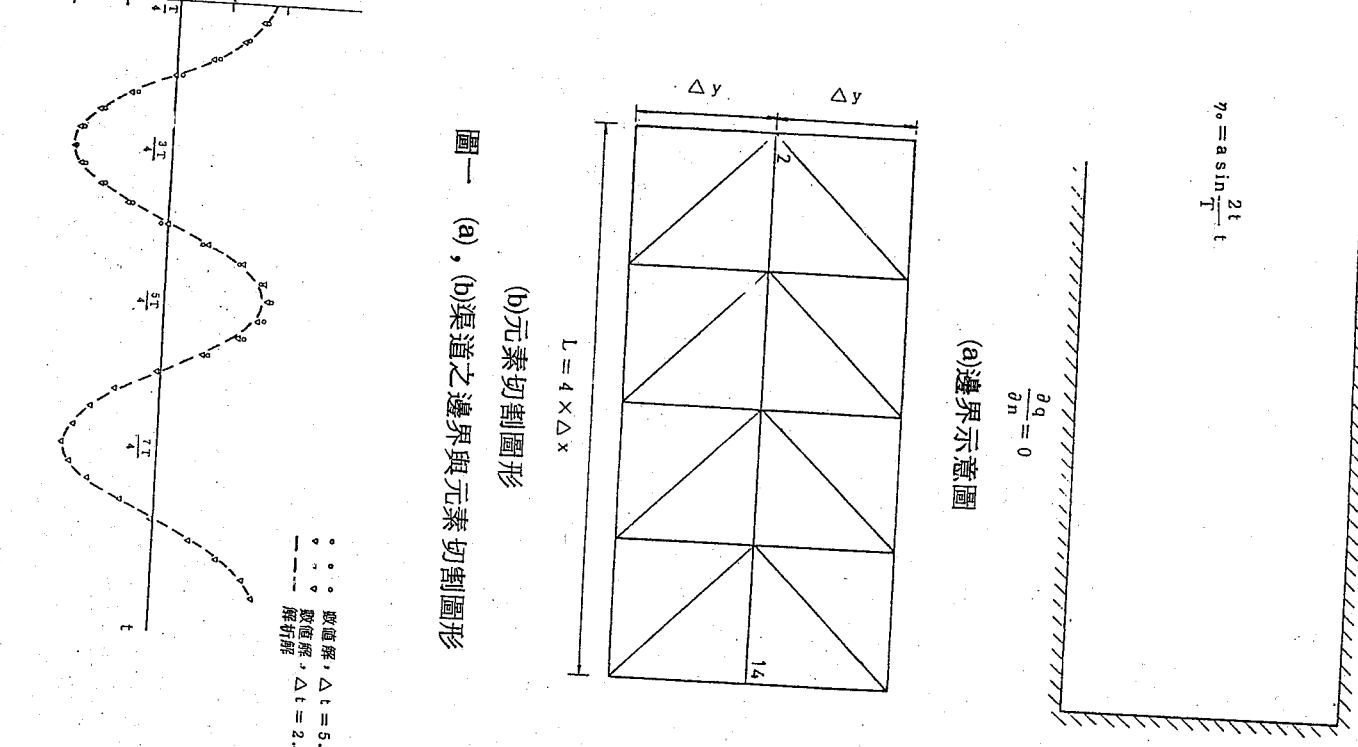

(a)邊界示意圖

(b)元素切割圖形

圖一　(a)，(b)渠道之邊界與元素切割圖形

圖二　x = L 處（節點 14）水位之變化情形

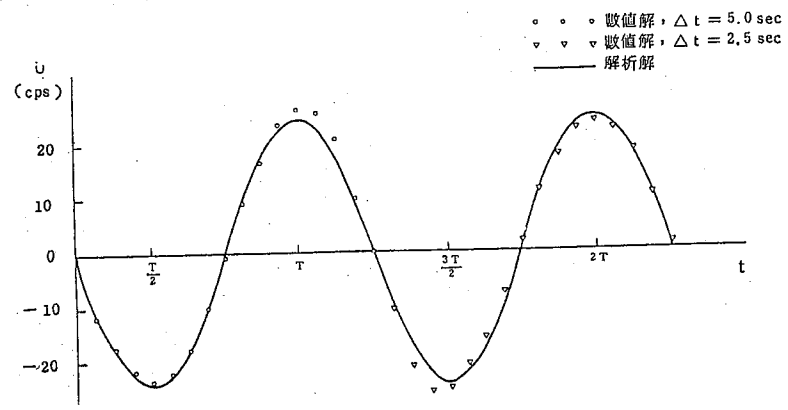

圖三　x = 0 處（節點 2 ）流速之變化情形

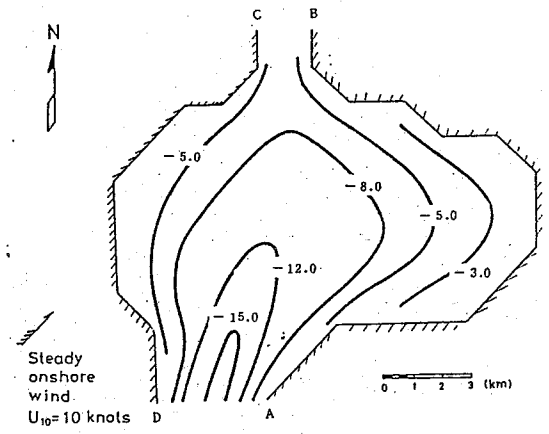

圖四(a)　地形變化之示意圖

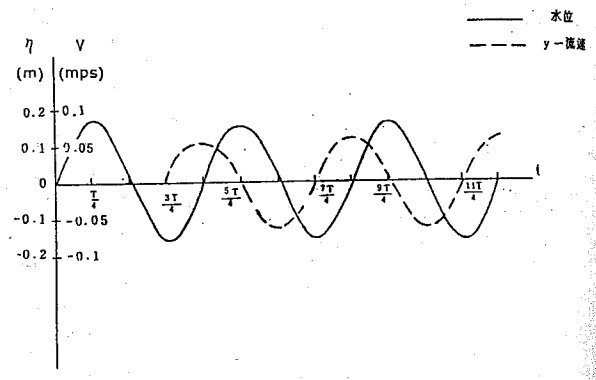

圖五(a)　節點 7 水位與 y－流速之變化圖形

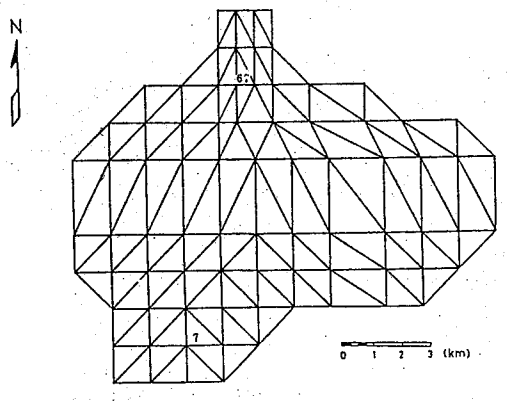

圖四(b)　元素切割示意圖

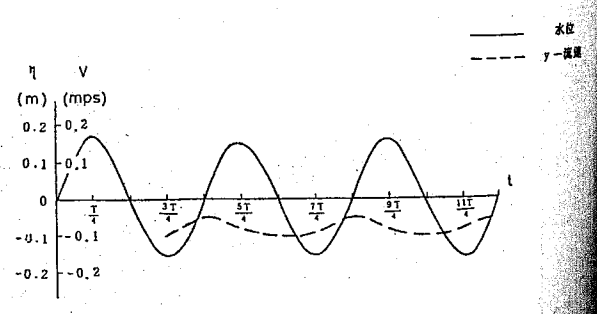

圖五(b)　節點 67 水位與 y－流速之變化圖形

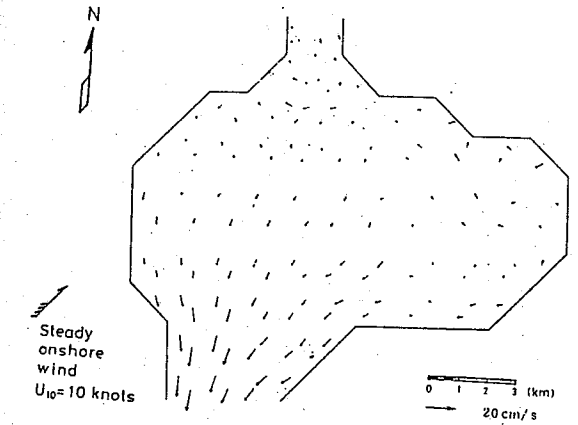

圖六(a)　t = 4.5 小時之速度場

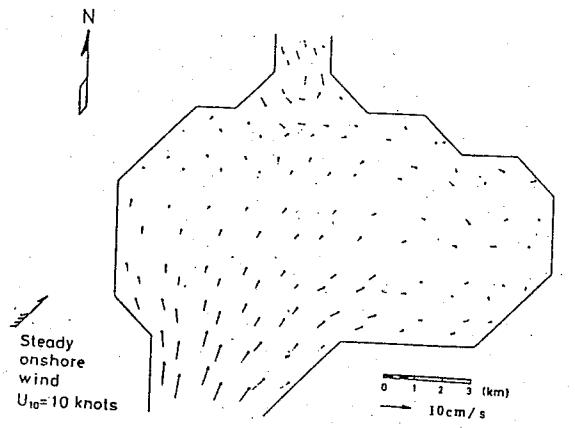

圖六(c)　t = 5.5 小時之速度場

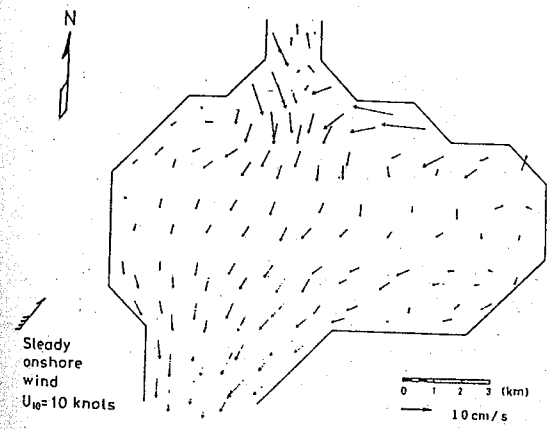

圖六(b)　t = 5.0 小時之速度場

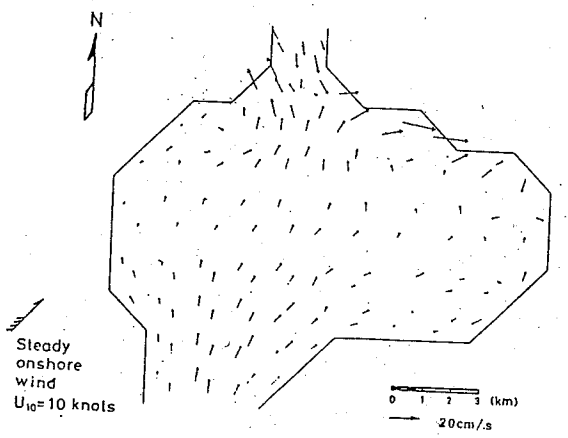

圖六(d)　t = 6.0 小時之速度場

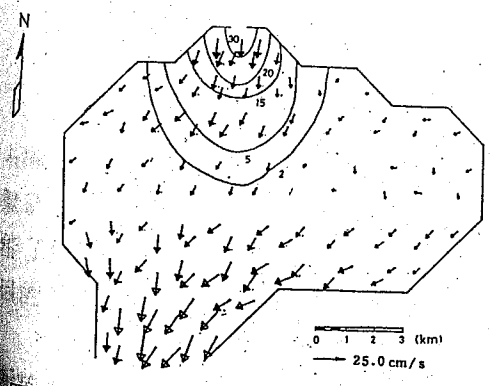

圖七(a)　t = 4.0 小時之等濃度線

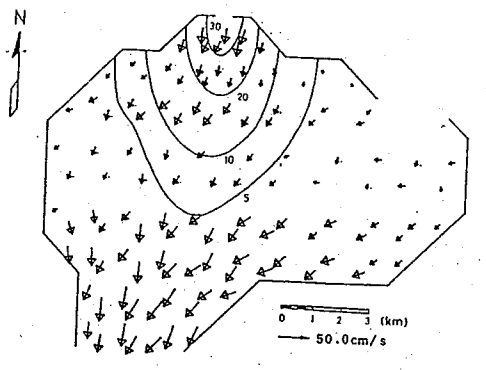

圖七(b)　t = 8.0 小時之等濃度線

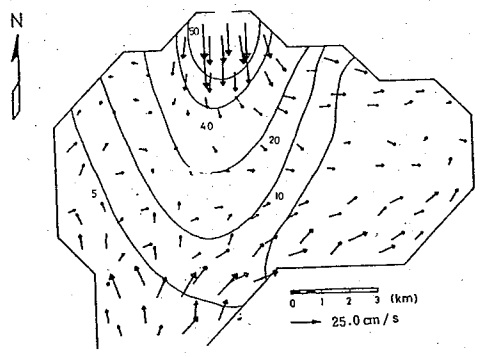

圖七(c)　t = 10.0 小時之等濃度線

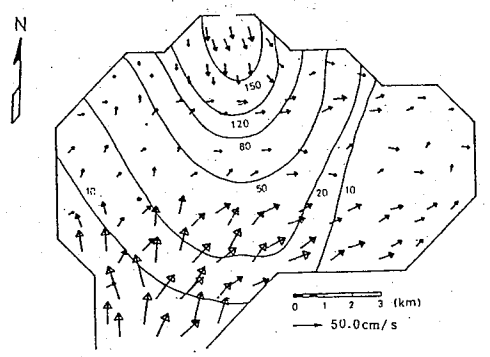

圖七(d)　t = 12.0 小時之等濃度線

大氣擴散參數時間序列預報之研究

梁　文　傑
中央研究院物理研究所
國立臺灣大學機械工程學系

張　瑞　宗
國立臺灣大學環境工程研究所

摘　要

本文是以各擴散參數小時平均值的逐時變化資料爲對象，來分析並建立各參數小時平均值的自迴歸積分移動平均（ ARIMA ）預報模式，以了解各擴散參數的小時變化。

研究結果顯示，此模式能對各大氣擴散參數如風向、風速、大氣穩定度、溫度的變化提供良好且可行的預報，對於週期性與季節性變化的情況，此模式亦能有效的掌握。對未來24小時（一天）的預報，文中以四組數據作個案研究，結果顯示，風向平均誤差爲25度，而大氣穩定度預報則準確性高，風速的平均預報誤差約爲0.45 公尺／秒，溫度的預報誤差則小於 1 ℃。

此研究可供區域性各擴散參數建立預報模式的參考，以預求未來短期內諸參數可能存有的擴散不利情況，儘早做適當的防制，以避免空氣品質的惡化。

壹、引　言

空氣品質是環境品質的重要指標，而空氣品質的好壞與氣象、氣候及地形狀況息息相關。由於因素甚多，使得空氣污染防治策略變得複雜。這些因素包括風向、風速、大氣穩定度（ Atmospheric Stability ）、溫度、太陽輻射（ Solar Radiation ）等。如能了解上述參數的變化，對於空氣污染的防治可得事半功倍的效果。因此本文最主要的目的，即爲對擴散參數在未來短期內的變化做一通盤的了解。

大氣擴散參數中，本文選定大氣穩定度、風向、風速及溫度進行研究，因爲穩定度對於大氣的擴散能力（即擴散係數）影響極大，風向與風速爲決定排放源（污染源）污染物質傳播的方向與速度，而溫度則會因影響煙囪排放的有效高度（Effective height），進一步影響到地面的濃度[1]。如能掌握上述四參數未來的變化，有助於求取其他有關的物理量，進而得知空氣污染擴散的大要。

空氣污染濃度的預報（即一般的擴散模式），通常是利用流體力學的制御方程式（

包括能量方程式），把當時風向、風速、大氣穩定度等氣象因素及污染源的分佈與排放量等資料全盤考慮，以推算下一時間濃度的分佈情形，然而因各種資料的取得受到經費與人力等現實因素的限制，再加上大氣紊流（Turbulence）過於複雜，所得的結果將不可能太密集且準確，必會有某種程度上的誤差，但儘管對局部性變化無法準確把握，就全面性的變化趨勢而言仍然提供了極爲有益的資訊。

本文鑑於擴散模式對局部性變化的掌握有其欠缺，乃另採途徑，直接以偵測站所得的資料，加以分析，利用統計方法，找出適合該區域各擴散參數的預報模式，因資料皆在該地實測，可使擴散模式中各參數的考慮更能反應出當地當時的實況及未來的變化，這些參數預測值應用於擴散模式或直接利用統計方法預測污染狀況，必能更有效的把握局部性變化，補一般大氣擴散模式的不足。

大氣擴散參數變化甚大，其預報雖十分困難，然由前人的研究可發現[2][3][4]以統計預報模式建立的各參數預報模式，如線性迴歸（Linear Regression）、複迴歸（Multi-Regression）及模式輸出統計法（Model Output Statistics）等，效果十分良好。

BOX與Jenkins[5]更於1970年提出時間序列分析法，依各種觀測物理量時間序列的特性，建立不同的隨機時序數學模式（Statistic Model），並應用所建立的隨機模式作預測。此隨機模式包括自迴歸（Auto-Regression簡稱AR）、積分（Integral簡稱I）與移動平均（Moving Average簡稱MA）三部分，故簡稱爲ARIMA，因其爲處理單一變數的問題，所以是單一變數ARIMA（Univariate ARIMA）的時間序列統計模式。此方法已被廣泛的應用在工程、水文、氣象、經濟、商業及自然科學的決策分析、控制研究及定量預測，其進一步的推廣應用是可預期的。本研究即嘗試以ARIMA對諸大氣擴散參數包括風向、風速、大氣穩定度及溫度做時序分析，並建立其預報模式。

貳、基本統計模式理論

一、基本定義

對一物理量做一等時距的連續量測，則量測所得的數列叫做時間序列，而時間序列的分析法，是以統計方法分析。由觀測所得的時間序列，如果它的分配機率，不因時間的移動而改變，稱爲嚴格穩定（Strictly Stationary），若此時序的前二階矩（Moment），不因時間的移動而改變，則稱爲二次穩定（Second-Order Stationary），但若所得的序列係非穩定性（Non-Stationary），則需藉數次的差分，以得新的穩定性時間序列。

一般說來一組時間序列，經由BOX與Jenkins氏所建議的方法，可以建立一個包含有三部分的隨機時間模式，包括自迴歸（AR）、積分（I）與移動平均（MA），其中積分（I）的部分，是當該序列爲非穩定性時才有，所以對一組穩定性的時間序列，它的預報模式將只包括自迴歸與移動平均（ARMA）兩個部分，非穩定性的時間序列，則藉差分的過程，使其穩定，然後再求其ARMA模式，最後合成ARIMA的模式。

二、模式的建立

ARIMA的基本觀念在於一物理量的過去觀測值Z_t，可由一線性隨機模式來代表，該物理量未來的變化，可藉此模式有限個過去觀測值與有限個過去擾動值的權重和來預測。AR（p）模式可寫成：

$$\tilde{Z}_t=\phi_1\tilde{Z}_{t-1}+\phi_2\tilde{Z}_{t-2}+\cdots+\phi_p\tilde{Z}_{t-p}+a_t, \quad \cdots\cdots(1)$$

此處$\tilde{Z}_t=Z_t-\mu$，μ爲觀測物理量的平均值，ϕ_1，$\phi_2\cdots\cdots\phi_p$爲AR（p）模式的p項參數，而$\{a_t\}$數列爲擾動（Shocks），統計上假設此擾動數列爲常態分配（Normal Distribution），其期望值（Expect Value）爲零，變異數（Variance）爲σ_a^2此數列的隨機變數（Random Variable），a_t，$a_{t-1}\cdots a_{t-p}$又稱爲白噪音（White Noise）。

若定義函數$\phi(B)$爲$(1-\phi_1B-\phi_2B^2-\cdots-\phi_pB^p)$，式中B爲後移運算子（Backshift Operator），即B^mZ_t爲Z_{t-m}，則(1)式可改寫爲：

$$\phi(B)\tilde{Z}_t=a_t, \quad \cdots\cdots(2)$$

而MA（q）模式可寫成：

$$\tilde{Z}_t=a_t-\theta_1a_{t-1}-\theta_2a_{t-2}-\cdots-\theta_qa_{t-q}, \quad \cdots\cdots(3)$$

式中θ_1，θ_2，$\cdots\theta_q$爲MA（q）模式的q項參數，a_t，a_{t-1}，$\cdots a_{t-q}$係白噪音。

若定義$\theta(B)$爲$(1-\theta_1B-\theta_2B^2-\cdots-\theta_qB^q)$則上式可寫成：

$$\tilde{Z}_t=\theta(B)a_t, \quad \cdots\cdots(4)$$

綜合(1)～(4)，ARMA（p,q）模式可寫成：

$$\tilde{Z}_t=\phi_1\tilde{Z}_{t-1}+\phi_2\tilde{Z}_{t-2}+\cdots+\phi_p\tilde{Z}_{t-p}+a_t-\theta_1a_{t-1}-\theta_2a_{t-2}-\cdots-\theta_qa_{t-q}$$

或簡寫成 $\cdots\cdots(5)$

$$\phi(B)\tilde{Z}_t=\theta(B)a_t, \quad \cdots\cdots(6)$$

上式適用於時間序列在一統計上的穩定狀況，即觀測數列的機率分配不因時間改變，實際上甚多時間序列傾向於非穩定性，此時則可用下式代表（即ARIMA（p·d·q）模式）：

$$\phi(B)\nabla^dZ_t=\theta(B)a_t, \quad \cdots\cdots(7)$$

上式中∇^d爲$(1-B)^d$，∇^d運算子的功用係將一非穩定性的時間序列Z_t，取d次差分後轉換爲穩定的時間序列。如對(6)式方程式兩邊取期望值，則因白噪音a_t的平均值爲零，我們發現對平均值不爲零的時間序列，需要先減去其平均值μ，以後我們就以$\tilde{Z}_t$代表$Z_t-\mu$。

由Jenkins與Watts[6]的理論ARMA（p,q）模式的變異數可寫爲：

$$\mathrm{Var}(Z_t)=\sigma_a^2\int_{-\frac{T}{2}}^{\frac{T}{2}}\left|\sum_{\alpha=0}^{q}\theta_\alpha e^{-i2\pi\omega\alpha}\right|^2\Big/\left|\sum_{j=0}^{p}\phi_je^{-i2\pi\omega Tj}\right|^2 d\omega, \quad \cdots\cdots(8)$$

式中T爲所取觀測值的總時間長度，ω是頻率（Frequency），σ_a是a_t的變異數。如分子部分的多項式θ_α，（$\alpha=0\cdots\cdots q$）的項數有限，則(8)式會收斂（Converge）

，但分母部份可表示爲（ $1-\phi_j \times e^{-i2\pi\omega T})^{mj}$ 的乘積，其中mj 是第 j 個因子的地方，(8)式的變異數在 $|\phi_j|<1$ 時會收斂，而(2)式方程式的根爲 $\frac{1}{\phi_j}$（ j = 1，2，…，p ），這意味著 $\phi(B)=0$ 的根必須在單位圓的外面，才會使變異數收斂，這就是穩定性的條件。例如對ARMA（1，0）模式：

$$(1-\phi_1 B)\tilde{Z}_t = a_t$$

則

$$\tilde{Z}_t = \phi_1 \tilde{Z}_{t-1} + a_t$$
$$\tilde{Z}_{t+1} = \phi_1^2 \tilde{Z}_{t-1} + \phi_1 a_t + a_{t+1}$$
$$\tilde{Z}_{t+2} = \phi_1^3 \tilde{Z}_{t-1} + \phi_1^2 a_t + \phi_1 a_{t+1} + a_{t+2}$$

以此類推，當 $|\phi_1|>1$ 時，則現在的值對愈遠的將來影響反而愈大，此不合理，而當 $|\phi_1|=1$ 時，則其影響力保持定值，不因時間而消退，即具有累積的作用，此時會產生不穩定的序列，所以穩定性的要求使 $\phi(B)=0$ 的解都必須位於單位圓外。

雖然穩定性對ARMA（p，q）的移動平均部分 θ_α 沒有什麼限制，但它仍必須滿足可逆性（ Invertibility ）的要求，這乃是爲了要使時間序列符合實際的物理現象。例如考慮ARMA（0，1）的情形：

$$\tilde{Z}_t = (1-\theta_1 B)a_t$$

則

$$a_t = (1-\theta_1 B)^{-1}\tilde{Z}_t$$
$$= (1+\theta_1 B+\theta_1^2 B^2+\cdots+\theta_1^k B^k)(1-\theta_1^{k+1}B^{k+1})^{-1}\tilde{Z}_t$$

所以

$$\tilde{Z}_t = -\theta_1\tilde{Z}_{t-1}-\theta_1^2\tilde{Z}_{t-2}-\cdots-\theta^k\tilde{Z}_{t-k}+a_t-\theta_1^{k+1}\tilde{Z}_{t-k+1}$$

若 $|\theta_1|>1$ 則現在的 Z_t 會受到 Z_{t-k} 的影響，k 隨時間的增加而增大，意即愈久遠以前的事件，對現在的情況影響愈大，此與一般現象不合，所以若 $\theta(B)$ 寫成（ $1-\theta_\alpha B)^{m_\alpha}$ 的乘積，其中 m_α 是 $\theta(B)$ 的第 α 根的次數，則 $|\theta_\alpha|<1$，（ $\alpha=1$，… q ），使得該時序可逆，也就是說，可逆的要求使得 $\theta(B)=0$ 的根都必須在單位圓的外面。

討論過穩定性與可逆性的問題後，將着手建立合適的模式。建立模式的過程如圖(一)所示，可概述如下：

1. 利用統計方法鑑定（ Identification ）模式。
2. 由已有的觀測序列來估計（ Estimation ）模式中未知的參數值。
3. 診斷檢驗（ Diagnostic Checking ）此模式是否適當，是否能正確代表觀測的時間序列，並符合精簡原則。
4. 如果模式適當則可用於分析預報，如果模式不適當，則重複進行第 1 至第 3 的步驟，直到尋獲適當的模式爲止。

作時間序列分析時，我們必須算出該序列遲滯 k 的自相關函數（ Autocorrelation Function，簡稱ACF ）及遲滯 k 的部份自相關函數（ Partial Autocorrelation

Function，簡稱PACF），求法詳述於後。但以上各值是由有限長度的序列所求出，並不全然就是理論上實際的值，有時在理論值消失後仍然可能出現相當大的估計值，所以我們需要一個判別方法來指出那些值不爲零，我們取ACF、PACF的標準離差（ Standard deviation ），作爲判斷的依據，如果理論值爲零，而估計值呈常態分佈，則估計值的絕大值大於一倍標準離差的可能性爲三分之一，大於兩倍標準離差的可能性只有二十分之一，所以我們把估計值大於兩倍離差者皆視爲理論值不爲零。

Bartlett[7] 證明ACF的標準離差爲：

$$\sigma[\gamma_k] \simeq \frac{1}{n^{1/2}}\left[1+\sum_{i=1}^{q}\gamma_i^2\right]^{1/2},\quad k>q$$

此處 γ_i 爲遲滯 i 的ACF。另外Quenouill[8] 證明了 PACF 估計標準離差爲：

$$\sigma[\phi_{kk}] = \frac{1}{n^{1/2}},\quad K>P$$

利用 ACF 及 PACF 的標準離差我們可找到理論值不爲零的 ACF 及 PACF，由其分佈的情形，可推論判斷出可能的 ARMA（p，q）模式。

三、模式的分類

(一)非季節性模式

對於穩定的非季節性模式，可用下列原則判斷：

1. 若ACF逐漸消失（ tail off ）而PACF在 $K\le P$ 時顯著，$K>P$ 時不顯著，此時爲 AR（p）模式，即：

$$\tilde{Z}_t = \phi_1\tilde{Z}_{t-1}+\phi_2\tilde{Z}_{t-2}+\cdots+\phi_p\tilde{Z}_{t-p}+a_t$$

或

$$\phi(B)\tilde{Z}_t = a_t$$

2. 若PACF逐漸消失而ACF 在 $K\le q$ 時顯著，$K>q$ 不顯著，則此模式爲MA（q）即：

$$\tilde{Z}_t = a_t-\theta_1 a_{t-1}-\cdots-\theta_q a_{t-q}$$

或可寫爲

$$\tilde{Z}_t = \theta(B)a_t$$

3. 若ACF於遲滯 q − p + 1 時間始呈現指數（ Exponential ）及阻尼正弦波（ Damped Sin Wave ），混合型消退，PACF亦呈現此現象，則此時適用模式爲ARMA（p，q）即：

$$\tilde{Z}_t = a_t-\theta_1 a_{t-1}-\theta_2 a_{t-2}-\cdots-\theta_q a_{t-q}+\phi_1\tilde{Z}_{t-1}+\phi_2\tilde{Z}_{t-2}$$
$$+\cdots+\phi_p\tilde{Z}_{t-p}$$

或可寫成

$$\phi(B)\tilde{Z}_t = \theta(B)a_t$$

然有時可能會發現ACF及 PACF 並沒有如上述的現象而沒有很快的消退，此時意味著可能是一非穩定性的序列。對非穩定的時間序列要經過數次的差分產生穩定性的新時序 W_t（ $W_t=\nabla^d Z_t$，d = 0，1，2，…），此處 $\nabla^d=(1-B)^d$，而 d 爲使 W_t 成爲

穩定的最小差分數，一般不大於 2 。而對於 W_t 我們就可利用前面所述的方法，得其合適的 ARMA（p，q）：

$$\phi(B)W_t = \theta(B)a_t,$$

再把 $W_t = \nabla^d Z_t$ 代入則得一完整的 ARIMA（p，d，q）模式：

$$\phi(B)\nabla^d Z_t = \theta(B)a_t$$

㈡季節性的模式（ Seasonal Model ）

當時間序列具有週期性變化時，其 ACF 及 PACF 也會有週期出現，無法用簡單的差分來消除，此時就要採用季節性模式，此模式分爲兩部份。

1. 週期性的部份

若時間序列具有週期 S ，可把相隔 S的 Z_t 運用前面所說過的方法來求取 ARIMA 模式，即：

$$(1-\phi_1^* B^S - \phi_2^* B^{2S} - \cdots - \phi_{p_1}^* B^{p_1 S})(1-B^S)^{d_1} Z_t$$
$$= (1-\theta_1^* B^S - \theta_2^* B^{2S} - \cdots - \theta_{q_1}^* B^{q_1 S})\rho_t \quad \cdots\cdots(9)$$

上式中 ρ_t 爲另一組時間序列，一般而言 ρ_t 不是白噪音，所以對於 ρ_t 我們仍需作如下操作。

2. 非週期性部份

⑼式中的 ρ_t 可以上述的非季節性時間序列加以判斷，而得一合適的 ARIMA（p，d，q）模式：

$$(1-\phi_1 B - \phi_2 B^2 - \cdots - \phi_p B^p)(1-B)^d \rho_t$$
$$= (1-\theta_1 B - \cdots - \theta_q B^q)a_t \quad \cdots\cdots(10)$$

把週期性及非週期性兩部分⑼及⑽式綜合起來，就得通用的相乘季節性模式（ General Multiplicative Seasonal Model ）：

$$\phi_p(B)(1-B^d)\phi_{p1}^*(B^S)(1-B^S)^{d_1} Z_t$$
$$= \theta_q(B)\theta_{q1}^*(B^S)a_t \quad \cdots\cdots(11)$$

其中

$$\phi_p(B) = (1-\phi_1 B - \cdots - \phi_p B^p)$$
$$\theta_q(B) = (1-\theta_1 B - \cdots - \theta_q B^q)$$
$$\phi_{p1}^*(B^S) = (1-\phi_1^* B^S - \cdots - \phi_{p1}^* B^{p_1 S})$$
$$\theta_{q1}^*(B^S) = (1-\theta_1^* B^S - \cdots - \theta_{q1}^* B^{q_1 S})$$

我們稱此爲（p，d，q）×（ p_1 ， d_1 ， q_1 ）s 的季節性 ARIMA模式。

我們可由理論利用圖表或公式先找出各參數 ϕ ， θ ， ϕ^* 及 θ^* 的起始值（Starting Values ），代入模式中可得一組同樣時間的預測值，我們稱其爲起始擬合（ Original Fitting ）Z_{tf} ，由 Z_{tf} 與 Z_t 的差得到一個殘差的平方和，利用非線性最小平方差法（ Non-Linear Least Square Error Method ），經過數次的迭代（ Iterations ），使殘差平方和爲最小的參數值，即爲所求的參數值。迭代的次數由我們所選的起始值與所要求的精度所決定。

求出各種參數值後，須做模式的診斷檢驗（ Diagnostic Checking ），以便對模式

的適性（ Goodness of Fit ）作診斷，以瞭解所求得的模式是否能最佳的代表觀測數列。第一個檢驗方法爲過度配合（ Overfitting ），在所求得的模式兩側各加一項，倘若原來的模式恰當，則會顯示加上去的項是多餘的，然此法並不表示所得模式爲最佳模式。另一方法是看 a_t 是否白噪音，首先把 a_t 的ACF算出，則因估計的殘差與 a_t 的實際餘差有如下的關係：

$$a_t = a_t + O\cdot\left(\frac{1}{\sqrt{N}}\right)$$

所以若有一個以上的 ACF 明顯的大於兩倍的 $\frac{1}{\sqrt{N}}$ 則考慮修改模式。

最後還要做殘差自相關總體鑑定，若在 k 項後的 a_t 的 ACF 可以忽略且令 $n = N - d - Sd_1$ ，定義下面的量 Q：

$$Q = n\sum_{k=1}^{k}\rho_k^2(a_t)$$

Q值可用來和 χ^2（K－P－d）比較，此處 χ^2 爲Chi-Square 分配，可取 90 %或 95 %。信賴區間來比較，而對 a_t 作一總體檢驗，看是否爲白噪音，若模式不太恰當，則可用殘差的 ACF 來修正。倘若在診斷模式後並未發現模式有不宜之處，則該模式可用來預報。

四、預報的原理

預報的方法是把ARIMA模式展開，若 $Z_t(\ell)$ 表示在時間 t 時預報 $t+\ell$ 時間的值，則對式中各項可用下面的值代入該模式中：

$$[Z_{t-j}] = E[Z_{t-j}] = Z_{t-j}\ ,\ j = 0,1,2$$
$$[Z_{t+j}] = E[Z_{t+j}] = Z_t(j)\ ,\ j = 1,2$$
$$[a_{t-j}] = E[a_{t-j}] = a_{t-j} = Z_{t-j} - Z_{t-j-1}\ ,\ j = 0,1,2$$
$$[a_{t+j}] = E[a_{t+j}] = 0\ ,\ j = 1,2$$

換句話說，若該值爲已發生事件，則用已知值代入，若該值尚未發生則代入期望值，如此一來，我們不僅可在時間 t 作預測，且隨時可因新資料的獲得而做即時預報（Updating Forecasting ），其方法爲首先我們定義無窮級數：

$$\Psi(B) = \sum_{j=1}^{\infty}\Psi_j B^j$$

令 $Z_t = \Psi(B)a_t$

則 $\varphi(B)Z_t = \theta(B)a_t$

$\varphi(B) = \phi(B)\Delta^d$

故 $\varphi(B)\Psi(B) = \theta(B)$

把多項式展開，比較兩邊係數可得：

$$\Psi_1 = \Psi_1 - \theta_1$$
$$\Psi_2 = \varphi_1\Psi_1 + \varphi_2 - \theta_2$$
$$\vdots \quad \vdots \quad \vdots \quad \vdots$$
$$\Psi_j = \varphi_1\Psi_{j-1} + \cdots + \varphi_{p+d}\Psi_{j-p-d} - \theta_j$$

此處 $\Psi_0 = 1$，對 $j < 0$ 之項 $\Psi_j = 0$，且 $j > q$ 時 $\theta_j = 0$，最後可得：

$$\Psi_j = \varphi_1\Psi_{j-1} + \varphi_2\Psi_{j-2} + \cdots + \varphi_{p+d}\Psi_{j-p-d}, \quad j > q$$

又因

$$Z_{t+1}(\ell) = \Psi_\ell a_{t+1} + \Psi_{\ell+1}a_t + \Psi_{\ell+2}a_{t-1} + \cdots\cdots$$
$$Z_t(\ell+1) = \Psi_{\ell+1}a_t + \Psi_{\ell+2}a_{t-1} + \cdots\cdots$$

所以

$$Z_{t+1}(\ell) = Z_t(\ell+1) + \Psi_\ell a_{t+1}$$

故隨時間的進行，每一個新發生的值都可以立刻用來得到一最新的預測。

五、基本資料的算法

對於一組 N 個的時間序列 Z_t 其平均值 μ 及變異數（Variance）σ_z^2 分別爲：

$$\mu = \left[\sum_{i=1}^{N} Z_t\right] / N$$

$$\sigma_z^2 = \left[\sum_{i=1}^{N} (Z_t - \mu)^2\right] / N$$

算出 μ 及 σ_z^2 後可接著計算遲滯 k 的自協變量數（Autocovariance）γ_k 及遲滯 k 自相關函數（ACF）ρ_k：

$$\gamma_k = E[(Z_t - \mu)(Z_{t+k} - \mu)]$$
$$\rho_k = \gamma_k / \gamma_0$$

此處 $E[Z_t]$ 爲統計上的求取期望值，顯然 $\gamma_0 = \sigma_z^2$，而 $\rho_0 = 1$。

得到自相關函數後，我們仍需計算部分自相關函數（PACF）ϕ_{kk}，其表示法爲：

$$\phi_{kk} = \frac{\begin{vmatrix} 1 & \rho_1 & \cdots & \rho_{k-2} & \rho_1 \\ \rho_1 & 1 & \cdots & \rho_{k-3} & \rho_2 \\ \vdots & \vdots & & \vdots & \vdots \\ \rho_{k-1} & \rho_{k-2} & \cdots & \rho_1 & 1 \end{vmatrix}}{\begin{vmatrix} 1 & \rho_1 & \cdots & \rho_{k-1} \\ \rho_1 & 1 & \cdots & \rho_{k-2} \\ \vdots & \vdots & & \vdots \\ \rho_{k-1} & \rho_{k-2} & \cdots & 1 \end{vmatrix}} \qquad \cdots\cdots(12)$$

由上式知 PACF 可由 ACF 而求得：

$$\text{PACF}(1) = \text{ACF}(1) = \rho_1$$
$$\text{PACF}(2) = \frac{\text{ACF}(2) - [\text{ACF}(1)]^2}{1 - [\text{ACF}(1)]^2} = \frac{\rho_2 - \rho_1^2}{1 - \rho_1^2}$$
$$\text{PACF}(3) = \frac{-2\,\text{ACF}(1)\,\text{ACF}(2) - [\text{ACF}(1)]^2\text{ACF}(3)}{1 + 2[\text{ACF}(1)]^2\text{ACF}(2) - [\text{ACF}(2)]^2 - [\text{ACF}(1)]^2}$$
$$= \frac{-2\rho_1\rho_2 - \rho_1^2\rho_3}{1 + 2\rho_1^2\rho_2 - \rho_2^2 - \rho_1^2}$$

六、模式的判斷

(一) AR (P) 模式的特性

AR (P) 的模式可展開如下：

$$\tilde{Z}_t = \phi_1\tilde{Z}_{t-1} + \phi_2\tilde{Z}_{t-2} + \cdots + \phi_p\tilde{Z}_{t-p} + a_t$$

兩邊同乘 Z_{t-k} 再取期望值可得：

$$\gamma_k = \phi_1\gamma_{k-1} + \phi_2\gamma_{k-2} + \cdots + \phi_p\gamma_{k-p} \qquad k > 0$$

兩邊同除 γ_0 則上式變爲：

$$\rho_k = \phi_1\rho_{k-1} + \phi_2\rho_{k-2} + \cdots + \phi_p\rho_{k-p} \qquad k > 0$$

或可寫成 $\phi(B)\rho_k = 0$，此處 $\phi(B) = 1 - \phi_1 B - \cdots - \phi_p B^p$ 而 B 爲對 k 作用而不是 t，若：

$$\phi(B) = \prod_{i=1}^{p}(1 - G_i B)$$

此處 G_1^{-1}，$G_2^{-1}\cdots\cdots G_p^{-1}$ 爲 $\phi(B) = 0$ 的根，則：

$$\rho_k = A_1G_1^k + A_2G_2^k + \cdots + A_pG_p^k$$

穩定性的條件要求 $|G_i| < 1$，假設 $\phi(B)$ 的根是分開（distinct）不連在一起，則：

1. G_i 是實數時，隨著 k 的增加 $A_iG_i^k$ 會呈指數衰減而衰減至零。
2. 若 G_i，G_j 爲成對的共軛複數，則它們會構成如下式的關係式：

$$d^k\sin(2\pi f k + F)$$

而使自相關函數成正弦阻尼波衰退。

再看 AR (P) 的 PACF，設此 AR 模式的次數爲 k，而 ϕ_{kj} 爲其第 j 個的係數，則 ϕ_{kk} 爲最後一個係數，所以由式

$$\rho_j = \phi_{k1}\rho_{j-1} + \cdots + \phi_{k(k-1)}\rho_{j-k+1} + \phi_{kk}\rho_{j-k} \qquad j = 1, 2\cdots k$$

就產生了 Yule-Walker 方程式：

$$\begin{vmatrix} 1 & \rho_1 & \rho_2 \cdots \rho_{k-1} \\ \rho_1 & 1 & \rho_1 \cdots \rho_{k-2} \\ \vdots & \vdots & \vdots \\ \rho_{k-1} & \rho_{k-2} & 1 \end{vmatrix} \begin{vmatrix} \phi_{k1} \\ \phi_{k2} \\ \vdots \\ \phi_{kk} \end{vmatrix} = \begin{vmatrix} \rho_1 \\ \rho_2 \\ \vdots \\ \rho_k \end{vmatrix}$$

所以有式(12)的表示法。

對於AR（P）而言，當k小於或等於ρ時，PACF、ϕ_{kk}會大於零，而在$k>\rho$時則會變成零。

㈡MA（q）模式的特性

MA（q）的模式可寫成：

$$\tilde{Z}_t = a_t - \theta_1 a_{t-1} - \cdots - \theta_q a_{t-q}$$

所以

$$\gamma_k = E[(a_t - \theta_1 a_{t-1} - \cdots - \theta_q a_{t-q})(a_{t-k} - \theta_1 a_{t-k-1} - \cdots - \theta_q a_{t-k-q})]$$

故

$$\gamma_0 = (1 + \theta_1^2 + \theta_2^2 + \cdots + \theta_q^2)\sigma_a^2$$

$$\gamma_k = \begin{cases} (-\theta_k + \theta_1\theta_{k+1} + \theta_2\theta_{k+2} + \cdots + \theta_{q-k}\theta_q)\sigma_a^2 & k = 1, 2, \cdots, q \\ 0 & k > q \end{cases}$$

所以

$$\rho_k = \begin{cases} -\theta_k + \theta_1\theta_{k+1} + \cdots + \theta_{q-k}\theta_q & k = 1, 2, \cdots, q \\ 0 & k > q \end{cases}$$

因此MA（q）的ACF在遲滯k大於q之後會變爲零。MA（q）的ϕ_{kk}除了在$q=1$時

$$\phi_{kk} = -\phi_{1k}(1 - \theta_1^2)/(1 - \theta_1^{2(k+1)})$$

呈現阻尼指數消退外，其他在$q \geq 2$時較複雜，但仍漸漸的消退，所以對MA（q）的判斷主要在依據ACF。

㈢ARMA（p，q）的特性

把ARMA（p，q）的模式展開成：

$$\tilde{Z}_t = \phi_1\tilde{Z}_{t-1} + \cdots + \phi_p\tilde{Z}_{t-p} + a_t - \theta_1 a_{t-1} - \cdots - \theta_q a_{t-q}$$

兩邊乘以Z_{t-k}再取期望值得：

$$\gamma_k = \phi_1\gamma_{k-1} + \cdots + \phi_p\gamma_{k-p} + \gamma_{za}(k) - \theta_1\gamma_{za}(k-1) - \cdots - \theta_q\gamma_{za}(k-q) \quad \cdots\cdots(13)$$

此處$\gamma_{za}(k) = E[Z_{t-k}a_t]$

所以：

$$\gamma_{za}(k) = 0 \quad \text{當 } k > 0$$

$$\gamma_{za}(k) \neq 0 \quad \text{當 } k \leq 0$$

當$k \geq q+1$時：

$$\gamma_k = \phi_1\gamma_{k-1} + \phi_2\gamma_{k-2} + \cdots + \phi_p\gamma_{k-p} \qquad k \geq q+1$$

同除γ_0後得：

$$\rho_k = \phi_1\rho_{k-1} + \phi_2\rho_{k-2} + \cdots + \phi_p\rho_{k-p} \qquad k \geq q+1$$

或可寫成$\phi(B)\rho_k = 0$。

所以ARMA（p，q）的ACF，ρ_1，ρ_2，…ρ_q由式(13)來決定，而此q個AC

，可用來算$k \geq q+1$時，$\phi(B)\rho_k = 0$的ACF，若$q-p<0$則ACF，ρ_j，$j=0$，1，2，會有混合的阻尼指數或阻尼正弦波。若$q-p \geq 0$則ρ_0，ρ_1，…，ρ_{q-p}，此$q-p+1$個起始的ACF，並不表示上述的一般型態，如此可用來鑑別ARMA（p，q）的型式，至於ARMA（p，q）的PACF，則會向無窮遠延伸，它最後會表現出純MA（q）的PACF型式，呈現出阻尼指數和（或）阻尼正弦波。

參、氣象資料分析

一、概　述

本文研究對象爲風向、風速、大氣穩定度與溫度。資料來源爲中央研究院物理研究所於民國71年秋季（10至12月）在南港工職所設的氣象觀測站測定的結果。一般習慣將風向劃分爲十六個方位，本文因研究的目的不同，所取的數據爲每小時平均風向的實測角度。風速採每小時風速的平均值，以公尺／秒表示。一般環境空氣品質模式中的穩定度，係依照Pasiquill(12)與Gifford(13)法，由日照、雲量與風速等觀測值而推算（簡稱P—G分類法），本文係依據Stoner(14)氏的分類法，以水平風向的標準偏差角σ_θ決定大氣穩定度，並將之分爲六級，根據Stoner氏建議，當風速過小時，大氣穩定度以P—G分類法較佳。本文並參考Mitchell和Timbre(15)氏的建議，考慮大氣穩定度的夜間修正。所謂夜間係指日落前一小時至日出後一小時，本文中設定爲下午六時至上午七時，氣溫也是取小時平均值，以℃表示。

二、氣象資料來源

㈠測站位置區域概述

由中央氣象局台北測站所得台北市各氣象要素的平均值，可看出風向於春秋多三季多爲東北季風（出現機會約70％左右），平均風速約爲2～3 m／sec。本研究所設的氣象測站，位於南港區南港工職行政大樓的四樓頂，其感應器高出樓頂約六公尺，即測站離地面的高度約18公尺左右，四周尚稱空曠，唯左方200公尺處有台北市垃圾堆積場，高度約30公尺。300公尺外有小丘陵存在，二者尚不致對測站構成顯著的影響。測站附近大多爲2或4樓的磚瓦房或鋼筋混凝土房，除西南方100公尺處的南港區公所爲十層建築物外，並沒有較高的建築物。

㈡測站使用儀器說明

測站使用的氣象觀測爲微電腦資料處理系統A—10，而記錄資料包括風向、風速、溫度及風向的變異量（即σ_θ）。各氣象因子先經感應器（Sensor），再經訊號調整器（Processor）轉換成爲線性電壓後，進入資料處理機（data logger）作資料分析與處理，經過處理的資料數據，由印刷機印於紙帶上，同時以磁帶記錄機記錄於磁帶上。

此處所用的風速與風向感應器，較一般氣象觀測者所用的精密，風速感應器的起動風僅需0.28 m／s，而一般則在0.6～1.0 m／s。可測得的風速範圍從0～45 m／s亦較一般氣象儀器爲寬，其風力訊號的轉換，係利用光電感應產生方波（脈波），不

同於一般發電式，前者爲一數字形式訊號，精確度與線性程度均較後者類比訊號者佳。風向感應器其起動風速亦爲0.28m／ s，用線圈感應發電，而非一般碳粉電阻感應，故解析力較高。溫度感應器係白金電偶式，其感應範圍從－30 ℃到 50 ℃，在此範圍內線性誤差小於 5 %。

訊號調整器調整各感應器測量的結果，使輸出成爲線性電壓訊號，處理過程是將各個不同位準（ level ）的輸入訊號，放大爲同一位準的輸出訊號，其輸出訊號及所代表的觀測量如下表：

因　子	輸　出（伏　特）	觀　測　值
風　向	0—5	0—360°
風　速	0—5	0—45 m／ s
溫　度	1.785—4.863	0—46.83 ℃

各感應器均爲瞬間訊號，其密度與精確度均高，爲能處理大量資料，本系統選用資料微處理機代替人爲處理。所用者爲 Acurox 的 Auto-data Ten-10 ，具各種算術運作能力，其處理訊號能力每秒35筆（ channel ），可接受 0 — 10 伏特的輸入訊號，有 4 K的儲存能力，除系統本身所用部分，尚有 1000 筆的日容量。輸入的電壓訊號進入微電腦，首先作單元換算，即爲將電腦轉換爲觀測物理量，然後各量依研究需要，計算一定時間內的平均值、最大值、最小值及標準偏差，依序存入微電腦內，經正式操作每分鐘可得 1000 個觀測值。輸出爲每十分鐘的風向最大、最小、平均值與標準偏差，及每小時的風速和溫度的平均值。

資料微處理機，本身有印刷機（ Printer ）一部，可記錄輸出結果，本系統爲使資料處理更爲迅速，另加二個卡式磁帶記錄器，直接記錄於磁帶上，再利用此磁帶直接進入電腦系統，以提高精確度，所用磁帶如坊間所見的卡式帶，攜帶方便，其儲存能力每面約 6000 筆資料，約可供記錄完整的六天資料。

三、研究步驟

由測站取得的氣象參數觀測資料其流程如圖二所示，因計算機容量的每組數據約爲 216 個小時平均值的時序，除溫度與風速以所得數據的時間序列直接建立各別的預報模式外，風向及大氣穩定度的數據，皆先經過處理。風向以向量型式建立預報模式，取風向平均角度的正弦（ Sine ）值及餘弦（ Cosine ）值形成爲 U 、V 的兩個分量，即將一時序分解爲二個長度相同的新時序U及V，而建立其各別的預報模式，本文將水平風向的標準偏差值做如下的處理：

處　理　前	處　理　後
$40 > \sigma_\theta \geq 30$	$\sigma_\theta = 22.5 + \sigma$
$50 > \sigma_\theta \geq 40$	$\sigma_\theta = 22.5 + 2\sigma$
$60 > \sigma_\theta \geq 50$	$\sigma_\theta = 22.5 + 3\sigma$
$\sigma_\theta \geq 60$	$\sigma_\theta = 22.5 + 4\sigma$

表中σ爲原資料的標準偏差值。

本研究使用的統計預報模式爲 Box and Jenkins 的時序預報模式，建立模式的流程如圖㈠所示。

風向及大氣穩定度的模式預報值，需經轉換成所要的結果。由U（ Sine ）及 V（ Cosine ）各別預報模式所得的預報值，取 $\theta = \tan^{-1}\frac{V}{U}$ ，可得對應的角度預報值，其象限的決定則需由U及V的正負號來決定。大氣穩定度預報所得數據需依表二的分類，轉換成穩定度級數。

四、結果與討論

本文主要探討空氣污染擴散參數包括風向、風速、大氣穩定度與溫度，其時序預報模式的可行性。本文取四組數據，每組皆由連續216小時（ 9 天）的小時平均值所組成，爲了解各參數在同一季的變化，數據時間皆屬秋季。四組數據時間爲 1982 年 10 月 1 日至 10 月 9 日（ A組）、 10 月 21 日至 10 月 29 日（ B組）、 11 月 7 日至 11 月 15 日（ C組）、 12 月 11 日至 12 月 19 日（ D組）。

一、統計預報模式

將各組中各參數的時序，利用前述統計理論，經鑑定、參數值估計及各項檢驗後，可得所求的預報模式，其流程見圖㈠。其 ACF 及 PACF 依前述的模式鑑定法，可判定模式的型式，再利用非線性最小平方差，估計出各模式的參數值。20個模式殘差遲滯（ lag ）1 至 36 的 ACF ，其值皆小於二倍標準偏差，與二倍標準偏差的比較參照圖十九，顯示此二十個預報模式皆合要求。自由度（ Degree of Freedom ）爲 30 的 Chi-square 值分別爲：

$$\chi^2_{30}\ (95\%) = 43.8$$
$$\chi^2_{30}\ (90\%) = 40.3$$
$$\chi^2_{30}\ (50\%) = 34.8$$
$$\chi^2_{30}\ (10\%) = 20.6$$
$$\chi^2_{30}\ (5\ \%) = 18.5$$

Q值爲殘差自相關總體檢定的依據，其定義爲：

$$Q = n \sum_{k=1}^{k} \rho_k^2\ (a_t)$$

當Q值愈小時，總體檢驗顯示出殘差與白噪音越相似，20個模式計算所得的Q值（參照表二），皆小於 χ^2_{30}（ 90 %），大部分在 χ^2_{30}（ 50 %）與 χ^2_{30}（ 10 ）之間，顯示所得的諸模式，皆能有效的代表該時序。圖三至圖十八是殘差時序對其標準偏差的累積機率分佈圖，這些圖顯示擬合（ Original Fitting ）的情形及其誤差的分佈情形。

二、各擴散參數連續小時變化的預報模式

㈠風　　向

風向U（Sine）及V（Cosine）的四組預報模式爲：

$$A:\begin{cases} U(\sin):(1-0.4275B-0.2755B^2+0.1364B^6)(Z_t-0.5924)=a_t \\ V(\cos):(1-0.4262B-0.1434B^3)(Z_t-0.4901)=(1+0.06485B^5+0.1253B^{26})a_t \end{cases}$$

$$B:\begin{cases} U(\sin):(1-B)Z_t=(1-0.6881B+0.1121B^7-0.1469B^{13}-0.1995B^{19}+0.035B^{20})a_t \\ V(\cos):(1-0.4112B-0.0544B^2-0.2055B^3-0.06736B^{13})(Z_t-0.3539)=(1-0.0839B^6)a_t \end{cases}$$

$$C:\begin{cases} U(\sin):(1-0.341B-0.1861B^2-0.1117B^5-0.07383B^8)(Z_t-0.651)=(1-0.04684B^3+0.1168B^6)a_t \\ V(\cos):(1-0.1034B-0.1147B^{11})(Z_t-0.3224) \\ \qquad =(1+0.1602B+0.2362B^2+0.2126B^3)a_t \end{cases}$$

$$D:\begin{cases} U(\sin):(1-0.6275B+0.0238B^6)(Z_t-0.7223) \\ \qquad =(1+0.2241B^3-0.1253B^7)a_t \\ V(\cos):(1-0.4053B-0.01276B^2-0.3389B^3-0.08769B^7)(Z_t-0.3998)=(1+0.03166B^3)a_t \end{cases}$$

實際數據與模式擬合值，皆由 $\theta=\tan^{-1}\frac{U}{V}$ 判定角度，再由U及V的正負判定象限以決定所要的角度，由擬合值與實際值之差所得的殘差時序（角度表示），其個別與總體檢定見圖十九與表二，殘差的累積機率分佈見圖三至圖六。

預報模式不具週期性，資料長度僅九天，故trend不明顯，所選取的資料同爲秋季，所以季節性的考慮亦可忽略。四組模式的階數及類型頗有差異，或是因風向本身變異程度頗大，或是因所取的資料太短。應用時需隨時修正模式，才能更吻合實際的情況。

㈡風　速

由ARIMA所建立的各組風速預報模式爲：

$$A:(1-0.0281B^6+0.1142B^{12})(Z_t-0.9327)=(1+0.4235B^6+0.2493B^{26})a_t$$

$$B:(1+0.06104B+0.1721B^{18}-0.1938B^{21})(1-B)Z_t=(1-0.3065B)a_t$$

$$C:(1-0.7578B+0.04903B^{11})(Z_t-0.7545)=a_t$$

$$D:(1-0.3554B-0.1441B^2)(Z_t-1.164)=a_t$$

實際數據與模式擬合值的差所得的殘差時序，其自相關個別及總體檢定見圖十九與表二，殘差的累積機率分佈見圖七至圖十。雖同爲東北季風，或因風速變異太大，或因所取數據太短，四組風速預報模式差異頗大。

㈢大氣穩定度

經第三章處理過的四組時序所建立的預報模式爲：

$$A:(1-0.1827B+0.0664B^2-0.0613B^3)(1-B)Z_t=(1-0.8902B)a_t$$

$$B:(1-0.2902B-0.312B^2+0.05326B^5)(Z_t-20.1)=(1+0.1646B^6)a_t$$

$$C:(1-0.5194B)(Z_t-22.71)=(1-0.1663B+0.02728B^4+0.116B^6-0.116B^6-0.1295B^{34})a_t$$

$$D:(1-0.0774B-0.0901B^5-0.1447B^6)(Z_t-22.21)=(1+0.249B+0.1004B^5-0.122B^{18}-0.1449B^{35})a_t$$

各組實際數據與預報模式擬合值所得的殘差時序，其自相關個別及總體檢定見圖十九與表二，其殘差的累積機率分佈見圖十一至十四。由Mitchell[16]氏的報告知，大氣穩定度的分類方式有數種，本文採 σ_θ 來分類是因爲：

1. σ_θ 可直接以數值表示，時序處理時較爲簡便。
2. 可直接以 σ_θ 之值判定穩定度等級，較其他分類法客觀，在氣象動力學上亦較具意義
3. σ_θ 的資料易於儲存及使用，以往使用較少，乃因資料獲得的不易，現因微處理器（Micro-processor）的進步，使此不利條件消失，則 σ_θ 應用的推廣是可預期的。

㈣溫　度

四組數據所建立的小時平均值預報模式爲：

$$A:(1-0.1793B+0.0177B^6+0.1191B^{13})(Z_t-25.19)=(1+0.346B^6+0.3778B^{13}+0.4409B^{19})a_t$$

$$B:(1-0.09897B+0.00266B^8-0.009B^{24})a_t=(1-0.6526B^{24})a_t$$

$$C:(1-0.969B-0.08775B^2+0.1327B^3)(Z_t-20.93)=(1+0.1191B^{23}+0.281B^{24}+0.1749B^{25})a_t$$

$$D:(1-0.01273B-0.00253B^2-0.00322B^3-0.00205B^4)(1-B)Z_t=(1-0.9222B)a_t$$

原始數據與預測模式擬合值的差值所得的殘差時序，其殘差時序自相關的總體及個別檢定見圖十九與表二，殘差的累積機率分佈見圖十五至圖十八。胡氏[17]曾以ARIMA做溫度預報，然其着眼點爲月平均溫度，而本文重點則爲小時變化。

四組數據中，除第四組外，其餘三組因寒潮的關係，小時值出現突變及跳動等不穩定現象，使得模式的擬合誤差達6.8 ℃。而除B組外，其餘各組模式週期性並不顯著。

三、預報模式特性

建立預報模式的目的在於了解空氣污染擴散參數對於未來短時間的變化。將上述所建立的20個預報模式，對各擴散參數進行未來24小時的預報，其結果列於表三至表十四，表中包括預報值與實際值的差異，絕對值平均誤差（Absolute Mean Error）及誤差的標準偏差。表十五則表示四組數據大氣穩定度的預報級數與實際級數的差異（以穩定度的級數表示）。

一般而言，各預報模式的階數增高，其參數值逐漸變小，但亦有甚多情況並不如此，於模式中亦有階數高達35者，此實爲一35階的微分方程式，但不爲零的參數個數並不多，亦即大部分的高階頂皆不顯著，所得的模式低階頂佔優勢，即時序最後幾個數據值，對未來預報值的影響最大。

㈠風　　向

表三至表六顯示絕對值平均誤差A組爲12.4°，B組爲68.1°，C組爲16.0°，D組爲10.3°，即B組外，其他三組所建立的預報模式，大致尚可吻合實際的變化情形。B組模式的預報會與實際情況有如此大的差異，乃由於在盛行東北季風的秋冬季，預報時間出現明顯的西南風或西北風，而此風向於建立模式的原始資料中，其出現機率尚不足百分之十，且以不規則的型態出現，由殘差的累積機率分佈圖（圖三至圖六），即可看出模式擬合時，對這些特殊值（西南風或西北風），即無法有效的掌握，因而其殘差有高達170°情況，另一原因則爲當時風速爲微風狀態（見表八），風向變化特別大。反觀A、C、D三組，因其預報時間的風向大體不脫東北季風的範圍，預報效果好，平均誤差約12.5°。

㈡風　　速

表七至表十顯示四組的平均誤差約0.4公尺／秒，因有許多靜風存在（風速＜0.5公尺／秒），使得預報模式即使即時預報（Updating Forecasting，見表十六、十七），亦無法有效的使誤差減少。

㈢大氣穩定度

表十五顯示模式預報所得的穩定度級數與實際穩定度級數常相吻合（約佔59％），而差一級者約佔30％（皆已考慮夜間的修正）。以前文獻中尚乏有關大氣穩定度的預報，本文首次嘗試，盼望以後做更多的探討與改進。

㈣溫　　度

表十一至十四顯示未來24小時預報的平均誤差除B組外，約爲0.6℃，B組的平均誤差約3℃，比較實際值與預報值（見表十二）可看出，預報的前8小時其平均誤差約爲0.4℃，8小時後有突變產生，此突變的高溫，於建立模式的原數據中，出現的機率過小而不規則，有賴即時預報來修正。將B組數據做即時預報，其結果列於表十八，從新輸入12個新的觀測值，作未來12小時預報，發現即時預報使原先的5.1℃誤差值降至1.9℃，其預報效果的改進十分顯然，各組參數預報模式的預報結果見表十九。

表二十顯示，殘差時序的標準偏差σ_{at}遠較原時序的標準偏差σ_{zt}爲小。風向、風速及大氣穩定度三參數的σ_{at}值仍大，雖然殘差時序經由診斷檢驗顯示爲白噪音，但其分佈範圍甚廣，顯示其預報的誤差尚大。

對各大氣參數建立AR（24）高階模式的結果與上文之ARMA 預報模式的比較見表二十一，表中顯示於擬合時AR（24）高階模式較原預報模式爲佳，顯示由BOX與Jenkins所建議的ARIMA模式建立法未必能得到最佳的時序預報模式，此或係ACF與PACF的採樣值與眞值頗有出入，或是ARMA混合模式的型式判斷不甚理想所致。

由於受小型電腦PDP-11容量的限制，本文僅取9天的各參數小時平均值做時序分

析，所建立的預報模式統計代表性略顯不足，如用大型電腦，取更長的數據來建立各參數的預報模式，將可得到更具代表性的結果。

伍、結論與建議

本文以Box and Jenkins所發展出的ARIMA時序分析法，來建立空氣污染擴散參數中的風向、風速、大氣穩定度與溫度的預報模式。結果顯示，此時序預報模式，對空氣污染擴散參數能提供良好的預報，此客觀的定量預報，對於溫度的突變情況，亦能利用即時預報法，做立即的修正。此時序預報法可推廣應用至下列範疇：

1. 建立空氣污染相關參數的預報模式，供大污染源廢氣排放控制的參考。
2. 由多數測站的參數及污染濃度預報資料，利用佳化評估理論[18]，而建立地區的空氣污染物質濃度的預報模式。

由於風向與風速的變異頗大，欲得良好的預報成果尚待作更多的研究與探討，以下爲將來研究的可行方向：

1. 將風向、風速等空氣污染擴散參數於頻率域，利用波譜分量（spectrum scale decomposition）分成幾個不同頻率域的時序，分別建立合適的ARIMA模式。
2. 以複變數ARIMA（Multi-ARIMA）建立這些參數的預報模式。
3. 利用辨別分析（Discriminant analysis）[19]先對原數據作詳細的分析，了解未來可能發生突變的機率，再分別考慮適合的統計預報模式。
4. 以高階AR(P)的模式作初步擬合，再將結果之殘差時序作ARMA。

參考文獻

1. John, S. I., Scheme For Estimating Dispersion Parameters As A Function of Release Height, U. S. Ehvironmental Protection Agency, EPA-600/4-79-069, 1979.
2. William, H.K. and F. Lewis, Computer Forecasting of Maximum and Minimum Temperatures, Journal of Applied Meteorology, Vol. 9, 350-359, 1970.
3. Russo, J. A., Jr., I. Enger and E. L. Sorenson, A Statistical Approach to the Short-Period Prediction of Surface Winds, J. Appl. Meteor., Vol. 3, 126-131. 1963.
4. Carter, G. M., Automated Prediction of Surface Wind From Numerical Model Output, Monthly Weather Review, Vol.103, 866-873, 1975.
5. Box, G. E. P. and G. M. Jenkins, Time Series Analysis Forecasting and Control, Holden-Day, San Francisco, 575p, 1976.
6. Jenkins, G. and G. Watts, Spectra Analysis and Its Applications, Holden Day, San Francisco, 523p, 1968.
7. Bartlett, M.S., On the Theoretical Specification of Sampling Properties of Autocorrelated Time Series, Journal Rayal Stal. Soc., B8, Vol.27, 1946.
8. Quenouille, M.H., Approximate Tests of Correlation in Time Series, Jour. Rayal Stal. Soc., B11, Vol. 68, 1949.

9. Turner, D. B., Workbook of Atmospheric Diffusion Estimates, Nat. Air Pollution Control Agency, Cincinnati, Ohio, 84p, 1970.
10. 蔡豐智，梁文傑，台北市二氧化硫時序預報模式之研究，中央研究院物理研究所集刊，第十卷，第 173～210 頁，1980。
11. KO, S. D., Surface Wind Field and Precipitation Activity over Taiwan in Meiyu Season, Annual Report of Institute of Physics, Academia Sinica, Vol. 4, 301-322. 1975.
12. Pasiquill, F., Atmospheric Diffusion John Wiley and Sons, New York, 429p, 1974.
13. Gifford, F. A., Use Routine Meteorological Observation for Estimating Atmospheric Dispersion, Nuclear Safety, Vol.2, 47-51, 1961.
14. Stoner, R. R., Procedures for Reduction of Meteorological data. Environmental Safegard Division, NUS. Corporation, NUS-757, 30p, 1971.
15. KAU, W.S., Lee, H. N. and Kao, S. K.A., Statistical Model for Wind Predication at a Mountain and valley Station Near Anderson Greek, California, J. Appl. Meteor., Vol. 21, 18-21, 1981.
16. Mitchell, A. E. Jr., A Comparison of Short-term Dispersion Estimates Resulting from Various Atmospheric Stability Classification Methods, Atmospheric Environmental, Vol. 16, No. 4, 765-773, 1982.
17. 胡仲英，應用 ARIMA 模式對台北市月平均溫度與降水量的分析與預報，氣象學報，二十三卷，第三期，第 15～16 頁，1977。
18. 梁文傑，空氣污染評估的佳化理論，中央研究院物理研究所集刊，第 8 卷，第 223～258 頁，1979。
19. Lin, G. Y., Oxidant Prediction By Discriminant Analysis in the South Coast Air Basin of California, Atmospheric Environmental, Vol. 16, No. 1, 135-143, 1982.
20. Mitchell, A. E. Jr. and Timbre K.O., Atmospheric Stability Class from Horizontal Wind Fluctuation, Paper 79-29.2 Air Pollution Control Association Annual Meeting, Cincinnati, OH. 1979.

表一　各組數據的說明：各組數據以小時平均值表示收集數據長度 9 天（連續 216 個小時）

組別	數據收集時間	數據內容	單位
A	71 年 10 月 1 日至 10 月 9 日	風向	度
		風速	公尺／秒
		大氣穩定度	度
		溫度	℃
B	71 年 10 月 21 日至 10 月 29 日	風向	度
		風速	公尺／秒
		大氣穩定度	度
		溫度	℃
C	71 年 11 月 7 日至 11 月 15 日	風向	度
		風速	公尺／秒
		大氣穩定度	度
		溫度	℃
D	71 年 12 月 11 日至 12 月 19 日	風向	度
		風速	公尺／秒
		大氣穩定度	度
		溫度	℃

表二　(A)爲各自由度之 χ_α 值，(B)爲二十個殘差時序自相關總體檢定，表中四組數據同表一，Q 爲殘差時序的自相關函數（遲滯 1 至 36）計算所得的 $\chi^2_{0.05}$ 值，括弧內爲自由度。

(A)

自由度 \ χ^2_α 值	$\alpha = 0.05$	$\alpha = 0.025$	$\alpha = 0.01$
28	41.5	44.5	48.3
29	42.6	45.7	49.6
30	43.8	46.9	50.9
40	55.8	59.3	63.6

(B)

組別	擴散參數	Q	組別	擴散參數	Q
A	風向（U）	19.36(32)	C	風向（U）	19.35(29)
A	風向（V）	20.73(31)	C	風向（V）	23.58(30)
A	風速	25.50(32)	C	風速	23.71(33)
A	大氣穩定度	21.71(31)	C	大氣穩定度	30.53(30)
A	溫度	18.62(29)	C	溫度	15.06(29)
B	風向（U）	31.36(31)	D	風向（U）	18.19(31)
B	風向（V）	20.79(20)	D	風向（V）	22.74(30)
B	風速	19.31(32)	D	風速	14.48(33)
B	大氣穩定度	27.06(31)	D	大氣穩定度	16.23(28)
B	溫度	22.70(32)	D	溫度	25.85(32)

表三　71年10月1日至9日風向數據的預報結果，單位爲度。預報值爲所建立風向預報模式，未來24小時預報結果，實際值爲當時風向的觀測值。

未來時間（小時）	預報值	實際值	誤差
1	56.6	56.0	0.6
2	60.1	51.0	9.1
3	53.0	73.0	-20.0
4	51.8	70.0	-18.2
5	47.4	32.0	15.4
6	46.0	58.0	-12.0
7	46.2	31.0	15.0
8	46.6	56.0	-9.4
9	46.5	32.0	14.5
10	47.8	76.0	-28.2
11	50.5	89.0	-38.5
12	50.0	59.0	-9.0
13	53.7	45.0	8.7
14	53.9	36.0	17.9
15	51.2	32.0	91.2
16	50.0	34.0	16.0
17	59.4	34.0	15.0
18	49.3	45.0	4.3
19	49.2	38.0	11.2
20	39.1	50.0	-0.9
21	49.1	48.0	1.1
22	49.1	45.0	4.1
23	49.1	55.0	-5.9
24	49.1	47.0	2.1

絕對值平均誤差＝ 12.38 標準偏差＝ 15.19

表四　71年10月21日至29日風向數據的預報結果，單位爲度，餘參照表三。

未來時間（小時）	預報值	實際值	誤差
1	74.7	85.0	-10.3
2	73.7	84.0	-10.3
3	72.0	75.0	-2.6
4	70.6	78.0	-7.4
5	70.0	115.0	-44.4
6	68.8	94.0	-25.2
7	69.2	87.0	-17.8
8	67.8	104.0	-36.2
9	67.1	231.0	-163.9
10	68.7	271.0	-157.7
11	67.4	260.0	-167.0
12	67.2	201.0	-133.8
13	67.7	242.0	-174.3
14	67.3	279.0	-148.3
15	66.9	286.0	-140.9
16	66.7	281.0	-145.7
17	66.6	36.0	30.6
18	66.5	57.0	9.5
19	66.5	47.0	19.5
20	66.5	112.0	-45.5
21	66.5	81.0	-14.5
22	66.5	107.0	-40.5
23	66.5	25.0	41.5
24	66.5	113.0	-46.5

絕對值平均誤差＝ 68.08 標準偏差＝ 70.50

表五　71年11月7日至15日風向數據的預報結果，單位爲度，餘參照表三。

未來時間（小時）	預報值	實際值	誤差
1	68.3	71.0	-2.7
2	64.6	106.0	-41.4
3	61.9	46.0	15.9
4	65.4	84.0	-18.6
5	66.4	75.0	-8.6
6	66.2	61.0	5.2
7	70.1	108.0	-37.9
8	66.0	81.0	-15.0
9	69.0	98.0	-29.0
10	68.3	100.0	-31.7
11	63.7	70.0	-6.3
12	65.3	79.0	-13.7
13	64.9	90.0	-25.1
14	64.3	83.0	-18.7
15	64.4	83.0	-18.6
16	63.9	35.0	28.9
17	63.8	74.0	-10.2
18	63.9	51.0	12.8
19	63.7	64.0	-0.3
20	63.7	63.0	0.7
21	63.7	102.0	-38.3
22	63.7	63.0	0.7
23	63.7	63.0	0.7
24	63.7	66.0	-2.3

絕對值平均誤差＝ 15.97 標準偏差＝ 17.53

表六　71年12月11日至19日風向數據的預報結果。單位爲度，餘參照表三。

未來時間（小時）	預報值	實際值	誤差
1	78.7	83.0	-4.3
2	76.9	84.0	-7.1
3	77.1	87.0	-9.9
4	72.9	49.0	23.9
5	71.9	66.0	5.9
6	71.6	70.0	1.6
7	70.2	74.0	-3.8
8	69.5	56.0	13.5
9	69.7	87.0	-17.3
10	69.3	89.0	-19.7
11	69.0	65.0	4.0
12	68.3	48.0	20.3
13	67.8	48.0	19.8
14	67.0	52.0	15.0
15	63.4	49.0	14.4
16	62.0	57.0	5.0
17	61.4	49.0	12.4
18	61.2	77.0	-15.8
19	61.2	61.0	0.2
20	61.1	59.0	2.1
21	61.0	74.0	-13.0
22	61.0	74.0	-13.0
23	61.0	60.0	1.0
24	61.0	51.0	10.0

絕對值平均誤差＝ 10.25 標準偏差＝ 12.14

表七　71年10月1日至9日風速數據的預報結果。單位爲公尺／秒，餘參照表三。

未來時間（小時）	預報值	實際值	誤差
1	1.56	1.00	0.56
2	1.25	1.14	0.11
3	0.85	0.75	0.10
4	0.68	0.92	-0.24
5	0.59	1.27	-0.68
6	0.57	1.30	-0.73
7	0.84	1.03	-0.19
8	0.90	0.70	0.20
9	0.82	1.44	-0.42
10	0.84	0.95	-0.11
11	0.96	0.92	0.04
12	0.99	0.65	0.34
13	0.87	1.38	-0.51
14	0.88	2.29	-1.41
15	0.93	2.26	-1.33
16	0.93	2.11	-1.18
17	0.93	2.61	-1.68
18	0.93	2.21	-1.28
19	0.93	1.94	-1.01
20	0.93	1.85	-0.92
21	0.93	1.48	-0.55
22	0.93	1.28	-0.35
23	0.93	0.80	0.13
24.0	0.93	1.30	-0.37

絕對值平均誤差＝ 0.61 標準偏差＝ 0.60

表八　71年10月21日至29日風速數據的預報結果，單位爲公尺／秒，餘參照表三。

未來時間（小時）	預報值	實際值	誤差
1	0.67	0.47	0.20
2	0.63	1.28	-0.65
3	0.65	0.90	-0.25
4	0.65	0.51	0.14
5	0.84	0.17	0.67
6	0.96	0.02	0.94
7	1.03	0.11	0.92
8	1.07	0.02	1.05
9	1.09	0.02	1.07
10	1.10	0.11	0.99
11	1.11	0.72	0.39
12	1.11	0.60	0.51
13	1.12	0.87	0.25
14	1.12	1.33	-0.21
15	1.12	1.97	-0.85
16	1.12	1.57	-0.45
17	1.12	1.14	-0.02
18	1.12	0.80	0.32
19	1.12	0.14	0.98
20	1.12	0.17	0.95
21	1.12	0.17	0.95
22	1.12	0.18	0.94
23	1.12	0.24	0.88
24	1.12	0.03	1.09

絕對值平均誤差＝ 0.65 標準偏差＝ 0.59

表九　71年11月7日至15日風速數據的預報結果，單位爲公尺／秒，餘參照表三。

未來時間（小時）	預報值	實際值	誤差
1	1.38	1.03	0.35
2	1.22	0.77	0.45
3	1.10	0.51	0.59
4	1.00	0.93	0.07
5	0.92	0.87	0.05
6	0.86	0.43	0.43
7	0.83	0.62	0.21
8	0.80	0.38	0.42
9	0.78	0.54	0.24
10	0.78	0.53	0.25
11	0.74	0.75	-0.01
12	0.71	0.69	0.02
13	0.70	1.18	-0.48
14	0.69	1.52	-0.83
15	0.71	1.55	-0.84
16	0.72	1.33	-0.61
17	0.73	1.81	-1.08
18	0.73	1.02	-0.29
19	0.73	1.10	-0.36
20	0.74	0.86	-0.12
21	0.75	0.81	-0.06
22	0.75	1.31	-0.56
23	0.75	0.13	0.62
24	0.75	1.27	-0.52

絕對值平均誤差＝ 0.39 標準偏差＝ 0.47

表十　71年12月11日至19日風速數據的預報結果，單位爲公尺／秒，餘參照表三。

未來時間（小時）	預報值	實際值	誤差
1	1.28	1.33	-0.05
2	1.24	1.14	0.09
3	1.21	1.52	-0.31
4	1.19	1.17	0.02
5	1.18	1.69	-0.51
6	1.17	0.66	0.51
7	1.17	0.46	0.71
8	1.17	1.06	0.11
9	1.17	0.78	0.38
10	1.17	1.64	-0.47
11	1.16	1.19	-0.03
12	1.16	1.37	-0.21
13	1.16	2.07	-0.91
14	1.16	1.58	-0.42
15	1.16	1.86	-0.70
16	1.16	1.70	-0.54
17	1.16	1.45	-0.29
18	1.16	1.09	0.07
19	1.16	1.10	0.06
20	1.16	1.55	-0.39
21	1.16	0.88	0.28
22	1.16	1.43	-0.27
23	1.16	1.42	-0.26
24	1.16	0.77	0.39

絕對值平均誤差＝ 0.33 標準偏差＝ 0.39

表十一　71年10月1日至9日溫度數據的預報結果，單位爲℃，餘參照表三。

未來時間（小時）	預報值	實際值	誤差
11	24.2	24.3	-0.1
2	24.1	23.9	0.2
3	23.8	23.6	0.2
4	23.7	23.6	0.1
5	24.1	23.8	0.3
6	23.9	23.2	0.7
7	23.5	23.5	0.0
8	23.5	23.7	-0.2
9	23.3	23.7	-0.4
10	23.1	23.6	-0.5
11	22.9	23.5	-0.6
12	23.1	23.6	-0.5
13	23.9	23.8	0.1
14	24.9	24.0	0.9
15	25.2	24.0	1.2
16	25.4	24.1	1.3
17	26.7	24.1	2.6
18	26.8	24.1	2.7
19	26.9	24.2	2.7
20	26.9	24.2	2.7
21	26.9	24.2	2.7
22	26.3	24.3	2.0
23	25.3	24.3	1.0
24	24.4	24.3	0.1

絕對值平均誤差＝ 0.99 標準偏差＝ 1.14

表十二　71年10月21日至29日溫度數據的預報結果，單位爲℃，餘參照表三。

未來時間（小時）	預報值	實際值	誤差
1	23.1	23.2	-0.1
2	22.8	23.2	-0.4
3	22.3	23.4	-1.1
4	22.1	23.0	-0.9
5	22.0	22.7	-0.7
6	21.8	22.2	-0.4
7	21.9	21.9	0.0
8	22.0	22.0	0.0
9	23.3	24.0	-0.7
10	25.0	26.0	-1.0
11	25.9	27.8	-1.9
12	27.0	30.1	-3.1
13	26.9	31.8	-4.9
14	26.6	31.2	-4.6
15	25.3	30.6	-5.3
16	24.2	29.8	-5.6
17	23.0	28.8	-5.8
18	22.0	26.6	-4.6
19	20.9	25.4	-4.5
20	20.0	24.7	-4.7
21	19.0	23.9	-4.9
22	18.1	23.3	-5.2
23	17.3	23.0	-5.7
24	16.5	22.4	-5.9

絕對值平均誤差＝ 3.00 標準偏差＝ 2.25

表十三　71年11月7日至15日溫度數據的預報結果，單位爲℃，餘參照表三。

未來時間（小時）	預報值	實際值	誤差
1	19.2	19.0	0.2
2	19.3	19.1	0.2
3	19.5	19.7	-0.2
4	19.6	19.4	0.2
5	19.8	19.6	0.2
6	20.1	20.2	-0.1
7	20.2	19.7	0.5
8	19.5	19.8	-0.3
9	18.5	19.5	-1.0
10	17.8	19.0	-1.2
11	17.6	18.9	-1.3
12	17.7	18.7	-1.0
13	18.0	18.6	-0.6
14	18.1	18.6	-0.5
15	18.2	18.6	-0.4
16	18.3	18.4	-0.1
17	18.4	18.5	-0.1
18	18.5	18.4	0.1
19	18.6	18.1	0.5
20	18.6	18.1	0.5
21	18.7	18.4	0.3
22	18.8	18.6	0.2
23	18.8	18.8	0.0
24	18.9	18.9	0.0

絕對值平均誤差＝ 0.40 標準偏差＝ 0.52

表十四　71年12月11日至19日溫度數據的預報結果，單位爲℃，餘參照表三。

未來時間（小時）	預報值	實際值	誤差
1	15.1	15.3	-0.2
2	15.1	15.4	-0.3
3	15.1	15.1	0.0
4	15.1	15.6	-0.5
5	15.1	16.4	-1.3
6	15.1	16.0	-0.9
7	15.1	16.1	-1.0
8	15.1	15.8	-0.7
9	15.1	16.0	-0.9
10	15.1	15.8	-0.7
11	15.1	16.2	-1.1
12	15.1	17.4	-2.3
13	15.1	18.1	-3.0
14	15.1	17.4	-2.3
15	15.1	15.9	-0.8
16	15.3	16.3	-1.0
17	15.3	16.5	-1.0
18	15.7	16.0	-0.3
19	15.9	16.0	-0.1
20	16.1	16.0	0.1
21	16.3	16.0	0.3
22	16.5	16.1	0.4
23	16.7	15.9	0.8
24	16.9	15.8	1.1

絕對值平均誤差＝ 0.88 標準偏差＝ 0.94

表十五　四組穩定度數據未來24小時預報結果。A與B級穩定度間級數差爲1，A與F級穩定度間級數差爲5。

收集數據時間	未來時間（小時）	1	2	3	4	5	6	7	8	9	10	11	12	13	14	15	16	17	18	19	20	21	22	23	24
71.10. 1. 至10. 9.	預報級數	F	F	F	F	F	F	F	B	B	B	B	B	B	B	B	B	A	F	F	F	F	F	F	F
	實際級數	F	E	F	F	F	E	E	B	B	C	B	B	B	B	B	B	B	F	F	F	F	F	F	E
	級數差	0	1	0	0	0	1	1	0	0	1	0	0	0	0	0	0	1	0	0	0	0	0	0	1
71.10.21. 至10.29.	預報級數	E	F	F	F	F	F	F	B	B	B	B	B	B	B	B	B	B	F	F	F	F	F	F	F
	實際級數	F	F	F	F	F	F	E	A	B	C	B	C	C	B	B	B	B	F	E	F	E	E	E	E
	級數差	1	0	0	0	0	0	1	1	0	1	0	1	1	0	0	0	0	0	1	0	1	1	1	1
71.11. 7. 至11.15.	預報級數	F	F	F	F	F	F	F	B	A	A	B	B	B	B	A	A	A	F	F	F	F	F	F	F
	實際級數	E	F	F	E	F	F	F	B	C	A	C	C	D	D	D	C	C	E	E	E	D	E	E	E
	級數差	1	0	0	1	0	0	0	0	2	0	1	1	2	2	3	2	2	1	1	1	0	1	1	1
71.12.11. 至12.19.	預報級數	F	F	F	F	F	F	F	B	A	B	B	B	A	A	B	B	B	F	F	F	F	F	F	F
	實際級數	F	F	F	F	F	F	F	A	B	B	B	B	B	A	B	B	B	F	F	F	F	F	F	F
	級數差	0	0	0	0	0	0	0	1	1	0	0	0	1	0	0	0	0	0	0	0	0	0	0	0

表十六　71年10月1日至9日風速數據即時預報的結果，單位爲公尺／秒。表中預報值爲表七原預報模式預報值中的後18個值，即時預報值爲將表七實際值中的前6個值輸入，做未來18小時的即時預報。

原預報值	即時預報值	實際值	原預報誤差	即時預報誤差
0.84	0.93	1.03	-0.19	-0.10
0.90	0.93	0.70	0.20	0.23
0.92	0.93	1.44	-0.52	-0.51
0.84	0.93	0.95	-0.11	-0.02
0.96	0.94	0.92	0.04	0.02
0.99	0.94	0.65	0.34	0.29
0.87	0.94	1.38	-0.51	-0.44
0.88	0.92	2.29	-1.41	-1.37
0.93	0.95	2.26	-1.33	-1.31
0.93	0.92	2.11	-1.18	-1.19
0.93	0.87	2.61	-1.68	-1.74
0.93	0.91	2.21	-1.28	-1.30
0.93	0.90	1.94	-1.01	-1.04
0.93	0.95	1.85	-0.92	-0.92
0.93	1.02	1.48	-0.55	-0.46
0.92	1.02	1.28	-0.35	-0.26
0.93	0.93	0.80	0.13	0.13
0.93	0.93	0.30	-0.37	-0.37
絕對值平均誤差			0.6733	0.6489

表十七　71年12月11日至19日風速數據即時預報的結果，單位爲公尺／秒。表中原預報值爲表十原預報模式預報值中的後19個值，即時預報值爲將表十實際值中的前5個數值輸入，作未來19小時的即時預報。

原預報值	即時預報值	實際值	原預報誤差	即時預報誤差
1.17	1.36	0.66	0.51	0.70
1.17	1.31	0.46	0.71	0.85
1.17	1.25	1.06	0.11	0.19
1.17	1.22	0.79	0.38	0.43
1.17	1.20	1.64	-0.47	-0.44
1.16	1.18	1.19	-0.03	-0.01
1.16	1.18	1.37	-0.21	-0.19
1.16	1.17	2.07	-0.91	-0.90
1.16	1.17	1.58	-0.42	-0.41
1.16	1.17	1.86	-0.70	-0.69
1.16	1.17	1.70	-0.54	-0.53
1.16	1.16	1.45	-0.29	-0.29
1.16	1.16	1.09	0.07	0.07
1.16	1.16	1.10	0.06	0.06
1.16	1.16	1.55	-0.39	-0.39
1.16	1.16	0.88	0.28	0.28
1.16	1.16	1.43	-0.27	-0.27
1.16	1.16	1.42	-0.26	-0.26
1.16	1.16	0.77	0.39	0.39
絕對值平均誤差			0.3684	0.3668

表十八　71年10月21日至29日溫度數據即時預報的結果，單位爲℃。表中原預報值爲表十二原預報模式預報值中的後12個值，即時預報值爲將表十二實際值中的前12個數值輸入，做未來12小時的即時預報，而表中實際值則爲表十二實際值中的後12個值爲預報值比較的依據。

原預報值	即時預報值	實際值	原預報誤差	即時預報誤差
26.9	29.8	31.8	-4.9	-2.0
26.6	29.5	31.2	-4.6	-1.7
25.3	29.3	30.6	-5.3	-1.3
24.2	28.8	29.8	-5.6	-1.0
23.0	28.1	28.8	-5.8	-0.8
22.0	28.0	26.6	-4.6	1.4
20.9	27.7	25.4	-4.5	2.3
20.9	27.6	24.7	-4.7	2.9
19.0	27.3	23.9	-4.9	3.4
18.1	26.8	23.3	-5.2	3.5
12.3	25.0	23.0	-5.7	2.0
16.5	23.2	22.4	-5.9	0.8
絕對值平均誤差				

表十九　各組參數預報結果表。四組數據同表一，表中預報誤差爲各組各參數24小時預報數值與實際數值差的標準偏差，四組平均誤差爲同一大氣參數四組數據預報誤差的平均值。

參數		預報誤差	四組平均誤差
風向	A	15.2°	28.8°
	B	70.5°	
	C	17.5°	
	D	12.1°	
風速	A	0.60 公尺／秒	0.51 公尺／秒
	B	0.59 公尺／秒	
	C	0.47 公尺／秒	
	D	0.39 公尺／秒	
大氣穩定度	A	＜1 級	＜1 級
	B	＜1 級	
	C	≒1 級	
	D	＜1 級	
溫度	A	1.14 ℃	1.21 ℃
	B	2.55 ℃	
	C	0.52 ℃	
	D	0.94 ℃	

表二十　原時序與殘差時序標準偏差之比較。四組數據同表一，σ_{zt}爲原時序Z_t的標準偏差，σ_{at}爲殘差時序a_t的標準偏差。

		σ_{zt}（樣本母體）	σ_{at}（殘差）
風向	A	68.2°	30.5°
	B	55.6°	35.7°
	C	70.3°	46.8°
	D	58.9°	28.7°
風速	A	0.72 公尺／秒	0.51 公尺／秒
	B	0.66 公尺／秒	0.33 公尺／秒
	C	0.63 公尺／秒	0.41 公尺／秒
	D	0.86 公尺／秒	0.43 公尺／秒
大氣穩定度	A	13.1°	5.7°
	B	9.0°	4.6°
	C	11.2°	7.1°
	D	8.6°	5.8°
溫度	A	2.64 ℃	0.91 ℃
	B	3.48 ℃	0.64 ℃
	C	4.87 ℃	0.85 ℃
	D	2.55 ℃	0.41 ℃

表二十一　原模式與AR（24）模式殘差時序的比較。四組數據同表一。表中原模式之σ_{at}爲原預報模式擬合後所得的殘差時序a_t的標準偏差，AR（24）模式之σ_{at}爲AR(24)高階模式擬合後所得殘差時序的標準偏差，表中最大殘差值爲各殘差時序的最大值。

		模式型式	σ_{at}	最大殘差值
風向	B	原模式	35.7°	156°
		AR（24）模式	26.5°	149°
	C	原模式	46.8°	175.5°
		AR（24）模式	33.4°	162°
風速	A	原模式	0.51 公尺／秒	2.62 公尺／秒
		AR（24）模式	0.38 公尺／秒	1.78 公尺／秒
	B	原模式	0.33 公尺／秒	1.14 公尺／秒
		AR（24）模式	0.34 公尺／秒	1.17 公尺／秒
	C	原模式	0.41 公尺／秒	2.05 公尺／秒
		AR（24）模式	0.39 公尺／秒	1.98 公尺／秒
	D	原模式	0.43 公尺／秒	2.36 公尺／秒
		AR（24）模式	0.36 公尺／秒	1.46 公尺／秒
溫度	A	原模式	0.91 ℃	6.80 ℃
		AR（24）模式	0.86 ℃	6.36 ℃
	B	原模式	0.64 ℃	2.73 ℃
		AR（24）模式	0.61 ℃	2.62 ℃
	C	原模式	0.85 ℃	4.49 ℃
		AR（24）模式	0.79 ℃	4.27 ℃
	D	原模式	0.41 ℃	2.26 ℃
		AR（24）模式	0.41 ℃	2.01 ℃

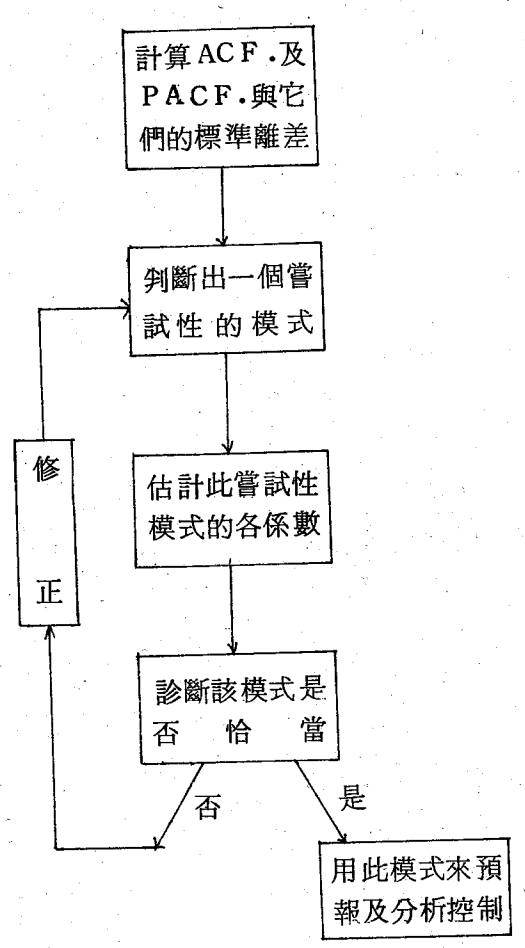

圖一　建立合適的ARIMA 模式的各個步驟

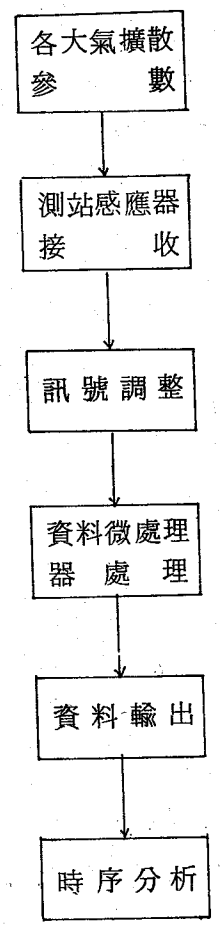

圖二　資料取得的流程

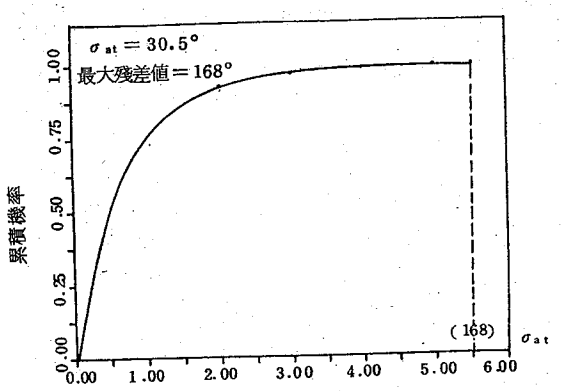

圖三　71年10月1日至9日風向數據殘差時序的累積機率分佈圖表中風向殘差時序爲上述收集時間風向實測值與同時間預報模式擬合值間之差值所組成的時序，σ_{at}參照表二十。

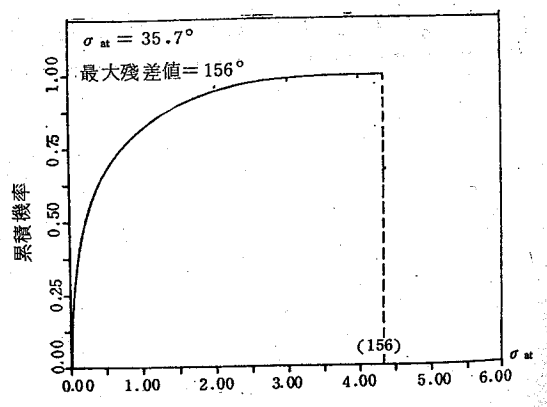

圖四　71年10月21日至29日風向數據殘差時序的累積機率分佈圖，餘同圖三。

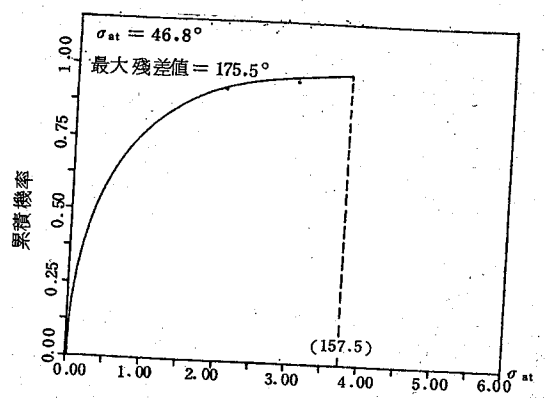

圖五　71年11月7日至15日風向數據殘差時序的累積機率分佈圖餘同圖三。

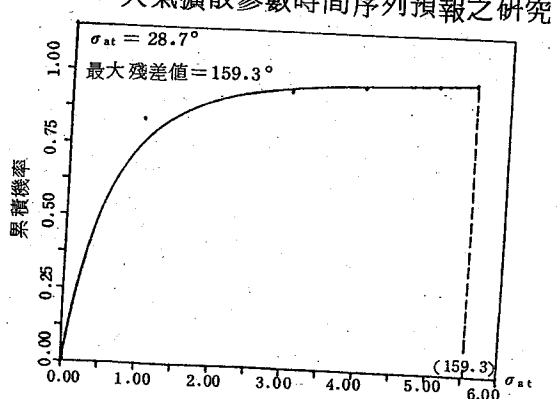

圖六　71年12月11日至19日風向數據殘差時序的累積機率分佈圖餘同圖三。

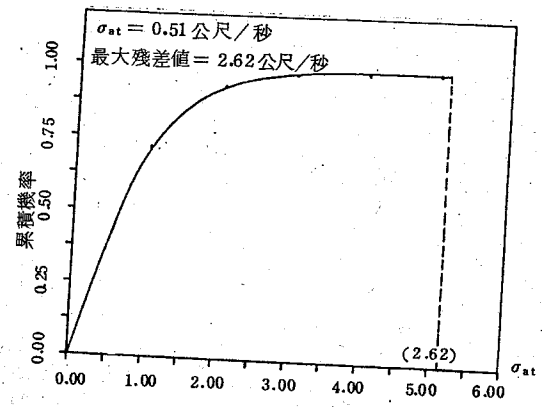

圖七　71年10月1日至9日風速數據殘差時序的累積機率分佈圖餘同圖三。

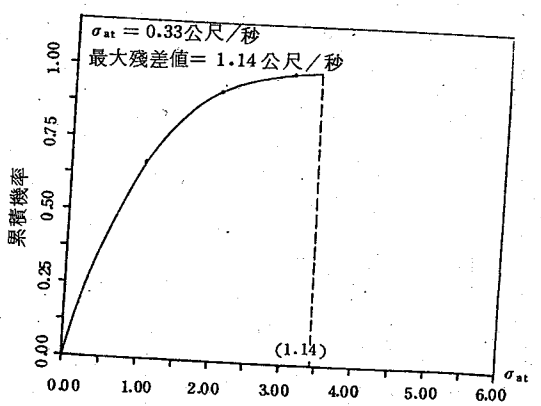

圖八　71年10月21日至29日風速數據殘差時序的累積機率分佈圖餘同圖三。

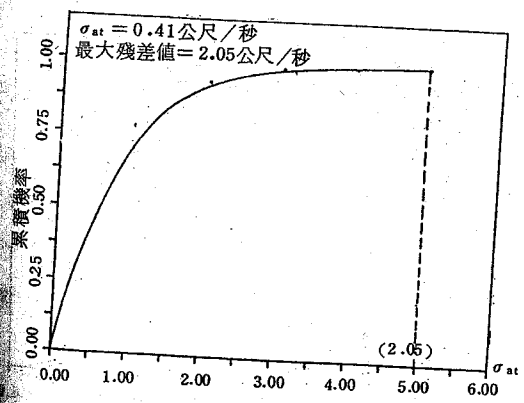

圖九　71年11月7日至15日風速數據殘差時序的累積機率分佈圖餘同圖三。

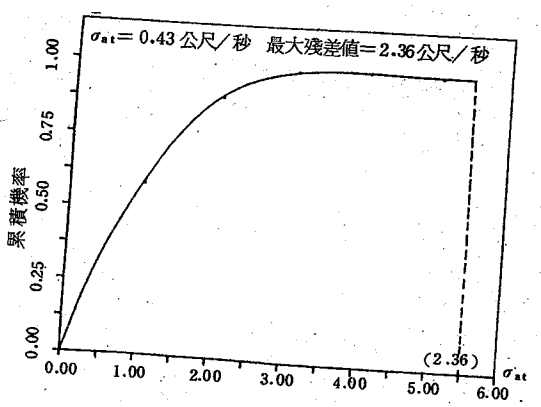

圖十　71年12月11日至19日風速數據殘差時序的累積機率分佈圖餘同圖三。

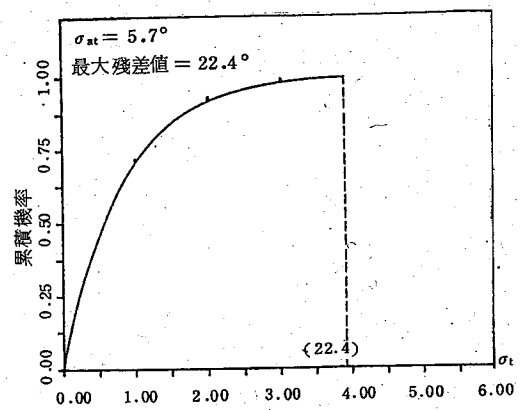

圖十一　71 年 10 月 1 日至 9 日大氣穩定度數據殘差時序的累積機率分佈圖，餘同圖三。

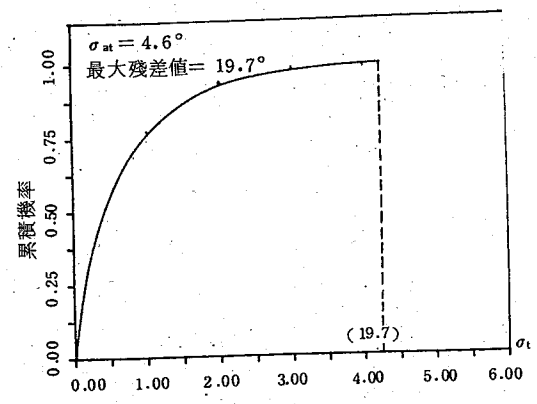

圖十二　71 年 10 月 21 日至 29 日大氣穩定度數據殘差時序的累積機率分佈圖，餘同圖三。

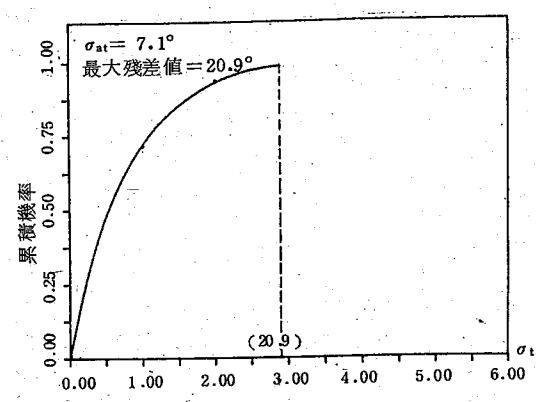

圖十三　71年 11 月 7 日至 15 日大氣穩定度數據殘差時序的累積機率分佈圖，餘同圖三。

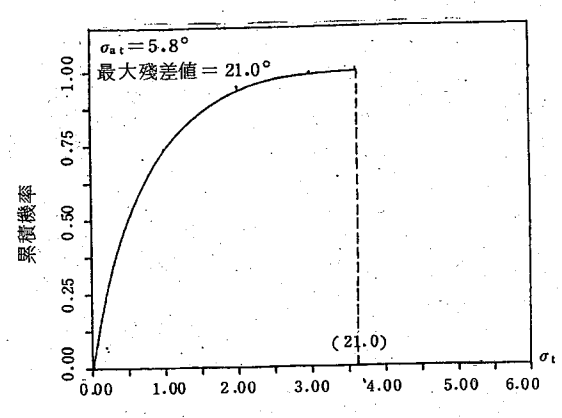

圖十四　71 年 12 月 11 日至 19 日大氣穩定度數據殘差時序的累積機率分佈圖，餘同圖三。

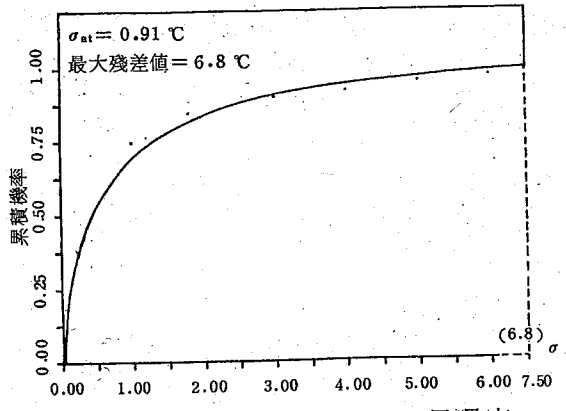

圖十五　71年 10 月 1 日至 9 日溫度數據殘差時序的累積機率分佈圖，餘同圖三。

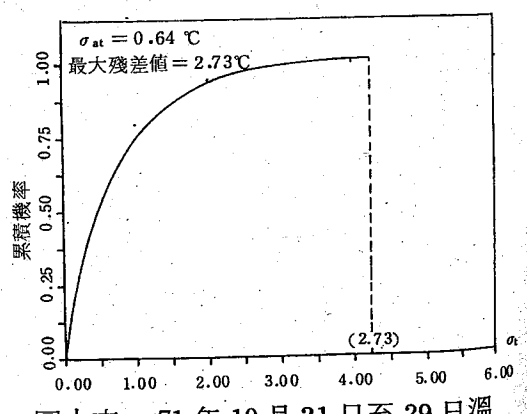

圖十六　71 年 10 月 21 日至 29 日溫度數據殘差時序的累積機率分佈圖，餘同圖三。

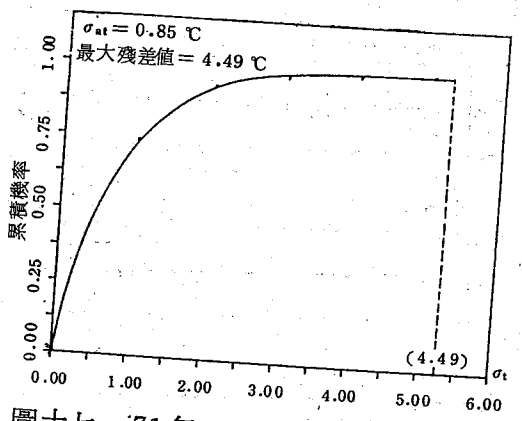

圖十七　71年11月7日至15日溫度數據殘差時序的累積機率分佈圖，餘同圖三。

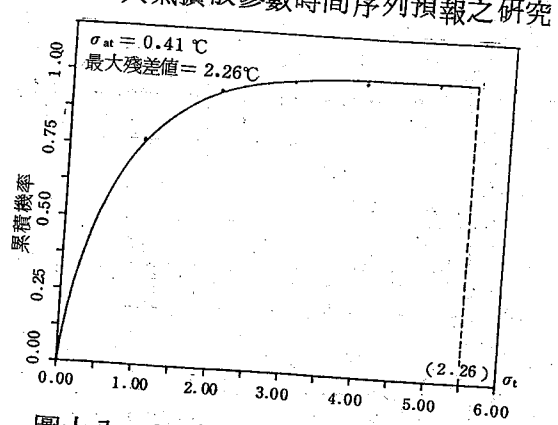

圖十八　71年 12 月 11 日至 19 日溫度數據殘差時序的累積機率分佈圖，餘同圖三。

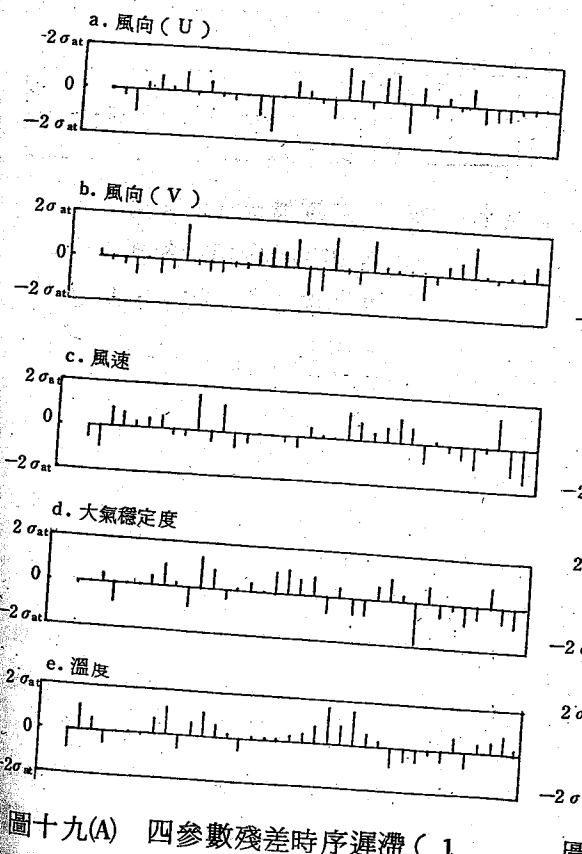

圖十九(A)　四參數殘差時序遲滯（1至36）的自相關對其二倍標準偏差值比較圖，餘參照表二十。

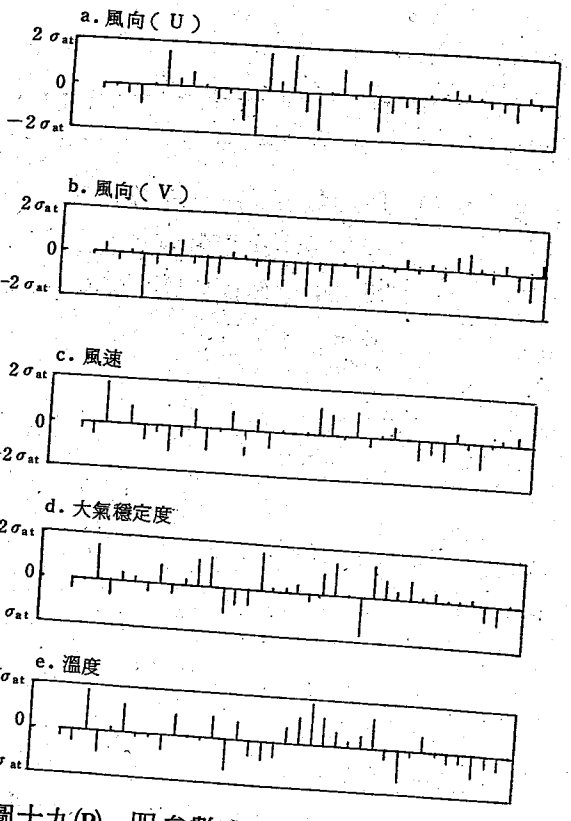

圖十九(B)　四參數殘差時序遲滯（1至36）的自相關對其二倍標準偏差值比較圖，餘參照表二十。

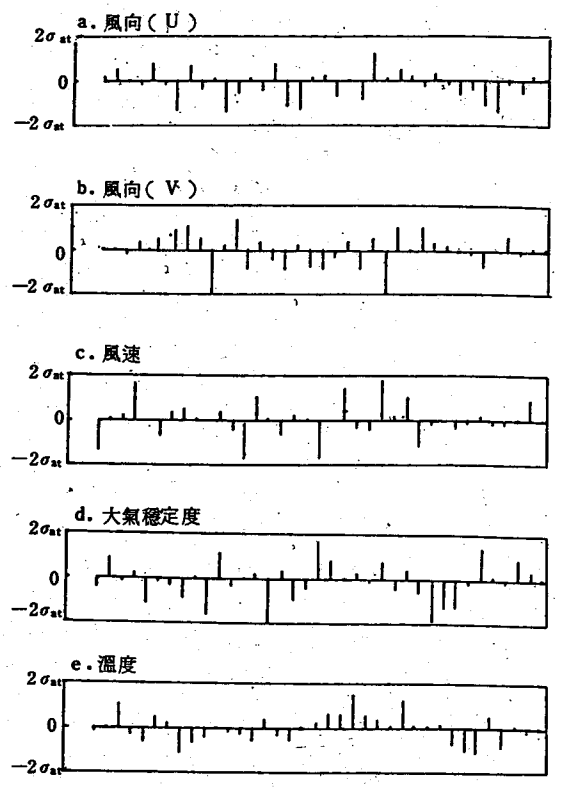

圖十九(C)　四參數殘差時序遲滯（1至36）的自相關對其二倍標準偏差值比較圖，餘參照表二十。

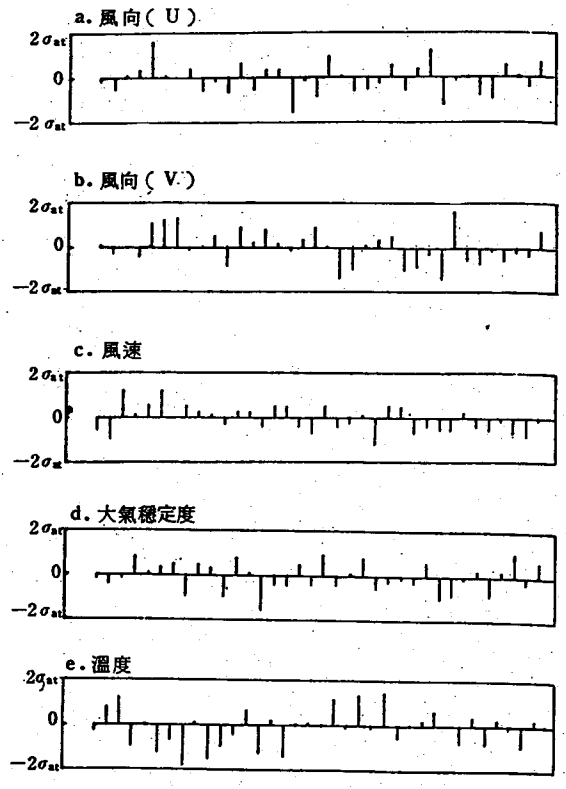

圖十九(D)　四參數殘差時序遲滯（1至36）的自相關對其二倍標準偏差值比較圖，餘參照表二十。

線源光化學污染物擴散模式之原理與應用

梁　文　傑
中央研究院物理研究所
國立臺灣大學機械工程學系
華　梅　英
國立臺灣大學環境工程研究所

摘　要

本研究是應用大氣擴散模式，將擴散空間分割成許多含有等量污染物質的巢空間，由於污染物的擴散，此巢空間也隨之變大，並依風向往下風處傳送，在傳送過程中，巢內產生光化學作用，使污染物濃度改變。此模式涉及數個至數十個光化學反應的聯解，就數學觀點而言，爲數個至數十個常微分方程式的聯解。

本研究自現有文獻選擇四組較具代表性的光化學反應方程式組，應用在實際大氣擴散上，並利用現場實際測定值與理論結果相較，以評估此線源光化學反應模式在台灣地區的可行性。

經由模式計算結果顯示，近距離沿下風方向，O_3、PAN和ALD 濃度會因化學作用而增加，其餘污染物濃度則減少，但無論污染物在擴散之初，濃度隨距離增加或減少，到某一距離後終會因擴散作用而遞減，與實際的污染物擴散情形相同。

壹、引　言

台灣地區人口密度高居世界第二位，工業急速發展，交通日益繁忙。道路的闢建與車輛數的增加，固然帶給人們莫大的便利，但就環境保護的立場，有必要對其可能造成的空氣污染問題加以研究，以供有關防治對策之參考。

空氣品質的改進，預防往往較防治更具效果，此時，數學模式扮演著極重要的角色，因爲它能預估某些情況下可能發生的情形。所以儘管空氣污染模式的發展，尚未達到完全的地步，但是它們在空氣品質的鑑定、預估及防治上仍然能提供許多有益的資訊。一般空氣污染模式，具有理論和經驗混合的特性，理論告訴我們方程式型式，經驗提供這些方程式中某些係數值，如化學反應速率和紊流擴散係數等。我們代入經驗數值，並以實測數據予以校正。經常一個特定的係數需要經過多次的更正，但無論如何，數學模式唯有經過實測數據的證實，才具有實用價值。

由於煙柱擴散問題相當複雜，無法用簡單的模式概括氣象、地形及污染源等所有因

素。當我們研究由單一污染源的擴散問題，經常不包括化學反應、落塵及生物吸收等作用。許多煙流擴散的研究上，大氣擴散參數僅依地區風速和穩定度而異。以高斯煙流擴散爲例，一次污染物濃度和垂直及水平方向擴散係數有關，並且依距離的增加呈現指數性的衰減。線源可視爲由無窮多個點源所組成，只是在濃度的計算上得加入積分的概念，其擴散特性和點污染源相似。一般而言，公路線源因汽車排氣不考慮浮場力的作用，污染物一經排出，能在很短的距離內和大氣混合，因此在接近排放源處的擴散型態和點源排放有些許出入。

光化學反應，和光的照射有關，低層大氣中所接受的可見光和紫外光，除直接來自太陽外，還有大氣散射以及地球表面的反射。其輻射强度的決定包括，太陽直接照射在大氣外層的强度、天頂角（ Zenith Angle ）、自然散射量、大氣散射或吸收性，以及地區的特性等。一般光化學污染物是指化學性轉變半衰期在數小時之內，如碳氫化物中丙烯、丁烯，以及臭氧等。其採樣分析和模式建立與惰性污染物有明顯差異。

以往的研究中，Wanta 與 Lowry[1] 對影響惰性污染物擴散情況的各種氣象條件，做過綜合性的整理。Graedel 等人[2] 研究都市對流層中光化學動力情形，合併化學動力，污染物的時間變化、陽光通量、空氣流和反應體積等因素，結果發現 NO-NO_3-O_3 間的反應，受自由基的影響較大，而自由基主要由乙醛經光分解後而得。Atkinson 等人[3] 爲配合使用大氣光化學空氣品質模擬模式，曾將部分反應機構更新，得知當 NO濃度比 1 ppb 大時，可大量減少反應方程式，而不會發生嚴重影響。1975 年 EPA [4] 刊行公路線源模式使用指針（ User's Guide ），介紹線源惰性污染物擴散模式的建立和使用方法。Dabberdt 等人[5] 研究在各種不同道路結構時，惰性污染物的擴散情形。Friendlander 與 Seinfeld[6] 嘗試使光化學煙霧於體積可膨脹反應器內發生反應。O'Brien 等人[7] 做過反應性污污物不同階段紊亂混合的研究。Steven 與 Philip 等學者[8][9][10] 在光化學煙霧擴散模式方面，由模式建立時方程式的選擇，各係數值的求取，至模式的驗證有一系列的探討。Eschenroeder 等人[11]也同樣有針對線源光化學模式的研究，考慮不同化學反應的影響。國內，有黃賢誠[12]將巢式擴散模式（ cell medel ），應用於光化學污染物擴散情形，此模式將空間分割爲許多含同量污染物的巢空間，隨著污染物的擴散，此巢空間亦隨之變大，並隨風速向下風方向傳送，在傳送過程中，巢內光化學性污染物與巢外加入之污染物起光化學作用，因而改變濃度。

本研究擬合併 Eschenroeder 及 EPA 公路線源模式，並將國內現有黃賢誠的光化學擴散模式加以改進，在污染擴散方面，線源和風向間的夾角可爲任意角度，巢的分格在下風向的長度，可隨濃度之遞減而增大，線源長度由無限線源改爲有限線源，並考慮線源的實際彎曲及不同强度線源的情況，改進近距離污染物的擴散模擬。在光化學反應方面，選擇四組做爲嘗試，比較化學反應的結果。由於國內在光化學污染方面的研究，多直接引用國外資料或數據，研究成果不能直接提供國內污染防治之用。本研究以台灣高速公路桃園至中壢段，作爲模式應用與探討對象，除從事模式的改良外，並利用實測數據求取模式中之參數。模式計算結果亦經實測數據證實。

貳、模式基本理論

一基本理論

在模擬光化學污染物時，最基本的目的，就是要描述一系列的非惰性污染物在大氣紊流中所呈現的結果。由於煙流擴散問題相當複雜，再加上化學反應的參與，使模式的建立必須綜合多項理論。

(一)基本污染擴散模式

假設在流體中含有 n 種污染物，則各污染物的濃度必須滿足擴散方程式[8]

$$\frac{\partial C_i}{\partial t}+\frac{\partial}{\partial x}(uC_i)+\frac{\partial}{\partial y}(vC_i)+\frac{\partial}{\partial z}(wC_i)$$

$$=D_i\left(\frac{\partial^2 C_i}{\partial x^2}+\frac{\partial^2 C_i}{\partial y^2}+\frac{\partial^2 C_i}{\partial z^2}\right)+R_i(C_1,\cdots,C_n,T)+$$

$$S_i(x,y,z,t)\qquad i=1,2,\cdots\cdots,n \qquad \cdots\cdots\cdots\cdots\cdots\cdots(1)$$

其中 u、v、w 爲紊流中三維度空間的風速分量，D_i 爲分子擴散係數，S_i 表排放源的排放率，T爲溫度，R_i 爲由化學反應所產生的污染物變化率，$R_i=R_i(\overline{C}_1+C_1',\overline{C}_2+C_2',\cdots,\overline{C}_n+C_n',T)$ 。在大多數包含化學反應的流體動力問題中，必須考慮質量、動量和能量方程式的聯立解，但是在研究空氣污染上，由於污染濃度極低，一般假定污染物不會影響氣象狀況。假設和紊流擴散比較之下，分子擴散可以忽略不計，且習慣上將風速 u 以 $\overline{u}+u'$表示，同理 $v=\overline{v}+v'$ 、$w=\overline{w}+w'$，代入(1)中，則反應污染物平均濃度變化爲

$$\frac{\partial \overline{C}_i}{\partial t}+\frac{\partial}{\partial x}(\overline{u}\overline{C}_i)+\frac{\partial}{\partial y}(\overline{v}\overline{C}_i)+\frac{\partial}{\partial z}(\overline{w}\overline{C}_i)+\frac{\partial}{\partial x}(\overline{u'C_i'})$$

$$+\frac{\partial}{\partial y}(\overline{v'C_i'})+\frac{\partial}{\partial z}(\overline{w'C_i'})$$

$$=R_i(\overline{C_1+C_1',\ C_2+C_2',\cdots,C_n+C_n',T})+S_i(x,y,z,t)$$

$$\cdots\cdots\cdots\cdots\cdots\cdots(2)$$

此處 $C_i=\overline{C}_i+C_i'$，$\overline{C}_i'=0$，並且溫度的變動予以忽略。(2)式中因爲 $\overline{u'C_i'}$，$\overline{v'C_i'}$，$\overline{w'C_i'}$ 等未知而無法直接求解。根據理論[13]

$$\overline{u'C_i'}=-K_{xx}\frac{\partial \overline{C}_i}{\partial x}\quad,\quad \overline{v'C_i'}=-K_{yy}\frac{\partial \overline{C}_i}{\partial y}\quad,$$

$$\overline{w'C_i'}=-K_{zz}\frac{\partial \overline{C}_i}{\partial z}$$

$$\cdots\cdots\cdots\cdots\cdots\cdots(3)$$

並假設平均反應速率極近於平均濃度的反應速率[14]，即

$$\overline{R_i(C_1+C_1',C_2+C_2',\cdots,C_n+C_n',T)}$$

$$\cong R_i(\overline{C}_1,\overline{C}_2,\cdots,\overline{C}_n,T) \qquad \cdots\cdots\cdots\cdots\cdots\cdots(4)$$

將(3)，(4)式代入(2)式得

$$\frac{\partial \bar{C}_i}{\partial t}+\frac{\partial}{\partial x}(\bar{u}\bar{C}_i)+\frac{\partial}{\partial y}(\bar{v}\bar{C}_i)+\frac{\partial}{\partial z}(\bar{w}\bar{C}_i)$$
$$=\frac{\partial}{\partial x}\left(K_{xx}\frac{\partial \bar{C}_i}{\partial x}\right)+\frac{\partial}{\partial y}\left(K_{yy}\frac{\partial \bar{C}_i}{\partial y}\right)+\frac{\partial}{\partial z}\left(K_{zz}\frac{\partial \bar{C}_i}{\partial z}\right)+$$
$$R_i(\bar{C}_1,\bar{C}_2,\cdots,\bar{C}_n,T)+S_i(x,y,z,t) \quad \cdots\cdots(5)$$

因爲本研究中所使用的時間、空間尺度，均大於單一顆粒運動的時間、空間尺度，因此(5)式能有效的代表大氣傳送和化學反應作用[15]。

二高斯模式

假設x軸與風向垂直，且x、y、z爲相互垂直的三度空間笛卡爾座標系統，則$\bar{u}=\bar{U}$，$\bar{v}=\bar{w}=0$。在x方向的紊亂擴散速率遠小於風所造成的對流擴散速率，即

$$\frac{\partial}{\partial x}\left(K_{xx}\frac{\partial \bar{C}_i}{\partial x}\right)\ll \bar{u}\frac{\partial \bar{C}_i}{\partial x}$$

若不考慮化學反應R_i，污染物由一穩定狀態（Steady state）且强度Q之點源（point source）連續放入風速爲常數並沿x軸吹向的大氣中。根據邊界條件[13]

$$\bar{C}_i=\frac{Q_i}{\bar{U}}\delta(x)\delta(y)\delta(z-h)$$

$$\frac{\partial \bar{C}_i}{\partial z}=0 \qquad z=0,\ x>0 \quad (\text{地面全反射})$$

$$\bar{C}_i=0 \qquad x,\ z\to\infty \quad y\to\pm\infty$$

$$\bar{U}\int_0^{\infty}\int_{-\infty}^{+\infty}\bar{C}_i\,dy\,dz=Q_i$$

則(5)式的解爲[16]

$$\bar{C}_i=\frac{Q_i}{2\pi\sigma_y\sigma_z\bar{U}}\exp\left(-\frac{y^2}{2\sigma_y^2}\right)\left[\exp\left(-\frac{(z+h)^2}{2\sigma_y^2}\right)+\exp\left(-\frac{(z-h)^2}{2\sigma_z^2}\right)\right] \quad \cdots\cdots(6)$$

其中σ_y、σ_z爲y、z方向的濃度擴散標準偏差[4][17]。

若將道路視爲由多點源所組成的定長度線源（Statistical base Finiteline Source），線源和風向的夾角爲θ，x軸沿風向而設，每單位長度線源放出污染强度爲Q_{Li}（參看圖一）。則由一定長線源對接收點（x_R,y_R,z_R）所產生的濃度爲

$$C_i(x,y,z)=\int_{x_L}^{x_u}\frac{Q_{Li}}{2\pi\bar{U}\sigma_y\sigma_z\cos\theta}\exp\left[-\frac{((x_0-x')\tan\theta)^2}{2\sigma_y^2}\right]\cdot$$

$$\left[\exp\left(-\frac{(Z+h)^2}{2\sigma_z^2}\right)+\exp\left(-\frac{(Z-h)^2}{2\sigma_z^2}\right)\right]dX' \quad (\theta\neq 90^\circ) \quad \cdots\cdots(7)$$

Z表示接收點離地面的高度。x_L表示線源對接收點有影響的下方x座標值。x_U表示線源對接收點有影響的上方x座標值。或

$$C_i(x,y,z)=\int_{Y_L}^{Y_u}\frac{Q_{Li}}{2\pi\bar{U}\sigma_y\sigma_z}\exp\left[-\frac{(y'-y_0)^2}{2\sigma_y^2}\right]\cdot$$
$$\left[\exp\left(-\frac{(Z+h)^2}{2\sigma_y^2}\right)+\exp\left(-\frac{(Z-h)^2}{2\sigma_z^2}\right)\right]dy' \quad (\theta=90^\circ) \quad \cdots\cdots(8)$$

此處h是表示排放源離地面的高度。y_L表示線源對接收點有影響的下方y座標值。y_u表示線源對接收點有影響的上方y座標值。對於線源濃度污染，經常以地面上的污染濃度最值得重視，因此，只要令Z＝0所求得的，即爲地面濃度（Ground-Level Concentration），可分別由下二式得之：

$$C_i(x,y,o)=\int_{x_L}^{x_u}\frac{Q_{Li}}{\pi\bar{U}\sigma_y\sigma_z\cos\theta}\exp\left[-\frac{((x_0-x')\tan\theta)^2}{2\sigma_y^2}+\frac{(h)^2}{2\sigma_z^2}\right]dx'$$
$$(\theta\neq 90^\circ) \quad \cdots\cdots(9)$$

或

$$C_i(x,y,0)=\int_{Y_L}^{Y_u}\frac{Q_{Li}}{\pi\bar{U}\sigma_y\sigma_z}\exp\left[-\frac{(y'-y_0)^2}{2\sigma_y^2}+\frac{(h)^2}{2\sigma_z^2}\right]dy' \quad (\theta=90^\circ) \quad \cdots\cdots(10)$$

很顯然的，污染物會在垂直於風向的方向上擴散。但是高斯煙柱模式至少有三項不得忽視的缺點，使它在應用於一般移散模式時受到限制。這三項缺點爲：

(1)無法適當說明經過一段時間後，污染物在大氣中的有效累積情形。

(2)在大空間尺度時，對於長範圍（long-range）作用下，紊亂擴散比起移流擴散將成爲微不足道。

(3)無法說明因各種化學反應存在時，各種污染物間的交互作用。

爲了解決高斯煙柱模式的不足，於是箱模式理論便應運而生[13]。

三箱模式

最早的箱模式理論是由Smith[18]所提出，用以說明非穩定（unsteady）污染物在都市中的累積效應。基本上，它是假設污染物在箱中迅速且均質（homogeneous）的混合。箱的體積是由都市的表面積和混合層高度而決定，然後將箱空間中的均勻（uniform）污染物，以一常微分方程式來表示濃度的變化情形，這時濃度會受移流、化學反

應和降雨的影響而改變。此均質混合的假設，有效解決了箱中紊流混合的問題，但是却無法顧及垂直方向濃度分佈的實際情形，如此將會造成較大誤差。針對這項缺點，Reiquam[19]、Seinfeld 和Mac Cracken et. al. 等人士提出了更進一步的箱模式，那就是把空間劃分成許許多多的小箱子，來解決不同濃度的分佈問題。其基本假設爲：

①污染物一旦進入箱中，能迅速且均勻的混合。

②箱中污染物濃度爲排放進入、移流和化學反應間的變數。

③忽略壁間的擴散作用。

箱模式的發展，彌補了高斯煙柱模式的不足，但是如何選擇合理的箱體積才能確實表示出擴散和化學反應的作用呢？

四可變體積分佈反應器理論（ VVBR ）[6]

所謂VVBR 理論（ Variable Volume Batch Reactor ），簡單的說就是假想將污染質放在體積能變化的反應器內，由擴散作用所引起污染質濃度的減小，可利用反應器體積作相對程度的擴大來模擬，而污染物的化學反應，就可視爲在此逐漸膨脹的虛構反應器內進行。假使暫時不考慮化學反應時，根據質量不滅定律：

$$C_i = \frac{AQ_i}{\bar{z}^3}$$

其中Q_i 爲 i 種污染物的排放量，A爲常數，$\bar{z}$ 爲反應器的長度，將隨時間的增加而增大，相反的，濃度C_i 將隨$\bar{z}$ 的增大而減小。這種觀念極具價值，但是它在求取反應器的體積變化與擴散速率間關係時，並沒有成功。不過VVBR的觀念却導致了環理論（ Ring Concept ）的產生[20]。

五環理論

環理論是由點源的煙柱擴散而發展出來的，將排放煙柱的橫截面上，劃分成許多的同心圓或橢圓，每二條分隔線間所圍成的區域，即爲每一環的面積。此面積大小分隔的決定，是將此橫截面的污染質作等量的分配，換句話說，於每一環中的污染質，其量相當於其他各環的污染量。因爲排放濃度在每一橫截面上，並不呈均勻狀態，而是以高斯分佈爲主，濃度的擴散以主軸最高，因此所區分出每環的面積並不相同。面積的大小，和所欲區分的環數N有關，與離排放源 x 軸的距離和 y 、 z 方向的擴散係數也有關。對於地面上的線源，則以 z 軸作爲每格的基本，利用 X－Y 平面，將 z 方向劃分成許多平行區間（ 見圖二 ），每一區間中，含有等量污染質。

環理論有幾項基本的假設：

1. 在每個環中污染物濃度相同。
2. 劃分等量污染質的區域時，是不考慮化學反應的情況下。
3. 因各環面積不同，相連兩環濃度爲不連續。
4. 當 x 增加時，因擴散作用而使環面積相對的擴大。

綜合環理論和箱模式的特性而導出推廣環理論的擴散模式[6]。

六推廣環理論的擴散模式

根據箱模式把擴散空間分格成許多小格子，每個小格子體積依 x 軸距離的增長而加大，此即推廣環理論。它充分表現了擴散的特性。對於線源，每一格的體積，除了 z 方向污染量分層外，y 方向因爲相同排放强度線源，通常以單位長度做爲區分，x 方向則視需要或誤差限度而定。則每單位長度層區域所含有污染物總量（ $\theta = 90°$ 時 ）爲

$$\int_{z_{ns-1}}^{z_{ns}} \bar{U}\,\bar{C}_i\,dz = \frac{Q_{Li}}{N} \qquad \cdots\cdots(12)$$

其中N表示總共區分的層數，Z_{ns} 表示第 ns 層的高度，Q_{Li} 表單位長度的線源排放强度。將式(8)代入(12)得

$$\int_{z_{ns-1}}^{z_{ns}} \bar{U} \int_{Y_L}^{Y_u} \frac{Q_{Li}}{2\pi\bar{U}\sigma_y\sigma_z} \exp\left[-\frac{(y')^2}{2\sigma_y^2}\right] \cdot \left[\exp\left(-\frac{(Z+h)^2}{2\sigma_y^2}\right) + \exp\left(-\frac{(Z-h)^2}{2\sigma_y^2}\right)\right] dy'dz = \frac{Q_{Li}}{N} \qquad \cdots\cdots(13)$$

同理，當 $\theta \neq 90°$ 時，每單位長度層區域含有污染物量爲：

$$\int_{z_{ns-1}}^{z_{ns}} \overline{U C_i}\,dz = \frac{Q_{Li}}{N\sin\theta} \qquad \cdots\cdots(14)$$

將式(7)代入(14)得

$$\int_{z_{ns-1}}^{z_{ns}} \bar{U} \int_{x_L}^{x_U} \frac{Q_{Li}}{2\pi\bar{U}\sigma_y\sigma_z\cos\theta} \exp\left[-\frac{((X_0 - X')\tan\theta)^2}{2\sigma_y^2}\right] \cdot \left[\exp\left(-\frac{(Z+h)^2}{2\sigma_z^2}\right) + \exp\left(-\frac{(Z-h)^2}{2\sigma_z^2}\right)\right] dx'dz = \frac{Q_{Li}}{N\sin\theta} \qquad \cdots\cdots(15)$$

在(12)～(15)式中 $\int_{z_{ns-1}}^{z_{ns}} \bar{U}\,dZ$ 的值，即爲每格的體積。層區域的區分由地表開始（ $Z_0 = 0$ ），式(13)、(15)可分別寫成：

$\theta = 90°$

$$\int_0^{Z_1} \left\{ \int_{Y_L}^{Y_u} \frac{1}{2\pi\bar{U}\sigma_y\sigma_z} \exp\left[-\frac{(y')^2}{2\sigma_y^2}\right] \cdot \left[\exp\left(-\frac{(z+h)^2}{2\sigma_y^2}\right) + \exp\left(-\frac{(Z-h)^2}{2\sigma_z^2}\right)\right] \cdot dy' \right\} dz = \frac{1}{N} \qquad \cdots\cdots(16)$$

$\theta \neq 90°$

$$\int_0^{Z_1} \bar{U} \left\{ \int_{x_L}^{x_U} \frac{1}{2\pi\bar{U}\sigma_y\sigma_z\cos\theta} \exp\left[-\frac{((X_0 - X')\tan\theta)^2}{2\sigma_y^2}\right] \cdot \right.$$

$$\left[\exp\left(-\frac{(Z+h)^2}{2\sigma_z^2}\right)+\exp\left(-\frac{(Z-h)^2}{2\sigma_z^2}\right)\right]\cdot dX'\Big\}dz$$

$$=\frac{1}{N\sin\theta} \qquad \cdots\cdots(17)$$

理論上由(16)、(17)兩式，可積分而解得 Z_1 的值，Z_1 值解出後，利用 $\int_0^{Z_1}\bar{U}\,dz$ 能求出連接地面的第一格其體積大小。將 z 軸分成許多高度極小的區域代入式(7)或式(8)中，算出各高度的濃度，再將各濃度乘以本身所代表極小區間的體積，可求出每極小區間中污染物的含有量，然後由下向上依序累加，直到所欲分得的 Q_{Li}/N（$\theta=90°$）或 $Q_{Li}/N\cdot\sin\theta$（$\theta\neq 90°$）爲止，如此次第累加，將可得到各層的高度。因濃度依 X 軸的延長而減小，在不同 x 點所得到的層高不同，且隨 x 軸增大而增大。其所涵蓋的體積，視爲 X－Z 二方向圍成的梯形和單位 Y 所構成的範圍，見圖三。其式如下：

$$V=\left[\left(Z^j_{ns}-Z^j_{ns-1}\right)+\left(Z^{j-1}_{ns}-Z^{j-1}_{ns-1}\right)\right]\times\left(X_j-X_{j-1}\right)/2 \qquad \cdots\cdots(18)$$

j 表 x 方向的分格代號

至此，由擴散所造成的影響，已由體積的變化取而代之。並且大氣中已存在的污染物，也可以和煙柱混合後，加入其中反應(7)(21)。這就是巢理論的基礎(12)。

七、巢理論

除了環理論的一些假設條件外，巢理論中必有二點基本假設：

1. 大氣中本身污染物能均勻分佈，並且能和煙柱中的污染物接觸，而以相同的速率進行化學反應。
2. 凡是參與化學反應的污染物，不論是否爲排放源所排放的，皆列入考慮。

大氣污染物儘管能與煙柱污染物紊亂混合，而進行化學反應，但是大氣污染物却沒有擴散因素的介入，因此這二種不同來源的污染質，在觀念上，仍然需要加以區分。也就是說，各個巢格子內部的化學反應，由大氣和煙柱的污染物同時參與，但是因爲大氣污染物的濃度並不擴散，故在巢與巢的交界處，應不斷地有大氣污染物補充。

對於固定的第 ns 區，$D^j_{i,ns}(X)$ 表示第 j 巢在 x 位置（$X_{j-1}\leq X\leq X_j$）所含有第 i 種污染物的總量，$C_{i,ns,b}$ 表示在 X 處 i 種污染物的濃度，則在 j－1 巢交界處（$X=X_{j-1}$），$D^{j-1}_{i,ns}(t_{j-1})$ 與 $D^j_{i,ns}(t_{j-1})$ 的關係爲：（參看圖四）

$$D^j_{i,ns}(t_{j-1})=D^{j-1}_{i,ns}(t_{j-1})+w\times C_{i,ns,b,x_{j-1}}\times\left(V_{ns,j}-V_{ns,j-1}\right) \qquad \cdots\cdots(19)$$

而 $D^j_{i,ns}(X)$ 的起始值爲：

$$D^j_{i,ns}(t_0)=\left(C_{i,ns,o}+WC_{i,ns,b,o}\right)\times V_{ns,1} \qquad \cdots\cdots(20)$$

其中 W 表示排放源與大氣混合程度的參數，（$0\leq W\leq 1$）。$V_{ns,j}$ 表第 j 巢的體積，

$C_{i,ns,j}$ 表示在 X_j 處的濃度值。則 $D^j_{i,ns}(X)$ 在 j 盒內因化學反應所引起的變化，可以由下式求得：

$$\frac{dD^j_{i,ns}(X)}{dt}=V_{ns,j}R_i \qquad \cdots\cdots(21)$$

$$C_{i,ns,t,j}=\frac{D^j_{i,ns}(X)}{V_{ns,j}}+(1-W)C_{i,ns,b,j} \qquad \cdots\cdots(22)$$

$C_{i,ns,t,j}$ 爲 ns 區域中，大氣與煙柱的污染總濃度。當 W＝0 時，巢理論將簡化爲推廣環理論。

在模式的建立過程中，巢體體積的計算，和光化學反應作用，被視爲二種完全獨立的過程。擴散所造成濃度減少的特性，用相對的體積增大來表示，已在前面敍述過，至於化學反應的計算也將於下節作一說明。

八、化學反應的計算(22)

以表一爲例，這一系列的反應中，各污染物濃度隨時間而變化，因此可以將各污染物的濃度變化寫成系列聯立常微分方程式：

$$\frac{dC_{NO_2}}{dt}=-P_1+P_3+P_6-P_8$$

$$\frac{dC_{NO}}{dt}=P_1-P_3-P_6$$

$$\frac{dC_{O_3}}{dt}=P_2-P_3-P_5+0.5P_7$$

$$\frac{dC_{O_2}}{dt}=-P_2+P_3-P_7$$

$$\frac{dC_{C_4H_8}}{dt}=-P_4-P_5$$

$$\frac{dC_{RCO_X}}{dt}=2.5P_4+2.5P_5-P_6-P_7-P_8$$

$$\frac{dC_{ALD}}{dt}=0.12P_4+0.12P_5$$

$$\frac{dC_{PAN}}{dt}=0.67P_8$$

其中 $P_1=\alpha_1C_{NO_2}$，$P_2=\alpha_2C_OC_{O_2}C_M$，$P_3=\alpha_3C_{O_3}C_{NO}$，$P_4=\alpha_4C_OC_{C_4H_8}$，$P_5=\alpha_5C_{O_3}C_{C_4H_8}$，$P_6=\alpha_6C_{RCO_X}C_{NO}$，$P_7=\alpha_7C_{RCO_X}C_{O_2}$，$P_8=\alpha_8C_{RCO_X}C_{NO_2}$，

α 爲化學反應速率 ……(24)

這最重要的 NO_2，NO，O_3 光化學反應循環中(23)(24)

$$NO_2 + h\nu \xrightarrow{1} NO + O$$
$$O + O_2 + M \xrightarrow{2} O_3 + M \qquad \cdots\cdots(25)$$
$$O_3 + NO \xrightarrow{3} NO_2 + O_2$$

$$\frac{dC_O}{dt} = K_1 C_{NO_2} - K_2 C_O C_{O_2} C_M \qquad \cdots\cdots(26)$$

若將(26)式的等號右方做數值上的估計，其值將非常趨近於 0，在物理意義上，反應 1 中氧原子的產生和反應 2 中氧原子的消耗量幾乎相等，因此習慣上將氧原子的濃度視爲定值，不隨時間而變，此稱爲穩定近似（ Steady-State Approximation ）。

同樣的在此處的光化學反應模式中，也採用穩定近似的假設：

$$\frac{dC_O}{dt} = P_1 - P_2 - P_4 = 0$$

即
$$C_O = \frac{\alpha_1 C_{NO_2}}{\alpha_2 C_{O_2} C_M + \alpha_4 C_{C_4H_8}}$$

在每一巢體積中氧原子的濃度不隨時間而變化。但巢與巢的比較，氧原子濃度則未必相同。

利用數值方法，求解聯立方程式[23]，可得到各種污染物經化學反應後的濃度。

九、模式的建立

模式的建立分爲二部份，第一部分求出巢體積。此巢體積隨著距離的增加而增加，將擴散濃度減小的特性，以巢體增大來代表。第二部分考慮巢內的化學反應。每個巢體視爲獨立的作用空間，化學反應在其中進行，污染物間濃度相互影響發生變化。

巢體積的計算，由於線源對接收點的影響範圍有限，式(7)、(8)中 X_L ，X_U 及 Y_L ，Y_U 的決定是以接收點向線源展開上下各 22.5° 的延伸線交點爲範圍。當線源和風向間夾角 θ 小於 22.5° 時，延伸線和線源將不會相交，使線源積分由負無窮大至 X_U 或 Y_U，爲減少計算上的困擾，當夾角小於或等於 30° 時，影響範圍下方 X_L 即以 30° 時計算的 X_L 長度爲主。選擇影響範圍之後，因式(13)或(15)的計算過於複雜，無法直接由數值方法求出 Z_{ns} 高度，所以自 $Z = 0$ 開始，先將 z 方向空間劃分成更細小的層區，計算每一層區的污染物量，再以式(14)或(12)判斷，累加各小層區污染物量，直到 Q_{Li}/N 或 $Q_{Li}/N \cdot \sin\theta$ 爲止的 Z 高度即爲 Z_1 ，依次類推求 $Z_2 \cdots Z_{ns}$ 高。層區高度求出後，以式(18)作爲基本計算各巢體積。式(13)、(15)中 σ_y 、σ_z 表示污染物在和風向呈直交的水平、垂直濃度擴散的標準偏差，其值和下風距離 x 有關，此處根據 P－G 曲線求取。污染物濃度以高斯求積法計算（ Gaussian Quaduature ）[24]，先將積分式做變數轉換，使積分區間成爲 -1 到 $+1$，然後在其中選定適當的節點，予以加權計算，此法既簡單又準確，但是當積分區間逐漸增長時，所取的節點數必須相對增加，否則誤差值將會跟著加大，表七爲各種穩定度情況下，節點數 n 和距離的關係。

模式中將空間劃分成許多小格，由於將連續空間改爲不連續空間，其中可能會引起相當的誤差。對於 $j-1$ 巢，當 $x = x_{j-1}$ 時(22)式成爲：

$$C^{j-1}_{i,ns,t} = \frac{D^{j-1}_{i,ns}(x_{j-1})}{\bar{V}_{ns,j-1}} + (1-W) \times C^{j-1}_{i,ns,b} \qquad \cdots\cdots(27)$$

對於 j 巢，當 $x = x_{j-1}$ 時(22)式成爲：

$$C^{j}_{i,ns,t} = \frac{D^{j}_{i,ns}(x_{j-1})}{\bar{V}_{ns,i}} + (1-W) \times C^{j-1}_{i,ns,b} \qquad \cdots\cdots(28)$$

理論上，同樣在 $x = x_{j-1}$ 處(27)應等於(28)，但實際上將二式相減得：

$$\triangle C^{j}_{i,t,ns} = \frac{D^{j}_{i,ns}(x_{j-1})}{\bar{V}_{ns,j}} - \frac{D^{j-1}_{i,ns}(x_{j-1})}{\bar{V}_{ns,j-1}} \qquad \cdots\cdots(29)$$

則 $\triangle C^{j}_{i,nn}$ 表示二者的誤差。將式(19)代入上式，則：

$$\triangle C^{j}_{i,t,ns} = \left[\frac{D^{j-1}_{i,ns}(x_{j-1})}{\bar{V}_{ns,j}} + W C^{j-1}_{i,ns,b}\left(1 - \frac{\bar{V}_{ns,j-1}}{\bar{V}_{ns,j}}\right)\right] - \frac{D^{j-1}_{i,ns}(x_{j-1})}{\bar{V}_{ns,j-1}}$$

$$= \left[W C^{j-1}_{i,ns,b} - \frac{D^{j-1}_{i,ns}(x_{j-1})}{\bar{V}_{ns,j-1}}\right]\left(1 - \frac{\bar{V}_{ns,j-1}}{\bar{V}_{ns,j}}\right)$$

$$= C^{j-1}_{i,ns}\left(\frac{\bar{V}_{ns,j-1}}{\bar{V}_{ns,j}} - 1\right) \qquad \cdots\cdots$$

由(30)可知，$\triangle C^{j}_{i,ns,t}$ 直接與 $\bar{V}_{ns,j-1}/\bar{V}_{ns,j}$ 有關，當 $\bar{V}_{ns,j-1} = \bar{V}_{ns,j}$ 時 $\triangle C^{j}_{i,ns,t} = 0$ 因此對相鄰兩巢的體積比，應控制在一定的程度下，以減少誤差。

參、模式的應用

本線源是以台灣南北高速公路爲模擬對象，高速公路由基隆起至高雄端，全長三百七十三點二四公里，道路二旁的地形，自北而南由丘陵起伏漸趨於平坦。爲有效配合模式的特性，選擇了桃園交流道至南中壢交流道間一段直線線源爲模擬，此路段附近以遼濶的田野爲主。在桃園交流道和南中壢交流道間，還有機場交流道、內壢交流道和北中壢交流道。由於中正國際機場的存在，桃園交流道至機場交流道間的車輛流量，很明顯的較機場交流道至南中壢交流道要高，因此本區的線源視爲二段強度不同的排放源。第一段爲桃園交流道至機場交流道間長二公里的區域，第二段爲機場交流道至南中壢交流道間長十點四公里的區域。由於只有在收費站處才有交通流量的記錄，因此第一段的流量以泰山收費站的記錄爲代表，第二段的流量以楊梅收費站的記錄代表。

模式資料的分析必需具有(1)氣象條件。(2)車輛流量。(3)排放因子。氣象條件包括風向、風速、大氣穩定度等，用以求得擴散的特性。大氣穩定度是由風向、風速、天頂角、總雲量、相對濕度、氣溫和露點等資料求得。車輛流量是根據泰山、楊梅收費站的記錄值。由於記錄值只有大客車、大貨車和輕型車三種，因此車輛種類的區分就分爲此三大類，表十爲交通量。排放因子(emission factor)的計算是根據美國環境保護署在1972曆年(calendar)做全國性調查時，加州的統計和計算法[25] 。排放因子是以車輛行一公里或一英哩所放出的污染物質量爲基本單位。因爲採樣時的氣溫不同，採樣點處的平均車速不同[26] ，所以排放因子會有差異，應予分別計算而得。計算時假設100%熱起動(hot start operation)。排放因子又依車種、柴油或汽油引擎而變化，但是限於資料的不足，此處假設輕型車全部爲汽油引擎，大客車和大貨車全部爲柴油引擎。將排放因子求出後(見表十一)，乘以當天車流量，即可得當天的污染物排放總量，在模式計算時線源污染物排放強度是以 $\mu g/sec\text{-}m$ 爲單位輸入，所以得再將每天排放總量除以86400，而得每秒平均排放量，見表五。

事實上汽車排出碳氫化合物的種類多不勝數，各種類的排出量也無法確定，再加上碳氫化合物的氧化過程非常複雜，因此要想得到確切的化學反應機構，是極爲困難的事。假使在模式建立之初，就以大量化學反應式作爲嘗試，將爲十分不智之舉，本研究以較具代表性的反應爲主，選擇四組基本光化學系列反應，分別予以嘗試(見表一～四)[11][3][27]，模式計算流程圖見圖六。

模式計算時的輸入資料：

1. 高斯求積法節點數n，權數，節點值。
2. 穩定度NS，風向和線源夾角 θ，氣溫T，風速U。
3. 總區分層數N。
4. 欲模擬之層號I。
5. 測點和線源的相對座標。
6. 控制巢體積x方向長度的係數 C_s。
7. 二不同強度排放源的比例QC。
8. 蘭吉固達法中的變幅H。
9. 混合係數W。
10. 排放準強度 Q_i。
11. 背景濃度 C_{ib}。
12. 各污染物的分子量。
13. 化學反應速率常數 α。

各種變數的輸入值列於表六。

四、結果與討論

根據數據組Ⅰ～Ⅳ以及光化學反應組PC-1～PC-4的計算機模擬計算得到：圖八

～圖十四爲數據組Ⅰ的計算結果。圖十五～圖二十一爲數據組Ⅱ的計算結果，圖二十二～圖二十八爲數據組Ⅲ的計算結果，圖二十九～圖三十五爲數據組Ⅳ的計算結果。圖形中若標明PC-n則表示第n組光化學反應。

圖七爲各數據組計算體積比較情形，Ⅳ曲線尾端分成編號爲1、2二條是由於有二段不同强度污染源的結果。當X < 620 m，接收點只受中壢—機場交流道間有限線源單一排放强度影響，但 x ≥ 620 m時，線源上端影響接收點的區域已開始涵蓋排放强度較大的桃園交流道—機場交流道的污染源，接收點的濃度較單一排放時爲高，因此層累積至 Q_L/N 或 $Q_L/N \times \sin\theta$ 的高度較低，使體積也略爲偏低。隨著距離繼續增加，較强污染源的影響增大，體積之間的差異也隨著增大。若以不同數據組體積的比較，理論上應與穩定度有直接關係，穩定度代表大氣紊亂狀況，穩定度愈小，亂流作用愈大，污染擴散情況愈好，也就是愈容易擴散。濃度減低，相對的巢體積則因而增大，所以穩定度由A→F，體積應有減少趨勢。圖七爲不同穩定度情況下，體積的變化情形，證明此項推論的正確。本文中計算影響接收點的線源長度，是以接收點向線源展開上下各22.5°的延伸線交接範圍內，假使線源和風向夾角愈小，影響接收點的線源將愈長，模式建立時線源影響的下方長度以夾角30°作爲限制，此假設經計算，當夾角爲25°時，所造成的誤差在十萬分之四以內，當夾角爲23°時，其誤差在十萬分之八以內，因此基於計算上的方便，當夾角小於或等於30°時。影響接收點的線源由原點以下長度以30°時的長度爲代表，將不會造成嚴重影響。

在體積求算過程中，流量值的輸入應屬不必要，因爲流量和濃度值之間呈正比例現象，求出的濃度作用只在於將它累積到流量的N分之一量(N爲Z方向的分格數)。因此可將流量視爲一定值代入。但是當線源車輛流量受地段影響，會有顯著差異而造成不同强度的排放量，這時各流量間的比例關係必需加以研究，因爲擴散的特性將由體積的大小代表之。此種强度不同的線源，在求取接收點濃度時依流量大小分成數段，各別積分之後累加。流量和流量間有一定比例關係，計算時加入一比例常數校正。此種强度比例校正在排放污染物量爲一定或在不起化學反應情形下，將不會產生任何困擾，但在本研究中以光化學反應爲主，而光化學反應爲一連串的反應，不同二路段間各種污染物排放會有不同的比例，究竟流量校正比例常數應如何選取，必需經由大量實測數據值和多次試誤法，來尋找較爲合理的代表。

濃度計算時以高斯積分法(Gaussian Quadrature)作爲線源的積分計算，高斯積分法的缺點在於係數及函數的幅數通常爲無理數。這在手算時會感到困難，若使用電腦計算，則不會受到影響，因此這項缺點在本模式上可以不必考慮。高斯積分法與使用合成牛頓—寇次(Newton-Cotes)法相比較，高斯公式能以較少的計算而獲得較高的準確度，在程式設計上也較爲簡單，所以本模式中即利用此法來做積分的計算。在排放因子中，NO_x 包括NO及 NO_2，於本模式中，二者皆爲排放源污染物，且視爲二種分別考慮的污染物，在 NO_x 中彼此所佔百分數並沒有明確的分析記錄。同樣的，H.C.是表示總碳氫化合物量，其中種類非常多，至於實際含 C_4H_8 或 C_3H_6 的量也沒有完整記錄。綜合這些不定值，在模式輸入值的選取上必須做多次試驗，以取得統計上的價值。

對於光化學反應方程式的選取，最基本的光分解循環爲式㉖的三項反應，其中M爲第三種介質用以吸收反應的能量，在空氣中M物質可能爲 O_2 或 N_2。根據實驗這三項反應作用非常迅速。若是所有光化學反應都能包括在式㉖中此項假設正確的話，則可推知 NO 、NO_2 、O_3 的濃度將爲定值，反應所產生穩定狀態的 O_3 ，濃度爲初始 NO_2的函數。因此由 NO_2 濃度可算出 O_3 的濃度，再因燃燒過程排入大氣中以 NO 爲主，NO_2 量極微，臭氧濃度應該維持在一定限度之內。然而，事實上 O_3 濃度遠大於此限度，因此可以斷定除式㉖之反應外還有其他反應存在使 NO 氧化成 NO_2 時不消耗 O_3 ，造成 O_3 累積成高濃度，而氮氧化物濃度則逐漸降低，正如大氣中所發生的情形一般。這一點由於碳氫化合物的存在而獲得解決。已存在有相當反應性的氧原子，能打擊碳氫化合物，尤其是穩定性較弱的烯屬烴（ olefin ），使雙鍵斷裂爲二，產生自由基（ free radical），此自由基具有高度反應性，能繼續參與其他的反應。這些有機性自由基與 O_2 形成過氧基（ Reroxy radicals ）能釋出一氧原子而使NO氧化爲 NO_2 ，因而干擾了上述所提及的 NO 、NO_2 、O_3 循環。在烯屬烴參與反應時形成另一種基，可能是醛類，因爲醛類爲氧原子與烯系烴反應所產生生成物的一種。過氧基的旁支反應，可能形成硝基過氧乙醯（PAN），這是一種非常强烈的眼睛刺激劑，對植物會造成傷害。硫化物在光化學煙霧中所扮演的角色，尚未能完全了解，因此在此暫時不予考慮。事實上光化學作用的連鎖反應非常多[27][28]，要推測光化學煙霧反應的模式，非常困難，爲了簡化極大數目可能反應，在複雜項目中僅選取速率較快的反應或較具代表性的反應。反應速率常數曾經多位專家在實驗室中研究並發表於報章雜誌上。本模式中第一組光化學反應，是根據A.Q. Eschenroeder et al.[11] 所做的研究，也就是取上面所述最基本又具代表性的反應爲主。因烯屬烴中以直鏈一二丁烯的活性較其他碳氫化合物爲多，因此以 C_4H_8 爲碳氫化合物的代表。第二組反應式中只將 C_4H_8 以 C_3H_6 取而代之，C_3H_6的氧化系統和空氣污染反應系統也十分接近，和 C_4H_8 比較起來 C_3H_6 的氧化速率較慢，PAN 產生量較少。第三、四組光化學反應是以 Seinfeld[22] 書中所選取化學反應組中具代表性的反應式做爲模擬對象。

模式根據上述資料進行計算機模擬，結果繪製成各種曲線，就第Ⅰ組數據結果顯示，經由PC-1，PC-2所計算出濃度沒有太大差異，而經PC-3，PC-4者除ALD 爲前二組的十倍外，其他濃度也差異有限。就Ⅲ所進行將Z空間分成三種層次：100，50 20 比較濃度計算值，結果三者之間並沒有固定關係存在。

縱觀圖形的趨勢。NO_2因原本就以固定量排入大氣中，排入時本身已到達某種濃度，因此儘管NO作用會增加 NO_2 量，但 NO_2 會進行相當快速光分降作用，形成NO，並產生最後污染物PAN ，在增加或減少總量上仍以減少爲多，因此其進入大氣之後呈現指數性衰減。NO分解爲 NO_2 的速度相當快速，假使 NO_2 排放量爲 0，則若干距離後，NO_2 量會累積至某特定高度，這都由於NO的氧化作用，因此NO 本身量會因快速分解而逐漸減少。O_3 如前所述，將NO氧化爲 NO_2 的速率較過氧基氧化速率慢，因此會逐漸累積，但是因爲擴散作用存在，使濃度的累積到達一定程度後，擴散的影響較化學作用要大，因而又有減小的趨勢。其濃度曲線爲起伏狀，先升後降。C_4H_8 因不停被氧原

子撞擊，形成自由基，又沒有其他的作用產生以增高濃度，因此爲一向下減小曲線。ALD和PAN 由於都是反應組的最後產物，所以濃度會逐漸增加，當增加至某一定程度後也因擴散作用而逐漸減小，如同 O_3 一般；但各污染物累積到何種程度才開始減少，依種類和擴散情況而異。

巢體積變化的限制已在前章敘述過，在愈遠離排放源時巢體積愈大，巢體的決定在 x 軸上的尺度可依距離增長而增加，因爲在近排放源處由於體積本身很小，邊長的尺度稍有變化就會造成無法忽略的影響，而依體積的增大，影響程度減小，因此只要在體積變化能允許的範圍內，隨距離增加將 x 方向尺度擴大，可減少部份計算機使用時間，却不會對結果產生影響。

對於式㉓聯立常微分方程式的求解，是利用四階蘭吉固達法計算（ Fourth - order Runge - Kutta Method ）。每一步驟需要計算 f （ x ，y ）四次，本模式選用蘭吉固達法的原因有：①步驟簡單，計算時只要知道前一點（ x_i ，z_i ）即可。②它的誤差與泰勒級數相合，可以 h^p 表示。③過程中不必計算 f （ x_i ，y_i ）的導數值，僅須重複計算函數 f 值即可。

由體積曲線（圖七）第Ⅳ組數據所計算的巢體積在 620 m處呈現略低的趨勢，在濃度計算上則會有較一般略高的結果（如圖二十九～圖三十五）。

伍、結論與建議

本文將巢理論運用於線源污染擴散上而做光化學模式的設計，經實際在中山高速公路上的模擬，結果能與實際量測值配合，因此模式的推估，仍有其價值存在。對高速公路的污染狀況，以 NO_2爲例，國內規定環境空氣品質爲一小時月平均值爲 0.05 ppm ，而量測結果約爲 0.005 ppm較限值低約一個數量級，污染情形尚不嚴重。但依六十八年至六十九年比較，以泰山收費站記錄結果，車輛增加率小型車約爲 10 %，重型客車爲 3.5 %，重型貨車爲 109 %。增加趨勢值得重視，可能造成的污染問題，應注意及早防範。

模式發展過程中，有幾點尚待改進或值得深入探討之處。第一，x 方向濃度必須由近而遠一個巢一個巢計算而得知，假使欲測數十公里遠處某點，將耗費大量時間計算此點之前的濃度，因此如何簡化過程有再研究的必要。第二，z 方向分層的計算，是先區分成更多更小的層區域，再累加至一定量爲止，假使能由計算中直接求出層區域的高度，可節省許多計算機時間。第三，模式中各輸入值，應加以確認。如排放因子、氣象狀況、不同來源强度間的比例值等，若能確定，計算結果的可信度將大爲提高。第四，採樣數目增加。有足夠採樣值才能驗證模式推估的正確性。第五，污染物量測種類增加。使污染物間化學作用得以證實。經過這些改進模式的彈性和價值將大爲增加。

參考文獻

1. Wanta, R. C., "Meteorology and Air Pollution", Chap, 7, in Air Pollution (A. C. Stern, ed.) Vol. I, 2nd ed. Academic Press, New York, (1976).
2. Graedel, T. E., Farrow, L. A., and Weber, T. A., "Kinetic Studies of the Photechemistry of the Urban Troposphere", Atmos. Envir., 10, 1095-1116, (1976).
3. Atkinson, R., Lloyd, A. C., Winges, L. "An Updated Chemical Mechanism for Hydrocarbon/NOx/SO2 Photooxidations Suitable for Inclusion in Atmospheric Simulation Models", Atmos. Environ. 16, No. 6, 1341-1355, (1982).
4. Zimmerman J. R., and Thompson, R. S. "User's Guide for Highway, A Highway Air Pollution Model", EPA-650/4-74-008, (1975).
5. Dabberdt, W. F., Shelar. E., Marimont, D. and Skinner, G., "Analysis, Experimental Studies, and Evaluations of Control Measures for Air Flow and Air Quality on and Near Highways", FHWA-RD-78-179, (1979).
6. Friendlander, S.K., and Seinfeld, J. H., "A Dynamic Model of Photochemical Smog", Envir. Sci. Tech., 3, 1175-1181, (1969).
7. O'Brein, E. E., "Turbulent Mixing of Two Rapidly Reacting Chemical Species", Phys. Fluids, 14, 1326-1331, (1971).
8. Reynolds, S. D., Roth, P. M., and Seinfeld, J. H. "Mathematical Modeling of Photochemical Air Pollution-I. Formulation of the Model", Atmos. Environ, 7, 1033-1061, (1973).
9. Roth, P. M., Roberts, P. J. W., Lin, M., Reynolds, S. D., and Seinfeld, J. H., "Mathematical Modeling of Photochemical Air Pollution-II. A Model and Inventory of Pollutant Emissions", Atmos. Environ. 8, 97-130, (1974).
10. Reynolds, S. D., Liu, M., Hecht, T. A., Roth, P. M., and Seinfeld, J. H., "Mathematical Modeling of Photochemical Air Pollution. III. Evaluation of the Model", Atmos. Envir, 8, 563-596, (1974).
11. Eschenroeder, A. Q., and Martinzs. J. R., "A Modeling Study to Characterize Photochemical Atmospheric Reactions to the Los Angeles Basin Area', General Research Cooperation, EPA-22-69-127, (1969).
12. 黃賢誠，“多目標式計算空氣污染擴散與化學反應濃度之計算機數學模式”，科學發展月刊，7,1,3-20,(1979)。
13. Calder, K. L., "Eddy Diffusion and Evaporation in Flow Over Aerodynamically Smooth and Rough Surfaces: A Treatment Based on Laboratory Laws of Turbulent Flow with Special Reference to Conditions in the Lower Atmosphere", Q. J. Mech. Appl. Math., 2, 153-176, (1949).
14. Hoffert, M. I., "Atmospheric Transport, Dispersion, and Chemical Reactions in Air Pollution: A Review", AIAA J., 10, 377-387, (1977).
15. Lamb, R. G., and Seinfeld, J. H. "Mathematical Modeling of Urban Air Pollution-General Theory", Envir. Sic. Tech. 7, 253-265, (1973).
16. Sutton, O. G., Micrometeorology, McGraw-Hill, New York, (1953).
17. Green, A. E. S., Singhal, R. P., and Venkateswar, R., "Analytic Extensions of the Gaussian Plume Model", JAPCA, 30, No. 7, 773-776, (1980).
18. Smith, M., "The Concentrations and Residence Times of Pollutants in the Atmosphere", Intercience, New York, 155-166., (1961).
19. Reiquam, H., "Sulfur: Simulated Long-Range Transport in the Atmosphere", Science, 170, 318-320, (1976).
20. Freiberg, J., "The Iron Catalyzed Oxidation of SO2 to Acid Sulphate Mist in Dispersing Plumes", Atmos. Environ. 10, 121-130, (1976).
21. Donaldson, C. du P., and Hilst, G. R., "Effect of Inhomogeneous Mixing on Atmospheric Photochemical Reactions", Envir. Sci. Tech. 6, 812-186, (1972).
22. Seinfeld, J. H., Air Pollution: Physical and Chemical Fundamentals, McGraw-Hill, Inc., (1975).
23. McGraw-Hill, A. J. "Chemistry and Physiology of Los Angeles Smog", Ind. Eng. Chem., 44, 1423-1438, (1952).
24. Gerald, C. F., Applied Numerical Analysis, 2nd ed., Addison-Wesley Publishing Company, (1969).
25. "Compilation of Air Pollutant Emission Factors, 3rd ed. EPA. No. AP-42, (1977).
26. 七十一年度高速公路交通動態資料調查報告，高速公路局，(1982)。
27. Cocks, A. T., and Fletcher, I. S., "Possible Effects of Dispersion on the Gas Phase Chemistry of Power Plant Effluents", Atmos. Environ. 16, No. 4, 667-678, (1982).
28. Augustsson, T. R., "The Effects of Isotropic Multiple Scattering and Surface Albedo on the Photochemistry of the Troposhere", Atmos. Environ. 16, No. 6, 1373-1380, (1982).

表一　第一組光學化學反應（PC-1）

此爲最基本的光化學反應式，H.C.是以C_4H_6的狀態排出

編號	反　　應	反應速率常數
1	$NO_2 + h\nu \rightarrow NO + O$	$0.072 \sim 0.05$ min^{-1}
2	$O + O_2 + M \rightarrow O_3 + M$	1.32×10^{-5} $ppm^{-2}min^{-1}$
3	$O_3 + NO \rightarrow NO_2 + O_2$	21.8 $ppm^{-1}min^{-1}$
4	$O + C_4H_8 \rightarrow 2.5RCO_x + 0.12ALD$	1.11×10^{-5} $ppm^{-1}min^{-1}$
5	$O_3 + C_4H_8 \rightarrow 2.5RCO_x + 0.12ALD$	6×10^{-1} $ppm^{-1}min^{-1}$
6	$RCO_x + NO \rightarrow NO_2$	50 $ppm^{-1}min^{-1}$
7	$RCO_x + O_2 \rightarrow 0.5\ O_3$	5×10^{-6} $ppm^{-1}min^{-1}$
8	$RCO_x + NO_2 \rightarrow 0.67$ PAN	6 $ppm^{-1}min^{-1}$

表二　第二組化學反應（PC-2）

假設H.C.是以C_3H_6的形式排出，所造成反應的變化。

編號	反　　應	反應速率常數
1	$NO_2 + h\nu \rightarrow NO + O$	0.4 min^{-1}
2	$O + O_2 + M \rightarrow O_3 + M$	1.32×10^{-5} $ppm^{-2}min^{-1}$
3	$O_3 + NO \rightarrow NO_2 + O_2$	21.8 $ppm^{-1}min^{-1}$
4	$O + C_3H_6 \rightarrow 2.5RCO_X + ALD$	4.97×10^{4} $ppm^{-1}min^{-1}$
5	$O_3 + C_3H_6 \rightarrow 2.5RCO_x + ALD$	1.8×10^{-1} $ppm^{-1}min^{-1}$
6	$RCO_x + NO \rightarrow NO_2$	50 $ppm^{-1}min^{-1}$
7	$RCO_x + O_2 \rightarrow 0.5O_3$	2.3×10^{-5} $ppm^{-1}min^{-1}$
8	$RCO_x + NO_2 \rightarrow 0.67PAN$	6 $ppm^{-1}min^{-1}$

表三　第三組光化學反應（PC-3）。此處存在NO_2和O_3之直接反應，且考慮N_2O_5的形成和對反應過程的影響。

編號	反　　應	反應速率常數
1	$NO_2 + h\nu \rightarrow NO + O$	$0.072 \sim 0.05$ min^{-1}
2	$O + O_2 + M \rightarrow O_3 + M$	1.32×10^{-5} $ppm^{-2}min^{-1}$
3	$O_3 + NO \rightarrow NO_2 + O_2$	21.8 $ppm^{-1}min^{-1}$
4	$O + C_4H_8 \rightarrow 2.5RCO_x + 0.12ALD$	1.11×10^{5} $ppm^{-1}min^{-1}$
5	$O_3 + C_4H_8 \rightarrow 2.5RCO_X + 0.12ALD$	6×10^{-1} $ppm^{-1}min^{-1}$
6	$RCO_X + NO \rightarrow NO_2$	50 $ppm^{-1}min^{-1}$
7	$RCO_X + O_2 \rightarrow 0.5O_3$	5×10^{-6} $ppm^{-1}min^{-1}$
8	$RCO_X + NO_2 \rightarrow 0.67PAN$	6 $ppm^{-1}min^{-1}$
9	$NO_2 + O_3 \rightarrow NO_3$	5.017×10^{-2} $ppm^{-1}min^{-1}$
10	$NO + NO_3 \rightarrow N_2O_5$	2640 $ppm^{-1}min^{-1}$
11	$N_2O_5 \rightarrow NO_2 + NO_3$	5.847 $ppm^{-1}min^{-1}$
12	$NO_3 + NO \rightarrow 2NO_2$	2.8×10^{5} $ppm^{-1}min^{-1}$

表四　第四組光化學反應（PC-4）。同表三但忽略N_2O_5的作用。

編號	反　　應	反應速率常數
1	$NO_2 + h\nu \rightarrow NO + O$	$0.072 \sim 0.05$ min^{-5}
2	$O + O_2 + M \rightarrow O_3 + M$	1.32×10^{-5} $ppm^{-2}min^{-1}$
3	$O_3 + NO \rightarrow NO_2 + O_2$	21.8 $ppm^{-1}min^{-1}$
4	$O + C_4H_8 \rightarrow 2.5RCO_X + 0.12ALD$	1.11×10^{5} $ppm^{-1}min^{-1}$
5	$O_3 + C_4H_8 \rightarrow 2.5RCO_X + 0.12ALD$	6×10^{-1} $ppm^{-1}min^{-1}$
6	$RCO_X + NO \rightarrow NO_2$	50 $ppm^{-1}min^{-1}$
7	$RCO_X + O_2 \rightarrow 0.5O_3$	5×10^{-6} $ppm^{-1}min^{-1}$
8	$RCO_X + NO_2 \rightarrow 0.67PAN$	6 $ppm^{-1}min^{-1}$
9	$NO_2 + O_3 \rightarrow NO_3$	5.017×10^{-2} $ppm^{-1}min^{-1}$
10	$NO_3 + NO \rightarrow 2NO_2$	2.8×10^{5} $ppm^{-1}min^{-1}$

表五　桃園交流道至機場交流道及機場交流道中至中壢交流道間高速公路污染物排放量（單位$\mu g/m\text{-}sec$）。

	2月22日		4月15日		4月16日	
	H.C.	NO_X	H.C.	NO_X	C.H.	NO_X
泰山	2,200	4,106	1,730	5,240	2,250	5,120
楊梅	-	-	1,133	4,310	1,570	4,290

表六　模式計算時的輸入資料（取表九中第4、5、6、8四組）。

項目 \ 組別		I	II	III	IV
高斯積分法選取點數	n	8	12	20	20
穩定度	NS	2	3	5	4
風向與線源夾角	θ	30	60	30	30
氣　溫	T	29	28	27	20
風　速	U	9	9	7	8
巢體長度控制係數	C_s	0.05	0.05	0.05	0.05
不同污染强度比例值	QC	1.2	1.2	1.2	1.2
蘭吉固達法增加係數	H	0.0025	0.0025	0.0025	0.0025
污染源與背景污染物混合係數	W	1	1	1	1
NO_2排放量	Q_{NO2}	300	700	300	300
NO排放量	Q_{NO}	1,200	2,000	1,200	1,000
H.C.排放量	$Q_{H\ C}$	400	400	400	450

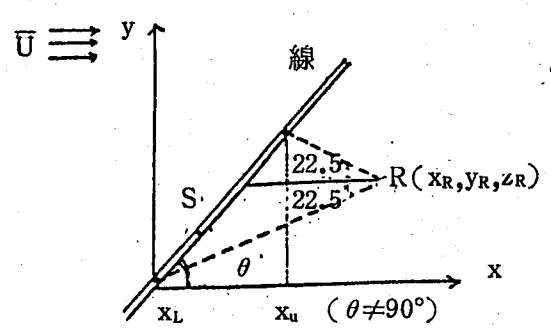

圖一　線源和風向夾角爲 θ（$\theta \neq 90°$），影響接收點的線源投影於 x 軸的長度爲 $x_L x_U$ 線段 R（x_R, y_R, z_R）爲接收點。S（$x^1, y^1, 0$）爲有限線源中任意點。

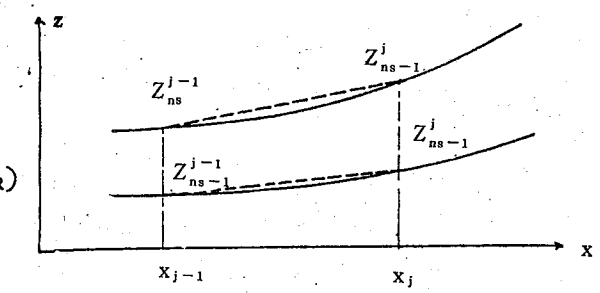

圖三　第 ns 個巢體積在 t_{j-1} 至 t_j 時爲 x－z 上的梯形面積（Z^{j-1}_{ns-1} Z^{j}_{ns-1} Z^{j}_{ns} Z^{j-1}_{ns}）和單位 y 長所圍成的範圍。

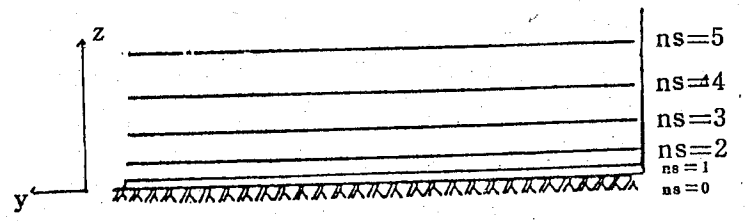

圖二　線源排放，與風向垂直的橫截面面上分成等污染物量的層區域

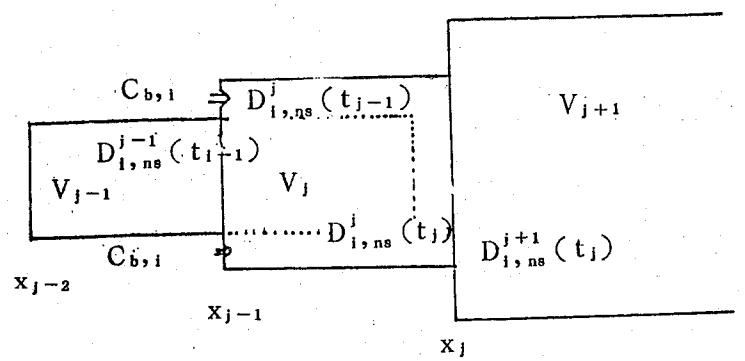

圖四　巢與巢的交界處二端，理論上污染物量會相同，但因背景濃度的加入，使結果並不相同。V_j 表示在 t 時之巢體積。$C_{b,i}$ 爲第 i 種污染物之背景濃度。x_j 爲 t_j 時之 x 軸向位置點。$D^{j}_{i,ns}(t_j)$ 和 $D^{j+1}_{i,ns}(t_j)$ 分別表示在 x_j 點區分成的左右二巢中接近 x_j 處，第 i 種污染物在第 ns 層區中的污染物總量。

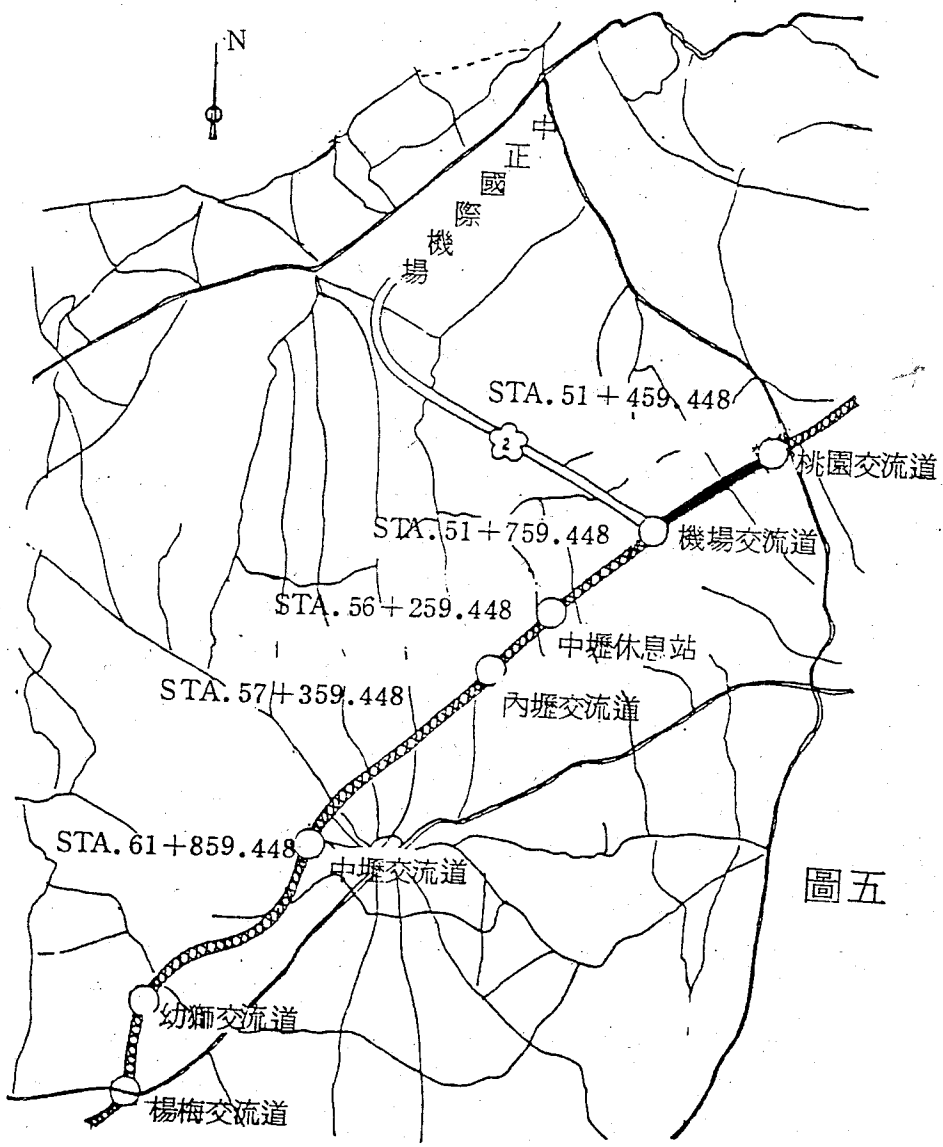

圖五

圖五　高速公路桃園交流道至楊梅交流道平面圖。此段可視爲直線線源，因排放强度不同，以機場交流道劃分成二段强度源。

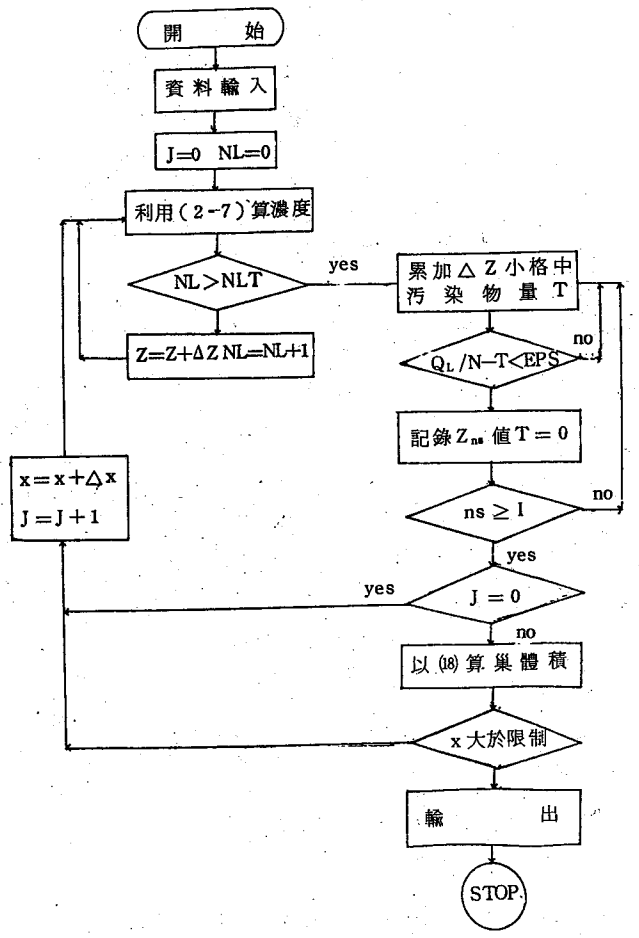

圖六 (a)體積計算流程圖

*NLT為預定計算的極小區域總數，EPS為誤差容許限度，I為欲模擬的層號，Z_{ns}為層ns 頂離地面高度，J為x方向分格數，△Z為Z方向之增加量。

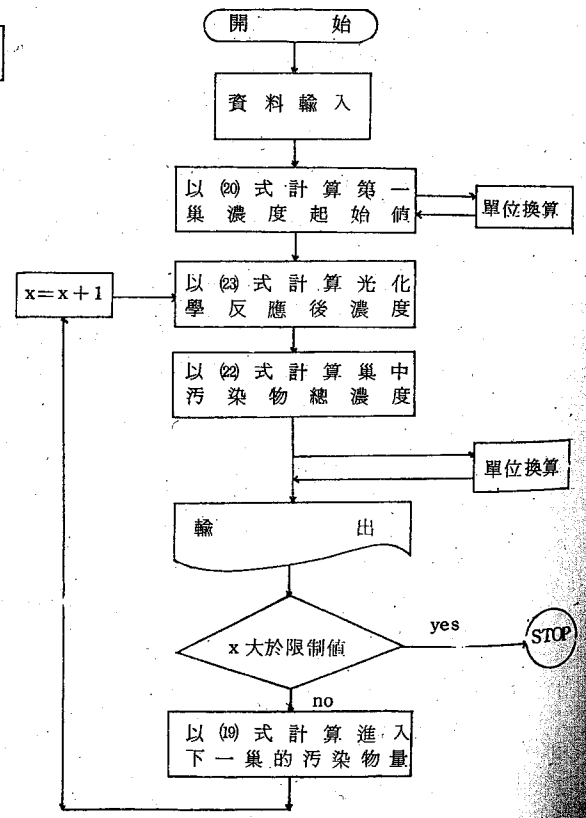

圖六 (b)進行光化學反應流程圖

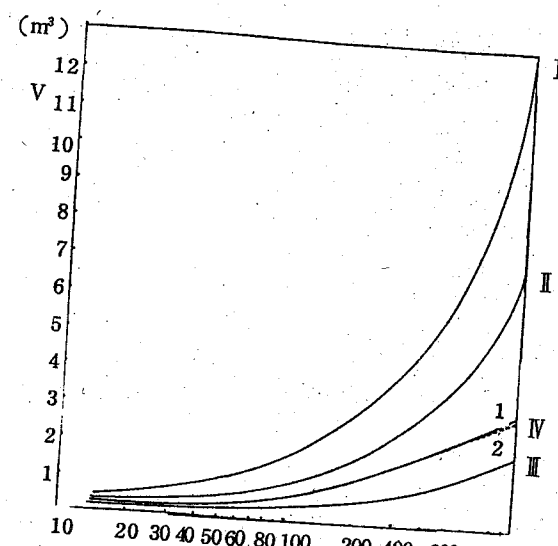

圖七 各數據組所計算巢體積和距離的關係。I為穩定度B級線源與風向之夾角30°。Ⅱ為C級穩定度，夾角60°。Ⅲ為E級穩定度，夾角30°。Ⅳ為D級穩定度，夾角30°。Ⅳ中實線表單一強度線源結果，虛線表620 m處起受強度較強線源加入影響，使濃度增加，體積減少。體積都由近而遠漸次增加。

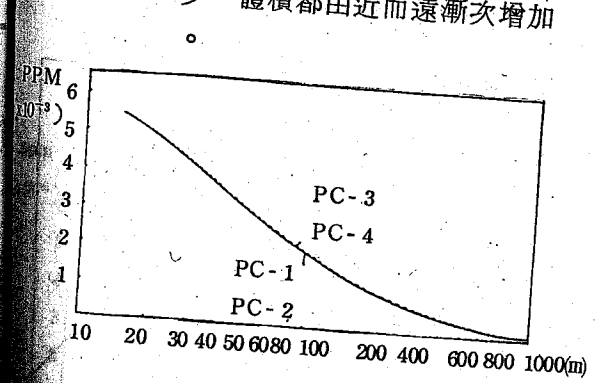

圖八 模式計算個案（見表九）第一組情況下，NO_2濃度隨距離變化的情形。實線表第一、二組光化學反應濃度變化情形，虛線表第三、四組情形。

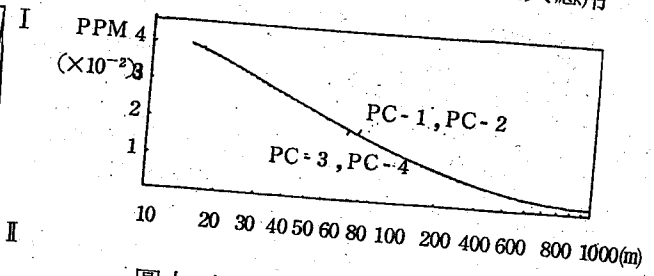

圖九 同圖十七唯係NO 濃度。採樣值和模式計算值間有4%的誤差。光化反應組1，2較3，4計算結果略大。

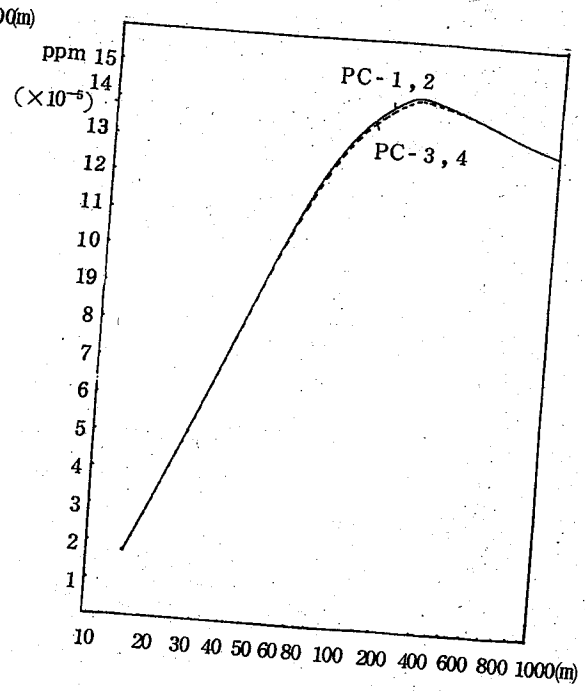

圖十 同圖十七唯係O_3 濃度。在220公尺遠處產生最大值後開始下降。光化學反應1，2組較3，4組在最大值附近，濃度稍大。

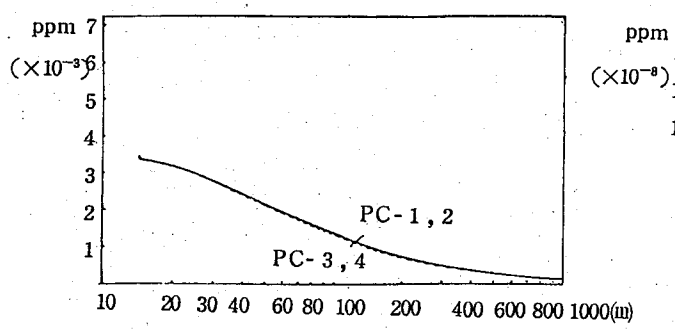

圖十一　同圖十七唯係C_4H_8 濃度。光化反應組 1，2較 3，4 計算濃度稍大。

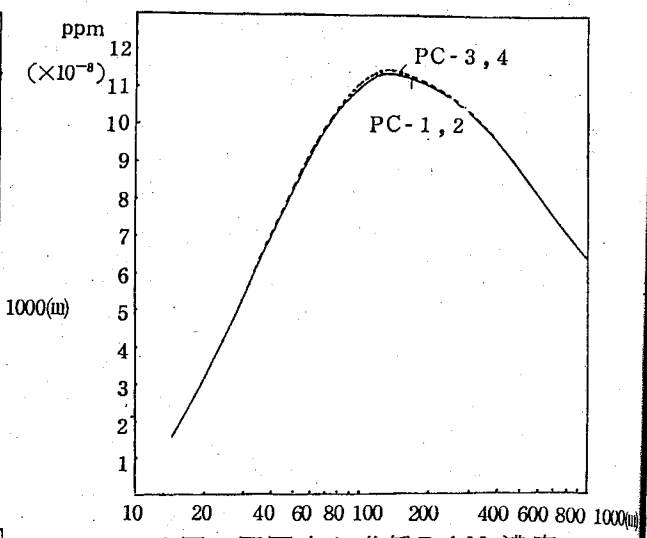

圖十四　同圖十七唯係PAN 濃度。約在 120 m處產生最大值，光化反應組 1，2 比 3，4 略小。

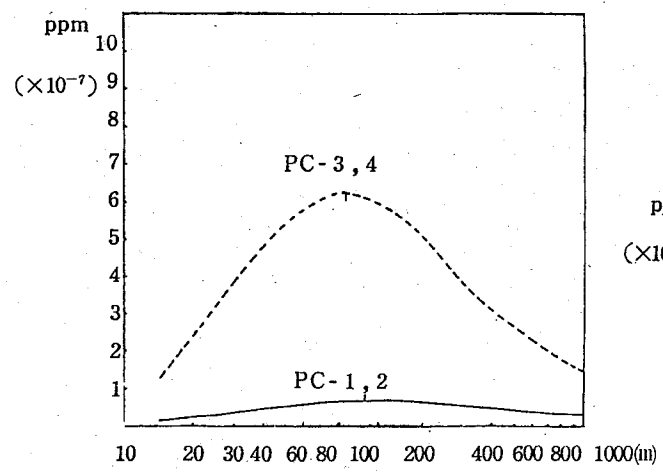

圖十二　同圖十七唯係ALD 濃度。光化反應組 1，2 約比 3，4 濃度小近一個數量級。前者最大濃度約在 130 m處。後者最大濃度約在 90m處。

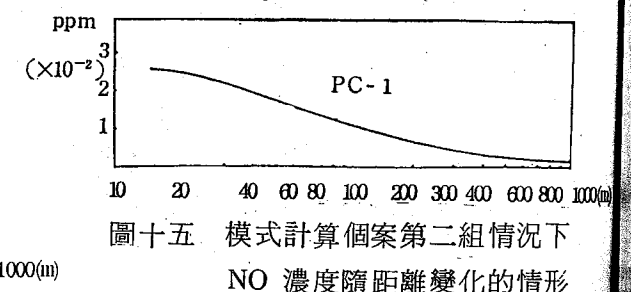

圖十五　模式計算個案第二組情況下 NO 濃度隨距離變化的情形（Ⅱ）。

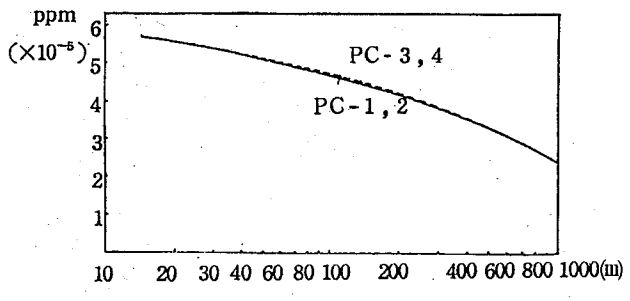

圖十三　同圖十七唯係RCO_X 濃度。光化反應組 1，2 比 3，4 略小。

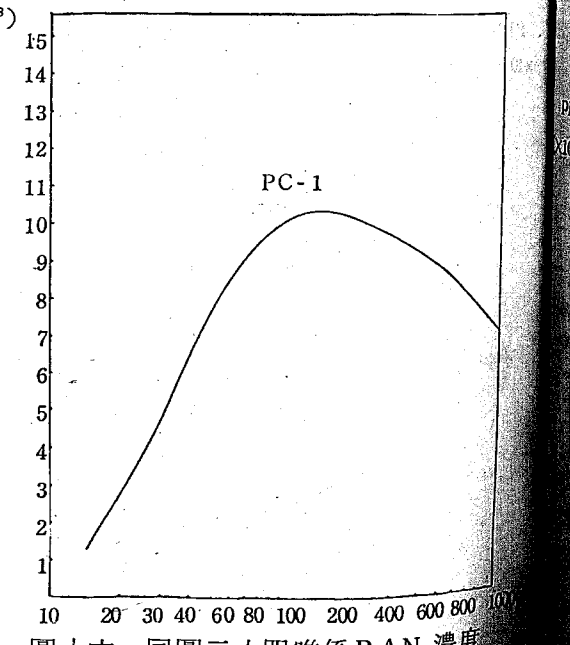

圖十六　同圖二十四唯係PAN 濃度。約在 160 m處產生最大值

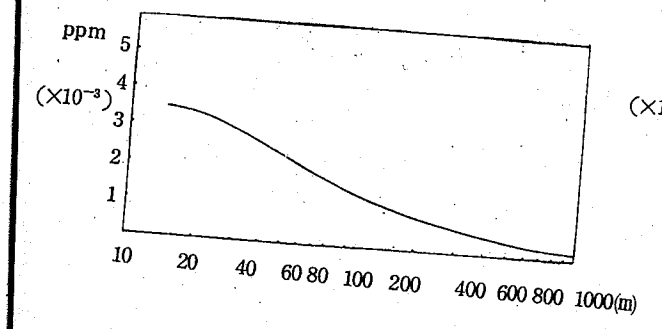

圖十七　同圖二十四唯係C_4H_8 濃度

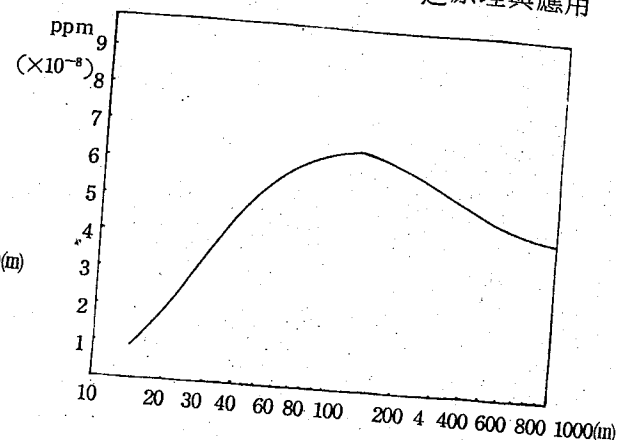

圖二十　同圖二十四唯係ALD 濃度。約在 120 m處產生最大值

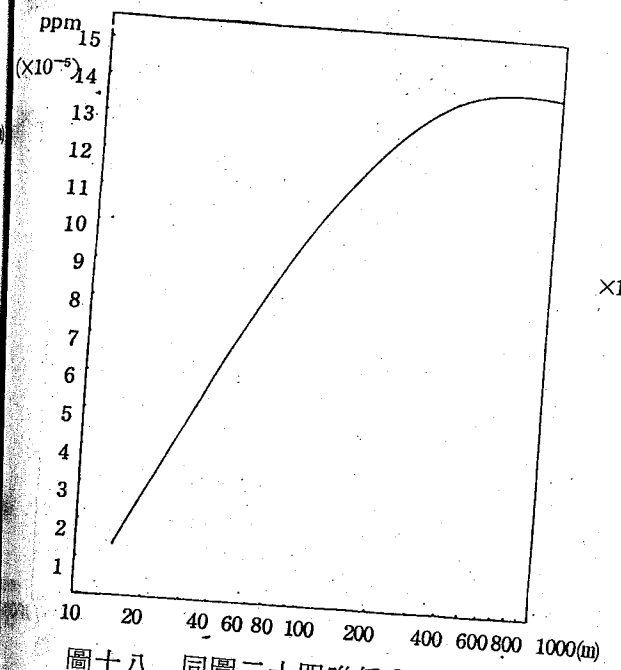

圖十八　同圖二十四唯係O_3 濃度，約在 650 m處產生最大值。

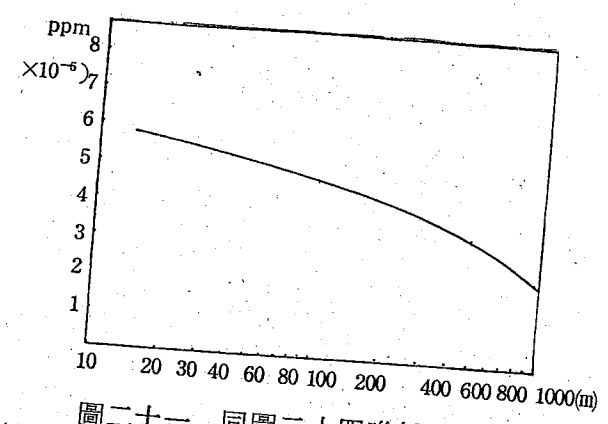

圖二十一　同圖二十四唯係RCO_X 濃度

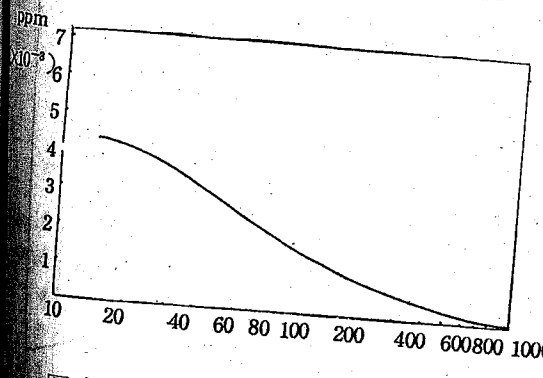

圖十九　同圖二十四唯係NO_2 濃度。採樣值與計算值間差約在12%之內。

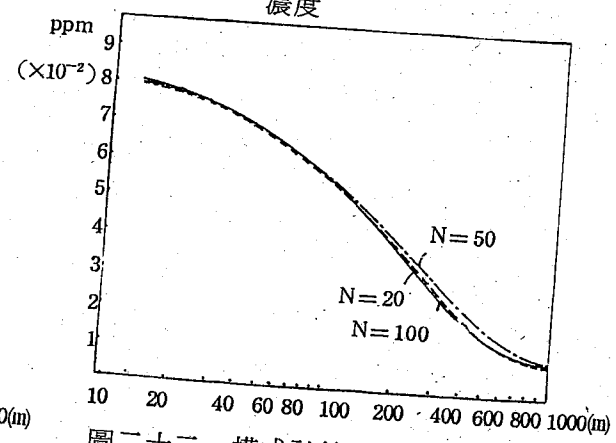

圖二十二　模式計算個案第三組情況下NO 濃度隨距離變化的情形。採樣點和計算點在層區間分 100 格時非常接近。N表層區間分格數。

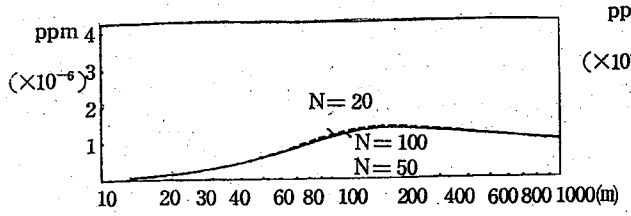

圖二十三　同圖三十一唯係ALD 濃度，約在 180 m處發生最大值。

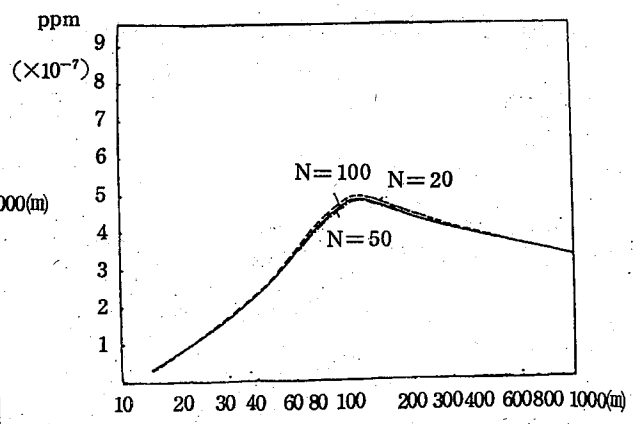

圖二十六　同圖三十一唯係PAN 濃度。約在 110 ～ 120 m附近產生最大值。N＝20者最大濃度處附近較其他二者略高。

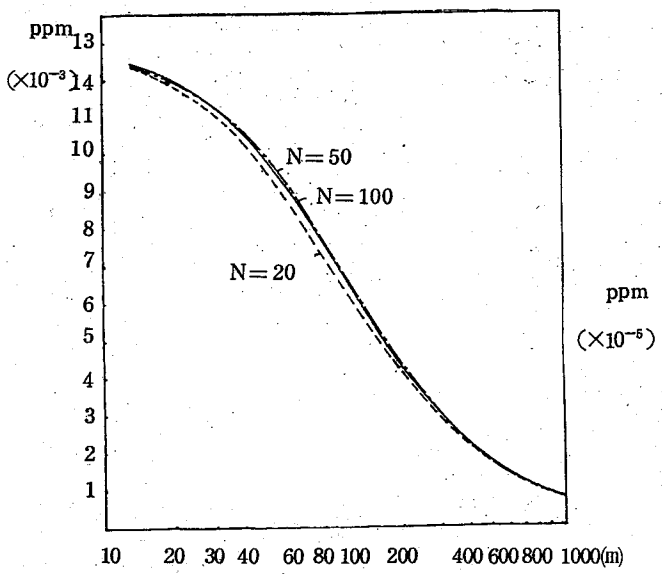

圖二十四　同圖三十一唯係NO 濃度。N＝20者較其他二者計算濃度值較小。

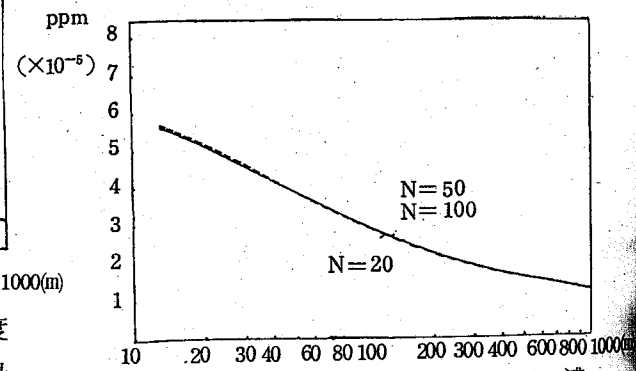

圖二十七　同圖三十一唯係RCOx 濃度。三者計算值相近。

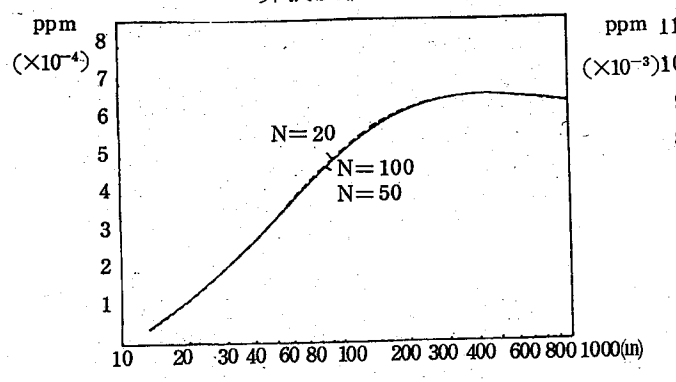

圖二十五　同圖三十一唯係 O_3 濃度。最大濃度值約在 400 m處。N＝50和 100 計算出濃度相差極微。虛線爲N＝20者計算之濃度。

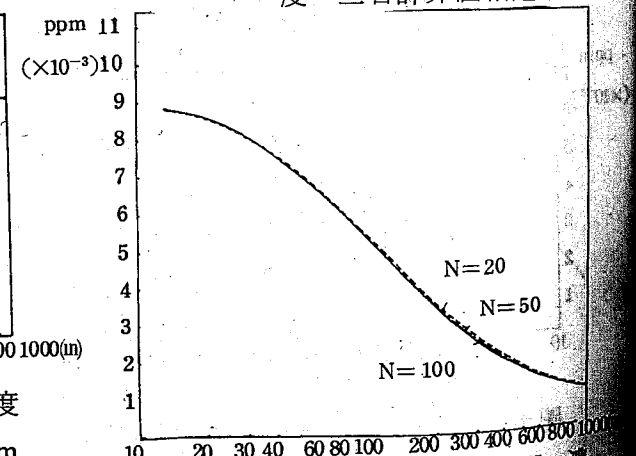

圖二十八　同圖三十一唯係 C_4H_8 濃度。N＝50和N＝100計算值極相近，在 150 m至 600 m間才稍有區別。

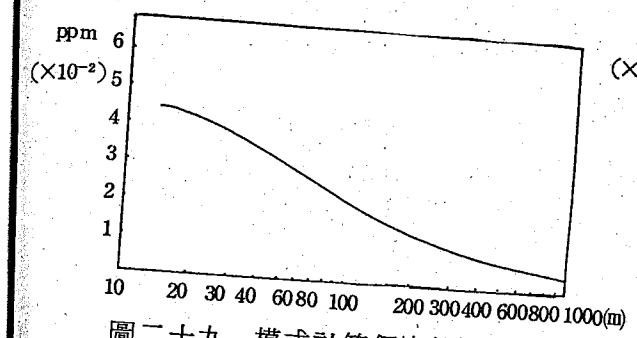

圖二十九　模式計算個案第四組情況下NO 濃度隨距離變化的情形。

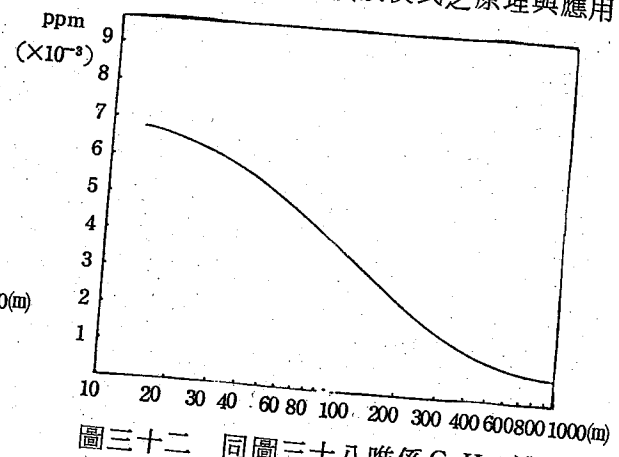

圖三十二　同圖三十八唯係 C_4H_8 濃度。

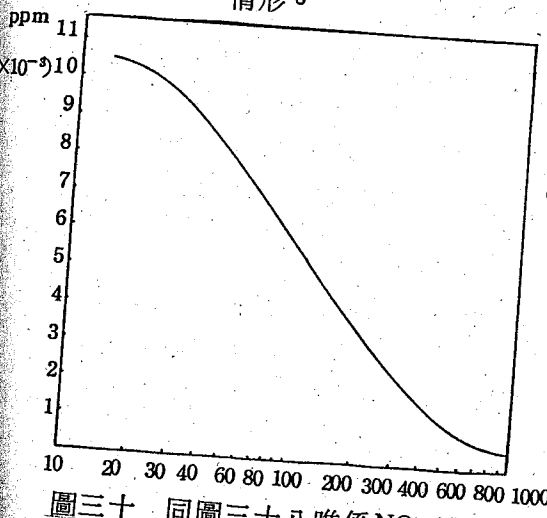

圖三十　同圖三十八唯係 NO_2 濃度

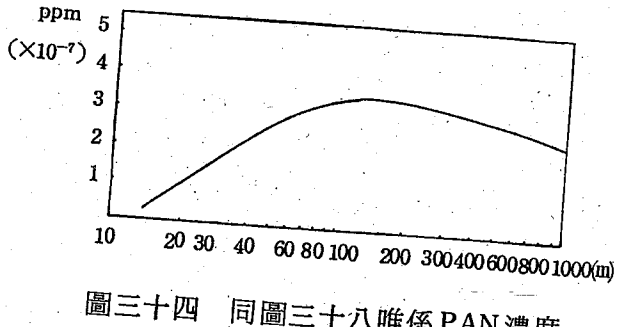

圖三十四　同圖三十八唯係PAN濃度

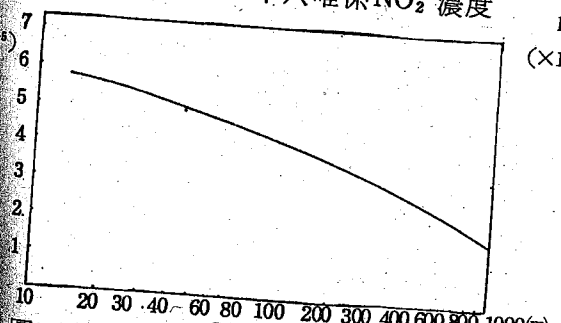

圖三十一　同圖三十八唯係 RCO_X 濃度。

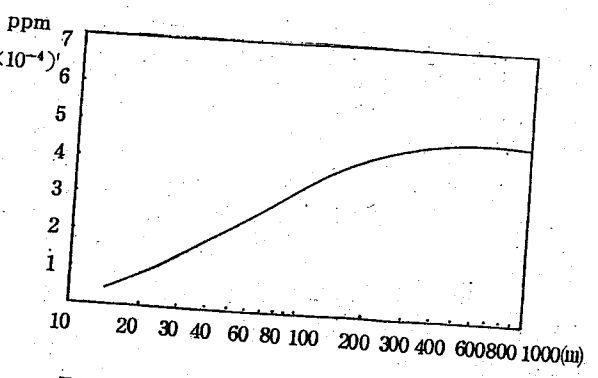

圖三十五　同圖三十八唯係 O_3 濃度

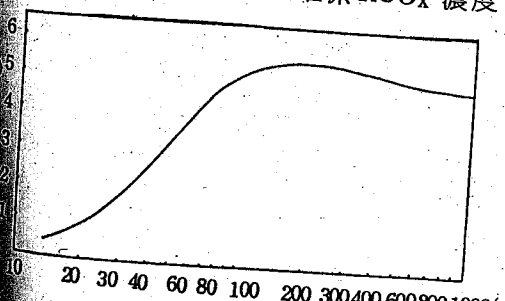

圖三十三　同圖三十八唯係ALD濃度

大氣自界層風洞之規劃與設計研究

大氣物理及流體力學組同仁

摘　要

本研究計劃之目的在研究大氣邊界層的紊流現象以風洞流體實驗可行性之探討，並進行規劃與設計研究。歐美國爲同等目的設計之風洞包括，美國克羅拉多州立大學流體與擴散實驗室（ FDDL ）之氣象風洞（ Meteorological Wind Tunnel ）與環境風洞（ Environmental Wind Tunnel ）。美國環境保護署（ EPA ）風洞實驗室之環境風洞，加拿大西溫特里（ Western Ontario ）大學之邊界層風洞實驗室設備。另外日本筑波科學園區亦設有同類型之風洞設備二～三組（分屬於日本國立公害研究所及產業資源研究所）。該類型風洞設備之主要特徵爲風洞試驗段的長度約爲其截面尺度的10～20倍，用以維持穩定之紊流邊界層，使得風洞內之紊流邊界層完全相似於大氣邊界層中近地之慣性次層（該慣性次層之氣象學俗名爲大氣近地層）。另外之特徵爲風洞內設置熱交換器，以維持垂直方向密度層變之流體。

中研院物理所籌建中之風洞主要之實驗問題包括：

(1)大氣近地層風力對建築結構物影響之研究，以配合國科會防災科技研究。

(2)複雜地形地物之紊流擴散現象研究。

(3)受小尺度地形影響之氣流現象研究。

(4)雷諾數與福祿數（或李查遜數）變化條件下之基本紊流現象研究。

爲達到上述主要之研究問題特徵之要求，籌建中之風洞之試驗段長60英呎（ 18.5 公尺），寬10英呎（ 3.048 公尺），高 7 英呎（ 2.13 公尺）。另外試驗段之高度可以變化，以調整流軸向壓力梯度。風洞之基本結構爲開放吸入式風洞，進口收縮比爲 4 ： 1 。試驗段內風速變化範圍爲 3～65英呎／秒（ 1～20m／sec ）。動力系統採用直流變速 200Hp馬達，帶動十六槳軸流式風扇（ axial fan ）。在試驗段內設置三個實驗轉盤，以配合不同之實驗問題。而試驗段之主要建造材料爲夾板，以便因應將來實驗之須求而變更。

壹、前　言

人類大部份之起居活動皆發生於地表附近，因此受近地表數百公尺高度以下之大氣流場强烈之影響。此流場可稱之爲大氣邊界層，乃是地表與高空大氣作動量，熱量和質量交換的主要場所。人類生活環境之品質與此大氣邊界層之特性有密不可分之關係，其中尤其以(1)建築物及結構之風力負荷及抗風設計，(2)大氣擴散之質量輸送及污染控制，(3)風能之利用，(4)局部區域性風場研究與風力行爲管制，四者與邊界層各個因子變化有直接之關聯。Cermak〔1〕指出此類問題之研究必須綜合流體力學，空氣動力學，氣象學，結構學之知識，而可稱之爲風力工程學（Wind Engineering）。在美國，The Office of Emergency Preparedness〔2〕之報告指出，過去50年來由於風災造成之經濟損失，每年平均約1億美元。Sander〔3〕估計於1963～1970年之間，暴風現象使年平均損失超過5億美元，並導致1667人死亡，18,285人受傷。在台灣每年夏季颱風襲擊，威力之强大，對建設、農作物破壞之嚴重，亦使人談颱變色。但台灣地區人口日增，其分佈亦日廣，將來向空中及風力條件不適合居住之環境發展，乃是必然之趨向。故風災損失之統計數字預計仍然會繼續增加。

今日，由於新建材之使用及新設計觀念之進步，得以造出更高、更龐大、重量更輕之建築物。但却使其機械阻尼（mechanical damping）不易平衡所承受之風力負荷。加上玻璃之廣泛使用，建築物之抗風設計不僅要考慮避免結構上之全盤性破壞，亦要減少脆弱部份之局部性損害。相同地，大氣層調整生態環境之能力已不足以應付人類產生之空氣污染。因此研究風力輸送現像使污染物集中度合乎人類生存之標準，亦是刻不容緩之工作。風力能源之利用是近年來替代能源開發之重點。唯有了解風場之特性才能作最有效地廠址選擇及效益評估。此外，局部區域性之風力行爲控制對於機場飛機之飛行安全，行人所受之風力擾動，社區之通風等問題非常重要。適當設計之風力行爲控制設備，積極地安排建築物位置及防風林，皆可使這些不利之條件獲得合理之改善。

研究風力工程學可利用三種方法，(1)流體力學之理論解析及數學模擬，(2)現場之實際測計，(3)實驗室內之風洞模擬。然而Corrsin〔4〕推測要解隨機起始條件（random initial conditions）之芮維爾－史脫克（Navier-Stokes）方程式，大約需要10^{18}位元（bit）之電腦記憶容量。因此即使是最新之電腦，其記憶體容量及速度仍不足以記錄紊流流場所產生大數量之渦漩（eddies）特徵。因此數學模擬僅能提供定性之參考。大氣邊界層之實際測計，無論在人力、物力，及時間上皆耗費甚大，有緩不濟急之勢，故最有效之法乃採用大氣風洞模擬實驗。且因風洞實驗流場可複製（reproductivity），控制性良好，故Houghton and Carruthers〔5〕，Davenport〔6〕，Cermak〔7〕等皆建議應用大氣風洞實驗模擬風力影響爲風力工程研究不可或缺之方法。

利用風洞研究流體力學之基本現象雖然非常普遍，然而國內已往所使用者大都屬於航空研究用風洞。其試驗段流場爲層流型態（laminar flow）且平均速度和溫度相當均勻。爲避免側壁邊界層之增厚，或形成紊流邊界層，故其試驗段長度與截面特徵寬度之比通常爲1～5，其模型尺寸不大，故試驗段截面亦相當小。而大氣邊界層風洞則不然，爲要實際模擬大氣近地層（surface layer）之高雷諾數（Reynolds number，超過10^7以上）剪力流場（shear flow），容納大面積之地形地物模型，故其試驗段截面積須較大。且試驗段長度與截面特徵寬度之比通常爲10～15，以維持紊流邊界層之發展及模擬上游地面邊界條件之相似性。因此，一般航空用之風洞特徵上和大氣邊界層風洞有極大之分野，也無法用來研究風力工程之問題。環顧國內已有之風洞設備，皆屬於航空或教學用風洞。中央研究院物理研究所流體力學組籌造大氣邊界層風洞之目的，即彌補國內在此方面研究之空白。本研究計劃即針對風洞實驗室之設立進行規劃與設計研究。

貳、理論根據

1 大氣邊界層之特性：

地球表面接受太陽輻射量的不一致造成壓力不平衡乃是形成風之基本原因。此外，由於地球的自轉，雲層之覆蓋，雨水之凝結，地表溫度及粗糙度之差異，地形變化等非線性因素和大氣流場之交互作用，使風之特性變化莫測。因此只能利用紊流統計法來描述風場現象。一般而言，由地表至1000公尺高度之間的大氣運動是屬於紊流邊界層型態，而稱之爲行星邊界層（planetary boundary layer）。山岳或丘陵背面流場的分離，颱風，狂飆（hurricanes）及龍捲風都有可能破壞此種邊界層結構。而在500公尺高度以上時，表面阻力（surface drag force）對空氣流之影響可忽略，且流場壓力梯度和地球自轉科氏力（Coriolis force）幾乎平衡，風向平行於等壓線（isobars），此時稱之爲地轉風（geostrophic wind）而自地表到500公尺高度之流場，Cermak〔8〕稱爲大氣邊界層。而由地表至150公尺高度之間大氣，其紊流動量、熱量及質量之傳遞速率隨地表之特性而不同，稱之爲大氣近地層。大部份風力工程問題皆發生於大氣近地層，故模擬此層之種種現象，即是大氣邊界層風洞之主要目的。Lettau〔9〕認爲行星邊界層之運動方程式可寫成

$$f(V-V_g)-\frac{\partial}{\partial z}<u'W'>=0 \tag{2.1}$$

$$f(U_g-U)-\frac{\partial}{\partial z}<v'W'>=0 \tag{2.2}$$

利用渦漩黏滯係數（eddy viscosity）K_M可將雷諾應力和平均速度表成：

$$<u'W'>=-K_M\frac{\partial U}{\partial z} \tag{2.3}$$

$$<v'W'>=-K_M\frac{\partial V}{\partial z} \tag{2.4}$$

而利用尺度長度（scale length）L_M 及混和長度（mixing length）可將 K_M 寫成

$$K_M = \ell^2(z)\left[\left(\frac{\partial U}{\partial z}\right)^2+\left(\frac{\partial V}{\partial z}\right)^2\right]^{1/2} \tag{2.5}$$

$$\frac{\ell(z)}{L_M} = \frac{0.4\,z/L_M}{1+4\,(z/L_M)^{5/4}} \tag{2.6}$$

$$\text{而 } L_M = 0.0736\,u_*/f \tag{2.7}$$

由此可獲得兩個無因次函數

$$U/u_* = F_1(fz/u_*,\ U_g/fz_0) \tag{2.8}$$

$$V/u_* = F_2(fz/u_*,\ U_g/fz_0) \tag{2.9}$$

此時 f 爲科氏參數（Coriolis Parameter）

V 爲 y 方向之平均速度，v′爲 y 方向速度變動（velocity fluctuation）

U 爲 x 方向之平均速度，u′爲 y 方向速度變動

$(\ )_g$ 爲在地轉風高度之值

u_* 爲摩擦速度（friction velocity）

z_0 爲地面粗糙長度（Surface Roughness length）。

由此可看出羅士培數（Rossby number $R_0 = U_g/fz_0$）固定時，無因次速度 U/u_* 及 V/u_* 乃是無因次高度 fz/u_* 之函數。

風力工程學之應用範圍最主要分成兩部分，即溫度層變現像與嚴重影響風力效應之邊界層區域。當考慮風力對建築物的影響效應時，最重要乃是獲得强風狀態下之邊界層特性。此時强風會加强流場混和之效果，而摧毀溫度層變之現像。然而研究區域性空氣污染或都市地區大氣質量輸送問題，則需要微風邊界層之資料。此時近地層之溫度層變會影響紊流場之混和作用。

强風狀態下之邊界層平均風速之垂直分佈可用次方律（power law）來描述

$$U/U_g = (Z/Z_g)^{1/n} \tag{2.10}$$

Houghton and Carruthers〔5〕認爲 1/n 值和地表粗糙度 z_0 及採樣時所取平均時間之長短有關。

欲模擬大氣流場之行爲，則不僅其速度分佈，其陣風强度及頻率亦須顧及。因流場之紊流强度乃是使建築物發生動力移動（dynamic movement）及流場分離、再密合（re-attach）之決定因素。Fichtl and McVehil〔10〕顯示在李查遜數（Richardson number）爲零時，近地層之紊流動能頻譜有下列之關係式

$$\frac{n\,S(n)}{u_*^2} = \text{const.}\left(\frac{nz}{U(z)}\right)^{-2/3} \tag{2.11}$$

此時 n 爲頻率，S(n)爲縱軸向頻譜（longitudinal spectrum）由此可看出紊流强度與高度變化之關係。

在大氣近地層，Monin and Obukhov〔11〕認爲具有均勻粗糙度、溫度及熱通量之表面，利用流場統計法可推測平行此表面之平面具有平面同質性（planar-homogeneity）

。此時影響流場結構之因子爲流體密度 ρ，表面剪應力 τ_0，表面熱通量 H_0，穩定參數 g/T，及突出邊界層之高度 z。將這些變數之無因次組合可得到大氣近地層之速度、溫度及長度尺度。

摩擦速度 $u_* = (\tau_0/\rho)^{1/2}$

摩擦溫度（friction temperature）$T_* = -H_0/(\rho C_p K' u_*)$ (2.12)

Monin-Obukhov 長度 $L = -u_*^3/[(K'g/T)H_0/\rho C_p]$ (2.13)

此時 K′爲 Kármán 常數 (2.14)

C_p 爲常壓之比熱

g 爲重力加速度

T 爲平均溫度。

無因次之風剪應力（wind shear）$(K'z/u_*)(\partial U/\partial z)$ 和溫度梯度 $(z/T_*)(\partial T/\partial z)$ 可用 (z/L) 之函數來代表。

$$U(z)-U(z_{ref}) = \frac{u_*}{K}\left[\ell n(z/z_{ref})+B_u(z-z_{ref})/L\right] \tag{2.15}$$

$$T(z)-T(z_{ref}) = T_*\left[\ell n(z/z_{ref})+B_T(z-z_{ref})/L\right] \tag{2.16}$$

而垂直速度變動之標準差爲

$$\frac{<W'^2>^{1/2}}{u_*} = \phi_1(z/L) \tag{2.17}$$

此時 B_U，B_T 皆爲成層穩定度 Z/L 之函數。

當雷諾數非常大時，Kolmogorov〔12〕認爲速度黏滯係數 ν 和紊流能量消散率 ϵ 控制高波數（high-wave-number）之紊流頻譜。其相對之速度及長度尺度分別爲 $(\nu\epsilon)^{1/4}$ 及 $(\nu^3/\epsilon)^{1/4}$。此時一維（one-dimension）之長軸向頻譜應爲

$$[(u'^2)E_u(K)]/(\epsilon\nu^5)^{1/4} = \phi_2[K(\nu^3/\epsilon)^{1/4}] \tag{2.18}$$

K 爲波數

E_u 爲長軸向之能量頻譜

以上(2.10)式至(2.18)式，皆是比照風洞模擬流場與大氣邊界層特性之良好指標。爲達成這些相似性之要求，Hunt and Fernholz〔13〕，Nee, Szewczyk and Yang〔14〕，Snyder〔15〕與 Cermak〔8, 16〕等文討論不同性質的風力工程學問題須要考慮之風洞設計因素。

2 風洞模擬之相似律

應用風洞進行模擬之流體力學原理包括：(1)幾何相似性，(2)動力相似性，(3)熱力相似性，與(4)起始及邊界條件相似性。由無因次的流體力學基本方程式：

$$\frac{\partial U_i^*}{\partial t^*}+U_j^*\frac{\partial U_i^*}{\partial X_j^*}+R_0^{-1}\,2\,\epsilon_{ijk}\Omega^* U^* = -\frac{\partial P^*}{\partial X_i^*}-R_1\theta^*\delta_{i3}+R_E^{-1}\frac{\partial^2 U_i^*}{\partial X_j^* \partial X_j^*} \tag{2.19}$$

$$\frac{\partial U_i^*}{\partial X_i^*} = 0 \tag{2.20}$$

$$\frac{\partial \theta^*}{\partial t^*}+U_j^*\frac{\partial \theta^*}{\partial X_j^*}=\frac{1}{P_r}\frac{1}{R_E}\frac{\partial^2\theta^*}{\partial X_j^*\partial X_j^*}+\frac{E_c}{R_E}\Phi^* \qquad (2.21)$$

$$R_o\ (\text{Rossby No.})=\frac{U_o}{\Omega_o L_o}$$

$$R_i\ (\text{Richardson No.})=g\frac{\triangle T_o\ L_o}{T_o\ \ U_o^2}$$

$$R_E\ (\text{Reynolds No.})=\frac{U_o L_o}{\nu}$$

$$P_r\ (\text{Prandtl No.})=\frac{\nu}{K/\rho_o C_p}$$

$$E_c\ (\text{Eckert No.})=\frac{U_o^2}{C_p\triangle T}$$

在上面無因次過程中

U_o ：流場之特徵速度尺度。
L_o/U_o ：流場特徵時間尺度。
ρU_o^2 ：流場之特徵壓力尺度。
L_o ：流場之特徵尺度。
$\triangle T_o$ ：流場之特徵溫度差。
g ：重力加速度。
Ω_o ：地球轉動座標之特徵角速度。
ν ：流體之運動黏滯係數。
K ：流體之導熱係數。
C_p ：空氣之定壓熱容。
Φ ：爲流體之焦耳加熱。

由方程式(2.19)～(2.21)可以看出，實際流場變化與風洞內之模擬流場之相似性要求爲：

(1)模型各方向之比例縮尺相同，滿足流體連續性。

(2)動力之相似性要求羅士培數、李查遜數、與雷諾數與實際流場情況相同。

(3)熱力之相似性要求普朗特數與艾卡數與實際流場情況相同。

在實際應用風洞進行模擬實驗時，上述之相似性要求不可能全部達到，因此設計實驗應依問題之特性，權衡輕重，考慮重要之相似性要求。Snyder〔15〕主張在嚴格要求下，如果應用非旋轉風洞模擬大氣邊界層現象時，模擬對象之水平尺度不可超過5公里。在這種情況下，羅士培數$R_o>10$，科氏力的效應可不予考慮。Cermak等〔17〕在較鬆的條件下，主張水平尺度小於150公里之大氣邊界層現象可以不考慮科氏力的效應。另外大氣邊界層屬於密度層變之流體(density stratified flow)，其特徵李查遜數在正負1之間，代表成層穩定或成層不穩定之流動狀態。因此浮揚力(buoyancy force)在大氣邊界層現象有其絕對之重要性。但是在研究防風問題時，主要之興趣對

象爲強風情況下地形或建築結構物與流體之交互作用，此時李查遜數趨近於零，故可應用一般之環境風洞(無加溫裝置)來模擬流體現象〔7〕。對於熱力相似性的要求，如果風洞內之空氣接近常溫與大氣壓，則普朗特數與實際大氣現象相同。另外艾卡數代表流體黏滯力之摩擦加熱作用。在低次音速流動情況下，這種黏滯力之焦耳加熱作用可以忽略〔1，7〕。

綜合上述對於流體模擬實驗相似性的要求，我們尚未討論雷諾數相似性的要求。一般言之，大氣邊界層之特徵雷諾數高達10^8以上，因此要求風洞內之雷諾數與實際情況相同幾無可能。所幸，目前對紊流現象之瞭解，紊流在高雷諾數具有雷諾數相似性之特徵(Reynolds number similarity)〔18〕，亦即當雷諾數超過某臨界值時，紊流結構之特徵不受雷諾數大小的影響。依照Kolmogorov的理論，當雷諾數夠大時，紊流頻譜(power spectrum)即有慣性次階(inertial subrange)的特徵出現，因此紊流的無因次頻譜(以Kolmogorov之紊流微尺度參數來常化)呈相似性。由很多的實驗數據顯示〔1，19〕。風洞內紊流邊界層之頻譜經常化後與實際大氣邊界層之紊流頻譜呈完全之相似性。而一般風洞內的雷諾數約比實際大氣邊界層之雷諾數要小二個數量級以上。這個事實說明，當風洞內之雷諾數達到臨界值以上時，大氣邊界層內的紊流結構可以應用環境風洞進行模擬。紊流結構的相似性，對於研究紊流振動對於結構物的影響具有重大的關係。另外研究紊流擴現像時亦須紊流頻譜之相似〔20〕。

由實驗結果〔8，15〕等顯示，風洞內的臨界雷諾數約爲10^4左右，這個條件決定風洞的模型縮尺比例，紊流邊界層的厚度與風洞試驗段的長度。

由上述雷諾數所影響的紊流邊界層特性，我們可以決定風洞內模型的縮尺比例，即

$$\frac{(R_E)_P}{(R_E)_M}\leq 10^4$$

可以得到 (2.22)

$$U_M L_M \geq 10^{-4} U_P L_P \qquad (2.23)$$

$(R_E)_P$ ：實體之雷諾數。
$(R_E)_M$ ：模型之雷諾數。
U_P ：實際情況之流速。
L_P ：實際情況之尺度。
U_M ：風洞內之流速。
L_M ：風洞內模型之尺度。

在應用(2.21)與(2.22)式時，假設風洞內模型屬於空氣動力之鈍型物(Bluff Body)，否則模型表面之滯性次層(viscous sublayer)受雷諾數的影響很大。

模型實驗之初始與邊界條件相似性要求迫近流易(approaching flow)與實際狀態相似。亦即

(1)迫近流場之平均流速分佈呈指數率分佈(logrithmic wind profile)。

(2)迫近流場內雷諾應力(Reynolds stress)與紊流動能分佈與大氣邊界層相似。

⑶迫近流場內之動能頻譜（ Power spectrum ）與實際狀態相似。

爲達到上述模擬的條件，風洞試驗段須有足夠的長度及適當的表面粗糙度（ Surface roughness ），以維持穩定之紊流邊界層。

參、大氣環境風洞基本設計

設計考慮因素：

環境風洞設備之主要實驗目的包括：

⑴大氣紊流邊界層之模擬。

⑵風力對於建築結構物的影響。

⑶大氣紊流邊界層之擴散現象。

⑷複雜地形對氣流之影響，風力能源開發之研究。

基於上述實驗目的考慮，環境風洞之基本特性爲發生（ generation ）及維持一穩定之紊流邊界層。爲達到上述的，風洞各項特性的決定，分述如后：

1. 風洞試驗段高度與寬度的決定：

由於試驗段高度影響模擬之紊流邊界層厚度。一般研究風力對於建築結構物之影響時，實體之高度約爲 100 ～ 200 公尺，如果模型之縮尺爲 1/200 ～ 1/500 ，風速的縮尺爲$\frac{1}{2}\sim\frac{1}{3}$，則風洞內模型之特徵雷諾數可以超過 10^5。在這種狀況下，風洞內求出之風阻係數（ $C_f=\triangle P/\frac{1}{2}\rho U^2$ ）較不受雷諾數大小的影響（ Reynolds number independency ）。故試驗風力對建築結構物之影響時，風洞內紊流邊界層之厚度須在 100 公分以上，而試驗段的高度須超過 150 公分以上。

試驗段寬度的決定，主要考慮模型放置於風洞內之阻檔效應（ Blockage effect ），及側壁邊界層的影響。一般風洞模擬實驗的指標原則爲模型面積之阻檔率（Blockage ratio ）以不超過 10 % 爲原則。另外試驗段的寬度亦影響試驗轉盤（ turntable ）的直徑。相對於模型之不同方向之迫近氣流（ approaching flow ），可以轉動試驗轉盤觀測模型物下游流場的變化。基於上述的考慮及各種可能的實驗狀況，環境風洞試驗段的高度決定爲 7 英呎（ 2133.6 mm ），寬度爲 10 英呎（ 3048 mm ）。

2. 試驗段長度的決定：

試驗段的長度爲影響紊流邊界層厚度與穩定性的主要因素。根據 Cermak 等人〔17〕，與 Counihan〔 21 〕的實驗研究，風洞內紊流邊界層可以由自然成長的方式或應用人工紊流發生器（ Vortex generator ）方式，模擬相似於大氣近地邊界層的流場（ Atmospheric surface boundary layer ）。於風洞底面加置粗糙元素之自然成長之紊流邊界層厚度在下游 10 公尺處約爲 50 公分以上。以渦流發生器置於試驗段入口，並於底面加置粗糙元素之紊流邊界層可達 100 公分以上，唯人工形成之邊界層約須 6 ～ 8 倍之邊界層厚度之下游距離形成穩定之邊界層（ Pertaka and Cermak ，〔 22 〕）。從風洞之實驗目的探討，一般紊流擴散實驗之模型比例縮尺以 1/500 ～ 1/1000 爲宜，

故風洞內模擬之邊界層厚度在 50 公分以上即可達到目的，但擴散實驗需要較長之下游距離，故以紊流擴散實驗實驗考慮風洞試驗段的長度以 10 ～ 15 公尺爲宜。一般風力對建築結構物影響的實驗，模型比例縮尺約爲 1/200 左右 ，以增高模型之雷諾數（ 10^5 ～ 10^6 ）。

在這種情況下，風洞內紊流邊界層的厚度約須 100 ～ 150 公分，須要 15 公尺以上長度的試驗段來維持穩定的邊界層，綜合以上的考慮，另外爲增加風洞實驗目的的多元性，決定風洞試驗段的長度爲 18.5 公尺（ 60.7 英呎 ）。

3. 風洞之動力與循環系：

一般低速風洞之動力與循環系有兩種型態：

㈠閉路循環系（ closed-circuit type ），㈡開放式風洞（ open-circuit type ）（ Pope and Harper ，〔 23 〕）。一般而言，閉路循環式風洞，能量效率高，但初始建造費用高。另外應用風洞進行紊流擴散現象模擬時皆須採用追踪劑（ tracer gas ）的技術來分析擴散現象，因此閉路式的風洞會累積追踪劑的濃度，引起實驗技術的困難。從初始造價與實驗目的考慮決定中研院物理所之大氣環境風洞爲開放式風洞（ open-circuit type wind tunnel ）。開放式風洞，因動力風扇（ fan ）與試驗段相對位置可分成㈠吸入式風洞（ suction type wind tunnel ）與㈡吹送式風洞（ blowing type wind tunnel ）。吹送式之風洞，風扇置於試驗段的上游，風扇的作用爲風洞管路之增壓站，整個試驗段之空氣之靜壓與大氣壓相同，故試驗段氣密（ air tight ）的問題不須考慮。但是風扇運動產生之螺狀渦流不易控制，影響試驗段氣流的均勻與穩定性。相反吸入式風洞之試驗段須有良好的氣密性，但風扇葉片的尾流作用可以不必控制。以吸入式安排之風洞，其整流段可以簡化（相對於吹送式）。總體考慮結果，中研院物理所風洞決定爲單向吸入式風洞（ open-circuit suction type ），整個風洞分爲三個單元，㈠進口整流收縮段，㈡試驗段，㈢風扇動力段。其空氣動力設計容後再述。

4. 風洞試驗段風速範圍之決定：

研究局部小地形或建築結構物對氣流之影響（或交互作用）時，風洞內主要量度的參數爲壓差係數 C_P，

$$C_P=\frac{\triangle P}{\frac{1}{2}\rho U_0^2} \qquad (3.1)$$

對於一般空氣動力鈍形物，壓差係數在雷諾數超過 10^4 時，趨近常數值，其值不隨著雷諾數的增大而變化。以 1/200 縮尺的模型，在風洞內的尺寸大約爲 50 ～ 100 公分 ，因此當風洞內的平均流速超過 2 m/ sec 時，模型的雷諾數即可超過 10^4 之臨界值。但在這種風速情況下，流場之靜壓差值約爲 10^{-1} 毫米水柱高 ，量度十分困難，一般之壓力感應器（ pressure transducer ）亦會受到風扇或周界噪音的影響，增高感應器的噪訊比（ noise to signal ratio ）。因此在量度壓差係數 C_P 時，爲降低噪訊比，風洞內操作風速 U_0 須提高至 10 ～ 15 m / sec 以上（ Personal communication with Prof. J.E.Cermak ）。爲了這個目的風洞設計之最大風速定爲每秒 20 公尺。〔註〕

另一方面爲了將來風洞從事密度變流（ density stratified flow ）現象之研究，例如熱噴流（ thermal plume ）現象，爲了維持福祿數（ Froude number ）或李查遜數的相似性，必須降低風洞試驗段內之風速至 1 ～ 2 m／sec 。基於上述二種考慮，風洞試驗段內之平均風速設計爲 1 ～ 20m／ sec ，連續可調整形式。

5. 試驗段流向靜壓差調整：

大氣邊界層流場，其於壓力梯度力主要由科氏力所平衡，沿風向的壓力梯度遠小於 10^{-4} dyne／cm^3 。反之，在風洞試驗段內，由於摩擦損耗，壓力梯度可達 10^{-1} dyne／cm^3 以上。更有甚者，由於模型引起流向截面積的改變，造成之壓差影響模擬相似性。由於上述的考慮，環境風洞之試驗段內須具備流向靜壓差調整裝置。規劃中之環境風洞試驗段之上壁可以調整其高度，其範圍爲 200 公分至 250 公分。

〔註〕：試驗段內之噪音強度以 80 分貝估計，產生之空氣壓力變差值爲 ± 2 dyne／cm^2 ，如氣流靜壓變化提升至 ± 100 dyne／cm^2 則噪訊比可降至 1／100 以下，此時風洞試驗段內之操作風速須提升至 15 ～ 20 m／ sec 。

肆、大氣環境風洞之進口整流設計

1. 風洞試驗段進口紊流強度控制：

吸入式風洞，空氣經由進口段內之紊流控制組合，包括蜂巢孔與整流細網，使紊流的強度降低，再經收縮段，可使流速均勻。下面討論蜂巢孔、整流細網與收縮段對於風洞內紊流強度的控制作用。

(1)蜂巢孔（ honey-cone ）的作用

一般蜂巢孔的管徑約爲數公分到十公分左右，因此其特徵雷諾數約爲數千以上（約爲 10^4 以上），經過蜂巢孔的氣流會以紊流的形態發生，唯其紊流的尺度約與蜂巢大小相當。且在蜂巢孔後的紊流接近等向性紊流（ isotropic turbuleuce ）。對於等向性紊流消散作用（ dissipation ）的理論可以根據 Taylor 之預測〔 24 〕：

$$\frac{U}{u'}=\frac{5x}{A^2M}+B \tag{4.1}$$

U：代表通過蜂巢孔之平均流速。

u′：代表紊流之平均異差值（ rms value ）。

M：代表蜂巢孔之尺寸。

x：代表離開蜂巢孔之下游距離。

A：爲一萬有常數（ universal constant ）。

B：常數，隨蜂巢孔之幾何形狀而異。

由英國 NPL（ National Physical Lab. ）Simmons 與 Salter 氏之實驗數據，孔徑在一英吋左右之蜂巢孔後之等向性紊流強度之變化可依據下式計算。

$$\frac{U}{u'}\doteq 1.30\frac{x}{M}+5.5 \tag{4.2}$$

(2)整流細網的作用

依據 Schubaner, Spangenberg 與 Klenbanoff 〔 25 〕等之研究，整流細網之特徵雷諾數須維持在 40 以下，$\frac{Ud}{\nu}<40$ 。通過整流細網後之紊流與前述之等向性紊流不同。整流細網後之紊流已屬於流體黏滯力直接作用之紊流（ turbulence in dissipation range ）。由 Dryden 與 Abbott 〔 26 〕之實驗數據，通過整流細網前後之紊流強度可以應用下式估計：

$$\left(\frac{u'}{U}\right)_{\substack{\text{with}\\ \text{screen}}}=\frac{1}{(1+k_s)^{n/2}}\left(\frac{u'}{U}\right)_{\substack{\text{without}\\ \text{screen}}} \tag{4.3}$$

n：整流細網的層數

$k_s=\triangle P / \frac{1}{2}\rho U^2$ ，爲整流細網的壓降係數。

ρ：空氣密度

$\triangle P$：通過細網前後之靜壓差。

一般設計之經驗建議風洞內的整流細網的壓降係數須避免採用超過 3 之細網。由於織網的不均勻的影響，太密的細網會使得風洞內平均流的均勻性破壞。故一般設計時採用 k_s 值較小之網，而抑制紊流的效果，可由多層細網來增强它的整流作用。

(3)收縮段對於紊流的抑制作用

收縮段對於不同方向之紊流渦旋會產生不同的作用。在估計收縮段的作用時，我們假設進入收縮段時之紊流屬於等向性紊流。如果 C 代表收縮段前後之截面積比，則沿流方向（ streamwise ）的紊流因渦度的擠壓作用（ vortex shrinking effect ）會減弱 C 倍，另外橫向（ transverse ）的紊流因渦度的抽拉作用（ vortex stretching effect ）增强$\sqrt{C}$倍（ Tennekes and Lumley ，〔 27 〕）。以公式表示

$$\frac{u'_{t_2}}{u'_{t_1}}=\sqrt{C} \tag{4.4}$$

$$\frac{u'_{l_2}}{u'_{l_1}}=\frac{1}{C} \tag{4.5}$$

u'_l ：streamwise 方向之紊流强度。

u'_t ：transverse 方向之紊流强度。

1 ：代表收縮段前之位置。

2 ：代表收縮段之位置。

則經過收縮段後之紊流強度可以導出爲

$$\frac{2u'^2_{t_2}+u'^2_{l_2}}{U_2^2}=\frac{2Cu'^2_{t_1}+\frac{1}{C^2}u'^2_{l_1}}{C^2U_1^2} \tag{4.6}$$

由 $u'^2_2=2u'^2_{t_2}+u'^2_{l_2}$ (4.7)

$u'^2_1=2u'^2_{t_1}+u'^2_{l_1}$ (4.8)

則 $\frac{u_2'}{U_2} = \sqrt{\frac{1}{3}\left(\frac{2}{c}+\frac{1}{c^4}\right)}\frac{u_1'}{U_1}$ (4.9)

應用(4.9)式估計收縮段對紊流強度作用時，並未考慮流體黏滯力之消散作用。

2 大氣環境風洞試驗段進口之紊流強度估計

(1)蜂巢孔設計規格

爲避免產生通過蜂巢孔後之大尺度渦流；蜂巢孔的長度與其直徑之比約須六倍至八倍（Bradshaw and Pankhurst，〔28〕）。籌建中風洞之進口因置於戶外，爲避免激流（surge flow）的發生，蜂巢孔（或蜂巢管）的長度與直徑比定爲10。

- 材料：PVC管。
- 直徑3公分，管壁厚度0.2公分，管長30公分。

(2)整流細網設計規格

- 材料：不銹鋼細絲。
- 網織：每英吋18方格織。
- 網絲直徑：0.011英吋。

(3)進口整流段收縮比，4：1。

應用前述之理論估計方法及蜂巢管，整流細網及收縮比之規格，籌建中風洞之紊流強度估計值列於下表。

試驗段風速 (m/s)	1.0	5.0	10.0	15.0	20.0	說明
進口段風速 (m/s)	0.25	1.25	2.5	3.75	5.0	
細網雷諾數	4.36	21.8	43.6	65.5	87.3	
k_s值	1.3	1.2	1.1	1.0	0.9	
蜂巢孔後紊流	5.4 %	5.4 %	5.4 %	5.4 %	5.4 %	下游30公分處
四層細網後紊流	1.02 %	1.12 %	1.22 %	1.35 %	1.49 %	
試驗段紊流	0.42 %	0.46 %	0.50 %	0.55 %	0.61 %	

註：k_s值參照Pope及Harper〔23〕。

伍、大氣環境風洞之規格與構造

㈠風洞整體構造說明：

大氣環境風洞爲一開放吸入式之風洞（open-circuit suction type）。其結構體包括進口整流段，收縮段，試驗段，與動力段，及風洞本體之支架。風洞本體之佈置，參閱圖一、圖二與圖三。風洞各段的內容說明如下：

1 進口整流段：內容包括

(a) Inlet Bell。

(b)蜂巢管及蜂巢管固定鐵絲網。

(c)四層整流細網。

(d)整流網與蜂巢管之清潔孔，該孔可以容許長柄吸塵器伸進蜂巢與細網內部進行維護清潔工作。

2 收縮段：

收縮段連結進口段與試驗段。該段斜面之彎輻主要以二個三次方程式曲線相接而成。在板金設計時須避免斜率的轉折點。

3 試驗段：

試驗段主要爲夾板結構構成，其上壁可以調整其高度位置，使得氣流通過試驗段時稍呈發散（divergent），以動壓彌補靜壓之摩擦損失，維持試驗段內流向之壓力梯度爲零的狀況（實際上壓力梯度小於 10^{-3} dyne/cm^3）。該上壁調整裝置的設計可參閱圖四。

試驗段內部設置感應器之三度空間活動機構，該儀器支架的位置可由風洞外之儀表遙控其位置。儀器支架調整位置的準確度小於2～3 mm。

另外試驗段內部亦考慮照明，實驗轉盤及照相孔的設計。

4 動力段：

動力段主要包括：

(1)動力段進口收縮管，承接試驗段長方形出口至風扇之圓形進口。

(2)風扇組合，內容包含風扇葉子轉子，軸承，整流片及傳動皮帶。

(3)風扇出口擴散管。

(4)動力段本體與動力馬達（置於風扇外側）之基座。

在動力段進口收縮管上設置人孔以備工作人員進入做風扇葉片調整工作。另外在上部設置照明設備。在設計動力段基座時考慮馬達及風扇振動的防止。動力段與風洞本體亦採分開結構之設計，附止振動之傳遞。

㈡風洞材料及尺寸規格：

1 進口整流段

對於蜂巢孔、整流細網、安全粗網及風扇葉片組之管流之壓降計算，則採用壓降係數之經驗公式

$$K=\frac{\triangle p}{\frac{1}{2}\rho u^2} \qquad (6.4)$$

在該式中 u 爲通過裝置之平均流速。

㈡最大壓降與風洞所需最大馬力計算：

由於摩擦與壓降損耗與風洞內，風速的平方成正比，故最大壓降與最大需要馬力可由風洞試驗段內最大風速情況估計。

(1)最大流量

$V_{max}=2.13\times3.048\times20\ m/sec$

$=129.8\ m^3/sec$

$=275.6\times10^3$ cubic feet per min.（CFM）

(2)空氣密度，ρ

在 25 °C，一大氣壓情況

$\rho=1.205\times10^{-3}\ gm/cm^3$

(3)空氣運動黏滯係數，ν（常溫，常壓狀態）。

$\nu=1.6\times10^{-5}\ m^2/sec$

(4)動壓（velocity pressure），P_v

①進口段　$u=5\ m/sec$

$P_v=150.6\ dyne/cm^2$

②收縮段

平均流速　$u=12.5\ m/sec$

$P_v=941.4\ dyne/cm^2$

③試驗段

平均流速　$u=20\ m/sec$

$P_v=2410\ dyne/cm^2$

③動力段之收縮管

平均流速　$u=36.4\ m/sec$

$P_v=7994\ dyne/cm^2$

(5)相當直徑，D_e

①進口段　$D_e=5.019\ m$

②收縮段　$D_e=4.1\ m$

③試驗段　$D_e=2.5\ m$

④動力段收縮管　$D_e=2.3\ m$

(6)摩擦係數，f

①進口段

$R_E=1.57\times10^6$

$\frac{\varepsilon}{D_e}=0.00001$　（commercial steel）relative roughness

$f=0.012$

②收縮段

$R_E=1.92\times10^6$

$\frac{\varepsilon}{D_e}=0.0001$　（commercial steel）

$f=0.01$

③試驗段

$R_E=3.1\times10^6$

$\frac{\varepsilon}{D_e}=0.005$　（木材與風洞內之粗糙元素）

$f=0.019$

④動力段收縮管

$R_E=4.0\times10^6$

$\frac{\varepsilon}{D_e}=0.00002$　（commerical steel）

$f=0.011$

(7)壓降係數，K

①蜂巢孔　$K=0.3$

②蜂巢孔前後之保護粗網　$K=0.2\times2=0.4$

③整流細網四層　$K=4\times0.9=3.6$

④安全網　$K=0.2$

⑤風扇組合　$K=0.075$　（由風扇原廠提供）。

(8)壓降，$\triangle p$

①進口段　$L=2\ m$，

$\triangle p=0.72\ dyne/cm^2$

②收縮段　$L=4\ m$，

$\triangle p=9.18\ dyne/cm^2$

③整流組合，包括蜂巢孔、細網與粗網

$\triangle p=647.6\ dyne/cm^2$

④試驗段　$L=18\ m$

$\triangle p=329.69\ dyne/cm^2$

⑤安全網

$\triangle p=482.0\ dyne/cm^2$

⑥風扇組合　$P_v=7994.8\ dyne/cm^2$

授 J: A. Peterka教授，及李文槐先生；對於風洞之特性規劃提供重要之建議。美國 Aerolab 公司陳兆梅博士，清華大學動力機械系巢慶成教授，台大機械系黃博治教授對於風洞動力段風扇與動力馬達之選擇亦提供寶貴之資料與建議。美國環境保護署（EPA），環境風洞實驗室Dr. W. H. Snyder 對於試驗段內儀器活動支架，及擴散實驗之儀器設備，提供了寶貴之規劃設計資料。中鼎工程公司設備設計部廖運焜經理及盧增輝先生對於風洞之結構及操作機構之設計，讓我們構想中之風洞變成可以施工製造之詳圖，尤其是盧增輝先生備極辛勞，對於風洞施工之每一步驟都詳細之檢查，確定其品質。我們都致以最大之敬意與謝意。中央研究院物理研究所所長林爾康先生對於風洞實驗室之設立，極力之支持與鼓勵，特此表示謝意。

參考資料

1. Cermak, J. E. 1975, "Applications of Fluid Mechanics to Wind Engineering - A Freeman Scholar Lecture" Trans. of the ASME, J. of Fluids Eng., Vol. 97, pp.9-38.
2. Disaster Preparedness, Report to the Congress, Office of Emergency Preparedness, U. S. Government Printing Office, 3 Vols., Jan. 1972.
3. Sander, F. 1971, "Toward Defining Human Needs: How Does the Atmosphere Hurt Us?" Bulletin of the American Meteorology Society, Vol. 52, pp.446-449.
4. Corrsin, S. 1961, "Turbulent Flow", Amer. Sci. 49, pp.300-325.
5. Houghton, E. L. and Carruther, N. B. 1976 "Wind Effects of Buildings and Structures", John Wiley & Sons, New York, p.243.
6. Davenport, A. G. 1967, "The Treatment of Wind Loading on Tall Buildings", Proc. of Symposium on Tall Buildings, Univ. of Southampton, Apr. 1966.
7. Cermak, J. E. 1976, "Aerodynamics of Buildings", Annual Review of Fluid Mechanics, Vol.8, pp.75-106.
8. Cermak, J. E. 1981, "Wind Tunnel Design, for Physical Modeling of Atmospheric Boundary Layers", J. of the Engineering Mechanics Division, ASCE, Vol. 107, No. EM3, pp.623-642.
9. Lettau, H. H. 1962, "Theoretical Wind Spirals in the Boundary Layer of a Barotropic Atmosphere", Beitr, Phys. Atmos., Vol. 35, pp.195-212.
10. Fichtl, G. H. and McVehil, G. F. 1970, "Longitudinal and Lateral Spectra of Turbulence in the Atmospheric Boundary Layer of the Kennedy Space Centor", J. Appl. Meteorol., 9, pp.51-63.
11. Monin, A. S. and Obukhov, A.M. 1954, "Basic Laws of Turbulent Mixing in the Ground Layer of the Atmosphere", Trudy Geofizs. Inst. An. SSSR, 2. No. 24, pp.163-187.
12. Kolmogorov, A. N. 1941, "The Local Structure of Turbulence in Incompressible Viscous Fluid for very Large Regnolds Number", Doklady AN SSSR, Vol. 30, No. 4, pp.299-303.
13. Hunt, J. C. R. and Fernholz, H. 1975, "Wind-Tunnel Simulation of the Atmospheric Boundary: A Report on Euromech 50", J. Fluid Mechanics., Vol. 70, Part 3, pp.543-559.
14. Nee, V. W., Szewczyk, A. A. and Yang, K.T. 1975, "Atmospheric Wind Tunnels - A Survey", ND-TR-WT-1, Oct., Univ. of Notre Dame ID.
15. Snyder, W. H. 1972, "Similarity Criteria for the Application of Fluid Models to the Study of Air Pollution Meteorology", Boundary Layer Meteorolgy, 3, pp.113-134.
16. Cermak, J.E. 1971, "Laboratory Simulation of the Atmospheric Boundary Layer", AIAA Journal, Vol. 9, No. 9, pp.1746-1754.
17. Cermak, J. E., Sandborn, V. A., Plate, E. J., Binder, G. H., Chuang, H., Meroney, R. N., and Ito, S., 1966 "Simulation of Atmospheric Motion by Wind Tunnel Flow", Report to Army under Contract DA-AMC-28-043-G20, Colo. State University.
18. Townsend, A.A., 1956: "The Structure of Turbulent Shear Flow", Cambridge University Press, p.315.
19. Jensen, M., 1958: "The Model-Law for Phenomena in a Natural Wind", Ingenioren Int., Ed. 2, No. 4,
20. Pasquill, F., 1974: "Atmospheric Diffusion", Second Ed., Ellis Horwood Publisher, Chichestor, p.429.
21. Counihan, J., 1973: "Simulation of an Adiabatic Urban Boundary Layer in a Wind Tunnel", Atmos. Environment, Vol. 7, pp.673-689.
22. Peterka, J. A., and Cermak, J. E., 1974: "Simulation of Atmospheric Flows in Short Wind Tunnel Test Section", FDDL, CER73-74 JAP-JEC32, Colo. State University, p.52.
23. Pope, A., and Harper, J.J., 1966: "Low-Speed Wind Tunnel Testing", John Wiley and Sons, New York, p.457.
24. Taylor, G. I., 1935:"Statistical Theory of Turbulence", Part I and II, Proc. Roy. Soc. A.
25. Schubauer, G. B., W. G. Spangenberg, and P. S. Klebanoff, 1950 "Aerodynamic Characteristics of Damping Screen", TN2001, NACA.
26. Drydon, H.L. and I.H. Abbott, 1950: "The Design of Low-Turbulence Wind Tunnel", NACA, Report, 940.
27. Tennekes, H. and J. L. Lumley, 1972: "A First Course in Turbulence", MIT Press. p.300.
28. Bradshaw, P. and R.C. Pankhurct, 1962: "The Design of Low-Speed Wind Tunnels", NPL-ARC 24041.

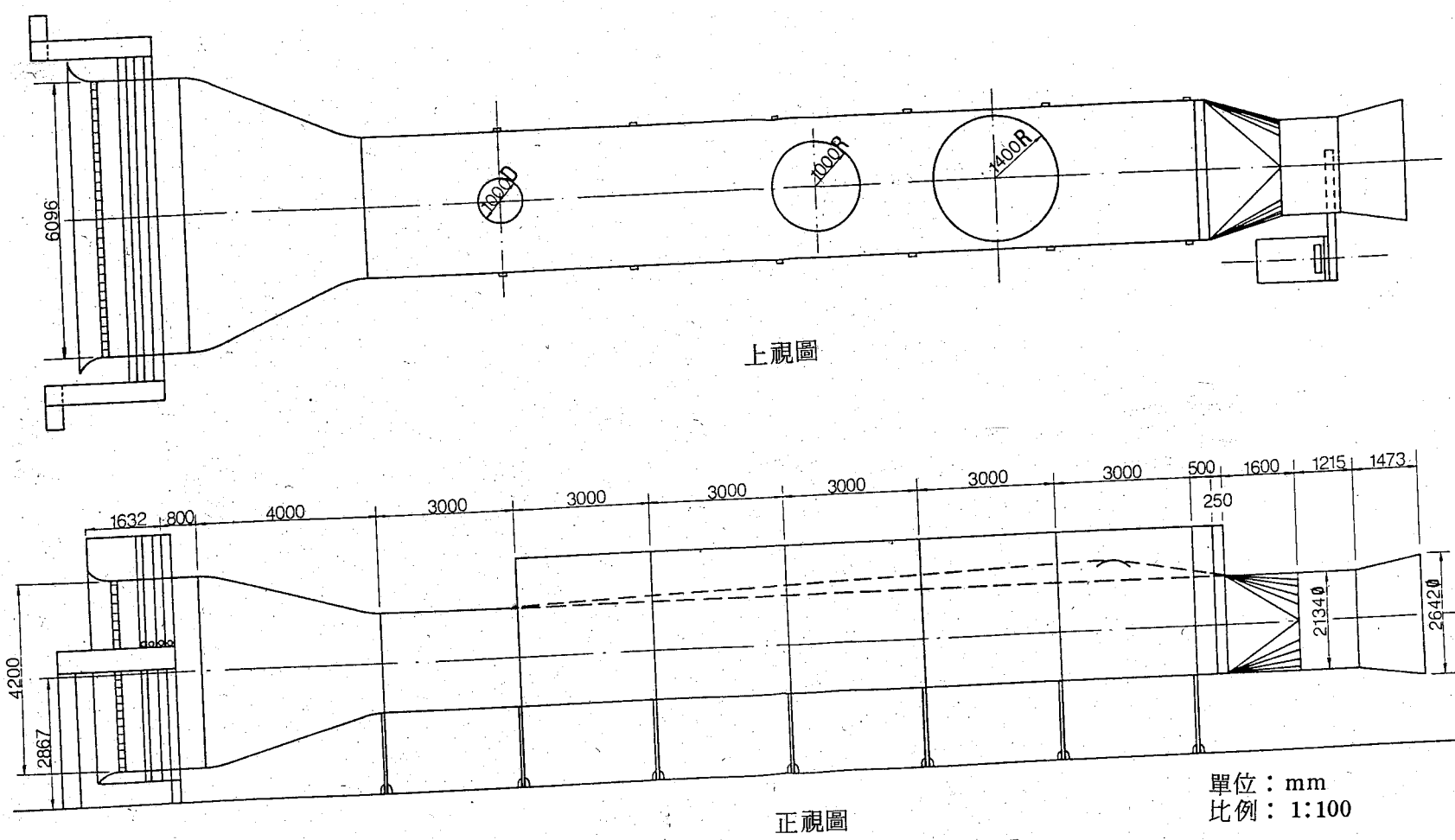

圖一、 大氣環境風洞上視圖與正視圖

No. 說明	No. 說明
1 保護網	7 試驗轉盤
2 蜂巢管	8 可調高度頂板
3 整流網	9 安全網
4 整流收縮段	10 風扇收縮管
5 收縮段	11 軸流風扇
6 試驗段	12 擴散管

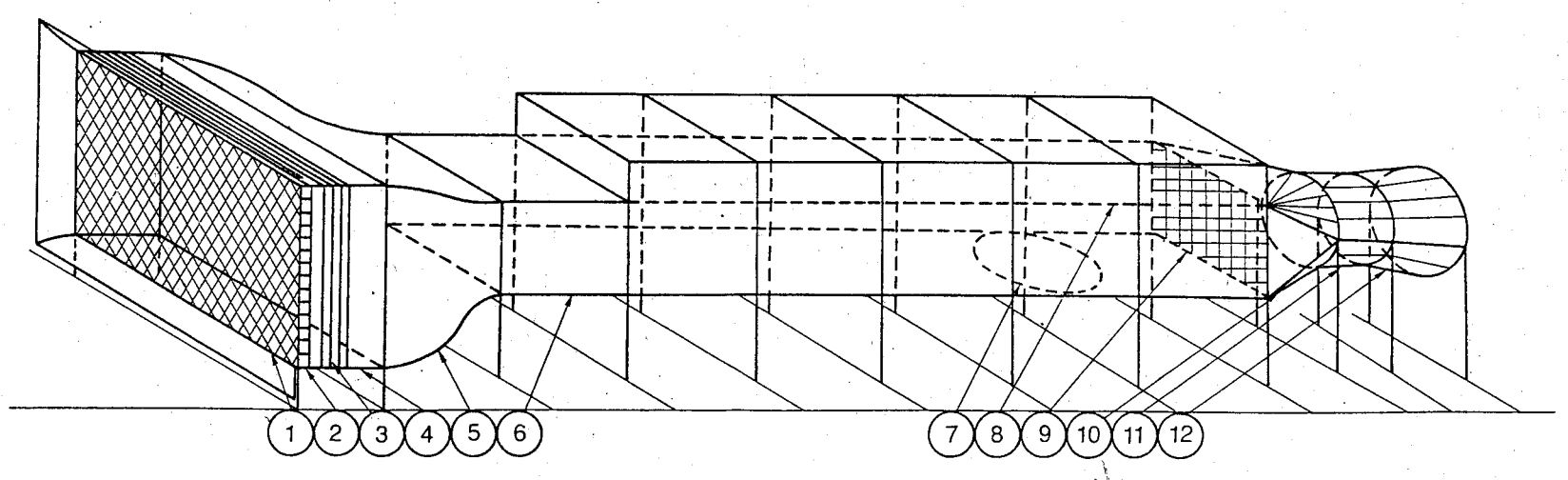

圖二、 大氣環境風洞立體圖

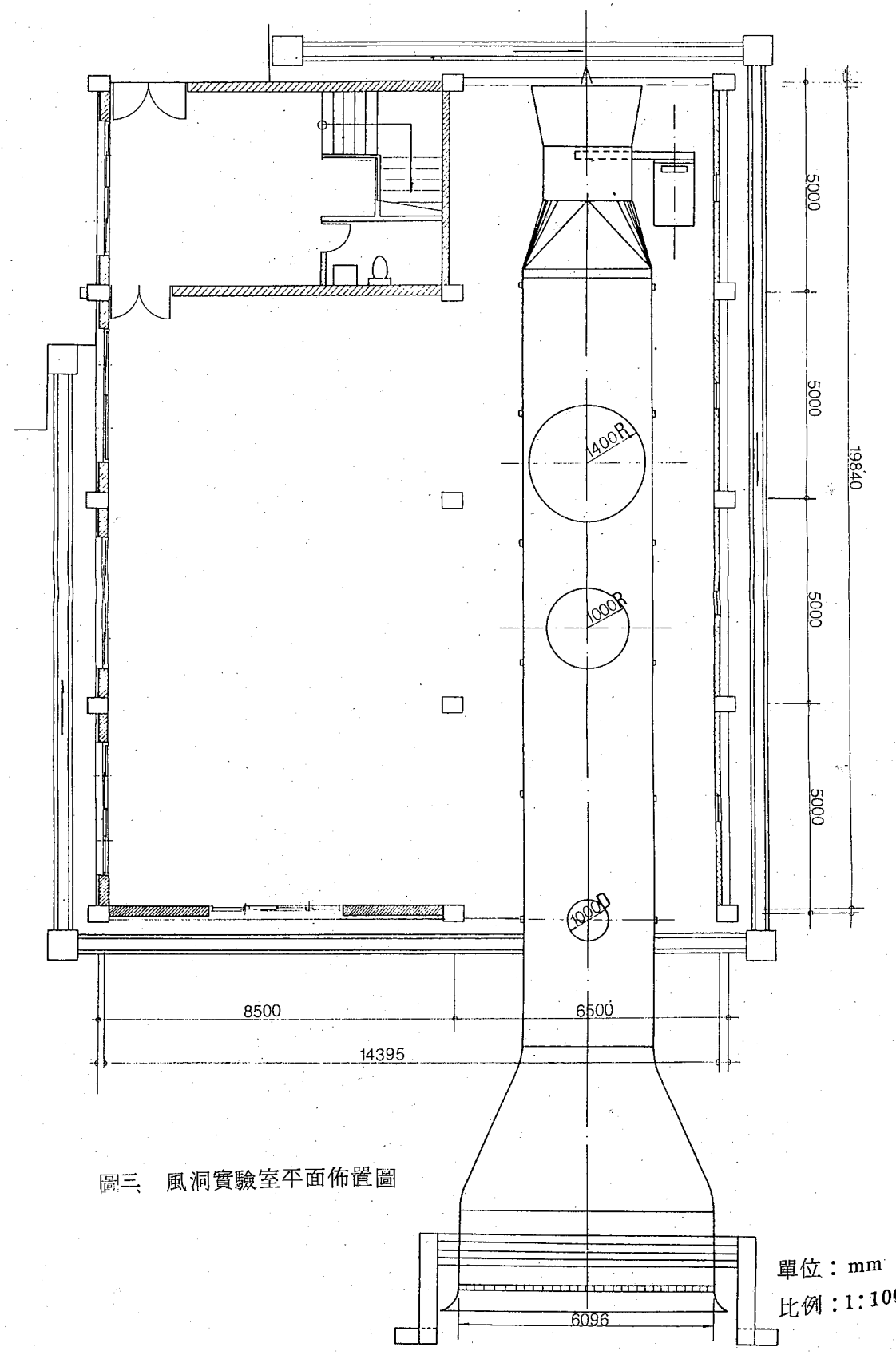

圖三、 風洞實驗室平面佈置圖

單位：mm
比例：1:100

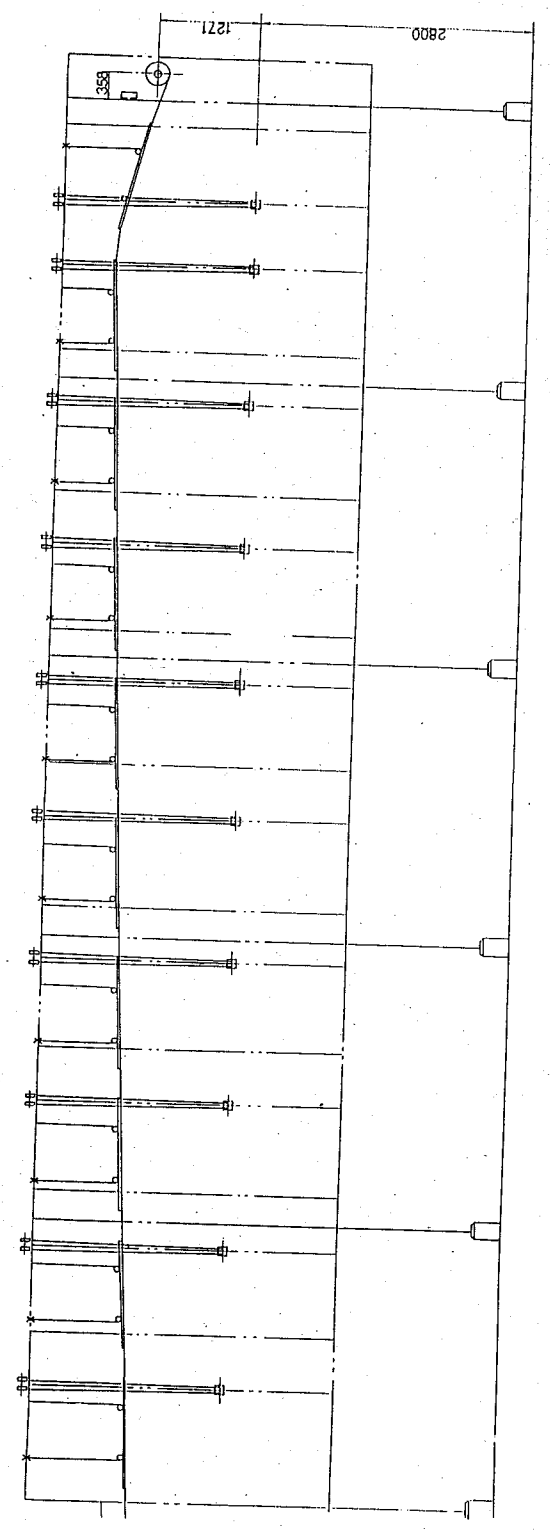

單位：mm
比例：1:45

圖四之一，風洞試驗段流軸向壓力調整裝置（側視圖）

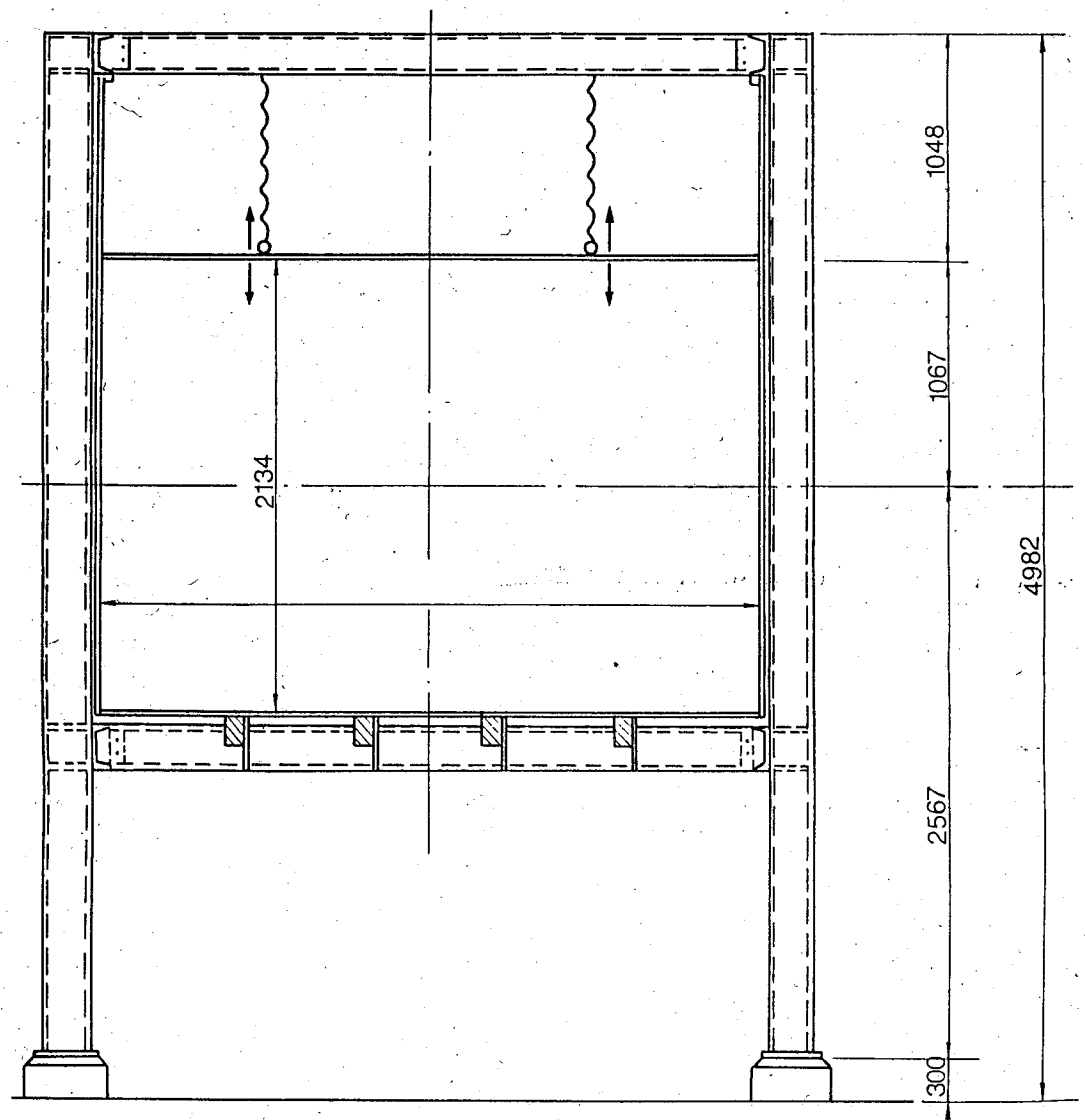

圖四之二，風洞試驗段流軸向壓力調整裝置（剖面圖）比例：1:30
單位：mm

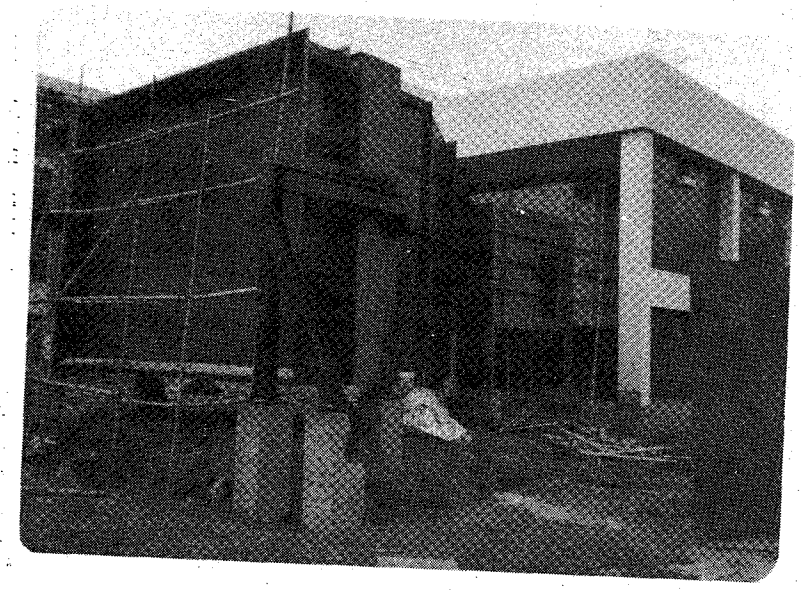

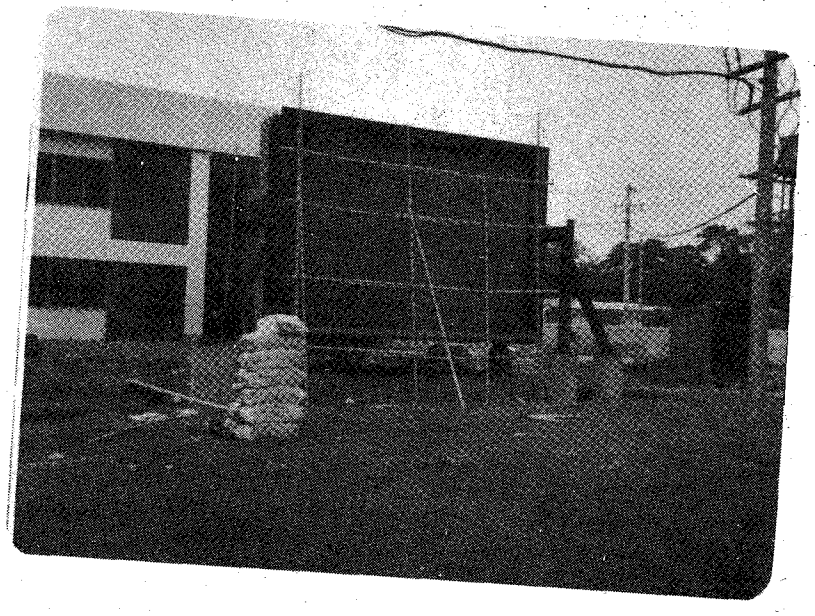

風洞進口收縮段

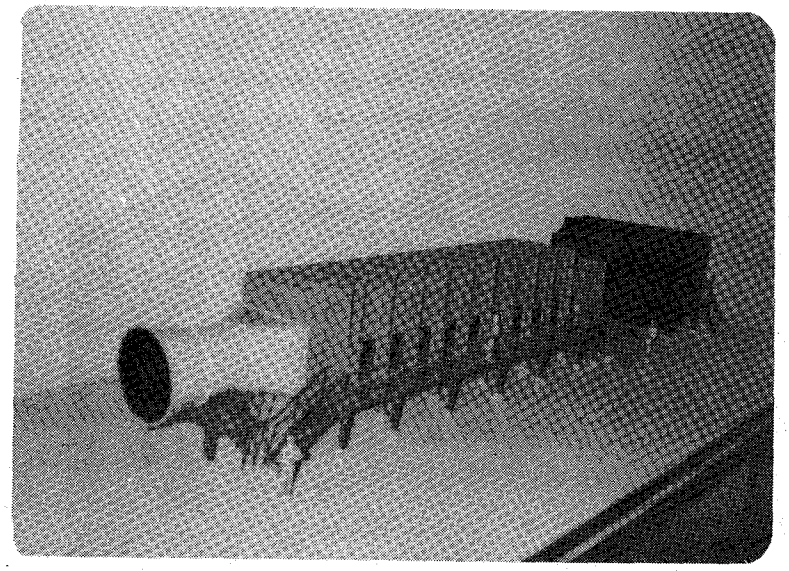

大氣環境風洞實體三十分之一模型

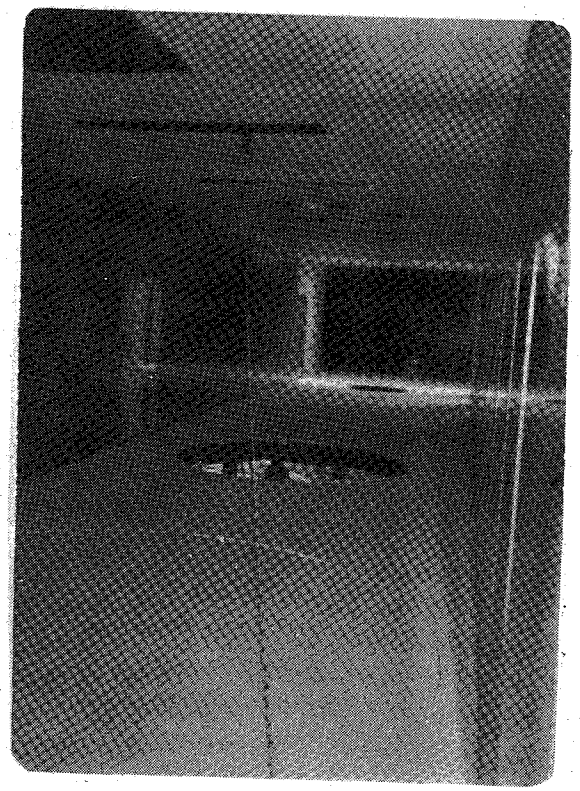

風洞試驗段內部

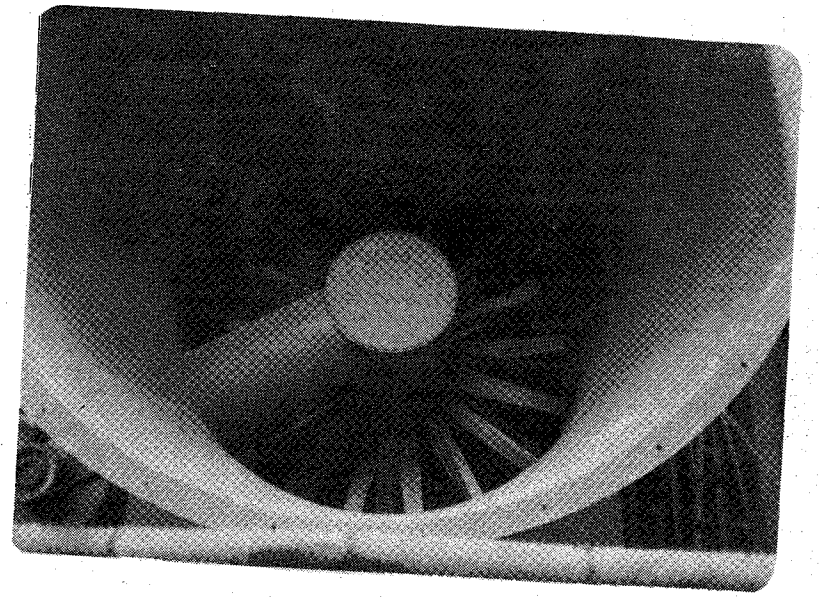

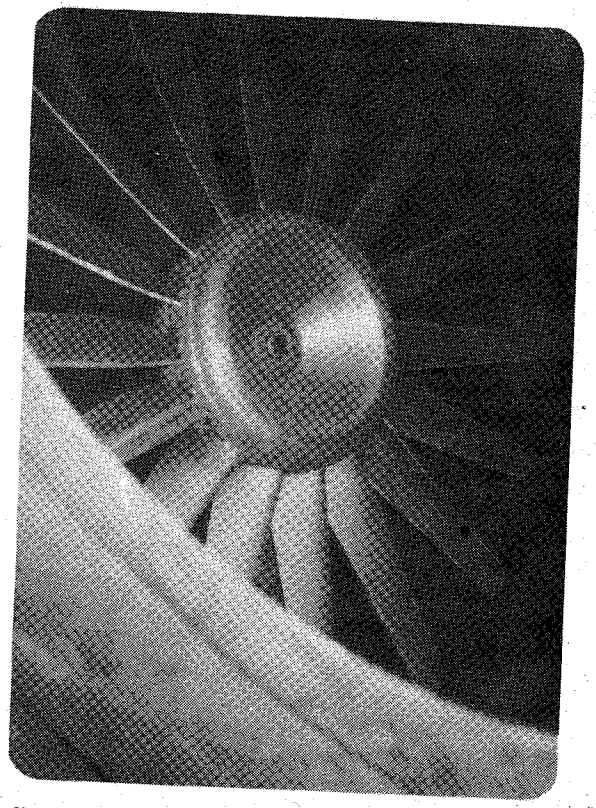

風洞動力段軸流式風扇（JOY AXIVANE FAN）

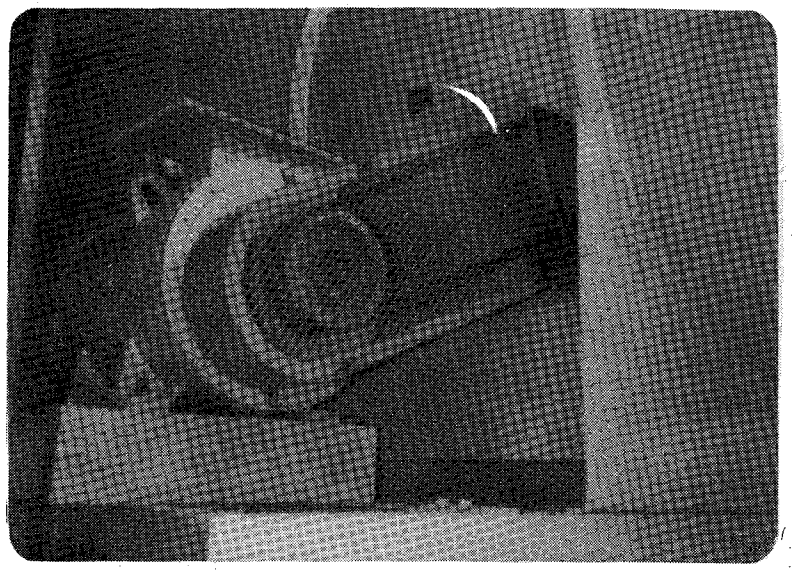

風洞動力段 200HP 直流變速馬達

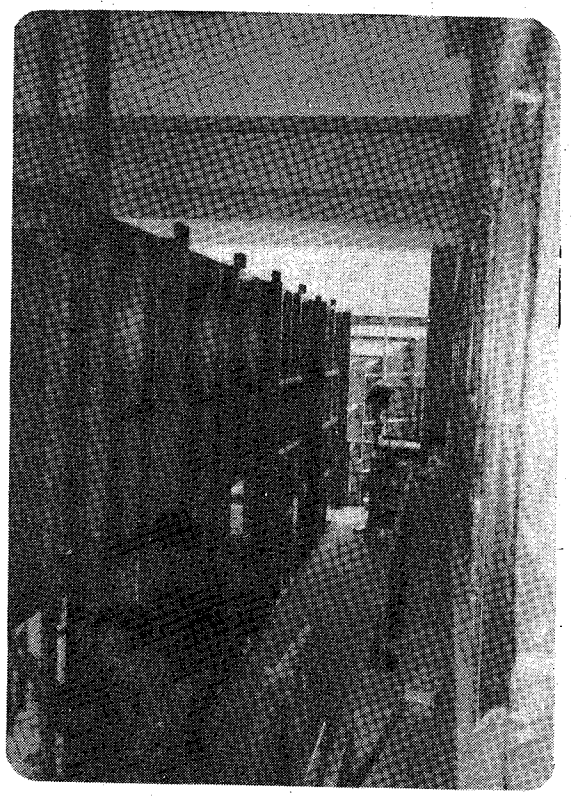

風洞施工過程

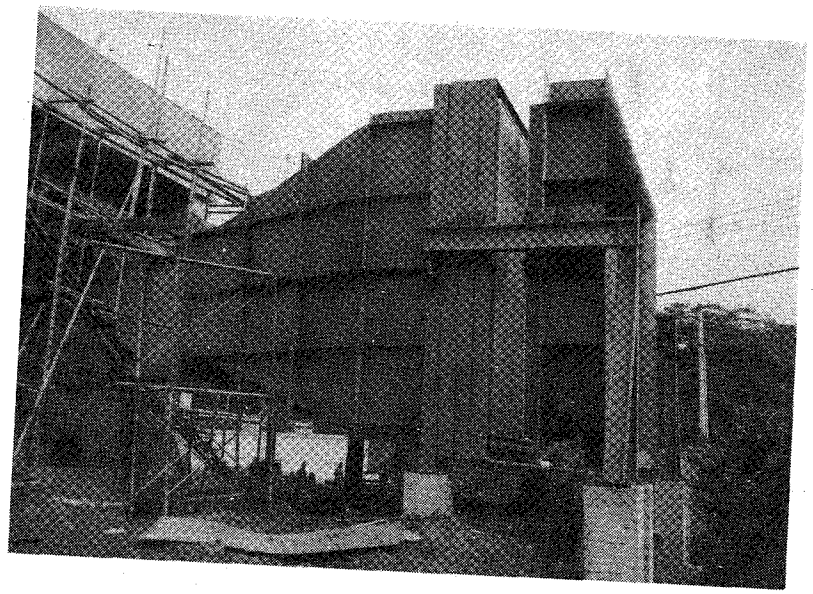

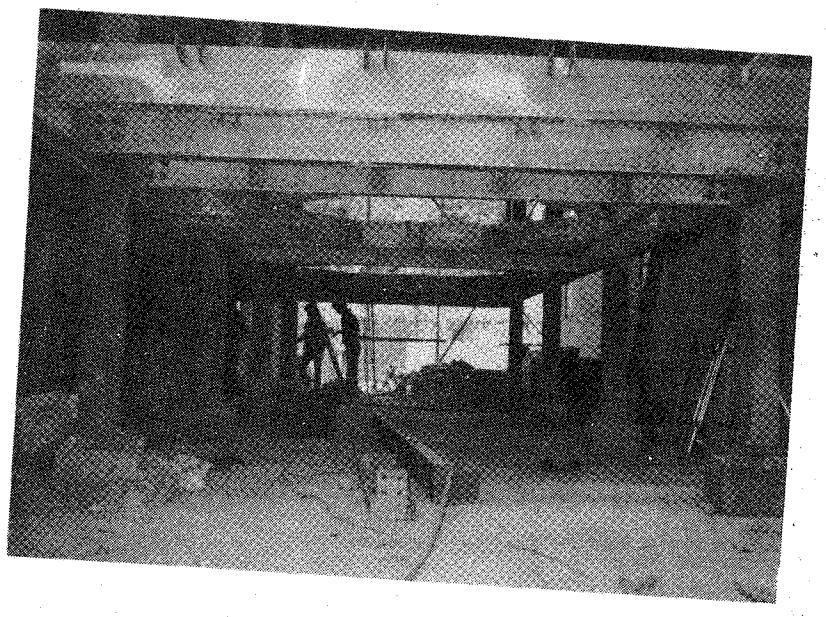

風洞施工過程

Annual Report of the Institute of Physics, Academia Sinica, Vol. 13, 1983

AN EXACT RENORMALIZATION GROUP TRANSFORMATION AND PROPERTIES OF POSITIVE SYMMETRY MATRICES

Chin-Kun Hu

Institute of Physics, Academia Sinica

Nankang, Taipei, Taiwan, R. O. C.

A positive symmetric m x m matrix P can be interpreted as the transfer matrix for an one-dimensional array of particles which have m-discrete energy levels and the most general nearest neighbor interactions. It is shown that $P' = P^2$ can be considered as exact renormalization group (RG) transformation applied on such one-dimensional system which does not have any phase transitions for $T > 0$. The exact RG transformation can be iterated to reach the high temperature fixed point. From the known asymptotic behaviour of RG transformations near the high temperature fixed point, we can derive and have a physical picture of properties of P^{2^n} as $n \to \infty$, which can also be derived directly from the matrix theory. We also show that the fixed point of the RG transformations can be obtained directly from the eigenvector corresponding to the largest eigenvalue of P. The formulation is applied to the spin-1/2 Ising model as an illustration.

Published in Chinese J. Phys. (Taipei), Vol. 21, No. 3, 4 (1983).

PERCOLATION, CLUSTERS, AND PHASE TRANSITIONS IN SPIN MODELS

Chin-Kun Hu

Institute of Physics, Academia Sinica

Nankang, Taipei, Taiwan, R. O. C.

The phase transition in the Ising model and the percolation transition in the lattice percolation model have many common characteristics, which have motivated researchers to explore whether the former is a percolation transition of a correlated percolation model. Previous attempts to draw such connection have been either unsuccessful or dissatisfactory. Considering each lattice site with an Ising spin occupied and the nearest-neighbor (NN) coupling between occupied sites as a bond with a bond probability p depending on the NN coupling constant J and the temperature T, we formally show that the partition function of the Ising model is the generating function of a bond-correlated percolation model (BCPM) with a bond probability $p = 1 - \exp(-2J/kT)$. The BCPM has the Ising critical temperature and exponents, including ν, ν', η, β, α, α' and γ (perhaps also γ'). From the connection between the Ising model and the BCPM, we also derive and hence give geometrical meaning of the finite-size scaling and broadening at first-order phase transitions of the Ising model. Our approach may easily be extended to many spin models and give geometrical meaning to other properties of spin models.

To be published in Physical Review B1, Vol. 29 (1984).

SITE-BOND-CORRELATED PERCOLATION AND A SUBLATTICE DILUTE POTTS MODEL AT FINITE TEMPERATURES

Chin-Kun Hu

Institute of Physics, Academia Sinica

Nankang, Taipei, Taiwan, R. O. C.

It is shown that the partition function of a sublattice dilute q-state Potts model (SDQPM) for even positive integer q at finite temperatures is the generating function of a site-bond-correlated percolation model (SBCPM) which favors subgraphs with larger numbers of disconnected finite clusters. The phase diagrams for the SBCPM are obtained from the corresponding phase diagrams for the SDQPM. A device is introduced to establish the connection between the SDQPM for $q \to 1$ and a site-bond (random) percolation model (SBPM). The results of this work contain those of some previous papers as special cases.

To be published in Physical Review B1, Vol.29 (1984).

CORRELATED PERCOLATION AND THE PHASE TRANSITIONS IN ISING-LIKE SPIN MODELS*

Chin-Kun Hu
Institute of Physics
Academia Sinica
Nankang, Taipei, R. O. C.

Considering each lattice site with a spin occupied and the lattice site without a spin unoccupied, we could formally show that the partition functions of many Ising-like spin models are the generating functions of correlated percolation models. Each correlated percolation model has the same critical properties as the corresponding spin model. From such connections, we could physically understand many properties of spin models. In this paper, we first formally show that the partition function of the q-state Potts model (QPM) is the generating function of a q-state bond-correlated percolation model (QBCPM) which has the same critical point and exponents as those of the QPM. From this connection, we propose a geometrical conditon of phase transitions and give geometrical reasons for the variation of the critical exponent α with q, the changeover from second-order to first-order phase transition as q increases, and the finite-size scaling and broadening at thermal and magnetic first-order phase transitions. Similar analyses for other spin models will be presented in other papers.

---

*Presented at Symposium on Condensed Matter Physics, November 25-26, 1983 at Institute of Physics, Academia Sinica, Taipei, Taiwan, R. O. C.

CORRELATED PERCOLATION AND THE PROPERTY OF MATTER*

Chinn-Kun Hu
Institute of Physics,
Academia Sinica
Nankang, Taipei, R. O. C.

Many physical systems may be represented by spin models. Using the method of the previous paper, we formally show that the partition functions of many spin models corresponding to physical systems are the generating functions of correlated percolation models. From such connections, we could physically understand many properties of matter, such as the unusual behavior of superooled water, sol-gel phase transition, etc.

---

*Presented at Symposium on Condensed Matter Physics, November 25-26, 1983 at Institute of Physics, Academia Sinica, Taipei, Taiwan, R. O. C.

Annual Report of the Institute of Physics, Academia Sinica, Vol. 13, 1983

MAGNETIC STATES OBSERVED IN HIGH-RESOLUTION (p, n) EXPERIMENTS

H. Orihara and C. D. Zafiratos

Cyclotron and Radioisotope Center,

Tohoku University, Sendai 980, Japan

S. Nishihara, K. Furukawa, M. Kabasawa and T. Nakagawa

Department of Physics, Faculty of Science,

Tohoku University, Sendai 980, Japan

K. Maeda

College of General Education, Tohoku University,

Sendai 980, Japan

K. Miura

Tohoku Institute of Technology,

Nagamachi-Koeji, Sendai 982, Japan

G. C. Kiang

Institute of Physics, Academia Sinica,

Taipei, 115, R. O. C.

H. Ohnuma

Department of Physics, Tokyo Institue of Technology,

Oh-okayama, Tokyo 152, Japan

A study of magnetic (unnatural-parity) states observed in charge-exchange (p, n) experiments is presented. The (p, n) reactions on ^{12}C, ^{14}C, ^{16}C, ^{24}Mg and ^{28}Si have been investigated at $E_p = 35$ MeV by means of time-of-flight technique. In the first half of this report, feasibility of analyses for the low-energy (p, n) data with use of the proposed realistic nucleon-nucleon interactions is discussed. In the next half analyses for angular distributions of the differential cross section for the transitions of the spin-isospin type such as from 0^+ to 0^-, 2^-, 4^- and 6^- states are presented.

---

*Proceedings of the 1983 RCNP International Symposium on Light Ion Reaction Mechanism, Osaka Japan, Research Center for Nuclear Physics, Osake University.

Annual Report of the Institute of Physics, Academia Sinica, Vol. 13, 1983

EXCITATION OF GIANT GAMOW-TELLER RESONANCES IN THE REACTION $^{140}Ce(p, n)\,^{140}Pr$

H. Orihara, G. C. Kiang

Cyclotron and Radioisotope Center,

Tohoku University, Sendai 980, Japan

S. Nishihara, T. Murakami, T. Nakagawa, K. Furukawa

Department of Physics, Faculty of Science,

Tohoku University, Sendai 980, Japan

K. Maeda

College of General Education,

Tohoku University, Sendai 980, Japan

K. Miura

Tohoku Institute of Technology,

Nagamachi-Koeji, Sendai 982, Japan

S. Adachi

Institute for Nuclear Study, University of Tokyo,

Tanashi, Tokyo 188, Japan

H. Ohnuma

Department of Physics, Tokyo Institute of Technology,

Oh-okayama, Meguro, Tokyo 152, Japan

Two broad peaks were observed at $E_x = 6.5$ and 12.1 MeV in the (p, n) reaction on ^{140}Ce at $E_p = 38$ MeV. They are interpreted as the $T = T_0 - 1$ Gamow-Teller resonances (GTR). A self-consistent TDA model with a Skymre type interaction predicts such a splitting of teh $T = T_0 - 1$ GTR, and reproduces the relative energies and strengths of the components. Experimental results are also compared with a recent RPA calculation which includes Δ—hole excitations.

---

*On leave from the Institute of Physics, Academia Sinica, Taipei, Taiwan, R. O. C.

Published in Physics Letters 118B, 283 (1982).

LOW-TEMPERATURE HEAT CAPACITIES OF SrF2 AND OTHER FLUORIDE COMPOUNDS

Lawrence T. Ho

Institute of Physics, Academia Sinica,

Taipei, Taiwan, R. O. C.

D. P. Dandekar

U. S. Army Materials and Mechanics Research Center,

Watertown, Massachusetts 02172

James C. Ho

Physics Department, Wichita State University,

Wichita, Kansas 67208

Heat-capacity measurements between 2 and 22 K have been made on SrF_2, yielding a limiting value of Debye temperature $\theta_D(0) = 385$ K. A brief review is then given, for various fluoride compounds XF_2 (X = Ba, Ca, Cd, Mn, Pb and Sr), on the general agreement between their $\theta_D(0)$ values as determined from calorimetric measurements and those from elastic-constant measurements, as well as on the general trend of deviations of their lattice heat capacity from a simple Debye behavior.

Published in Phys. Rev. B27, 3881, (1983).

EXCITATION SPECTRA OF GROUP II IMPURITIES IN Ge: Ge(Mg^o), Ge(Be^o) and Ge(Be^-)

L. T. Ho

Academia Sinica, Taipei, R. O. C.

J. W. Cross and A. K. Ramdas

Purdue University, Indiana, U. S. A.

R. Sauer

University of Stuttgart, Stuttgart, Germany

E. E. Haller

University of California, Berkeley, U. S.A.

Magnesium diffused into germanium behaves as an acceptor. The high resolution far infrared absorption spectrum of Ge(Mg^o) reveals a Lyman spectrum characteristic of a neutral double acceptor[2] with the G, D, C, B, A″, A′, and A lines at 31.22, 32.97, 33.72, 34.34, 34.69, 34.88, and 35.15 meV respectively, in turn yielding an ionization energy of 35.85 meV. The excitation spectrum of Ge(Be^o) examined under the high resolution shows that all the excitation lines have additional structure. We ascribe this to the $\{\Gamma_8 \times \Gamma_8\} = \Gamma_1 + \Gamma_3 + \Gamma_5$ ground state structure of a double acceptor. Excitation lines with spacing four times that of Ge(Be^o) have been observed in samples with compensating donors; we ascribe them to Ge(Be^-). When this compensation is large, broadenings and asymmetries characteristic of the Stark effect due to charged centers are observed.

Published in Bulletin of the American Physical Society Vol. 28, 339 (1983).

THE BEHAVIOR OF MAGNESIUM IMPURITIES IN GERMANIUM

L. T. Ho.

Institute of Physics Academia Sinica

Nankang, Taipei, Taiwan, R. O. C.

A solid solubility of the order of 10^{16} atoms/cm^3 has been found for magnesium impurities in germanium by the diffusion technique. Unlike being an interstitial donor in silicon[1], electrical measurement indicates that magnesium enters germanium lattice substitutionally and behaves like an acceptor[2]. The infrared absorption spectrum of magnesium impurities in germanium shows excited states similar to those of group III and other group II acceptors. Contrary to the believe that the depth of the acceptor level within the same group increases as the row number in the periodic table increases, magnesium is found to be a deeper impurity in germanium than zinc.

---

1. L. T. Ho and A. K. Ramads, Phys. Rev. B5, 462 (1972).
2. L. T. Ho. Appl. Phys. Lett. 35, 409 (1979).

Presented at Asia Pacific Physics Conference, Singapore, June, 1983.

DEVIATIONS FROM MATTHIESSEN'S RULE IN THE NICKEL-CHROMIUM SYSTEM*

Y. D. Yao

Institute of Physics, Academia Sinica

Taipei, Taiwan, R. O. C.

S. Arajs

Department of Physics, Clarkson College of Technology

Potsdam, N. Y. U. S. A.

E. E. Anderson

The University of Alabama in Huntsville

Huntsville, Alabama, U. S. A.

The deviations from Matthiessen's rule are studied between 4 and 300 K for Ni-Cr alloys containing Cr up to 27 at %. For Ni-Cr alloys with Cr concentration smaller than about 5 at %, the deviations from Matthiessen's rule of the resistivity can be explained by a two-current model. However, this model is not valid for Ni-Cr alloys with Cr concentration larger than about 11 at %.

---

*Published in Phys. Stst. Sol. (a) 79, 327 (1983).

FERROMAGNETIC MULTIFILAMENTARY Fe AND Ni WIRES WITH HIGH COERCIVE FIELDS PRODUCED BY POWDER METALLURGY PROCESSING*

Y. D. Yao

Institute of Physics, Academia Sinica,

Taipei, Taiwan, R. O. C.

S. Foner

Francis Bitter National Magnet Laboratory,

Massachusetts Institute of Technology, Cambridge

Massachusetts, 02139, U. S. A.

Powder metallurgy processed multifilamentary Cu-Fe, Cu-Ni, and Nb-Ni ferromagnetic composite wires were fabricated with a relatively high coercive field H_c at room temperature. Compacts of Cu-36 wt. % Fe, Cu-36 wt.% Ni, and Nb-36 wt.% Ni powders were reduced in cross section to produce ferromagnetic multifilamentary materials. Nominal areal reduction ratios of 10^8 for Cu-36 wt.% Fe and 10^4 for Nb-36 wt.% Ni and Cu-36 wt.% Ni resulted in values of $H_c \sim 195$ Oe, 95 Oe, and 77 Oe, respectively. A final 300°C anneal of the Cu-36 wt.% Fe composite gave $H_c \sim 460$ Oe. The average ferromagnetic fiber diameters are estimated to be 100 - 1000 A for the Fe fibers and are about 1 μm for the Ni fibers.

---

*Published in Appl. Phys. Lett. 43, 697 (1983).

島狀銻薄膜的非晶體與晶形相變

梁　乃　崇

中央研究院物理研究所

摘　要

島狀銻薄膜的非晶形與晶形相變可用拉曼散射觀察到，銻島的表面積與其體積之比（S／V）愈大愈難結成晶體，島狀銻薄膜的平均厚度與其等效結晶活化能大約成反比，平均厚度爲 200 Å 時，其等效結晶活化能爲 0.75 eV；20 Å 時爲10eV，由實驗結果推斷，銻的表面結晶活化能應在 10 eV 以上。

RAMAN SCATTERING FROM WEDGE-SHAPE Sb FILMS ON Ag FILMS

N. T. Liang

Institute of Physics, Academia Sinica

Nankang, Taipei, R. O. c.

T. T. Chen and Shou-Yih Wang

Department of Physics, National Tsing-Hua University

Hsinchu, Taiwan, R. O. C.

The resonance Raman scattering from an Sb wedge of variable effective thickness with underlayer or overlayer Ag has been studied. On the Sb wedge there was found a boundary line below which the wedge was Sb islands while above which the wedge was continuous. The normalized Raman signal from the Sb wedge was found to become enlarged in the island region whereas to become reduced in the continuous reg ion when a Ag island film was added as underlayer or overlayer.

Published in Chinese J. Phys. (Taipei), Vol. 21, No. 3, 4, (1983).

RESONANCE RAMAN SCATTERING FROM CRYSTAL VIOLET DEPOSITED ON ROUGH Ag FILMS

Y. C. Chou

Department of Physics, National Tsing Hua University

Hsinchu, Taiwan 300, R. O. C.

N. T. Liang

Institute of Physics, Academia Sinica

Nankang, Taipei, R. O. C.

The observed thickness dependence and excitation profiles of the surface enhanced resonance Raman scattering (SERRS) from crystal violet (CV) on Ag films demonstrated the importance of surface roughness and chemical effects. A tentative argument based on the overlap between the molecular resonance and the excitable surface resonances could reasonably explain the observed excitation profiles.

To be published in Chinese J. Phys. (Taipei), Vol.21, submitted for publiscation.

LATTICE VIBRATIONS OF CRYSTALLINE TITANIUM AND TIN TETRACHLORIDES

W. S. Tse

Institute of Physics, Academia Sinica,

Taipei, Taiwan (115), R. O. C.

C. C. Chen

Department of Physics, Soochow University

Taipei, Taiwan (111), R. O. C.

H. Chang

Department of Chemistry, National Tsing Hua University,

Hsinchu, Taiwan (300), R. O. C.

N. T. Liang

Institute of Physics, Academia Sinica,

Taipei, Taiwan (115), R. O. C.

The vibrational spectra of polycrystalline samples of titanium and tin tetrachlorides at 80 K have been investigated by Raman spectroscopic techniques. In the intramolecular region, isotopic and crystalline field splittings are observed, in substantial agreement with earlier work. In the lattice region, ten of the twelve Raman-active lattice modes are observed. A simple model is suggested and used to distinguish the low-frequency lattice translational from librational modes.

To be published in Journal of Raman Spectroscopy (1984).

ON THE STABILITY, SWITCHING VOLTAGE AND TRANSIENT ON-CHARACTERISTICS OF AMORPHOUS THIN FILMS

Chun Chiang

Institute of Physics Academia Sinica,

Nankang, Taipei, Taiwan, R. O. C.

By proposing that two types of reversible configurations co-existing in the film, that the ratio of two configurations is determined by current according to the law of mass action and the electronic energy transfer, that the difference of configurations may be due to phase, bonding state, filament formation, valence alternation pair, etc., mathematical equations can be derived to explain the threshold switching, the time dependence of the threshold voltage, transient ON characteristics and the non-linearity of the conductance.

Published in Physics Letters 99A, 453 (1983).

A DYNAMIC EQUATION FOR SWITCHING IN AMORPHONS THIN FILMS

Chun Chiang
Institute of Physics Academia Sinica,
Nankang, Taipei, Taiwan, R. O. C.

Base on Chiang's previous theory of threshold switching in amorphous thin films, a dynamic switching equation is formulated for the first time; numerical calculation of this equation shows that it can predict the experimental results very well. It is also pointed out that the differentiation of delay time and switching time may be misleading theoretically and it is proposed to use instead the smooth switching time, during which no appreciable change is observed and the drastic switching time during which appreciable change is observed.

To be published in Physica Status Solidi (a) (1984).

THE EXCITATION PROPERTIES OF NERVE MEMBERANES

Chun Chiang
Institute of Physics, Academia Sinica,
Nankang, Taipei, Taiwan, R. O. C.

With the assumption of coupling between the membrane dipoles and the phonons, it is possible to explain sodium activation, sodium inactivation, potassium activation with time delay, the nerve action potential, after-potential oscillation and gating currents in a coherent way. While it is possible that some polishing and modification may be needed in the future, it seems at present that this theory is able to explain a large amount of data satisfactorily.

Published in Neural Membranes, Edited by Grace Y. Sun, Nicolas Bazan, Jan-Yen Wu, Guiseppe Porcellati, and Albert Y. Sun. (The Humana Press, 1983).

Annual Report of the Institute of Physics, Academia Sinica, Vol. 13, 1983

A STUDY OF THE PLANETARY BOUNDARY LAYER WITH HIGHER-ORDER CLOSURE MODEL

Len-Fu W. Chang

Institute of Physics, Arademia Sinica,

Nankang, Taipei, Taiwan, R. O. C.

In this study, the continuous evolution of a convective planetary boundary layer (PBL) is simulated by turbulence higher-order-closure model. The closure assumptions include the return-to-isotropy effect proposed by Rotta (1951), the universal theory about turbulence dissipation by Kolmogoroff (1941), and the down-the-gradient transport analogy relating thirdmoment quantities to second-moment quantities.

Statistics of turbulence in a convective PBL simulated by model are compared with experimental data. The detailed turbulence structure predicted by model is reasonably well.

As inferred from the simulation study, a convective PBL can be conceived as comprising three layers; the surface layer, the well-mixed layer, and the turbulent inversion layer. Below the turbulent inversion layer, ensemble mean profiles of a convective PBL reveal similarity, regardless of the baroclinic geostrophic shear. This is due to the existence of two distinct time scales associated with geostrophic forcing and convective turbulence mixing. The geostrophic shear is not effective in changing the ensemble mean profiles, because of its long-time scale process compared to convective turbuelent mixing. Finally, the turbulent inversion layer serves as the matching layer which connects the mixing layer from below to the free atmosphere above, both dynamically and thermodynamically.

To be published in Proceeding of the National Science Council of the Republic of China, Vol. 8, No. 2, (1984).

本文主要討論應用紊流高階收合模式研究對流性大氣邊界層的變化。紊流收合模式的主要假設爲紊流回復等向性效應(Rotta,1951)，紊流動能滯耗效應(Kolmogoroft, 1941)，及第三階與第二階紊流統計量間之逆梯度傳遞性效應。

從模式模擬之紊流邊界層各種總集平均量與實驗觀測數據比較相當一致。進一步的檢討模擬結果可以發現，對流性大氣邊界層可以定性上分成三層：近地層、混合層與紊流逆溫層。在紊流逆溫層以下之總集平均速度與位溫變化呈高度之相似性，而地轉風切變對該種相似性沒有影響。本文另以定性理論分析，發現地轉風切變屬於長時間(在中緯度爲 3 ～ 6 小時)之效應，而紊流對流混合作用屬於短時間之效應(數分鐘)。模式研究結果印證這種推論。在整個對流邊界層與自由大氣層接合過程中，紊流逆溫層之熱力與動力作用不可忽略。

AUTHOR INDEX

本集刊每年出版一次

非　賣　品

中　央　研　究　院

物　理　研　究　所　集　刊

第　十　三　卷

發行人：林　　爾　　康

編輯者：中央研究院物理研究所集刊編輯委員會

出版者：中央研究院物理研究所　　臺北市南港區

印刷者：萬　達　打　字　印　刷　有　限　公　司

電　話：三　九　四　〇　七　一　八

中　華　民　國　七　十　二　年　十　二　月　出　版